

NASA/CP—2001-210826



Sixth International Microgravity Combustion Workshop

Proceedings of a conference sponsored by
NASA Office of Biological and Physical Research
hosted by NASA Glenn Research Center
Cleveland, Ohio
May 22–24, 2001

National Aeronautics and
Space Administration

Glenn Research Center

May 2001

Trade names or manufacturers' names are used in this report for identification only. This usage does not constitute an official endorsement, either expressed or implied, by the National Aeronautics and Space Administration.

Available from

NASA Center for Aerospace Information
7121 Standard Drive
Hanover, MD 21076

National Technical Information Service
5285 Port Royal Road
Springfield, VA 22100

Available electronically at <http://gltrs.grc.nasa.gov/GLTRS>

PREFACE

The Sixth International Microgravity Combustion Workshop, planned at this writing for May 22–24, 2001, in Cleveland Ohio near the NASA John Glenn Research Center at Lewis Field, is to occur at a time when the combustion science community has solidly established reduced gravity as a powerful tool for fundamental advancements in our field. We will also gather at a time when the role of combustion research supporting NASA's future missions and our ongoing contributions to fundamental science are being re-examined. The contents of this workshop volume and the substantial journal literature that stands behind it should leave no doubt over the contributions of this program to fundamental science; a small logical step suggests substantial future applications of this research to technologies crucial to the economy, the intelligent use of limited energy resources, and increasingly safe space travel.

The workshop we gather to conduct is intended to be 3 days of learning, teaching, and creativity. The environment for this experience was created by the dedicated conference team from the National Center for Microgravity Research in Fluids and Combustion (NCMR) including Beatrix Norton, Sandra Jones, Sharon Guerra, Cynthia Rosenberger, William Yanis, Evan Halprin, Norman Weinberg, Melissa Rogers, and the conference coordinator, Dr. Christine Gorecki. My thanks to the Director of the NCMR, Professor Simon Ostrach, the Deputy Director, Dr. Thomas Labus, and Chief Scientist, Professor James S. T'ien for their indispensable technical and organizational contributions. I also wish to thank the Microgravity Combustion Discipline Working Group (DWG) for their technical guidance and support including Professor Robert Altenkirch, Dr. Meredith Colket, Professor Gerard Faeth, Professor Jack Howard, Professor Mitchell Smooke, Dr. Julian Tishkoff, Professor Forman Williams, DWG Chair Professor Chung K. Law and Dr. Merrill King of NASA Headquarters. Finally, the book you hold is the product of the effort and expertise of the NCMR staff and the NASA Logistics and Technical Information Division and its support service contractors.

No matter what curves in the programmatic road we may be asked to follow during the coming months and years, this research community will rise to the occasion with the energy, innovation, and foresight that has brought us to our current success. With that in mind I hope that you find the workshop useful.

Kurt Sacksteder
NASA Glenn Research Center
March 2001

TABLE OF CONTENTS

Paper No.		Page No.
1	FLUID MANAGEMENT OF AND FLAME SPREAD ACROSS LIQUID POOLS H.D. Ross, NASA Glenn Research Center; and F.J. Miller, National Center for Microgravity Research.....	1
2	THREE-DIMENSIONAL IGNITION AND FLAME PROPAGATION ABOVE LIQUID FUEL POOLS: COMPUTATIONAL ANALYSIS Jinsheng Cai, Feng Liu, and William A. Sirignano, University of California, Irvine	5
3	SOLID INFLAMMABILITY BOUNDARY AT LOW-SPEED (SIBAL) James T'ien, Case Western Reserve University; Paul Ferkul, National Center for Microgravity Research; Kurt Sacksteder, NASA Glenn Research Center; Hsin-Yi Shih, Amit Kumar, Julie Kleinhenz, and Hasan Bedir, Case Western Reserve University; Richard Pettegrew, National Center for Microgravity Research; and Nancy Piltch and David Frate, NASA Glenn Research Center	9
4	TRANSPORT AND CHEMICAL EFFECTS ON CONCURRENT AND OPPOSED-FLOW FLAME SPREAD AT MICROGRAVITY Y. Son, L.K. Honda, and P.D. Ronney, University of Southern California	13
5	EFFECT OF SLOW EXTERNAL FLOW ON FLAME SPREADING OVER SOLID MATERIAL— OPPOSED SPREADING OVER POLYETHYLENE WIRE INSULATION O. Fujita, K. Nishizawa, and K. Ito, Hokkaido University; S.L. Olson, NASA Glenn Research Center; and T. Kashiwagi, National Institute of Standards and Technology	17
6	SMOLDERING, TRANSITION AND FLAMING IN MICROGRAVITY A.C. Fernandez-Pello, A. Bar-Ilan, T.L. Lo, and D.C. Walther, University of California, Berkeley; and D.L. Urban, NASA Glenn Research Center	21
7	QUANTITATIVE STUDIES ON THE PROPAGATION AND EXTINCTION OF NEAR-LIMIT PREMIXED FLAMES UNDER NORMAL- AND MICRO-GRAVITY F.N. Egolfopoulos, Y. Dong, and G. Spedding, University of Southern California; and B. Cuenot and T. Poinso, CERFACS	25
8	CHARACTERISATION OF A LAMINAR FLAT PLATE DIFFUSION FLAME IN MICROGRAVITY USING PIV, VISIBLE AND CH EMISSIONS P. Joulain and P. Cordeiro, ENSMA—Université de Poitiers; and J.L. Torero, University of Maryland	29
9	THICKNESS EFFECTS ON FUEL FLAMMABILITY (TEOFF) Paul Ferkul and Richard Pettegrew, National Center for Microgravity Research; and John Oerther, University of Michigan	33
10	THREE-DIMENSIONAL UPWARD FLAME SPREADING IN PARTIAL-GRAVITY BUOYANT FLOWS Kurt R. Sacksteder, NASA Glenn Research Center; and Ioan I. Feier, Hsin-Yi Shih, and James S. T'ien, Case Western Reserve University	37
11	LASER VELOCIMETER FOR STUDIES OF MICROGRAVITY COMBUSTION FLOWFIELDS P.L. Varghese and J. Jagodzinski, University of Texas at Austin	41

12	PIV MEASUREMENTS IN WEAKLY BUOYANT GAS JET FLAMES Peter B. Sunderland, National Center for Microgravity Research; Paul S. Greenberg, David L. Urban, and Mark P. Wernet, NASA Glenn Research Center; and William Yanis, National Center for Microgravity Research	45
13	THE "ADVANCED DISK LASER" (ADL): INSTRUMENTATION FOR LASER DIAGNOSTICS IN MICROGRAVITY COMBUSTION RESEARCH D. Grebner, D. Müller, and W. Triebel, IPHT; J. König, ZARM; and I. Johannsen and A. Giesen, IFSW	49
14	THE POTENTIAL APPLYING THE "ADVANCED DISC LASER" (ADL) IN MICROGRAVITY- COMBUSTION FOR OH-LIF DIAGNOSTICS USING THE (A-X; 2,0)-ELECTRONIC EXCITATION SCHEME J. König, ZARM; D. Grebner and W. Triebel, IPHT; and I. Johannsen and A. Giesen, IFSW	53
15	HYPERSPECTRAL IMAGING OF FLAMES USING A SPECTRALLY SCANNING FABRY-PEROT FILTER W.T. Rawlins, W.G. Lawrence, W.J. Marinelli, and M.G. Allen, Physical Sciences Inc.	57
16	QUANTITATIVE SPECIES MEASUREMENTS IN MICROGRAVITY COMBUSTION FLAMES Joel A. Silver and William R. Wood, Southwest Sciences, Inc.; Shin-Juh Chen and Werner J.A. Dahm, University of Michigan; and Nancy D. Piltch, NASA Glenn Research Center	61
17	TURBULENT FLAME PROCESSES VIA DIFFUSION FLAME-VORTEX RING INTERACTIONS Werner J.A. Dahm and Shin-Juh Chen, University of Michigan; Joel A. Silver, Southwest Sciences, Inc.; and Nancy D. Piltch and Randall L. Vander Wal, NASA Glenn Research Center	65
18	QUANTITATIVE MICROGRAVITY CHEMILUMINESCENCE DIAGNOSTICS: RATE CONSTANTS FROM LOW PRESSURE METHANE FLAMES Gregory P. Smith, SRI International; Jorge Luque, LAM Research Corp.; Jay B. Jeffries, Stanford University; and David R. Crosley, SRI International	69
19	QUANTITATIVE DETECTION OF COMBUSTION SPECIES USING ULTRA-VIOLET DIODE LASERS J.S. Pilgrim and K.A. Peterson, Southwest Sciences, Inc.	73
20	DEVELOPMENT OF AN EARLY WARNING FIRE DETECTION SYSTEM USING CORRELATION SPECTROSCOPY K. Goswami, G. Voevodkin, V. Rubstov, and R. Lieberman, Intelligent Optical Systems; and N. Piltch, NASA Glenn Research Center	77
21	MULTIDIMENSIONAL EFFECTS ON IGNITION, TRANSITION, AND FLAME SPREAD IN MICROGRAVITY T. Kashiwagi, National Institute of Standards and Technology; W.E. Mell, University of Utah; Y. Nakamura, National Institute of Standards and Technology; S.L. Olson, NASA Glenn Research Center; and H.R. Baum and K.B. McGrattan, National Institute of Standards and Technology	81
22	THEORETICAL PREDICTION OF MICROGRAVITY IGNITION DELAY OF POLYMERIC FUELS IN LOW VELOCITY FLOWS A.C. Fernandez-Pello, University of California, Berkeley; J.L. Torero, University of Maryland; Y.Y. Zhou and D. Walther, University of California, Berkeley; and H.D. Ross, NASA Glenn Research Center	85

23	FLAMMABILITY OF POLYMERS IN MICROGRAVITY A. Tewarson, S. Nam, and M. Whitbeck, Factory Mutual Research Corporation	89
24	LOW STRETCH PMMA BURNING IN MICROGRAVITY: STATUS OF THE GROUND-BASED PROGRAM AND NEW ISS GLOVEBOX EXPERIMENT SALSA S.L. Olson, NASA Glenn Research Center; J.S. T'ien and J.B. Armstrong, Case Western Reserve University	93
25	PATTERN FORMATION IN DIFFUSION FLAMES EMBEDDED IN VON KARMAN SWIRLING FLOWS Vedha Nayagam, National Center for Microgravity Research; and Forman A. Williams, University of California, San Diego	97
26	SUPPRESSION OF LOW STRAIN RATE NONPREMIXED FLAMES BY AN AGENT A. Hamins and M. Bundy, National Institute of Standards and Technology; I.K. Puri, University of Illinois at Chicago; K. McGrattan, National Institute of Standards and Technology; and W.C. Park, Pukyong National University	101
27	THE WATER-MIST FIRE SUPPRESSION EXPERIMENT: PROJECT OBJECTIVES AND HARDWARE DEVELOPMENT FOR THE STS-107 MISSION J.T. McKinnon, A. Abbud-Madrid, E.P. Riedel, S. Gökoğlu, W. Yang, and R.J. Kee, Colorado School of Mines	105
28	DETAILED STUDIES ON FLAME EXTINCTION BY INERT PARTICLES IN NORMAL- AND MICRO-GRAVITY M.G. Andac, F.N. Egolfopoulos, and C.S. Campbell, University of Southern California	109
29	UNSTEADY SPHERICAL DIFFUSION FLAMES IN MICROGRAVITY Arvind Atreya, S. Berhan, and M. Chernovsky, University of Michigan; and Kurt R. Sacksteder, NASA Glenn Research Center	113
30	REACTION KERNEL STRUCTURE OF A SLOT JET DIFFUSION FLAME IN MICROGRAVITY F. Takahashi, National Center for Microgravity Research; and V.R. Katta, Innovative Scientific Solutions, Inc.	117
31	FIELD EFFECTS OF BUOYANCY ON LEAN PREMIXED TURBULENT FLAMES R.K. Cheng and R. Dimalanta, Lawrence Berkeley National Laboratory; and M.P. Wernet and P.S. Greenberg, NASA Glenn Research Center	121
32	FLAME-VORTEX INTERACTIONS IMAGED IN MICROGRAVITY—TO ASSESS THE THEORY OF FLAME STRETCH James F. Driscoll, University of Michigan	125
33	CHARACTERISTICS OF NON-PREMIXED TURBULENT FLAMES IN MICROGRAVITY U. Hegde and Z.G. Yuan, National Center for Microgravity Research; D.P. Stocker, NASA Glenn Research Center; and M.Y. Bahadori, Science and Technology Development Corp.	129
34	LARGE-SCALE FLOW STRUCTURE IN TURBULENT NONPREMIXED FLAMES UNDER NORMAL- AND LOW-GRAVITY CONDITIONS N.T. Clemens, C.A. Idicheria, and I.G. Boxx, University of Texas at Austin	133

35	THE IMPACT OF BUOYANCY AND FLAME STRUCTURE ON SOOT IN A TURBULENT DIFFUSION FLAME W. Kollmann, University of California, Davis; R.L. Vander Wal, National Center for Microgravity Research; and I.M. Kennedy, University of California, Davis	137
36	AN INVESTIGATION OF FULLY-MODULATED, TURBULENT DIFFUSION FLAMES IN REDUCED GRAVITY J.C. Hermanson, H. Johari, J.E. Usowicz, and R. Sangras, Worcester Polytechnic Institute; D.P. Stocker and U.G. Hegde, NASA Glenn Research Center; T. Nagashima, University of Tokyo; and S. Obata, National Defense Academy	141
37	LARGE EDDY SIMULATION OF GRAVITATIONAL EFFECTS ON TRANSITIONAL AND TURBULENT GAS-JET DIFFUSION FLAMES Peyman Givi, University at Buffalo, SUNY; and Farhad A. Jaber, Michigan State University	145
38	VORTEX/FLAME INTERACTIONS IN MICROGRAVITY PULSED JET DIFFUSION FLAMES M.Y. Bahadori, Science and Technology Development Corp.; U. Hegde, National Center for Microgravity Research; and D.P. Stocker, NASA Glenn Research Center	149
39	EFFECTS OF FLAME STRUCTURE AND HYDRODYNAMICS ON SOOT PARTICLE INCEPTION AND FLAME EXTINCTION IN DIFFUSION FLAMES R.L. Axelbaum and R. Chen, Washington University; P.B. Sunderland, National Center for Microgravity Research; D.L. Urban, NASA Glenn Research Center; and S. Liu and B.H. Chao, University of Hawaii	153
40	STRUCTURE AND STABILITY OF MICRO-BUOYANT SPHERICAL DIFFUSION FLAMES C.K. Law, W.S. Yoo, and E.W. Christiansen, Princeton University; and S.D. Tse, Rutgers, The State University of New Jersey	157
41	THE ONSET OF OSCILLATIONS IN NON-PREMIXED COMBUSTION Moshe Matalon, Northwestern University	161
42	NUMERICAL SIMULATION OF AN ENCLOSED LAMINAR JET DIFFUSION FLAME IN MICROGRAVITY ENVIRONMENT: COMPARISON WITH ELF DATA Kezhong Jia, Rajasekhar Venuturumilli, Brandon J. Ryan, and Lea-Der Chen, University of Iowa	165
43	STRUCTURE AND EARLY SOOT OXIDATION PROPERTIES OF LAMINAR DIFFUSION FLAMES A.M. El-Leathy, F. Xu, and G.M. Faeth, University of Michigan	169
44	SUPPRESSION OF SOOT FORMATION AND SHAPES OF LAMINAR JET DIFFUSION FLAMES F. Xu, Z. Dai, and G.M. Faeth, University of Michigan	173
45	COSMIC: CARBON MONOXIDE AND SOOT IN MICROGRAVITY INVERSE COMBUSTION L.G. Blevins, Sandia National Laboratories; M.G. Fernandez, G.W. Mulholland, R.W. Davis, E.F. Moore, E.B. Steel, and J.H.J. Scott, National Institute of Standards and Technology	177
46	ELECTRICAL ASPECTS OF MICROGRAVITY COMBUSTION Derek Dunn-Rankin, University of California, Irvine; and Felix J. Weinberg, Imperial College	181
47	COUNTER-FLOW DIFFUSION FLAMES OF AMMONIUM PERCHLORATE WITH GASEOUS FUELS M.D. Smooke, Yale University; R.A. Yetter, Pennsylvania State University; T.P. Parr and D.M. Hanson-Parr, Naval Air Warfare Center	185

48	STATUS REPORT ON MARS ISRU CO/O ₂ HYBRID ENGINE DEVELOPMENT AND TESTING E.E. Rice, M.J. Chiaverini, M.M. Malecki, C.P. St. Clair, W.H. Knuth, R.J. Gustafson, and D.J. Gramer, Orbital Technologies Corporation	189
49	COMBUSTION OF INTERACTING DROPLET ARRAYS IN A MICROGRAVITY ENVIRONMENT D.L. Dietrich, NASA Glenn Research Center; P.M. Struk, National Center for Microgravity Research; and M. Ikegami, H. Nagaishi, S. Honma, and K. Ikeda, Hokkaido National Industrial Research Institute	193
50	HIGH-PRESSURE COMBUSTION OF BINARY FUEL SPRAYS F.A. Williams, University of California, San Diego; and Daniel L. Dietrich, NASA Glenn Research Center	197
51	MICROGRAVITY EXPERIMENT ON FLAME SPREAD OF A BLENDED-FUEL DROPLET ARRAY AT SUPERCRITICAL PRESSURE Takeshi Iwahashi, Toyota Motor Corp.; and Hideaki Kobayashi and Takashi Niioka, Tohoku University	201
52	AUTO-IGNITION AND FLAME SHAPES OF GEOMETRICALLY WELL-CONTROLLED GROUP OF FUEL DROPLETS IN HIGH TEMPERATURE GASEOUS ENVIRONMENT UNDER MICRO-GRAVITY Hiroshi Enomoto, Hitoshi Nagata, Daisuke Segawa, and Toshikazu Kadota, Osaka Prefecture University	205
53	FROM A SINGLE DROP TO 2-D AND 3-D ARRAYS: ACOUSTO-ELECTRIC MANIPULATION OF DROPS AND PARTICLES Robert E. Apfel and Yibing Zheng, Yale University	209
54	HETEROGENEOUS COMBUSTION OF POROUS GRAPHITE PARTICLES IN NORMAL AND MICROGRAVITY Harsha K. Chelliah, University of Virginia; Fletcher J. Miller, National Center for Microgravity Research; and Andrew J. Delisle, University of Virginia	213
55	REACTION MECHANISMS AND PARTICLE INTERACTION IN BURNING TWO-PHASE SYSTEMS Edward L. Dreizin, Yuriy L. Shoshin, and Ruslan S. Murdy, New Jersey Institute of Technology; and Vern K. Hoffman, AeroChem Research Laboratory, Titan Corp.	217
56	BURNING VELOCITY MEASUREMENTS IN ALUMINUM-AIR SUSPENSIONS USING BUNSEN-TYPE DUST FLAMES John Lee, Samuel Goroshin, and Massimiliano Kolbe, McGill University	221
57	COMBUSTION OF MAGNESIUM PARTICLES IN CARBON DIOXIDE UNDER MICROGRAVITY CONDITIONS B. Legrand and C. Chauveau, Centre National de la Recherche Scientifique; E. Shafirovich and U. Goldshleger, Russian Academy of Sciences; E. Carrea, University of Genoa; C. Mounaim-Rousselle, Université d'Orléans; and J.P. Rouan and I. Gökalp, Centre National de la Recherche Scientifique	225
58	EXPERIMENTS ON DROPLET COMBUSTION IN SPACELAB AND SPACE STATION: PLANNING, DATA ANALYSIS AND THEORETICAL INTERPRETATIONS OF RESULTS F.A. Williams, University of California, San Diego	229
59	SOME RECENT OBSERVATIONS ON THE BURNING OF ISOLATED N-HEPTANE AND ALCOHOL DROPLETS F.L. Dryer, A. Kazakov, and B.D. Urban, Princeton University	233

60	DROPLET COMBUSTION IN A SLOW CONVECTIVE FLOW V. Nayagam, National Center for Microgravity Research; M.C. Hicks, NASA Glenn Research Center; N. Kaib, National Center for Microgravity Research; M. Ackerman, University of California, San Diego; J.B. Haggard, Jr., NASA Glenn Research Center; and F.A. Williams, University of California, San Diego	237
61	CONTROL OF DROPLET COMBUSTION VIA ACOUSTICAL EXCITATION O.I. Smith, A.R. Karagozian, C. Ghenai, R. Lobbia, and S. Datterajan, University of California, Los Angeles	241
62	EXPERIMENTS AND MODEL DEVELOPMENT FOR THE INVESTIGATION OF SOOTING AND RADIATION EFFECTS IN MICROGRAVITY DROPLET COMBUSTION Mun Young Choi and Ahmet Yozgatligil, Drexel University; Frederick L. Dryer and Andrei Kazakov, Princeton University; and Ritsu Dobashi, University of Tokyo	245
63	COMBUSTION OF SOOTING MIXTURE DROPLETS AT LOW GRAVITY C.T. Avedisian and J.H. Bae, Cornell University	249
64	BI-COMPONENT DROPLET COMBUSTION IN REDUCED GRAVITY B.D. Shaw, University of California, Davis	253
65	COMBUSTION OF HAN-BASED MONOPROPELLANT DROPLETS IN REDUCED GRAVITY B.D. Shaw, University of California, Davis	257
66	COMBUSTION STAGES OF A SINGLE HEAVY OIL DROPLET IN MICROGRAVITY M. Ikegami, G. Xu, K. Ikeda, S. Honma, and H. Nagaishi, National Institute of Advanced Industrial Science and Technology; D.L. Dietrich and P.M. Struk, NASA Glenn Research Center; and Y. Takeshita, Japan Space Utilization Promotion Center	261
67	COMBUSTION OF INDIVIDUAL BUBBLES AND SUBMERGED GAS JETS Daniel E. Rosner, Manuel Arias-Zugasti, and Barbara La Mantia, Yale University	265
68	COMBUSTION OF METALS IN CARBON DIOXIDE AND REDUCED-GRAVITY ENVIRONMENTS M.C. Branch, A. Abbud-Madrid, A. Modak, C.B. Dreyer, and J.W. Daily, University of Colorado at Boulder	269
69	EFFECT OF GRAVITY ON THE COMBUSTION SYNTHESIS OF ENGINEERED POROUS COMPOSITE MATERIALS John J. Moore, Franklin D. Schowengerdt, Reed Ayers, X. Zhang, and M. Castillo, Colorado School of Mines	273
70	MECHANISTIC STUDIES OF COMBUSTION AND STRUCTURE FORMATION DURING SYNTHESIS OF ADVANCED MATERIALS A. Varma, C. Lau, and A.S. Mukasyan, University of Notre Dame	277
71	FILTRATION COMBUSTION IN SMOLDERING AND SHS Bernard J. Matkowsky, Northwestern University	281
72	EFFECT OF MICROGRAVITY ON HIGH-TEMPERATURE SELF-PROPAGATING REACTIONS G. Cao, R. Orrù, E. Medda, A. Locci, and A. Cincotti, Università di Cagliari	285

73	KISS: KINETICS AND STRUCTURE OF SUPERAGGLOMERATES PRODUCED BY SILANE AND ACETYLENE G.W. Mulholland, J.C. Yang, and J.H. Scott, National Institute of Standards and Technology; and Y. Sivathanu, En'Urga, Inc.	289
74	FORMATION OF CARBON NANOTUBES IN A MICROGRAVITY ENVIRONMENT J.M. Alford and G.R. Mason, TDA Research, Inc.; and D.A. Feikema, NASA Glenn Research Center ..	293
75	GAS-PHASE COMBUSTION SYNTHESIS OF NONOXIDE NANOPARTICLES IN MICROGRAVITY R.L. Axelbaum, B.M. Kumfer, and Z. Sun, Washington University; and B.H. Chao, University of Hawaii	297
76	FLAME SYNTHESIS OF SINGLE- AND MULTI-WALLED CARBON NANOTUBES AND NANOFIBERS R.L. Vander Wal, National Center for Microgravity Research; and Thomas M. Tcich, Centenary College of Louisiana	301
77	OUTWARDLY PROPAGATING FLAMES AT ELEVATED PRESSURES C.K. Law and G. Rozenchan, Princeton University; S.D. Tse, Rutgers, The State University of New Jersey; and D.L. Zhu, Princeton University	305
78	STUDIES OF PREMIXED LAMINAR AND TURBULENT FLAMES AT MICROGRAVITY M. Abid, K. Aung, C. Kaiser, J.-B. Liu, P.D. Ronney, and J. Sharif, University of Southern California ...	309
79	THE COOL FLAMES EXPERIMENT Howard Pearlman, University of Southern California; Richard Chapek, Donna Neville, and William Sheredy, NASA Glenn Research Center; Ming-Shin Wu, National Center for Microgravity Research; and Robert Tornabene, ZIN Technologies	313
80	THE BEHAVIOR OF METHANE-AIR PARTIALLY PREMIXED FLAMES UNDER NORMAL- AND ZERO-G CONDITIONS Ishwar K. Puri, Suresh K. Aggarwal, and Chun Wai Choi, University of Illinois at Chicago; and Uday Hegde, National Center for Microgravity Research	317
81	GRAVITATIONAL INFLUENCES ON FLAME PROPAGATION THROUGH NON-UNIFORM, PREMIXED GAS SYSTEMS Fletcher J. Miller and John Easton, National Center for Microgravity Research; Howard D. Ross, NASA Glenn Research Center; Anthony Marchese, Rowan University; and David Perry and Michael Kulis, University of Akron	321
82	STRUCTURE AND SOOT FORMATION PROPERTIES OF LAMINAR FLAMES A.M. El-Leathy, F. Xu, and G.M. Faeth, University of Michigan	325
83	CANDLE FLAMES IN MICROGRAVITY D.L. Dietrich and H.D. Ross, NASA Glenn Research Center; and P. Chang and J.S. T'ien, Case Western Reserve University	329
84	SIMULATION OF COMBUSTION SYSTEMS WITH REALISTIC g-JITTER W.E. Mell, University of Utah; K.B. McGrattan, Y. Nakamura, and H.R. Baum, National Institute of Standards and Technology	333
85	HYDRODYNAMIC STABILITY OF LIQUID-PROPELLANT COMBUSTION: LANDAU'S PROBLEM REVISITED S.B. Margolis, Sandia National Laboratories	337

86	LARGE LEWIS NO. EDGE-FLAME INSTABILITIES J. Buckmaster, University of Illinois at Urbana—Champaign	341
87	DESIGN AND FABRICATION OF A HELE-SHAW APPARATUS FOR OBSERVING INSTABILITIES OF DIFFUSION FLAMES I.S. Wichman, L. Oravec-Simpkins, and S. Olson, Michigan State University	345
88	EFFECTS OF GRAVITY ON TRIPLE FLAME PROPAGATION AND STABILITY J.-Y. Chen, University of California, Berkeley; Tarek Echekki, Sandia National Laboratories; and Uday Hegde, National Center for Microgravity Research	349
89	ESA—INSERT FOR NASA’S CIR: ENVIRONMENT FOR COMBUSTION EXPERIMENTS UNDER ELEVATED TEMPERATURE AND PRESSURE Ch. Eigenbrod, J. König, and H.J. Rath, ZARM; and E. Kufner, ESA/ESTEC	353
90	SPACE-DRUMS™—CONTAINER AND CONTAINERLESS PROCESSING ON THE ISS Ron Davidson, Jacques Guigné, and Peter Everett, Guigné Technologies Ltd.	357
91	HOLOGRAPHIC INTERFEROMETRY AND LAMINAR JET DIFFUSION FLAMES IN THE PRESENCE OF NON-UNIFORM MAGNETIC FIELDS J. Baker and M.E. Calvert, University of Alabama at Birmingham; K. Saito, University of Kentucky; and R. Vander Wal, NASA Glenn Research Center	361
92	RETRIEVAL OF TEMPERATURE AND SPECIES DISTRIBUTIONS FROM MULTISPECTRAL IMAGE DATA OF SURFACE FLAME SPREAD IN MICROGRAVITY K.D. Annen and John A. Conant, Aerodyne Research, Inc.; and Karen J. Weiland, NASA Glenn Research Center	365
93	FAN BEAM EMISSION TOMOGRAPHY FOR TRANSIENT FIRES Yudaya Sivathanu, Jongmook Lim, Vinoo Narayanan, and Rony Joseph, En’Urga, Inc.	369
94	FULL NAVIER-STOKES MODELING OF A BOUNDARY-LAYER DIFFUSION FLAME OVER A POROUS FLAT PLATE Ramagopal Ananth, Chuka C. Ndubizu, and P.A. Tatem, Navy Technology Center for Safety and Survivability; and Gopal Patnaik and K. Kailasanath, Naval Research Laboratory	373
95	COMBUSTION OF GASEOUS FUELS WITH HIGH TEMPERATURE AIR IN NORMAL- AND MICRO-GRAVITY CONDITIONS Y. Wang and A.K. Gupta, University of Maryland	377
96	AN ANALYTICAL MODEL FOR NON-UNIFORM MAGNETIC FIELD EFFECTS ON TWO-DIMENSIONAL LAMINAR JET DIFFUSION FLAMES M.E. Calvert and J. Baker, University of Alabama at Birmingham; K. Saito, University of Kentucky; and R.L. Vander Wal, NASA Glenn Research Center	381
97	TRIOXANE-AIR COUNTERFLOW DIFFUSION FLAMES IN NORMAL AND MICROGRAVITY Gregory T. Linteris, National Institute of Standards and Technology; Marc D. Rumminger, Ceryx, Inc.; and David L. Urban, NASA Glenn Research Center	385
98	COMBUSTION OF UNCONFINED DROPLET CLUSTERS IN MICROGRAVITY G.A. Ruff, NASA Glenn Research Center; and S. Liu, Drexel University	389

99	HIGH PRESSURE, TRANSPORT PROPERTIES OF FLUIDS: THEORY AND DATA FROM LEVITATED FLUID-DROPS AT COMBUSTION-RELEVANT TEMPERATURES J. Bellan, Jet Propulsion Laboratory; and K. Ohaska, University of Southern California	393
100	QUENCHING OF PARTICLE-GAS COMBUSTIBLE MIXTURES USING ELECTRIC PARTICULATE SUSPENSION (EPS) AND DISPERSION METHODS Gerald M. Colver, Iowa State University; and Samuel Goroshin and John H.S. Lee, McGill University .	397
101	"SMOKE:" CHARACTERIZATION OF SMOKE PARTICULATE FOR SPACECRAFT FIRE DETECTION D.L. Urban, NASA Glenn Research Center; G. Mulholland, National Institute of Standards and Technology; Z.G. Yuan, National Center for Microgravity Research; and J. Yang and T. Cleary, National Institute of Standards and Technology	401
102	FLAME SPREAD IN A MICROGRAVITY ENVIRONMENT—ROLE OF FUEL THICKNESS Subrata Bhattacharjee, San Diego State University; and Kazunori Wakai and Shuhei Takahashi, Gifu University	405
103	AN EARTH-BASED EQUIVALENT LOW STRETCH APPARATUS TO ASSESS MATERIAL FLAMMABILITY FOR MICROGRAVITY AND EXTRATERRESTRIAL FIRE-SAFETY APPLICATIONS S.L. Olson, NASA Glenn Research Center; and H. Beeson and J. Haas, NASA White Sands Test Facility	409
104	FIRE ACCIDENT TESTING EVALUATION (FATE) H.D. Ross, NASA Glenn Research Center; W. Mell, University of Utah; R. Pettegrew, National Center for Microgravity Research; and M. Hicks and D. Urban, NASA Glenn Research Center	413
105	PHYSICAL AND CHEMICAL ASPECTS OF FIRE SUPPRESSION IN EXTRATERRESTRIAL ENVIRONMENTS F. Takahashi, National Center for Microgravity Research; G.T. Linteris, National Institute of Standards and Technology; and V.R. Katta, Innovative Scientific Solutions, Inc.	417
106	COOL FLAME QUENCHING Howard Pearlman, University of Southern California; and Richard Chapek, NASA Glenn Research Center	421
107	SPHERICAL ETHYLENE/AIR DIFFUSION FLAMES SUBJECT TO CONCENTRIC DC ELECTRIC FIELD IN MICROGRAVITY Z.-G. Yuan and U. Hegde, National Center for Microgravity Research; and G.M. Faeth, University of Michigan	425
108	PARTICLE GENERATION AND EVOLUTION IN SILANE/ACETYLENE FLAMES IN MICROGRAVITY D.G. Keil, AeroChem Research Laboratory, Titan Corp.	429
109	COUPLED RADIATION AND THERMOPHORETIC EFFECTS IN SOOTING MICROGRAVITY FLAMES D.W. Mackowski, Auburn University; and V. Nayagam and P.B. Sunderland, National Center for Microgravity Research	433
110	LAMINAR FLAME SPEEDS OF SOOT-FORMING FLAMES C.J. Sung, Case Western Reserve University and the National Center for Microgravity Research; and H. Wang, University of Delaware	437

111	MICROGRAVITY PRODUCTION OF NANOPARTICLES OF NOVEL MATERIALS USING PLASMA SYNTHESIS Michael Frenklach and Carlos Fernandez-Pello, University of California, Berkeley	441
112	CARBON NANOSTRUCTURE: ITS EVOLUTION DURING AND ITS IMPACT UPON SOOT GROWTH AND OXIDATION R.L. Vander Wal, National Center for Microgravity Research	443
113	ELECTRIC FIELD EFFECTS IN SELF-PROPAGATING HIGH-TEMPERATURE COMBUSTION SYNTHESIS UNDER MICROGRAVITY CONDITIONS Z.A. Munir and B.D. Shaw, University of California, Davis	447
114	INVESTIGATION OF THE LIFTOFF AND BLOWOUT OF TRANSITIONAL AND TURBULENT JET FLAMES James J. Riley, George Kosály, and John C. Kramlich, University of Washington	451
115	UNSTEADY MULTIDIMENSIONAL NUMERICAL SIMULATIONS OF FLAME VORTEX INTERACTIONS—A NEW STUDY G. Patnaik and K. Kailasanath, Naval Research Laboratory	455
116	FLAME PROPAGATION IN LOW-INTENSITY TURBULENCE UNDER MICROGRAVITY CONDITIONS R.C. Aldredge, University of California, Davis	459
117	PIV MEASUREMENT OF TRANSIENT 3-D (LIQUID AND GAS PHASES) FLOW STRUCTURES CREATED BY A SPREADING FLAME OVER 1-PROPANOL M.I. Hassan, K. Kuwana, and K. Saito, University of Kentucky	463
AUTHOR INDEX.....		467

FLUID MANAGEMENT OF AND FLAME SPREAD ACROSS LIQUID POOLS

H. D. Ross¹ and F. J. Miller², ¹NASA Glenn Research Center; MS 500-115, 21000 Brookpark Road, Cleveland, OH 44135-3191; Howard.D.Ross@grc.nasa.gov; ²National Center for Microgravity Research; MS 110-3, 21000 Brookpark Road, Cleveland, OH 44135-3191

INTRODUCTION

The goal of our research on flame spread across pools of liquid fuel remains the quantitative identification of the mechanisms that control the rate and nature of flame spread when the initial temperature of the liquid pool is below the fuel's flash point temperature. As described in [1,2], four microgravity (μg) sounding rocket flights examined the effect of forced opposed airflow over a 2.5 cm deep x 2 cm wide x 30 cm long pool of 1-butanol. Among many unexpected findings, it was observed that the flame spread is much slower and steadier than in 1g where flame spread has a pulsating character. Our numerical model, restricted to two dimensions, had predicted faster, pulsating flame spread [3] in μg . In a test designed to achieve a more 2-D experiment, our investigation of a shallow, wide pool (2 mm deep x 78 mm wide x 30 cm long) was unsuccessful in μg , due to an unexpectedly long time required to fill the tray [4].

As such, the most recent Spread Across Liquids (SAL) sounding rocket experiment had two principal objectives: 1. determine if pulsating flame spread in deep fuel trays would occur under the conditions that a state-of-the-art computational combustion code and short-duration drop tower tests predict, and 2. determine if a long, rectangular, shallow fuel tray could achieve a visibly flat liquid surface across the whole tray without spillage in the μg time allotted. If the second objective was met, the shallow tray was to be ignited to determine the nature of flame spread in μg for this geometry. For the first time in the experiment series, two fuel trays – one deep (30 cm long x 2 cm wide x 25 mm deep) and one shallow (same length and width, but 2 mm deep)-- were flown. By doing two independent experiments in a single flight, a significant cost savings was realized. In parallel, the computational objective (work conducted at Univ. of California at Irvine by W. Sirignano and collaborators) was to modify the code to improve agreement with earlier results. This last objective was achieved by modifying the fuel mass diffusivity and adding a parameter to correct for radiative and lateral heat loss [5].

GROUND-BASED TESTING AND RESULTS

The following types of flame spread experiments were performed in 1g and in μg prior to the sounding rocket flight: (a) flame spread across shallow pools (2 mm deep, 20 mm wide, and 165 mm long) in ambient air and in enriched O₂ subject to a 30 cm/s opposed flow inside a flow duct; and (b) flame spread experiments as in (a) but with a deeper trays (10 & 25 mm) in μg at varying temperatures. As discussed later, tests were also performed to validate a new fluid filling technology.

Flame spread results: The pool width was selected based on recent work that showed that the 20 mm wide pools suppress unstable flame front shapes that appear in 80 mm wide trays [6], and on the need to fit two trays into the flow duct. The length was selected based on available test time and room in the experimental chamber. The trays were filled with 1-butanol in 1g, and then ignited after release in μg . For the 2 and 10 mm deep trays, the experimental realization of pulsating flame spread across a flammable liquid in μg was accomplished for the first time [5]. For the shallow tray at either

gravity level, the pulsation frequency increases as O_2 concentration increases, until the flame spread character becomes uniform at sufficiently high O_2 concentration (e.g. 25-26%), as shown in Fig. 1.

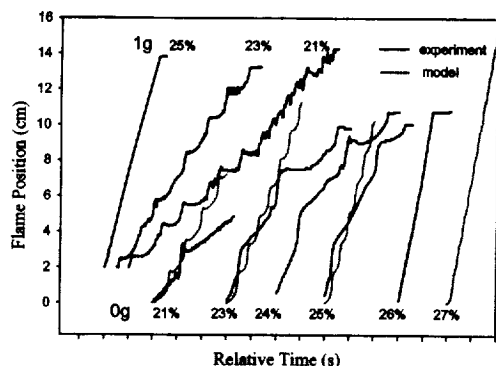


Figure 1. Flame position for a 2 mm deep tray.

This is consistent with the model (thin red lines on Fig. 1) and our earlier conclusion that gas-phase phenomena (not just liquid-phase phenomena) contribute to the onset or elimination of pulsating spread [6]. The pulsation frequency in 1g is higher than in μg , even at elevated O_2 concentration, and the transition to uniform spread occurs at slightly higher O_2 concentration in the μg experiments. Thus, while O_2 concentration and shallow pool depth can yield similar flame spread character at either gravity level, they alone cannot render the spread behavior identical in μg and 1g in the pulsating spread regime. In tests with the 10 mm deep pools, the sequential transition through all three subflash flame spread regimes -- from pseudo-uniform to pulsating to uniform spread -- was achieved in μg . As was predicted by the model, pulsating spread for the deeper 10-mm pools appears to be achievable only in a narrow band of O_2 concentrations (between 23 and 25%) in μg .

For the 25mm deep pools, a temperature-controlled tray was employed. We conducted μg experiments at fuel temperatures from 23 °C to 26 °C and O_2 concentrations from 21 to 25 %. For 21% O_2 , steady flame spread rates between 1 cm/s (23 °C) and 2 cm/s (27 °C), as shown in Fig.2, were obtained in the 3 s that the flame had spread far enough from the igniter to be reliably tracked. As the O_2 level was increased, two new phenomena were noted. At O_2 levels of 23% and 24% the flame wobbled side to side as it spread. This was not classical pulsating spread, in which the flame brightness increases markedly just before the flame (or a large part of its front) jumps, but a higher speed, side-to-side wobble. At 25% O_2 , regardless of temperature, the flame-front shape changed from convex to concave, i.e., the edges along the sides of the flame led the portion in the middle. This is the first time such a flame shape was observed in our tests (though it has been seen with solids' flame spread). A preliminary 3D version of the model, however, predicted such a shape.

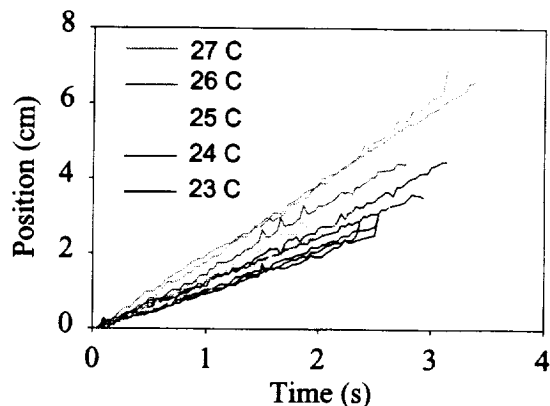


Figure 2. Flame position vs. time for a 25 mm deep tray in μg

Fluid filling re-design and testing: Each experiment on the sounding rocket required 1-butanol to be pumped from a reservoir into an open tray in μg . For the 25 mm deep tray, 1-butanol was pumped into one end of the tray and allowed to fill the tray lengthwise by inertial and capillary forces (as had been done on previous flights). The same design could not be used for the 2 mm shallow tray because the time required for fuel spreading exceeded the available microgravity time. This conclusion was reached based on both the previous sounding rocket experiment as well as additional tests that were run in a freely floated rig on the NASA low-gravity aircraft. With such a configuration, the rate at which liquid spread and wetted the shallow tray bottom was measured to be less than 1 mm/s, so that the time needed to completely

cover the 300 mm long tray, with filling from one end, was excessive. The 'free float' approach was vital to reach this conclusion, as the observed spread rate was much faster in a 'bolted down' configuration on the aircraft, owed to the latter's much higher residual acceleration and g-jitter.

A redesign was then performed for the shallow fuel tray and a manifold was utilized, from which fuel slowly issued from 10 small capillary holes (of diameter 0.33 mm) located 2 cm apart along the tray bottom. From a theoretical perspective, if the Weber¹ number of the fuel leaving each hole is too large, then the fuel stream leaving the hole will jet, i.e. it will no longer stick to the fuel tray bottom (as in Fig. 3a), but proceed in a column away from the tray (Fig. 3b). This can be avoided by filling with a sufficiently small fuel velocity leaving each hole. If, however, the velocity is too small, then not enough fuel would be pumped into the tray in the allowable (2 minutes) time in microgravity. In addition, it was necessary to choose the fill holes' diameter small enough such that the pressure drop through them was much larger than through the manifold to assure an even distribution of fuel along the tray bottom, but making the holes more prone to jetting (since V increases for small holes with the same volume flow rate). Further complicating the design was the possibility that one or more fill holes might clog with debris or bubbles, and potentially increase the Weber number of the others above the critical value. Numerous 1g tests were performed with upward and downward facing holes. This design was tested in the free-float rig, with transparent parts utilized initially to visualize the flow in the manifold and capillaries. Later tests were also performed with a metal tray bottom whose anodized surface roughness matched that planned for flight. The degree of roughness was optimized based on sessile droplet tests performed in 1g and μ g that examined the rate of spread of liquid along a flat surface.

From the 1g tests a critical Weber number of between 5 and 10 was found, with the higher numbers applying to downward facing holes. Although one might expect gravity to enhance jetting and lower the critical We for downward facing holes, in fact it tends to pull the liquid into a hanging mound that absorbs some of the jet momentum. For upward facing holes the fluid does not mound, but gravity does act to pull down on a fluid column. Thus, it was unknown how the fluid would behave in microgravity; if it wetted the surface well, it might jet more easily than in either 1g configuration. The KC-135 tests

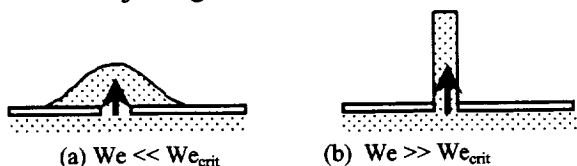


Figure 3. For low We liquid adheres to the tray bottom (a); for high We it breaks free into a jet.

were not able to answer this question directly because the pump used for filling the trays was a positive displacement pump with two pistons. Thus, the We number was not constant over the whole pump cycle. An average critical We number of 3 was found in microgravity, though the instantaneous value was higher. From all of these tests, the liquid pumping rate was optimized, such that the shallow tray could be filled completely within 42 seconds in μ g. As the aircraft test periods were less than this requirement, a complete test in μ g was performed for the first time in the sounding rocket experiment itself.

SOUNDING ROCKET TESTING

¹ Weber number is the dimensionless ratio of inertial to surface tension forces, $We = \rho V^2 D / \sigma$, with ρ the liquid density, V the mean velocity, D the hole diameter and σ the surface tension.

A sequence of operations was selected such that two or three tests could be run. After the deep tray was filled with liquid, the shallow tray was filled during the time period normally allotted to the damping of liquid motion in the deep tray. After both trays were full, the opposed airflow fan was energized, followed by two 'smoke wires' to visualize near-surface and bulk streamlines in the air flow, and then the deep tray was ignited and flame spread was observed. As in our other sounding rocket experiments, particle image velocimetry and rainbow schlieren deflectometry (RSD) were utilized to observe the liquid-phase flow and temperature fields in the central portion of the deep fuel tray. In addition, infrared (IR) thermography provided the surface temperature in the same region of the tray. After the flame spread and extinguished in the deep tray, the smoke wires were de-energized, and viewing and ignition switched to the shallow fuel tray. Diagnostics for this tray included only flame imaging, IR thermography, and strobe-light imaging to check for fuel spills during flame spread.

The sounding rocket flight took place on February 12, 2001, and so the data have not yet been analyzed in detail. An initial condition was selected as air at 1 atm and 25 C. The fluid management designs were successful as the trays filled completely and yielded a flat liquid surface. Upon sequential ignitions, each tray remarkably exhibited pulsating flame-spread behavior, which was anticipated for the shallow tray based on drop tower tests and modeling, but never before seen in previous μg experiments for the deep tray. Finally, the detailed diagnostics all performed nominally and yielded novel observations. The IR showed that twin vortices formed with the deep pool in both 1g and in μg during the crawl phase of the pulsating spread; similar vortices formed with the shallow pool in 1g, but surprisingly not in μg . Instead a long preheat region was observed in μg during the crawl phase of the pulsating flame spread in the shallow tray. The RSD showed vortices in the liquid phase of the deep tray that resembled those seen in 1g, a finding very different than that observed in earlier sounding rocket flights.

SUMMARY

The fluid management design achieved the largest-ever flat rectangular free liquid surfaces in μg , without jetting or spilling of any liquid. A classical manifold design can be made to work well in μg , if attention is given to the Weber number limitations and to the spreading characteristics on the tray surface. Pulsating spread in μg , heretofore never seen, has now been achieved for several pool depths, O_2 concentrations, and temperatures. For fixed pool depth, pulsation frequency increases with O_2 concentration and temperature until a limit is reached, and spread becomes rapid and uniform. On the other hand, pulsation frequency decreases with pool depth for all O_2 concentrations and temperatures. Modeling improvements have yielded sharply better agreement with experiments, though experimental flame spread across liquid pools continues to exhibit some behaviors that are unpredicted.

REFERENCES

1. Ross, H.D. and Miller, F.J. Proceedings of The Combustion Institute, 26, 1327-1334, 1996.
2. Miller, F.J. and Ross, H.D., Proceedings of The Combustion Institute, 27, 2715-2722, 1998.
3. Schiller, D.N., Ross, H. D. and Sirignano, W. A., Combust. Sci. Tech., 1997. 118: 203-255.
4. Ross, H.D., and Miller, F. J., NASA/CP-1999-208917, p. 321-324.
5. Miller, F.J., *et al.* Proceedings of The Combustion Institute, 28, 2000, to appear.
6. Ross, H.D. and Miller, F.J. Proceedings of the Sixth Intl Assoc .of Fire Safety Science Symposium. 2000.

Three-Dimensional Ignition and Flame Propagation Above Liquid Fuel Pools: Computational Analysis

Jinsheng Cai, Feng Liu, and William A. Sirignano

*Department of Mechanical and Aerospace Engineering
University of California, Irvine, CA 92697-3975*

Abstract: A three-dimensional unsteady reactive Navier-Stokes code is developed to study the ignition and flame spread above liquid fuels initially below the flashpoint temperature. Opposed air flow to the flame spread due to forced and/or natural convection is considered. Pools of finite width and length are studied in air channels of prescribed height and width. Three-dimensional effects of the flame front near the edge of the pool are captured in the computation. The formation of a recirculation zone in the gas phase similar to that found in two-dimensional calculations is also present in the three-dimensional calculations. Both uniform spread and pulsating spread modes are found in the calculated results.

Introduction: Schiller, Ross, and Sirignano [1] studied ignition and flame spread above liquid fuels initially below the flashpoint temperature by using a two-dimensional computational fluid dynamics code that solves the coupled equations of both the gas and the liquid phases. Their computational studies and analysis identified the mechanisms for uniform and pulsating flame spread and studied the effects of gravity level, pool depth, fluid properties, and chemical kinetic coefficients on flame spread across liquid fuel pools. Pulsating flame spread was attributed to the establishment of a gas-phase recirculation cell that forms just ahead of the flame leading edge because of the opposing effect of buoyancy-driven flow in the gas phase and the thermocapillary-driven flow in the liquid phase. Schiller and Sirignano [2] extended the same study to include flame spread with forced opposed flow in the gas phase. A transition flow velocity was found above which an originally uniform spreading flame becomes pulsating. The same type of gas-phase recirculation cell caused by the combination of forced opposed flow, buoyancy-driven flow, and thermocapillary-driven concurrent flow was found to be responsible for the pulsating flame spread. Ross and Miller [4] and Miller and Ross [5] performed experimental work that generally corroborate many of the computational findings in References 1 and 2.

In this paper, we extend previous two-dimensional and axisymmetric studies in References 1, 2, and 3 to three-dimensions. Figure 1 shows the geometry of the three-dimensional model. The mathematical formulation of the problem and assumptions are the same as those in References 2.

Results and Discussion: Four cases of different initial temperature T_0 at normal gravity and zero gravity are studied: (1) $T_0 = 21^\circ\text{C}$ at normal gravity; (2) $T_0 = 21^\circ\text{C}$ at zero gravity; (3) $T_0 = 25^\circ\text{C}$ at zero gravity. (3) $T_0 = 15^\circ\text{C}$ at normal gravity; The flow velocity at the exit of the wind tunnel is fixed at 30 cm/s for all four cases.

Figure 2 shows the contours of fuel consumption rate 0.89 seconds after ignition in the $x-y$ plane at $z/L = 0.02$ for Case 1. Figure 3 shows contours of temperature and flow velocity vectors in the same plane. The spatial coordinates presented here are non-dimensionalized by the total length of the wind-tunnel, i.e., 36 cm. Near the surface of the liquid pool, surface tension pulls the fluid forward ahead of the flame while the forced flow velocity goes against this motion. This causes small vortex cell in front of the flame as shown by the velocity vectors shown in Figure 3. A top view of the flame ($x-z$) plane at a dimensionless distance of $y/L = 0.0022$ from the liquid fuel surface is shown in Figure 4. The flame at the corner curves around and bends at the edge of the fuel pool. The flame reaches out of the fuel pool and attaches to the wind-tunnel floor by the pool edge. Figure 5 shows the contours of fuel consumption rate in a cross-section at $x/L = 0.805$. Figure 6 plots the velocity vectors and contours of temperature in the same plane. Buoyancy effects pull the flow into the flame from the side very near the wind tunnel floor and close to the flame whereas the flow expands out from the pool away from the wind-tunnel wall.

Figure 7 shows the calculated history of the position of the maximum fuel consumption rate location for all four cases within the computed time period. At the time of the writing of this abstract, computations for Cases (2) and (4) have been performed for the longest time to show pulsating features of the flame spread.

In summary, A three-dimensional computational code has been developed to solve the coupled reactive flow problem of forced gas phase flow over liquid fuel. Three-dimensional effects of the flame front near the edge of the pool are captured in the computation. The flame curves backwards near the pool edge and extends beyond the edge of fuel pool to be attached to the wind-tunnel wall. Thermal expansion and buoyancy effects create a streamwise vortex near the two edges of the liquid pool. Despite the three-dimensional effects, computations show that the basic features of the flame propagation process is the same as those in the two-dimensional simulations. The formation of a recirculation zone in the gas phase is necessary for pulsating spread of the flame. Further studies will include more detailed simulation of the propagation of the flame over the whole pool surface and also variation of parameters such as forced flow speed, initial temperature, liquid pool width and depth.

Acknowledgments: This research was conducted in support of NASA Grant No. NAG3-2024 under the technical monitoring of Dr. Howard Ross. Computer time was provided by the San Diego Supercomputer Center, the NASA Center for Computational Sciences, and the UCI Office of Academic Computing.

References

- [1] D. N. Schiller, H. D. Ross, and W. A. Sirignano, "Computational analysis of flame spread over alcohol pools," *Combustion Science and Technology*, vol. 118, pp. 205-258, May 1996.
- [2] D. N. Schiller and W. A. Sirignano, "Opposed-flow flame spread across n-propanol pools," in *Proceedings of the Twenty-Sixth International Symposium on Combustion*, pp. 1319-1325, 1996.
- [3] I. Kim, D. N. Schiller, and W. A. Sirignano, "Axisymmetric flame spread across propanol pools in normal and zero gravities," *Combustion Science and Technology*, vol. 139, no. 1-6, p. 249, 1999.
- [4] H. D. Ross and F. J. Miller, "Flame spread across liquid pools with very low-speed opposed or concurrent airflow," in *Proceedings of the Twenty-Seventh International Symposium on Combustion*, pp. 2723-2729, 1998.
- [5] F. J. Miller and H. D. Ross, "Smoke visualization of the gas-phase flow during flame spread across a liquid pool," in *Proceedings of the Twenty-Seventh International Symposium on Combustion*, pp. 2715-2722, 1998.

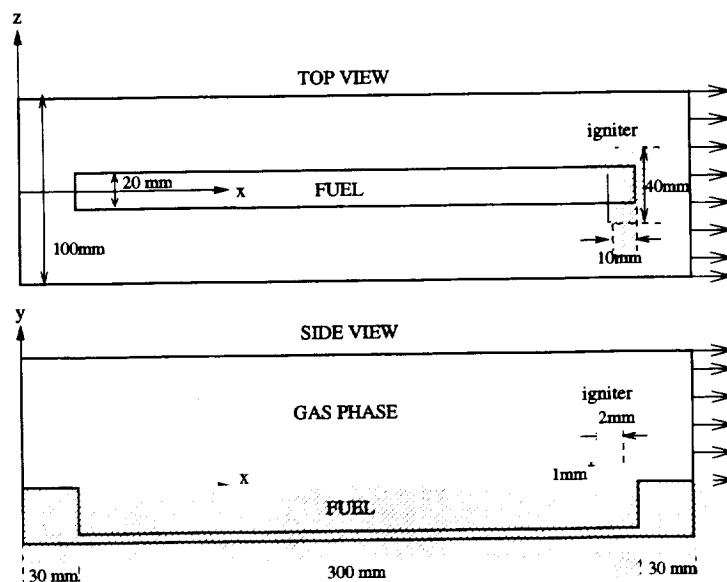


Figure 1: Geometry for the three-dimensional liquid fuel pool in a wind-tunnel with forced flow

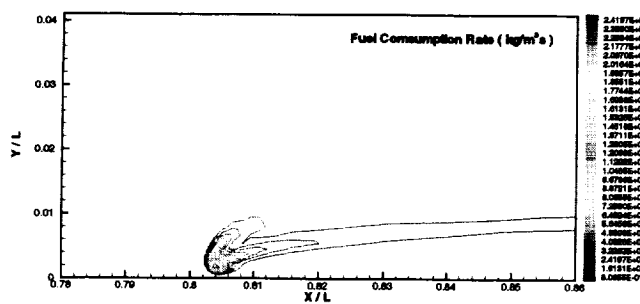


Figure 2: Contours of fuel consumption rate in the $x - y$ plane at $z/L = 0.02$, $t = 0.89s$

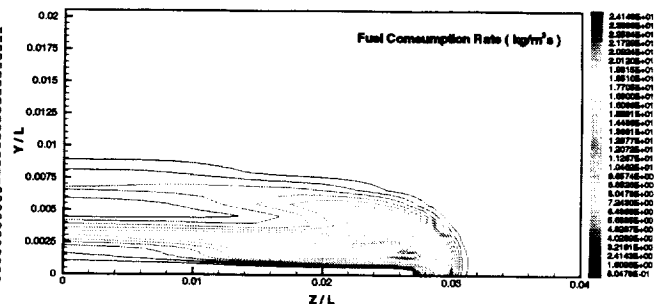


Figure 5: Contours of fuel consumption rate in the $y - z$ plane at $x/L = 0.805$, $t = 0.89s$

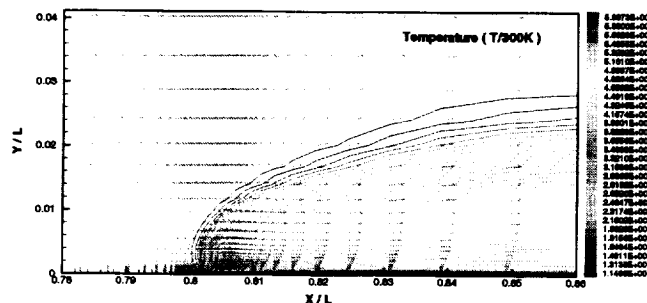


Figure 3: Velocity vectors and contours of temperature in the $x - y$ plane at $y/L = 0.0022$, $t = 0.89s$

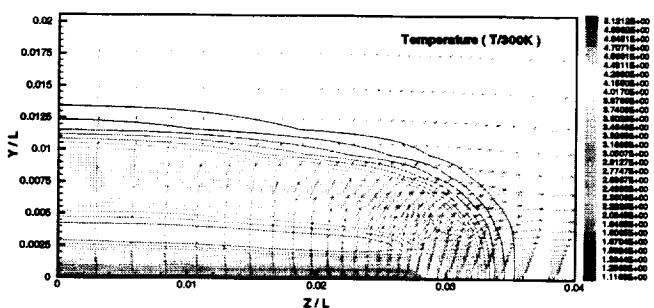


Figure 6: Velocity vectors and contours of temperature in the $y - z$ plane at $x/L = 0.805$, $t = 0.89s$

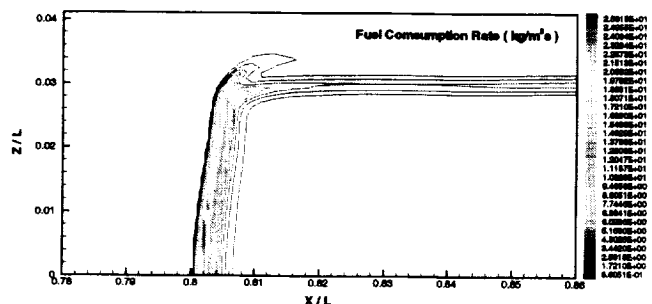


Figure 4: Contours of fuel consumption rate in the $x - z$ plane at $y/L = 0.0022$, $t = 0.89s$

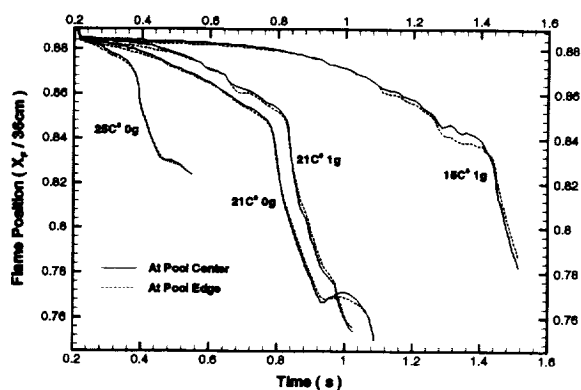


Figure 7: Position of the maximum fuel consumption rate location near the edge of the fuel pool

SOLID INFLAMMABILITY BOUNDARY AT LOW-SPEED (SIBAL)

James T'ien*, Paul Ferkul[†], Kurt Sacksteder[#], Hsin-Yi Shih*, Amit Kumar*,
Julie Kleinhenz*, Hasan Bedir*, Richard Pettegrew[†], Nancy Piltch[#] and David Frate[#]

*Case Western Reserve University, Cleveland, Ohio 44106

[†]National Center for Microgravity Research, Cleveland, Ohio 44135

[#]NASA Glenn Research Center, Cleveland, Ohio 44135

INTRODUCTION

This research program is concerned with the effect of low-speed, concurrent flow on the spreading and extinction processes of flames over solid fuels. The primary objective is to verify the theoretically predicted extinction boundary, using oxygen percentage and flow velocity as coordinates. Of particular interest are the low-speed quenching limits and the existence of the critical oxygen flammability limit. Detailed flame spread characteristics, including flame spread rate, flame size, and flame structure are sought. Since the predicted flame behavior depends on the inclusion of flame and surface radiation, the measured results will also be used to assess the importance of radiative heat transfer by direct comparison to a comprehensive numerical model.

The solid fuel used in this experiment is a custom-made fabric consisting of a 1:1 blend of cotton and fiberglass. This choice was made following an extensive search to yield a material with favorable properties, namely, rollability, non-cracking behavior during combustion, strength after combustion, and flammability in a range of oxygen limits permissible within the Combustion Integrated Rack (CIR) on the International Space Station. At the present time, an effort is being made to characterize both the radiative properties of the fuel and the flame spreading behavior in normal gravity at reduced pressure. These will provide a basis for comparison with the microgravity results as well as aid in bracketing the anticipated flammability boundary for the flight experiment.

An overview of recent work, with emphasis on theoretical results, is presented below.

THREE-DIMENSIONAL FLAME SPREAD MODEL

A previously established two-dimensional laminar flame spread model over a thin solid in low-speed concurrent flow has been extended to three-dimensions. The model consists of the full Navier-Stokes equations for the conservation of mass, momentum energy and species in the gas-phase. The species equations are for the fuel vapor, oxygen, carbon dioxide and water vapor. A one-step, second-order, finite-rate Arrhenius reaction between fuel vapor and oxygen is assumed. The solid obeys a zeroth-order pyrolysis relation and is thermally and aerodynamically thin. Both surface and gas radiation are included in the model. However, the coupled computation with the three-dimensional gas-phase radiative transfer equation is very time-consuming. Thus far, the computed solutions are restricted to the case with surface radiative loss only.

Computations have been performed with the solid fuel inside a three-dimensional flow tunnel. In the first configuration examined, the tunnel height is fixed at 10 cm, and the solid fuel is placed at the middle height. The solid is fed into the tunnel at the steady burnout rate (only steady solutions are being sought). Laterally, the fuel spans the entire tunnel width (i.e., from wall to wall). The tunnel width (which is identical to the solid fuel width) is a parameter in the numerical study (varied from 2 cm to infinity).

In addition to the fuel width, the incoming flow velocity and the oxygen percentage are varied. The fuel burnout is fixed at 6 cm from the tunnel entrance. In this configuration, several three-dimensional effects due to the presence of the tunnel walls are observed. First, the wall

changes the velocity profiles due to the no-slip boundary condition. Second, the cold sidewalls conduct heat away from the flame, which produces heat loss and a quenched layer. Third, the quenched layer near the walls creates a space for oxygen side diffusion to the flame.

At higher flow velocities (away from limit cases), the three-dimensional effect is mostly heat transfer in origin, as the flames spread faster for wider samples. However, near the low-speed, low-oxygen limit, many unexpected results appear. The competition between wall heat loss, wall quenching, and oxygen side diffusion creates a number of unusual phenomena for the near-limit flames. These include faster spread for narrower samples and an extension of flammability beyond the two-dimensional limit for moderately narrow samples (about 4 cm wide for the specified conditions) [1,2]. The key mechanism responsible for these unusual phenomena appears to be the side diffusion of oxygen, which finds its way to the flame through quenched wall layers. Oxygen side diffusion strengthens the oxygen-starved near-limit flames. It also pushes the flames closer to the solid surface, which increases the flame heat feedback and the spread rate.

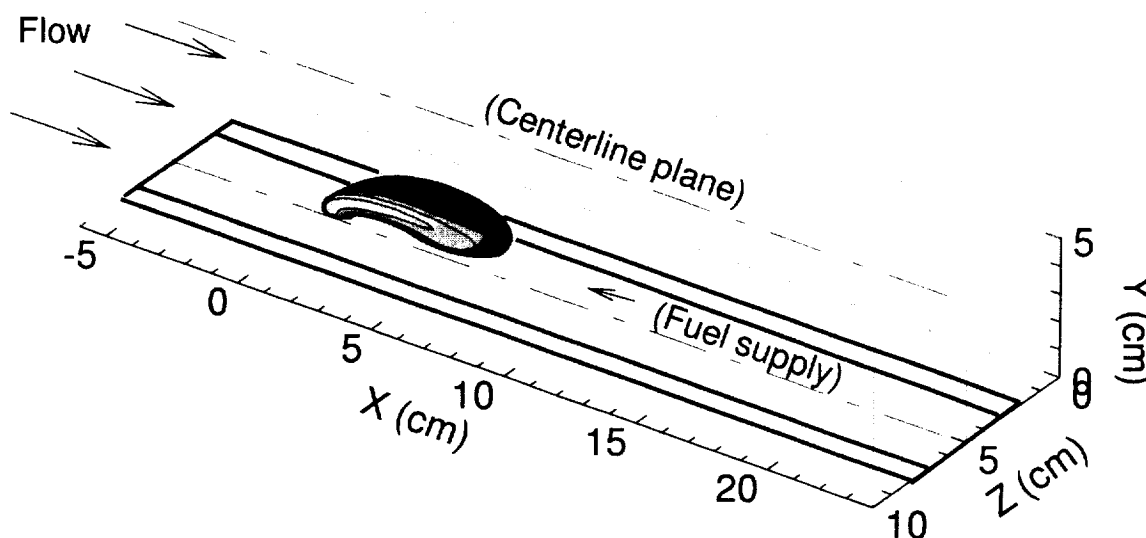


Figure 1. Schematic of the three-dimensional flame in the flow tunnel. Upper half of the tunnel configuration is shown. The 4-cm wide solid fuel ($Y = 0$) is fitted with a 1-cm inert strip on each side. The computed flame (only half of the upper flame) is shown stabilized over the solid where the flame base position ($X = 0$) is 6 cm away from the tunnel entrance. A forced oxidizer flow is imposed at the entrance and the solid fuel is fed into the flame.

In the proposed flight experiment, the tunnel flow cross section is fixed (10 cm x 10 cm) but the fuel sample width can be varied. In addition, to facilitate the translation of the sample and to eliminate edge effects, two inert strips are mounted on the sample sides (fig. 1). This realistic geometry is the second configuration examined numerically. With the inert strips, the flame spread rate increases due to the decrease of the wall heat loss and the promotion of the oxygen side diffusion. To demonstrate the modeling capability, Figures 2 and 3 give an illustration of the types of results computed.

Figure 2 shows the non-dimensional solid thickness and surface temperature contours of a 4-cm wide solid fuel (thin cellulosic sheets with 20% noncombustible material) in 5 cm/s, 15% O_2 flow. The pyrolysis front (thickness ~ 0.95) and burnout front are seen clearly to exhibit a three-dimensional effect. This three-dimensional feature is even more pronounced in the preheat zone as shown by the surface temperature contours. It is expected from the consideration of the length-to-width ratio. The curvature of the contours in the downstream region is opposite to those in the

upstream flame base region. It is also noteworthy that in this calculation, the area thermal inertia of the inert strips is assumed to be 100 times that of the fuel. Consequently, the strip temperature is low. The strip thermal inertia is a parameter in the model and in the experiment.

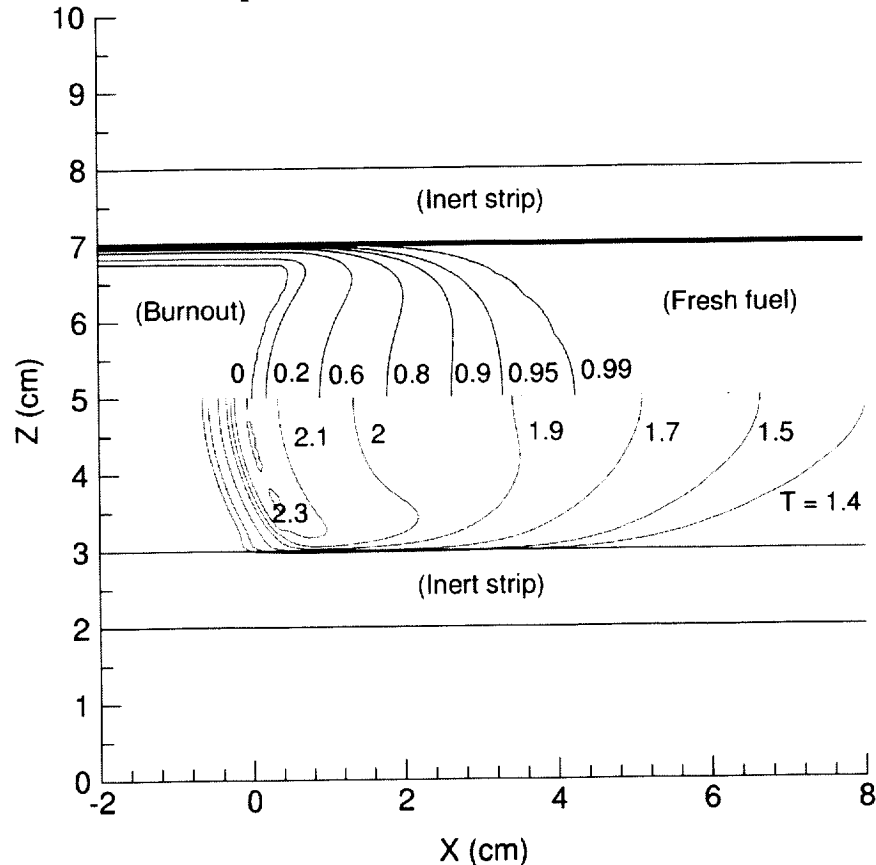


Figure 2. The solid thickness (upper half) and temperature contours (lower half, 1 unit = 300 K).

Figure 3 presents the projections of the streamlines and velocity vectors on the plane 8.5 mm above the solid surface. Also shown are the oxygen mass flux vectors, temperature contours, and fuel reaction rate contours. Note that due to thermal expansion, the hot temperature contours (e.g., $T = 2$) are extended beyond the width of the sample, consistent with experimental observations. Also note that side diffusion of oxygen is very pronounced near the flame base region. These computed results will provide guidance on the types of flame structure measurements that should be performed in the flight experiment.

OPPOSED AND CONCURRENT SPREADING FLAMES COMPARISON

In order to fully understand the relationship between flame spread in concurrent and in opposed flows, a two-dimensional opposed-flow model with the same assumptions as the two-dimensional concurrent spread model is developed [3]. Both contain gas radiation.

Flammability limits and spread rates are computed using oxygen percentage and free stream velocity as parameters. The opposed flow result is compared to that of concurrent flow. In both cases, the flammability boundary is a typical U-shaped curve which consists of two branches, namely a low-speed quenching branch which is due to radiative losses from both the gas phase and the fuel surface, and a high-speed blowoff branch which is due to inadequate flow residence time. Although

qualitatively similar, the comparison of the two flammability boundaries shows that there is a crossover. When the flow velocity is sufficiently low, the flame in opposed flow can be more flammable, while at higher flow velocities the flame in concurrent flow is more flammable. This is an unusual and intriguing discovery but can be explained based on the relative flow velocity with respect to the flame.

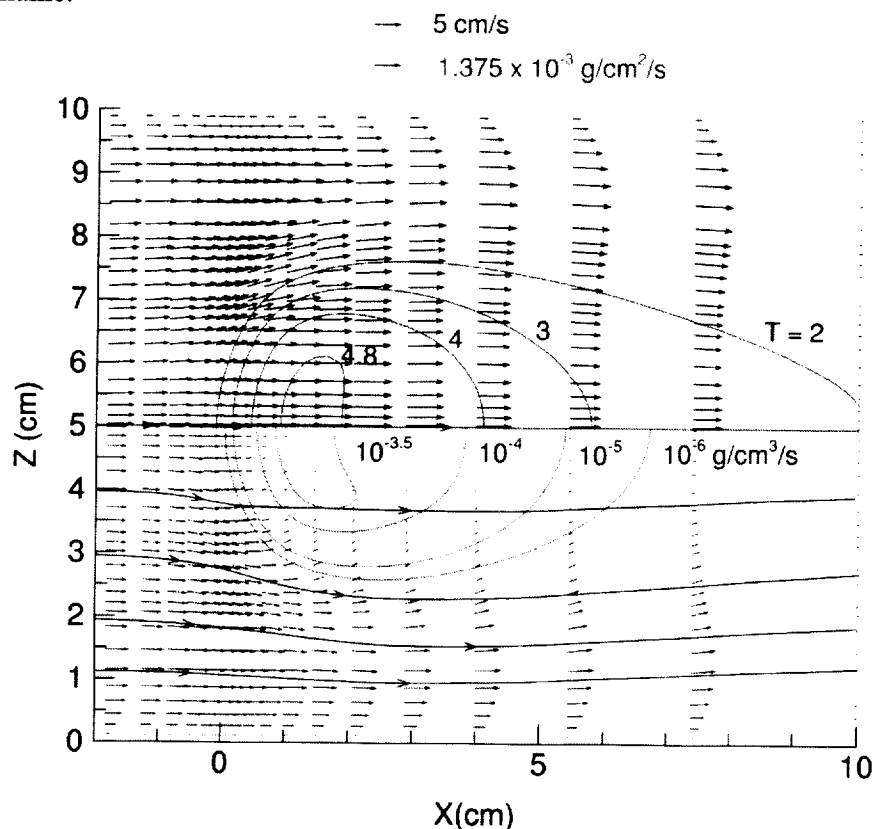


Figure 3. The detailed flame structure on the plane at height $Y = 8.5$ mm above the solid. Upper half: velocity vectors, temperature contours (1 unit = 300 K). Lower half: velocity streamlines, fuel reaction rate contours, and oxygen mass flux vectors. The vectors are projections on this plane.

The flame-spread rates in opposed and concurrent flow exhibit different trends. The flame-spread rate in concurrent flow is approximately proportional to the flow velocity while in opposed flow the variation of spread rate with flow velocity has a maximum at an intermediate flow velocity and drops near both the high and the low velocity limits. The two spread rate curves again can crossover. The spread rates for opposed flow can be higher than those for concurrent flow when the flow velocity is sufficiently low.

REFERENCES

1. Shih, H. Y.: "A Three-Dimensional Model of Flame Spread Over a Thin Solid in Low-Speed Concurrent Flow," Ph.D. Dissertation, Case Western Reserve University, Cleveland, Ohio (January 2000).
2. Shih, H. Y. and T'ien, J. S.: "Modeling Concurrent Flame Spread Over a Thin Solid in a Low-Speed Flow Tunnel," Proceedings of the Combustion Institute 28, to appear (2000).
3. Kumar, A., Shih, H. Y. and T'ien, J. S.: "A Comparison of Extinction Limits and Spreading Rates in Opposed and Concurrent Spreading Flames Over Thin Solids," Presented at the 2nd Joint Meeting of the US Sections of the Combustion Institute (March 2001).

TRANSPORT AND CHEMICAL EFFECTS ON CONCURRENT AND OPPOSED-FLOW FLAME SPREAD AT MICROGRAVITY

(NASA GRANT NO. NCC3-671)

Y. Son, L. K. Honda and P. D. Ronney

Department of Aerospace and Mechanical Engineering
University of Southern California, Los Angeles, CA 90089-1453

INTRODUCTION

Flame spread over flat solid fuel beds is a useful means of understanding more complex two-phase non-premixed spreading flames, such as those that may occur due to accidents in inhabited buildings and orbiting spacecraft. The role of buoyant convection on flame spread is substantial, especially for thermally-thick fuels. With suitable assumptions, deRis [1] showed that the spread rate (S_f) over thick fuels is given by:

$$S_f = U \frac{\lambda_g \rho_g C_{p,g}}{\lambda_s \rho_s C_{p,s}} \left(\frac{T_f - T_v}{T_v - T_\infty} \right)^2 \quad (1),$$

where U is the buoyant or forced convection velocity, λ , ρ , C_p and T are the conductivity, density, specific heat and temperature, and the subscripts s , g , v and ∞ refer to the solid fuel, gas-phase, vaporization condition and ambient condition, respectively. Equation (1) indicates that for thick fuels $S_f \sim U$, and thus suggests that S_f is indeterminate at g (since $S_f = U$) unless a forced flow is applied. (In contrast, for thermally thin fuels, the ideal S_f is independent of U [1].) The conventional view [2], as supported by computations and space experiments, is that for quiescent g conditions, S_f must be unsteady and decreasing until extinction occurs due to radiative losses. However, this view does not consider that radiative transfer to the fuel surface can enhance flame spread. While Eq. (1) presumes no radiation, deRis [1] also showed that when radiation from a prescribed radiative flux per unit area (q) dominates heat transfer to the fuel bed,

$$S_f = \frac{q^2 \delta}{\rho_s C_{p,s} \lambda_s (T_v - T_\infty)^2} \quad (2),$$

indicating that conductive transfer from the flame to fuel bed is not required for steady spread.

In this work we suggest that radiative transfer from the flame itself, not just from an external source, can lead to steady flame spread at g over thick fuel beds. As a first estimate, we assume the flame to be an isothermal volume of optically-thin radiating gas at temperature T_f with dimension δ in both the directions parallel to and perpendicular to the fuel bed, where δ is presumed to be the convective-diffusive zone thickness $\delta \sim \alpha_g / U = \alpha_g / S_f$ and $\alpha_g = \lambda_g / \rho_g C_{p,g}$ is the thermal diffusivity. The heat flux per unit area to the fuel surface due to radiation is estimated as $\Lambda \delta_g$, where $\Lambda = 4\sigma a_p (T_f^4 - T_v^4)$ is the radiant heat emission rate per unit volume, σ is the Stefan-Boltzman constant and a_p is the Planck mean absorption coefficient. The combined effects of gas-phase radiation and thermal conduction is then given by $q = \Lambda \delta + \lambda_g (T_f - T_v) / \delta$. Substituting this into Eq. (2) leads to (assuming unit fuel bed emissivity):

$$S_f = \left[\frac{\Lambda \alpha_g^2}{\sqrt{\alpha_g \rho_s C_{p,s} \lambda_s (T_v - T_\infty)} - \lambda_g (T_f - T_v)} \right]^{1/2} \quad (3)$$

Equation (3) predicts that without gas-phase radiation, no steady spread is possible ($S_f = 0$) and with gas-phase radiation, steady spread with $S_f \sim \Lambda^{1/2}$ is possible. Hence, the goal of this study is to determine if flame-generated radiation can in fact lead to steady spread over thick fuels at g .

EXPERIMENTAL APPARATUS

Experiments were conducted in a 20 liter combustion chamber as shown in Fig. 1. O_2-N_2 and O_2-CO_2 atmospheres were employed since they have very different radiative properties - CO_2 radiates strongly whereas N_2 does not radiate, and thus for O_2-N_2 atmospheres only the combustion products, not the ambient atmosphere, radiate. Equations 1 and 3 indicate that S_f in a given atmosphere S_f can be much higher for fuels with low $\rho_s C_{p,s} \lambda_s$. This led us to use polyphenolic foam (used in floral arranging) having low ρ and λ to study flame spread in short-duration drop tower tests. The samples were ignited by an electrically-heated Kanthal wire imbedded in a nitrocellulose sheet attached to the fuel surface. The flames were imaged via CCD cameras whose signals are connected via fiber-optic cables to ground-based S-VHS video recorders. A shearing interferometer was used for the side view since the flames were sometimes too dim for direct video. Thermopile-type radiometers were used to determine flame radiation; a "front" radiometer viewed a hole in the flame side of the fuel surface, and a "back" radiometer viewed the non-burning side of the hole. By viewing a hole, interference from surface radiation was eliminated.

RESULTS

Figure 2 shows examples of the progress of flame spread (flame position vs. time) at $1g$ and g . The slope of these plots gives the spread rate; a straight line indicates a constant spread rate and thus steady spread. From these tests, it can be seen that that in O_2-CO_2 atmospheres, steady flame spread is possible over thick fuels at quiescent g conditions when gas-phase radiation effects are significant, as suggested by our model (Eq. 3).

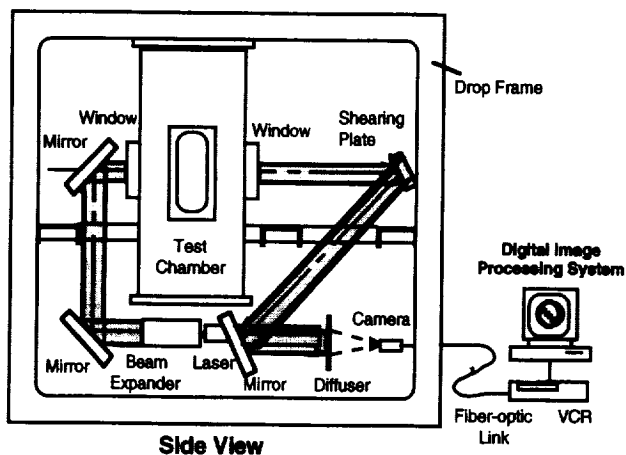


Figure 1. Schematic of drop frame and camera apparatus. The fuel bed is mounted inside the chamber parallel to the plane of the page.

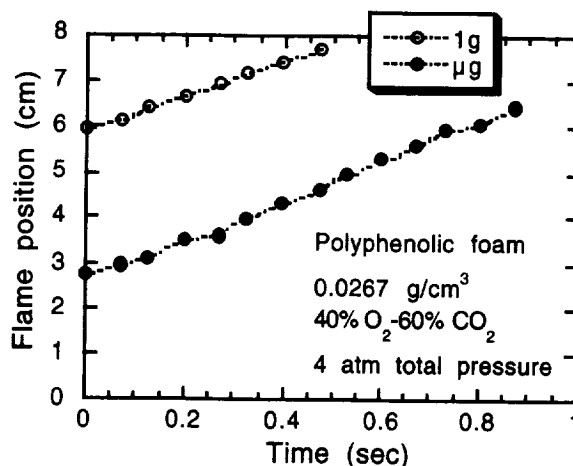


Figure 2. Position of spreading flames as a function of time in a 40% O_2 - 60% CO_2 mixture at 4 atm at earth gravity and g .

Figure 3 shows example images of spreading flames at $1g$ and g . From these images the effect of buoyancy can be seen at $1g$. Figure 4 shows example side-view images obtained using the interferometer. As expected, the flame is thicker at g than $1g$, indicating that g flames have more volume and thus more radiation to fuel bed.



Figure 3. Images of flame spread over a thick solid fuel bed in a 40% O_2 - 60% CO_2 mixture at 4 atm. Flame spreads from top to bottom. Width of samples is 10 cm. Left: microgravity (bright band in the lower part of image is the flame front.) Right: earth gravity.

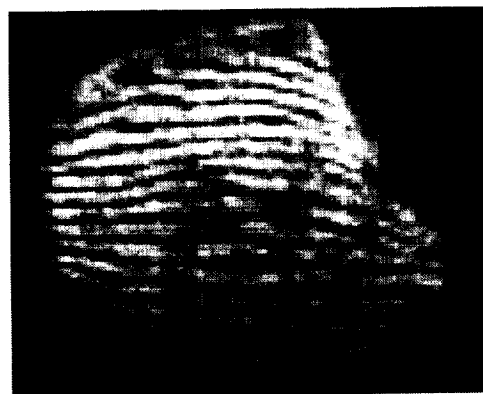


Figure 4. Side-view interferometer images of flame, same conditions as Fig. 3. Width of images is 5 cm. The upper black region is the combustion products. Left: microgravity. Right: earth gravity.

Figure 5 shows that, as was also seen in prior tests using thermally-thin fuels [3], for thick fuels the quiescent g_{eff} can be higher than its 1g (downward) counterpart for CO_2 -diluted atmospheres but not N_2 -diluted atmospheres. Figure 6 shows that a transition from S_f increasing rapidly with pressure (P) to S_f nearly independent of P at $P \sim 5$ atm. While the cause of this transition is uncertain, it may be due to a transition from radiation dominated by optically-thin behavior to optically-thick behavior. Figure 7 shows that S_f becomes less dependent on fuel bed thickness as thickness increases, indicating the approach to the thermally-thick limit. The transition thickness is about 2 mm for the case shown. Figure 8 the radiative emission from a O_2 - CO_2 atmosphere test at g_{eff} , which are the only cases tested where the back radiometer showed significant flux. This is because only in this case is there substantial emission, absorption and re-emission, which is the only means to obtain substantial radiative flux to the back radiometer. O_2 - N_2 atmospheres (not shown) do not exhibit this behavior at all [4], and even for O_2 - CO_2 atmospheres this was seen only at g_{eff} where δ is larger and thus the total radiative flux is greater.

CONCLUSIONS

Our results indicate that, in contrast conventional understanding, steady spread can occur over thick fuels in quiescent microgravity environments, especially when a radiatively active diluent gas such as CO_2 is employed. We propose that this is due to radiative transfer from the

flame to the fuel surface. Additionally, the transition from thermally thick to thermally thin behavior with decreasing bed thickness is demonstrated. It was found that foam fuels enabled steady spread to be obtained over thermally thick fuels at μg even in short-duration drop tower experiments. These results are being used to define a space flight experiment called Radiative Enhancement Effects on Flame Spread (REEFS) planned for the International Space Station in the Combustion Integrated Rack facility.

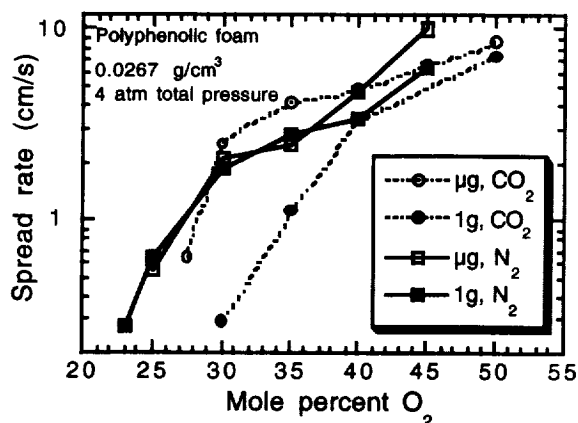


Figure 5. Effect of O₂ concentration on S_f over thick solid fuel beds at μg and earth gravity.

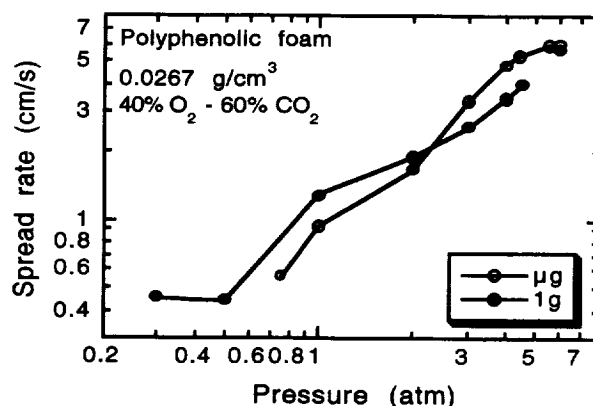


Figure 6. Effect of pressure on S_f over thick solid fuel beds at μg and earth gravity.

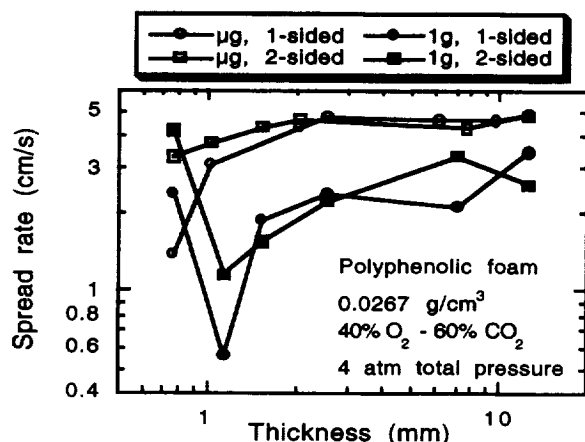


Figure 7. Effect of fuel bed thickness on S_f over thick solid fuel beds at μg and earth gravity.

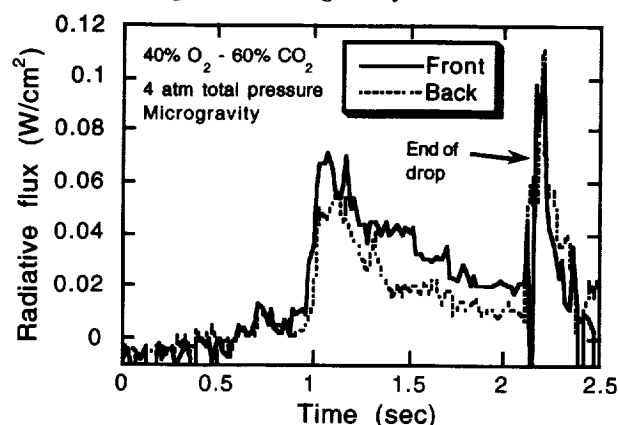


Figure 8. Radiative flux characteristics of a flame spreading over a thick solid fuel bed at μg in a 40% O₂ - 60% CO₂ mixture at 4 atm.

REFERENCES

- [1] deRis, J. N., *Twelfth Symposium (International) on Combustion*, Combustion Institute, Pittsburgh, 1969, p.241.
- [2] Bhattacharjee, S., West, J., Altenkirch, R. A. *Twenty-Sixth Symposium (International) on Combustion*, Combustion Institute, Pittsburgh, 1996, p. 1477; Altenkirch, R.A., Tang, L., Sacksteder, K., Bhattacharjee, S., Delichatsios, M. A., *Twenty-Seventh Symposium (International) on Combustion*, Combustion Institute, Pittsburgh, 1998, p. 2515.
- [3] Honda, L., Ronney, P. D., *Combust. Sci. Technol.* **133**, 267 (1998).
- [4] Honda, L., Son, Y., Ronney, P. D., AIAA Paper No. 2001-0467 (2001).

EFFECT OF SLOW EXTERNAL FLOW ON FLAME SPREADING OVER SOLID MATERIAL -OPPOSED SPREADING OVER POLYETHYLENE WIRE INSULATION-

O.Fujita, K.Nishizawa, K.Ito, Hokkaido University, Sapporo 060-8628, Japan

S. L.Olson, NASA GRC, USA

and T. Kashiwagi, NIST, USA

INTRODUCTION

The effect of slow external flow on solid combustion is very important from the view of fire safety in space because the solid material in spacecraft is generally exposed to the low air flow for ventilation. Further, the effect of low external flow on fuel combustion is generally fundamental information for industrial combustion system, such as gas turbine, boiler, incinerator and so on. However, it is difficult to study the effect of low external flow on solid combustion in normal gravity, because the buoyancy-induced flow strongly disturbs the flow field, especially for low flow velocity. In this research, therefore, the effect of slow external flow on opposed flame spreading over polyethylene (PE) wire insulation have been investigated in microgravity. The microgravity environment was provided by Japan Microgravity Center (JAMIC) in Japan and KC-135 at NASA GRC. The tested flow velocity range is 0-30cm/s with different oxygen concentration and inert gas component.

EXPERIMENTAL

Figure 1 shows the test section of the wire combustion. The sample wire is horizontally fixed at the center of the duct and is ignited at the left end of the wire with Kanthal wire coil. At the left end of the duct a

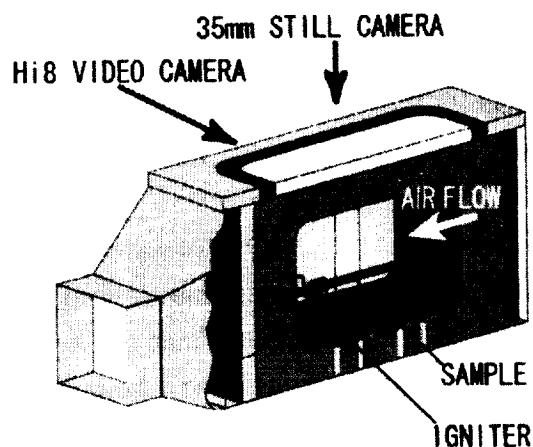


Fig.1 Cross section of combustion chamber

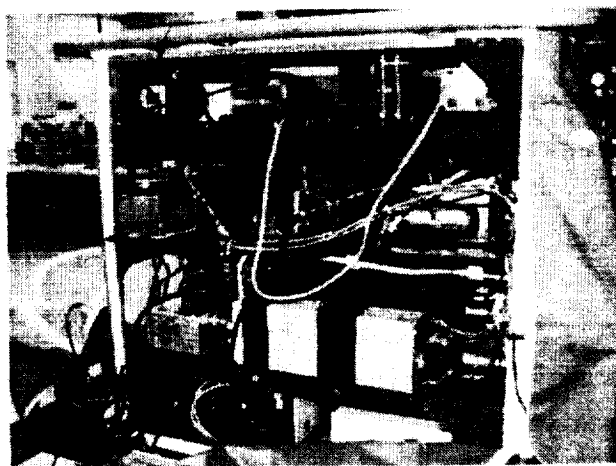


Fig.2 Rig for KC-135 experiments

suction fan is installed and uniform external flow along the wire is given from right to left. Therefore, opposed flow flame spreading over wire insulation is achieved. Flame spread phenomenon is observed from the top and rear window with 35mm still camera and Hi-8 video camera, respectively. Flame spread rate is measured from the motion picture taken by Hi-8 video camera. Figure 2 shows the experimental rig used for KC-135 parabolic flight experiments. The test section described above is located on the second shelf of the rig. The rig is originally designed for TIGER-3D project and is modified for the wire insulation combustion test within a low external flow.

Microgravity tests were performed with KC-135 parabolic flight for high flow velocity case (mainly larger than 10 cm/s) and with JAMIC for low flow velocity case (mainly less than 10cm/s) and high O₂ concentration case. The experimental sample used in the test is polyethylene insulated microm wire as was used with WIF experiments[1], whose the core diameter is 0.5mm and insulation thickness 0.15mm.

RESULTS AND DISCUSSION

Figures 3 and 4 show a flame in normal gravity and microgravity, respectively. In normal gravity, flame plume appears naturally because of buoyancy induced flow. In microgravity the plume does not appear and flame locates along the wire. The flame in microgravity is darker, which implies the lower flame temperature even with external flow. In the discussion below flame spread rate over horizontal wire as shown here is compared between normal gravity and microgravity.

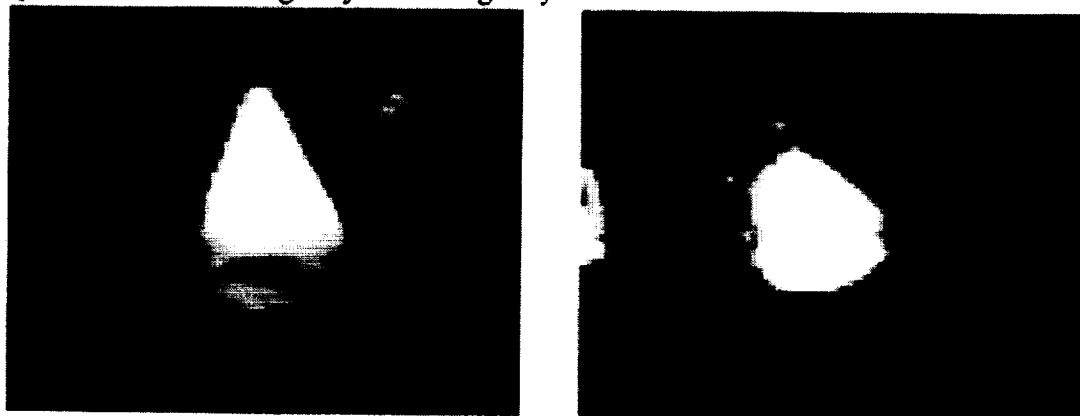


Fig.3 Flame in normal gravity(O₂=35%, V=1.3cm/s) Fig.4 Flame in microgravity(O₂=35%, V=1.3cm/s)

Figure 5 shows the flame spread rate in normal gravity. As seen in the figure, spread rate decreases monotonously with increase in flow velocity for each O₂ concentration, while the effect of O₂ concentration to increase the spread rate is significant. In microgravity, as shown in Fig.6, trend is different from that in normal gravity. Flame spread rate increases with increase in flow velocity in low velocity range and it shows a maximum value at a certain flow velocity. This trend is more obvious at higher O₂ concentration. Figures 7 and 8 show the change in the spread rate versus external flow velocity with different balance gas taken in

normal gravity and microgravity, respectively. The effect of balance gas on the spread rate is also strong as well as O₂ contestation. According the comparison of the two figures, it is understood the trends in normal and microgravity is different each other as was seen in the comparison between Figs. 5 and 6. Flame spread rate tends to show a peak value at a certain flow velocity in normal gravity, while it monotonously decreases in normal gravity.

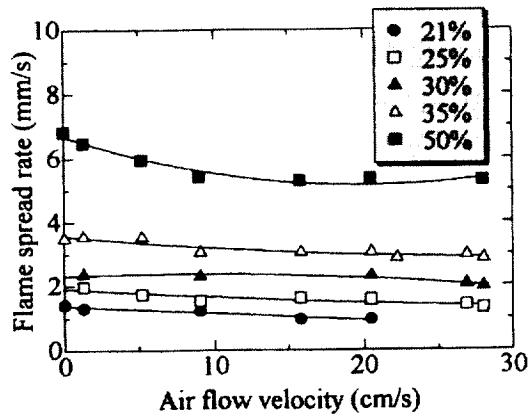


Fig.5 Spread rate vs. external flow velocity in 1G

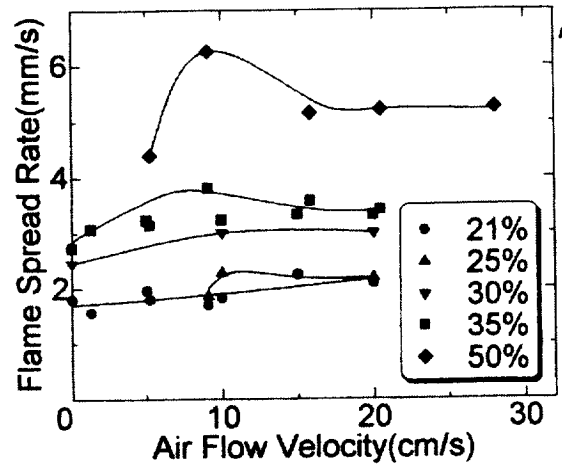


Fig.6 Spread rate vs. external flow velocity in μ G

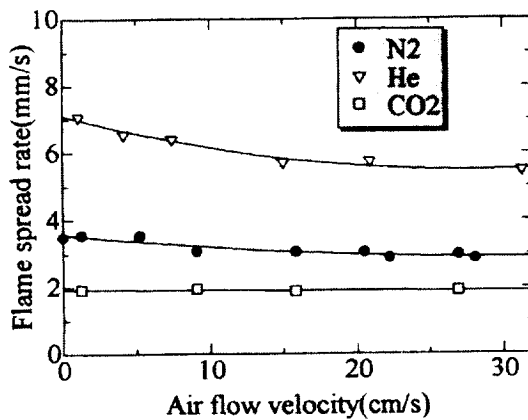


Fig.7 Effect of balance gas on flame spread rate in 1G (O₂=35%)

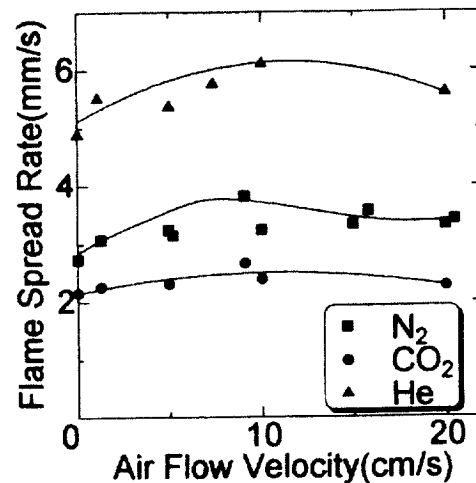


Fig.8 Effect of balance gas on flame spread rate in μ G (O₂=35%)

This trend in microgravity is very essential because it implies the presence of the most flammable region of wire insulation. The flow velocity to give a maximum spread rate is close to the ventilation flow in spacecraft. In the previous research on paper sheet combustion [2], the trend to appear maximum spread rate was shown even for thermally thin fuel. This trend was explained by the transition from oxygen transport control region to the kinetic control region. In the case, the appearance of a peak value was more obvious in lower oxygen concentration. On the other hand, the trend to show peak value in Fig.6 is more obvious in

higher oxygen case and it is assumed that the reason to appear the peak value is different from the transition from the oxygen supply control to the kinetic control.

One of the explanations to appear the maximum value is the increase of preheat zone thickness in low flow velocity under microgravity condition [3,4]. With increase in preheat zone thickness heat flux to the unburned region increases. However, when the external flow velocity is very low close to the quiescent condition flame temperature decreases. Therefore, spread rate decreases again in the low flow velocity region, while the preheat zone is thicker with lower flow velocity. As a result the maximum spread rate appears at a certain flow velocity region. In normal gravity, flame temperature is kept high even in low external flow because of vertical buoyancy induce flow. If the flame temperature is kept high enough, flame spread rate increases with decrease in external flow velocity because of thicker preheat zone as well as larger radiation heat to the unburned fuel.

Another important fact is the comparison of spread rate with CO₂ balance in normal gravity and microgravity. The spread rate in microgravity is higher than horizontal flame spread rate in normal gravity, while other balance gas gives the lower spread rate in microgravity than normal gravity. A possible mechanism to explain the effect of CO₂ is reabsorption of radiation heat from the flame. The CO₂ gas ahead of the flame front is heated with radiation heat and it makes the preheat zone thickness wider in microgravity. In normal gravity preheated CO₂ gas ahead of flame flows away upward because of buoyancy force and the reabsorption effect becomes negligible.

SUMMARY

Flame spreading over wire insulation within low external flow has been investigated in microgravity by KC-135 at NASA GRC and Japan Microgravity Center (JAMIC). The tested flow velocity range is 0-30cm/s with different oxygen concentration and inert gas component. The results showed that the flame spread rate was almost constant for different flow velocity, when the flow velocity is higher than 10cm/s within the tested range. In the very low flow velocity range, less than 10cm/s, maximum flame spread rate appeared. It means more flammable regime on external flow velocity than the so-called thermal regime. This phenomena is explained by the increase of preheat zone thickness in low flow velocity region as well as flame temperature decrease by radiation heat loss.

ACKNOWLEDGEMENT

This work was performed under the NASA/NEDO Cooperative Research Project under management of JSUP (*Japan Space Utilization Promotion Center*).

Reference

- [1] Greenberg, J. B., Sacksteder, K. R., and Kashiwagi, T., NASA CP 3272 Vol. II: pp.631-655, (1994).
- [2] Olson, S.L., Comb. Sci. Tech, Vol.76, pp.233-249.
- [3] Kikuchi, M., Fujita, O., Ito, K., Sato, A. and Sakuraya, T., *Proc. Combust. Inst.* 27: 2507-2514, (1998).
- [4] Fujita, O., Kikuchi, M., Ito, K., and Nishizawa, K., *Proc. Combust. Inst.* 28: (2000), in print.

SMOLDERING, TRANSITION AND FLAMING IN MICROGRAVITY

A.C. Fernandez-Pello¹, A. Bar-Ilan¹, T.L. Lo¹, D.C. Walther¹, and D.L. Urban²

¹University of California, Berkeley, 94720, ferpello@newton.berkeley.edu,

²NASA Glenn Research Center, Cleveland, OH 44135

INTRODUCTION

A research project is underway to study smolder and the transition to flaming in microgravity. The Microgravity Smoldering Combustion (MSC) flight project is an ongoing research project to provide a better understanding of the controlling mechanisms of smoldering combustion. The Smoldering Transition and Flaming (STAF) project is a recently established research program that will utilize the Fluids and Combustion Facility (FCF) of the ISS [1] to examine the transition from smolder to flaming in microgravity.

In forced flow smolder experiments ambient pressure in the MSC chamber rises, thus motivating the need to understand the effects of pressure on smoldering combustion. Further, the STAF experiment has constraints on experimental scale and testing at elevated pressure may be a mechanism to reduce the sample size by enhancing the smolder reaction. In the work we are reporting here, a series of ground-based tests determine the effects of pressure on smoldering combustion. These tests are compared with data obtained from experiments conducted aboard the Space Shuttle in flights STS-69 and STS-77. Measurements of one-dimensional smolder propagation velocity are made by thermocouple probing and a non-intrusive Ultrasound Imaging System (UIS) [2, 4]. Thermocouples are also used to obtain reaction temperatures and the UIS is used to determine permeabilities of the fuel in real-time.

EXPERIMENTAL HARDWARE AND PROTOCOL

Ground-based and microgravity tests were conducted in the MSC flight hardware on 120mm diameter and 150mm length cylindrical samples of open-cell, unretarded, polyurethane foam [5]. The tests were conducted in 3 configurations: opposed forced flow in normal gravity and microgravity, and natural convection. A range of ambient pressures from 1.0 to 3.5 atm was tested.

In normal gravity forced flow experiments, the oxidizer mass flux was a controlled parameter. Tests were conducted at a specific pressure, which was held constant throughout the test via a pressure relief valve. A constant oxidizer mass flux was delivered by a mass flow controller (MFC). The experimental setup was similar in the forced flow microgravity tests [5]. In both of these forced flow tests, an igniter setting of 90W for 600 seconds was chosen to simulate the mission ignition criteria [5].

In the natural convection tests, the ends of the fuel sample were exposed to the ambient chamber pressure. The igniter power chosen was 70W for 1200 seconds, similar to STS-69 and STS-77 quiescent tests [6], as well as previous natural convection smolder experiments [7].

BACKGROUND

Smolder often occurs under oxygen-limited conditions [8], in which case the rate of heat release from the smolder reaction is directly proportional to the oxidizer mass flux. The smolder propagation velocity is then proportional to the heat release rate minus heat losses to the environment [9]. The effect of pressure on the oxidizer mass flux will be discussed in order to clarify the experimental results. With buoyancy as the driving force the pressure gradient along the length of the cylindrical sample can be written as $dP/dz = -\rho g$. For a flow in a porous

medium Darcy's Law is applicable [10] $dP/dz = -(\mu/K)u_D$ and equating these two gives an estimate of the buoyant flow velocity, u_D , through the medium. The resulting oxidizer mass flux is $\dot{m}''_{O_2, Buoyant} = y_{O_2} \rho_{air} u_D = y_{O_2} (\rho_{air})^2 gK/\mu$. A calculation of the buoyancy-induced oxidizer mass flux is conducted based on data from the natural convection tests. It has been observed that permeability changes with the passage of the smolder propagation front and the final char permeability increases with increasing oxidizer mass flux [2, 7]. An increased oxidizer mass flux leads to a more vigorous reaction, which consumes more fuel, and leads to a higher permeability of the residual char. In normal gravity tests, increased pressure leads to increased buoyancy-induced oxidizer mass flux, and consequently to an increased permeability.

The pressure effects on diffusive transport of heat and mass are determined by examining the effects of pressure on the binary diffusion coefficient. The diffusive mass flux is given by $\dot{m}''_{O_2, Diffusive} = \rho D \nabla y_{O_2}$. The binary diffusion coefficient is proportional to $T^{1.5}/P$ [11]. Thus it is expected that the diffusive mass flux is relatively independent of the pressure inasmuch as the reaction temperatures are not significantly changed over the range of pressures tested.

The forced oxidizer mass flux is given by $\dot{m}''_{O_2, Forced} = y_{O_2} \rho_{air} u_{forced}$. In the present experiments the mass flux is controlled through the MFC, and therefore is independent of pressure.

The total oxidizer mass flux is the sum of oxidizer mass fluxes from buoyancy-induced flow, diffusive transport, and controlled forced flow. The total oxidizer mass flux is therefore expressed as:

$$\dot{m}''_{O_2, Total} = \frac{y_{O_2} (\rho_{air})^2 gK}{\mu} + \rho_{air} D \nabla y_{O_2} + \dot{m}''_{O_2, Forced} \quad (1)$$

Concerning the heat losses to the environment, an analysis of free convection on the outside of the sample cylinder indicates that heat losses, as described by the Nusselt number, are proportional to the Rayleigh number to the power of $1/4$. Since the Rayleigh number is proportional to the square of the pressure, then the heat losses from the smoldering sample are expected to rise as $P^{1/2}$ [12].

For an oxygen-limited reaction the heat release rate can be estimated by multiplying the oxidizer mass flux by the heat of smolder combustion (per unit mass of oxidizer). The effect of pressure on the heat of smolder combustion is not well known, although since the heat of combustion depends on the products of combustion it should depend on the characteristics of the smolder reaction. The effect of pressure on heterogeneous reaction chemistry is difficult to quantify, but assuming that the reaction rate behaves as an Arrhenius reaction of first order in oxidizer, then the reaction rate should be proportional to pressure [13]. Thus it could be inferred that the rate of heat release would be proportional to pressure, although most likely weakly.

RESULTS & DISCUSSION

Figure 1 presents the effect of pressure on the smolder velocity for three smolder test configurations – opposed forced flow smolder in normal- and microgravity, and natural convection downward smolder. It is observed that under similar ignition conditions and for the present sample size, there exists a minimum ambient pressure at which a self-sustaining smolder reaction is observed. In the microgravity tests, this minimum pressure is 1.0 atm, although it is difficult to quantify, because initially smolder occurs under the influence of the igniter. In the forced flow normal gravity tests this minimum pressure is 1.2 atm, and in the natural convection tests it is 2.0 atm.

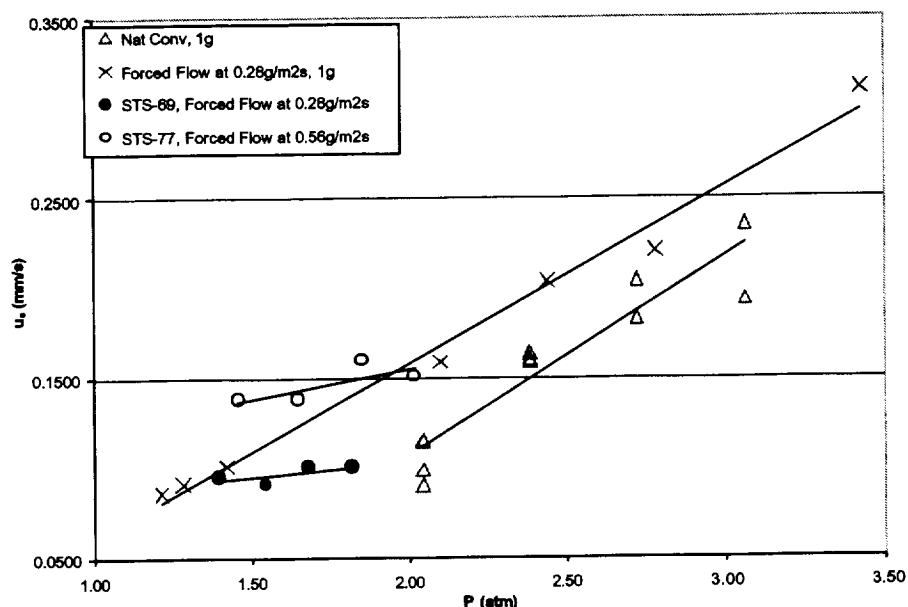


Figure 1 Effect of pressure on the smolder velocity for opposed forced flow smolder in normal- and microgravity, and natural convection downward smolder.

From Eq. 1 it is calculated that in the normal gravity forced flow testing, at 1.2 atm, the oxidizer mass flux is $0.50\text{g/m}^2\text{s}$. Also using Eq. 1, in the natural convection tests at 2.0 atm the calculated oxidizer mass flux is $0.53\text{g/m}^2\text{s}$, which is consistent with the previous result. These calculations seem to indicate that for the present experimental conditions and sample size, a critical oxidizer mass flux of roughly $0.5\text{g/m}^2\text{s}$ is needed to achieve a self-sustaining smolder reaction in normal gravity.

In the microgravity forced flow tests where there is no augmentation of oxidizer mass flux due to buoyancy, the smolder propagation velocity is observed to increase slightly with pressure. Since the mass flux of oxidizer is constant, this indicates that there may be little or no dependence on pressure of the rate of heat release, although it may be difficult to separate the effects of pressure on the rate of heat release from the effects of pressure on heat losses. For the STS-69 tests in which the oxidizer mass flux was $0.28\text{g/m}^2\text{s}$, the smolder velocity is basically the same as that of the forced flow test in normal gravity at 1.4 atm. At this pressure, the forced oxidizer mass flux is calculated as $0.53\text{g/m}^2\text{s}$, which shows that the lack of convective heat losses in microgravity enhance the smolder reaction to the point that nearly half the oxidizer mass flux is needed to sustain the smolder reaction in microgravity.

Figure 1 also shows that the smolder velocity in microgravity at an oxidizer mass flux of $0.56\text{g/m}^2\text{s}$ (STS-77) is the same as that of a normal-gravity forced flow with an oxidizer mass flux of $0.81\text{g/m}^2\text{s}$ (Eq. 1), corroborating the above finding that a significantly lower oxidizer mass flux is needed to attain a self-propagating smolder reaction in microgravity than in normal gravity.

It should be noted that the pressure dependence of the buoyancy-induced heat losses is less than that of the buoyancy-induced mass flux, which explains why the difference in the critical mass flux between normal- and microgravity for self-propagating smolder decreases as the pressure increases. Furthermore these results appear to indicate that the effect of pressure on transport is dominant over its effect on chemical kinetics. In microgravity, where there is no

buoyancy, the effect of pressure on the smolder velocity is weak ($\sim P^{1/3}$), and the smolder velocity is proportional to the oxidizer mass flux. Also, in normal gravity for the same pressure and consequently the same buoyant heat losses, the smolder velocity is proportional to the oxidizer-mass flux in natural and forced flow smolder.

CONCLUDING REMARKS

A comparison of the tests conducted in normal- and microgravity indicates that there is a critical oxidizer mass flux to attain a self-propagating smolder reaction, and that this critical mass flux is significantly smaller in microgravity than in normal gravity. This finding has important implications from the point of view of fire safety in a space-based environment, since smolder can be initiated at lower oxygen concentrations or mass flows than in normal gravity. Since buoyant heat losses are the primary reason for these results, the quantitative differences are a function of the sample size, decreasing as the sample size increases.

A comparison of only smolder propagation velocities ignores differences in reaction temperatures, in the extent of reaction and/or char conversion, conductive and/or forced convection heat losses. Examination of these effects is ongoing.

ACKNOWLEDGEMENTS

This work is funded by the National Aeronautics and space Administration under NASA grant number NAG3-2026.

References:

- ¹ Zurawski, R., "The FCF Combustion Integrated Rack", *38th AIAA Space Sciences & Exhibit*, AIAA 2000-0425, January 2000.
- ² Walther, D.C., R.A. Anthenien, M. Roslon, D.L. Urban and A.C. Fernandez-Pello, *37th AIAA Space Sciences & Exhibit*, AIAA 99-0699, January 1999.
- ³ D.C. Walther, A.C. Fernandez-Pello, R.A. Anthenien and D.L. Urban, *5th Microgravity Combustion Workshop*, NASA/CP-1999-208917, 193-196, Cleveland, OH., May 18-20, 1999.
- ⁴ Tse, S.D., Anthenien, R.A., Miyasaka, K. and A.C. Fernandez-Pello, *Combustion and Flame*, V.116, No. 12, 120-135, 1998
- ⁵ Walther, D.C., A.C. Fernandez-Pello, Urban, D.L., *Comb. and Flame*, 116:398-414, 1999.
- ⁶ Walther, D.C., A.C. Fernandez-Pello and D.L. Urban, *Proc. of the 1st Pan-Pacific Basin Workshop and 4th Japan/China Workshop on Microgravity Sciences*, pp.260-265, Tokyo, Japan, 8-11 July, 1998.
- ⁷ J. L. Torero, A.C.Fernandez-Pello and M.Kitano, *Fourth International Symposium on Fire Safety Science*, pp. 409-420, 1994.
- ⁸ Ohlemiller, T.J., *Prog. Ener. & Comb. Sci.*, 11:277, (1986).
- ⁹ Dosanjh, S., P.J. Pagni and A.C. Fernandez-Pello, *Combustion and Flame*, 68, 131-142, (1987).
- ¹⁰ Nield, D.A. and A. Bejan, *Convection in Porous Media*, Springer-Verlag, New York (1992).
- ¹¹ Bird, R.B., W.E. Stewart and E.N. Lightfoot, *Transport Phenomena*, John Wiley & Sons, New York, (1960).
- ¹² Incropera, F.P. and D.P. DeWitt, *Fundamentals of Heat and Mass Transfer*, John Wiley & Sons, New York, (1996).
- ¹³ Alberty, R.A. and R.J. Silbey, *Physical Chemistry*, John Wiley & Sons, New York, (1992).

QUANTITATIVE STUDIES ON THE PROPAGATION AND EXTINCTION OF NEAR-LIMIT PREMIXED FLAMES UNDER NORMAL- AND MICRO-GRAVITY

F. N. EGOLFOPOULOS¹, Y. DONG¹, G. SPEDDING¹, B. CUENOT² & T. POINSOT²

¹Department of Aerospace & Mechanical Engineering

University of Southern California
Los Angeles, California 90089-1453

²CERFACS, Toulouse, France

INTRODUCTION

Strained laminar flames have been systematically studied, as the understanding of their structure and dynamic behavior is of relevance to turbulent combustion [e.g. 1,2]. Most of these studies have been conducted in opposed-jet, stagnation-type flow configurations. Studies at high strain rates are important in quantifying and understanding the response of vigorously burning flames and determine extinction states. Studies of weakly strained flames can be of particular interest for all stoichiometries. For example, the laminar flame speeds, S_u^o , can be accurately determined by using the counterflow technique [2] only if measurements are obtained at very low strain rates [3]. Furthermore, near-limit flames are stabilized by weak strain rates. Previous studies [4] have shown that near-limit flames are particularly sensitive to chain mechanisms, thermal radiation, and unsteadiness. The stabilization and study of weakly strained flames is complicated by the presence of buoyancy that can render the flames unstable to the point of extinction. Thus, the use of microgravity (μ -g) becomes essential in order to provide meaningful insight into this important combustion regime.

In our past studies [5,6] the laminar flame speeds and extinction strain rates were directly measured at ultra-low strain rates. The laminar flame speeds were measured [5] by having a positively strained planar flame undergoing a transition to a negatively strained Bunsen flame and by measuring the propagation speed during that transition. The extinction strain rates of near-limit flames were measured [6] in μ -g. Results obtained for CH_4/air and $\text{C}_3\text{H}_8/\text{air}$ mixtures are in agreement with those obtained by Maruta *et al.* [7]

OBJECTIVES

The objective of this research is twofold. First, to develop accurate Digital Particle Image Velocimetry (DPIV) technique capable to accurately measure flow velocities and introduce it to the 2.2 sec drop tower. Current μ -g practices include global descriptions of fluid mechanics effects, which may not be accurate. Second, to perform Direct Numerical Simulations (DNS) of the counterflow in order to describe phenomena related to the phenomenon of transition to Bunsen flame and also provide insight into the effects of buoyancy for weakly burning flames.

EXPERIMENTAL APPROACH

Strained flames are produced by impingement of a round jet on a flat plate. The plate is also round to reduce slow time-scale instabilities caused by jet flow-boundary layer interactions on the plate. The jet is illuminated by a pulsed sheet of laser light, provided by a 2W A^+ laser, modulated by a polarizing shutter. The shutter pulses are phase-locked with the vertical drive signal from the Pulnix TM9701N (full frame, asynchronous reset) CCD camera. A custom timing circuit then generated pairs of pulses that straddle frame pairs. The effective exposure time (δt) for DPIV calculations is determined by the inter-pulse time, and the maximum repetition rate is 15 Hz. Frame pair sequences of 768 x 484 x 8 bit images are saved direct to PC RAM, and then saved to disk. Seeding is provided by particle with diameters less than 10 μm . Correlation Image Velocimetry (CIV) is used to calculate displacement fields from each image pair. CIV has the

useful property that the search distances for performing correlations is decoupled from the search box size itself. This allows displacements and vector densities to be tuned independently to the appropriate flow characteristics. The former is determined exclusively by δt , the latter by the seeding density and flow complexity.

NUMERICAL APPROACH

The phenomenon of transition from flat to Bunsen flame in a stagnation flow configuration can not be described by quasi one-dimensional codes. Instead a DNS study was done by using a second order, fully compressible code developed at CERFACS. The simulations were conducted for conditions that closely resemble those of the experiments. One-step chemistry that results in $S_u^o \approx 33$ cm/s for a $\phi = 1.0$ CH₄/air atmospheric flame was used. Special treatment of the boundary conditions was implemented in order to minimize the effect of numerical waves.

SUMMARY OF RESEARCH

Development of DPIV for flame studies

Measurements were confined very close to the flow centerline, and Fig. 1 depicts a particle image and corresponding velocity field for a jet exit velocity of $U_{\text{exit}} = 61.6$ cm/s. The particle image streaks represent a necessary compromise between spatial resolution and available light from the shuttered 2W A+ laser. The vector field shows dense coverage (the vectors are independent) and measurements that pass through the flame front. The maximum correlation peak location is independent of secondary peaks caused by the image of the flame front itself. No extra optical filter was required.

Figure 2a is a spline-interpolated reconstruction of the velocity field, which corrects for systematic bias in vector location due to particle displacements and also provides analytical calculation of spatial derivatives (and not grid-dependent finite differences). The development of the combined experimental/analytical technique has focused on the accurate determination of the minimum flow speed, $S_{u,\text{ref}}$, close to the flame front, and the maximum strain rate, $K \equiv -\partial U / \partial x$, occurring immediately before this point. Figure 2 depicts an example, where $S_{u,\text{ref}} = 27.6$ cm/s at $x = 1.55$ cm, and $\partial U / \partial x = -K = -107.3$ s⁻¹ at $x = 1.44$ cm. The data come from time-averaged ensembles of velocity profiles and are correct if and only if the flow is steady. The variation of $S_{u,\text{ref}}$ and K themselves within each time series can be used as diagnostics of this. For a given (ϕ, U_{exit}) pair, each experiment is conducted at least 4 times, each involving sequences of at least 15 time-steps. Figure 3 depicts 10 separate points, from analysis of approximately 600 velocity fields. The standard deviation in both $S_{u,\text{ref}}$ and K are shown, and accounts for most, but not all of the deviation from the linear least squares fit. Improvements and modifications to the experimental design (to increase seeding scattering efficiency and light intensity) are adapted to microgravity application of these techniques.

DNS of the Phenomenon of Transition from Planar to Bunsen Flames

Transient simulations were conducted for a nozzle diameter $D = 2$ cm and a nozzle-plate separation distance $L = 3.5$ cm corresponding to $L/D = 1.75$. A $\phi = 1.0$ atmospheric CH₄/air flame was modeled for U_{exit} 's ranging from 140 cm/s to 65 cm/s.

It was found that for large U_{exit} 's the flow is of the stagnation-type throughout the domain of interest. For low U_{exit} 's, however, it was found that the flow is hybrid between a near-jet flow close to the nozzle and a stagnation-type flow close to the stagnation plate. Furthermore, as the U_{exit} decreases from 140 cm/s to values higher than about 65 cm/s, the flame is stabilized as nearly planar and at greater distances from the stagnation plane. The shape of such flames was found to be in general planar but with a small concave curvature around the centerline and a stronger

convex curvature at larger radii. It was found that while the concave curvature around the centerline results from the radial pressure gradients of the stagnation-type flow, the shear layer that develops between the jet and the surrounding gas causes the convex curvature at the larger radii. The presence of the shear layer results in reduced flow velocities and the flame moves further upstream in order to be stabilized at locations at which its speed equals the local flow velocity. It should be noted that the DNS results also reveal that there is no noticeable fuel dilution within the immediate vicinity of the jet to cause local reduction of the flame speed.

For $U_{\text{exit}} = 65$ cm/s, however, the flame can not be stabilized at a given location and undergoes an unassisted transition to conical Bunsen flame, in close agreement with the experimental observations. The phenomenon of transition was captured numerically at different times and insight was provided into the underlying mechanisms. Analysis shows that when $U_{\text{exit}} = 65$ cm/s the radial pressure gradients that are responsible for the establishment of planar, stagnation-type flames are so weak that the effect of flame curvature at the edges of the jet, which tends to favor the Bunsen flame configuration, dominates. Thus, there is a gradual movement of the curvature towards the system centerline resulting eventually in a Bunsen-type flame.

During that transition the minimum pre-flame flow velocity, $S_{u,\text{ref}}$, was monitored and is shown in Fig. 4. It first decreases as the flame moves slightly downstream with a very low displacement velocity. This physically happens because the radial pressure gradients are very weak and the radial profile of the axial velocity becomes planar eliminating thus the flame curvature around the centerline. Then, and after reaching a minimum value, $S_{u,\text{ref}}$ starts increasing due to the combined effect of moving curvature and the significant displacement velocity. The DNS confirm that during the transition there is a state at which the $S_{u,\text{ref}}$ equals the true laminar flame speed S_u^0 . Detailed analysis of the numerical results reveal that both the strain rate and the total stretch (strain rate plus curvature) become zero at the state of $S_{u,\text{ref}} = S_u^0$. These results support the validity of the original thesis behind the proposed methodology for the direct measurement of S_u^0 [5].

REFERENCES

1. Peters, N., *Prog. Energy Combust. Sci.* 10, pp. 221-252 (1984).
2. Law, C.K., *Proc. Combust. Inst.* 22: 1381-1402 (1988).
3. Vagelopoulos, C.M., Egolfopoulos, F.N. & Law, C.K., *Proc. Combust. Inst.* 25: 1341-1347 (1994).
4. Egolfopoulos, F.N., *Proc. Combust. Inst.* 25: 1375-1381 (1994).
5. Vagelopoulos, C.M. & Egolfopoulos, *Proc. Combust. Inst.* 27: 513-519 (1998).
6. Zhang, H. & Egolfopoulos, F.N. "Extinction of Near-Limit Premixed Flames in Microgravity," by H. Zhang and F.N. Egolfopoulos, *Proc. Combust. Inst.* 28, in press.
7. Maruta, K., Yoshida, M., Ju, Y. & Niioka, T., *Proc. Combust. Inst.* 26: 1283-289 (1996).

ACKNOWLEDGMENTS

This work is supported by NASA (Grant NCC3-678) and under the technical supervision of Dr. Fletcher Miller of the Glenn Research Center

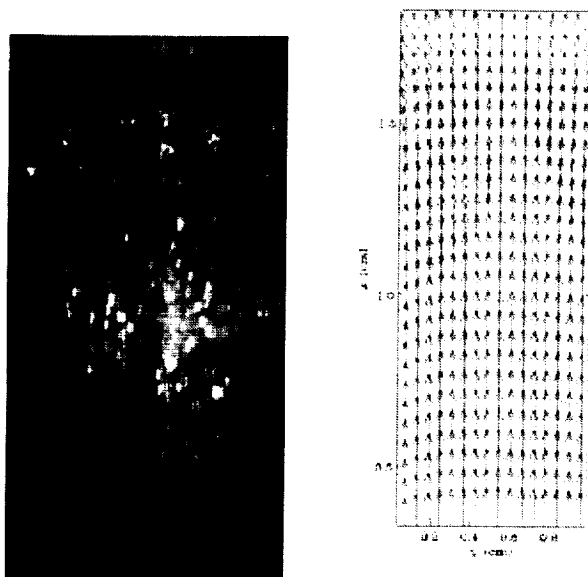


Figure 1. DPIV image and calculated velocity field for a $\phi=0.75$ flame close to the jet centerline.

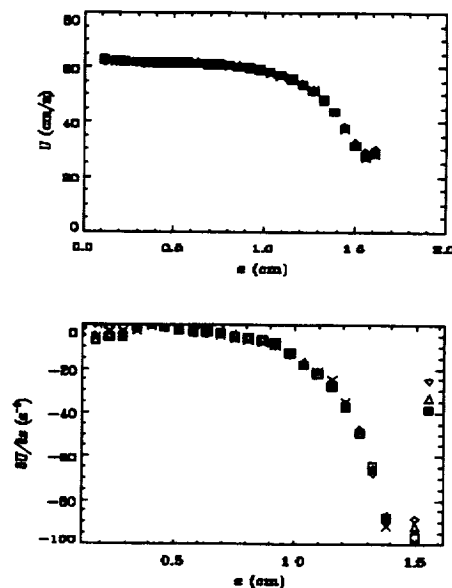


Figure 2. (a) $U(x)$ close to the jet centerline, and (b) $-K = \partial U / \partial x$ for a $\phi=0.75$ flame

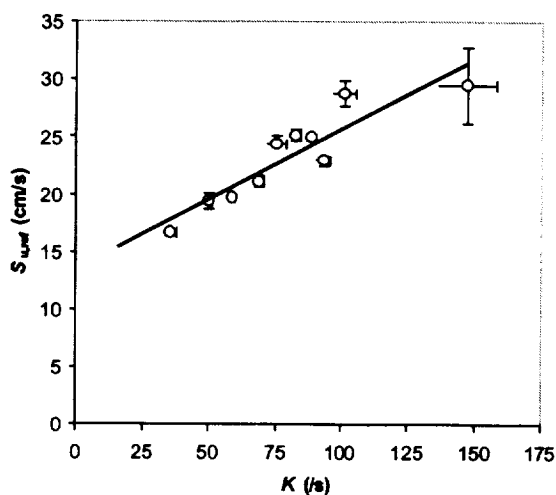


Figure 3. DPIV results for the variation of $S_{u,ref}$ with K for a $\phi=0.75$ flame

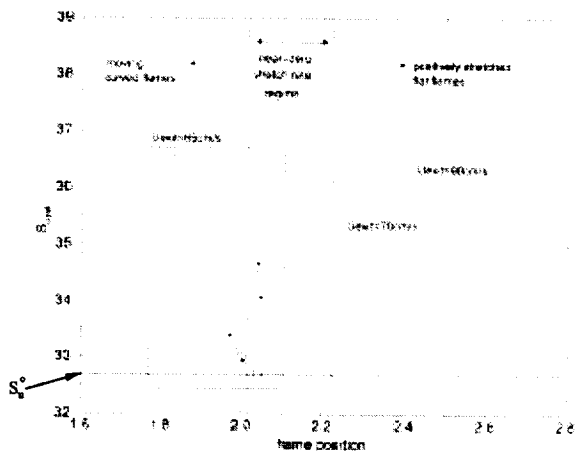


Figure 4. DNS results for the variation of $S_{u,ref}$ with flame position for a $\phi=1.0$ flame. Note the variation of $S_{u,ref}$ for the same $U_{exit} = 65$ cm/s and that the state for which $S_{u,ref} = S_u^0$ is achieved.

CHARACTERISATION OF A LAMINAR FLAT PLATE DIFFUSION FLAME IN MICROGRAVITY USING PIV, VISIBLE AND CH EMISSIONS

P. Joulain, P. Cordeiro,
Laboratoire de Combustion et de Détonique - UPR 9028 au CNRS
ENSMA – Université de Poitiers, BP 40109
86961 Chasseneuil Futuroscope Cedex
France

J. L. Torero
Department of Fire Protection Engineering
University of Maryland
College Park, MD, 20742 – 3031
USA

INTRODUCTION

Motivated by fire safety concerns and the advent of long-term micro-gravity facilities, a cooperative program has been developed to study the mechanisms and material properties that control flow assisted (co-current) flame spread. This program has used as a common fire scenario a reacting steady-state boundary layer. Preliminary studies explored the aerodynamics of a reacting boundary layer by simulating a condensed fuel by means of a gas burner. Stability curves for ethane air flames were obtained and different burning regimes were identified [1,2]. An important feature of this study was the independent identification of the different mechanisms leading to the instability of the flow. It was observed that fuel injection velocity and thermal expansion independently contributed to the separation of the flow at the leading edge of the burner. The occurrence of separation resulted in complex three-dimensional flow patterns that have a dominant effect on critical fire safety parameters such as the stand-off distance and flame length. This work was extended to a solid fuel (PMMA) [3] leading to a Sounding Rocket experiment (Mini-Texus-6) [4]. The solid phase showed similar flow patterns, mostly present at low flow velocities (<100 mm/s) but the results clearly demonstrated that the thermal balance at the pyrolyzing fuel surface is the dominant mechanism that controls both stand-off distance and flame length. This thermal balance could be described in a global manner by means of a total mass transfer or "B" number. This "B" number incorporates surface re-radiation, radiative feedback and in-depth heat conduction as first prescribed by Emmons [5]. The mass transfer number becomes the single parameter that determines the evolution of these fire safety variables (flame length, stand-off distance) and therefore can be used as a ranking criterion to assess the flammability of materials. The particular configuration is representative of the NASA upward flame spread test (Test 1 [6]) therefore this approach can be used in the interpretation of the results obtained from this test. Nevertheless, complete validation of this approach has not been fully achieved due, mainly because all the measurements necessary to compare with the theoretical predictions have not been obtained.

Following these studies two different directions have been taken. The first attempts to elucidate the details of the gas phase combustion reaction and the associated flow field by means of quantitative and qualitative measurements. The second approach, a more practical one, is to apply this methodology to the assessment of material flammability. The former is

currently being conducted with a gas burner because it allows for easier control and longer experimentation time. The results obtained so far will be presented in more detail. The latter is a new program therefore only a brief summary of the objectives will be presented.

CHARACTERIZATION OF THE LAMINAR DIFFUSION FLAME

The experiments are conducted in a test facility that involves a small scale, horizontally oriented, combustion tunnel along with the supporting instrumentation, already described elsewhere [2]. Ethane, 99.4% pure, is uniformly injected through a porous burner (50mmx50mm) mounted on the centre of the flat plate. Compressed air flows through a settling chamber before entering the test section. The air and fuel velocities are governed with controlled mass flow meters and varied respectively from 20 to 70 mm/s and 1 to 5 mm/s. Information on the flame and the flow is obtained from three CCD video cameras. A standard colour CCD video camera is used to obtain images of the visible flame. Hydrocarbon emissions are recorded with a high speed intensified CCD video camera, 50Hz, 256x256 pixels with an interferential filter centred at 532nm. And a high definition CCD video camera (1300x1000 pixels) is used for flow velocity measurements using PIV. For PIV measurements air is seeded with zirconium oxide 5 μ m particles illuminated by a 26mJ mini-YAG.

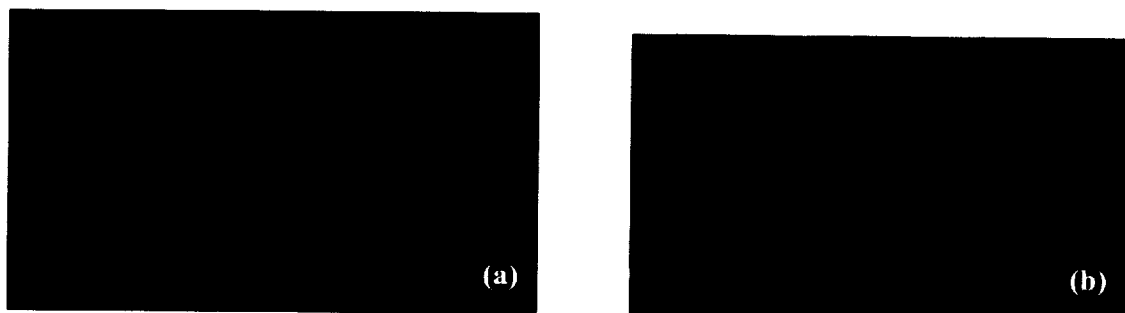


Figure 1 - Image obtained by a CCD camera of a flame for ethane-air and air velocity of 20 mm/s and a fuel velocity of 4 mm/s (a) visible flame (b) CH emission from the reacting zone.

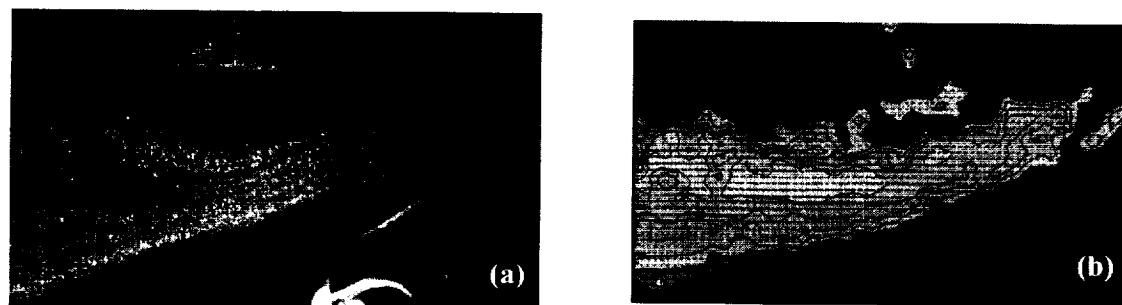


Figure 2 – (a) Image obtained by a CCD camera of the illuminated seeding particles for an ethane-air flame (air velocity of 20 mm/s and a fuel velocity of 4 mm/s) (b) corresponding velocity vectors after a PIV treatment.

The image of a flame obtained at the ZARM (5 sec.) Drop Tower is presented in Figure 1. The visible flame is presented in Figure 1(a) and Figure 1(b) shows the CH emission from the reacting zone. Figure 2 shows the corresponding velocity measurements.

Figure 2(a) shows an image of the particles captured by the CCD camera and Figure 2(b) shows the velocity vectors after PIV treatment. The example presented corresponds to an air velocity of 20 mm/s and a fuel velocity of 4 mm/s, with a $\Delta t = 4$ ms between two pictures. The ZARM drop tower in Bremen provides a stable gravity level of $10^{-5}g$ and the images presented were taken 3 s after the drop. For these low velocities at least 3 s are needed to completely annihilate the influence of the initial buoyancy forces. Therefore the image still shows perturbations of the flow above the flame. It is important to note that the area where the flame is present remains un-seeded, showing that the flames deflect the airflow. Figure 1 shows good coincidence between the visible flame and the recorded CH emissions, the CH zone being, as expected, slightly below the visible flame zone. The complete analysis of the different video and PIV recordings leads to a detailed description of the low velocity reacting flow, especially on the influence of the flame on the flow field. Furthermore, these measurements provide a better definition of the flame length and stand-off distance, since they allow to identify the presence of a reacting zone beyond the limits of the visible flame.

THE MASS TRANSFER NUMBER

The analysis of Test 1 equates the experimentally obtained stand-off distance for the upward propagating flame with the theoretical solution of an existing quasi-steady model of a reacting natural boundary layer. Comparison of theory [5] and experiments allows the determination of the evolution of the mass transfer number, B_T [4]. An expression for B_T was

first provided by Emmons [5] and is given by: $B_T = \frac{(1-\chi)(\Delta H_C Y_{O_2,\infty}) - Cp_\infty (T_{ig} - T_\infty)}{\Delta H_p + Q}$

where $Q = \frac{(\dot{q}_C + \dot{q}_{s,r} - \dot{q}_{f,r})}{\dot{m}_f}$, the heat fluxes correspond to in-depth conduction, surface re-

radiation and flame radiative feedback respectively. The denominator is the fuel mass production rate. The evolution of B_T can be obtained by matching the theoretical predictions to the experimental measurements of the stand-off distance. An example of this matching is shown in Figure 3.

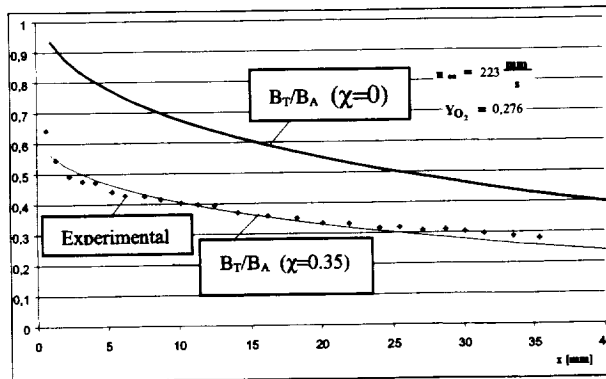


Figure 3 Variation of B_T/B_A as a function of the streamwise coordinate, x . The experimental data was extracted from Vietoris et al. [7].

Subsequently, three characteristic mass transfer numbers can be defined:

$$B_A = \frac{(\Delta H_C Y_{O_2,\infty}) - Cp_\infty (T_w - T_\infty)}{\Delta H_p}, \quad B_R = \frac{(1-\chi)(\Delta H_C Y_{O_2,\infty}) - Cp_\infty (T_{ig} - T_\infty)}{\Delta H_p} \quad \text{and}$$

$$B_C = \frac{(1-\chi)(\Delta H_C Y_{O_2,\infty}) - Cp_\infty (T_{ig} - T_\infty)}{\Delta H_p + Q_C}. \quad B_A \text{ and } B_C \text{ correspond to extreme values, the}$$

former being the resulting mass transfer number in the absence of all losses and the latter the lowest mass transfer number that can sustain a flame (non-propagation condition as defined by Test 1). Modelling of a fire using B_A will provide an estimate of the “worst possible scenario” and using B_C of the “best possible scenario.” B_R corresponds to a “realistic scenario” that includes heat exchange between the flames and the environment. A similar approach can be followed in normal and micro-gravity leading to the quantification of the same parameters. The theoretical analysis of both natural and forced flow problems has been available in the literature since the 70’s and leads to the same controlling parameters for both cases.

Evaluating independently all the properties involved in the mass transfer number (Heat of Combustion, Temperature and Heat of Pyrolysis) the theoretical value of B_A can be calculated. In a similar way, to obtain B_R , an effective heat of combustion needs to be determined and can be obtained by means of oxygen consumption calorimetry (Test 2 [6]). Estimation of the in-depth conduction and surface re-radiation by means of thermocouples and IR-Thermography provides the necessary information to compute B_C . Independent calculation of these “material properties” provides validation to this methodology.

Determination of these parameters is of great value for material selection and as criteria for the design of engineered materials since it provides a ranking criterion based on fundamental combustion principles. Furthermore, the definition of B_A , B_R and B_C allows to bound the possible evolution of a fire in a space facility and also serve as an estimate of the possible error.

ACKNOWLEDGEMENTS

This work has been funded in Europe by CNES and ESA and in the USA by NASA and the Minta Martin Research Foundation at the university of Maryland. The authors wish to acknowledge the support of personnel at ZARM for the performance of micro-gravity tests.

REFERENCES

- [1] Torero, J.L., Bonneau, L., Most, J.M. & Joulain, P., *Twenty-Fifth Symposium (International) on Combustion*, The Combustion Institute, 1701-1709, 1994.
- [2] Brahmi, L., Vietoris, T., Joulain, P. & Torero J.L., *Fourth International Microgravity Combustion Workshop*, May, 1997, p.99-104.
- [3] Vietoris, T., Joulain, P. & Torero J.L., *Fifth International Microgravity Combustion Workshop*, May 1999, NASA/CP-1999-208917, p.101-104.
- [4] Vietoris T., Ellzey, J.L., Joulain, P., Mehta, S.N. and Torero J.L., *Twenty-Eight Symposium (International) on Combustion*, The Combustion Institute, August 2000, Edinburgh (in press).
- [5] Emmons H. , *The Film Combustion of Liquid Fuel*, *Zeitschrift für Angewandte Mathematik und Mechanik*, Vol. 36, pp. 60, 1956.
- [6] “Flammability, Odor, Offgassing, and Compatibility Requirements and Test Procedures for Materials in Environments that Support Combustion” NASA-NHB 8060.1, 1981.
- [7] Vietoris, T., Joulain, P. and Torero, J.L., “Experimental Observations on the Geometry and Stability of a Laminar Diffusion Flame in Micro-Gravity,” *Sixth International Symposium on Fire Safety Science*, 1999.

THICKNESS EFFECTS ON FUEL FLAMMABILITY (TEOFF)

Paul Ferkul, Richard Pettegrew,
(National Center for Microgravity Research, Cleveland, OH),
And John Oerther (University of Michigan)

INTRODUCTION

The U-shaped flammability boundary for a thermally-thin fuel (defined as one where the rate of conduction into the depth of the fuel is much faster than the rate of conduction ahead of the flame through the gas phase) burning in low-speed flows has been well established.^{1,2,3,4} The importance of radiative loss is evident in leading to flame extinction when the flow velocity (or ambient oxygen concentration) is reduced sufficiently. This quenching extinction occurs when the flame power output decreases, and the radiative heat loss rate becomes a significant fraction of the flame power. Observation of the quenching extinction branch is only possible at microgravity, since otherwise any buoyant flow generated would take the system out of the low-speed flow regime. The blowoff branch can be studied in normal gravity.

The existence of a similar boundary, more specifically the quenching branch of this boundary, is hypothesized for fuels that are not thermally thin. For such fuels, heat conduction in the solid will become increasingly important as the thickness is increased, especially near the flammability limit.

For downward flame spread in normal gravity, the dominant mode of heat transfer is conduction through the solid for thick fuels, but conduction through the gas phase becomes more important as the thickness decreases.⁵ Near the blowoff limit, the gas-phase length scale becomes so small that conduction through the solid may again become significant.^{5,6} Thus, even though a fuel may be thermally-thin (conduction into the depth is fast), forward conduction through the solid may become important enough to affect the flame spread rate and flammability.

In a related study,⁷ fuel thickness effects on the blowoff branch of the flammability boundary were extrapolated using a variety of normal and microgravity opposed-flow data. Results suggested that in the near quenching regime (high Damkohler number), the effect of increasing fuel thickness would be to shift the flammability boundary towards higher flow velocities and oxygen concentrations (effectively making it less flammable). This is contrary to observations in the blowoff regime (low Damkohler number), where flame spread is enhanced as thickness increases since forward heat conduction through the solid can serve to help stabilize the flame.

In this new research effort, we began with an extremely thin fuel in order to provide the baseline for studying thicker materials in microgravity. In the course of our testing, it became evident that there was a discernible difference in burning for two different orientations. This provided a convenient way to assess the role of solid phase conduction for a thin fuel, for which it is deduced that solid conductivity in the two directions is substantially different.

The effect of fuel thickness and solid conductivity has applications to fire safety. Consider a flammability ranking for a set of materials with a given thickness. One can imagine that a different ranking may result for the same materials as the relative contribution of

conduction heat transfer changes for a different thickness. Furthermore, a real material that does not have isotropic properties may be more or less flammable depending on the direction in which it is burned. This has been shown in studies of wood combustion (thick fuels), where the assumption of constant thermal conductivity cannot be made, as typically its value along the grain is approximately twice that across the grain.⁸

NORMAL GRAVITY EXPERIMENTS

Individual sheets of tissue paper measuring 5cm wide by 17cm long were ignited on top using a hot wire and allowed to burn downward inside a combustion chamber.⁹ The igniter voltage was computer controlled so as to provide nearly the same ignition energy for each test. The resulting flame spread was recorded on videotape.

In preparing the thin, cellulosic fuel samples, it was noted that they tended to tear much more easily in one direction than the other. This suggested the individual fibers of the paper were generally aligned with the preferential tear direction, and furthermore that certain solid phase properties might be substantially different as well in the two directions. Thus, by examining burns in the preferential tear direction (parallel to the fibers) compared to those at right angles to it (orthogonal to the fibers) there was an easy way to determine how anisotropic thermal properties might affect flammability and flame spread. Ultimately, some insight into the fundamental importance of thermal conductivity for varying fuel thickness is sought.

While the thermal conductivity of the tissue paper samples in the two directions was not measured, the sample strength was substantially different (by about a factor of 2 or 3). With tension applied parallel to the general fiber orientation, the sample resists tearing much more than when it is stressed in the orthogonal direction. Thus, by analogy, conduction in the parallel orientation is presumed to be higher. Similarly, in the orthogonal direction, the fibers are more loosely intertwined on average, creating reduced conductivity through poorer surface contact. In the parallel direction, the fibers have greater extent on average providing a more direct conduction path. Note that at a casual glance, the tissue paper samples seem quite uniform in both directions.

Figure 1 is a representative plot of the flame base position as a function of time for all tests at the same condition. Both the parallel and the orthogonal tests are plotted, and it can be seen that the spread rates of the parallel samples are generally higher than those of the orthogonal tests.

Figure 2 shows a comparison of the average spread rates for both orientations for each of the tested pressure conditions. Error bars are displayed for the spread rate, while the width of the data symbol is greater than the error bars in the pressure axis (the uncertainties listed are typical for all of the test data). This plot shows a clear difference in the spread rate between the two orientations at lower pressures (very near the limit). At higher pressure, the difference between the two orientations is less evident.

Additional tests were performed at 1 atm. pressure, for several oxygen concentrations using both fuel orientations. The qualitative trend for these tests is similar to that seen in the reduced pressure tests: the parallel fiber orientation has a greater spread rate than the orthogonal direction. The difference in the spread rates increases as the oxygen concentration is reduced.

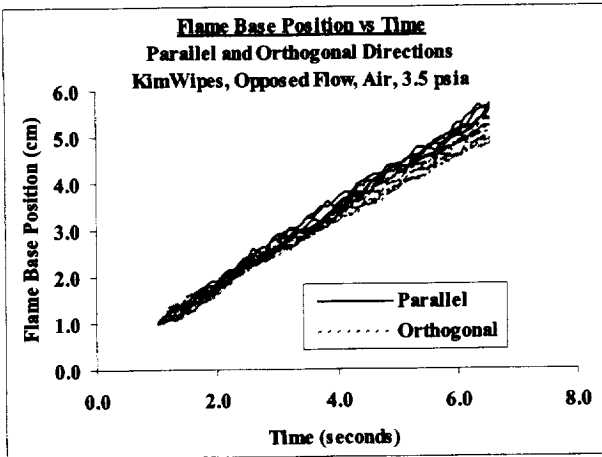


Figure 1

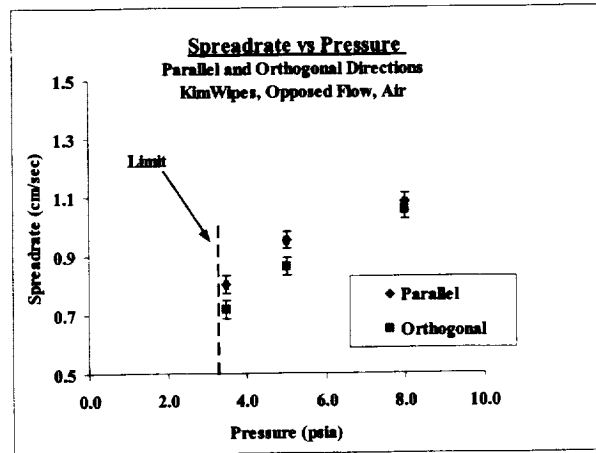


Figure 2

The flammability limit (with respect to oxygen) was also found to be lower for the parallel orientation (15.6% for parallel, 15.7% for orthogonal).

ZERO GRAVITY EXPERIMENTS

Tests were conducted in the NASA Glenn Research Center 5.18-sec Zero Gravity Facility. Two samples (same thin fuel used in the normal gravity experiments described above) were mounted in a combustion chamber; one was ignited in the parallel orientation and the other in the orthogonal. Quiescent, opposed-flow flame spread ensued. Differences in spread rate and flammability limit were sought. Given the time limitation of this drop tower, there were significant ignition transients evident. Nevertheless, there were differences for the two orientations.

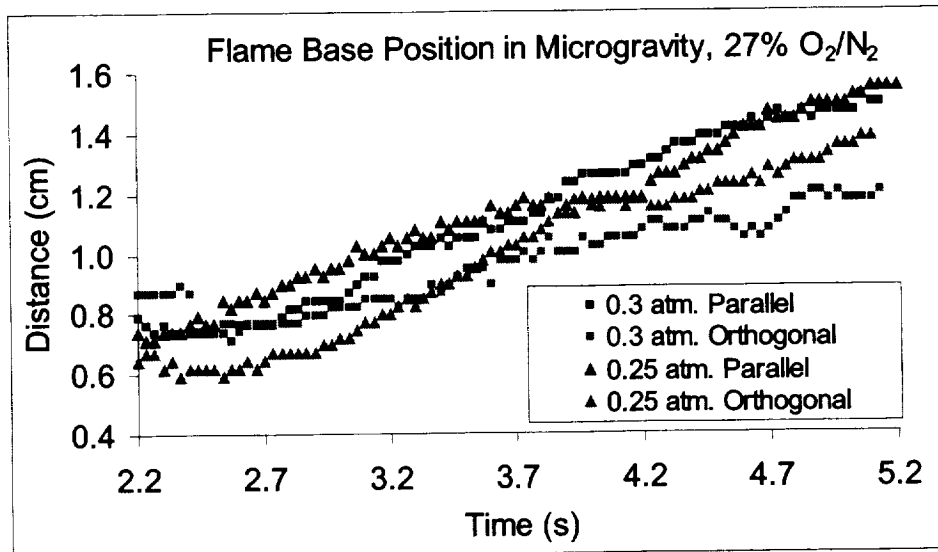


Figure 3 shows a sample of some of the data obtained. The spread rate variation in a 27% O₂/N₂ environment at reduced pressure is plotted. Consistent with normal gravity tests, the samples burning in the parallel orientation spread faster than the orthogonal ones. Furthermore, when the pressure was reduced to 0.22 atm., the parallel sample could be ignited while the orthogonal one could not. This suggests a difference in the limiting pressure for the two orientations. (Only the last 3 seconds of the drop are plotted, away from the ignition transient.)

DISCUSSION

Consider the ratio of thermal length scales, Λ , which is a measure of the importance of forward conduction heat transfer through the gas compared to the solid:⁹

$$\Lambda \equiv L_{\text{TH,G}} / L_{\text{TH,S}} = (\alpha_{\text{G}} V_{\text{F}}) / (\alpha_{\text{S}} U_{\text{R}}),$$

where L_{TH} is thermal length, α is thermal diffusivity, V_{F} is flame spread rate, U_{R} is characteristic gas-phase velocity, and subscripts "G" and "S" refer to the gas and solid phase, respectively.

For a typical thin fuel, Λ is large as most of the forward heat transfer occurs through the gas phase. (When the fuel is thermally thin, the gas-phase length scale is effectively "impressed" upon the solid fuel ahead of the flame.) However, as this ratio is reduced, the forward heat conduction through the solid phase becomes more important. For example, this occurs as the flow velocity U_{R} is increased near blowoff, as suggested by others.^{5,6,10}

Since Λ is inversely proportional to solid conductivity, it decreases as solid conductivity in the forward direction increases, hence suggesting that forward heat conduction through the solid phase becomes more important, especially near the flammability limit for these very thin fuels. Indeed, our results show that when the fuel is oriented such that forward heat conduction occurs in the direction of higher fuel conductivity (the parallel direction) a higher spread rate and lower flammability limit are achieved compared to the orthogonal orientation. This is true both for normal gravity blowoff and microgravity quenching extinction.

REFERENCES

1. Olson, S. L., Ferkul, P. V., T'ien, J. S. (1988): Near-Limit Flame Spread Over a Thin Solid Fuel in Microgravity, 22nd Symposium (International) on Combustion, The Combustion Institute, pp. 1213-1222 and NASA TM 100871.
2. Ferkul, P. V. and T'ien, J. S. (1994): A Model of Low-Speed Concurrent Flow Flame Spread Over a Thin Solid, Combustion Science and Technology, Vol. 99, pp. 345-370.
3. T'ien, J. S. and Bedir, H. (1997): Radiative Extinction of Diffusion Flames - A Review, Asia-Pacific Conference on Combustion, Osaka, Japan.
4. Sacksteder, K.R. and T'ien, J.S. (1995): A New Formulation of Damkohler Number for Studying Opposed Flow Flame Spread and Extinction, AIAA 33rd Aerospace Sciences Meeting, AIAA-95-0150.
5. Fernandez-Pello, A.C. and Santoro, R.J. (1978): On the Dominant Mode of Heat Transfer in Downward Flame Spread, 17th Symposium (International) on Combustion, The Combustion Institute, pp. 1201-1209.
6. Chen, C.H. (1986): Flame Propagation: Effect of Solid Phase Heat Conduction, Chemical and Physical Processes in Combustion, Fall Meeting.
7. Olson, S. L. (1991): Fuel Thickness Effects on Flame Spread and Extinction Limits in Low Gravity as Compared to Normal Gravity, Eastern States Technical Meeting of the Combustion Institute.
8. Roberts, A.F. (1971): Problems Associated with the Theoretical Analysis of the Burning of Wood, 13th Symposium (International) on Combustion, The Combustion Institute, pp. 893-903.
9. Ferkul, P., Pettegrew, R. D., and Kletecka, C. (2000): Effect of Sample Orientation on the Flammability of Thin Paper, AIAA 38th Aerospace Sciences Meeting, AIAA-2000-0846.
10. Frey, A.E. and T'ien, J.S. (1977) A Theory of Flame Spread Over a Solid Fuel Including Finite Rate Chemical Kinetics, Case Western Reserve University, FTAS/TR-77-134.

THREE-DIMENSIONAL UPWARD FLAME SPREADING IN PARTIAL-GRAVITY BUOYANT FLOWS

Kurt R. Sacksteder, NASA Glenn Research Center, Cleveland OH

Ioan I. Feier, Hsin-Yi Shih, and James S. T'ien, Case Western Reserve Univ., Cleveland OH

Introduction

Reduced-gravity environments have been used to establish low-speed, purely forced flows for both opposed- and concurrent-flow flame spread studies. Altenkirch's group obtained space-based experimental results and developed unsteady, two-dimensional numerical simulations of opposed-flow flame spread including gas-phase radiation, primarily away from the flammability limit for thin fuels, but including observations of thick fuel quenching in quiescent environments¹. T'ien's group contributed some early flame spreading results for thin fuels both in opposed flow^{2,3} and concurrent flow⁴ regimes, with more focus on near-limit conditions. T'ien's group also developed two- and three-dimensional numerical simulations of concurrent-flow flame spread incorporating gas-phase radiative models,^{5,6,7,8} including predictions of a radiatively-induced quenching limit reached in very low-speed air flows. Radiative quenching has been subsequently observed in other studies of combustion in very low-speed flows including other flame spread investigations,⁹ droplet combustion and homogeneous diffusion flames, and is the subject of several contemporary studies reported in this workshop.

Using NASA aircraft flying partial-gravity "parabolic" trajectories, flame spreading in purely-buoyant, opposed-flow (downward burning) has been studied.¹⁰ These results indicated increases in flame spread rates and enhanced flammability (lower limiting atmospheric oxygen content) as gravity levels were reduced from normal Earth gravity, and were consistent with earlier data obtained by Altenkirch using a centrifuge.¹¹

In this work, experimental results and a three-dimensional numerical simulation of upward flame spreading in variable partial-gravity environments were obtained including some effects of reduced pressure and variable sample width. The simulation provides physical insight for interpreting the experimental results and shows the intrinsic 3-D nature of buoyant, upward flame spreading. This study is intended to link the evolving understanding of flame spreading in purely-forced flows to the purely-buoyant flow environment, particularly in the concurrent flow regime; provide additional insight into the existence of steady flame spread in concurrent flows; and stimulate direct comparisons between opposed- and concurrent-flow flame spread. Additionally, this effort is intended to provide direct practical understanding applicable to fire protection planning for the habitable facilities in partial gravity environments of anticipated Lunar and Martian explorations.

Experiments

Upward flame spreading was observed in reduced-pressure air environments in normal-gravity and in partial-gravity environments using the GIFFTS test apparatus¹⁰ with slight modifications. Fig.1 shows the test apparatus. Fuel samples were a thin cellulosic tissue, trade name "Kimwipes," used by others.^{2,3,4,10} An improved, repeatable sample-drying procedure was developed using a hot-air gun. Test pressures between 0.2-0.4 atmospheres were established using primary standard, precision mixtures of 21% O₂, balance N₂. Flight tests were performed

onboard the NASA KC-135 aircraft providing partial-gravity environments of 0.1, 0.16, and 0.38 g_{earth} . Chamber pressure and 3-axis accelerations were recorded by the GIFFTS computer. Conventional video and a FSI Inc. Prism DS IR camera with a flame filter at $3.8\mu\text{m}$ (to reject emissions from H_2O , CO_2) were used to image the solid surface.

Numerical Flame Spread Simulation

A 3-dimensional model developed to simulate steady laminar flame spread and extinction over a thin solid fuel in low-speed forced concurrent flows⁸ was modified to simulate purely buoyant flow in partial-gravity and reduced-pressure environments. For the gas phase, full three-dimensional, steady, laminar Navier-Stokes equations for conservation of mass, momentum, energy and species (O_2 , N_2 , CO_2 , H_2O and fuel vapor) were solved. Gas-phase reactions were modeled using one-step, second-order Arrhenius kinetics. The thermally thin solid model consists of continuity and energy equations with a surface radiative loss ($\epsilon=0.92$) whose solutions provide the boundary conditions for the gas phase. Fuel pyrolysis is modeled as a one-step, zeroth-order Arrhenius process; manifested as shrinking fuel thickness. Gas-phase radiation was neglected at this stage of the buoyant model development.

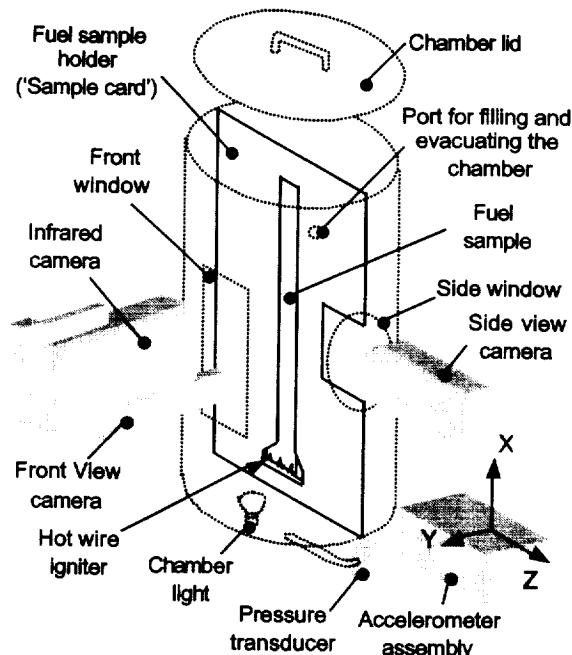


Figure 1. GIFFTS Apparatus Schematic: Combustion chamber (27 liter), thin stainless-steel sample-holder cards with 1,2 and 4 cm wide gaps for fuel exposure on both sides, conventional video imaging of the fuel surface and edge, infrared camera for imaging the fuel surface through a $3.8\mu\text{m}$ flame reject filter, a pressure transducer and 3-axis accelerometer. Samples are ignited using a resistively heated Kanthol alloy wire (approximately 100J ignition energy). An embedded computer controls the experiment operation and data acquisition sequence.

Results of Experiments and the Numerical Simulation

A more detailed summary of the experimental and numerical results can be found in reference 12. Figure 2 shows a comparison of a visible flame and the computed gas-phase reaction rates from the numerical simulation. The computed flames are longer than the experimental counterparts, but the shape of the experimental flames are well reproduced by the simulation. Experimentally, short flame shapes were steady and regular; longer flames exhibited oscillating tips and irregular shapes. Figure 3 shows a comparison of an image of the pyrolyzing fuel and the computed fuel thickness. In both cases, the downstream pyrolysis front is pointed, suggesting the three dimensional nature of the flames. Figure 4 shows comparisons between IR camera indications of fuel surface temperature and the computed values. The centerline temperature profiles in Fig. 4c are qualitatively similar; but the computed surface temperatures are higher than the equivalent blackbody temperature indicated by the camera detector. Surface emissivity less than unity would increase the temperatures indicated by the camera data, but the actual emissivity of partially pyrolyzed Kimwipes at elevated temperatures is not known. Figure 5 shows a comparison of measured and experimental pyrolysis and flame lengths for 2 cm wide samples burning at different gravity levels at 0.27 atm pressure. While the trend with gravity level is the same, the computed lengths are consistently longer than the measured values. (A pre-

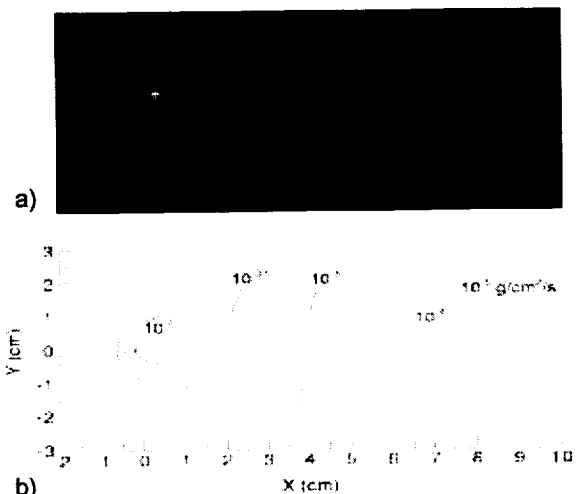


Figure 2. (a) Experimental and (b) numerical results showing upward flame spread over thin fuel samples 2cm wide in $0.16 \text{ g/g}_{\text{earth}}$ (g vector toward the left) and 0.27 atm pressure. Computed fuel reactivity contours shown are values integrated over the 3D flame width. Values of approximately $10^{-4} \text{ g/cm}^2/\text{s}$ correspond to the visible flame length.

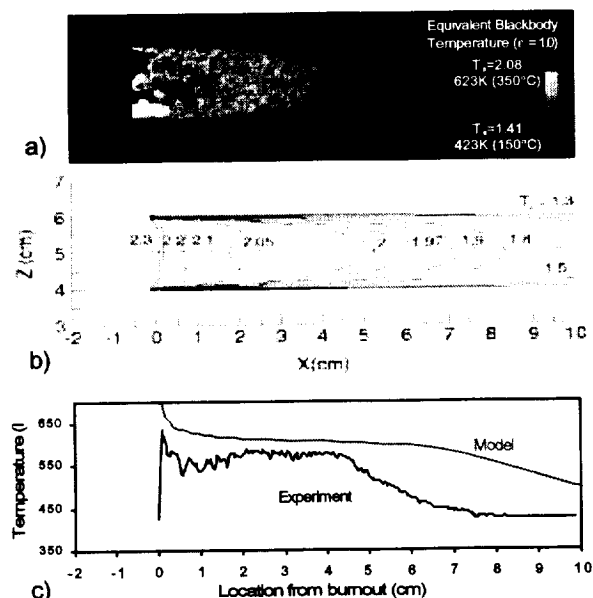


Figure 4. Comparison of (a) fuel surface infra-red image, (b) computed dimensionless fuel surface temperatures, and (c) centerline fuel surface temperatures from (a) and (b) for 2-cm wide fuel burning in $0.16 \text{ g/g}_{\text{earth}}$ and 0.27 atm pressure. The IR camera reports equivalent blackbody temperatures, and its sensitivity limits the lowest detectable temperature to 423K.

fuel. In this buoyancy-driven case, flow is induced by density gradients and accelerates inside the flame from 10cm/s just upstream of the flame to 60 cm/s downstream. In purely forced-flow, the downstream flames and streamlines diverge from the fuel,^{4,5} unless the flow is confined by a

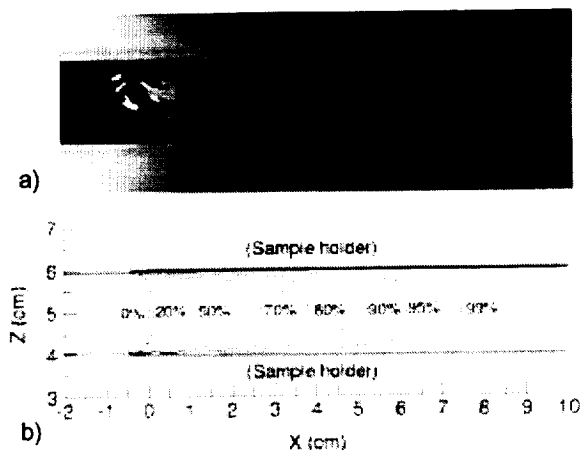


Figure 3. (a) Experimental and (b) numerical results showing the visible degradation of the fuel compared to computed fuel thickness contours for upward flame spread over thin fuel samples 2cm wide in $0.16 \text{ g/g}_{\text{earth}}$ (g vector toward the left) and 0.27 atm pressure. Computed fuel thicknesses of approximately 95% of the unburnt fuel correspond to the onset of visible discoloration.

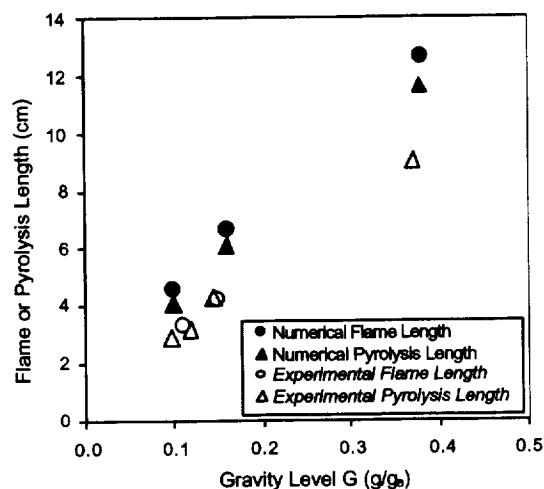


Figure 5 Comparison of experimental and computed flame and pyrolysis lengths of 2 cm wide samples burning at 0.27 atm pressure in various gravity levels.

vious 2-D flame-spread simulation,⁶ showed that including flame radiation shortens the flame and pyrolysis lengths in low-speed flow with little affect on spread rates.) Figure 6a shows computed results in a plane perpendicular to the fuel surface. Downstream, the temperature contours are nearly parallel to the

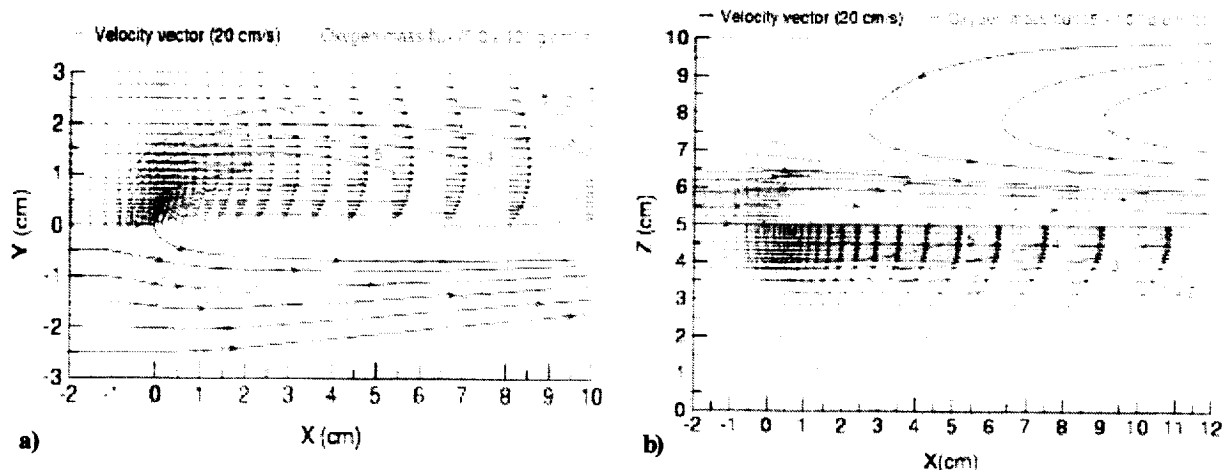


Figure 6. Flame structure and flow field in two-dimensional slices through an upward spreading flame over a 2cm wide sample in $0.16g/g_{earth}$, 0.27atm pressure, oriented a) perpendicular to fuel surface and b) parallel to and 1 cm above the fuel surface. In a), the top half of the image shows velocity vectors, non-dimensional temperature ($T=1$ is 300K). Bottom half shows streamlines, oxygen mass flux vectors, and fuel reaction rate contours (10^{-3} , 10^{-4} , 10^{-5} g/cm³/s from smallest to largest contour.) In b), the data presentation is reversed. Note the characteristic buoyant velocity profile in a), with the local peak inside the flame, and in b) the lateral entrainment of air and the substantial diffusion of oxygen across the streamlines.

small wind tunnel.^{7,8} Figure 6b shows computed results in a plane parallel to and offset by 1cm from the fuel surface. In the purely buoyant flow, the gas accelerates throughout the length of the flame, entraining air from the sides and pulling the streamlines toward the central plane. Flow recirculation occurs beside the flame. Oxygen diffuses into the flame from the side at fluxes comparable to the convective oxygen stream. The entrainment, recirculation and lateral diffusion could not be observed in a two-dimensional simulation. Although not shown here, the computed flame spread rates closely predicted corresponding experimental rates. The simulation predicted significantly wider flammability limits than were observed in the experiments. As forced-flow simulations have shown,⁷ flame and pyrolysis lengths shrink and flammability limits narrow when gas-phase radiation is included in the flame spread simulations. Better agreement between the experimental and simulation results can be expected once the existing gas radiation model is coupled to the 3D buoyant code. Despite this limitation, the model shows agreement with the flame behavior trends that were experimentally observed.

References

1. Sacksteder, K.R., ESA SP-454, 1st Int. Symp. Microg. Res. & Appl., Sorrento, Italy, (2000).
2. Olson, S.L., Ferkul, P.V., and T'ien, J.S., Proc. Combust. Inst. Vol. 22, pp.1213-1222 (1988).
3. Olson, S.L., Comb. Sci. Tech., Vol. 76, pp. 233-249, (1991).
4. Grayson, G.D., Sacksteder, K.R., Ferkul, P.V., T'ien, J.S., Microg. Sci. Tech. VII-2 (1994).
5. Ferkul, P.V., and T'ien, J.S., Vol. 99, pp. 345-370 (1994).
6. Jiang, C.B., T'ien, J.S. and Shih, H.Y., Proc. Combust. Inst. Vol. 26, pp.1353-1360 (1996).
7. Shih, H.Y. and T'ien, J.S., AIAA 97-0236, 35th Aerospace Sciences Meeting, (1997).
8. Shih, H.Y. and T'ien, J.S. Proc. Combust. Inst. Vol. 28, to appear.
9. Honda, L. K. and Ronney, P. D., Proc. Combust. Inst. Vol. 28, to appear.
10. Sacksteder, K.R., and T'ien, J.S., Proc. Combust. Inst., Vol. 25, pp. 1685-1692 (1994).
11. Altenkirch, R.A., Eichorn R., Shang, P.C., Combust. Flame, Vol. 37, pp. 71-83 (1980).
12. Feier, I.I., Shih, H-Y, Sacksteder, K.S., and T'ien, J.S., AIAA-2001-0466, 39th Aerospace Sciences Meeting, (2001).

LASER VELOCIMETER FOR STUDIES OF MICROGRAVITY COMBUSTION FLOWFIELDS

P. L. Varghese, PI

J. Jagodzinski, Graduate Student

Center for Aeromechanics Research

University of Texas at Austin, Austin, TX 78751-1085

INTRODUCTION

We are currently developing a velocimeter based on modulated filtered Rayleigh scattering (MFRS), utilizing diode lasers to make measurements in an unseeded gas or flame. MFRS is a novel variation of filtered Rayleigh scattering, utilizing modulation absorption spectroscopy to detect a strong absorption of a weak Rayleigh scattered signal. A rubidium (Rb) vapor filter is used to provide the relatively strong absorption and semiconductor diode lasers generate the relatively weak Rayleigh scattered signal. Alkali metal vapors have a high optical depth at modest vapor pressures, and their narrow linewidth is ideally suited for high-resolution velocimetry; the compact, rugged construction of diode lasers makes them ideally suited for microgravity experimentation. Molecular Rayleigh scattering of laser light simplifies flow measurements as it obviates the complications of flow-seeding. The MFRS velocimeter should offer an attractive alternative to comparable systems, providing a relatively inexpensive means of measuring velocity in unseeded flows and flames.

Filtered Rayleigh scattering is an established technique for measuring flow velocity and thermodynamic properties in a gas or flame. We improve the detectability of the weak Rayleigh scattered signal by using modulation techniques, utilizing the tunability of diode lasers to implement heterodyne detection.¹ The injection current, and hence the frequency, of the diode laser is dithered at the rate of several kHz. The high frequency modulation results in a modulated absorption through the rubidium filter in a reference and a scattering arm, and a corresponding modulation appears in the detector outputs that are fed into two separate lock-in amplifiers. If these lock-in amplifiers are synchronized with the function generator that drives the frequency modulation, then very high levels of background rejection are possible since the lock-ins are both frequency and phase selective.²

Two basic modes of operation have been devised for the MFRS velocimeter: the sweep mode of operation and the frequency-locked mode of operation.³ In sweep mode of operation the laser is tuned relatively slowly across the entire profile of the rubidium D₂ transition (approximately 11 GHz centered at 780 nm), while simultaneously dithering the frequency. In preliminary experiments the lock-in amplifier was set to extract the 2nd-harmonic of the modulation frequency ($2f$ detection). The Doppler frequency shift due to velocity in the probe volume is measured by cross-correlating the shifted $2f$ scattering profile to the $2f$ reference profile. The S/N is poor for Rayleigh scattering measurements, and so the lock-in output time constant has to be relatively long to collect reliable data. The sweep period must be correspondingly increased, which is the primary disadvantage of the sweep mode of operation. In preliminary investigations of the sweep mode of operation, with 25 mW of laser power in the probe volume an output time constant of at least 100 ms was required to measure the Rayleigh scattered signal reliably. Ideally the ramp period should be much longer than the output time constant, and modulation period much less. With this time constant, ramp frequencies greater than 0.1 Hz distorted the profile, and so the temporal resolution of the MFRS velocimeter was limited to 10 s.

An alternative to sweeping the laser across the Rb D₂-profile is to tune the diode to the edge of one of the Doppler broadened components in the multiplet and lock the laser to a desired frequency while modulating about this frequency. A shift in the Rayleigh scattered frequency due to changes in Doppler shift would result in a change in absorption and thus in the magnitude of the $2f$ signal. There is additional experimental complexity in the frequency-locked mode of operation, because of the need to stabilize the laser and to account for density fluctuations in the probe volume. A drift in laser frequency would be misinterpreted as a Doppler frequency shift of the Rayleigh scattered signal and attributed to a change in flow velocity. In addition, in the frequency-locked mode of operation the velocity can only be correlated to the amplitude of the filtered Doppler-shifted Rayleigh scattered signal provided that scattering intensity fluctuations due to density fluctuations are normalized out.

An extended-cavity diode laser (ECDL) is currently being built to obviate difficulties associated with preliminary attempts to stabilize a free-running diode. Specifically, we are building an ECDL that uses a grazing-incidence diffraction grating as the wavelength selective element.^{4,5} Laser power in the probe volume is a concern since the power output from ECDLs is practically limited to < 50 mW. We therefore intend to inject the cavity output into an AR-coated broad stripe diode (P=1.5 W). The resulting extended cavity diode laser master oscillator power amplifier (ECDL-MOPA) system should provide frequency stable, single-mode, relatively high power lasing for the MFRS velocimeter in frequency-locked mode of operation.

We are also currently developing a ratioed detection scheme for the Rayleigh scattered signal that will provide a frequency reference that is independent of the signal intensity. The Rayleigh scattered signal from the photomultiplier tube (PMT) in the scattering arm is output to two separate lock-in amplifiers. The outputs from the lock-in amplifiers, each set to extract a different harmonic of the modulated signal from the PMT, are ratioed, resulting in a frequency dependent, scattering-intensity independent signal. In essence, we extract different Fourier components of the modulated signal and ratio them.

EXPERIMENTAL SETUP

The experimental setup for the sweep mode of operation is shown in Figure 1. The single-mode GaAlAs diode (Hitachi HL7851), mounted in a diode laser head (ILX Lightwave LDM-4420), is excited with an ultra-low noise current controller (ILX Lightwave LDX-3620) that is specified to be stable to ≤ 10 ppm over 10-30 minutes. The temperature of the diode was controlled with a spectroscopic grade thermoelectric temperature controller (ILX Lightwave LDT-5910B) with a long-term stability of less than $\pm 0.01^\circ\text{C}$. Dry nitrogen is bled into the laser head to prevent condensation during operation. The diode emits at 780 nm when operating at approximately 125 mA and -3°C with a linear tuning rate of approximately -2.1 GHz/mA. Therefore, a triangular current ramp of amplitude 5 mA scans repetitively across the entire hyperfine structure of the D₂ line that extends over approximately 10.5 GHz at Doppler limited resolution. A good compromise between lock-in signal strength and profile resolution was established with a modulation current amplitude of 0.20 mA. The modulation sine wave and triangular sweep are produced by separate function generators (Exact 200MSP and Stanford Research Systems DS345) and combined in a summing amplifier (Stanford Research Systems SR560) before input to the current driver.

The laser beam is collimated and a small portion (< 1%) of the beam is split off to a reference arm, and passes through a 10 cm long room temperature cell containing Rb vapor in natural isotopic abundance (72.2% ^{85}Rb and 27.8% ^{87}Rb) before being recorded by an avalanche

photodiode (Hamamatsu C5460). The majority of the laser beam passes to the probe volume. A series of six anti-reflection coated lenses are used to collect the scattered light from the probe volume and relay it through a Rb cell identical to that in the reference arm, a ± 1 nm narrow-band filter (Barr Associates) and focus it onto a side-looking PMT (Hamamatsu R636-10). The PMT is biased at ~ 1000 V to give good radiant sensitivity while maintaining a linear response. The narrow band filter greatly reduces interference from ambient light while passing the Rayleigh scattered signal with high efficiency (80% peak transmittance). For these preliminary experiments we chose standard off-the-shelf lenses for the scattering arm optics. The lenses were chosen with the help of OSLO LT freeware, with a design objective of filling the PMT photocathode with high transmission efficiency. The collection F/# of ~ 1.2 was achieved using a pair of 100mm diameter, 120.8 mm focal length plano-convex lenses (Melles Griot LPX215/076).

Two lock-in amplifiers (Stanford Research Systems SR830) are synchronized with the modulation signal and run in $2f$ mode so that their output approximates the 2^{nd} -derivative of the

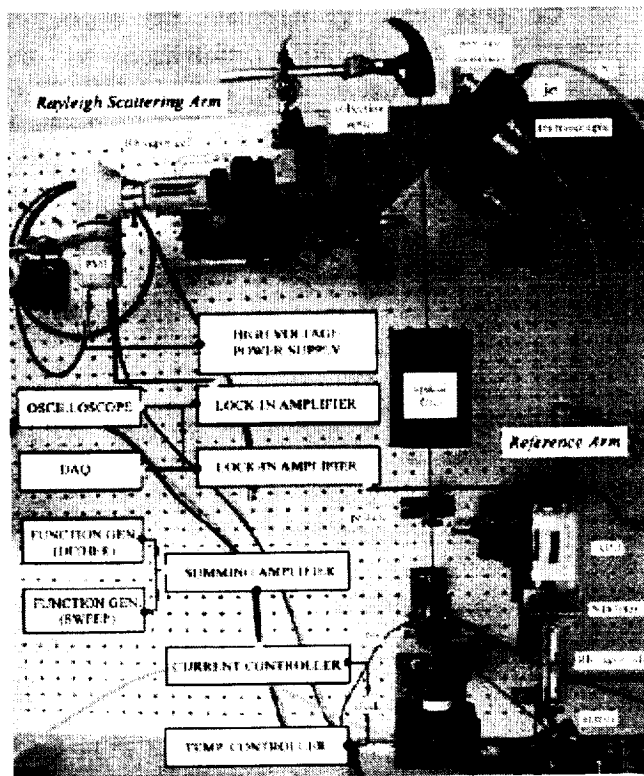


Figure 1. MFRS experimental setup.

Rb D_2 -profile. The lock-in output signals are digitized with a 1.25 Msample/s, 12-bit National Instruments data acquisition board (PCI-MIO-16E-1). A virtual instrument (VI) was developed with National Instruments LabView G-programming language to trigger acquisition and save the acquired profiles to a binary file.

In the frequency-locked mode of operation, the reference arm is used to lock the ECDL-MOPA system to the edge of some feature in the absorption profile. A proportional-integral-differential (PID) controller was built, and will eventually stabilize the ECDL-MOPA system at the zero crossing of this edge. The error signal due to drift in laser frequency is fed back to a piezoelectric transducer that tunes the wavelength selective element in the cavity. One additional lock-in amplifier in the scattering arm completes the required modifications for operation of the MFRS velocimeter in frequency-locked mode.

RESULTS

We have demonstrated measurement of gas velocity in an unseeded nitrogen jet.³ Velocity measurements were made nominally 9 nozzle diameters (28 mm) downstream of a converging nozzle. The geometry of the velocimeter was set to measure the axial velocity of the jet. A post-processing VI was written to cross correlate the signal and reference profiles, and to convert the Doppler frequency shift to a velocity measurement. Figure 2 shows a sample screen from this VI after post-processing a series of velocity measurements obtained during a single run. The sweep frequency for this run was 0.1 Hz and the laser was swept through approximately 4 GHz to cover

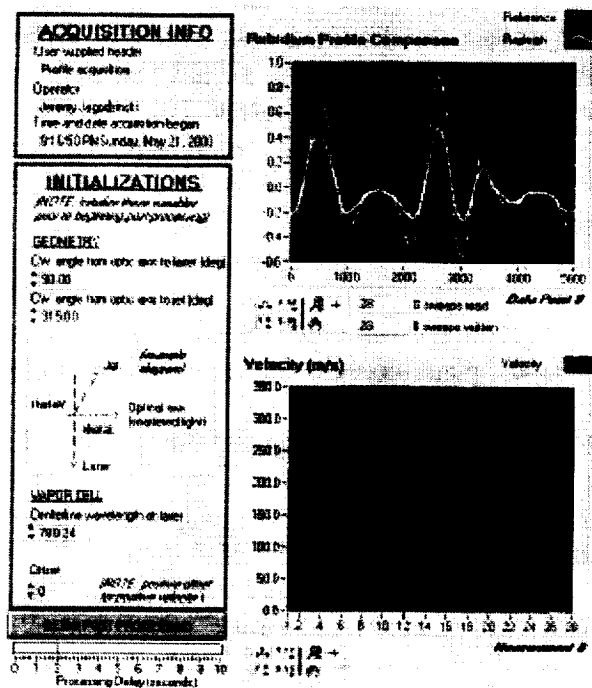


Figure 2. LabView post-processing routine

CONCLUSIONS

We have demonstrated preliminary velocity measurements in an unseeded nitrogen jet by MFRS. The current spatial and temporal resolution are limited to ~ 5 mm and 10 s respectively, and work is in progress to improve the system performance.

ACKNOWLEDGMENT

This work was initiated with sponsorship from the Texas Advanced Technology Program under grant 003658-454 and continued with support from the National Science Foundation under grant CTS-9871249 and by NASA under grant NAG3-2240.

REFERENCES

1. C. E. Weiman and L. Hollberg, "Using diode lasers for atomic physics," *Rev. Sci. Instr.* **62**(1), pp. 1-20 (1991).
2. Stanford Research Systems, "Application note #3: About lock-in amplifiers," Scientific and Engineering Instruments Catalog (1998-1999).
3. J. Jagodzinski and P. L. Varghese, "Velocity measurements by modulated filtered Rayleigh scattering using diode lasers," AIAA Paper 2001-0848, 39th AIAA Aerospace Sciences Meeting, Reno, NV (2001).
4. I. Shoshan, N. N. Danon, and U. P. Oppenheim, "Narrowband operation of a pulsed dye laser without intracavity beam expander," *J. Appl. Phys.* **48**(11), pp. 4495-4497 (1977).
5. M. G. Littman and H. J. Metcalf, "Spectrally narrow pulsed dye laser without beam expander," *Applied Optics* **14**, pp. 2224-2227 (1978).

the two strong absorption features of ^{85}Rb that are separated by about 3 GHz. The reduced sweep range enables the profile to be scanned with lower distortion for a given sweep rate. The laser frequency was modulated at the rate of 2 kHz with a modulation amplitude of approximately 300 MHz and the lock-in output time constant was set to 100 ms.

The plenum pressure and temperature were recorded manually for each laser sweep (duration 10 s). A relatively rapid acceleration is provided by a 12.5 mm (1/2-in) radius of curvature up to the throat of the converging nozzle, and isentropic expansion was assumed in the core flow to calculate the maximum theoretical velocity for comparison to the measured velocity. In these preliminary experiments with molecular Rayleigh scattering the imaged length of the probe volume is estimated to be ~ 5 mm so the measurements average over flow gradients and cannot be directly compared to a calculated jet velocity field.

PIV MEASUREMENTS IN WEAKLY BUOYANT GAS JET FLAMES*

Peter B. Sunderland¹, Paul S. Greenberg², David L. Urban²,

Mark P. Wernet³, and William Yanis⁴

¹PI, NCMR, ²Microgravity Combustion Branch,

³Optical Instrumentation Technology Branch, ⁴NCMR

NASA Glenn Research Center

INTRODUCTION

Despite numerous experimental investigations, the characterization of microgravity laminar jet diffusion flames remains incomplete. Measurements to date have included shapes, temperatures, soot properties, radiative emissions and compositions, but full-field quantitative measurements of velocity are lacking (Law and Faeth 1994). Since the differences between normal-gravity and microgravity diffusion flames are fundamentally influenced by changes in velocities, it is imperative that the associated velocity fields be measured in microgravity flames. Velocity measurements in nonbuoyant flames will be helpful both in validating numerical models and in interpreting past microgravity combustion experiments.

Pointwise velocity techniques are inadequate for full-field velocity measurements in microgravity facilities. In contrast, Particle Image Velocimetry (PIV) can capture the entire flow field in less than 1% of the time required with Laser Doppler Velocimetry (LDV). Although PIV is a mature diagnostic for normal-gravity flames (Mungal et al., 1995; Goss et al., 1991), restrictions on size, power and data storage complicate these measurements in microgravity (Kato et al., 1998).

Results from the application of PIV to gas jet flames in normal gravity are presented here. Ethane flames burning at 13, 25 and 50 kPa are considered. These results are presented in more detail in Wernet et al. (2000). The PIV system developed for these measurements recently has been adapted for on-rig use in the NASA Glenn 2.2-second drop tower.

EXPERIMENTAL METHODS

Burner Configuration

The PIV measurements were conducted inside a windowed pressure vessel with optical access for introducing the laser light sheet and imaging the scattered light. The chamber is 53 cm long by 25 cm diameter. A vacuum pump was used to maintain the pressure in the chamber and remove product gases during the tests.

The tests were conducted at pressures of 13-50 kPa. These low pressures were selected to minimize flame flicker and to allow consideration of flames of varying levels of buoyancy.

The burner was a 75 mm long stainless tube with an inside diameter of 1.5 mm. This length ensured fully developed laminar flow at the jet discharge. The burner was placed on the chamber centerline and oriented so that its tip was within the view of the PIV camera. Mass flow controllers regulated the ethane and air streams. Most of the air was unseeded and entered the chamber bottom through a small frit. The remainder of the air was seeded and was supplied via a 22 cm diameter ring of 9.5 mm diameter tubing. The ring was perforated with twenty 1 mm holes and was mounted just above the bottom of the chamber.

*Presented at the Sixth International Microgravity Combustion Workshop, Cleveland, 2001.

PIV Technique

A dual head mini-Nd:YAG laser operating at 532 nm was used to generate 50 mJ pulses. A 50 mm by 100 μ m light sheet was generated using a 25 mm cylindrical and a 300 mm spherical lens.

A 1000x1000 pixel Kodak ES 1.0 camera equipped with a 50 mm Schneider lens (set at f/5.6) was used to record the PIV image data. An interference filter (532 \pm 10 nm) was used to attenuate the flame luminosity. The first exposure had a 250 μ s integration period to limit the influence of flame luminosity. The second frame was integrated for 33 ms (while the first frame was being read from the sensor), which yielded an image of both the seed particles and the flame. The scale of the images was 53 μ m/pixel, corresponding to a magnification of 0.17.

TSI's Insight software and Synchronizer were used to control and synchronize the laser and camera. Image frame pairs were obtained by straddling adjacent frames, allowing acquisition of independent vector maps at 15 Hz. A digitizer was used to acquire image data in 200 image sequences. The present results were obtained by averaging 100 frames, yielding estimated velocity uncertainties of \pm 1% near the flame centerline and somewhat higher uncertainties elsewhere.

The data were cross-correlation processed using 32x64 pixel subregions with r and z spacings of 16 and 32 pixels, respectively, corresponding to grid point separations of 0.85x1.7 mm in the velocity vector maps. The analysis of the present PIV images uses the correlation software of Wernet (1999) and is discussed in detail in Wernet et al. (2000).

Seeding

The seed particles for the present tests were 2.5 μ m silica particles. One seeder was used for the fuel gas and another was used for the air entering the perforated ring. Microgravity rules out traditional seeders such as fluidized or packed beds, which can produce uncontrolled or overseeded conditions in microgravity (Greenberg et al., 1997). Prior work in the microgravity facilities at NASA Glenn demonstrated the viability of orifice-inlet seeders (Greenberg et al., 1997). By introducing gas into the seeder via a small orifice, sufficiently high velocities are generated for controllable particle entrainment.

The most difficult region to seed was the outer edge of the flame, where thermophoresis deflected many particles. Despite low seed concentrations, we were able to obtain velocities in this region.

RESULTS AND DISCUSSION

PIV data were collected at 3 ambient pressures: 13, 25 and 50 kPa. The ethane flow was maintained at 1.9 mg/s for all conditions. The air flow was 160 mg/s for the 25 and 50 kPa cases, but was reduced to 120 mg/s for the 13 kPa case to minimize turbulence in the ambient air.

The flow streamlines computed using the PIV data show that the ambient air in the chamber was disturbed owing to the nonuniformities in the air supply which will be corrected in future work. The measured burner exit velocities were generally higher than expected for fully-developed flow at 300 K, indicating that the burner gas was heated above ambient temperature.

The processed PIV velocity vector map for the 50 kPa flame is shown in Figure 1. The burner location is shown. The flame shapes have been included to show the location and extent of the flame. Streamlines have been determined from the measured velocities and are overlaid on the flow field. The streamline starting points are roughly equally spaced at the upstream boundary. The 50 kPa flame was observed to be slightly flickering.

The flow centerline velocities are plotted as a function of height above the burner in Figure 2. The 25 and 50 kPa flames exhibit centerline velocities which are affected by buoyancy. Only the 50 kPa flame has accelerating flow near its tip.

The PIV system described here has been reassembled on a rig suitable for testing in the 2.2-second drop tower.

ACKNOWLEDGMENTS

This work was supported by NASA RTOP 101-12-0A.

REFERENCES

- Goss, L.P., Post, M.E., Trump, D.D., and Sarka, B. (1991), "Two-Color Particle Image Velocimetry," *J. of Laser Applications*, winter, pp. 36-42.
- Greenberg, P.S., Griffin, D.W., Weiland, K.J., and Yanis, W. (1997), "Selected Diagnostics for Microgravity Combustion Science;" *Fourth International Workshop on Microgravity Combustion*, Cleveland, pp. 275-280.
- Kato, H., Kunieda, S., Enomoto, H., Okai, K., Kaneko, T., Chauveau, C., Gökalp, I., Sato, J., Tsue, M. and Kono, M. (1998), "Effects of Co-Flowing Air on Behavior of Gas Jet Diffusion Flames Under Normal- and Micro-gravity Fields," Drop Tower Days, JAMIC, paper 12-B-11, Sapporo, Japan.
- Law, C.K. and Faeth, G.M. (1994), "Opportunities and Challenges of Combustion in Microgravity," *Prog. Energy Combust. Sci.* 20:65.
- Mungal, M.G., Lourenco, L.M., and Krothapalli, A. (1995), "Instantaneous Velocity Measurements in Laminar and Turbulent Premixed Flames Using On-Line PIV," *Combust. Sci. Technol.*, 106:239.
- Wernet, M.P. (1999), "Fuzzy Logic Enhanced Digital PIV Processing Software", 18th *International Congress on Instrumentation for Aerospace Simulation Facilities*, Toulouse, France.
- Wernet, M.P., Greenberg, P.S., Sunderland, P.B., and Yanis, W. (2000), "A PIV Investigation of Weakly Buoyant Laminar Jet Diffusion Flames," AIAA-2000-0694, Reno.

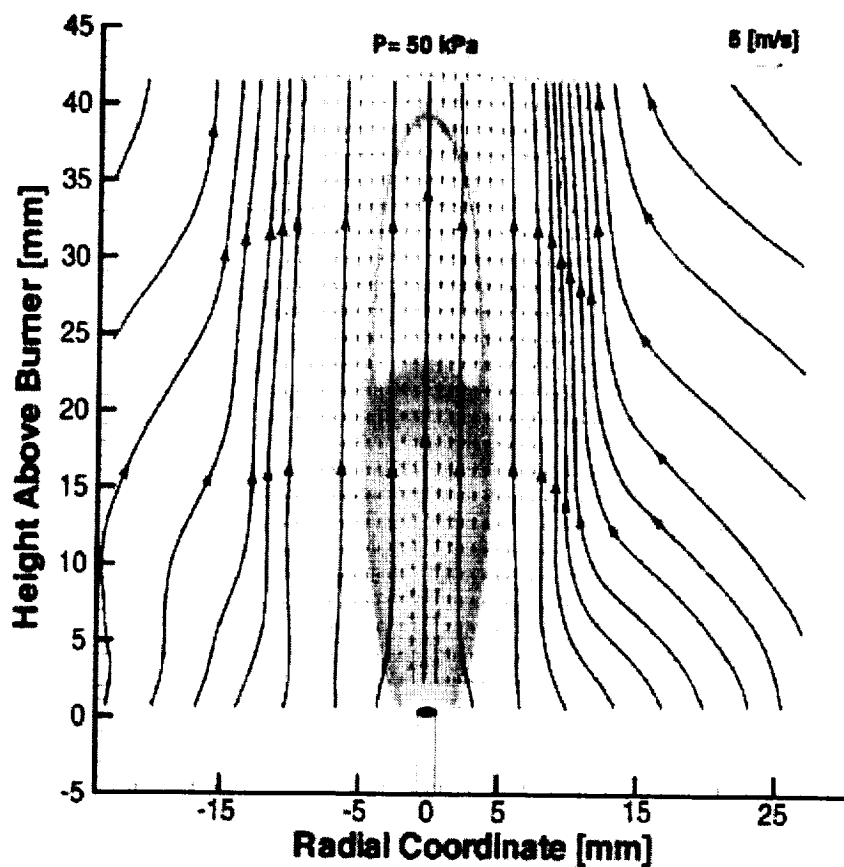


Figure 1. Velocity vectors, streamlines, and flame outline for the 50 kPa flame.

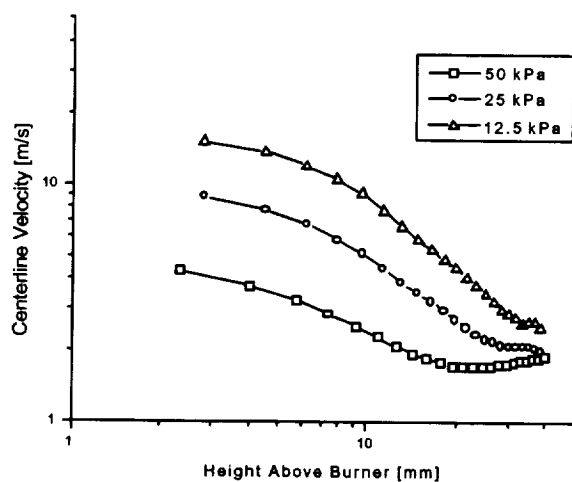


Figure 2. Centerline velocity as a function of height above burner.

THE "ADVANCED DISK LASER" (ADL): INSTRUMENTATION FOR LASER DIAGNOSTICS IN MICROGRAVITY COMBUSTION RESEARCH

Grebner, D., Müller, D., Triebel, W., König, J.*, Johannsen, I.**, Giesen, A.**

IPHT, POB 100239, D-07702 Jena, Germany, grebner@ipht-jena.de

* ZARM, Am Fallturm, D-28359 Bremen, Germany,

** IFSW, Pfaffenwaldring 43, D-70569 Stuttgart, Germany

Introduction

Laser based diagnostics of combustion processes using wavelengths in the UV-VIS spectral range have been developed extensively during the last decades [1]. Methods like planar laser induced fluorescence (PLIF), Raman, Rayleigh and MIE scattering, laser induced incandescence (LII) or particle imaging velocimetry (PIV) supply information about combustion relevant species and temperature distributions, soot formation or flow field properties. The application of these measurement techniques "in-flight" under microgravity requires compact but highly efficient pulsed laser systems. Moreover, the restricted experimental time at short term microgravity facilities favors high repetition rate lasers to allow fast scan process diagnostics. Laser diagnostic experiments using a high repetition rate excimer laser (250 Hz) in combination with intensified camera systems (250 fps) have successfully been performed at Bremen drop tower [2, 3].

Diode pumped solid state lasers generate high output power from a compact device with high efficiency. Pulsed systems can operate with kHz repetition rate. Recently the development of the diode laser pumped Yb:YAG thin disk laser [4] resulted in 100 W TEM₀₀ operation [5]. Electrical efficiencies of 20 % and an optical efficiency of 58 % were demonstrated as well as a laser power of up to 1 kW [6].

Based on the disk laser, a combustion diagnostic system for in-flight experiments under microgravity is under development. The system will be tested and applied for fast scan measurements (kHz repetition rate) under short term microgravity conditions (drop tower, parabolic flights). Its installation at the CIR for combustion experiments at the ISS is proposed.

The ADL diagnostics system

The laser system consists of a two-stage oscillator-amplifier arrangement (Fig. 1). Narrow bandwidth radiation is generated by a cw Yb:YAG thin disk laser ($P = 12$ W). Single frequency operation is realized by etalons and wavelength tuning by rotating a birefringent filter, both intracavity.

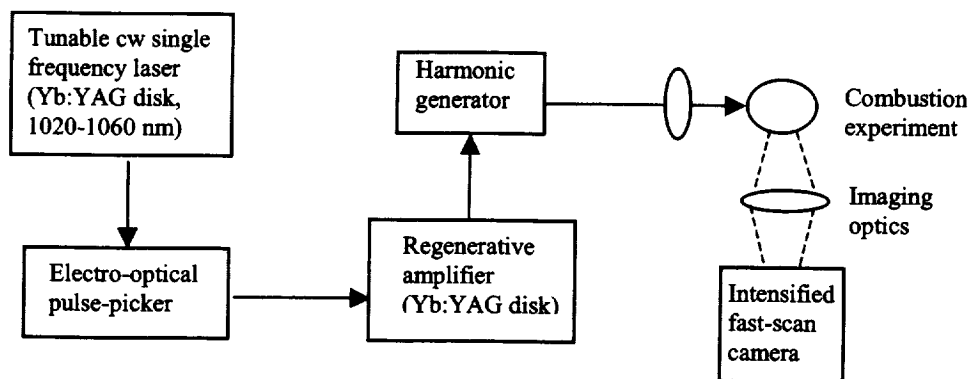


Fig. 1. "Advanced Disk Laser" (ADL) for combustion diagnostics under microgravity.

Using an output coupler of low transmission ($T=0.6$ %) compared to the outcoupling of 2-3 % for maximum output power a large wavelength tuning range from 1020-1060 nm is obtained (Fig. 2). The tunable laser in single frequency operation serves as seed laser in a regenerative amplification scheme (Fig. 1, [7]).

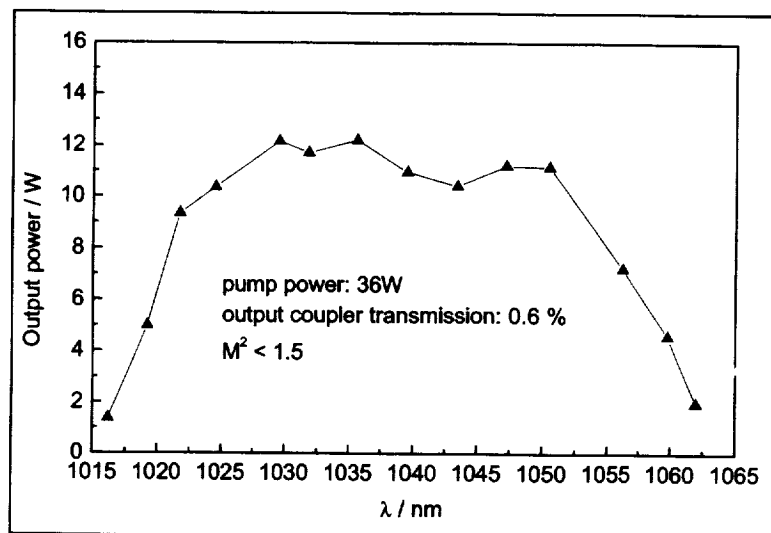


Fig. 2. Tuning curve of the cw Yb:YAG thin disk laser emission.

Using a Pockels cell in a pulse picker setup rectangular pulses with repetition rates up to 10 kHz are generated. By means of an adapted synchronization electronics the radiation is

trapped in the regenerative amplifier using a second Pockels cell. Amplification is achieved within several passes through an Yb:YAG thin disk as the active medium. After amplification the infrared pulses of 15 ns pulse duration are coupled out after switching the Pockels cell. The tunable narrow bandwidth high energy pulses (1020 – 1060 nm) will be frequency converted into second harmonic (SHG, 510-530 nm), third harmonic (THG, 340-353 nm) and fourth harmonic (FHG, 255-265 nm) by LBO and BBO nonlinear optical crystals.

The maximum output power depends mainly on the available pump power and the apertures of the Pockels cell in the amplifier resonator. A first system is tested applying a fibercoupled pump diode of 60 W output power. Here an average infrared power of 10 W (e.g. 10 mJ @ 1 kHz) is expected. Up to 5 W in the VIS and 2-3 W in the UV spectral ranges are expected after frequency conversion. In the near future a 250 W pump diode will replace the 60 W unit and in combination with an adapted resonator design lead to an increase of the available infrared laser power. This system with the 250 W pump unit is proposed to be installed at the ISS. The requirements for its integration are evaluated. Due to the modular design and the scaleable concept further improvements of the laser properties and output power are possible and planned.

In stationary combustion experiments the ADL laser system can be applied in combination with standard intensified slow scan camera systems at low repetition rate. Alternatively both, the laser and the image intensifier, can operate at a kHz rate, while the signal integration at the CCD chip is realized with small rates (e.g. 10 Hz). However, a main advantage of the laser system is its kHz repetition rate allowing fast scan process diagnostics. The fast scan camera system (Reticon, Princeton), available at the moment, can record up to 4000 frames at a rate of 1000 fps with 256×256 pixels. An image intensifier is adapted to the CCD according to the frame rate for signal amplification and gating (minimal gate duration: 5 ns). Using further developed camera systems together with the ADL, species selective single shot imaging can be performed with a rate of several kHz.

ADL applications

The ADL laser system is well suited for fast imaging of flow fields, species concentrations and temperatures. The preferred method for evaluating the laser system is PLIF for detection of different minor and major species in flames and reactive flows. Table 1 gives an overview of the tuning ranges with frequency converted radiation of the Yb:YAG laser and of expected PLIF applications.

Table 1. Yb:YAG harmonics generation and species which can be detected via laser induced fluorescence (LIF).

Yb:YAG-Laser ($\Delta\lambda$ / nm)	Species to detect by LIF
Fundamental (1020 – 1060)	---
SHG (510 – 530)	C ₂ (516 nm, $v'=0$, $v''=0$) NO ₂ (509.5 nm, A ² B ₁ -X ² A ₁)
THG (340 – 353)	HCHO (343 nm, 4 ³ ₀ ; 352 nm, 4 ¹ ₀) OH (342.8 – 347.2 nm, $v'=0$, $v''=1$)
FHG (255 – 265)	OH (260.8-262.2 nm, $v'=2$, $v''=0$) O ₂ (257.0 nm, $v'=2$, $v''=8$) NO (259.6 nm, $v'=0$, $v''=3$) HCO (258.4 nm, B-X,000)

Preparatory experiments were performed with a pulsed dye laser system in the laboratory to estimate realistic light sheet dimensions for recording 2D distributions under microgravity conditions with the Yb:YAG laser. LIF spectra were recorded for OH, NO, formaldehyde and C₂ at laser energies in the μ J range. To observe PLIF of formaldehyde in cool and hot flames, a light sheet of 5 mm x 200 μ m was formed using a 500 μ J dye laser pulse and the intensified fast scan camera for single pulse recording. PLIF profiles of formaldehyd were obtained with good signal to noise ratio in different flames. Further applications like PIV, LII or Raman- Rayleigh- and MIE-scattering are under evaluation.

Acknowledgements

We thank the DLR for financial support by contract no. 50 WP 0004. We thank Martin Jordan (Astrium) for advice concerning the laser implementation at ISS.

References

- [1] E. W. Rothe and P. Andresen, Appl. Opt. 36, (1997) 3971.
- [2] W. Triebel, Space Forum 4 (1998) 121.
- [3] Ch. Eigenbrod, J. König, W. Triebel, Proc. 4th Int. Comb. Worksh., NASA Conf. Publ. 10194, Cleveland (1997) 311.
- [4] A. Giesen, H. Hügel, A. Voss, K. Wittig, U. Brauch, H. Opower, Appl. Phys. B 58 (1994) 365.
- [5] M. Karszewski, U. Brauch, K. Contag, S. Ehrhard, A. Giesen, I. Johannsen, C. Stewen, A. Voss, OSA TOPS 19 Adv. Solid-State Lasers (1998) 296.
- [6] C. Stewen, K. Contag, A. Larionov, A. Giesen, H. Hügel, IEEE J. Sel. Top. Quant. Electr. 6 (2000) 650.
- [7] I. Johannsen, S. Ehrhard, A. Giesen, OSA TOPS (2001) to be published.

THE POTENTIAL APPLYING THE "ADVANCED DISC LASER" (ADL) IN MICROGRAVITY-COMBUSTION FOR OH-LIF DIAGNOSTICS USING THE (A-X; 2,0) -ELECTRONIC EXCITATION SCHEME

König, J., Grebner, D.*, Triebel, W.*, Johannsen, I.**, Giesen, A.**

Center of Applied Microgravity and Space Technology, ZARM; Hochschulring/ Am Fallturm, D-28359 Bremen, Germany, koenig@zarm.uni-bremen.de;

* Institut für Physikalische Hochtechnologie IPHT, Helmholtzweg 4, D-07743 Jena, Germany

** Institut für Strahlwerkzeuge IFSW, Pfaffenwaldring 43, 70569 Stuttgart, Germany

Introduction

The OH-radical is one of the most important reaction intermediate in combustion. Detection of planar laser induced fluorescence (PLIF) of OH is a frequently used technique to visualize the location of the reaction zone or the structure of various types of flames. Qualitative two-dimensional mapping of OH-concentration-fields is commonly used in laboratory- and technical applications, quantitative concentration values can be determined for many selected cases. Employing LIF-techniques in microgravity combustion research is currently very limited due to the lack of appropriate laser sources with respect of size, efficiency and spectral performance. Within the $A^2\Sigma^+ \rightarrow X^2\Pi$ electronic transition, OH exhibits the strongest favorable experimental features for LIF exciting the X ($v''=0$) state to the A state at ($v'=0, 1, 2$ and 3) at wavelengths centered at 308nm, 283nm, 262nm and 246nm respectively, with drastically declining absorption efficiencies to the UV. Thus, in particular for planar LIF application, diagnostics using the $v'=2$ or 3 excited state, the only appropriate excitation sources have been excimer based systems or, in few cases, specially modified Nd:YAG-lasers with low pulse repetition rates. Consequently,

Fig.1a: Low-resolution absorption spectrum of OH (simulated with LIFBASE[3]) at $v''=0 \rightarrow v'=2$ and $v''=1 \rightarrow v'=3$ band position; overlap with available laser sources.

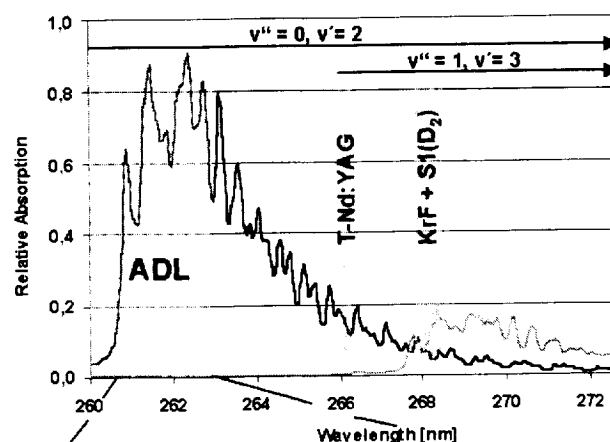
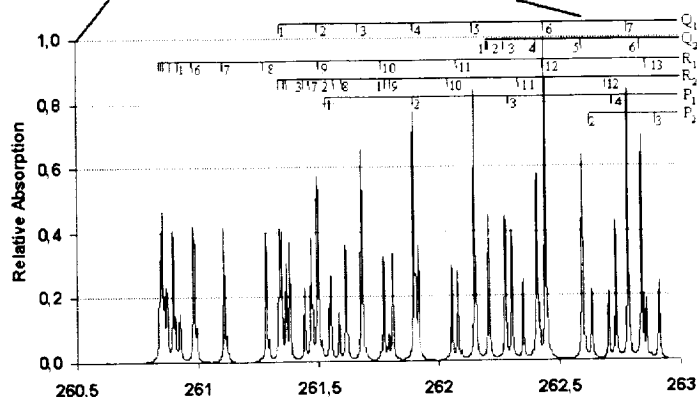


Fig.1b: High resolution absorption spectrum of OH (simulated with LIFBASE, wavelengths in air) at the ADL-overlap position



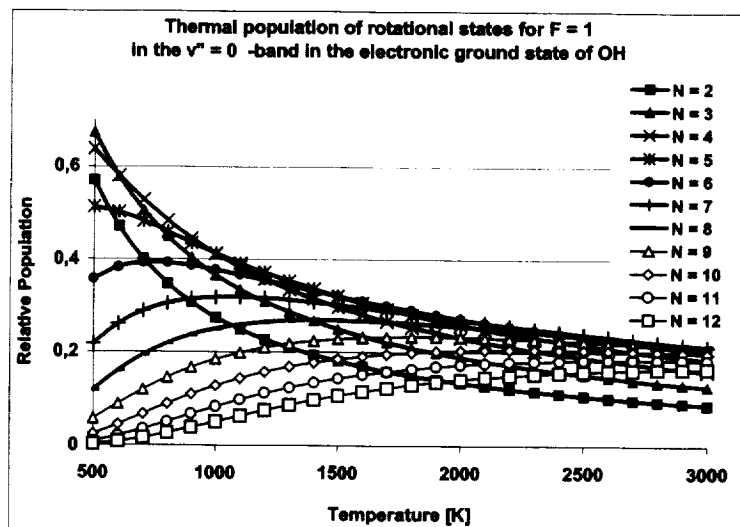
the choice of the rotational transition used to excite LIF was very limited by the spectral properties of the laser source. Exciting the lower vibrational bands in the excited state of OH, diverse configurations with dye-lasers provide sufficient energy for PLIF-applications. However, these setups are not suitable for microgravity experiments.

The "Advanced Disc Laser" (ADL), especially designed for laser diagnostic applications on microgravity platforms, will provide narrow-bandwidth pulsed UV-emission covering an wide tuning range of 254nm to 263nm. Figure 1a displays the spectral overlap of the ADL-tuning range with the (2,0) vibrational band within the OH (A-X) electronic transition in addition to the spectral emission ranges of the tunable Nd:YAG- and a Raman (D₂)- converted KrF-excimer laser. Both latter sources are the only practical means known to the author actually available to be applied for OH-LIF in the (2,0) band for combustion diagnostics [e.g. 1,2].

Brief Discussion of OH-LIF using the (2,0) -band

Beyond the practical importance of diagnostic application of OH and other radicals like NO, CH etc., the relatively simple electron structure of these small species yielded a quite comprehensive numerical treatment with respect of spectroscopic features in the recent years. That is why a sound base of data is available on absorption and excitation spectroscopy involving the $A^2\Sigma^+ \rightarrow X^2\Pi$ transition. A systematic compilation of numerous works in this field, either experimental and theoretical has been done by the group of Luque and Crosley, and Jeffries, resulting in the *LIFBASE*- program [3]. Using this program, predictions on absorption line strengths, transition probabilities, fluorescence yields and spectral overlap with other important radicals and molecules abundant in flames are being made for electronic excitation of OH with the expected spectral performance of the Advanced Disc Laser. Figure 1b shows a high spectral resolution simulation of the (2,0) absorption band of OH at gas phase conditions of 0.1 MPa and 2000K overlapping the ADL-tuning range. Owing to the spectral bandwidths of the ADL below a FWHM of 2pm, most of the rotational lines are supposed to have the potential for selective excitation at atmospheric flame conditions. However, there are sufficient rotational levels substantially separated from neighboring lines to enable selective excitation even at high pressures. Due to the large amount of candidate rotational transitions, a suitable spectral filtering to account for VET and RET is not presented yet. It should be noted that, due to the large number of rotational levels that can be excited in the (2,0) vibrational band by means of the ADL, there is a considerable "available" variety of thermal population profiles for the individual lines. Figure 2 shows the thermal population profiles for spin state $F = 1$ and rotational numbers in the tuning range of the ADL-laser overlapping the (2,0) band system. Disregarding the effect of thermally dependent quenching which influences the final yield of emitted fluorescence, there are rotational levels (e.g. $N = 6, 7, 8$) which exhibit population densities in the ground state

Fig.2: Thermal population of selected rotational lines excitable with the ADL-source in the (2,0) vibrational band of OH for spin state $F=1$



changing less than 10% in absolute value within the range of typical flame temperatures. Beyond that, intentionally selecting two rotational lines with highly temperature dependant population profiles, 2-dimensional mapping of temperatures should be a promising technique for selected experimental cases as demonstrated earlier for the (3,0) band [4].

Generally, exciting higher vibrational levels in the upper electronic state, the probability of molecular predissociation increases. It is well investigated that, exciting the third vibrational excited state manifold, predissociation rates exceed collisional quenching rates in typical atmospheric pressure flames [5]. Thus, on one hand side, quenching independent "quantitative" fluorescence measurements are possible, yielding undesired potential photochemical reactions in the probed gas volume on the other hand side [e.g. 6]. LIF following the excitation of the (2,0)-band is only very slightly predissociating [7] and can be accounted to have neither of the latter effects.

Experimental performance estimates

One of the most important issue introducing the ADL for planar LIF-diagnostics is to proof, whether sufficient pulse energy at reasonable pulse repetition rate is available to generate single shot images with appropriate signal-to-noise ratio [8]. Even though, as mentioned in the introduction, the absorption coefficient of the (2,0) band is considerably lower than for the commonly used (0,0) and (1,0) band transition ($B_{20}/B_{00} \sim 0.05$ and $B_{20}/B_{10} \sim 0.2$), the transition is much stronger than the (3,0) band ($B_{20}/B_{30} \sim 10$), the latter favorably be excited with available strong KrF-excimer laser sources. To estimate practical values to assess the OH-LIF performance with ADL, number of photon/ pixel and signal/ noise values were calculated for a typical experiment setup extending the data listed by Seitzmann [7]. It was found that, exciting the $Q_1(6)$ line in atmospheric hydrogen-flame in the (2,0) band with a 10mJ pulse emitted by the ADL-system (light sheet of 100mm height and 500 μ m thickness) will yield a signal-to-noise ratio of approximately 200, which is slightly less than that achieved with dye-laser of identical pulse energy and light sheet-size exciting the $Q_1(6)$ rotational transition in the (1,0) vibrational band. One reason for this result is, that at the current state of hardware development the spectral emission bandwidths of the ADL is essentially lower than that of the excimer-pumped dye laser sources, thus giving a better matching with the OH-absorption lines. Signal/ noise values for 2-dimensional XeCl- LIF applications exciting lines in the (0,0) band are at least a factor of 20 larger than those achievable with ADL- induced OH-fluorescence. However, effects like self absorption of fluorescence emission, difficulties in spectral separation of excitation- and emission radiation and, if undesired, saturation effects using the (0,0) band have to be considered.

Preparatory experiments

To estimate the measurement opportunities of the ADL laser, experiments were performed using a tunable, spectrally narrowed frequency converted dye laser (Scanmate, Lambda Physik). Radiation between 255 and 262.5 nm was generated with a spectral bandwidth of about 2 pm. Spectroscopic experiments were performed on a H₂-O₂ diffusion flame using an intensified OMA-system (OMA IV, Princeton) combined by a spectrometer. In figure 3 the OH fluorescence emission following excitation at 261.191 nm ($R_1(7)$ -transition) is demonstrated, showing the typical rotational structure. Integrating the emission band at 290 nm (2,1) band scanning the excitation wavelength, the resulting fluorescence excitation spectrum is shown in figure 4. The recorded fluorescence excitation spectrum can completely be assigned to the excitation of OH (Fig. 1). It is important to note that no spectral overlap by hot O₂ or NO was observed, although

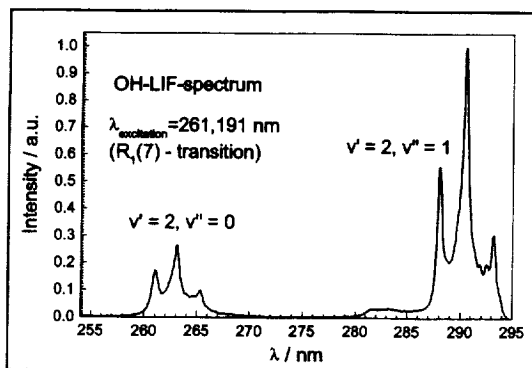


Fig. 3. OH fluorescence emission spectrum

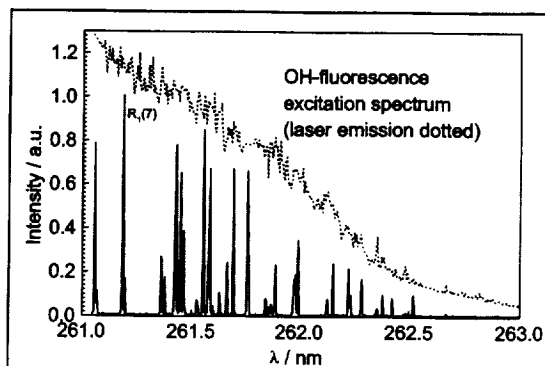
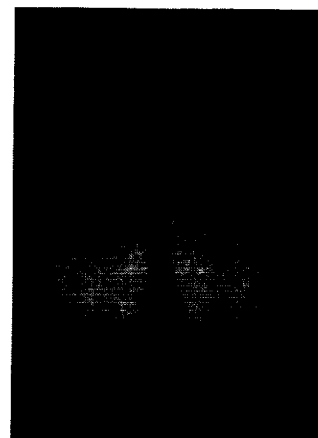


Fig. 4. OH fluorescence excitation spectrum and dye laser emission curve

these species were found in high concentrations in this flame. NO-LIF excitation was found to excited with wavelengths between 255 nm and 260 nm, also supplied by the ADL laser system. Due to the limited tuning range of the available laser dye (Fig.4) LIF excitation with wavelengths longer than 262.5nm was not possible, but may result in even higher intensities as shown by the *LIFBASE*-calculations (Fig.1).

To estimate the excitation efficiency for radiation at 261.191 nm, pulse energy of 100 μ J was used in a PLIF test measurement. It was possible to detect OH-LIF in a partially premixed ethene-air-flame (Fig.5). According to these investigations UV laser pulse energies of 2-3 mJ will be sufficient for PLIF measurements with a laser light sheet of 3 cm. An even higher signal intensity is expected after excitation around 263 nm (see Fig.1)

Fig.5: OH-PLIF after dye laser excitation 261.119 nm,
R1(7) -transition ($E = 100\mu$ J).



References

1. Dreier, T., Dreizler, A., Wolfrum, J.: "The Application of Raman-Shifted Tunable KrF Excimer Laser for Laser Induced Combustion Diagnostics", *Appl. Phys.*, B55, 381 (1992)
2. Versluis, M., Queeney, K.L., Springfield, J.L., Dreier, T., Dreizler, A.: "Laser Induced Fluorescence Detection of OH in a Flame near 268nm", *J. Mol. Spectrosc.*, 166, 486 (1994)
3. Luque, J., Crosley, D.R.: "LIFBASE: Database and Simulation Program (V.1.6)", SRI International Report MP 99-009 (1999)
4. Kohse-Höinghaus, K.: "Laser Techniques for the Quantitative Detection of Reactive Intermediates in Combustion Systems", *Prog. Energy Comb. Sci.*, 20, 203 (1994)
5. Spaanjars, J.J.L., ter Meulen, J.J., Meijer, G.: "Relative Predissociation Rates of OH A: $v' = 3$ from combined Cavity Ring-Down/ Laser Induced Fluorescence", *J. Chem. Phys.*, 107, 2242 (1997)
6. Seitzmann, J.M.: "Quantitative Application of Fluorescence Imaging in Combustion", HTGL Report No. T-275 (1991)
7. Yarkony, D.R.: "A Theoretical Treatment of the Predissociation of the Individual Revibronic Levels of OH/ OD A", *J. Chem. Phys.*, 97, 1838 (1992)
8. Grebner, D., Müller, D., Tirebel, W., König, J., Johannsen, I., Giesen, A.: "The "Advanced Disc Laser" (ADL): Instrumentation For Laser Diagnostics in Microgravity Combustion Research", 6th Intl. Microgravity Comb. Workshop, to be presented, Cleveland (2001)

Aknowlegdement

We hereby wish to thank the "Deutsches Zentrum für Luft- und Raumfahrt (DLR)" for funding the presented work in the frame of the contract No 50 WP 9840.

HYPERSPECTRAL IMAGING OF FLAMES USING A SPECTRALLY SCANNING FABRY-PEROT FILTER

W.T. Rawlins, W.G. Lawrence, W.J. Marinelli, and M.G. Allen
Physical Sciences Inc.
20 New England Business Center
Andover, MA 01810

INTRODUCTION

Investigations of the dynamics of flame spread over combustible surfaces in microgravity are critical to spacecraft fire safety, as well as to the understanding of fundamental fire phenomena. In the absence of gravity-induced buoyancy and forced convection, heat transfer between the flame and the fuel surface is dominated by conductive and radiative mechanisms. The detailed understanding of these mechanisms requires direct observations of the spatial propagation and radiative fluxes of key flame product species such as CO₂ and H₂O. We are developing a method to perform such measurements non-intrusively by observing spatially and spectrally resolved infrared emission from flame-produced molecular species including CO₂, H₂O, and CO. The species-specific rovibrational band structures of the spectra enable discrimination between gas phase, particulate, and hot surface contributions to the observed emission, as well as determinations of path-integrated species concentrations and temperatures.

The overall goal of this 4-year project is to develop a design for a hyperspectral infrared imaging instrument to be used in flame spread and other combustion experiments in space and/or low-gravity conditions. This design is based on a hyperspectral infrared imaging device previously developed at Physical Sciences Inc. (PSI) and used in several laboratory and ground based applications. During the currently funded project, we are using this instrument, named AIRIS (Adaptive Infrared Imaging Spectroradiometer), in laboratory flame measurements to characterize its performance and to develop the necessary data analysis tools. We also plan to use this instrument in test flights on the KC-135 airplane, interfaced to GIFFTS (Gravitational Influences on Flammability and Flamespread Test System), a NASA/GRC and CWRU flame spread experiment. Ultimately, the AIRIS instrument will use three or four mirror sets to operate over the spectral range 2 to 5 μm , encompassing the molecular bands of H₂O, CO₂, CO, and hydrocarbons. The instrument produces spatially resolved images of the scene at each wavelength, with a spectral resolution on the order of 0.03 to 0.05 μm . At present we are focusing on spectrally scanning imaging measurements in the 3.7 to 5.0 μm region.

INSTRUMENT DESCRIPTION

We have assembled a fully operative AIRIS Fabry-Perot filter, and have interfaced it to an infrared focal plane array (FPA) camera/dewar system obtained on loan from NASA/GRC. The fully assembled instrument is shown in Figure 1. The AIRIS filter consists of a high-finesse, low-order Fabry-Perot interferometer, using a pair of high-reflectivity mirrors which are coated for the 3.7 to 5.0 μm spectral region. The mirrors are driven at high precision (~ 4 nm) by a set of three inchworm motors controlled by a four-point capacitance micrometer circuit which measures the mirror spacing and parallelism. The instrument includes a computer system and a

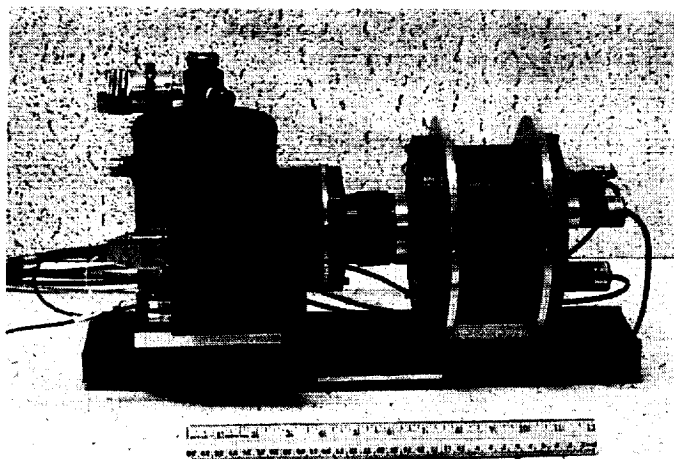


Figure 1. Photograph of the AIRIS instrument, consisting of scanning Fabry-Perot filter, collection lens, and InSb camera/dewar system.

data acquisition board. The computer, camera controls, and AIRIS motor controls are housed in an instrument rack modified for aircraft use as recommended by NASA/GRC. The camera is an Amber 4128C InSb focal plane array, 128 x 128 (6.4 mm x 6.4 mm), with a 50 μm pitch. The FPA is integral with a liquid nitrogen dewar which is specially designed for microgravity measurements on the KC-135. We have developed a data acquisition interface for this camera using an Imaging Technologies Inc. (ITI) framegrabber board and custom software.

The optical collection system, diagrammed in Figure 2, consists of a 50 mm DIOP multi-element lens, positioned 9 cm in front of the FPA to give 1/10 magnification of the object plane. This results in a field of view 6.4 x 6.4 cm (0.5 x 0.5 mm per pixel) at the object plane, which is 55 cm from the lens. The AIRIS filter is 18 cm long and 15 cm OD with a 36 mm clear aperture, and is positioned immediately in front of the lens. An f/4.8 aperture between the lens and the AIRIS filter controls the collection solid angle, and elongates the depth of field near the image plane. A cold bandpass filter mounted on the FPA restricts the spectral range to 3.7 to 5.0 μm , eliminating higher-order radiation transmitted by the AIRIS filter. The entire assembly of camera, lens, and filter are mounted on an optical rail 46 cm (18 in.) long. Quantitative testing of the imaging system using screens of known dimensions and a modulation transfer function analysis has confirmed ray-tracing computations of the field of view. The observed spatial resolution near 4 μm is limited by diffraction, and is intermediate between 0.5 and 1 mm. The observed depth of field for the f/4.8 system is ~4 cm.

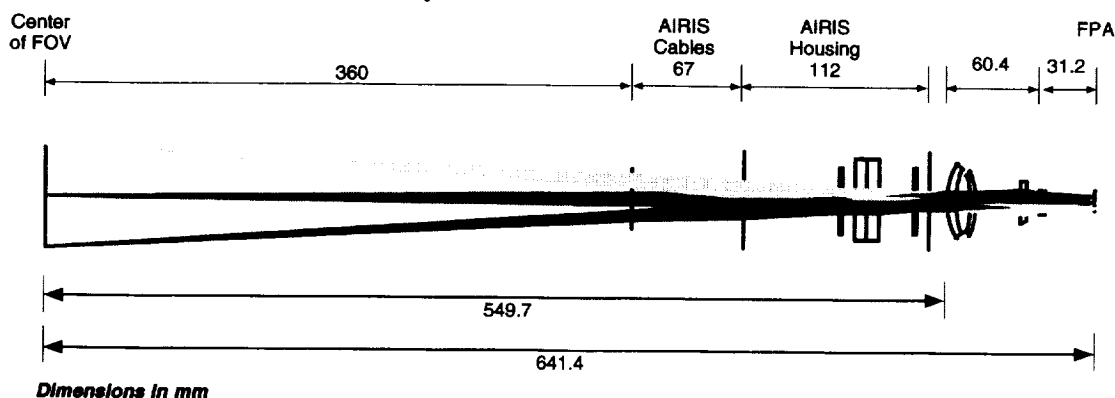


Figure 2. Diagram of AIRIS optical train.

We have performed several sets of wavelength calibrations of the AIRIS filter, using an FTIR spectrometer to test the filter's wavelength precision, spectral resolution, and scan rate. For second-order operation of the Fabry-Perot filter between 3.5 and 5 μm (i.e., mirror spacing = wavelength), the free spectral range is 1.48 μm , the spectral resolution is 0.043 μm (FWHM),

and the finesse is 34, all of which are consistent with our expectation and slightly improved over the design goals. In current laboratory testing, we typically scan the instrument at ~ 10 Hz per wavelength, however detailed tests of the scanning control algorithm (not including the frame capture) have achieved scan rates up to 40 Hz per wavelength. Based on these results, we expect to achieve our target scan rate of 20 to 30 Hz per wavelength including frame capture. Detailed testing of the wavelength accuracy as a function of scan rate is in progress.

LABORATORY FLAME MEASUREMENTS

We have acquired preliminary spectral images of the exhaust plume of a laboratory CH_4/air flame generated by a flat flame, Hencken-style burner. These images qualitatively confirm the expected instrument field of view and sensitivity, and the spectra illustrate spectral resolution of the prominent $4.3\text{ }\mu\text{m}$ CO_2 feature in the hot exhaust gas. The measurements were made 10 to 16 cm above the burner surface using a stoichiometric CH_4/air flame at 1 atm. The fuel and oxidizer are not premixed, but are injected separately through a set of small, alternating tubes in a honeycomb arrangement; this produces a set of small diffusion flamelets immediately above the burner surface which blend into a radially uniform flat flame. The flame is surrounded and stabilized by an annular flow of nitrogen. Previous temperature, OH PLIF, and LII imaging measurements on this burner indicate flame diameters of 2 to 3 cm at heights up to 4 cm above the burner surface. For the exhaust plume IR imaging measurements, a circular 1/8-in. thick aluminum plate, with a central hole 2.5 in. (6.35 cm) in diameter, was placed over the flame at a height 10 cm above the burner surface. This plate was used to define the bottom edge of the imager's field of view. The AIRIS imager was positioned to view the flame exhaust stream from the top of the plate to a height some 6 cm above the plate (i.e., 10 to 16 cm above the burner surface) with a magnification of 1/10 (6.4 x 6.4 cm image). At this position, the active flame zone is not directly in the field of view. An FTIR spectrometer with a HgCdTe detector viewed the same region at 90 deg to the sight line of the imager. For these preliminary measurements, neither the imager nor the FTIR spectrometer was calibrated for relative spectral or absolute responsivity, nor were any corrections made for room temperature absorption by CO_2 or H_2O .

The imager acquired spectral images from 3.65 to 5.00 μm at 0.05 μm intervals, with a frame acquisition rate of 3 Hz. Example images at three wavelengths within the $\text{CO}_2(\nu_3)$ band are shown in Figure 3. The image intensities are displayed on a linear gray scale, bitmapped from the original 12-bit image onto an 8-bit image. Near the bottom of the image, the 6.35 cm hole in the plate is illuminated by reflections from the flame zone below. Above the plate, the hot exhaust stream can be seen extending up ~ 6 cm to the top edge of the field of view. The diameter of the exhaust stream ranges from ~ 1.4 cm near the bottom of the image to ~ 1.1 cm near the top of the image. The image at 4.35 μm samples radiation near the center of the CO_2 band, and is therefore the most intense. The decrease in intensity with increasing height signifies decreasing gas temperature; this is especially apparent at 4.2 μm , near the temperature-sensitive band edge. Some of this decrease may also be due to dilution of the post-flame CO_2 concentration, which will affect all three wavelengths similarly.

Example spectral distributions near the center of the image are shown in Figure 4. The figure shows two AIRIS spectra compared with two spectra from the FTIR spectrometer, acquired at spectral resolutions of 2 cm^{-1} (0.003 μm), and also at 16 cm^{-1} (0.025 μm) to more closely match

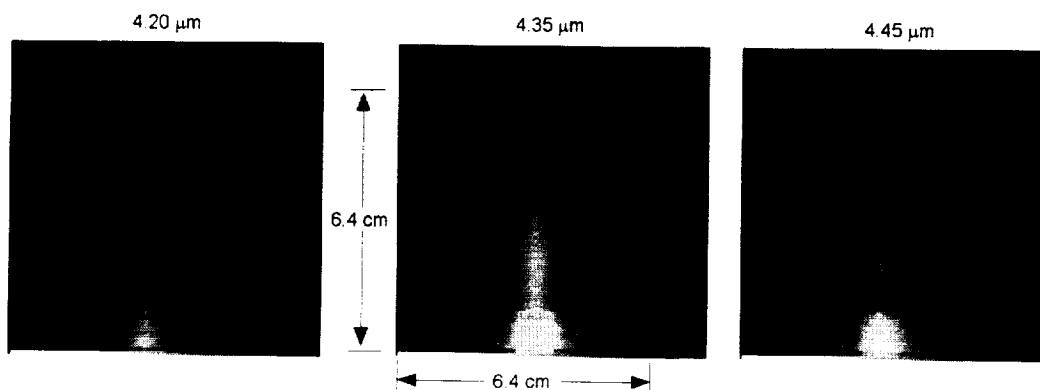


Figure 3. Spectrally resolved images of the exhaust stream of a stoichiometric CH_4/air flame at 4.20, 4.35, and 4.45 μm . The exhaust stream is observed at heights of 10 to 16 cm above the burner surface. The 6.4 x 6.4 cm field of view is indicated on the center frame.

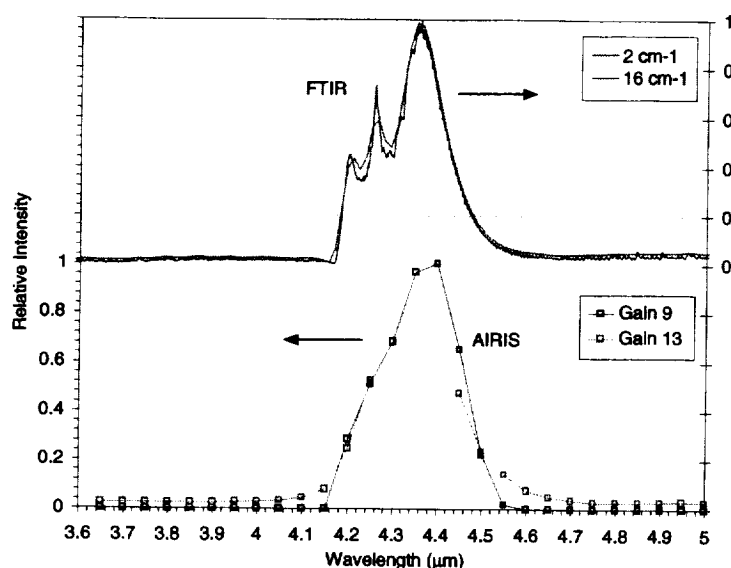


Figure 4. Comparison of concurrent AIRIS and FTIR spectra of the flame exhaust stream from Figure 3. The spectral data are not corrected for the wavelength-dependent responsivities of the two instruments.

the resolution of AIRIS (0.043 μm). The two AIRIS spectra were obtained at different gain settings on the Amber camera. At the more sensitive gain setting, the intensities near the band center were in saturation, and are not plotted in the figure. Absorption by room CO_2 can be clearly observed in the higher-resolution FTIR spectra. The general spectral shapes and widths observed by the two instruments are in good agreement. The primary band feature is indeed the $\text{CO}_2(\nu_3)$ band, centered at 4.26 μm and extending from about 4.15 to 4.55 μm . Based on a preliminary band model analysis, the shape and width of the band

indicate a rotational/ vibrational temperature of roughly 1300 K near the center of the image, consistent with our expectations for exhaust gas temperatures above this flame. In addition, features due to CO and H_2O are observable in the 2 cm^{-1} FTIR spectrum between 4.5 and 5 μm .

SUMMARY

This paper describes a hyperspectral Fabry-Perot infrared imager for quantitative infrared emission spectroscopy and imaging of flames. We plan to apply this non-intrusive measurement method to investigations of flame spread in microgravity and reduced gravity environments. Although specifically focused toward implementation in a solid fuel flame spread experiment, the IR imaging spectrometer will be widely applicable to other microgravity combustion experiments, such as diffusion and premixed flame structure, soot formation, and droplet combustion investigations.

QUANTITATIVE SPECIES MEASUREMENTS IN MICROGRAVITY COMBUSTION FLAMES

Joel A. Silver¹, William R. Wood¹, Shin-Juh Chen², Werner J.A. Dahm², and Nancy D. Piltch³

¹Southwest Sciences, Inc., 1570 Pacheco Street, Suite E-11, Santa Fe, NM 87505

²Laboratory for Turbulence & Combustion (LTC), Department of Aerospace Engineering, The University of Michigan, Ann Arbor, MI 48109-2140

³NASA Glenn Research Center, MS 110-3, Cleveland, OH 44153

INTRODUCTION

Flame-vortex interactions are canonical configurations that can be used to study the underlying processes occurring in complicated turbulent reacting flows. The elegant simplicity of the flame-vortex interaction permits the study of these complex interactions under relatively controllable experimental configurations, in contrast to direct measurements in turbulent flames. The ability to measure and model the fundamental phenomena that occur in a turbulent flame, but with time and spatial scales which are amenable to our diagnostics, permits significant improvements in the understanding of turbulent combustion under both normal and reduced gravity conditions.

In this paper, we report absolute mole fraction measurements of methane in a reacting vortex ring. These microgravity experiments are performed in the 2.2-sec drop tower at NASA Glenn Research Center. In collaboration with Drs. Chen and Dahm at the University of Michigan, measured methane absorbances are incorporated into a new model from which the temperature and concentrations of all major gases in the flame can be determined at all positions and times in the development of the vortex ring. This is the first demonstration of the ITAC (Iterative Temperature with Assumed Chemistry) approach, and the results of these computations and analyses are presented in a companion paper by Dahm and Chen [1] at this Workshop. We believe that the ITAC approach will become a powerful tool in understanding a wide variety of combustion flames under both equilibrium and non-equilibrium conditions.

EXPERIMENTAL

Determination of the gas concentrations and temperatures is accomplished by tunable diode laser absorption using 2f wavelength modulation spectroscopy (WMS) [2-3]. With an axisymmetric flame, line-of-sight absorption measurements are inverted [4] to provide radial mole fraction profiles with high spatial and temporal resolution. The new system used in this work is more compact and uses much less power than earlier designs. This accomplishment arises from the use of a digital signal processor (DSP) to control the hardware, acquire and process the data, and then transmit the data to a laptop computer after the drop.

The vortex ring is generated by issuing methane into an air environment through the exit of an axisymmetric nozzle. The experiments are conducted under microgravity conditions in order to remove the undesirable effects of buoyancy that can affect both the flame structure and ring dynamics resulting in possibly asymmetric and non-repeatable interactions [5]. Figure 1 is a photograph of the experiment drop package, showing the vacuum system, vortex generator system,

nozzle/plenum assembly, WMS controller and data acquisition system on the top shelf. The laser absorption system and test section hang below the center of this, where the laser beam scanning region can be adjusted to any distance below the nozzle plane. The power supply for spark generation, power distributor, batteries, B/W CCD camera, and video transmitters reside on the bottom shelf.

The vortex ring and drop rig have been described in detail previously [6,7]. The ring diameter in these experiments is 2 cm. Since methane is lighter than air, the flame is pointed downward so that the pre-drop mixing with air for proper ignition can be accomplished. The laser DSP system has also been

described in a prior publication [8], but in brief, comprises a 1-mm dia. collimated laser beam pointed onto a raster scanner mirror. The center of this mirror is located at the focal point of an off-axis paraboloidal reflector (OAP). As the scanner is rotated over an angle of $\sim 13^\circ$, the laser beam tracks in parallel lines across the flame. A second OAP collects the beam and refocuses it onto an extended-wavelength InGaAs photodiode. The result of this process is that data acquired sequentially in time can be used to obtain spatially-resolved line-of-sight measurements through the flame.

In these experiments, a Sensors Unlimited diode laser is used to detect the nearly degenerate rotational triplet R3 A2 in the $2\nu_3$ vibrational band of methane at 1652.9 nm. Spectroscopic parameters used to analyze these spectra are obtained from the HITRAN database [9]. Each spectrum of 65 points, spanning a 1.38 cm^{-1} wavelength range, are recorded in 3.0 msec. The raster scanner is set up so that the product of spatial steps and scans/second is constant, so that for a scan range of 30 mm at a resolution of 2 mm, a full spatial map is acquired in 51 msec. A number of runs were made with higher spatial resolution (1 mm) over a shorter total range of 16 mm, and higher temporal resolution (25 msec) with a 2 mm spacing over a 16 mm range. These help us to interpolate all of the data to higher resolution.

The DSP board controls all laser and scanner ramps, and acquires the raw data from the photodiode. These data are then $2f$ demodulated at the correct phase, normalized to the incident laser intensity and stored for subsequent download. The vortex ring is ignited approximately 0.5 seconds after the rig is released.



Figure 1 - Experimental drop rig package.

RESULTS

Spatial-temporal maps of methane in the microgravity flame vortex were recorded at heights of 5.0 mm, 12.7 mm and 19.1 mm. Noise and background terms (offsets and optical interference fringes) are removed using a singular valued decomposition (SVD) approach which determines a set of orthogonal basis functions to represent the data where no true absorptions of methane are present (*i.e.*, at times before the vortex ring is released). The actual integrated absorbance of each projection and time is found by a multi-linear least-squares fit of the experimental spectrum to a design matrix comprised of a reference spectrum (0.10 mole fraction methane at 733 Torr and 296 K) and the largest fifteen background basis vectors. An example of filtered spectra at a particular drop time is shown in Fig. 2. The 16 spectra correspond to each of the spatial locations between the center of the flame and 30 mm away at 2 mm increments. Larger absorbances closer to the vortex centerline (0 mm) are observed.

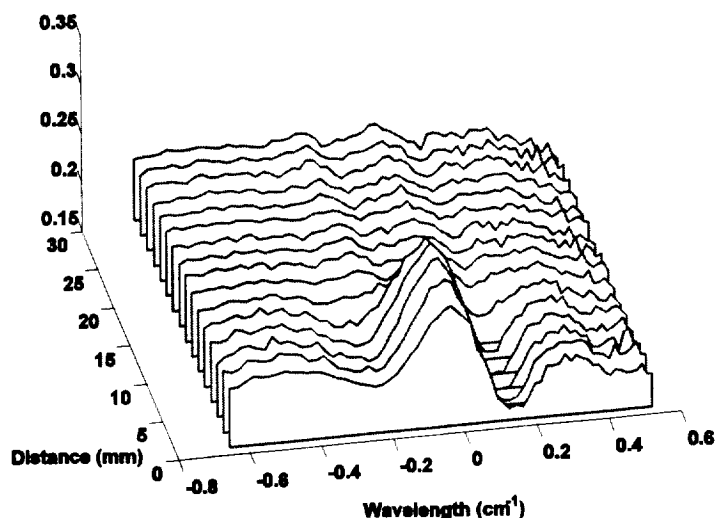


Figure 2 - $2f$ WMS spectra of methane for different distances from flame center at a height of 12.5 mm, 0.75 seconds after the package was released.

The resulting absorbance maps as a function of projection distance are then inverted to radial maps using the Abel inversion routines of Dasch [4]. From the radial absorbances, we then determine absolute mole fractions at each position and time assuming methane is at the reference condition. Contour maps of these results are shown in Fig. 3.

Collapsing the spectra to a single absorbance before the radial inversion is truly valid only if the $2f$ line shape is independent of temperature and mole fraction. While not strictly true, we can compute correction factors that can be applied to the radial absorbances to accommodate these effects. These correction terms, as well as factors for temperature-dependent cross sections, are applied in the ITAC iterations to produce final temperature and concentration maps. These are presented in the companion paper by Dahm and Chen [1].

DISCUSSION

As confirmed by the video record of the vortex ring, the flame front rapidly expands into its characteristic shape with a diameter of approximately 2 cm. As will be shown [1], the nominal mole fractions observed here will significantly increase to expected levels when the temperature corrections are applied.

Besides our earlier work [8,10], there are no other published results of quantitative species concentration measurements in microgravity combustion. This paper demonstrates that these type

of measurements can provide detailed spatial and temporal information that can be of great assistance toward improving the detailed models and our understanding of combustion phenomena under microgravity conditions. The ITAC method may prove to be a very powerful tool in elucidating the composition of many flames.

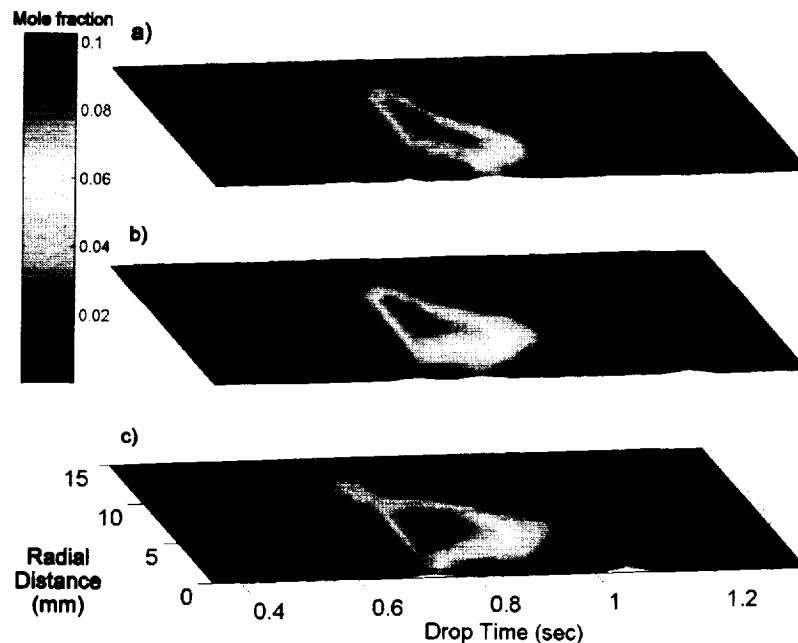


Figure 3 - Contour maps of nominal mole fraction (at reference conditions) at heights of a) 19.1 mm, b) 12.7 mm and c) 5.0 mm from the nozzle plane as a function of drop time and radial distance from the flame center axis.

As part of this effort, we plan to expand these measurements to other gases such as CO_2 or H_2O to fill in the spatial regions where methane has been consumed, as well as measure OH radical mole fractions. Hydroxyl measurements would allow the ITAC method to be expanded to reacting flows where non-equilibrium chemistry effects are important. We also hope to compare these measurements to other combustion system in both normal and reduced gravity.

ACKNOWLEDGMENT

This work was performed under NASA Contract NAS3-99140 and Grant NAG3-1639.

REFERENCES

1. Dahm, W.J.A., Chen S.-J., Silver, J.A., Piltch, N.D. and VanderWal, R.L., "Turbulent flame processes via diffusion flame-vortex ring interactions", *Sixth International Microgravity Combustion Workshop*, (2001).
2. Silver, J.A., *Appl. Opt.* **31**, 707-717 (1992).
3. Bomse, D.S., Stanton, A.C. and Silver, J.A. *Appl. Opt.* **31**, 718-731 (1992).
4. Dasch, C.J., *Appl. Opt.* **31**, 1146-152 (1992).
5. Chen S.-J., Dahm, W.J.A., Silver, J.A. and Piltch, N.D., *AIAA Paper* 2001-0187 (2001).
6. Chen S.-J. and Dahm, W.J.A., *Fourth International Microgravity Combustion Workshop*, NASA CP-10191, 191-196 (1997).
7. Chen, S.-J., Dahm, W.J.A., *Proc. Combust Institute* **27**, 2579-2586 (1998).
8. Silver, J.A., and Kane, D.J., *Meas. Sci. Technol.* **10**, 845-852 (1999).
9. L.S. Rothman et al., *J. Quant. Spectrosc. Radiat. Transfer* **48**, 469 (1992); updates 1998, 2001.
10. Silver, J.A., Kane, D.J. and Greenberg, P.J., *Appl. Opt.* **34**, 2787-2801 (1995).

TURBULENT FLAME PROCESSES VIA DIFFUSION FLAME-VORTEX RING INTERACTIONS

**Werner J.A. Dahm¹, Shin-Juh Chen¹, Joel A. Silver²,
Nancy D. Piltch³, Randall L. Vander Wal³**

¹Laboratory for Turbulence and Combustion (LTC), Department of Aerospace Engineering
The University of Michigan, 1320 Beal Avenue, Ann Arbor, MI 48109-2140

²Southwest Sciences, Inc., 1570 Pacheco Street, Suite E-11, Santa Fe, NM 87505

³NASA Glenn Research Center, MS 110-3, Cleveland, OH 44153

INTRODUCTION

Flame-vortex interactions are canonical configurations that can be used to study the underlying processes occurring in turbulent reacting flows. This configuration contains many of the fundamental aspects of the coupling between fluid dynamics and combustion that could be investigated with more controllable conditions than are possible under direct investigations of turbulent flames. Diffusion flame-vortex ring interaction contains many of the fundamental elements of flow, transport, combustion, and soot processes found in turbulent diffusion flames. Some of these elements include concentrated vorticity, entrainment and mixing, strain and nonequilibrium phenomena, diffusion and differential diffusion, partial premixing and diluent effects, soot formation and oxidation, and heat release effects. Such simplified flowfield allows the complex processes to be examined more closely and yet preserving the physical processes present in turbulent reacting flows. Furthermore, experimental results from the study of flame-vortex interactions are useful for the validation of numerical simulations and more importantly to deepen our understanding of the fundamental processes present in reacting flows.

Experimental and numerical results obtained under microgravity conditions of the diffusion flame-vortex ring interaction are summarized in this paper. Results are obtained using techniques that include Flame Luminosity Imaging (FLI), Laser Soot-Mie Scattering (LSMS), Computational Fluid Dynamics and Combustion (CFDC), and Diode Laser Spectroscopy/Iterative Temperature with Assumed Chemistry (DLS/ITAC).

RESULTS

Experiments were conducted under microgravity conditions at the NASA Glenn Research Center 2.2 seconds drop tower facility. Details of the experiment drop rig and its operations can be found in [1, 2]. A reacting vortex ring is generated by first establishing a diffusion flame at the exit of a 2-cm dia. nozzle. Fuel is then impulsively forced through the circular nozzle to generate a vortex ring which wraps the diffusion flame as it rolls up and propagates upstream. The configuration is analogous to the 2-D vortex pair analyses of Karagozian & Manda [3] and Manda & Karagozian [4]. Fuels include methane, ethane, propane, and nitrogen-diluted propane.

Flame luminosity from the burning vortex rings was imaged by a B/W CCD camera. Two cases of methane-air combustion are shown in Figs. 1 and 2. FLI was useful in the analysis of the flame



Figure 1. FLI results showing time evolution of methane-air combustion for $\Gamma = 482 \text{ cm}^2/\text{s}$ and $V=22 \text{ cc}$. Frame rate is 30 Hz.



Figure 2. FLI results showing time evolution of methane-air combustion for $\Gamma = 212 \text{ cm}^2/\text{s}$ and $V=21 \text{ cc}$. Frame rate is 30 Hz.

structure and ring dynamics of reacting vortex rings [1]. Ring trajectories have shown to have an increase in ring speed in the early stage of interaction, and a drastic decrease in ring speed in the latter stage. Fuel volume V and ring circulation Γ also played a role in the resulting flame structure and ring dynamics. Comparisons of propane and ethane cases have shown that radiative heat loss due to the presence of soot can also have an impact on the flame structure and ring dynamics [5]. Comparing Figs.1 and 2 shows that doubling the ring circulation while keeping fuel volume constant led to an increase in fuel consumption rate and flame height. Observations made from FLI were further examined using laser diagnostic tools and numerical simulations.

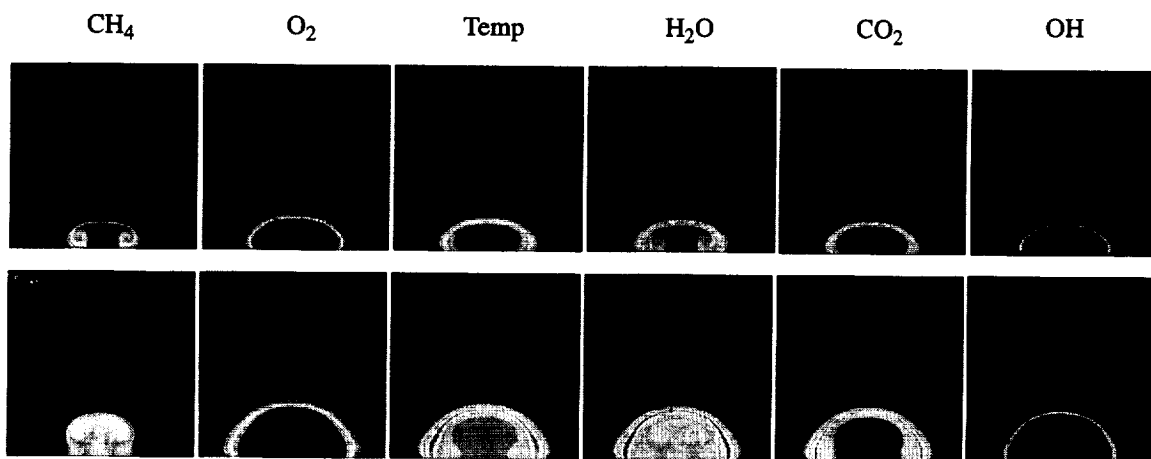


Figure 3. CFDC results showing mole fractions of chemical species and temperature for methane-air combustion with $\Gamma = 100 \text{ cm}^2/\text{s}$ and $V=10.5 \text{ cc}$. Time between top and bottom frames is 0.2 sec. Color bars are as follow: 0-1 for CH_4 , 0-0.21 for O_2 , 300-2200 K for temperature, 0-0.19 for H_2O , 0-0.086 for CO_2 , and 0-0.0064 for OH.

The coupling between fluid dynamics and combustion was examined using numerical simulations by incorporating the conserved scalar approach in which the chemical species and temperature are functions of the conserved scalar (e.g. mixture fraction) and scalar dissipation rate [6, 7]. Chemistry assumptions included flame sheet modeling, equilibrium and non-equilibrium chemistry. Figure 3 is a methane-air reaction case showing results at two different times for temperature and mole fractions of CH_4 , O_2 , H_2O , CO_2 , and OH . Dilatation was found to be the dominant effect of combustion heat release in reacting vortex rings [5]. Note that no CO_2 was found inside the ring in regions where the fuel is still present. On the other hand H_2O is present throughout the interaction. Since no O_2 is found inside the vortex ring, modeling the fuel consumption as a diffusion-limited reaction seems appropriate [1].

The configuration of flame-vortex interaction allows the effects of fluid dynamics and chemistry on the soot processes to be studied. LSMS results can be used as tests for the numerical simulations of soot processes. Details of the experimental setup can be found in Chen *et al.* [8]. LSMS revealed new insights of the soot field inside reacting vortex rings which could not have been possible from inspection of FLI results. Soot was not present in regions of high strain and was found to be along the periphery of reacting vortex ring but inside the flame zone, as shown in Figs. 4 and 5. Future quantification of soot concentrations, such as Laser-Induced Incandescence technique, should be of great interest to the modeling of soot formation and oxidation.

DLS/ITAC was implemented to quantify CH_4 concentration in reacting vortex rings under microgravity conditions [9, 10]. The method of ITAC eliminates the need to directly measure temperature in order to quantify DLS measurements. The conserved scalar approach with the assumption of equilibrium chemistry or non-equilibrium chemistry allows the temperature to be determined via the mixture fraction and scalar dissipation rate. With the measurement of a single major species (e.g. CH_4) all the

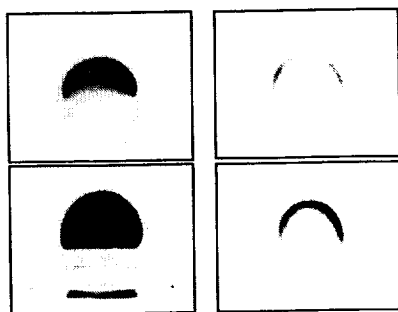


Figure 4. Propane-air combustion results from (left) FLI and (right) LSMS. Frame rate is 10 Hz. $V = 22$ cc and $\Gamma = 80$ cm^2/s .

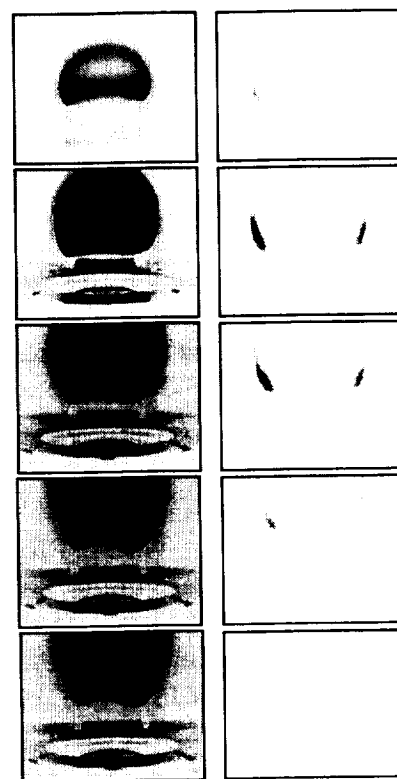


Figure 5. Propane-air combustion results from (left) FLI and (right) LSMS. Frame rate is 10 Hz. $V = 22$ cc and $\Gamma = 190$ cm^2/s .

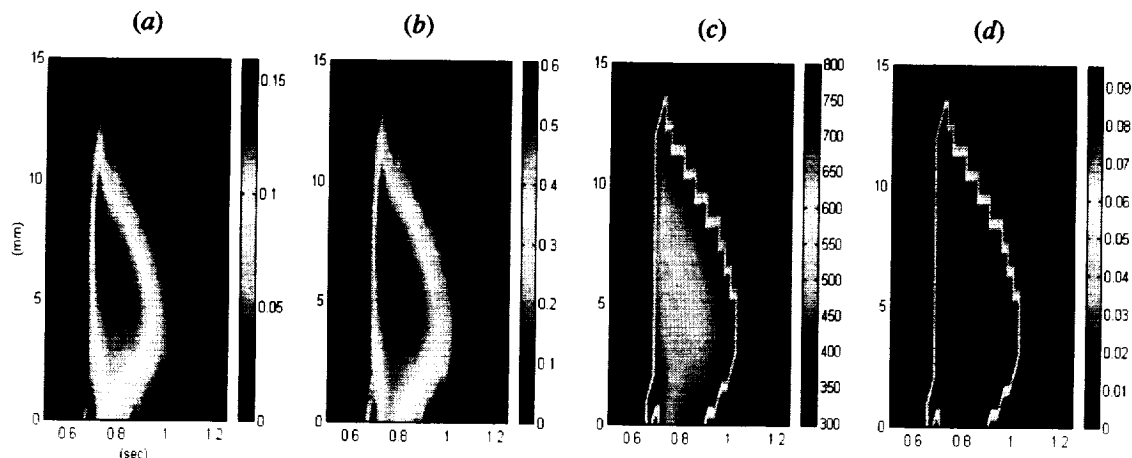


Figure 6. DLS/ITAC results for methane-air combustion at 0.2 inch above nozzle. $V = 21$ cc and $\Gamma = 212$ cm^2/s . (a) Uncorrected CH_4 mole fraction from DLS [10], (b) corrected CH_4 mole fraction using ITAC, (c) temperature field in K, and (d) H_2O mole fraction as a function of drop time and radial distance from center of nozzle.

other major species (H_2O , CO_2 , N_2) and temperature can be determined using ITAC via an iterative process. The method of ITAC extends diode laser spectroscopy measurement technique of a single species to a much broader measurement technique. Figure 6 shows the uncorrected and corrected CH_4 mole fraction along with the temperature field and H_2O mole fraction. The sawtooth edges in (c) and (d) are due to a lack of resolution. Future DLS/ITAC experiments will include measurements of H_2O or CO_2 which are useful in determining other major species in regions where CH_4 is not present. Measurements of OH will extend ITAC to flows where non-equilibrium chemistry effects are important.

Part of this work has been a collaborative effort with Joel A. Silver (Southwest Sciences, Inc.) for the Diode Laser Spectroscopy and Randall L. Vander Wal (NCMR) for the Laser Soot-Mie Scattering. Funding is provided by the NASA Microgravity Combustion Science Program under contract Nos. NAG3-1639 at the University of Michigan, and NAS3-99140 at Southwest Sciences, Inc. A portion of NAG3-1639 was awarded through NASA cooperative agreement NCA3-544 with the National Center for Microgravity Research on Fluids and Combustion.

REFERENCES

1. Chen, S.-J. and Dahm, W.J.A., *Proc. Combust. Inst.* **27**:2579-2586 (1998).
2. Chen, S.-J., *Ph.D. Dissertation*, University of Michigan (2000).
3. Karagozian, A.R. and Manda, B.V.S., *Comb. Sci. Tech.* **49**:185-2000 (1986).
4. Manda, B.V.S. and Karagozian, A.R., *Comb. Sci. Tech.* **61**:101-119 (1988).
5. Chen, S.-J., Dahm, W.J.A., and Tryggvason G., *Proc. Combust. Inst.* **28** (2000). To Appear.
6. Chen, S.-J., Dahm, W.J.A., and Tryggvason, G., AIAA 2000-0433 (2000).
7. Chen, S.-J., Dahm, W.J.A., and Tryggvason, G., AIAA 2000-2468 (2000).
8. Chen, S.-J., Dahm, W.J.A., and Millard, M., & Vander Wal, R.L., AIAA 2001-0786 (2001).
9. Chen, S.-J., Dahm, W.J.A., Silver, J.A., and Piltch, N.D., AIAA 2001-0187 (2001).
10. Silver, J.A. Wood, W.D., Chen, S.-J., Dahm, W.J.A., & Piltch, N.D., *Sixth International Microgravity Combustion Workshop* (2001).

QUANTITATIVE MICROGRAVITY CHEMILUMINESCENCE DIAGNOSTICS: RATE CONSTANTS FROM LOW PRESSURE METHANE FLAMES

Gregory P. Smith, Jorge Luque,* Jay B. Jeffries,[†] David R. Crosley
Molecular Physics Laboratory, SRI International, Menlo Park CA 94025

* Current address: LAM Research Corp. Fremont CA

[†] Current address: Dept. of Mechanical Engineering, Stanford University, Stanford CA

INTRODUCTION

Optical emission signatures from combustion experiments provide a convenient chemically based diagnostic for microgravity and space-based flame experimentation. Sophisticated laser diagnostics require optical and laser equipment that are often in need of adjustment or repair, require high electrical power, and are quite massive to transport and accommodate. However, quantitative implementation of emission diagnostics requires a model-based interpretation, with improved kinetics for excited state production.

We report here experiments in 3 25-30 torr methane-air premixed flames of different stoichiometry to determine these rate constants for CH(A), OH(A), and C₂(d) production. A camera with appropriate optical filters records spatially resolved 2-D profiles of the emissions. An Abel inversion converts these images into flame-center height profiles. Rayleigh scattering from N₂ is recorded with the same system to calibrate the measurements. Using a 1-D flame model validated by previous flame radical measurements, prior LIF determinations of CH(A) and OH(A) quenching rate constants, and these results, we then derive formation rate constants.

For hydrocarbon-air flames,¹ most light comes from OH(A-X) at 280-310 nm, CH(A-X) at 430 nm, CH(B-X) at 390 nm, C₂(d-a) Swan bands found mostly between 470-550 nm, the CO₂ flame band continuum between 320-500 nm, and polynuclear aromatic molecules and soot luminescence in rich systems emitting in the visible. Walsh et al^{2,3} quantitatively measured and modeled the optical emission intensities from CH(A) at 431 nm and OH(A) at 308 nm in a methane jet diffusion flame. Similar experiments are being performed under microgravity.⁴

The reliability of the model comparison, and its validation for use on the flight experiments, depends largely on the availability of reliable kinetics for the production of the excited state species that emit. The loss rates through collisional quenching are well known from experiment and theory.⁵ The current model of Walsh's data^{2,3} errs in predicting the results by factors of 2-6, so quantitative success and interpretation for these diagnostics depends on obtaining improved measurements of the CH(A) and OH(A) production reactions.

EXPERIMENTAL

The three premixed methane-air flames studied here are those labeled Standard ($\Phi = 1.07$, 25 torr), Lean ($\Phi = 0.81$, 25 torr), and Rich ($\Phi = 1.28$, 30 torr) in previous LIF studies of methane flame chemistry.⁶ Operation at low pressure allows good spatial resolution of the species, by which the progress of the flame chemistry can be followed. The flames are supported on a 6 cm diameter sintered plug McKenna burner, housed inside a vacuum chamber designed for optical probing. A laser beam traverses the chamber with power monitored at the exit for the Rayleigh scattering calibration of the optical detection system. A filtered CCD camera detection system images light through a large silica window perpendicular to the laser path.

In order to compare experimental results for the excited state species concentrations and derive production rate constants, we performed one-dimensional flame model calculations using the GRI-Mech 3.0 chemical mechanism for methane oxidation.⁷ Measured flow rates and temperature profiles are also inputs. Reactions are added for excited state species OH(A) and CH(A) – radiative decay, collisional quenching,⁵ and potential production steps – plus a few steps involving C and C₂, since these species are likely involved in the production kinetics.

The likely OH chemiluminescence source cited by Gaydon¹ is CH + O₂; our initial rate constant of 6×10^{10}

comes from flame studies by Porter et al.⁸ The reaction responsible for CH chemiluminescence is less certain. Three reactions have been proposed, and literature analysis of experiments often conflict or omit the other possible steps. For $C_2H + O_2$, an Arrhenius fit to the 300K result of Devriendt et al.⁹ and shock tube emission results at 2000-2600K from Hwang et al.,¹⁰ gives $4.1 \times 10^{13} e^{-2265/T}$. (Merten's recent 3000K shock tube results¹¹ suggest a higher activation energy and a 16-fold reduction at 1500K flame temperatures.) For the reaction $C_2H + O$ at 300K, Devriendt et al.⁹ measure $1.1 \times 10^{13} \text{ cm}^3 \text{ mole}^{-1} \text{ s}^{-1}$ but Grebe and Homann¹² propose a much lower value, 7.0×10^{11} . Joklik et al.¹³ estimate 7.0×10^{12} from a low pressure C_2H_2 flame. An average value of 6.2×10^{12} is used in the preliminary mechanism, temperature independent with large error limits. Finally, the step $C_2 + OH \rightarrow CH^*$ is favored by Bulewicz¹⁴ and Porter.⁸ The mechanism $k = 1.1 \times 10^{13}$ from a reanalysis of Porter's results is about twice Bulewicz's estimate. For $C_2(\text{d-a})$ emission, quenching loss rates need measurement. Isotope work by Ferguson¹⁵ suggests C_2^* production reactions $C+CH$, $CH+CH$, and $C+CH_2$ – operationally and experimentally hard to distinguish.

Low resolution spectra show features clearly identifiable as OH(A-X), CH(B-X), CH(A-X), and $C_2(\text{d-a})$ bands. CH and especially C_2 emissions are very dependent on stoichiometry, and C_2 Swan bands are absent in the lean flame. Some underlying emission, particularly near 350 nm and >430 nm, likely the CO_2^* continuum, is too faint for analysis. We assume light at 280-340 nm is OH(A-X), 380-450 nm is excited CH, and >450 nm is C_2 .

A set of 2-D flame emission images from a gated intensified CCD camera record line-of-sight integrated luminescence signals at 0.0135 cm resolution. Five calibrated filters examine $\lambda > 455$ nm (Swan bands), $\lambda > 375$ (CH and C_2), 430 ± 10 nm for CH(A-X), 300 ± 10 nm or 275-370nm for OH(A-X). The difference image between the 375 and 455 filters covers the 370-460 nm window to isolate the CH emissions. The intensifier gain calibration versus wavelength adds uncertainty to the OH(A) determination. (The optical system was calibrated at 434 nm.) In addition to these gain and transmission terms, recorded emission intensities must be multiplied by the ratio of observation time to radiative lifetime to obtain excited state concentrations.

The images measure integrated emissivities through the depth dimension of the cylindrical flames, but comparison to 1-D chemical models requires localized excited state concentrations near the uniform center of the flame, as a function of height above the burner. An Abel inversion of the data must be performed, using the code of Walsh et al.² Binning of data pixels and operation at lower spatial resolution is necessary to avoid excessive noise in the inverted result. The current analysis resolution is 0.05 cm height and 0.43 cm radial. The inversion results provide emission intensities for each species and flame from specific local volume elements. A flattening of the profiles is seen, as might be expected from the inversion and the general saucer shape of species distributions in these flames. Vertical cuts to provide height distributions show that the inversion has minor effects on most excited state peak positions, widths, and amounts. If one assumes that the excited CH is uniformly distributed over the nominal 6 cm burner diameter instead of taking the radial data and performing the inversion, only a 5% error is introduced. Traces of an uneven pattern are apparent in some Abel results, suggesting 10% inversion uncertainty.

To relate the point emission intensities of the Abel inverted images to excited state concentrations, the system optical detection efficiency is calibrated using the Rayleigh scattering method previously employed to determine ground state concentrations from flame LIF measurements⁶. The CCD camera system with 375nm filter is operated with a 50 ns gate triggered by the firing of an excimer pumped dye laser at 434 nm. The laser beam traverses the chamber above the burner, filled with 50-100 torr N_2 , and the power (20 $\mu\text{J/pulse}$) is measured. 600 shots are averaged, and the process is repeated with the N_2 and laser beam replaced by the standard flame $CH + C_2$ luminescence. The Rayleigh signal is integrated over a 2.16cm (160 pixel) length and 6 pixel height-width of the laser beam.

RESULTS

Table 1 shows results and model comparisons. $C_2H + O_2$ dominates model CH^* production and greatly overpredicts results. A second model result without this step, in the penultimate column, gives better predictions. At 1700K 25 torr, 10^7 cm^{-3} is 70 parts per trillion. Uncertainties are 20% relative, 35% absolute. CH(A) interference filter results are consistent with the glass filter difference image. From CH(A)/ CH^* ratios, 80% is A state emission (60% lean).

Flame ratios are well reproduced by the model, supporting the chosen chemistry and ability to predict the stoichiometry dependence. The lean CH ratio is high for the 370-460nm glass filter result, but matches predictions for the narrow band CH(A-X) value, suggesting that some non-CH background may contribute. The rich CH^* ratio lies between the values from models dominated by $C_2H + O_2$ and $C_2H + O$, which suggests both reactions may contribute. The model underpredicts absolute OH(A) by 2, and overpredicts CH^* by up to a factor of 40. If the reaction $C_2H + O_2 \rightarrow CH^* + CO_2$ is removed, however, good agreement is obtained.

Table 1. Maximum Excited State Concentrations (cm^{-3}) ($\text{e}8 = \times 10^8$)

Species	Flame(s)	Experiment	Model	w/o C ₂ H+O ₂	Exper./Model	C ₂ *
OH*	Rich	1.53e8	9.03e7		1.69	1.06e7
OH*	Standard	1.02e8	5.38e7		1.90	1.26e6
OH*	Lean	7.91e7	3.79e7		2.09	0
CH*	Rich	5.57e7	2.11e9	4.41e7	.026, 1.26	
CH*	Standard	9.62e6	3.09e8	9.93e6	.031, 0.97	
CH*	Lean	2.36e6	4.66e7	1.62e6	.051, 1.46	
OH*	Rich/Standard	1.49	1.68			
OH*	Lean/Standard	0.77	0.70			
CH*	Rich/Standard	5.8	6.8	4.4		
CH*	Lean/Standard	0.24 (.17 A)	0.15	0.16		

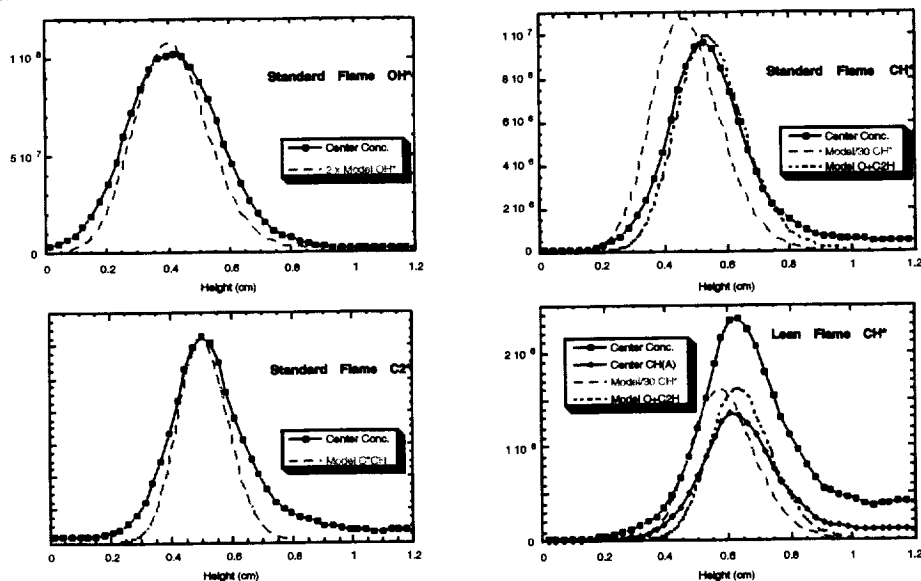


Figure 1. Experimental and model excited state profiles in 25 torr CH₄-air flames (see text).

Abel inversions also provide height profiles of the excited state concentrations at flame center for comparison with model results. Some results are shown in Figure 1. Model curves are plotted for twice the OH* prediction, 1/30 the CH* predictions, and for the CH* formed from the $\text{O} + \text{C}_2\text{H}$ reaction only. Model results for C₂*, C times CH, reflect one likely production reaction.

The zero height location of the profiles derived from the images is uncertain. Repeat runs can differ by 0.05 cm, and the average peak position is unexpectedly 0.1 cm above the model prediction. Previous agreement of the model with CH(X) LIF peak positions,⁶ the OH(A) precursor, implies the model should predict the chemiluminescence peak positions well. Previous data places the peak of the CH* emission (at $0.60 \pm .02$ cm) with respect to the CH LIF maximum in the standard flame, and all profiles shown in Fig. 1 are adjusted backward 0.12 cm.

DISCUSSION

The data and model order of the peaks in these flames is OH* before C₂* and then CH*. Model widths are slightly narrower than Abel-inverted measurements. Two model predictions included for the CH* results correspond to $\text{C}_2\text{H} + \text{O}_2$ and $\text{C}_2\text{H} + \text{O}$ production reactions. C₂H + O fits peak position and amount better. Standard flame profiles show good model agreement.

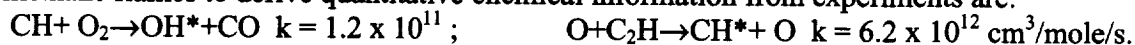
The interference filter results, labeled CH(A), are plotted in the Lean CH* panel along with the glass filter 370-460 nm profile. The tail in the broadband profile into the burnt gases, and the larger than expected difference in peak magnitudes, indicates a significant minority of the broadband emission is not associated with CH*. Model agreement then improves.

The starting model predicts about 30 times too much excited CH. Analysis shows the $C_2H + O_2$ reaction is responsible for nearly all CH* production. Even reducing this rate by 16, as Mertens' work indicates,¹¹ is insufficient. A second model without this reaction predicts the measured amounts (multiplier of 1.1 ± 0.2). Here, the $C_2 + OH$ reaction only contributes about 10%; for this to be a significant cause of the chemiluminescence, k must be 10 times higher and nearly gas kinetic – unlikely. We recommend $k = 6.2 \times 10^{12} \text{ cm}^3 \text{ mol}^{-1} \text{ s}^{-1}$ for $O + C_2H$ as the CH* source, although any combination of O and O_2 reactions with the same net rate is acceptable. Determining this division requires experiments in flames with significantly different O/O_2 ratios. The rich/standard flame CH* ratio results in Table 1 suggest nearly equivalent participation. Note our $k(O + C_2H)$ nearly equals Joklik's¹³ C_2H_2 flame value (7×10^{12}), half the 300K value.⁹

The Walsh diffusion flame results^{2,3} for CH* are overpredicted by 3 by a model that uses GRI-Mech 2.11 chemistry and chemiluminescence rate constants from Devriendt et al.⁹ This data suggests $k(O + C_2H) = 3.6 \times 10^{12}$, only 40% below our recommendation.

The results for OH*, a multiplier of 1.9 ± 0.2 , suggest a faster rate constant for $CH + O_2$, $1.2 \times 10^{11} \text{ cm}^3/\text{mole/s} (\pm 35\%)$. Modeling the Walsh diffusion flame OH* observations^{2,3} using GRI-Mech 2.11 and the same OH* mechanism implies a nearly identical multiplier of 1.6; the predicted position of the chemiluminescence is poor, however. Future experiments in other low pressure flames, including C_2H_x fuels, will refine these rate constant values. Flames with N_2O oxidizer and H_2 flames seeded with hydrocarbons will provide the varied O/O_2 ratios needed to decipher CH* production reaction(s). LIF quenching decay measurements of $C_2(d-a)$ will enable deduction of excited state C_2 production rate parameters from the emission data.

Recommended rate constants for use in modeling chemiluminescence measurements in methane flames to derive quantitative chemical information from experiments are:



The results do not rule out the $C_2H + O_2$ reaction as an alternative source of CH* ($k < 4 \times 10^{11}$).

REFERENCES

1. A. G. Gaydon, "The Spectroscopy of Flames," 2nd ed., John Wiley & Sons, New York, NY, 1974.
2. K. T. Walsh, M. B. Long, M. A. Tanoff, and M. D. Smooke, *Proc. Combust. Inst.* **27**: 615-623 (1998).
3. J. Luque, J. B. Jeffries, G. P. Smith, D. R. Crosley, K. T. Walsh, M. B. Long, and M. D. Smooke, *Combust. Flame* **122**: 172-175 (2000).
4. K. T. Walsh, J. Fielding, M. D. Smooke, and M. B. Long, *Proc. Combust. Inst.* **28**, in press (2000).
5. M. Tamura, P. A. Berg, J. E. Harrington, J. Luque, J. B. Jeffries, G. P. Smith, and D. R. Crosley, *Combust. Flame* **114**: 502-514 (1998).
6. P. A. Berg, D. A. Hill, A. R. Noble, G. P. Smith, J. B. Jeffries, D. R. Crosley, *Combust. Flame* **121**: 223 (2000).
7. G. P. Smith, D. M. Golden, M. Frenklach, N. W. Moriarty, B. Eiteneer, M. Goldenberg, C. T. Bowman, R. K. Hanson, S. Song, W. C. Gardiner, V. Lissianski, Z. Qin, GRI-Mech 3.0 Web site, www.me.berkeley.edu/gri_mech/, 1999.
8. R. P. Porter, A. H. Clark, W. E. Kaskan, and W. E. Browne, *Proc. Combust. Inst.* **11**: 907-917 (1966).
9. K. H. Devriendt, H. VanLook, B. Ceusters, and J. Peeters, *Chem. Phys. Lett.* **261**: 450-456 (1996).
10. S. Hwang, W. C. Gardiner, M. Frenklach, and D. Hidaka, *Combust. Flame* **67**: 65-76 (1987).
11. J. D. Mertens, "A Shock Tube Study of CH* Reaction Kinetics in CH_4 and C_2H_2 Oxidation," 22nd Intl. Symp. On Shock Waves, Paper 4510, London, 1999.
12. J. Grebe, and K. Homann, *Ber. Bunsenges. Phys. Chem.* **86**: 581-586; *ibid.* 587-596 (1982).
13. R. G. Joklik, J. W. Daily, W. J. Pitz, *Proc. Combust. Inst.* **21**: 895-904 (1986).
14. E. M. Bulewicz, P. L. Padley, and R. E. Smith, *Proc. Roy. Soc. (London)* **A315**: 129-146 (1970).
15. R. E. Ferguson, *J. Chem. Phys.* **23**: 2085-2089 (1955).

Quantitative Detection of Combustion Species using Ultra-Violet Diode Lasers

J. S. Pilgrim and K. A. Peterson

Southwest Sciences, Inc. 1570 Pacheco Street, Suite E-11 Santa Fe, NM 87505

INTRODUCTION

Southwest Sciences is developing a new microgravity combustion diagnostic based on UV diode lasers. The instrument will allow absolute concentration measurements of combustion species on a variety of microgravity combustion platforms including the Space Station. Our approach uses newly available room temperature UV diode lasers, thereby keeping the instrument compact, rugged and energy efficient. The feasibility of the technique was demonstrated by measurement of CH radicals in laboratory flames. Further progress in fabrication technology of UV diode lasers at shorter wavelengths and higher power will result in detection of transient species in the deeper UV. High sensitivity detection of combustion radicals is provided with wavelength modulation absorption spectroscopy.

It has long been recognized that absorption spectroscopy can provide quantitative species number densities, but the technique has not been used widely by combustion researchers because of poor sensitivity. In addition, one has to perform multiple line-of-sight measurements followed by tomographic inversion in order to retrieve spatial distribution information. We have been developing high frequency wavelength modulation spectroscopy (WMS) techniques utilizing commercially available visible, near-infrared, and mid-infrared diode lasers.¹⁻⁷ We have demonstrated minimum detectable absorbances of $\sim 10^{-6}$ while retaining the inherent quantitative aspects of traditional absorption methods. This level of sensitivity—about a thousand times better than traditional absorption methods—allows detection of trace species including free radicals in flames.

In an earlier SBIR project sponsored by NASA Glenn Research Center, we successfully demonstrated high sensitivity detection of CH radicals in laboratory diffusion flames using $\sim 100\mu\text{W}$ of tunable 426 nm generated by doubling 85 mW of 852 nm diode laser output in a nonlinear crystal. Results from the study are detailed in Optics Letters.⁷ In another earlier SBIR project sponsored by NASA Lewis Research Center, we performed multiple line-of-sight measurements of H_2O and CH_4 under microgravity conditions to reconstruct 2-D distributions using the Abel inversion technique.⁸ We have also extended the diode laser-based WMS technique to 308 nm by sum frequency mixing 488 nm Ar^+ laser light and 835 nm diode laser light, and we demonstrated the high sensitivity detection of OH by WMS.⁹

Recently, GaN-based ultraviolet diode lasers became commercially available from Nichia Corporation in the 390 – 420 nm wavelength region. Operating at room temperature and emitting $> 5\text{ mW}$ of continuous output, they were developed primarily for high density storage and printing applications. We recognize that new sensing applications may be available with ultraviolet diode lasers including combustion diagnostics and chemical analysis. In order to examine the spectroscopic properties and the feasibility of optical diagnostics based on UV diode lasers, we chose to monitor the CH radical in laboratory flames. The direct UV output from a GaN diode laser

bypasses the requirement for a complex nonlinear upconversion step as performed in the earlier Phase I study.

Table I lists some of the combustion species that may be amenable to detection using the present diagnostic technique. The last two entries in the table, NO and O₂, require deep UV generation by first amplifying the UV diode laser output in a GaN power amplifier diode, followed by doubling in a nonlinear crystal. Such GaN power amplifier diodes have been demonstrated in the laboratory and are slowly becoming commercially available.

Table I. Combustion species amenable to UV diode lasers .

Species	Transition	Wavelength (nm)
CH	$A^2\Delta \leftarrow X^2\Pi$	413 – 440
	$B^2\Sigma^- \leftarrow X^2\Pi$	387 – 408
C ₂	$d^3\Pi_g \leftarrow a^3\Pi_u$ (Swan band)	438 – 516
CN	$B^2\Sigma^+ \leftarrow X^2\Sigma^+$	359 – 422
NO ₂	$B^2B_2 \leftarrow X^2A_1$	350 – 780
NO	$A^2\Sigma^+ \leftarrow X^2\Pi_2$ (γ -band)	227, 215, 205 (x2)
O ₂	$B^3\Sigma_u^- \leftarrow X^3\Sigma_g^-$ (Schumann-Runge)	175 – 205 (x2)

SPECTROSCOPIC APPLICATION OF GaN LASERS

One of the most serious impediments to applying GaN blue lasers to spectroscopic detection of combustion species is the erratic spectral coverage. Because only about 10 % of the wavelengths in the laser's nominal operating range are accessible for single mode tuning and modulation, there is no guarantee that an absorption feature of the target molecular species will be accessible. This limitation becomes even more disabling for molecules with sparse absorption features where there may be no absorption lines accessible to the GaN laser. Our solution is the development of a new type of external cavity diode laser (ECDL) that allows complete spectral coverage and agile wavelength tuning and modulation using GaN blue lasers.

The Southwest Sciences ECDL design allows the laser to be tuned by varying the diode gain element injection current. Thus, wavelength modulation frequencies may be orders-of-magnitude higher than with competitive presently commercialized designs (New Focus, Newport, and TuiOptics). Fig. 1 shows the wavelength tuning of our ECDL with diode laser injection current. Competitive designs approach wavelength modulation frequencies of about 1500 Hz limited by piezo-electric driven mechanical movement of an optical element. Our ECDL has been modulated at over 10 kHz and frequencies in the MHz regime are possible. The wavelength modulation frequency has important ramifications for implementation as a microgravity combustion diagnostic. First, the 1/f noise term dictates that higher frequency operation will result in increased sensitivity. Since we are interested in looking at weak molecular optical transitions of gaseous species that are present at low concentrations in a flame, the highest sensitivities are required. Secondly, the

modulation frequency determines the temporal measurement resolution during the microgravity drop experiment; a higher frequency permits faster measurements. Thus, we can acquire data with higher temporal and spatial resolution during a 2.2 or 5.18 second drop than possible with slower commercial off-the-shelf ECDLs.

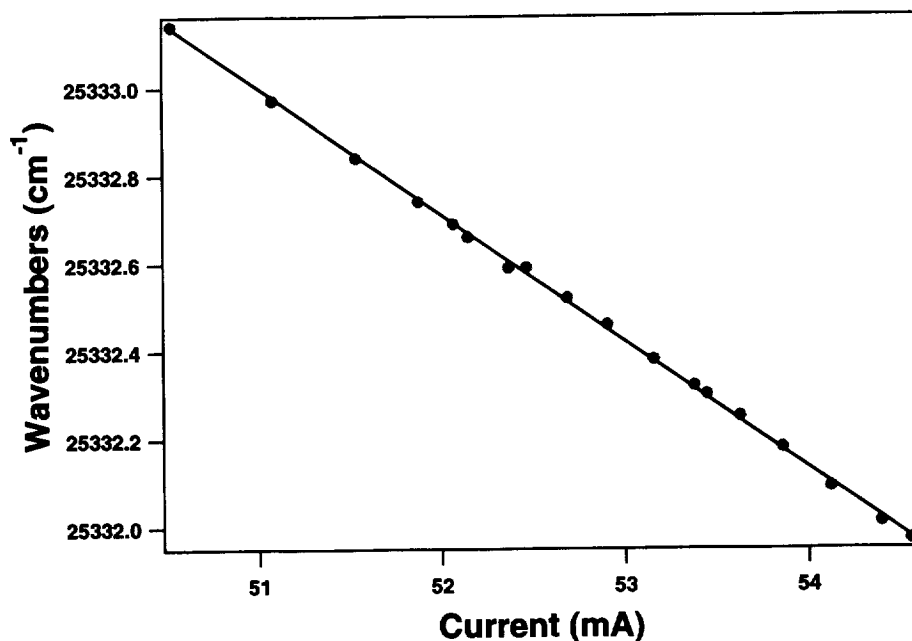


Figure 1- Wavelength tuning of the ECDL with diode laser injection current.

Incorporating the standard Fabry-Perot GaN laser into an external cavity allows recovery of the basic features that make a semiconductor device operating in the ultra-violet appealing for microgravity combustion diagnostics. Operation in an ECDL configuration allows inclusion of a separate wavelength-selective optical element that ensures operation at any desired wavelength within the device gain curve. We have constructed our ECDL around the well-known Littman-Metcalf¹⁰ resonator. Fig. 2 shows a schematic diagram of the major components of this type resonator. In the Littman-Metcalf design the zeroth order output of the diffraction grating is used as the laser output. The first order diffraction is retroreflected by a cavity feed back mirror which establishes one end of the resonator. The other end of the resonator is the outboard surface of the Fabry-Perot diode element. Wavelength selectivity is achieved by the angle of the diffracted return beam as determined by the cavity feed back mirror position.

PRESENT WORK

The goal of the present project is to develop a deliverable instrument for the quantitative detection of CH radicals in combustion studies and use this instrument in the 2.2 second drop tower at NASA Glenn Research Center. This instrument will be compatible with NASA Glenn microgravity drop tower facilities. The light source will consist of a frequency-agile, UV, external cavity diode laser that will be used to make high sensitivity line-of-sight absorption measurements.

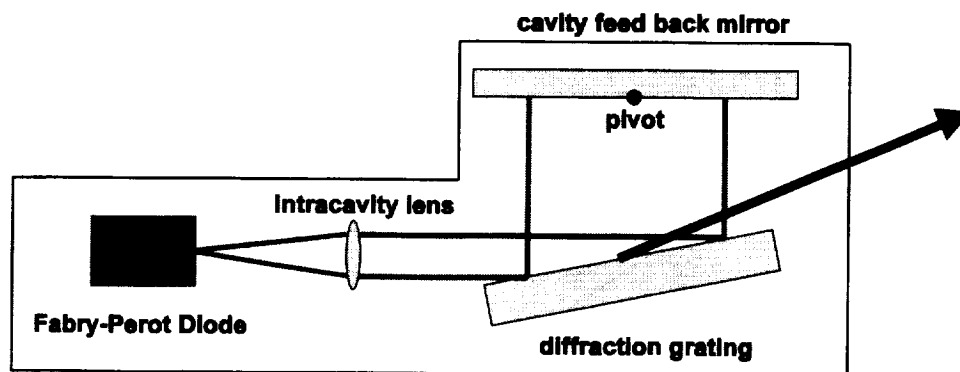


Figure 2 - A block diagram of a Littman-Metcalf external cavity diode laser.

This instrument will be compatible with our 1-D and 2-D imaging technology which we have utilized in previous NASA projects. We anticipate CH detection limits of 0.1 ppm over a 1 cm path and a spatial resolution of 0.5 mm with a 10 Hz measurement rate. Our present effort is directed toward optimizing the ECDL design for maximum wavelength tuning range with injection current and maximum wavelength modulation frequency. The basic optical elements are being engineered into an integrated and rugged package to withstand the rigors of the microgravity drop tower.

REFERENCES

1. D. B. Oh, A. C. Stanton and J. A. Silver, *J. Phys. Chem.* **97**, 2246 (1993).
2. D. B. Oh and A. C. Stanton, *Appl. Opt.* **36**, 3294 (1997).
3. J. A. Silver and D. C. Hovde, *Rev. Sci. Instrum.* **65**, 1691 (1994).
4. D. C. Hovde, T. P. Meyers, A. C. Stanton and D. R. Matt, *J. Atmos. Chem.*, **20**, 141 (1995).
5. J. A. Silver, *Appl. Opt.*, **31**, 707 (1992) and references therein.
6. D. S. Bomse, A. C. Stanton and J. A. Silver, *Appl. Opt.* **31**, 718 (1992) and references therein.
7. K. A. Peterson and D. B. Oh, *Opt. Lett.* **24**, 667 (1999).
8. J. A. Silver, D. J. Kane and P. J. Greenberg, *Appl. Opt.*, **34**, 2787, (1995).
9. D. B. Oh, *Opt. Lett.*, **20**, 101 (1995).
10. M. G. Littman and H. J. Metcalf, *Appl. Opt.* **17**, 2224 (1978).

This work is being performed under NASA Glenn Research Center contract NAS3-01007.

DEVELOPMENT OF AN EARLY WARNING FIRE DETECTION SYSTEM USING CORRELATION SPECTROSCOPY

K. Goswami, G. Voevodkin, V. Rubstov, and R. Lieberman
Intelligent Optical Systems
2520 West 237th Street
Torrance, CA 90505, USA

N. Piltch
NASA - Glenn Research Center
21000 Brookpark Road, MS 110-3
Cleveland, OH 44135

INTRODUCTION

Combustion byproducts are numerous. A few examples of the gaseous byproducts include carbon dioxide, carbon monoxide, hydrogen chloride, hydrogen cyanide and ammonia. For detecting these chemical species, classic absorption spectroscopy has been used for many decades, but the sensitivity of steady-state methods is often unsuitable for the detection of trace compounds at the low levels (parts per million to parts per billion) appropriate for scientific purposes. This is particularly so for monitoring equipment, which must be compact and cost-effective, and which is often subjected to shock, vibration, and other environmental effects that can severely degrade the performance of high-sensitivity spectrometers in an aircraft. Steady-state techniques also suffer from a lack of specificity; the deconvolution of the spectra of complex mixtures is a laborious and error prone process. These problems are exacerbated in remote fiber-optic monitoring where, for practical reasons, the fundamental absorbance region of the spectrum (often between 3 and 8 μm) is inaccessible, and the low-strength, closely spaced, near-infrared overtone absorbance bands must be used. *We circumvented these challenges by employing correlation spectroscopy, a variation of modulation spectroscopy.*

In correlation spectroscopy, a dramatic increase in sensitivity is achieved by phase- or wavelength-modulation of a very narrow band optical source whose natural wavelength coincides with one of the absorbance lines of the target compound. Highly specific chemical detection is accomplished by using a sample of the target compound itself as an optical filter. The positions of the absorbance maxima in the filter sample are modulated via an external physical process, such as an electric field (Stark effect modulation) or pressure. This modulation, which brings the reference sample's absorbance bands periodically into and out of registry with the absorbance bands of the target gas in the substance under test, creates a modulated signal at the detector whose intensity is directly related to the concentration of the target. This technique can achieve one or two orders of magnitude better sensitivity than simple modulation of the source intensity, and has the added benefit of rendering the detection system virtually insensitive to other gases. Because the detailed structure (e.g., the manifold of rotational states on infrared vibrational absorbance bands) is unique for each compound, the use of tunable fiber

Bragg grating (FBG) filters matched to the spectral properties of the target compound makes correlation-spectroscopy systems extremely good at detecting trace quantities of target molecules in complex mixtures.

EXPERIMENTAL SETUP AND RESULTS

Currently, we are developing a prototype instrument, which will use the correlation spectroscopic approach for detecting trace gases. We have targeted the detection of carbon monoxide in the near infrared (NIR) region. Figure 1 shows the NIR spectrum of carbon monoxide.

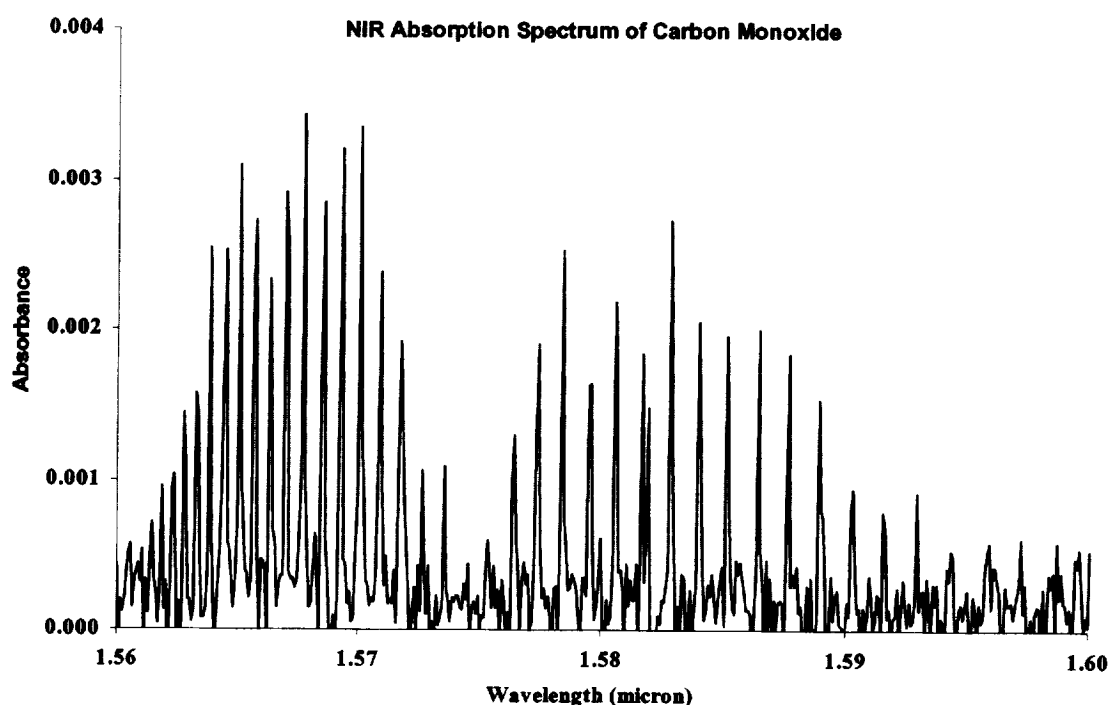


Figure 1
Absorption spectra of 100% CO acquired with FT-NIR (15 cm pathlength)

Figure 2 shows the schematic diagram of the experimental arrangement.

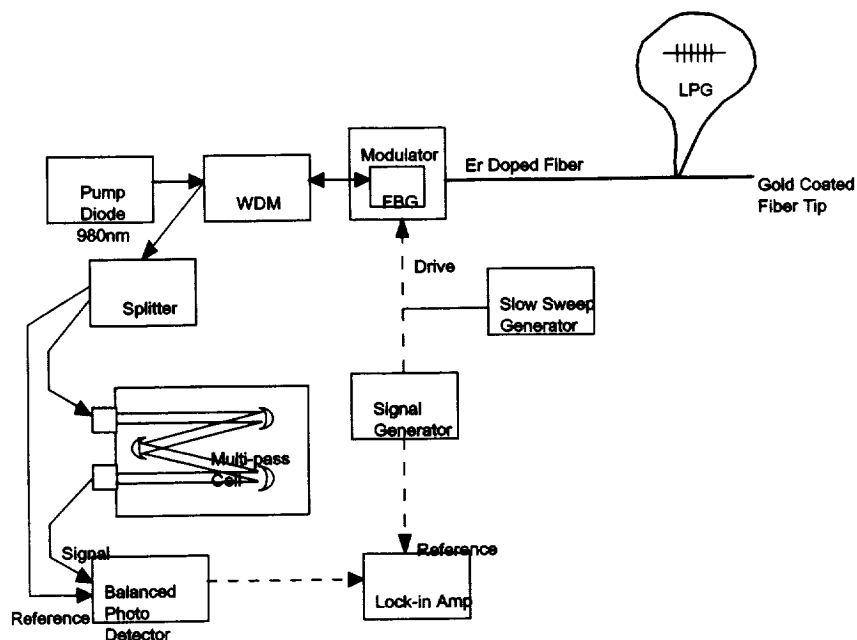


Figure 2
Schematic diagram of the experimental setup showing the Erbium fiber-doped fiber laser as the light source.

Spectroscopic detection of carbon monoxide requires a light source. Because commercially available light emitting diodes do not have sufficient power, we are utilizing Erbium-doped fiber laser (EDFL) in the L-band (power 10 mW). As Figure 2 shows, the output of the EDFL is coupled to a splitter. One fraction of the laser power directly goes to a reference photodiode, and the other fraction (the signal) passes through a multipass cell. We have utilized a GRIN (GRaded INDEX) lens for collimating the signal beam before entering into the multipass cell. After traversing through the multipass cell, the modified signal beam is detected by another photodetector. The reference and signal beams are converted to electrical parameters. By using a processing chip we are able eliminate the common mode noise of the EDFL.

As can be seen from Figure 1, the absorption lines of carbon monoxide span nicely over the 1560 – 1590 nm range. We designed our EDFL to yield output in this region. We achieve this control of wavelength selection by utilizing fiber Bragg grating (FBG). The laser cavity consists of the FBG on one side of an Er^{3+} -doped fiber, and a gold coated mirror on the other.

The Bragg wavelength is dependent on strain and temperature. Thus, by varying either strain or temperature, we can tune the EDFL for a match with any absorption line of carbon monoxide. The strain-induced shift in wavelength is typically 1.2 nm/mε, and temperature-induced shift is about 0.1 nm per degree C. The FBG will break if the strain exceeds 1%. This implies a theoretical tuning range of 12 nm where the lower wavelengths are accessed by compressing the grating. Experimentally, we produced 1584

nm gratings that could be tuned from 1584 to 1590 nm using a compact fiber-holding device. This pencil-like device is shown in Figure 3.



Figure 3

A PZT driven fiber stretcher

To apply strain to the Bragg grating in a controllable manner, we attached the grating to a PZT actuator. When connected to a function generator, the PZT stack vibrates at a set frequency. The resonance of the modulator was kept around 3000 Hz. Following the manufacturer's instructions, we did not operate the device at resonance or above resonance frequencies. We demonstrated 0.5 nm tuning at a modulation frequency around 3 kHz.

CONCLUSION

This is an ongoing project. During the actual presentation, we will show data on the performance of the system with respect to detecting low concentrations of carbon monoxide.

ACKNOWLEDGEMENT

Intelligent Optical Systems gratefully acknowledges funding support for this project from NASA-GRC through a Phase II SBIR contract (NAS3-00016).

MULTIDIMENSIONAL EFFECTS ON IGNITION, TRANSITION, AND FLAME SPREAD IN MICROGRAVITY

T. Kashiwagi¹, W. E. Mell², Y. Nakamura¹, S. L. Olson³, H. R. Baum¹, K. B. McGrattan¹

¹Mail Stop 8662, NIST, Gaithersburg, MD 20899

² Mechanical Engineering, University of Utah, Salt Lake City, UT 84112

³Mail Stop 500-115, NASA Glenn Research Center, Cleveland, OH 44135

INTRODUCTION

Localized ignition is initiated by an external radiant source at the middle of a thermally thin sample under external slow flow, simulating fire initiation in a spacecraft with a slow ventilation flow. Two ignition configurations are simulated, one across the sample surface creating a line shaped flame front (two-dimensional, 2-D, configuration) and the other a small circular ignition (three-dimensional, 3-D, configuration). Ignition, subsequent transition to simultaneously upstream and downstream flame spread, and flame growth behavior are studied experimentally and theoretically. Details of our theoretical models and numerical techniques can be found in previous publications ^{1,2}.

The effects of the sample width on the transition and subsequent flame spread, and flame spread along open edges of a thermally thin paper sample are determined. Experimental observations of flame spread phenomena were conducted in the 10 s drop tower and also on the space shuttle STS-75 flight to determine the effects of oxygen concentration and external flow velocity on flame spread rate and flame growth pattern. Finally, effects of confinement in a small test chamber on the transition and subsequent flame spread are examined. The results of these studies are briefly reported.

EFFECTS OF SAMPLE WIDTH

Many flame spread studies over a solid fuel surface in microgravity, by necessity, were conducted in spatially limited experimental volumes which resulted in relatively narrow samples despite the original intention of a 2-D experimental configuration. It is, therefore, critically important to determine whether these sample widths will produce truly 2-D flame spread behavior. In this study, our 2-D and 3-D numerical simulation codes were used to investigate the effects of sample width on flame spread. Heat loss effects at the interface of the sample and the sample holder were tested by varying the thermal properties of the sample holder. It was found that heat losses to the sample holder affected the flame spread rate in the case of the narrower sample with slower external flow velocity as shown in Figure 1. Sample width effects were most significant when the external flow was relatively small (limited oxygen supply case) as shown in Figure 2. The incoming flow speed towards the flame front was dramatically reduced by thermal expansion (the flame acts as an obstacle to the incoming flow). In such environments, the net inflow of oxygen is reduced enough to significantly affect flame spread behavior. Since a full 2-D flame generates more heat release (larger thermal expansion) than a narrow 2-D flame (a smaller flame with less heat release), the net inflow of oxygen for the full 2-D flame is less than for the narrow 2-D flame³. This is the reason why flame spread rate of a narrow sample is faster than that of a wider sample. The results shown in Figure 1 indicate that attainment of a truly 2-D flame configuration tends to be difficult at external flow velocities less than 5 cm/s.

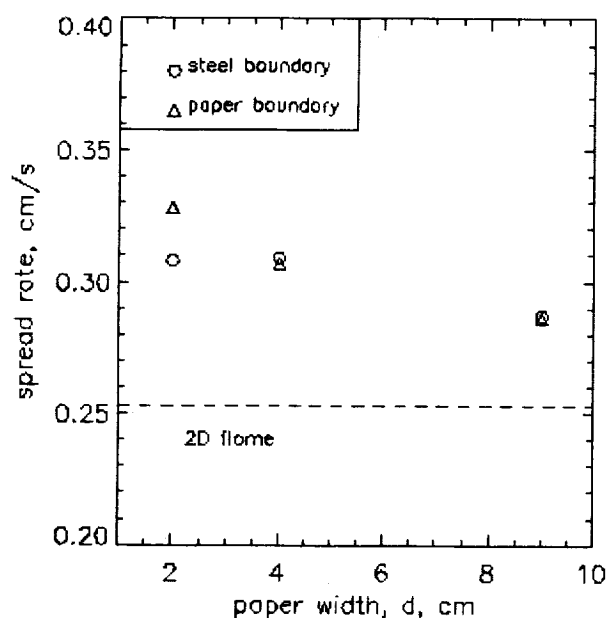


Figure 1. An external flow of 2 cm/s.

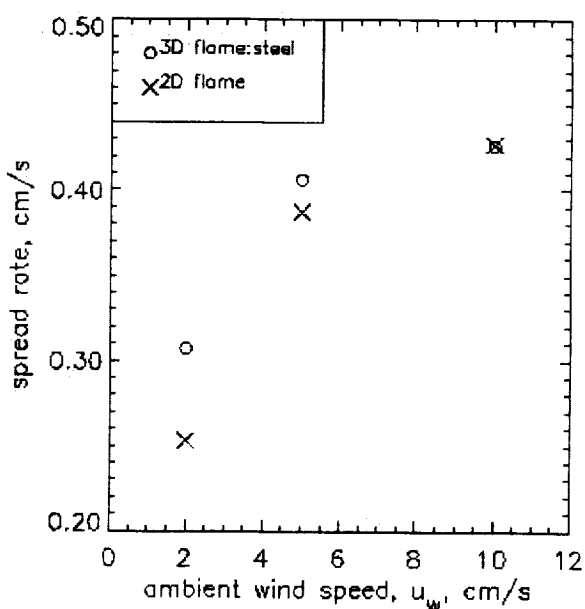


Figure 2. 9 cm width for 3-D with steel holder

FLAME SPREAD ALONG FREE EDGES

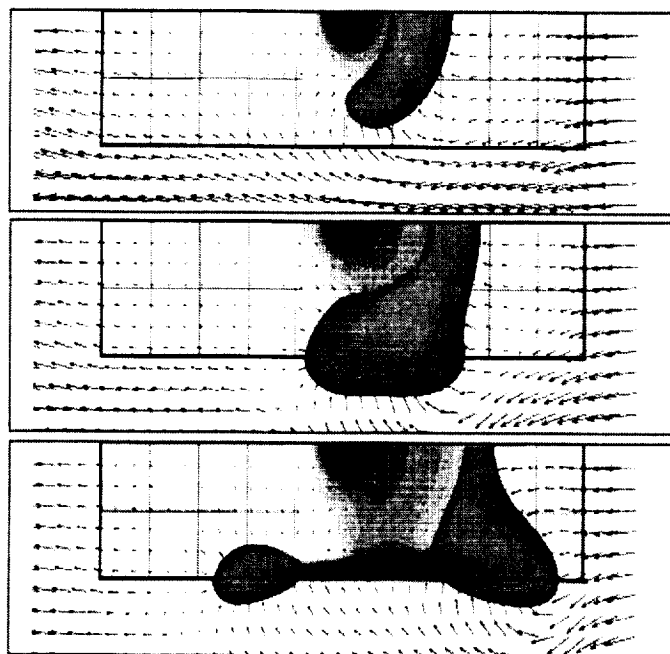


Figure 3 Calculated sequence images of isosurface of gas phase reaction rate with net oxygen mass flux vectors at flow of 2 cm/s from right to left .

In this theoretical and experimental study, the sample is ignited locally at the middle of the 4 cm wide sample and the subsequent flame spread reaches both open edges of the sample oriented along the direction of the flow. Figure 3 shows the flame is more or less semicircular shortly after ignition, and slightly extended upstream (top figure). Later the flame spreads to free edges (middle figure) and starts to spread both upstream and downstream. The following trends are observed in the experiments and predicted by the numerical calculation⁴ in the order of increasing imposed flow velocity; (1) ignition but subsequent flame spread is not attained, (2) flame spreads upstream (opposed mode) without any downstream flame, and (3) the upstream flame and downstream flames separately travel simultaneously along the two open edges. For the upstream edge flame, the flame spread rate is nearly independent

of, or decreases gradually, with the imposed flow velocity as shown in Figure 4. The spread rate of the downstream edge flame, however, increases significantly with the imposed flow velocity. Generally, the upstream and downstream edge flame spread rates are faster than the central flame spread rate for an imposed flow velocity of up to 5 cm/s as shown in Figure 3. This is due to greater oxygen supply from the outer free stream to the edge flames shown in Figure 3 and more efficient heat transfer from the edge flames to the sample surface than the central flames.

SPOT RADIATIVE IGNITION AND SUBSEQUENT 3D FLAME SPREAD

It was experimentally observed that non-piloted radiative ignition of the paper occurred more easily in microgravity than in normal gravity. The ignition delay time was a much stronger function of flow at low oxygen concentrations. After ignition, the flame spread only upstream, in a fan-shaped pattern. The fan angle increased with increasing external flow velocity and oxygen concentration from zero angle (narrow flame with width of the beam diameter) at the limiting 0.5 cm/s external air flow, to 90 degrees (semicircular flame) for external flow velocities at and above 5 cm/s and higher oxygen concentrations as shown in Figure 5⁵. Predicted fan angles based on a simple analysis that estimates the air flow normal to the flame front including the effects of diffusion qualitatively agree with the experimentally obtained results as shown in the figure. A surface energy balance using the measured surface temperature histories from fine thermocouples reveals the heat feedback rate from the upstream flame to the surface decreases with decreasing oxygen mass transport to the flame via either imposed flow velocity or ambient oxygen concentration⁵. Despite the convective heating from

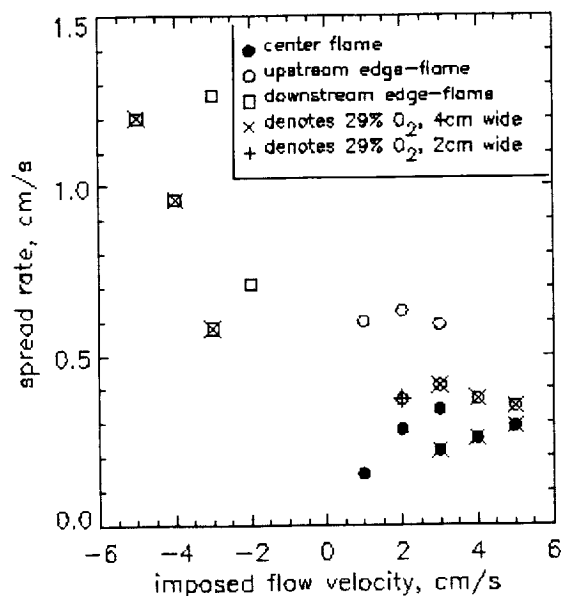


Figure 4. Calculated flame spread rates.

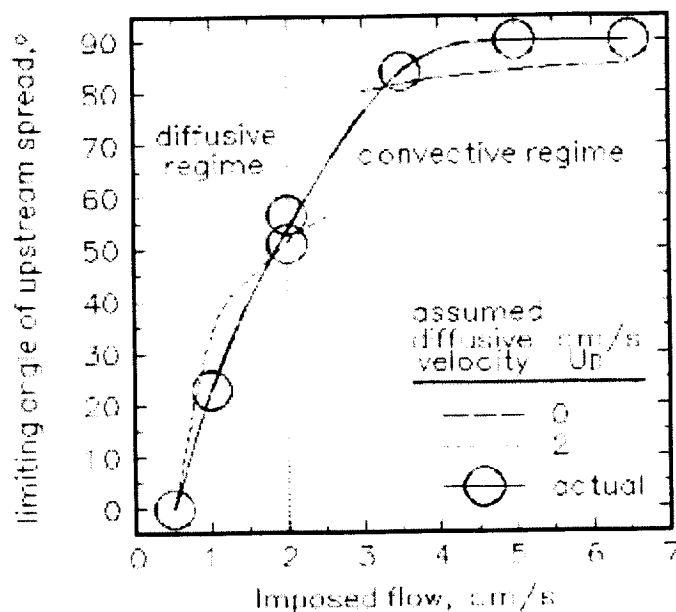


Figure 5. Measured fan angle with circle vs. calculated results with lines.

the upstream flame, the downstream flame spread did not occur due to lack of oxygen caused by the upstream flame, 'oxygen shadow', for the flow conditions studied.

EFFECTS OF TEST CHAMBER CONFINEMENT

Generally, the size of many test chambers for microgravity combustion experiments is due to low flow velocities. It is quite possible that surrounding test chamber walls might have significant effects on flame behavior. In this study, the confinement effects are determined by comparing the calculated results obtained from the open, unconfined case with the results with the confinement of the test chamber used in our experiments. The effects of the confinement on flame spread rate in the 2-D configuration are shown in Figure 6. Since the fan used in the

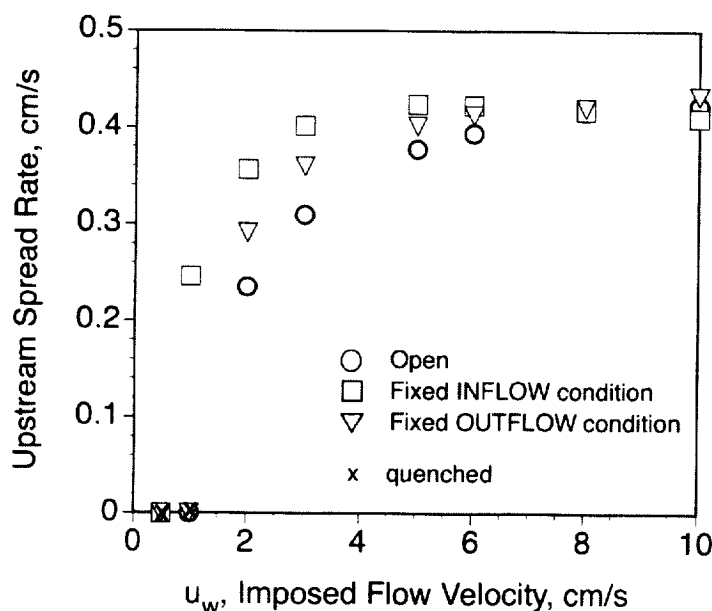


Figure 6. Effects of confinement on flame spread rate in 40% oxygen Concentration.

experiment was calibrated without any combustion in the test chamber, the effects of heat and mass addition to the performance of the fan could not be determined. Therefore, two different boundary conditions for the flow field were selected; specifying a constant inflow condition and fixing a constant outflow condition. The results show significant acceleration of flow and subsequent increase in flame spread rate compared to that without any confinement (open) at low imposed flow velocities. The length of flame is more extended and flame gets closer to the sample surface with the confined case. Since the size of flame is initially small in the 3-D configuration, the effects of the confinement on flame behavior are initially less than in the 2-D configuration.

ACKNOWLEDGMENTS

This study is supported by the NASA Microgravity Science Program under the Inter-Agency Agreement No. C-32090-K.

¹ McGrattan, K.B., Kashiwagi, T., Baum, H.R., and Olson, S.L., *Combust. Flame*, 106:377-391(1996).

² Mell, W.E. and Kashiwagi, T., *Proc. Combust. Inst.* 27:2635-2641(1998).

³ Mell, W.E. and Kashiwagi, T., "Effects of Finite Sample Width on Transition and Flame Spread in Microgravity", *Proc. Combust. Inst.* 28, in press.

⁴ Mell, W.E., Olson, S.L., and Kashiwagi, T., "Flame Spread Along Free Edges of Thermally Thin Samples in Microgravity", *Proc. Combust. Inst.* 28, in press.

⁵ Olson, S.L., Kashiwagi, T., Fujita, O., Kikuchi, M., and Ito, K., "Experimental Observations of Spot Radiative Ignition and Subsequent Three-Dimensional Flame Spread over Thin Cellulose Fuels", *Combust. Flame*, in press.

THEORETICAL PREDICTION OF MICROGRAVITY IGNITION DELAY OF POLYMERIC FUELS IN LOW VELOCITY FLOWS

A.C. Fernandez-Pello¹, J.L. Torero², Y.Y. Zhou¹, D. Walther¹ &
H.D. Ross³

¹University of California, Berkeley, CA 94720-1740

²University of Maryland, College Park, MD 20742-3031

³NASA Glenn Research Center, Cleveland, OH 44135-3191

Overview

A new flammability apparatus and protocol, FIST (Forced Flow Ignition and Flame Spread Test), is under development. Based on the LIFT (Lateral Ignition and Flame Spread Test)[1] protocol, FIST better reflects the environments expected in space-based facilities. The final objective of the FIST research is to provide NASA with a test methodology that complements the existing protocol [2] and provides a more comprehensive assessment of material flammability of practical materials for space applications. Theoretical modeling, an extensive normal gravity data bank and a few validation space experiments will support the testing methodology. The objective of the work presented here is to predict the ignition delay and critical heat flux for ignition of solid fuels in microgravity at airflow velocities below those induced in normal gravity. This is achieved through the application of a numerical model previously developed [3] of piloted ignition of solid polymeric materials exposed to an external radiant heat flux. The model predictions will provide quantitative results about ignition of practical materials in the limiting conditions expected in space facilities.

Experimental data of surface temperature histories and ignition delay obtained in the KC-135 aircraft [4,5] are used to determine the critical pyrolysis mass flux for ignition and this value is subsequently used to predict the ignition delay and the critical heat flux for ignition of the material. Surface temperature and piloted ignition delay calculations for Polymethylmethacrylate (PMMA) and a Polypropylene/Fiberglass (PP/GL) composite were conducted under both reduced and normal gravity conditions. It was found that ignition delay times are significantly shorter at velocities below those induced by natural convection.

Introduction

Long-term missions in space facilities bring concern about the possibility of an accidental fire [6,7], since there are combustible materials and sources of ignition aboard. In fact, there have been some minor incidents reported on Space Shuttle flights [8] and aboard MIR [9].

Space facilities typically have low air currents of the order of 0.1 m/s induced by HVAC systems, and variable oxygen concentration due to CO₂ scrubbers. Unfortunately, natural convection flows induced by gravity impose a limitation on the lowest velocities that can be tested on earth, and consequently on determining microgravity fire properties. Moreover, ground based microgravity facilities can only provide short periods of reduced gravity, e.g. about 25 seconds for a NASA KC-135

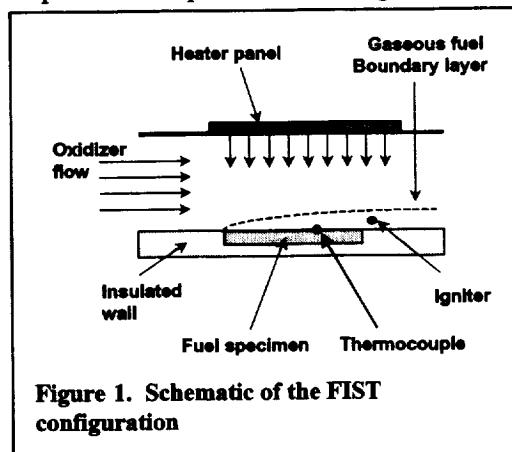


Figure 1. Schematic of the FIST configuration

aircraft. Therefore, ignition tests in these ground based facilities can only be conducted at very high heat fluxes, which result in ignition delays less than this time. Thus, until experiments are conducted in space based facilities, the results must be extrapolated, and are consequently limited in scope. Theoretical modeling, therefore, becomes a promising means to predict fire properties under microgravity and low velocity conditions.

Ignition of solid combustible materials has been extensively investigated theoretically [10-13]. Many investigators have focused on the condensed phase by introducing an empirical criterion for ignition. Among these, the critical pyrolysate mass flow rate at ignition is physically the most relevant [10,14-16], because it is logically related to the lean flammability limit. For this reason, this criterion is adopted here in conjunction with the available experimental data. This strategy assumes fast chemistry in the gas phase.

Problem configuration

A schematic of the FIST apparatus is shown in Fig. 1. It consists of a small-scale combustion wind tunnel with a fuel sample mounted into a low conductivity, inert slab on one wall of the test section, and a radiant panel on the opposite wall. The surface of the fuel sample is impulsively exposed to a uniform and constant, external radiant heat flux, 5–40 kW/m². A known oxidizer forced flow is established parallel to the sample surface. A pilot is located downstream of the fuel sample. More detail is given in [4]. Experiments are conducted with two different fuels in both normal and reduced gravity. The first is clear, 1/2" thick PMMA and the other is a 1/8" thick commercially made polypropylene (70% by mass) and loose glass fiber (30%)(PP/GL) blend, typically used for electronic casings and paneling.

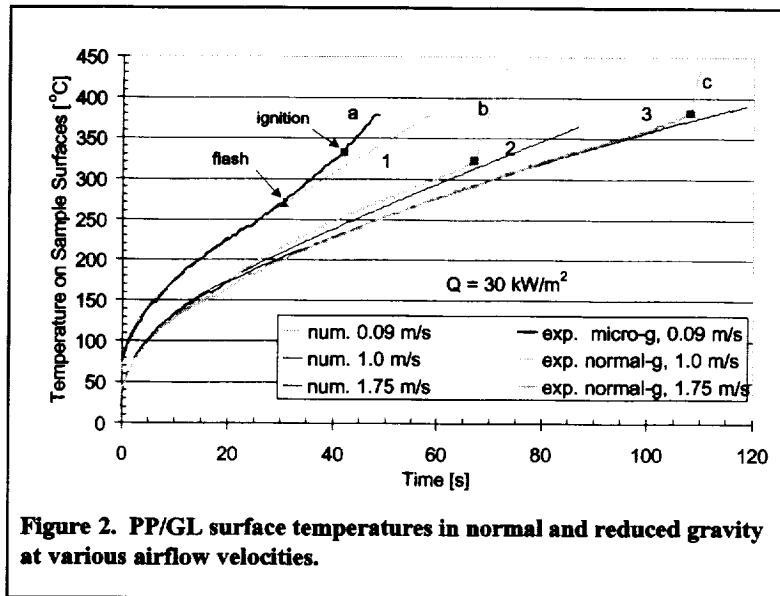


Figure 2. PP/GL surface temperatures in normal and reduced gravity at various airflow velocities.

Normal gravity tests are conducted at airflow velocities of 1.0, 1.75 and 2.5 m/s; larger than the limited values of natural convection. The experiments at forced airflow of 0.09 and 0.15 m/s are conducted in a KC-135 aircraft following parabolic flight trajectories. The FIST testing apparatus is similar to the normal gravity test facility, albeit slightly reduced in scale [17] and is placed within the Spacecraft Fire Safety Facility (SFSF)[18]. Although these experiments are subject to the g-jitter and resulting buoyant flows of the aircraft, zero gravity and no buoyancy is assumed in modeling the low gravity experiments. The governing equations, boundary conditions, and the properties of PMMA and PP/GL can be found in [3] and [5]. Both thermal and oxidative pyrolysis are considered in the model together with in-depth absorption and phase change when appropriate.

For ignition to occur, the solid must first pyrolyze. The pyrolyzed fuel then mixes with the oxidizer in the boundary layer to produce a flammable mixture, which is ignited

by the pilot. In order to determine the pyrolyzate mass flow rate at which ignition occurs, the numerical and FIST experimental surface temperature are compared at each specific airflow velocity. The value of the pyrolyzate mass flow rate at the experimentally observed ignition time is considered to be the critical pyrolyzate mass flow rate for those particular test conditions. This value is subsequently used to predict the ignition delay diagram (ignition delay vs. heat flux) and the critical heat flux for ignition.

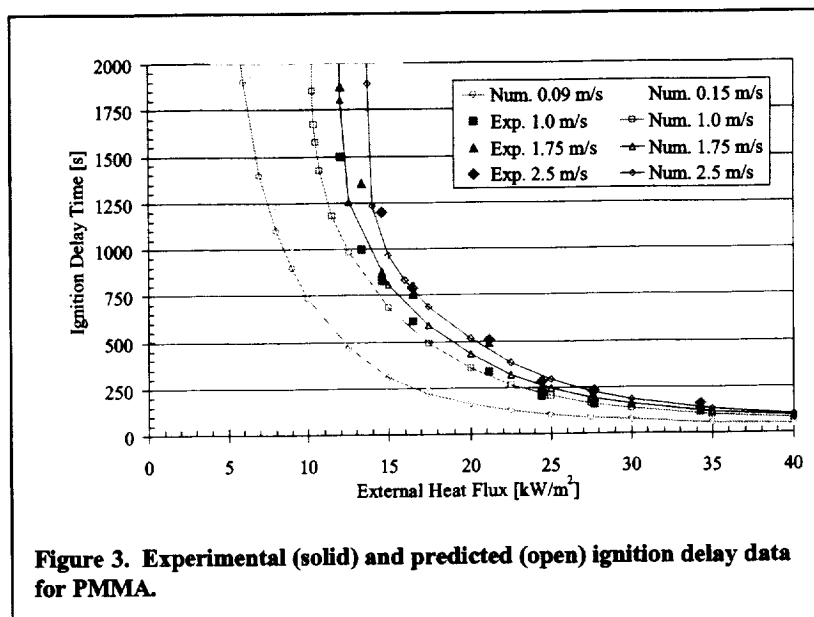


Figure 3. Experimental (solid) and predicted (open) ignition delay data for PMMA.

Results and discussion

The measured and predicted surface temperature histories at various airflow velocities are shown in Fig. 2 for PP/GL composite (30 kW/m^2). The numerical results agree well with the experimental data up to the point of ignition. The experimentally observed sharp increase in temperature at ignition is not predicted by the model since the gas phase is not considered. Similar temperature histories are observed for PMMA[5].

The numerically predicted and experimentally measured ignition delays are plotted in Fig. 3 for PMMA and Fig. 4 for PP/GL. The critical heat fluxes can be deduced from the ignition diagrams by noting the external radiant flux at which the ignition delay approaches infinity. The ignition delay and critical heat flux for ignition decrease as the forced-flow velocity decreases, consistent with the findings of [16]. This suggests that materials will ignite more easily under the low velocity conditions of space facilities. The critical heat flux for ignition as the forced flow velocities approach zero is close to half of the value measured in normal gravity. It should also be noted that since the gas phase is not considered in this model, oxygen limitation effects are not examined.

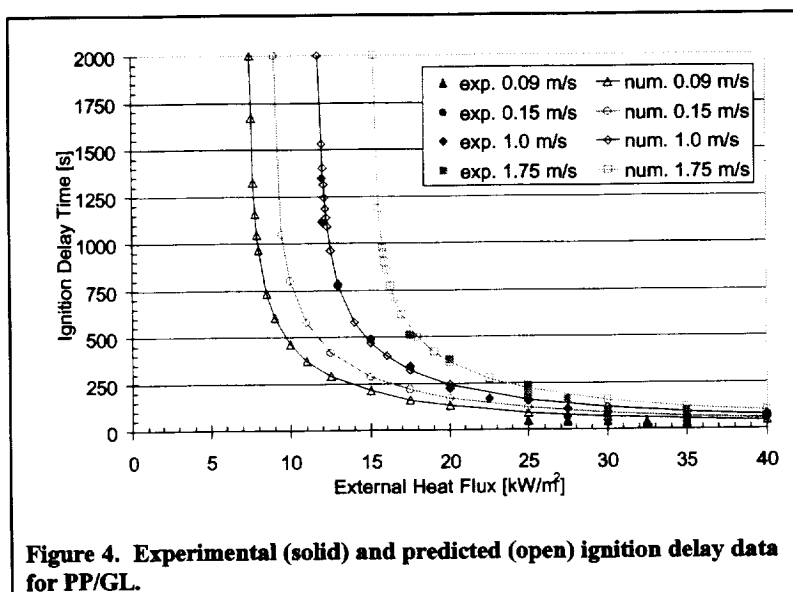


Figure 4. Experimental (solid) and predicted (open) ignition delay data for PP/GL.

Conclusions

The ignition delay, critical pyrolysis mass flow rate, and critical heat flux for ignition depend strongly on the airflow, and decrease as the airflow velocity decreases. This indicates that the environmental conditions must be considered in determining their values. In microgravity conditions, where airflows can be reduced significantly below natural convection limited values, the ignition delay times and the critical heat fluxes have been predicted to be close to half of the value in normal gravity. The results, if confirmed with longer duration microgravity tests, have very important implications since they indicate that materials will ignite easier under the conditions expected in space facilities, and that consequently stricter design specifications may be needed for fire safety.

Acknowledgments

This work was supported by NASA under Grant NCC3-478. The authors thank Messrs. S. Olenick, M. Roslon, J. Beck, A. Stevanovic, and T. Steinhaus for their experimental work. The authors would also like to thank the NASA reduced gravity aircraft team and support staff.

References

1. Annual Book of ASTM Standards, Vol. 04-07, 1055-1077 (1993).
2. Friedman, R., NASA TM-1999-209285.
3. Zhou, Y., and Fernandez-Pello, A. C., *29th Symp. (Int.) on Combust.*, The Combust. Institute (2000)
4. Roslon, M., Olenick, S., Walther, D., Torero, J.L., Fernandez-Pello, A.C., and Ross, H.D., *38th AIAA Space Sciences & Exhibit*, AIAA 2000-0580 (2000).
5. C. Fernandez-Pello, Y. Zhou, D. Walther; J. Torero, and H. Ross, *39th AIAA Space Sciences & Exhibit*, AIAA 2001-0471 (2001).
6. Palmer, H., Intl Microgravity Combustion Workshop, NASA LeRC, Cleveland, OH (1987).
7. Faeth, G., Space Station Freedom Modular Combustion Facility Assessment Workshop, NASA LeRC, Cleveland, OH (1989).
8. Friedman, R., NASA TM 106403 (1994).
9. Ross, H. D.: "Burning To Go: Combustion On Orbit and Mars", Fall Technical Meeting of the Eastern States Section of The Combustion Institute, Hartford CT (1997).
10. Atreya, A., *Phil. Trans. R. Soc. Lond. A* **356**:2787-2813 (1998).
11. Di Blasi, C., Crescitelli, S., Russo, G., and Cinque, G., *Combust. Flame*, **83**:333-344 (1991).
12. Nakabe, K., McGrattan, K. B., Kashiwagi, T., Baum, H. R., Yamashita, H., and Kushida, G., *Combust. Flame*, **98**:361-374 (1994).
13. Park, S. H., and Tien, C. L., *Combust. Sci. Tech.* **95**:173-192 (1994).
14. Bamford, C. H., Crank, J., and Malan, D. H., *Proc. Camb. Phil. Soc.* **42**:166-182 (1946).
15. Drysdale, D. D., and Thomson, H. E., *Fire Safety Journal*, **14**:179-188 (1989).
16. Cordova, J.L. and Fernandez-Pello, A.C., *Combust. Sci. Tech.* **156**:271-289 (2000)
17. Long, R.T., Quintiere, J.G, Torero, J.L. and Fernandez-Pello, A.C., *Fire Safety Sci.-6th Intl Symp.*, pp.567 (2000).
18. Goldmeer, J.S., NASA, TM-2000-210375.

FLAMMABILITY OF POLYMERS IN MICROGRAVITY

A. Tewarson, S. Nam, and M. Whitbeck
Factory Mutual Research Corporation,
1151 Boston-Providence Turnpike, Norwood, MA 02062

INTRODUCTION

NASA uses techniques for enhancing fire safety in spacecrafts by precluding the use of flammable materials, allowing the use of flammable materials only in controlled containment-separated from possible ignition sources or to use habitable atmospheres that do not support combustion in μg [1]. Diverse uses of the planned laboratory facilities in the International Space Station (ISS), however, will undoubtedly tax this prevention system [1]. NASA is considering a variety of strategies to enhance fire safety on the ISS [1] including the use of specialized-engineered polymers. Reliable implementation of these strategies, however, requires a μg fire property database for polymers [1]. Since all possible polymers cannot be tested in μg , it is necessary to find a way of assessing flammability behaviors of polymers under μg conditions using 1g fire property data [1]. The μg fire property database that is established by flammability experiments for carefully selected polymers on the ISS and its relationship with the corresponding 1g fire property database could provide the means of extending the larger 1g database to μg conditions. Also, such a μg fire property database would become a standard reference for the assessment of fire safety in space.

An examination of the literature on the μg combustion science research [1,2,3] suggests possible explanations for the range of variations in fire property values due to reduced gravity. It appears that fire property values of melting type polymers and polymers with higher halogen-to-carbon atoms relative to hydrogen-to-carbon atoms and polymers with high chemical bond strengths are more sensitive to effects of gravity than non-melting type polymers having large hydrogen-to-carbon-atom ratios.

We have examined each major fire property associated with the ignition, combustion, and fire propagation behaviors of polymers for the possible effects of μg .

FIRE PROPERTIES ASSOCIATED WITH THE IGNITION BEHAVIOR

The properties are [4]:

- 1) *Critical heat flux, CHF* (\dot{q}_{cr}''), is the external heat flux at or below which there is no sustained-piloted ignition. Polymers with higher *CHF* values have higher resistance to ignition. It is related to the ignition temperature, T_{ig} .
- 2) *Thermal response parameter, TRP* ($\Delta T_{\text{ig}} \sqrt{\pi k \rho c / 4}$), is an indicator of ignition delay under thermally thick condition and relates time-to-ignition (t_{ig}) to external heat flux \dot{q}_e'' :

$$1/t_{\text{ig}}^{1/2} = (\dot{q}_e'' - \dot{q}_{\text{cr}}'') / \text{TRP} \quad (1)$$

where ΔT_{ig} is the excess ignition temperature above ambient, k is the thermal conductivity, ρ is the density, and c is the heat capacity. Polymers with higher *TRP* values have higher resistance to ignition. Figure 1 shows that highly halogenated and high temperature specialized-engineered polymers have higher ignition resistance compared to the ordinary polymers under 1g conditions.

The values of k , ρ , and c for polymers are very similar and are not expected to depend on gravity as they are material properties. Thus, the differences in the TRP values of polymers would primarily be due to differences in the ΔT_{ig} values.

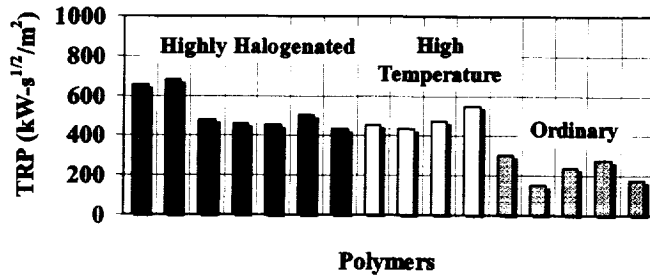


Figure 1. TRP values for highly specialized-engineered and ordinary polymers for 1g conditions.

$T_{ig} > 1000$ K for a PVDF grade with high molecular weight, narrow molecular weight distribution, and high crystallinity. Such a high T_{ig} value appears to be associated with large amounts of HF and other gaseous fluorinated compounds generated during the decomposition of PVDF.

Since T_d is a material property, it is not expected to depend on the changes in the gravity, thus the ignition resistance of ordinary polymers in 1g and μg conditions should be very similar. However, the ignition resistance of specialized-engineered polymers in μg conditions may be different compared to 1g conditions if, as it appears, fuel-rich combustion is favored due to longer residence times and reduced fresh air supply to the flame. Under these conditions, enhancement of flame inhibition by the combustion products may also be favored.

FIRE PROPERTIES ASSOCIATED WITH THE COMBUSTION BEHAVIOR

The properties are [4]:

- 1) *Heat release parameter, HRP* ($\Delta H_{ch}/\Delta H_g$): it is an indicator of the heat release rate at a specified heat flux and heat loss [4]:

$$\dot{Q}_{ch}'' = (\Delta H_{ch} / \Delta H_g)(\dot{q}_e'' + \dot{q}_f'' - \dot{q}_{rr}'') = \chi(\Delta H_T / \Delta H_g)(\dot{q}_e'' + \dot{q}_f'' - \dot{q}_{rr}'') \quad (2)$$

- 2) *Product generation parameter, PGP* ($y_j/\Delta H_g$): it is an indicator of mass generation rate of product j at a specified heat flux and heat loss [4]:

$$\dot{G}_j'' = (y_j / \Delta H_g)(\dot{q}_e'' + \dot{q}_f'' - \dot{q}_{rr}'') = f_j(\Psi_j / \Delta H_g)(\dot{q}_e'' + \dot{q}_f'' - \dot{q}_{rr}'') \quad (3)$$

where \dot{Q}_{ch}'' is the chemical heat release rate, \dot{G}_j'' is the generation rate of product j , ΔH_{ch} is the chemical heat of combustion, ΔH_g is the heat of gasification, y_j is the yield of product j , \dot{q}_f'' is the flame heat flux, \dot{q}_{rr}'' is the reradiation loss, χ is the combustion efficiency, ΔH_T is the net heat of complete combustion, f_j is the generation efficiency of product j , and Ψ_j is the maximum possible mass stoichiometric yield of product j .

$\Delta H_T/\Delta H_g$ and $\Psi_j/\Delta H_g$ are material properties and thus are not expected to depend on gravity. As a result, the effects of the μg conditions on heat release rates and generation rates of products would be due to the gravity effects on χ , f_j , \dot{q}_f'' , and \dot{q}_{rr}'' . In addition, fuel-rich

combustion that appears to be favored under μg conditions would further reduce χ and increase f_i for products of incomplete combustion.

Currently there is little information on this subject except the information derived indirectly from other studies, such as an order of magnitude higher amount of CO generated from smoldering flexible polyurethane foam found under μg conditions than found under 1g conditions, despite similar temperatures and char patterns [6].

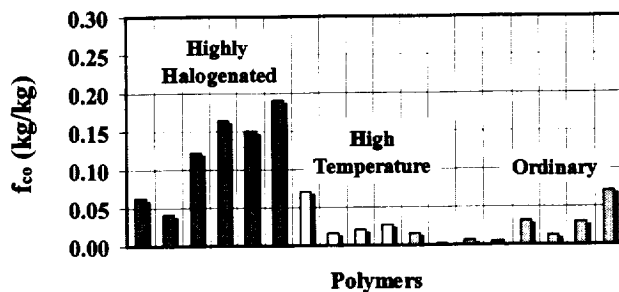


Figure 2. CO generation efficiency for specialized-engineered and ordinary polymers for 1g conditions.

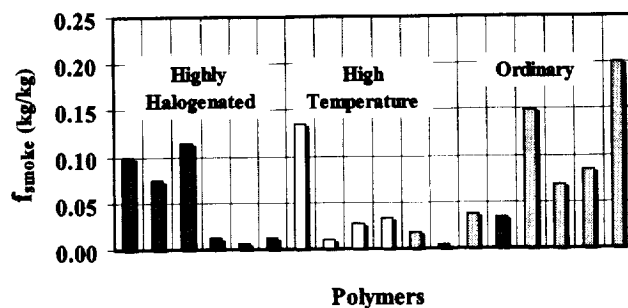


Figure 3. Smoke generation efficiency for specialized-engineered and ordinary polymers for 1g conditions.

Figures 2 and 3 show values of f_{CO} and f_{smoke} under 1g conditions. These values would increase further in μg conditions, if, as it appears, fuel rich conditions and flame inhibition by the products are favored.

In general, polymers with higher halogen-to-carbon atom ratios (highly halogenated polymers) have higher f_{CO} values and polymers with higher hydrogen-to-carbon atom ratios (ordinary polymers) have higher f_{smoke} values. Similar trends are expected for other products of incomplete combustion. Some of these products could be toxic, corrosive, and be responsible for circuit failures.

The expected decrease in the value of χ , increase in the values of f_i for products of incomplete combustion, and variations in the \dot{q}_f'' , and \dot{q}_{rr}'' values under μg conditions would present very different types of fire hazards compared to 1g conditions. These hazards would be associated with heat

damage, reduced visibility, toxicity, corrosivity, and circuit failures.

FIRE PROPERTY ASSOCIATED WITH THE FIRE PROPAGATION BEHAVIOR

Fire propagation index, FPI, is used to describe the fire propagation behaviors of materials [4]. The FPI concept has been developed for fire safety assessment [4] and has been adopted by industry [7,8]. The principle associated with the FPI concept for vertical fire propagation in coflowing air with 40% oxygen concentration and external heat flux performed in the ASTM E 2058 apparatus [8] is very similar to the principle associated with the NASA's standard test for upward fire propagation under variable oxygen concentration and pressure [9].

FPI is expressed as $750(\dot{Q}_{ch}/w)^{1/3}/TRP$, where \dot{Q}_{ch} is the chemical heat release rate and w is the width. *FPI* values for 1g conditions are shown in Fig. 4. The *FPI* values indicate that highly halogenated and high temperature specialized-engineered polymers have high resistance to fire propagation (*FPI* values less than 10) compared to ordinary polymers (*FPI* values in the range of 13 to 36). *FPI* values combined with the large-scale upward fire propagation behavior shows the following classification for various polymers [4]: 1) no propagation: $FPI \leq 6$; 2)

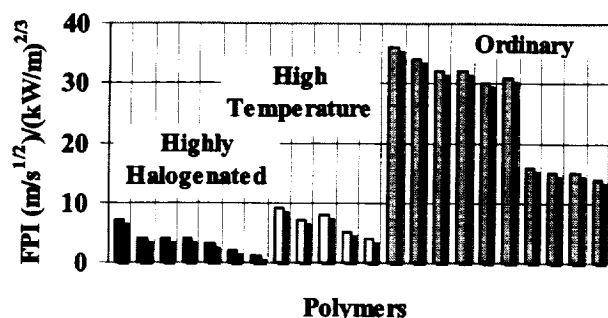


Figure 4. Fire propagation index for specialized-engineered and ordinary polymers for 1g conditions.

SUMMARY

Fire hazards due to heat damage, reduced visibility, toxicity, corrosivity, and circuit failures may be very different between 1g and μg conditions. Fire properties of polymers that melt and/or have high ratios of halogen-to-carbon atoms appear to be more sensitive to gravity changes than non-melting polymers with high hydrogen-to-carbon atom ratios. Ignition temperature, combustion efficiency, generation efficiencies of products, flame heat flux and reradiation loss may account for this distinction. The extension of 1g fire property data to μg conditions may be possible with a better understanding of the relationships between these properties at 1g and μg conditions.

A limited number of experiments for carefully selected polymers under μg and 1g conditions need to be performed to utilize the voluminous 1g fire property data for polymers for fire safety in space.

REFERENCES

1. Sacksteder, K.R., *Twenty-third Symposium (International) on Combustion*, 1990, pp.1589-1596.
2. Kono, M., Ito, K., Niioka, T., Kadota, T., and Sato, J., *Twenty-Sixth Symposium (International) on Combustion*, 1996, pp. 1189-1199.
3. Ronney, P., *Twenty-Seventh Symposium (International) on Combustion*, 1998, pp.2485-2506.
4. Tewarson A. Generation of Heat and Chemical Compounds in Fires. Section 3, Chapter 4. *The SFPE Handbook of Fire Protection Engineering*, Second Edition. The National Fire Protection Association Press, Quincy, MA, 1995; p. 3-53 to 3-124.
5. Tewarson, A., Abu-Isa, I. A., Cummings, D.R., and LaDue, D.E., *Fire Safety Science, Sixth International Symposium*, pp. 991-1002, 2000.
6. Stocker, D.P., Olson, S.L., Urban, D.L., Torero, J.L., Walter, D.C., and Fernandez-Pello, A.C., *Twenty-sixth Symposium (International) on Combustion*, 1996, pp.1361-1368.
7. Class # 4910 Test Standard (1997), Class #3972 (1989), and Class #4998 (1995), Factory Mutual Research Corporation, Norwood, MA.
8. ASTM E2058 (2000) and NFPA 287 (2000).
9. NASA Technical Standard NASA-STD-6001, February 9, 1998.

deceleration fire propagation: $6 < FPI \leq 10$; 3) normal fire propagation: $10 < FPI < 16$, and 4) accelerating fire propagation: $FPI \geq 30$.

The fire propagation behavior of polymers under μg conditions could be examined in a fashion similar to 1g conditions using the FPI values. However, it would be necessary to account for the possibility of fuel-rich combustion and flame inhibition by the products in the FPI format for μg conditions.

LOW STRETCH PMMA BURNING IN MICROGRAVITY: STATUS OF THE GROUND-BASED PROGRAM AND NEW ISS GLOVEBOX EXPERIMENT SALSA

S.L. Olson, NASA Glenn Research Center

J.S. T'ien, CWRU, and

J.B. Armstrong, CWRU

Abstract

The objective of this ground-based program is to study low stretch diffusion flames burning PMMA as the solid fuel to determine the relationship between buoyant low stretch burning in normal gravity and forced flow low stretch burning in microgravity. The low stretch is generated in normal gravity by using the buoyant convection induced by burning the bottom of a large radius of curvature sample. Low stretch is also generated using the Combustion Tunnel drop tower rig (2.2 and 5.2 second facilities), which provides a forced convective low velocity flow past smaller radius of curvature samples. Lastly, an ISS glovebox investigation is being developed to study low stretch burning of PMMA spheres to obtain long duration testing needed to accurately assess the flammability and burning characteristics of the material in microgravity. A comparison of microgravity experiment results with normal gravity test results allows us to establish a direct link between a material's burning characteristics in normal gravity (easily measured) with its burning characteristics in extraterrestrial environments, including microgravity forced convective environments. Theoretical predictions and recent experimental results indicate that it should be possible to understand a material's burning characteristics in the low stretch environment of spacecraft (non-buoyant air movement induced by fans and crew disturbances) by understanding its burning characteristics in an equivalent Earth-based low stretch environment (induced by normal gravity buoyancy). Similarly, Earth-based stretch environments can be made equivalent to those in Lunar- and Martian-surface stretch environments (which would induce partial-gravity buoyancy).

Surface Regression Rates

Figure 1 shows the surface regression rates for PMMA cylinders over the full range of flammability in air, from blowoff at high stretch, to quenching at low stretch, observed for the first time in the normal gravity experiments^[1], which are represented by the data circles. Previous higher stretch results^[2,3] are represented by the squares and triangles. The solid line drawn through the central portion of the data ($3 < a < 100 \text{ s}^{-1}$) has a slope of unity, which indicates regression is proportional to stretch. Infinite kinetics theory and experiments find a square root relationship^[2] between regression and stretch at high stretch rates. The figure coordinates assume that the values of stretch are equivalent, whether derived from forced stretch or from buoyant stretch. The excellent correlation of the regression-rate data over the two-order-of-magnitude variation of stretch shows the reasonableness of this assumption.

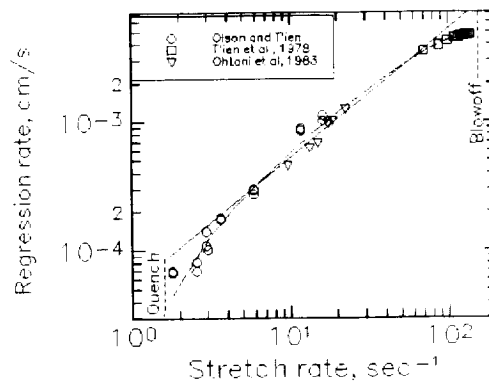


Figure 1: Surface regression rates for PMMA as a function of stretch rate. Data spans from blowoff extinction at high stretch rate to quenching extinction at low stretch rate.

In Figure 1, the stretch rate below which uniform flame burning was not achieved is 3 s^{-1} , where departure from the linear correlation occurs. Flamelets^[1] which only partially cover the fuel surface are observed in this region. Similarly, the overall extinction limit is marked simply as a Quench limit, where no flame could be sustained at these large radii (low stretch rates).

Surface Energy Balance

Burning rate data and temperature measurements (gas and solid-phase) were used to evaluate each term of a surface energy balance at the solid surface. To determine overall trends, the terms of the surface balance are compared as ratios as defined below. The ratio $F_{\text{reutilization}}$ is the fraction of gas-to-surface net heat flux used to vaporize more fuel, and another ratio, F_{loss} , is the fraction of gas-to-surface net heat flux that is lost to the solid interior and radiated from the surface. In this way, $F_{\text{loss}} + F_{\text{reutilization}} = 1$. These ratios are plotted in Fig. 2 as a function of stretch rate. At the Quench limit, only 10% of the heat flux is reused; 90% of it is lost.

PHI, the fraction of gas-to-surface net heat flux that is conducted in depth, is defined for comparison with Yang and T'ien's theory^[4]. The flammability of a thick solid is modified considerably by solid-phase heat loss, so the solid phase heat loss is an important additional parameter in experiments with thick solids. The value of PHI at the Quench limit of $a=2 \text{ s}^{-1}$ agrees well with the value of ≈ 0.55 predicted by Yang and T'ien^[4] for the same stretch rate in air. It is important to note that over the range of stretch rates studied, that in-depth solid-phase losses are comparable to surface radiative losses, whose strong effect on flammability was shown in Fig. 1. Thus for thick fuels, the solid-phase heat loss is expected to be a significant factor in a material's flammability characteristics.

Modeling

A numerical model of the combustion of the solid fuel is being developed concurrently. The theoretical model makes use of an advanced, one-dimensional, gas-phase combustion model implementing a narrow-band radiation model. The gas-phase model is currently being coupled with a transient solid heat conduction model to simulate our drop experiments. The solid model was designed to provide an accurate simulation of the temperature profile within the solid. The transient heat conduction equation with surface regression is:

$$\rho c_s \frac{\delta T}{\delta t} = k_s \frac{\delta^2 T}{\delta x^2} + \rho c_s r \frac{\delta T}{\delta x}$$

where ρ represents the density of the solid, c_s represents the local heat capacity, k_s represents the local thermal conductivity (see below), and the regression rate is given as r . The equation was discretized using a Crank-Nicolson scheme to allow for a time-stepping solver to be used. The discretization employed the finite difference method. The solid model is able to respond to rapid changes in incident heat flux and has shown stability at time steps equal to those used by the gas phase model.

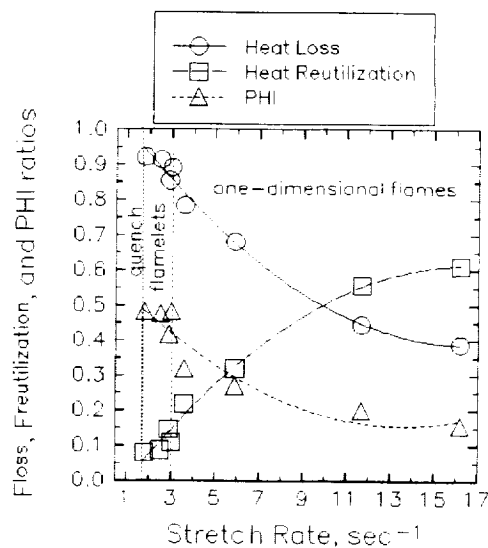


Figure 2: Loss, Reutilization, and PHI ratios as a function of stretch rate.

Experiments have shown the formation of bubbles within the plastic, as shown in Figure 3. In order to improve the accuracy of the solid phase model, the heat capacity and thermal conductivities vary with temperature. The thermal conductivity was further modified using a bubble model to correct for the porosity of the burning molten plastic. The bubble model is still under development, but will incorporate bubble nucleation theory and bubble growth dynamics.

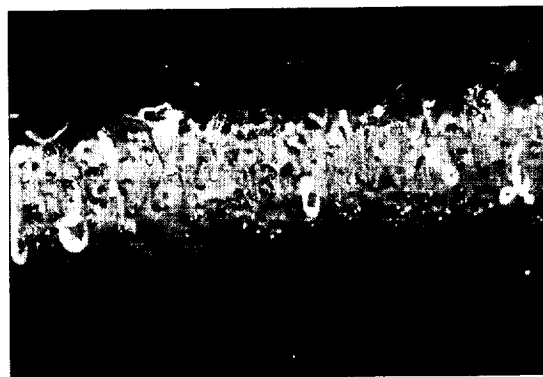


Figure 3: bubble layer in PMMA sample under low stretch burning conditions (1g)

Drop Tower Test Results

Testing is underway using the Combustion Tunnel drop rig, a droppable wind-tunnel capable of low velocity forced flow. The rig has been dropped in both drop towers available at the Glenn Research Center (2.2s and 5.2 s). Cylindrical samples approximately 2 cm in radius are ignited in normal gravity and dropped after stable 1g burning of the sample in air is achieved. The experiment also features the ability to control the rear surface temperature of the PMMA tube. This control over the rear surface is achieved using a combination of a thin heater and a water coolant system. The system may be set to maintain temperature at any value up to 140 deg C.

During an experimental run, data taken include pressures at various points in the flow system to insure proper experiment operation, thermocouples on the front and rear surfaces of the PMMA at the stagnation point to record preheating and surface degradation temperatures, and a heat flux sensor between the rear surface of the PMMA and the inner water coolant system to measure the heat flow from the heated fuel into the central heat sink. Also recorded are two orthogonal video views of the experiment.

Flame standoff distance is very sensitive to the surface energy balance. The flame standoff distance data are shown in Figure 4, and indicate that stable flame standoff distances are obtained for stretch rates above 3 s^{-1} . Preliminary results of microgravity forced stretch gas-phase flame standoff distances agree well with normal gravity buoyant stretch flame standoff distances. However, the limited time available in drop towers do not permit the even the gas-phase to stabilize at very low stretch ($<3 \text{ sec}^{-1}$). The solid phase in drop tower experiments has too little time to respond to the g change, and reflects the normal gravity burning heat balance, so these results are qualitative in nature. The microgravity experiments have shown good agreement with the previous 1g tests at similar stretch rates. However, the nature of the experiment requires more time for steady state flames to form in microgravity.

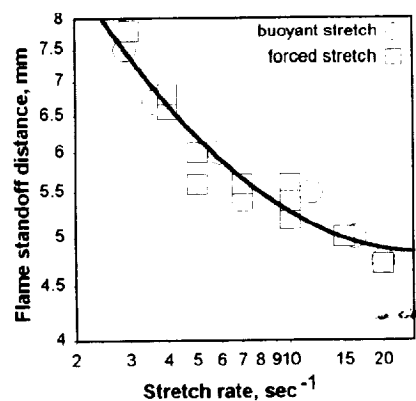


Figure 4: Flame standoff distances for forced and buoyant stretch rates.

Recently published Mir experiments^[5] revealed that 4.5 mm diameter cylinders, which were aligned with a low speed concurrent flow (0.5-8 cm/s), burned as low stretch candle-like stagnation flames, as shown in Figure 5, rather than as concurrently spreading flames, which

was the intended configuration. The molten ball of fuel remained at roughly twice the initial radius of the sample, and the flames remained stable to equivalent stretch rates of down to approximately 1.5 sec^{-1} . Oscillating flames were observed prior to extinction at this low stretch rate. Unfortunately, diagnostics were limited to visual images, so detailed energy balances and the quantification of solid phase heat loss, such as those described above for the normal gravity experiments, cannot be made.

Description of the SALSA Investigation in ISS MSG

The SALSA investigation, Solids Aflame in Low Stretch Air, which was recently awarded as an extension of this program, is to study a low stretch flame stabilized at the forward stagnation point of a cast PMMA sphere immersed in a low velocity air flow (Fig. 5). The experiment concept is inspired by recently published results of Mir Skorost experiments^[5] where low stretch candle-like flames were obtained. Quantitative temperature measurements of the gas-phase and solid-phase will be obtained, as well as regression rate of the solid sphere.

The data will be used to make a surface balance for the space experiments, in a manner very similar to the normal gravity data presented above. This data, and numerical modeling of the geometrically-simple experiment, will allow a comparison of the forced and buoyant stretch effects on the heat fluxes balances and flame standoff distances. In addition, the curvature effects will be separated from stretch effects for the small scale flames. Curvature effects on flame standoff distances can be significant compared to the stretch effects for small radii samples. The normal gravity data shown is for large radii cylinders, and provides a baseline set of data with negligible curvature effect. In the proposed experiments, stretch will be varied by varying R as well as U_∞ , to provide independent variation of curvature and stretch. Understanding these effects will provide new fundamental information on multidimensional effects on flames.

The experiment requires the use of an infrared camera which will provide a gas-phase SiC fiber temperature and surface temperature field diagnostic. An example IR image is shown in Figure 6, which clearly shows the burning fuel surface and the fiber extending out into the gas phase. The IR camera is narrow-band filtered at 3.8 microns. This diagnostic will provide a much better method of recording the surface temperatures than discrete location thermocouples. The solid thermocouple(s) will provide in-depth heat flux measurements to characterize solid phase heat loss, as well as a temperature reference for emissivity evaluation.

References

- ¹Olson, S.L and T'ien, J.S.; *Combustion and Flame*, V. 121, pp. 439-452, 2000.
- ²T'ien, J.S., Singhal, S.N., Harrold, D.P., and Pahl, J.M.; 1978; *Combustion and Flame*, Vol. 33, pp.55-68.
- ³Ohtani, H., Akita, K., and Hirano, T., 1983; *Combustion and Flame*, Vol. 53, pp. 33-40.
- ⁴Yang, C. T., and T'ien, J.S., 1998, *Journal of Heat Transfer*, Vol. 120, pp. 1055-1063.
- ⁵Ivanov, A.V, et. al.; NASA Contract NAS3-97160 final report, Russian Space Agency, Keldysh Research Center, Moscow 1999, NASA CP-1999-208917, pp 47-50.

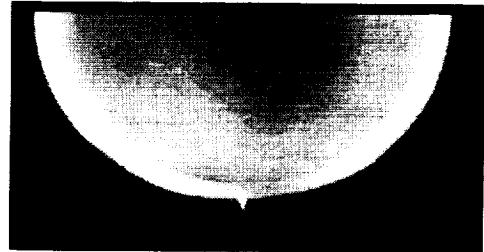


Figure 5: Color visible image of burning PMMA sphere (1g) with SiC fiber shown extending through the flame zone at the buoyant stagnation point.

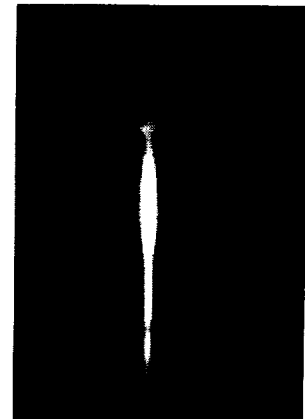


Figure 6: IR image of 1G burning PMMA ball with a SiC fiber extending through the flame zone at the stagnation point.

PATTERN FORMATION IN DIFFUSION FLAMES EMBEDDED IN VON KARMAN SWIRLING FLOWS

Vedha Nayagam¹ and **Forman A. Williams²**, ¹National Center for Microgravity Research
21000 Brookpark Road, Cleveland, OH 44135, email: v.nayagam@grc.nasa.gov

²Center for Energy Research, University of California, San Diego, La Jolla, CA 92093.

INTRODUCTION

Pattern formation in nonlinear, excitable systems has been a subject of intense research over the past few decades, primarily by biologist, chemists, physicist, and mathematicians. In these systems when a control parameter is smoothly varied, at a critical point the previously stable pattern suddenly breaks up and reestablishes a new pattern with different symmetry characteristics. Examples of such systems include electrical pulses in cardiac muscles, slime-mold amoeba aggregation, catalytic surface reactions, and chemical-reaction fronts in premixed combustion. Although wave propagation, pattern formation and reaction-front instabilities historically have been major subjects in the field of combustion, few observations of pattern formation have been reported in the literature thus far for diffusion flames. Recently, we showed that during near-limit combustion of a downward-facing polymer disks spinning in quiescent air the diffusion flame established adjacent to the fuel disk can exhibit pattern formation [1]. Depending on the rotational speed of the fuel disk, these flames burn steadily after growing to cover the entire fuel disk [2], extinguish by contracting axisymmetrically [3], or form spiral patterns [1]. Over a very narrow window of rotational speeds, flame holes were also observed in this configuration. By extending Buckmaster's [4] edge-flame model a generalized stability map was developed in a plane of Damköhler number and flame-disk or hole radius, normalized by diffusion length scale, showing regimes of dynamics of hole-disk combinations [3,5]. Experimentally measured flame-disk radii as functions of time were shown to compare favorably with the theory.

The axisymmetric configuration is broken in the spiral flames (see, Fig.1) and the dynamics of these flames are more complex. The tail of the spiral flame rotates rigidly while the tip executes a compound, meandering motion sometimes observed in Belousov-Zhabotinskii reactions. A model assuming a rigid-body rotation with constant speed of propagation relative to the swirling gas flow generated by the spinning fuel disk predicts the observed spiral shapes well [1]. However, further studies are needed to understand the tip meandering patterns. In further theoretical works, an AEA model was developed to define the flammability boundaries for a flat laminar diffusion-flame adjacent to a solid fuel disk, rotating about its axis and subjected to an impinging flow of oxidizer. The details of this last study can be found in Ref. [6].

One of the finding of our earlier work is that the burning rate of the condensed fuel is such that steady conditions are not achieved in air at normal atmospheric pressure for experimentally reasonable fuel thickness. Therefore in this continuation effort we employ a gas-fueled, rotating porous-disk burner to further examine the effects of stretch on diffusion-flame dynamics. The results of the experiment for methane burning in air are discussed in this report.

EXPERIMENTS

A schematic illustration of the burner assembly is shown in Fig. 1. The burner assembly consisted of a sintered, porous, bronze disk of diameter 7.8 inches and thickness $\frac{1}{2}$ inch, mounted on a perforated water-cooled copper back-plate and a cup-shaped housing chamber which also serves as the plenum for the injected fuel gas. The fuel gas and the cooling water are supplied through concentric tubes located along the axis of this assembly. The concentric supply tubes are connected to external feed tubes through O-ring seals so that the entire burner assembly can be rotated around its axis with a stepper motor. During an experiment the burner is placed horizontally with the exposed porous surface facing downward and then spun at a desired rotational speed with the cooling water supply turned on. Fuel gas is fed to the burner from a compressed-gas bottle through a programmable mass-flow controller at a specified flow rate and ignited by a propane torch. The entire experimental setup is enclosed in a large plexiglass box to prevent draft. All the flames observed in this study were blue and clearly visible to the naked eye. Since, commercially available color CCD cameras are not sensitive enough to capture the flame emission in this wavelength, in this study we used an intensified array camera (Xybion) and video-taped the flames using a 45° mirror at 30 frames per second.

RESULTS AND DISCUSSIONS

Experiments were conducted for methane burning in air at atmospheric pressure. The rotational speed of the fuel disk Ω , was varied from 0 to 20 revolutions per second (rps), and the fuel flow rate from 0.5 to 5 standard liters per minute (slpm). Steadily burning flat flames covering the entire burner surface are established at low rotational speeds and at high flow rates. As Ω is increased or the fuel flow rate is decreased, localized quenching occurs within the flat diffusion-flame. These quenched flame-fronts take up different patterns depending upon the fuel flow rate and Ω . Typically, starting from a steadily burning flame, as the disk rotation speed is increased we first observe a pulsating flame hole, followed by rotating spirals, multi-tongued flames, flame rings and finally extinction. A similar behavior is observed when the fuel flow rate is decreased for a constant Ω . Figure 2 shows a map of the different flame patterns in coordinates of the flow rate and rotation speed, and Fig. 3 illustrates some the observed flame shapes. In the following we describe the dynamics of the flame shapes by traversing a horizontal line across the map in Fig. 2, starting at a small Ω .

Starting from a steadily burning flame that covers the entire fuel disk, as Ω increases the flame develops a circular hole that originates at the center of the disk and propagates outward (Fig. 3a). Once the hole reaches a critical diameter, the circular configuration becomes unstable, and a small perturbation with the positive curvature develops and propagates quickly over the quenched hole area, reestablishing the flat diffusion flame; in other words, the hole closing is not axisymmetrical. This process repeats itself with a characteristic frequency as shown in Fig. 4 where the flame intensity at a point (fixed to the laboratory reference frame) within the hole region is plotted as function of time. For the range of parameters examined in this study the pulsation frequencies varied over a range of 1 to 4 Hz. As the burner speed is further increased, the pulsating hole configuration transitions into a rotating single-armed spiral flame (Fig. 3b), whose characteristics are similar to the spirals observed before with the solid fuels and described earlier [3]. The single-spiral flame rotates in the opposite direction to that of the burner, slowing down and eventually reaching a stationary state at a critical burner speed.

The next mode shapes observed are the multi-armed spirals (see, Fig. 3c-3g). Originating closer to the burner edge, the spirals arms extend toward the center of the disk, terminating at a finite radius. Spiral flames with two to seven arms were observed during the present experiments, with the number of arms increasing with Ω . The transition from one configuration to another is much more abrupt for the multi-armed spirals compared to the previous transitions. Also, these flames rotate in the same direction as that of the burner with increasing velocities, as observed from the laboratory frame of reference. When the number of spiral arms reaches more than seven, the flame rotational speed becomes sufficiently high and the standard video framing rate (30 fps) cannot resolve the flame shapes accurately. It is also interesting to note in Fig.3 that the radius of the central, quenched core region increases with Ω . Eventually, the central core region expand almost to the edge of the burner with the arms of the spirals completely disappearing, leaving only a ring shaped flame (Fig. 3h). Further increase in Ω completely blows the flame off.

A similar scenario develops when one travels vertically down a line in Fig. 2. This similarity can be explained by considering the stoichiometric flame location within the flow field. Similarity solutions to the von Karman flows with an embedded diffusion flame show that the flame moves into regions of higher strain when the rotational speed is increased or the surface blowing is decreased. It is also clear from the Fig. 2 that pattern formation occurs close to the extinction boundary. The Damköhler number close to the boundary is sufficiently close to the extinction Damköhler number, so that local flame extinction is possible. The quenched "edge-flames" propagate against the flow with a characteristic velocity determined by the supporting flames strength as well as their curvature toward the quenched region. Currently, studies are underway to predict the mode shapes as well as their dynamics. In future experiments we plan use a high-speed intensified camera to temporally resolve the flame shapes at higher rotational rates.

CONCLUDING REMARKS

The porous-disk burner experiments have confirmed the earlier observations of rotating spiral flames and disk flames. These experiments have also revealed pattern formation behavior previously unobserved due to the limitations inherent to solid-fuel experiments. Theoretical modeling effort aimed at predicting the conditions at which these phenomena occur are currently underway.

REFERENCES

1. Nayagam, V. and Williams, F. A., "Rotating Spiral Edge-Flames in von Karman Swirling Flows," *Physical Review Letters*, Phys. Vol. 84, 2000, pp. 479-482.
2. King, M., Nayagam, V. and Williams, F. A., "Measurements of Polymethylmethacrylate diffusion flames in von Karman Swirling Flows," (to appear) *Combustion Science and Technology*, 2001.
3. Nayagam, V., and Williams, F. A., "Diffusion-Flame Dynamics in Von Karman Boundary Layers," (to appear) *Combustion and Flame*, 2001.
4. Buckmaster, J., "Edge-flames," *J. Eng. Math.* 31:269-284 (1997).
5. Nayagam, V., Balasubramaniam, and Ronney, P. D., "Diffusion Flame-Holes," *Combust. Theory Modelling*, Vol. 3, 1999, pp. 727-742.
6. Nayagam, V., and Williams, F. A., "Diffusion-Flame Extinction for a Spinning Fuel Disk in an Oxidizer Counterflow," (to appear) *Proc. Combust. Inst.*, Vol. 28, 2001.

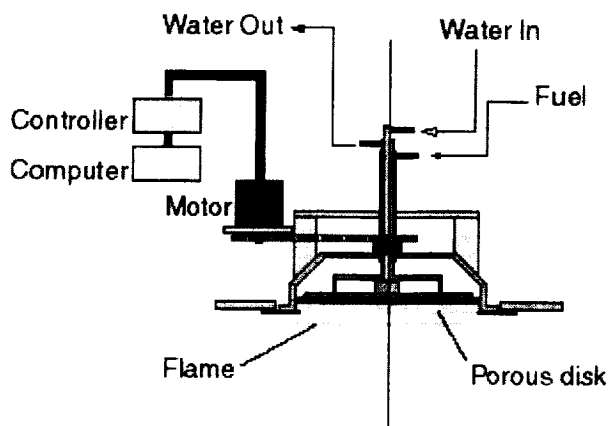


Figure 1. Schematic illustration of the porous-disk burner.

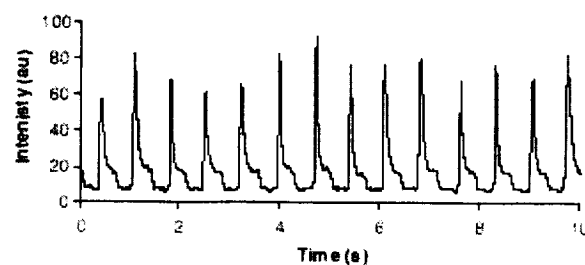


Figure 4. Flame intensity versus time for a pulsating flame hole; flow rate 3 slpm, disk rotation 4.25 rps.

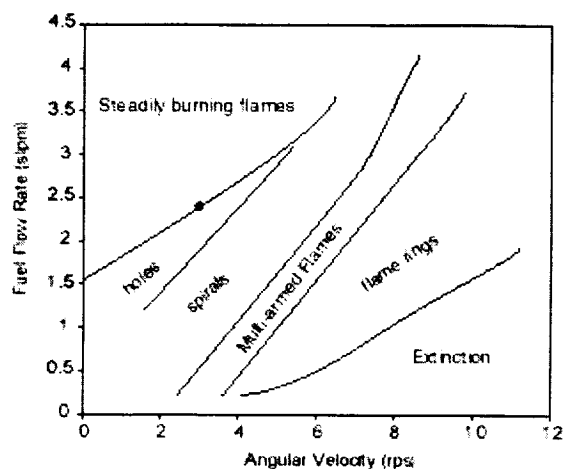


Figure 2. Flame-pattern map for methane burning in air.

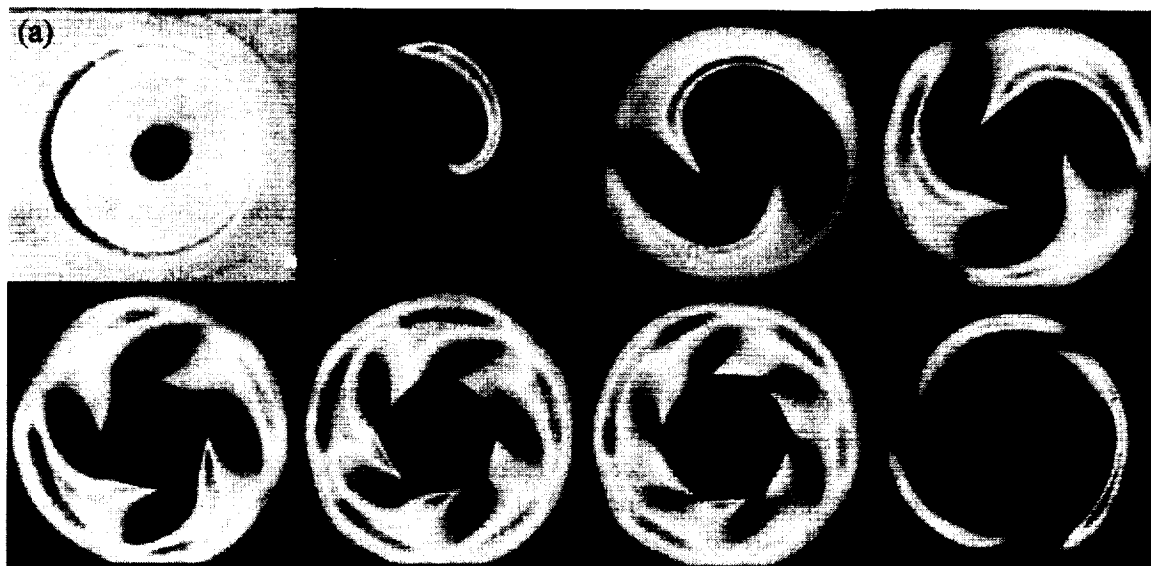


Figure 3. Various flame patterns for methane burning in air.

Suppression of Low Strain Rate Nonpremixed Flames by an Agent

A. Hamins, M. Bundy, I.K. Puri*, K. McGrattan, and W.C. Park**

NIST, Gaithersburg, Maryland 20899-8640

* Dept. Mechanical Engineering, University of Illinois at Chicago, Chicago, Illinois 60607-7022

** Permanent address: Safety Engineering, Pukyong National University, Pusan, 608-739, Korea

INTRODUCTION The agent concentration required to achieve the suppression of low strain rate nonpremixed flames is an important consideration for fire protection in a microgravity environment such as a space platform. Currently, there is a lack of understanding of the structure and extinction of low strain rate ($<20 \text{ s}^{-1}$) nonpremixed flames [1]. The exception to this statement is the study by Maruta et al. [2], who reported measurements of low strain rate suppression of methane-air diffusion flames with N_2 added to the fuel stream under microgravity conditions. They found that the nitrogen concentration required to achieve extinction increased as the strain rate decreased until a critical value was obtained. As the strain rate was further decreased, the required N_2 concentration decreased. This phenomenon was termed "turning point" behavior and was attributed to radiation-induced nonpremixed flame extinction. In terms of fire safety, a critical agent concentration assuring suppression under all flow conditions represents a fundamental limit for nonpremixed flames.

Counterflow flames are a convenient configuration for control of the flame strain rate. In high and moderately strained near-extinction nonpremixed flames, analysis of flame structure typically neglects radiant energy loss because the flames are nonluminous and the hot gas species are confined to a thin reaction zone. In counterflowing CH_4 -air flames, for example, radiative heat loss fractions ranging from 1 to 6 percent have been predicted and measured [3,4].

The objective of this study is to investigate the impact of radiative emission, flame strain, agent addition, and buoyancy on the structure and extinction of low strain rate nonpremixed flames through measurements and comparison with flame simulations. The suppression effectiveness of a number of suppressants (N_2 , CO_2 , or CF_3Br) was considered as they were added to either the fuel or oxidizer streams of low strain rate methane-air diffusion flames.

EXPERIMENTAL METHOD Flame structure and extinction was investigated in normal gravity using a water-cooled counterflow burner with a diameter of 23.4 mm and a duct separation of 25 mm. Four 200 mesh stainless steel screens were secured at the opening of each duct to impose a top-hat velocity profile. The flow of dry air (with $[\text{O}_2]=20.94\%\pm0.04\%$) and methane (99.99%) were controlled using mass flow controllers that were calibrated using a dry cell primary flow meter with an uncertainty of better than 0.5%. The oxidizer flowed from the top duct, which was aligned with the gravity vector. The ratio of the velocity of the oxidizer stream to the velocity of the fuel stream was varied from 1:1 to 4:1 to position the flame such that conductive heat transfer losses to the burner were negligible, as verified by temperature measurements using 50 μm diameter thermocouples (see Fig.1). Analogous experiments are being prepared for the NASA/Cleveland drop towers.

Extinction measurements were performed by incrementally increasing the agent flow, while maintaining a constant global strain rate (a_g), accomplished by simultaneously reducing the air or fuel flow. The value of (a_g) was varied from 12 s^{-1} to 120 s^{-1} and is defined as:

$$a_g = (-2V_O/L) \cdot (1 + [(V_F/V_O) \cdot (\rho_F/\rho_O)^{1/2}]) \quad (1)$$

The parameters V and ρ denote the velocity and density of the reactant streams at the boundaries, L is the duct separation distance, and the subscripts O and F represent the oxidizer and fuel streams, respectively. Extinction measurements were repeated at least four times. The combined standard uncertainty (with a coverage factor of 2) in the agent extinction concentration based on repeat measurements and a propagation of error analysis was typically 1.3%.

Flame unsteadiness was reduced by placing the burner in an enclosure ($0.5 \times 0.5 \times 0.6 \text{ m}^3$), which isolated it from ambient flow disturbances and facilitated experimentation on flames with a_g as low as 12 s^{-1} . The enclosure had a 10 cm exhaust port and was placed inside a chemical hood. Combustion products were removed by buoyancy, not forced ventilation.

NUMERICAL METHODOLOGY

Two flame codes were utilized. The structure and extinction of methane-air flames with CO_2 and N_2 addition were investigated using a one-dimensional numerical simulation [5] that employs detailed models of molecular transport and chemistry [6], but ignores buoyancy. A term for the radiative heat loss rate was added to the energy equation in the one-dimensional flame code. Radiative losses were modeled with either a narrowband spectral model [7] or as an optically thin gray gas with temperature dependent Plank mean absorption coefficients for the participating gas species (CH_4 , CO_2 , H_2O and CO) [8]. A transient two-dimensional (axisymmetric) solution to the Navier-Stokes equations using a mixture fraction approach and including buoyancy [9] was used to investigate the impact of G -level on the structure of near-extinction methane-air diffusion flames with N_2 added to the fuel.

RESULTS AND DISCUSSION

Observations Undiluted, low strain rate counterflow methane-air flames are luminous. As CO_2 or N_2 was added to either reactant stream, flame luminosity decreased. Near extinction, the flames appeared to be completely nonluminous. This observation motivated simplification of the radiation model for these diluted flames, permitting exclusion of radiative emission by particulates. This was not the case for CF_3Br inhibited flames, which were very luminous.

Suppressant added to the Fuel Stream Equation 1 implies that a_g can be held constant for varying values of (V_O/V_F) . A series of measurements and one-dimensional calculations were performed that determined the agent concentration required to achieve extinction as a function of (V_O/V_F) for constant a_g . The computations showed that while the flame position shifted, the maximum flame temperature and the required agent concentration was invariant. This was experimentally confirmed. Using this strategy, Fig. 2 shows measurements of the required N_2 , CO_2 , and CF_3Br concentration in the oxidizer stream of nonpremixed CH_4 -air flames as a function of the global strain rate for normal gravity and flames free of conductive losses. The most effective suppressant was CF_3Br , followed by CO_2 and then N_2 . The critical suppressant concentration increased as the strain rate decreased, with its value leveling off near 30 s^{-1} , except for CF_3Br , which flattened near 40 s^{-1} . The results demonstrate the existence of turning point behavior in normal gravity diffusion flames, but at higher values of a_g than the microgravity measurements of Maruta et al. [2]. This implies that buoyancy impacts the near-extinction flame structure. These differences are being studied experimentally and computationally. Both the measurements and calculations show that as a_g decreases, the near-extinction peak flame temperature decreases and the flames broaden spatially. Removal of gravity also broadens the

flames spatially (as well as shifting the flame location) as seen in Fig. 3, which compares the calculated temperatures from the two-dimensional code to thermocouple measurements conducted in normal gravity and the one-dimensional calculations for near-extinction N_2 diluted flames. Removal of gravity does not significantly change the calculated peak temperatures.

Suppressant added to the Oxidizer Stream Figure 4 shows measurements of the required N_2 , CO_2 , and CF_3Br concentrations as a function of the global strain rate for agent added to the oxidizer stream. Similar to the results for agent added to the fuel stream (Fig. 2), the results flattened at low strain rates suggestive of turning point behavior. Again, the most effective suppressant was CF_3Br , followed by CO_2 and then N_2 . Flames with N_2 and CF_3Br addition showed turning point behavior at $40\ s^{-1}$ and $30\ s^{-1}$, respectively. The larger turning point strain rate value for CF_3Br is attributed to enhanced radiative emission associated with CF_3Br addition.

SUMMARY AND CONCLUSIONS An experimental and computational study is underway to investigate the extinction of low strain rate diffusion flames by an agent. To illuminate the mechanisms of flame suppression at low strain rates, computational simulations that include radiative heat transfer were compared with measurements. An experimental apparatus is being completed for low strain rate microgravity experiments using the 2.2 s drop tower. The microgravity measurements will be compared to numerical predictions and 1G measurements.

ACKNOWLEDGEMENTS This research was partially supported by the NASA Microgravity Research Division through Contract No. C-32066-T (NIST) and Grant No. NCC3-694 (UIC), with Sandra Olson serving as Technical Monitor. M. Bundy was supported by the National Research Council as a NIST Post-Doctoral Research Associate (1999-2001).

REFERENCES

1. Hamins, A., Trees, D., Seshadri, K., & Chelliah, H., *Combust. Flame*, 99:221 (1994).
2. Maruta, K., Yoshida, M., Guo, H., Ju, Y., & Niioka, T., *Combust. Flame*, 112:181 (1998).
3. Lee, K. Y., Cha, D. J., Hamins, A., & Puri, I. K., *Combust. Flame* 104:27 (1996).
4. Chan, S. H., Pan, X. C., & Abou-Ellail, M. M. M., *Combust. Flame*, 102:438 (1995).
5. Lutz, A., Kee, R. J., Grcar, J., & Rupley, F. M., "A Fortran Program Computing Opposed Flow Diffusion Flames", SAND96-8243, Sandia National Labs, Livermore (1997).
6. Bowman, C. T., Hanson, R. K., Davidson, D. F., Gardiner, Jr., W. C., Lissianski, V., Smith, G. P., Golden, D. M., Frenklach, M., & Goldenberg, M., "GRI-MECH 2.11", URL: <http://www.me.berkeley.edu/gri-mech/>, 1995.
7. Grosshandler, W.L., RADCAL: NIST Technical Note 1402, National Institute of Standards and Technology, Gaithersburg, Maryland, 1993.
8. Tien, C. L., Thermal Radiation Properties of Gases in *Advances in Heat Transfer* (T. F. Irvine Jr. and J. P. Hartnett, Eds.), Vol. 5, 1968, p. 311.
9. Floyd, J., McGrattan, K., & Baum, H., *A Mixture Fraction Combustion Model for Fire Simulation Using CFD*, International Conference on Engineered Fire Protection Design, to appear, June 2001.

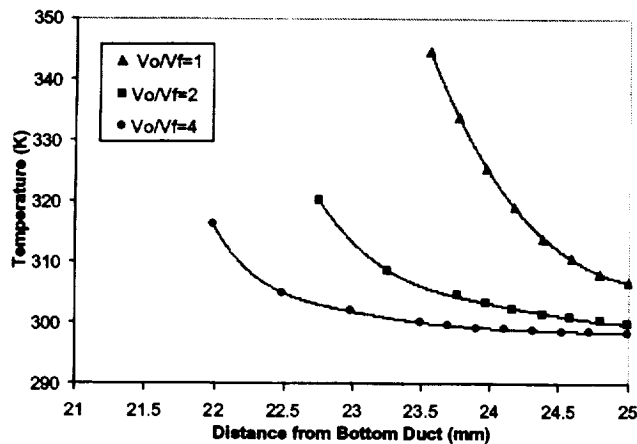


Figure 1. Thermocouple measurements in near-extinction CH_4 -air nonpremixed flames with N_2 added to the fuel stream as a function of distance from the bottom (fuel) duct in normal gravity. The ratio of the velocity of the oxidizer stream to the velocity of the fuel stream (V_o/V_f) was varied from 1 to 4 with all flames at a global strain rate of 12 s^{-1} .

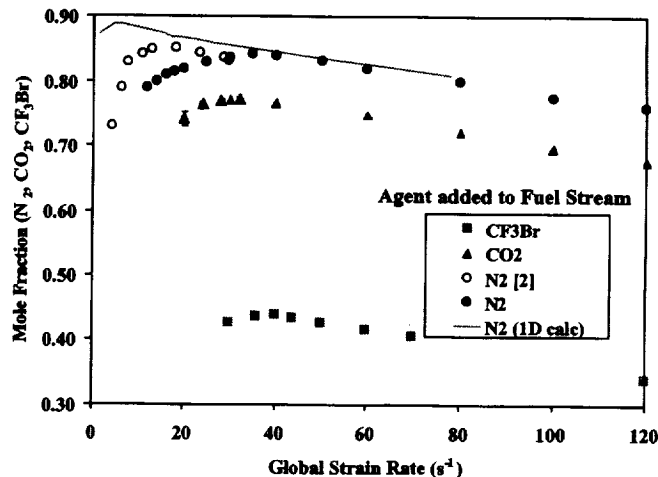


Figure 2. The critical agent mole fraction in the fuel stream required to extinguish CH_4 -air nonpremixed flames measured in normal gravity. Also shown are Maruta's microgravity results for N_2 [2], and the one-dimensional (1D) flame calculations (using the narrowband model), which show agreement with the N_2 measurements for $a_g \geq 40 \text{ s}^{-1}$.

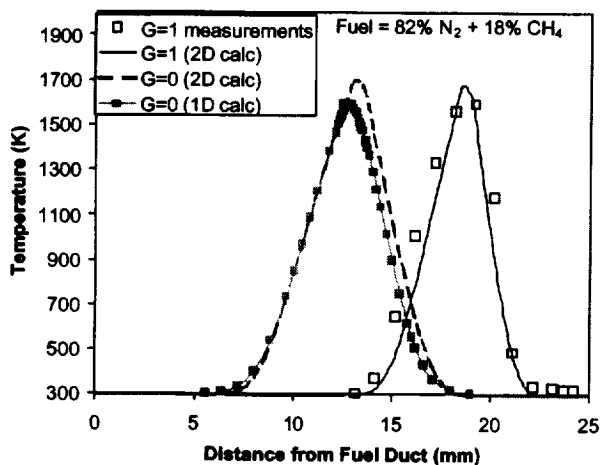


Figure 3. The temperature of near-extinction CH_4 -air nonpremixed flames with N_2 added to the fuel stream as a function of distance from the fuel duct. The global strain rate = 20 s^{-1} and $V_o/V_f = 1$. Normal gravity ($G=1$) thermocouple measurements (uncorrected for radiative losses) are compared to the results from the two-dimensional (2D) calculation. In addition, results from the one-dimensional (1D) calculation (using the narrowband model) are compared to those of the two-dimensional calculation with the buoyancy force set to zero ($G=0$).

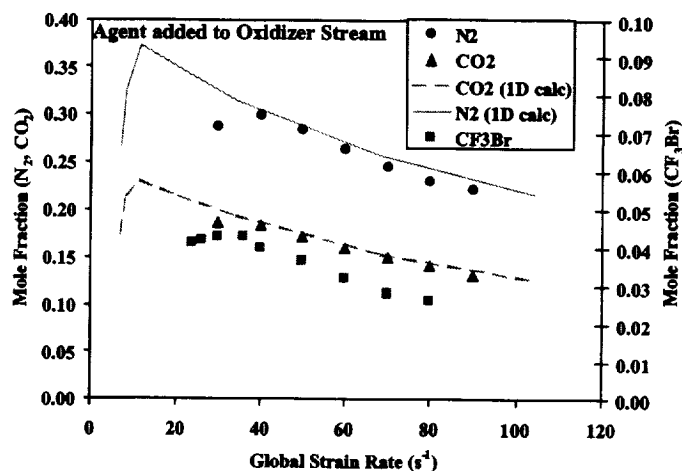


Figure 4. The critical agent mole fraction in the oxidizer stream required to extinguish CH_4 -air nonpremixed flames measured in normal gravity. Also shown are the one-dimensional (1D) flame calculations (using the narrowband model), which show agreement with the measurements for $a_g \geq 40 \text{ s}^{-1}$.

THE WATER-MIST FIRE SUPPRESSION EXPERIMENT: PROJECT OBJECTIVES AND HARDWARE DEVELOPMENT FOR THE STS-107 MISSION

J. T. McKinnon, A. Abbud-Madrid, E. P. Riedel, S. Gökoğlu, W. Yang, R. J. Kee
Center for Commercial Applications of Combustion in Space
Colorado School of Mines
Golden, Colorado 80401

INTRODUCTION

Fire protection systems in areas which are susceptible to water damage or where there is a significant weight penalty for water-based systems have historically used halon-based chemical fire suppression agents such as Halon 1301 (CF_3Br). Halons are so effective at fire suppression that in the past it was not necessary to evaluate other options. However, halons are also powerful ozone-depleting agents due to their ability to transport bromine into the stratosphere. This attribute of halons led to the ban of their manufacture in the industrialized world by the Montreal Protocols starting in 1995. Despite the urgent need to find an alternative replacement, no environmentally acceptable chemical agent as effective as Halon 1301 has been identified.

The deficiency in replacing chemical agents has lead to an increasing interest in fine water mists as fire suppressants since mists pose no adverse environmental or health issues and they offer the promise of meeting the requirements of protecting both water- and weight-sensitive areas due to the low requirements for total water flow, typically about one order of magnitude less than conventional water sprinklers. Water mist technology has already been found effective for extinguishing fires in shipboard machinery, aircraft cabins, and computer rooms.

Unfortunately, there is to date no widely accepted interpretation of the critical concentration of droplets or the optimum droplet size required to suppress a flame, or more importantly, of the fundamental mechanisms involved in flame extinguishment by a water mist. One of the main obstacles to obtaining such understanding is the difficulty of providing a simple, well-characterized experimental setup for the flame front/water mist interaction. A weightless environment provides an ideal place to study this interaction by eliminating the distorting effects of gravity on the generation and prolonged suspension of a uniform concentration of droplets and on the complex flow patterns induced by natural convection between the flame front and the water droplets. The objective of the Water-Mist Fire Suppression experiment (*Mist*) is to provide information on the flame-front/water-mist interaction by conducting a series of experiments on the Combustion Module (CM-2) facility in the STS-107 mission of the Space Shuttle. The results from these tests will be used to assess the feasibility of using water mists as the new generation of fire suppressants on earth as well as in spacecraft systems. In preparation for the orbital flights, numerical simulations and low-gravity ground experiments have been conducted to obtain the data necessary to define the test matrix and the important technical issues for the spacecraft experiments.

DESCRIPTION OF THE *MIST* EXPERIMENT

The *Mist* experimental apparatus has been described previously [1] so only a short description will be given here. Figure 1 shows a three-dimensional model of the flight apparatus with the main components of the experiment. A mixture of propane (C_3H_8) and air is loaded in a transparent cylindrical tube of 6.3-cm diameter and 49.5-cm length. The two gases are

introduced in the tube from separate tanks through a static mixer using mass flow controllers. A water mist generated by an ultrasonic atomizer is introduced in one half of the tube separated by an iris from the dry region. A light extinction system consisting of three diode lasers shining radially through the tube into three photodiode detectors is used to obtain droplet concentration data in different parts of the wet section. After the mist injection, the iris opens and the mixture is ignited in the dry section while keeping the valve at that end of the tube open for an isobaric combustion process. In order to measure the fire suppression ability of a given water-mist droplet size and water concentration, the propagation velocity of the premixed flame is measured by a video camera and by an array of 16 photodiodes installed along the tube. The *Mist* experiment was designed, fabricated, and assembled at the Center for Commercial Applications of Combustion in Space (CCACS) at the Colorado School of Mines and later tested and integrated to CM-2 along with the SOFBALL and LSP experiments.

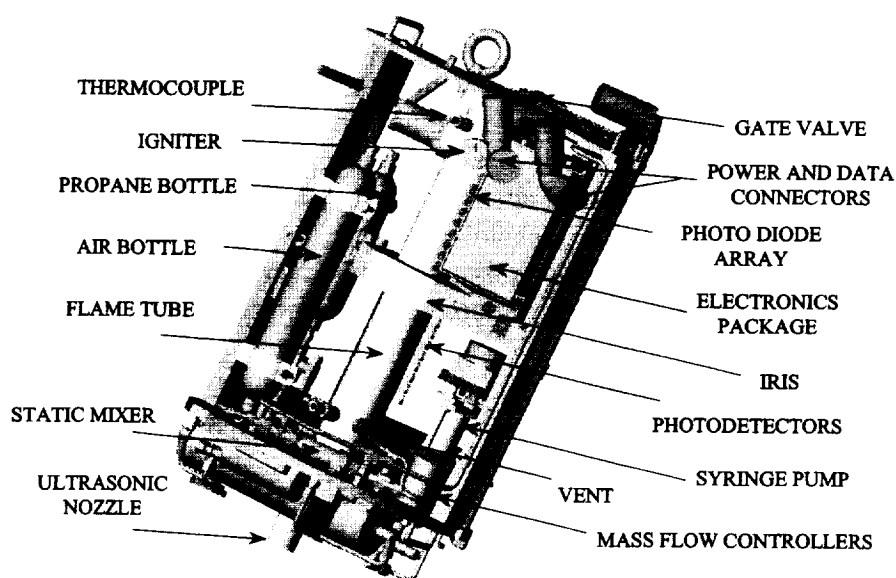


Figure 1. The *Mist* experiment flight unit.

NUMERICAL MODELING

In this investigation, a computational model has been developed that uses a hybrid Eulerian-Lagrangian formulation to simulate the two-phase, flame/mist interaction. Currently, the model is capable of simulating the free propagation of methane (CH_4)-air, planar, premixed laminar flames of various stoichiometries and their interaction with monodisperse water droplets. Gas-phase chemical kinetics, thermodynamic, and transport properties are handled by the PREMIX software [2] and are used in the Eulerian representation of the propagating flame. The GRI-MECH 3.0 database [3] is used as the methane-air reaction mechanism. This formulation is then coupled with droplet source terms from Lagrangian equations of mass, momentum, energy, and particle flux fraction. The interaction between the two phases is modeled using an imaginary gas packet that follows the droplet. This algorithm facilitates a stable coupling between the phases, yet permits solving the gas-phase equations and droplet equations separately.

EXPERIMENTAL AND NUMERICAL RESULTS

Low-gravity experiments conducted in NASA's KC-135 airplane showed two different types of flame behavior in the presence of water mists depending on the mixture stoichiometry. In the case of lean C_3H_8 -air mixtures, the flame speed increases at first with low water mist concentrations and then decreases below its dry value when higher water mist volumes are introduced in the tube. An increase in flame thrust due to thermal expansion of the high-density, water-laden combustion gases may account in part for the increase in flame propagation speed at low water mist volumes. For rich C_3H_8 -air mixtures, similar behavior of flame speed vs. water concentration is encountered, but in this case the higher flame speed is mostly due to the formation of cellular flames which acquire higher temperatures and consequently become more resistant to extinction by the water mist. Reference [1] describes these experimental findings in more detail.

The first numerical simulation consists of two freely propagating, stoichiometric, CH_4 -air flames—one wet and the other dry. Both cases are at atmospheric pressure with an inlet gas temperature of 298 K. The inlet mixture for the wet case has water vapor in the unburned mixture at 100% relative humidity (roughly 3% water vapor). The dry case contains no inlet water vapor. Due to the thermal, physical, and chemical effects of the steam, the burning velocity for the wet case is about 34 cm/s, which is considerably lower than the dry flame speed of about 39 cm/s. As anticipated, the post-flame temperature is higher for the dry case.

After establishing the two base cases mentioned above, different droplet sizes and concentrations are introduced in the wet-gas mixture case. These simulations show that larger droplets penetrate further into the post-flame region than smaller droplets which undergo rapid vaporization. Near the end of the droplet lifetime, the vaporization rate accelerates due to the rapidly increasing surface-area-to-volume ratio. Also, as more condensed water is added into the gas mixture, the maximum and post-flame temperatures are reduced. Consequently, the burning velocities are also reduced with increasing water-mass loading. At some point, the amount of water mist is sufficient to extinguish the flame. There is also a significant effect of droplet size on the flame temperature profiles. Smaller droplets tend to be more effective in the active flame zone itself and in the immediate post-flame gases. This is due to their higher vaporization rate. Larger droplets, which persist farther into the post-flame gases, are more effective in decreasing post-flame temperatures, away from the flame front itself. It is well known that a flame propagates by diffusion of energy and radicals towards the unreacted zone and the intensity of the diffusion is proportional to the temperature and concentration gradients. The smaller droplets vaporizing in the reaction zone tend to flatten gradients, so they are more effective in reducing the flame speed. Figure 2a shows the effect of water concentration and droplet size on burning speed. As clearly seen in the plot, very fine mists should be more efficient fire suppressants than larger droplets. Mathematically speaking, the flame-extinction point itself is a turning point where the steady-state conservation equations are singular.

An advantage of the numerical model is the capability of de-coupling the various suppression mechanisms to evaluate their relative importance. As an example, Fig. 2b shows the quenching magnitude of the sensible and latent heats of water on stoichiometric methane-air flames. For this case, it is clearly evident that the sensible heat component of the thermal effect is larger than the latent heat of vaporization of the water due to the high temperature of the flame. Also shown is the dominant quenching effect of thermal heat removal as compared to physical and chemical suppression mechanisms.

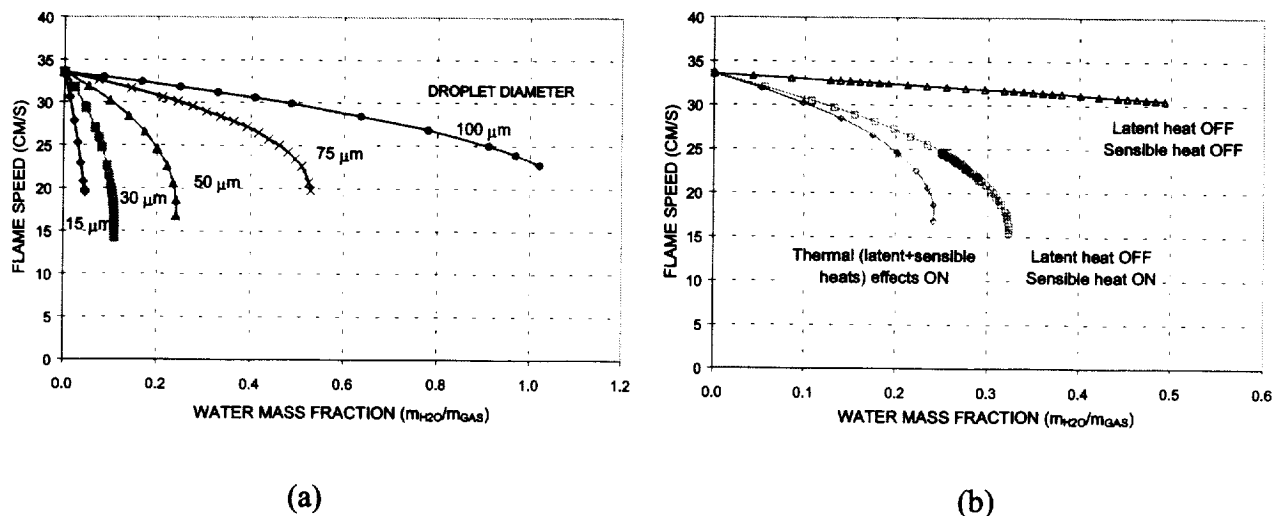


Figure 2. (a) Effect of droplet diameter and (b) effect of sensible and latent heats (50- μm water droplets), at various mass fractions of water on the flame speed of a planar, stoichiometric CH_4 -air premixed flame obtained by numerical simulation.

CONCLUSIONS

A preliminary investigation of the effect of water mists on premixed flame propagation under low-gravity conditions has been conducted to define the scientific and technical objectives of the experiments to be performed on the Space Shuttle microgravity environment. Based on the numerical modeling and ground-based experimental tests, the *Mist* test matrix will consist of 36 tests using 3 droplet median diameters (20, 30, and 40 μm), 3 water loadings (0.06, 0.12, and 0.18 water mass fractions), and 3 different mixture stoichiometries (0.7, 1.0, and 1.3). The last six tests will be allocated to explore the effect of mists on mixtures near their flammability limits.

It is suspected that the unusual flame behavior observed in the low- g experiments may be a result of the non-uniform droplet concentrations caused by residual convective currents, g -jitter, and short low- g times available in the aircraft. The elimination of these effects on the Shuttle experiments should provide a better environment to study this phenomenon. The lessons learned from the hardware development of the *Mist* experiment and its integration into CM-2 will surely benefit the design of future fire-suppression experiments which will take advantage of the versatility of the Combustion Integrated Rack (CIR) onboard the International Space Station.

REFERENCES

1. Abbud-Madrid, A., Riedel, E. P., and McKinnon, J. T., "A Study of Flame Propagation on Water-Mist Laden Gas Mixtures in Microgravity," *Fifth International Microgravity Combustion Workshop*, NASA CP 1999-208917, NASA GRC, Cleveland, pp. 65-68, 1999.
2. Kee, R.J., Grcar, J.F., Miller, A., and Meeks, E., "PREMIX: A Fortran Program for Modeling Steady Laminar One-Dimensional Premixed Flames," Sandia National Laboratories, 1998.
3. Smith, G.P., Golden, D.M., Frenklach, M., Moriarty, N.W., Eiteneer, B., Goldenberg, M., Bowman, C.T., Hanson, R.K., Song, S., Gardiner, W.C., Lissianski, V., and Qin, Z., "GRI-MECH—an Optimized Detailed Chemical Reaction Mechanism for Methane Combustion," Tech. Report http://www.me.berkeley.edu/gri_mech, Gas Research Institute, 2000.

DETAILED STUDIES ON FLAME EXTINCTION BY INERT PARTICLES IN NORMAL- AND MICRO-GRAVITY

M.G. ANDAC, F. N. EGOLFOPOULOS & C. S. CAMPBELL

Department of Aerospace & Mechanical Engineering

University of Southern California

Los Angeles, California 90089-1453

INTRODUCTION

The combustion of dusty flows has been studied to lesser extent than pure gas phase flows and sprays. Particles can have a strong effect by modifying the dynamic response and detailed structure of flames through the dynamic, thermal, and chemical couplings between the two phases. A rigorous understanding of the dynamics and structure of two-phase flows can be attained in stagnation flow configurations, which have been used by others to study spray combustion [e.g. 1-3] as well as reacting dusty flows [e.g. 4, 5].

In earlier studies on reacting dusty flows [e.g.4, 5], the thermal coupling between the two phases as well as the effect of gravity on the flame response were not considered. However, in Ref. 6, the thermal coupling between chemically inert particles and the gas was addressed in premixed flames. The effects of gravity was also studied showing that it can substantially affect the profiles of the particle velocity, number density, mass flux, and temperature. The results showed a strong dynamic and thermal dependence of reacting dusty flows to particle number density. However, the work was only numerical and limited to twin-flames, stagnation, premixed flames.

In Ref. 7 the effects of chemically inert particle clouds on the extinction of strained premixed and non-premixed flames were studied both experimentally and numerically at 1-g. It was shown and explained that large particles can cause more effective flame cooling compared to smaller particles. The effects of flame configuration and particle injection orientation were also addressed. The complexity of the coupling between the various parameters in such flows was demonstrated and it was shown that it was impossible to obtain a simple and still meaningful scaling that captured all the pertinent physics.

OBJECTIVES

The objective of the present work was to conduct a combined experimental and numerical study to assess the effects of chemically inert particles on flame extinction in 1-g and μ -g environments. Numerical simulations were compared with experimental results to verify the validity of theoretical models. The results were used to derive physical insight into the mechanisms that control the dynamic and thermal interactions between the two phases.

EXPERIMENTAL APPROACH

The experimental configuration includes the use of two counterflowing jets. Particles are fed into the flow by using a particle seeder unit, which utilizes a piston feeder similar to that used in [8]. This feeder is attached beneath the bottom burner and feeds the particles into the flow at a constant rate. This design allows for seeding under both 1-g and μ -g. However, it is apparent that the particle pickup is strongly affected by gravitational forces so that the seeder had to be calibrated separately in 1-g and μ -g. Chemically inert aluminum oxide and nickel-alloy particles were used. (While nickel burns, these fuel-lean flames are too cool to cause nickel ignition).

Premixed and non-premixed flame extinction experiments were conducted, by varying the particle type, size, and mass delivery rate, as well as the gas phase equivalence ratio, fuel type, flame configuration, and strain rate. In all these experiments, the particles were seeded from the lower burner. The experiments in μ -g were conducted on board the KC-135 plane.

Two types of premixed flame configurations were studied. The first included the use of the symmetric twin-flame that results by impinging on each other two fuel/air jets of identical composition. In this configuration, two flames form and the particles, which are injected only through the lower burner, preferentially cool the first flame that they encounter and may or may not have a chance to directly cool the second flame. That depends both on the ability of the particles to penetrate the gas phase stagnation plane (GSP) and on the particle's thermal state as they reach the second flame. The second configuration used is a single flame that results by impinging a fuel/air jet on an opposing air jet. In the non-premixed flame experiments, the mixture of fuel and nitrogen gas was supplied from the bottom burner, while the air jet was supplied from the upper burner.

For all cases, the flames are first established at conditions close to the extinction state. Then, the local strain rate, based on the maximum velocity gradient in the hydrodynamic zone, is measured by using Laser Doppler Velocimetry at 1-g, and is globally determined at μ -g. Subsequently, the piston seeder is turned on, feeding the particles at a constant rate. The fuel flow rate is then decreased very slowly, until the flames are extinguished.

NUMERICAL APPROACH

A set of quasi-one-dimensional equations along the system centerline has been developed for both phases [6]. The particle equations were formulated for small particle number densities. The gas phase continuity and species equations for the inert particles are identical to those of Ref. 9. However, the gas phase momentum equation was modified by adding a term representing the Stokes drag and thermophoretic forces exerted between the particles and the gas, as well as the gravitational force on the particles. (The system configuration is assumed to be vertical so that gravity acts in the axial direction.) Including terms describing the conductive/convective/radiative heat exchange between the two phases also modified the gas phase energy equation. The particle energy equation includes the contributions of conductive/convective heat exchange between the two phases. A conservation equation was also formulated for the particle number density.

The solutions are obtained by simultaneously integrating the entire system of equations for both phases. An Eulerian frame of reference is used for the integration of the gas phase equations. The particle equations are integrated in a Lagrangian frame of reference in order to describe properly the particle reversal phenomenon [1,6]. Detailed kinetics are used, and the code is integrated with the CHEMKIN [10] and Transport [11] subroutine libraries.

SUMMARY OF RESEARCH

It was previously shown experimentally and explained numerically [7] that at low strain rates the cooling efficiency of large particles may be greater compared to that of small particles for the same amount of particle mass delivered into the flow. This counterintuitive finding results from the fact that while similar masses of small particles possess more total surface area, the large particles can establish large temperature differences with the gas phase within the reaction zone, and thus more effectively cool the flame. However, the numerical simulations shown in Fig.1 indicate that as the strain rate increases, the smaller particles cool more effectively. This is also

supported by the experimental results for methane/air premixed flames shown in Fig. 2. At high strain rates large particles are quickly transported through the flame and do not remove much heat compared to smaller particles, which more closely follow the flow as they are slowed near the stagnation plane and have a larger residence time in the main reaction zone.

Flame extinction experiments were conducted for twin flames performed in 1-g and μ -g. The experimental data of Fig. 3 indicate that with the same particle mass delivery rate and the same strain rate values (i.e. the same nozzle exit velocity), the particles extinguish stronger flames in μ -g compared to 1-g. This is because at μ -g the particles penetrate all the way to the top flame and thus can affect both flames directly. In 1-g, however, gravity opposes the particle motion so that they can barely cross the GSP and as a result, only the lower flame is cooled. Figure 5 depicts the results of flame extinction experiments conducted by 25- and 60- μ m aluminum-oxide particles. It can be seen that the large particles cool the flames to extinction more effectively as they remove more heat from the bottom flame due to their larger thermal inertia and they also affect the top flame directly due to their larger dynamic inertia.

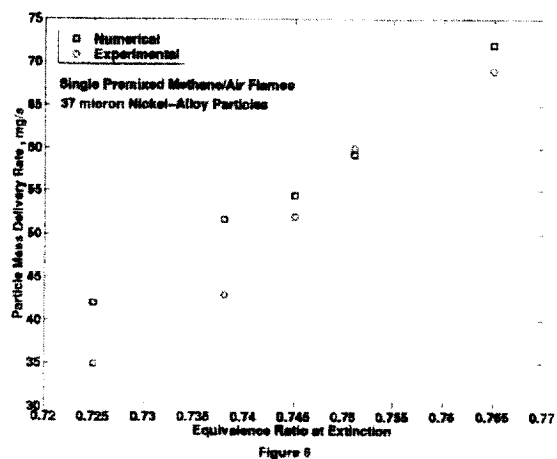
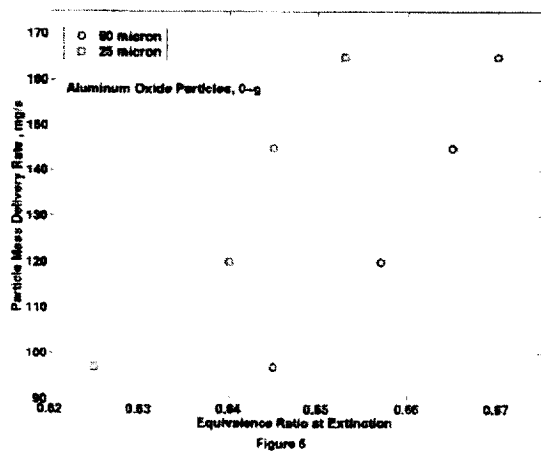
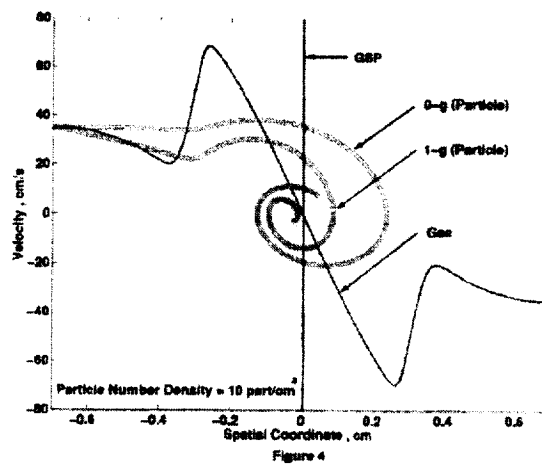
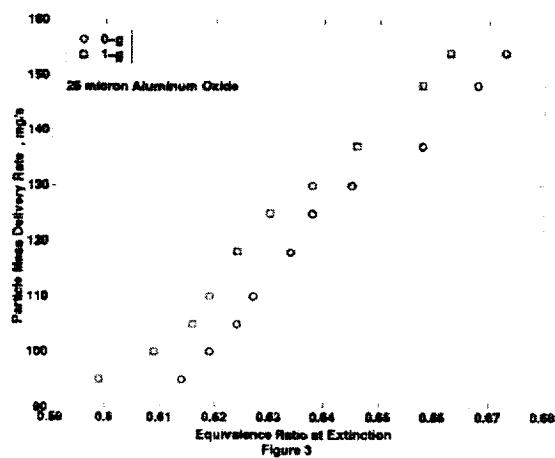
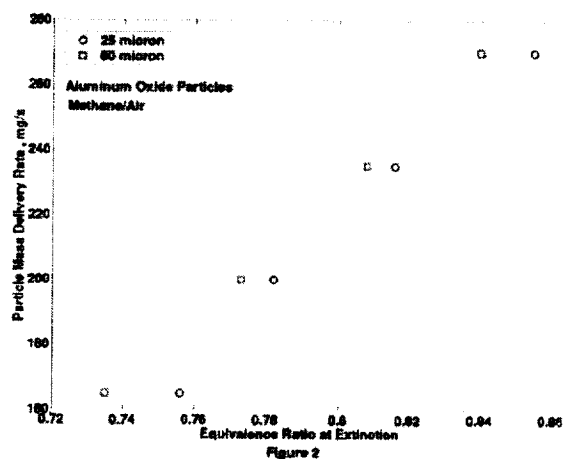
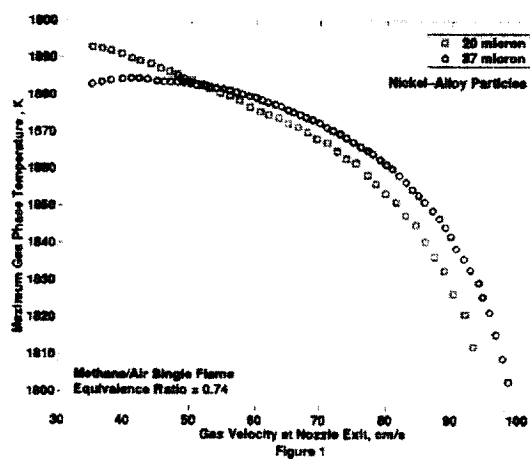
Figure 6 depicts comparisons of experimental and predicted extinction conditions for single premixed methane/air flames stabilized below GSP and seeded with 37- μ m nickel-alloy particles in 1-g. It is apparent that a good agreement exists, considering that various assumptions are involved in both experiments and simulations. However, the simulations systematically predict larger particle mass delivery rates for a particular extinction equivalence ratio. This may result from the fact that the code is quasi-one dimensional while the actual flow field is axisymmetric. In other words the code only defines properly the dynamic and thermal behavior of the particles along the stagnation streamline, which may be different from the behavior of the particles that are not at the vicinity of the centerline.

REFERENCES

1. Continillo, G. & Sirignano, W.A., *Combust. Flame* 81:325-340 (1990).
2. Chen, N.H., Rogg, B. & Bray, K.N.C., *Proc. Combust. Inst.* 24: 1513-1521 (1992).
3. Chen, G. & Gomez, A., *Proc. Combust. Inst.* 24: 1531-1539 (1992).
4. Gomez, A. & Rosner, D.E., *Combust. Sci. Tech.* 89, pp. 335-362, (1993).
5. Sung, C.J., Law, C.K. & Axelbaum, R.L., *Combust. Sci. Tech.* 99:119-132, (1994).
6. Egolfopoulos, F.N. & Campbell, C.S., *Combust. Flame* 117, pp. 206-226, (1999).
7. Andac, M.G., Egolfopoulos, F.N., Campbell, C.S. & Lauvergne, R. "Effects of Inert Dust Clouds on the Extinction of Strained, Laminar Flames at Normal- and Micro-Gravity," *Proc. Combust. Inst.* 28, in press.
8. Goroshin, S., Kleins, H., Lee, J.H.S. & Frost, D., "Microgravity Combustion of Dust Clouds. Quenching Distance Measurements," *Third International Microgravity Combustion Symposium*, NASA Lewis Research Center, Cleveland, Ohio, April 1995.
9. Kee, R. J., Miller, J. A., Evans, G. H. & Dixon-Lewis, G., *Proc. Combust. Inst.* 22: 1479-1494 (1988).
10. Kee, R. J., Warnatz, J. & Miller, J. A., Sandia Report SAND83-8209, 1983.
11. Kee, R. J., Rupley, F. M. & Miller, J. A., Sandia Report SAND89-8009, 1989.

ACKNOWLEDGMENTS

This work is supported by NASA under Grants NAG3-1877 and NCC3-834 under the technical supervision of Dr. Ming-Shin Wu of the Glenn Research Center



UNSTEADY SPHERICAL DIFFUSION FLAMES IN MICROGRAVITY

Arvind Atreya, S. Berhan, M. Chernovsky

Department of Mechanical Engineering & Applied Mechanics

University of Michigan; Ann Arbor, MI 48109

and

Kurt R. Sacksteder

NASA Glen Research Center; Cleveland, OH 44135

INTRODUCTION

The absence of buoyancy-induced flows in microgravity (μg) and the resulting increase in the reactant residence time significantly alters the fundamentals of many combustion processes. Substantial differences between normal gravity (ng) and μg flames have been reported in experiments on candle flames [1, 2], flame spread over solids [3, 4], droplet combustion [5,6], and others. These differences are more basic than just in the visible flame shape. Longer residence times and higher concentration of combustion products in the flame zone create a thermochemical environment that changes the flame chemistry and the heat and mass transfer processes. Processes such as flame radiation, that are often ignored in ng , become very important and sometimes even controlling. Furthermore, microgravity conditions considerably enhance flame radiation by: (i) the build-up of combustion products in the high-temperature reaction zone which increases the gas radiation, and (ii) longer residence times make conditions appropriate for substantial amounts of soot to form which is also responsible for radiative heat loss. Thus, it is anticipated that radiative heat loss may eventually extinguish the "weak" (low burning rate per unit flame area) μg diffusion flame. Yet, space shuttle experiments on candle flames show that in an infinite ambient atmosphere, the hemispherical candle flame in μg will burn indefinitely [1]. This may be because of the coupling between the fuel production rate and the flame via the heat-feedback mechanism for candle flames, flames over solids and fuel droplet flames. Thus, to focus only on the gas-phase phenomena leading to radiative extinction, aerodynamically stabilized gaseous diffusion flames are examined. This enables independent control of the fuel flow rate to help identify conditions under which radiative extinction occurs. Also, spherical geometry is chosen for the μg experiments and modeling because: (i) It reduces the complexity by making the problem one-dimensional. (ii) The spherical diffusion flame completely encloses the soot which is formed on the fuel rich side of the reaction zone. This increases the importance of flame radiation because now both soot and gaseous combustion products co-exist inside the high temperature spherical diffusion flame. (iii) For small fuel injection velocities, as is usually the case for a pyrolyzing solid, the diffusion flame in μg around the solid naturally develops spherical symmetry. Thus, spherical diffusion flames are of interest to fires in μg and identifying conditions that lead to radiation-induced extinction is important for spacecraft fire safety.

EXPERIMENTS

The experiments were conducted in the 2.2 sec drop tower at the NASA Lewis Research Center. The drop-rig used is described in detail elsewhere [8]. Briefly, it consists of a cylindrical test chamber (0.38m dia.; 0.43m deep) that houses the spherical burner, the hot-wire igniter and the photodiodes and thermocouples used for making radiation and temperature measurements. The spherical burner (19mm dia.) was constructed from a low heat capacity porous ceramic material (93% porosity). Two

gas cylinders (150 cc & 500 cc) were charged with various gases up to 45 psig and were used to supply the fuel to the porous spherical burner. Fuel flow rates to the burner were controlled by a calibrated needle valve and a gas solenoid valve was used to open and close the gas line to the burner upon computer command. The test chamber also had a 125mm diameter Lexan window which enabled the camera to photograph the flame.

Several μg experiments under ambient pressure and oxygen concentration conditions, were conducted with methane (less sooty), ethylene (sooty), and acetylene (very sooty) fuels for flow rates ranging from 3 to 45 cm³/s. Some experiments with ethylene were repeated with various amounts of CO₂ added to the fuel to increase the radiative heat loss. The following measurements were made and data was collected by an onboard computer during these experiments: (i) *Flame radius* - measured from photographs taken by a color CCD camera. (ii) *Flame radiation* - measured by photodiodes with different spectral characteristics ranging from UV to IR. (iii) *Flame temperature* - measured by five S-type thermocouples and the sphere surface temperature was measured by a K-type thermocouple.

RESULTS

Flame Radius: For all fuels (methane, ethylene and acetylene), initially the flame was blue (non-sooty) but becomes very bright yellow (sooty) under μg conditions. Later, as the flame grew in size it became orange and less luminous and eventually the soot luminosity disappeared. CO₂ diluted flames, however, were mostly blue due to the fuel dilution effect. Both simple analytical and numerical models with one-step chemistry have been developed to explain and understand the expansion rate of these flames. Detailed chemistry models are also being developed. By defining a stream function ' ψ ' to satisfy the mass conservation equation as follows:

$$\frac{\partial \psi}{\partial t} = -r^2 \rho v; \quad \frac{\partial \psi}{\partial r} = r^2 \rho; \quad \rightarrow \left(\frac{\partial r}{\partial t} \right)_{\psi} = v$$

The equation for the conserved scalar ' Z ' can be analytically solved with the constant pressure ideal gas assumption and by requiring that $\psi = \text{constant}$ at the flame front. The solution for the flame radius ' r_f ' at time ' t ' is given by the following equation:

$$r_f(t) = \left(R^3 + \left(\frac{3\dot{V}(\rho_o h_{\infty}^f + Q \rho_o Y_{F_{\infty}} Z_c)}{4\pi(\rho_o h_{\infty}^f + \bar{\eta} t)} \right) \times t \right)^{1/3}$$

Where, ' R ' is the sphere radius; \dot{V} is the volumetric fuel flow rate; $\rho_o, h_{\infty}^f, Y_{F_{\infty}}$ and Q are the ambient density, enthalpy, fuel mass fraction and heat released per unit mass of fuel respectively. The flame exists at the conserved scalar value $Z=Z_c$, where ' Z ' is given by the expression:

$$Z = 1 - \operatorname{erf}\left(\frac{\psi}{2\sqrt{\tau}}\right) / 1 + \operatorname{erf}\left(\frac{M(t)}{8\pi\sqrt{\tau}}\right)$$

Here, $\bar{\eta}$ is the average heat loss rate by radiation per unit volume and $M(t)$ is the fuel mass injected until time ' t '. Note that the effect of heat release, mass flow rate, radiation heat loss rate and diffusion are contained in the factor multiplying ' t ' in the expression for ' r_f '. While these equations

are unlikely to provide comparison with experiments because infinite reaction rates and constant properties are assumed. However, the expression for ' r_f ' may be used to correlate the experimental and numerical results obtained with one-step kinetics. Such a correlation is shown in Figure 1 for several experiments conducted on methane. Similar results were also obtained for other fuels. This correlation shows that the flame radius growth rate is slightly less than $t^{1/3}$.

Flame Temperature:

Figure 2 shows the measured evolution of radial temperature profiles for methane ethylene, acetylene and CO₂ diluted flames. In all cases the fuel flow

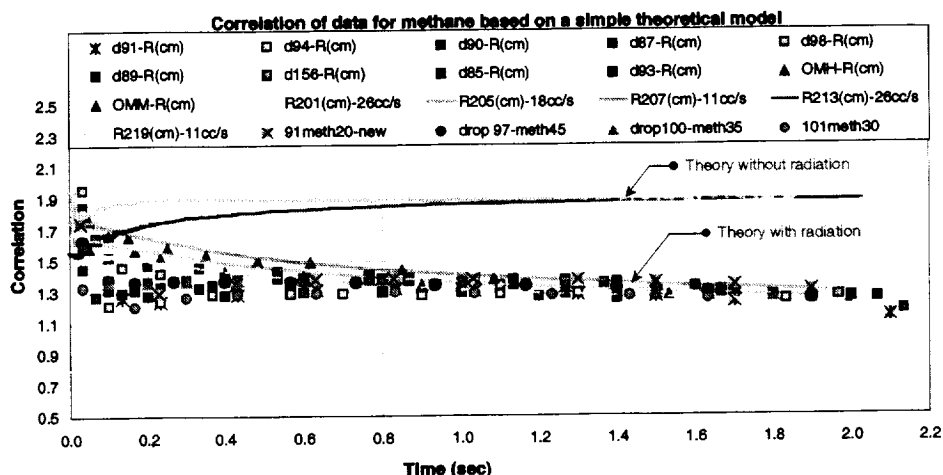


Figure 1: Correlation of data and numerical calculations.

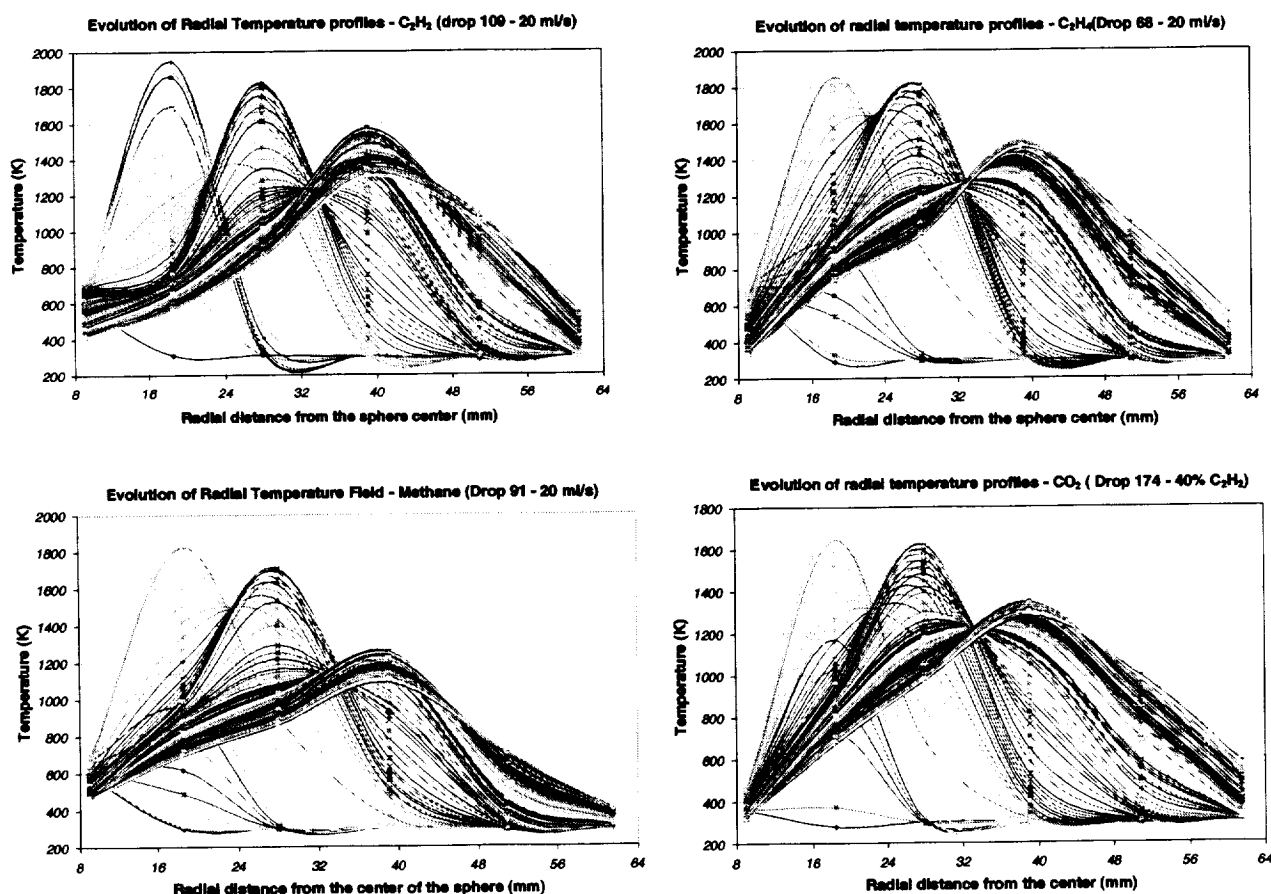


Figure 2: Evolution of radial temperature profiles for four representative cases.

rate was 20 ml/s except for the CO₂ diluted case where the C₂H₄ flow rate was 16 ml/s and the total flow rate was 40 ml/s. Clearly, the temperature fell as time progressed. Also, $T_{C_2H_2} > T_{C_2H_4} > T_{CH_4}$ at all times in the entire domain for the same fuel flow rate. The temperature for T_{CO₂+C₂H₄} was the lowest. The sooting propensity of these fuels is also in the same order, i.e. C₂H₂ > C₂H₄ > CH₄. Thus, we expect that C₂H₂ flames will be the most radiative. It turns out that C₂H₄ + CO₂ flames are the least radiative due to fuel dilution that reduces the temperature. This is shown in Figure 3 below. Only radiation in the CO₂ wavelength for CH₄ & C₂H₄ is shown due to space limitations.

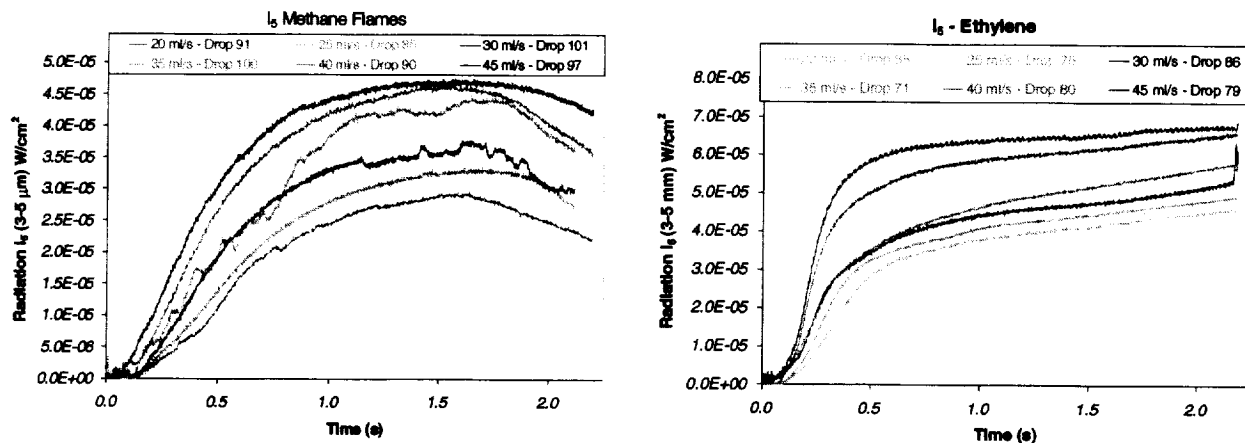


Figure 3: Radiation from CH₄ & C₂H₄ flames in the CO₂ wavelength band.

Figure 3 shows that the flame radiation was reduced roughly by a factor of two for all flames. This is true for all wavelengths as well. Likewise, the radiation from C₂H₂ is higher than C₂H₄ and radiation from CO₂ diluted flames is lower than CH₄ flames for all wavelengths and all flames. This indicates that the effect of temperature is dominant. Interestingly, the total radiation from the pure ethylene flame becomes constant (a trend that is true regardless of the fuel type and the flow rate; in fact for CH₄ it begins to fall) but the total radiation from CO₂ diluted flames continues to increase.

REFERENCES

- [1] Dietrich, D. L., Ross, H. D. and T'ien, J. S. "Candle Flames in Microgravity," Third Microgravity Combustion Workshop, Cleveland, Ohio, April, 1995.
- [2] Ross, H. D., Sotos, R. G. and T'ien, J. S., Combustion Science and Technology, Vol. 75, pp. 155-160, 1991.
- [3] T'ien, J. S., Sacksteder, K. R., Ferkul, P. V. and Grayson, G. D. "Combustion of Solid Fuels in very Low Speed Oxygen Streams," Second International Microgravity Combustion Workshop, NASA Conference Publication, 1992.
- [4] Ferkul, P., V., "A Model of Concurrent Flow Flame Spread Over a Thin Solid Fuel," NASA Contractor Report 191111, 1993.
- [5] Jackson, G., S., Avedisian, C., T. and Yang, J., C., Int. J. Heat Mass Transfer., Vol.35, No. 8, pp. 2017-2033, 1992.
- [6] Tsue, M., Segawa, D., Kadota, T. and Yamasaki, H. Twenty-Sixth (International) Symposium on Combustion, The Combustion Institute, 1996, pp. 1251-1258.
- [7] Atreya, A. and Agrawal, S., "Effect of Radiative Heat Loss on Diffusion Flames in Quiescent Microgravity Atmosphere," Combustion & Flame, (accepted for publication), 1997.
- [8] Atreya, A., Agrawal, S., Sacksteder, K., and Baum, H., "Observations of Methane and Ethylene Diffusion Flames Stabilized around a Blowing Porous Sphere in μg Conditions," AIAA # 94-0572.

REACTION KERNEL STRUCTURE OF A SLOT JET DIFFUSION FLAME IN MICROGRAVITY

F. Takahashi¹ and V. R. Katta²

¹National Center for Microgravity Research on Fluids and Combustion, Cleveland, Ohio

²Innovative Scientific Solutions, Inc., Dayton, Ohio

INTRODUCTION

Diffusion flame stabilization in normal earth gravity (1 g) has long been a fundamental research subject in combustion [1]. Local flame-flow phenomena, including heat and species transport and chemical reactions, around the flame base in the vicinity of condensed surfaces control flame stabilization and fire spreading processes. Therefore, gravity plays an important role in the subject topic because buoyancy induces flow in the flame zone, thus increasing the convective (and diffusive) oxygen transport into the flame zone and, in turn, reaction rates.

Recent computations [2-5] show that a peak reactivity (heat-release or oxygen-consumption rate) spot, or *reaction kernel*, is formed in the flame base by back-diffusion and reactions of radical species in the incoming oxygen-abundant flow at relatively low temperatures (~1550 K). Quasi-linear correlations were found between the peak heat-release or oxygen-consumption rate and the velocity at the reaction kernel for cases including both jet and flat-plate diffusion flames in airflow. The reaction kernel provides a stationary ignition source to incoming reactants, sustains combustion, and thus stabilizes the trailing diffusion flame. In a quiescent microgravity environment, no buoyancy-induced flow exists and thus purely diffusive transport controls the reaction rates. Flame stabilization mechanisms in such purely diffusion-controlled regime remain largely unstudied. Therefore, it will be a rigorous test for the reaction kernel correlation if it can be extended toward zero velocity conditions in the purely diffusion-controlled regime.

The objectives of this study are to reveal the structure of the flame-stabilizing region of a two-dimensional (2D) laminar jet diffusion flame in microgravity and develop a unified diffusion flame stabilization mechanism. This paper reports the recent progress in the computation and experiment performed in microgravity.

EXPERIMENTAL TECHNIQUES

Microgravity experiments were conducted using the 2.2-s drop tower in the NASA Glenn Research Center. Figure 1 shows a conceptual sketch of a slot burner (1.02×25.4 mm inner cross-section, 152 mm length, 0.25 mm lip thickness; 360 brass) placed in a combustion chamber (255 mm i.d. \times 533 mm length). Methane jet was ignited using an electrically heated kanthal wire (29 AWG, ~30 mm length) ~2 cm above the jet exit in microgravity. Standard color video recording via a fiber-optic link was made for the mean fuel jet velocity of $U_j = 0.236$ m/s in still air and $U_j = 0.142$ m/s and 0.071 m/s in a still 30 mol.% O_2 /70 mol.% N_2 mixture. Diagnostic techniques to be used in the near future include Mach-Zehnder interferometry and particle image velocimetry.

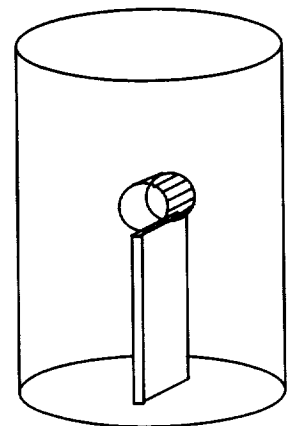


Fig. 1 Slot jet diffusion flame concept.

NUMERICAL METHODS

In this study, the structure of a 2D methane jet diffusion flame was simulated in zero-gravity (0 g) using a transient two-dimensional code (known as UNICORN [6, 7]). Time-dependent governing equations, expressed in Cartesian coordinates, consist of mass continuity, axial and transverse momentum conservation, energy conservation, and species conservation equations with the ideal-gas equation of state. The transport coefficients are estimated using molecular dynamics and mixture rules. The enthalpy of each species is calculated from polynomial curve-fits. The detailed chemistry model [8] for 24 species and 81 elementary steps is used. The finite-difference forms of the momentum equations are integrated using an implicit QUICKEST scheme, and those of the species and energy equations are obtained using a hybrid scheme of upwind and central differencing. Computations were performed using a 601×201 non-uniform grid system covering a physical domain of $60 \times 40\text{ mm}$. The grid system is clustered near the flame zone to resolve the large gradients in flow variables. The slot burner width of 3 mm , a lip thickness of 0.5 mm , and constant wall temperature of 500 K are used in computations. In this paper, the results obtained for the mean jet velocity of $U_j = 0.236\text{ m/s}$ and the near-still external air velocity of $U_a = 0.001\text{ m/s}$ are reported.

RESULTS AND DISCUSSION

Figure 2 shows video images (end view) of methane jet diffusion flames on a slot burner in microgravity. The flame in air (Fig. 2a) showed a round shape with a distortion due to initial ignition non-uniformity. Debris of the igniter wire is seen in the image. Because of the end effect allowing diffusion of the fuel and oxygen in the direction parallel to the long side of the slot, the flame was elongated hemispherical rather than cylindrical. There were relatively large quenched regions near the base on both sides of the burner. The flames in an oxygen-enriched atmosphere (Figs. 2b and 2c) appeared more cylindrical and blue. For $U_j = 0.142\text{ m/s}$ (Fig. 2b), a luminous zone presumably due to soot formation at ignition remained inside the blue flame envelop, while for $U_j = 0.71\text{ m/s}$ (Fig. 2c), it disappeared.

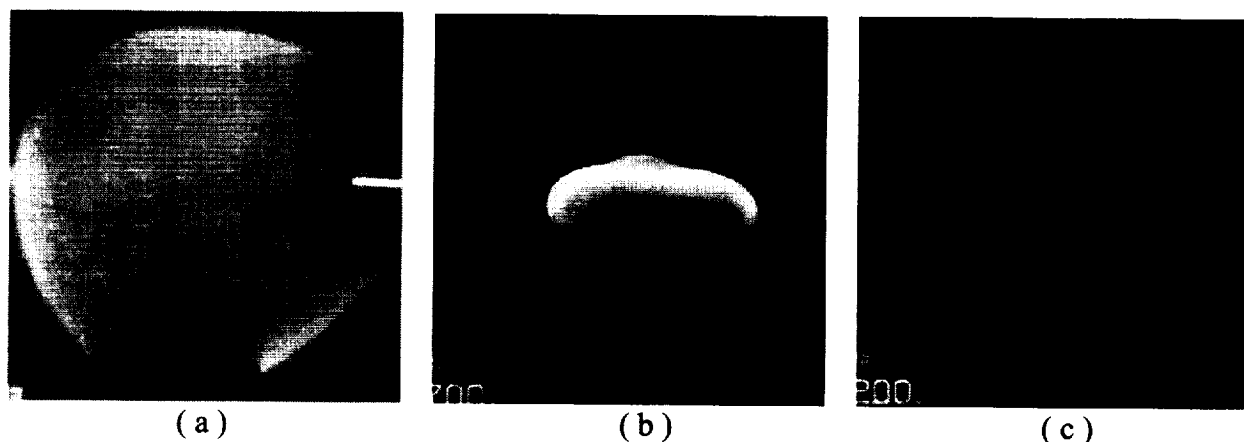


Fig. 2 Video images of methane jet diffusion flames on a slot burner in various still oxidizing atmospheres in microgravity. (a) $U_j = 0.236\text{ m/s}$, air; (b) $U_j = 0.142\text{ m/s}$, $30\%\text{O}_2/70\%\text{N}_2$; (c) $U_j = 0.071\text{ m/s}$, $30\%\text{O}_2/70\%\text{N}_2$.

Figure 3 shows the calculated velocity vectors, isotherms, and heat-release rate. The

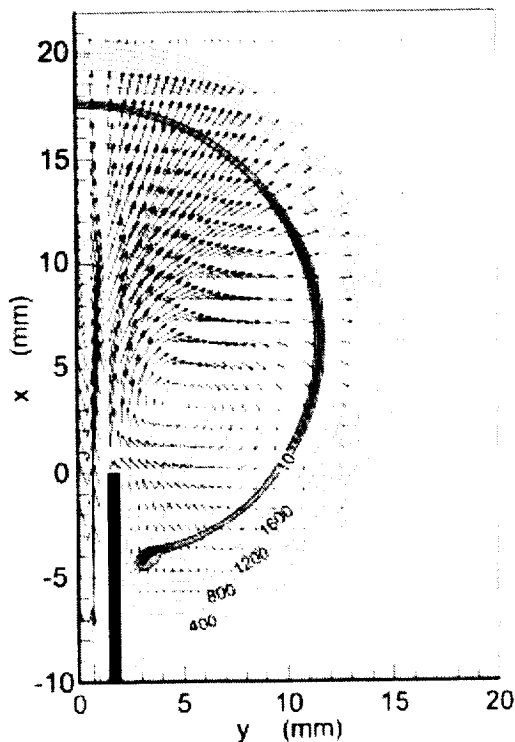


Fig.3 Calculated velocity vectors, isotherms (K), heat-release rate (J/cm³s).

computed flame was nearly circular (cylindrical) with a quenched region near the burner wall. The velocity vectors show the expanded fuel jet downstream and the air entrainment in the flame base region. The maximum flame temperature was approximately 1900 K in the upper portion of the flame. There existed a peak heat-release rate spot, i.e., reaction kernel, at the flame base as was observed in the jet and flat-plate diffusion flames in moderate airflow calculated previously [2-5]. However, the magnitude of the heat-release rate peak (~29 J/cm³s) in the present flame was an order of magnitude smaller, and the reaction kernel temperature (~1370 K) and velocity (~0.013 m/s) were much lower as well.

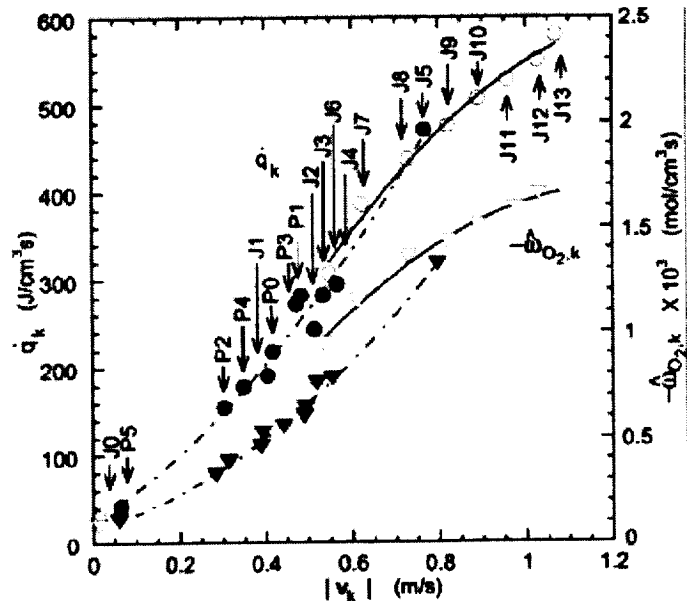


Fig. 4 Reaction kernel correlations. $\circ\bullet$, \dot{q}_k ; $\nabla\nabla$, $-\dot{\omega}_{O_2,k}$. Open, C₂-chemistry; filled, C₁-chemistry.

Table 1 Test conditions

Case No.	Air Velocity (m/s)	Fuel Velocity (m/s)	Chem. model
<i>2D Jet Diffusion Flame (0 g)</i>			
J0	0.001	0.236	C ₂
<i>Axisymmetric Jet Diffusion Flames (1 g, upward)</i>			
J1	0.19	1.7	C ₁
J2	0.19	11.5	C ₁
J3	0.36	1.7	C ₁
J4	0.36	6.9	C ₁
J5	0.72	1.7	C ₁
J6	0.36	1.7	C ₂
J7	0.50	1.7	C ₂
J8	0.66	1.7	C ₂
J9	0.72	1.7	C ₂
J10	0.75	1.7	C ₂
J11	0.78	1.7	C ₂
J12	0.80	1.7	C ₂
J13	0.80	1.7	C ₂
<i>Flat-Plate Burner Flames</i>			
P0	0.65 (0 g)	0.02 (0 g)	C ₁
P1	0.65 (upward)	0.02 (horizontal)	C ₁
P2	0.65 (downward)	0.02 (horizontal)	C ₁
P3	0.65 (horizontal)	0.02 (upward)	C ₁
P4	0.65 (horizontal)	0.02 (downward)	C ₁
P5	1.2 (horizontal)	0.008 (downward)	C ₁

Figure 5 shows the reaction kernel correlations of the peak heat-release rate or oxygen consumption rate with the total velocity. The test conditions for the data points are listed in

Table 1. The data set includes the results for the 2D (case J0, this study) or axisymmetric jet- (J1-J13) and flat-plate diffusion flames (P0-P5) [2-5]. Either C₁- or C₂-chemistry model [8] was used. All cases are for 1 g except for cases P0 and J0 for 0 g. There exist strong positive correlations between the reactivity and the incoming velocity at the reaction kernel. A previous paper [4] extended the correlations at higher ends (cases J6-J13) and successfully predicted the lifting limit of jet diffusion flames. The data points for the present results (case J0) further extended the correlation at lower ends toward a non-convective, pure diffusion-controlled regime. Extrapolations of the curves for $|v_k| = 0$ would give the heat-release rate or oxygen consumption rate in the pure diffusion-controlled regime.

CONCLUSIONS

The slot jet diffusion flames were observed experimentally in microgravity and simulated numerically. In the experiment, the end effect of the slot burner resulted in the formation of an elongated hemispherical flame. The computation showed that the peak reactivity spot, reaction kernel, was formed at the flame base of a 2D jet diffusion flame even under a low-convective zero-gravity condition. The computational results extended the reaction kernel correlations toward the pure diffusion-controlled regime. Thus, the flame stabilization mechanism based on the reaction kernel hypothesis derived previously is applicable to extremely low convective conditions as well.

ACKNOWLEDGMENTS

This work was supported under the Cooperative Agreement No. NCC3-675 by the NASA Office of Biological and Physical Research, Washington, DC. V. R. Katta was supported by the Air Force Office of Scientific Research in performing these calculations. Assistance by Peter Sunderland in conducting the microgravity test is acknowledged.

REFERENCES

1. Gaydon, A. G., and Wolfhard, H. G., *Flames—Their structure, radiation and temperature*, 4th Ed., Chapman and Hall, London, 1979, p. 39.
2. Takahashi, F., Schmoll, W. J., and Katta, V. R., "Attachment Mechanisms of Diffusion Flames," *Proceedings of The Combustion Institute*, Vol. 27, 675-684 (1998).
3. Takahashi, F., and Katta, V. R., "Chemical Kinetic Structure of the Reaction Kernel of Methane Jet Diffusion Flames," *Combustion Science and Technology*, 155, 243-279 (2000).
4. Takahashi, F., and Katta, V. R., "A Reaction Kernel Hypothesis for the Stability Limit of Methane Jet Diffusion Flames," *Proceedings of The Combustion Institute*, Vol. 28, (in press).
5. Takahashi, F., and Katta, V. R., "A Numerical and Experimental Study of the Structure of a Diffusion Flame Established in a Laminar Boundary Layer Along a Vertical Porous Plate," *Proceedings of the Third International Symposium on Scale Modeling*, Nagoya, Japan, September 2000.
6. Katta, V. R., Goss, L. P., and Roquemore, W. M., "Numerical Investigations of Transitional H₂/N₂ Jet Diffusion Flames," *AIAA Journal* 32, 84 (1994).
7. Roquemore, W. M., and Katta, V. R., "Role of Flow Visualization in the Development of UNICORN," *Journal of Visualization*, Vol. 2, No. 3/4 (2000).
8. Peters, N., "Flame Calculations with Reduced Mechanisms—An Outline," *Reduced Kinetic Mechanisms for Applications in Combustion Systems*, Springer-Verlag, Berlin, 1993, p. 3.

FIELD EFFECTS OF BUOYANCY ON LEAN PREMIXED TURBULENT FLAMES

R. K. Cheng¹, R. Dimalanta¹, M. P. Wernet², and P. S. Greenberg²

¹Lawrence Berkeley National Laboratory, Berkeley, CA

² NASA John H. Glenn Research Center at Lewis Field, Cleveland OH

INTRODUCTION

Buoyancy affects the entire flowfield of steady turbulent flames and this aspect of flame buoyancy coupling is largely unexplored by experiments or by theory. Open flames and flames within large confinements are free to expand and interact with the surrounding environment. In addition to fluid and combustion conditions, their aerodynamic flowfields are determined by the flame brush orientation and geometry, wake of the stabilizer, enclosure size, and of course, the gravitational field. Because the flowfield consists mainly of cold reactants (mostly in the nearfield) and hot products (mostly in the farfield), buoyancy effects are manifested in the farfield region. In upward pointing flames, an obvious effect is a favorable axial pressure gradient that accelerates the products thereby increasing the axial aerodynamic stretch rate. Intrinsic to turbulent flows, changes in mean aerodynamic stretch also couple to the fluctuating pressure field. Consequently, buoyancy can influence the turbulence intensities upstream and downstream of the flame. Flame wrinkling process, and heat release rate are also directly affected. This backward coupling mechanism is the so-called elliptic problem. To resolve the field effects of buoyancy would require the solution of three-dimensional non-linear Navier Stokes equations with full specification of the upstream, wall and downstream boundary conditions.

BACKGROUND

The objective of our experimental study is to characterize the field effects of buoyancy through an extensive laboratory study of flames in normal gravity (+1g), and reversed gravity (-1g) that cumulate to a microgravity (μg) flight experiments to quantify the velocity and scalar flow fields of lean premixed turbulent flames. By comparing the results obtained at different gravitational levels and orientations, it would be possible to decipher the mechanism associated with the upstream coupling effects of buoyancy so that they can be treated properly in turbulent flame model.

Thus far, we have conducted laboratory studies of the effects of buoyancy on flame flickering frequency, stabilization limits, flame wrinkle structures, and mean and rms velocities for several flame configurations. Exploration of these phenomena helps to gain a knowledge base to define the appropriate configuration and conditions for microgravity flight experiments. As reported in our papers [1-3], these studies show that the effects of buoyancy can be prevalent and persist beyond the limits predicted by simple scaling arguments.

A significant finding of our investigations is that the premixed flame configuration is an important experimental parameter that controls which buoyancy phenomenon can be observed. For example, buoyancy driven flame flickering frequency is a distinctive and stable property of both laminar and turbulent conical flames. These frequencies can be correlated for a broad range of conditions including enhanced gravitational forces and sub-atmospheric pressures [1]. However, conical flames are not ideal for investigating buoyancy effects on the flowfield.

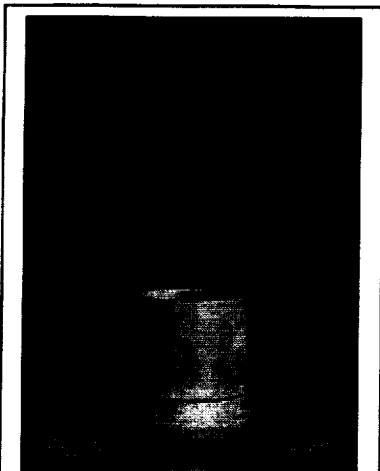


Figure 1 "Funnel" flame stabilized by a bluff body

Because of the divergent nature of the flow in the products counteracting buoyancy-induced acceleration, changes in the flowfields are not easily detectable. This is not the case for rod-stabilized v-flames. The products region is convergent and the presence (+1g) and absence (μ g) of flow acceleration in the products show the influence of buoyancy. However, the coupling of the v-flames' plumes with the surrounding atmosphere is quite complex. Due to the flame edge effects that originate at the ends of the stabilizer rod, the flame flickering frequencies are not consistent and do correlate well with flow and mixture parameters. Velocity profiles made above the stabilizer rod also indicate the existence of a slight inflow due to an entrainment effect associated with the accelerating products. Therefore, the v-flame configuration is not ideal for our microgravity studies despite the large body of experimental and theoretical work available in the scientific literature.

For our flight experiments, we have chosen to use an inverted conical flame configuration that we called a "funnel" flame. This flame is stabilized by a small bluff body placed at the center of a premixed flow of fuel and air. The small recirculation zone generated in the wake of the bluff-body provides the flame anchoring mechanism. This flowfield is axisymmetric and has most of the attributes of the v-flame, i.e. an inclined flame brush with products converging to the centerline.

Bluff-body stabilized flames in 1g

Despite the fact that there have been many studies of bluff body stabilized flames, a majority of them focuses on investigating the wake effects of large bluff-bodies. As our goal is to use the bluff body for flame attachment, the wake effects need to be de-emphasized by employing small bluff bodies. For our 25mm diameter burner, we constructed a 45° steel cone of 6.5 mm diameter. It was attached to a steel support rod centered at the burner nozzle. To infer the effects of buoyancy on the flames' flowfields, we used two component LDV to investigate +1g and -1g flames.

Figure 2 compares the centerline velocity profiles obtained for laminar +1g and -1g "funnel" flames and V-flames with Reynolds number $Re = 1880$ and equivalence ratio, ϕ of 0.7. For the +1g flames, both configurations has similar characteristics with the velocity

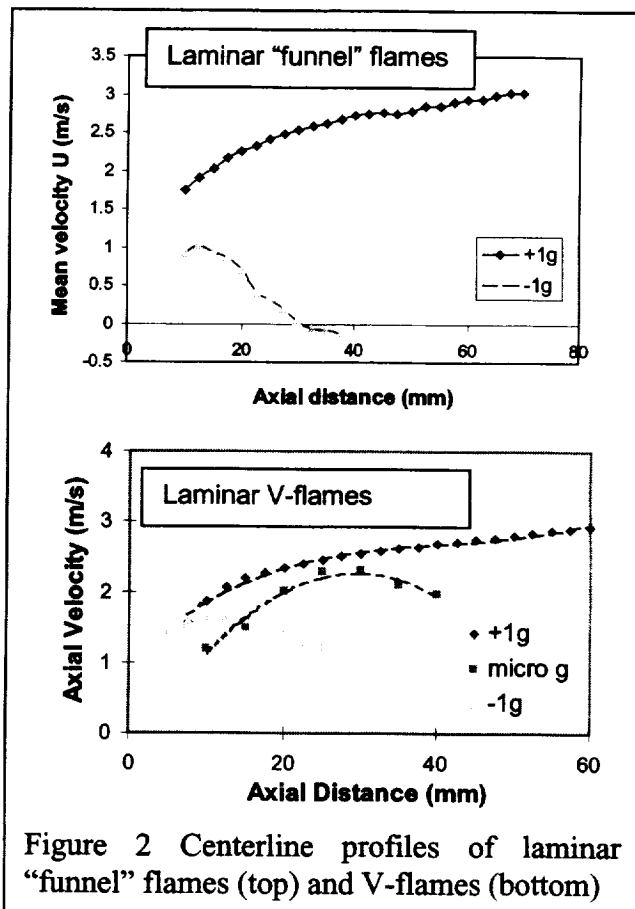


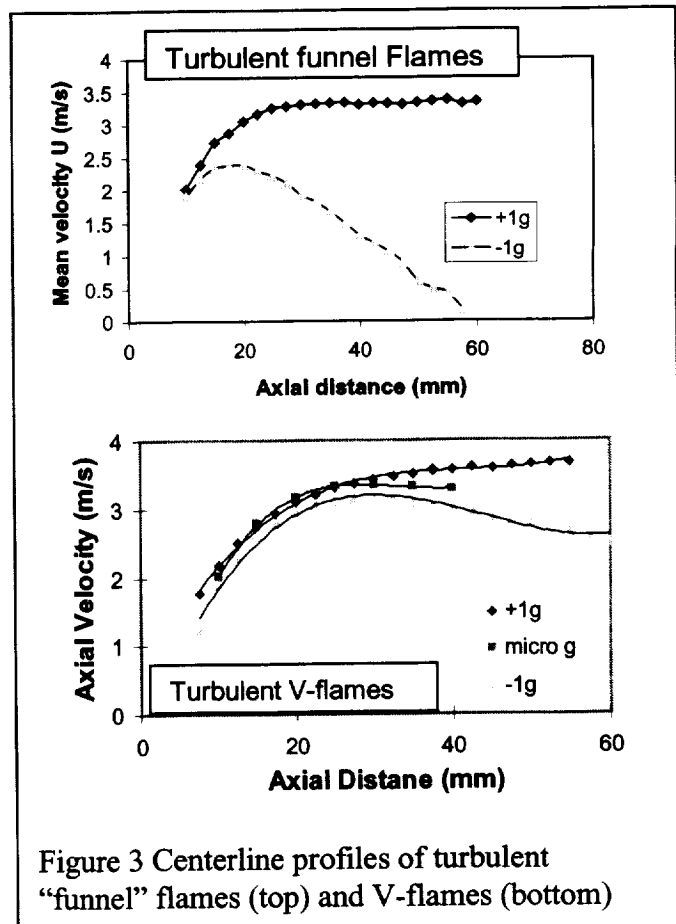
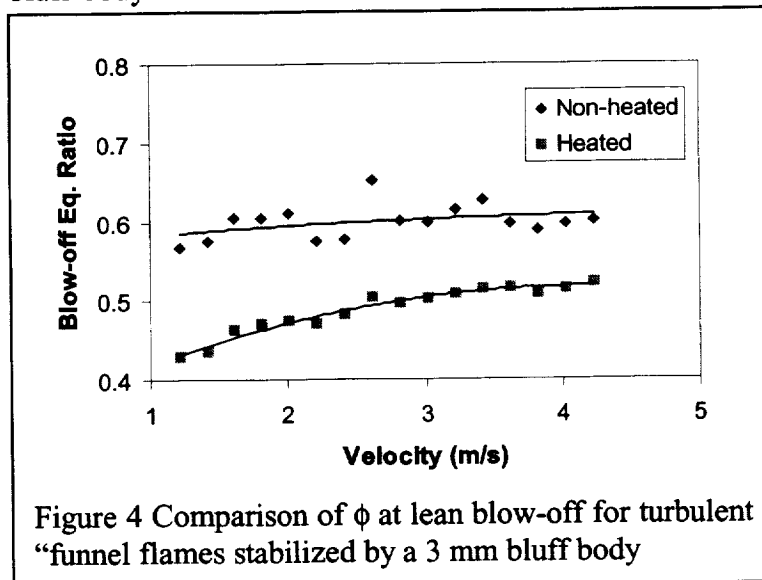
Figure 2 Centerline profiles of laminar "funnel" flames (top) and V-flames (bottom)

increasing rapid for $x < 20$ mm then leveling off to a more gradual acceleration. Differences shown by the $-g$ flames are more drastic. At $x > 30$ mm, the “funnel” flame has a stagnation point with a slight flow reversal forming further downstream.

Centerline profiles measured in turbulent “funnel” flames and v-flames of $Re = 2500$ and $\phi = 0.75$ are compared in Figure 3. It is clear that the deviations between the $+1g$ and $-1g$ “funnel” flame profiles occur much farther upstream and are more substantial. These results indicate that under identical flow conditions, buoyancy has a stronger effect on the flowfields of “funnel” flames than on those of v-flames. Therefore, “funnel” flames should be a more suitable configuration for characterizing field effects of buoyancy.

Flight experiments

To design a flight experiment, one of the most important issues is whether or not our experiment can be scaled down to the flow and energy release requirements of the Combustion Integrated Rig (CIR) while preserving its integrity in terms of allowing the flame to interact with turbulence without extrinsic impediments. Using constant velocity scaling law and the integral turbulence length scale (3mm) as a criterion, the optimum burner diameter is established to be 18mm. To maximize the residence time for flame/turbulence interaction, the bluff-body stabilizer is reduced to 3 mm. As this stabilizer is the same size as the turbulence



scale, concerns exist on how stable the flames would be. To ensure that the flame remains robust after ignition, engineers at NASA Glenn Research Center designed a ceramic conical bluff body that can be electrically heated. Figure 4 compares the lean-blow off ϕ for this stabilizer with and without heating. As can be seen, with a heated bluff-body, the lean blow-off ϕ is lowered to about 0.5 close to the flammability limits of laminar flames.

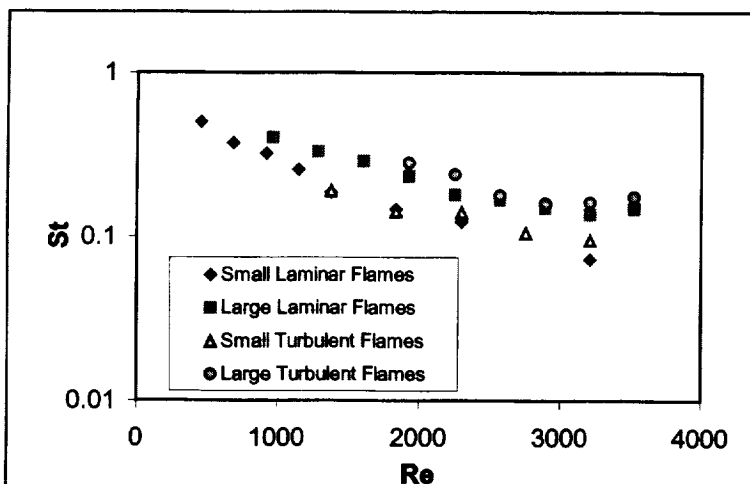


Figure 5 Comparison Strouhal number, St , based on flickering frequencies of funnel flames ($0.75 < \phi < 0.8$)

Figure 5 compares the Strouhal numbers, St , obtained from flickering frequencies of laminar and turbulent “funnel” flames in a 18mm and a 25mm burner. Unlike the conical flames where St increases with Re , St is a decreasing function of Re for funnel flames. None the less, the fact that the results are independent of turbulence level shows them to be consistent properties of flame buoyancy coupling. Comparison of St with and without CIR chamber will allow a first estimate on whether or not the enclosure effects would be significant.

Particle Image Velocimetry (PIV)

We also investigated the feasibility of using PIV to measure the flowfield of microgravity flames. An example of the 1g data is shown in Figure 6. The results are very encouraging and the velocity contours clearly show the converging plume at $x > 15$ mm. Comparison of these features with those measured in μg would be very useful to quantify the contributions of buoyancy to different flame flowfield regions.

ACKNOWLEDGEMENT

This work is supported by NASA Microgravity Combustion Science through the U. S. Department of Energy Contract No. DE-AC03-76F00098.

REFERENCES

- [1] Kostuik, L. W. and Cheng, R. K., *Combustion and Flame*, 103, 27-40 (1995)
- [1] Bédard, B. and Cheng, R. K., *Combustion and Flame*, 107, 13-26 (1996).
- [2] Cheng, R. K., Bédard, B., Kostuik, L. W. *Combustion and Flame*, 116 (1999).

CIR Chamber Effects

To date, all our microgravity flames are not enclosed. To investigate if there would be effects associated with enclosing these flames in the CIR chamber, we plan a 1g flame study in a CIR Chamber Simulator. Our first experiment will be to measure flame flickering frequency. This parameter encapsulates the overall field effects of buoyancy because our study of flame flickering frequencies in conical flames shows it to be sensitive to both upstream and downstream boundary conditions [1].

Figure 5 compares the Strouhal

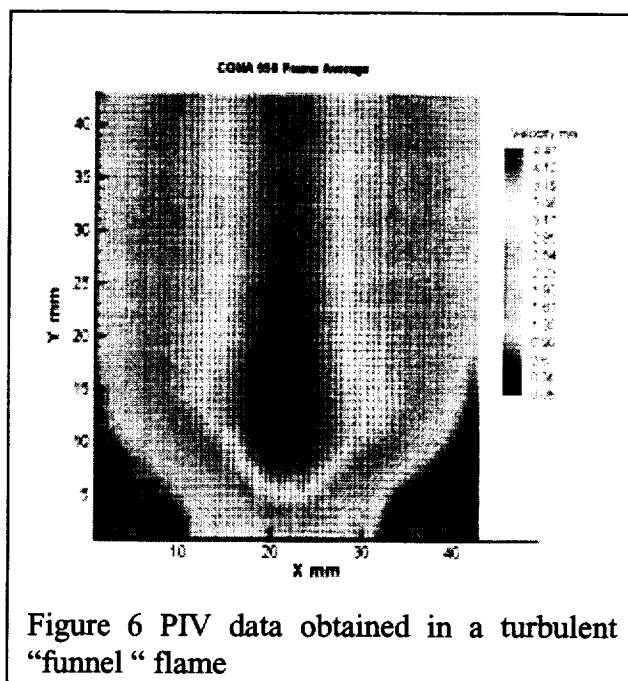


Figure 6 PIV data obtained in a turbulent “funnel” flame

Flame-Vortex Interactions Imaged in Microgravity - To Assess the Theory of Flame Stretch

James F. Driscoll, University of Michigan

(COTR: Douglas A. Feikema, NASA Glenn)

Ph.D. candidate: Alfonso Ibarreta, Univ. of Michigan

NASA Contract NCC3 - 656

Abstract. The goals of this research are to:

1. Assess the Theory of Flame Stretch by operating a unique flame-vortex experiment under microgravity conditions in the NASA Glenn 2.2 Second Drop Tower (drops to identify operating conditions have been completed);
2. Obtain high speed shadowgraph images (500-1000 frames/s) using the drop rig (images were obtained at one-g, and the NASA Kodak RO camera is being mounted on the drop rig);
3. Obtain shadowgraph and PIV images at 1-g while varying the effects of buoyancy by controlling the Froude number (completed);
4. Numerically model the inwardly-propagating spherical flame that is observed in the experiment using full chemistry and the RUN 1DL code (completed);
5. Send images of the flame shape to Dr. G. Patniak at NRL who is numerically simulating the entire flame-vortex interaction of the present experiment (data transfer completed); and
6. Assess the feasibility of obtaining PIV velocity field images in the drop rig, which would be useful (but not required) for our assessment of the Theory of Flame Stretch (PIV images were obtained at one-g using same low laser power that is available from fiber optic cable in drop tower).

The motivation for the work is to obtain novel measurement needed to develop a physically accurate model of turbulent combustion that can help in the control of engine pollutants. The unique experiment allows, for the first time, the detailed study of a negatively-curved (negatively stretched) flame, which is one of the five fundamental types of premixed flames. While there have been studies of flat flames, positively-curved (outwardly-propagating) cases and positively-strained (counterflow) cases, this is the first detailed study of a negatively-curved (inwardly-propagating) flame.

The first set of drops in the 2.2 Second Drop Tower showed that microgravity provides more favorable conditions for achieving inwardly-propagating flames (IPFs) than 1-g. A vortex interacts with a flame and creates a spherical pocket, which burns inwardly.. Shadowgraphs at 1000 frames/sec quantify the Markstein number and flame speed. A Low-Laser Power PIV System was developed and is being added to the drop package.

Numerical computations were required to explain why the Markstein numbers measured for the inwardly-propagating flames differ from those of outward propagating flames; this is an important research issue in the assessment of the Theory of Flame Stretch. The RUN-

1DL code (developed by Prof. B. Rogg) was run for IPF and OPFs with complex methane and propane chemistry. Results confirmed that Ma for the IPFs are larger than for OPFs as was observed experimentally. Physical reasons for these new findings about the Theory of Flame Stretch are being determined from the experiments and the computations.

Several journal papers have been published; the drop package is described in the AIAA Journal [1], while the one-g results appear in three other journal papers [2-4].

Experimental Apparatus and Results:

Figure 1 shows the University of Michigan Microgravity Flame-Vortex Drop Rig. A chamber is filled with a lean mixture (either propane-air or methane-air). Two electrodes ignite a flame kernel that becomes a flat flame. Pulsing a loudspeaker creates a laminar toroidal vortex ring that moves upward and interacts with the flame. For the proper conditions, the interaction creates a pocket of unburned reactants that is surrounded by an inward-propagating spherical flame. Figure 2 shows images of the spherical flame in the microgravity environment during drop tests. The third image on the left side of Fig. 2 shows that a spherical pocket has been formed. The bottom two images on the right side of Fig. 2 shows how a pocket is first forming and then how it burns out. The pocket is typically 5 mm in diameter initially. The propagation flame is dR/dt , where R is the radius of the pocket determined from shadowgraphs. The stretch rate is $(2/R) dR/dt$ and also is determined from shadowgraphs. The Theory of Flame Stretch predicts that propagation speed S_L and the nondimensional stretch rate Ka are related by :

$$S_L/S_{L0} = (1 + Ma \ Ka)^{-1} \quad (1)$$

Ma is the Markstein number. Faeth [5] and Law [6] have determined Ma for outward-propagating flames, but our experiments [2] have shown that Ma of IPFs are 2-3 times larger than for OPFs, as seen in Fig. 3. Microgravity conditions on the drop rig provide a larger range of conditions for which spherical flames can be produced, so that values of Ma can be obtained using Eq. 1 for a wider range of fuel types and equivalence ratios than at one-g. Computations using RUN 1DL [7] were run in this study and they confirm our measurements; Fig. 4 shows that Ma is larger for an IPF than for an OPF. The physical reason for our findings is being determined from the experiments and the computations.

1. Sinibaldi, J.O., Mueller, C.J., Tulkki, A. and Driscoll, J.F., "Suppression of Flame Wrinkling by Buoyancy - the Baroclinic Stabilization Mechanism", *AIAA Journal* Vol. 36, p. 1432-1438, 1998.
2. Ibaretta, A. F., and Driscoll, J.F., "Measured Burning Velocities of Stretched Inwardly-Propagating Premixed Flames", *Proc. of the Combustion Inst.*, Vol 28, 2000.
3. Sinibaldi, J.O., Mueller, C. J., and Driscoll, J. F., "Local Flame Propagation Speeds Along Wrinkled Stretched Premixed Flames", *Proc. of Comb Inst.*, 27, 1998, 827.
4. Mueller, C., Driscoll, J. F., Reuss, D. and Drake, M., *Comb. Flame*: 112, 342 (1998).
5. Tseng, L., Ismail, M., and Faeth, G.M., *Comb. Flame* 95:410-426 (1993).
6. Sun, C., Sung, C. He, L., and Law, C.K., *Comb. Flame* 118: 108-128 (1999).
7. Rogg, B. *Reduced Kinetics Mechanisms*, Peters, N. and Rogg, B., (Eds), Springer-Verlag, Berlin, 1993.

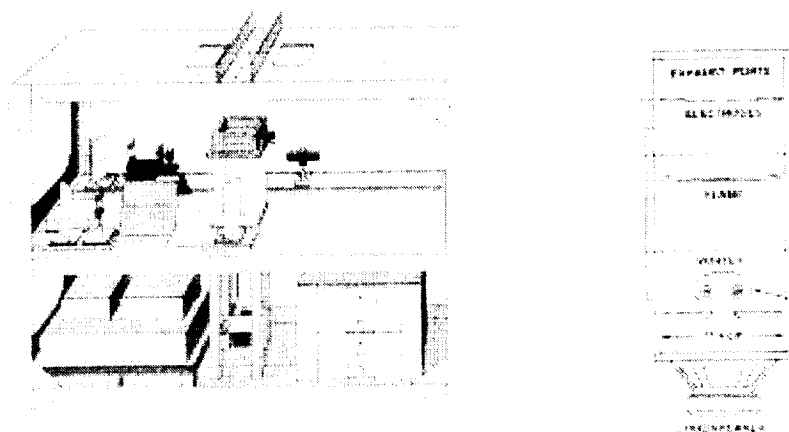


Figure 1. Schematics of the University of Michigan Premixed Flame-Vortex Interaction Drop Rig and the Combustion Chamber

Top Shelf: Pulsed Xenon Shadowgraph White Light Source, Shadowgraph optics, NASA Glenn Kodak RO High Speed Video Camera, Sony low-speed Video Camera. Bottom Shelf: Light source power supply, batteries, power distribution box, Tattletale computer, video optical cable transmitter, solenoids for flame-vortex experiment.

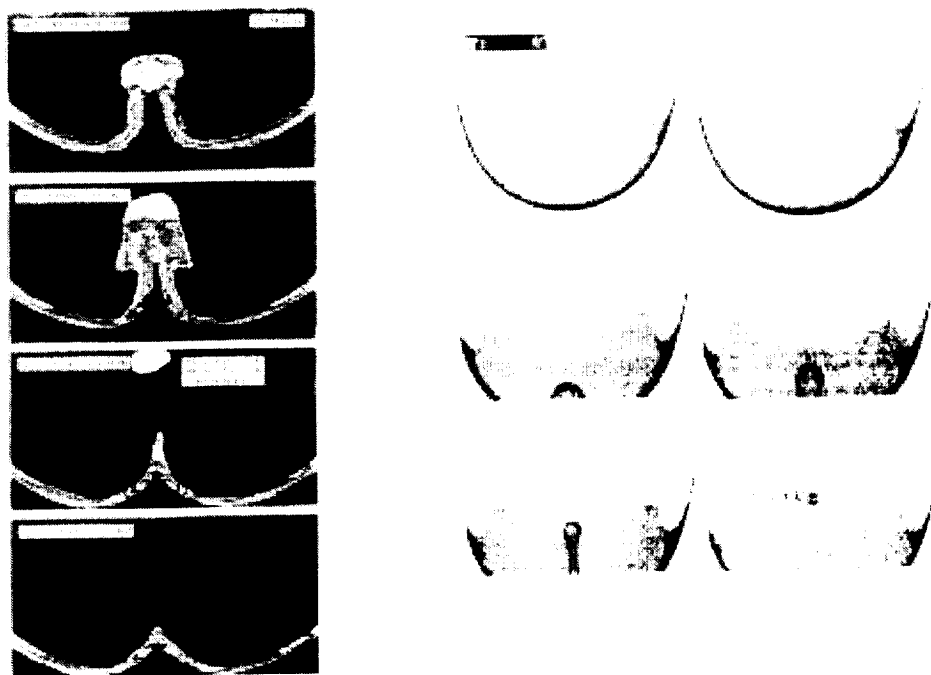


Figure 2. Video Images Obtained During Microgravity Drops - of a Vortex Creating a Pocket of Reactants Surrounded by an Inwardly-Propagating Spherical Flame

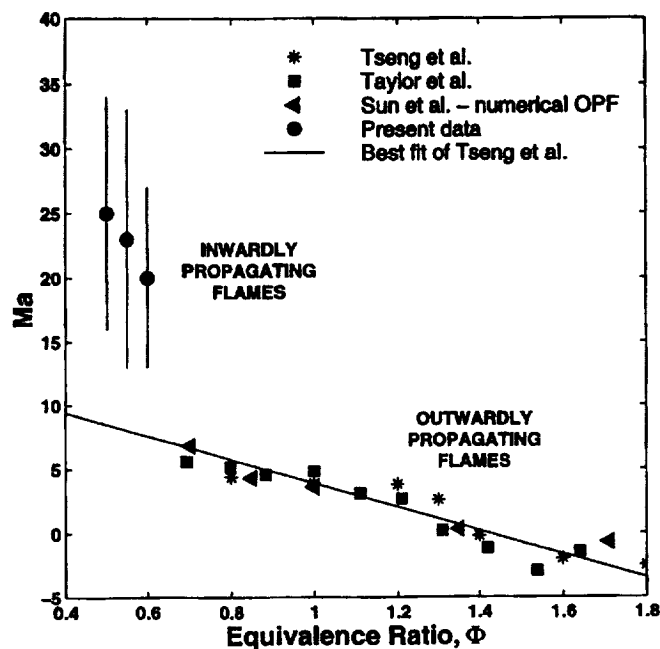


Figure 3. Measured Markstein Numbers of the Inward Propagating Flame in the Flame-Vortex Interaction Drop Rig at One-g [2]. Only a limited range of equivalence ratios create spherical flames at one-g; microgravity conditions provide a wider range of test conditions.

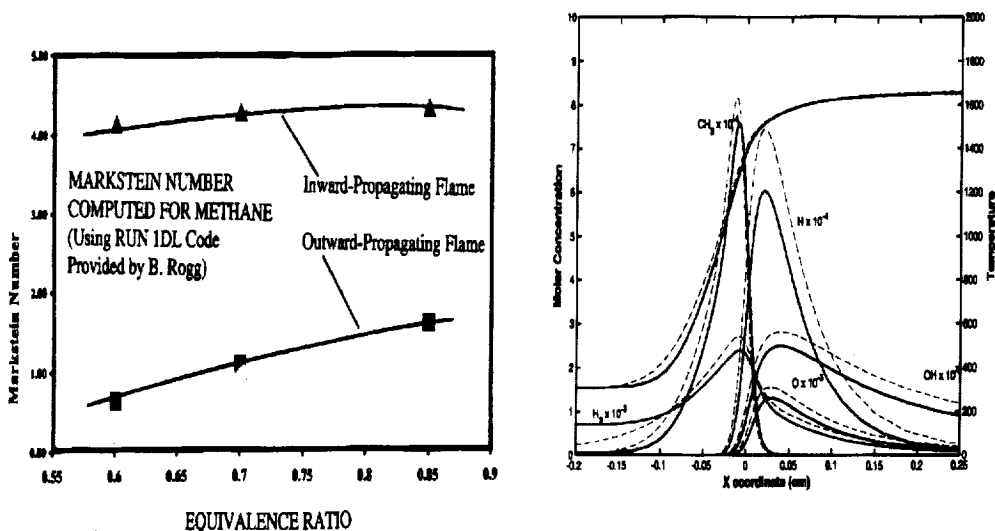


Figure 4. Computations Using Full Methane-Air Chemistry of the Inward-Propagating Flame Observed in the Experiment. RUN 1DL Code was used and conditions were set equal to our experimental operating conditions. Computations explain our significant experimental finding that Markstein number of inward-propagating flames is larger than that of outward-propagating flames.

CHARACTERISTICS OF NON-PREMIXED TURBULENT FLAMES IN MICROGRAVITY

U. Hegde and Z. G. Yuan, National Center for Microgravity Research, Cleveland, OH

D. P. Stocker, NASA John H. Glenn Research Center, Cleveland, OH

M. Y. Bahadori, Science and Technology Development Corp., Los Angeles, CA

INTRODUCTION

This project is concerned with the characteristics of turbulent hydrocarbon (primarily propane) gas-jet diffusion flames in microgravity. A microgravity environment provides the opportunity to study the structure of turbulent diffusion flames under momentum-dominated conditions (large Froude number) at moderate Reynolds number which is a combination not achievable in normal gravity. This paper summarizes progress made since the last workshop¹. Primarily, the features of flame radiation from microgravity turbulent jet diffusion flames in a reduced gravity environment are described. Tests were conducted for non-premixed, nitrogen-diluted propane flames burning in quiescent air in the NASA Glenn 5.18 Second Zero Gravity Facility. Measured flame radiation from wedge-shaped, axial slices of the flame are compared for microgravity and normal gravity flames. Results from numerical computations of the flame using a k- ϵ model for the turbulence are also presented to show the effects of flame radiation on the thermal field.

Flame radiation is an important quantity that is impacted by buoyancy as has been shown in previous studies by the authors² and also by Urban et al³. It was found that jet diffusion flames burning under microgravity conditions have significantly higher radiative loss (about five to seven times higher) compared to their normal gravity counterparts because of larger flame size in microgravity and larger convective heat loss fraction from the flame in normal gravity. These studies, however, were confined to laminar flames. For the case of turbulent flames, the flame radiation is a function of time and both the time-averaged and time-dependent components are of interest. In this paper, attention is focused primarily on the time-averaged level of the radiation but the turbulent structure of the flame is also assessed from considerations of the radiation power spectra.

APPROACH

Fuel-nitrogen mixtures are injected into quiescent air through a nozzle (i.d. of 1.65 mm) made of stainless steel tubing. A mixture of 60% propane-40% nitrogen was used. For the results presented here, injection Reynolds number was about 3000. Side views of the flame are imaged by means of video cameras at 30 frames per second. The radiometer assembly utilized for the flame radiation measurements is shown in Fig. 1. It consists of a thermopile radiometer and an optical assembly consisting of a biconvex lens, a plano-cylindrical lens, and a narrow bandpass filter. The filter is centered at 1870 nm which corresponds to a water vapor band. The restriction to the narrow bandpass wavelength range enables the limited field of view desired. This design in conjunction with the placement distance of the radiometer assembly from the nozzle centerline (see Fig. 1) results in a field of view which has an axial extent of approximately 6 mm at the flame centerline. The axial location of the radiometer assembly was varied to obtain the axial distribution of the flame radiation signal. A 16-bit data acquisition system is utilized to record the radiometer signal at sampling rates up to 2000 Hz.

The numerical model utilizes standard turbulent models in conjunction with state relationships for chemistry for predicting the time-averaged flow field. A single step chemical reaction between fuel and oxidizer is assumed. The model solves for pressure, velocity,

temperatures, species concentrations, and turbulent kinetic energy and dissipation rate. The code utilizes a discrete transfer radiation model⁴ for CO₂ and H₂O emissions for radiative transport. This is a grey gas model where the predicted intensity is an integrated intensity over all wavelengths. With this model, the equation for the radiant intensity, dI , along a path ds is

$$dI/ds = \alpha I + \beta \sigma T^4/\pi$$

where α is the net absorption and scattering coefficient, β is the emission coefficient, T is the local temperature, and σ is Boltzmann's constant. In the present computations, the emission and absorption coefficients are assumed equal at each point in the flow field and scattering in the gas is neglected. The absorption coefficient is a function of the local concentrations of carbon dioxide and water vapor. The above equation must be integrated for a number of rays emanating from a point in the flow field so that the hemispherical solid angle about that point is covered by the rays.

RESULTS AND DISCUSSION

A typical radiation signal obtained in the drop test for the microgravity flame is shown in Fig. 2 for the final two seconds of the drop. For this test, the axial location of the radiometer was at a x/d of approximately 150. The radiation signal exhibits a fluctuating behavior consistent with the turbulent nature of the flame. A mean level of the radiation may be obtained during this time frame, but due to the limited time duration of the test, it is not clear whether the signal has achieved a statistically stationary state.

Figure 3 plots the mean measured radiation signal for different axial locations, x/L , of the radiometer. The results for both the microgravity flame and the corresponding normal gravity flame are shown. It is seen that for the normal gravity flame, the radiation signal increases with axial distance up to approximately the flame tip before beginning to decay. For the microgravity flame, however, the mean radiation signal peaks upstream of the flame tip before decaying. Since radiation is proportional to the fourth power of temperature, the above finding suggests that flame temperatures near the tip for the microgravity flame are reduced compared to the normal gravity case. This is confirmed by the numerical computations as shown in Fig. 4 which plots computed flame centerline temperatures as a function of the distance from the nozzle tip, non-dimensionalized in the same manner as for Fig. 3.

The numerical computations also show that the axial velocity profile for the normal and microgravity flames begin to differ significantly within thirty nozzle diameters axially from the nozzle tip for the flow conditions studied here. This corresponds to roughly 20% of the normal gravity flame height. The effects of buoyant acceleration in the velocity field (for example, higher velocity and velocity gradient) are clearly evident at further downstream locations. This is shown in Fig. 5 which plots the computed radial profile of the axial velocity (non-dimensionalized with respect to the injection velocity) for both normal gravity and microgravity cases at an axial location corresponding to the mean normal-gravity flame height.

Figures 4 and 5 indicate that in normal gravity, a larger fraction of the heat release is lost by convection. This follows by noting that the flame heat release, Q , can be related to the heat lost by convection downstream of the flame, Q_c , and the radiative heat loss, Q_r , as

$$Q = Q_c + Q_r$$

where, for simplicity, conduction is assumed to be negligible compared to the radiative and convective losses. The axial convection of enthalpy downstream of the flame is proportional to the product of velocity and temperature at the flame tip which from Figs. 4 and 5 is greater for

the normal gravity case. Consequently, radiative transfer becomes more dominant in the absence of buoyancy.

The microgravity flame radiation power spectra for three locations, $x/d = 30, 120$ and 180 , respectively are shown in Fig. 6. At the lowest location, the spectral magnitude levels are the smallest of the three. Further downstream, at $x/d = 120$ (in the region where the time-averaged radiation levels reaches a maximum), the magnitude of the spectra increases over the entire frequency range of interest. This indicates an increase in the magnitude of the turbulent fluctuations. However, further downstream, at $x/d = 180$, while the lower frequency components (up to 30 Hz, approximately) are of similar magnitude compared to those at $x/d = 120$, the higher frequency components are of smaller magnitude. This result is consistent with computations that indicate that the axial velocity near the flame tip of the microgravity flame is only a few percent of the injection velocity i.e., an order of magnitude lower. Hence, the local Reynolds number based upon the local centerline velocity is also expected to decay significantly. Furthermore, if it is assumed that the local turbulent velocity magnitude scales with the local centerline velocity, and that the local integral length scales with the local flame width which is relatively invariant over the flame length, then it is clear that the local turbulent Reynolds number, Re_T , also decays. The smallest scale of turbulence, that is, the dissipation length scale, varies as $Re_T^{-0.75}$ [e.g. Tennekes and Lumley⁵] indicating that the size of the smallest scales increases with increasing distance along the flame (since Re_T decreases). This is also consistent with turbulence dissipation behavior. The turbulence dissipation is of order u'/l where u' is the turbulent velocity fluctuation magnitude and l is the integral length scale [e.g., Spalding⁶]. This is a measure of the highest frequencies (i.e., the smallest scales) in the turbulent spectrum. The integral length scale is expected to be relatively invariant over the flame length whereas u' will scale with the mean velocity which decreases axially. Thus, u'/l is expected to decrease downstream indicating a decrease in the highest frequencies and an increase in the size of the smallest scales.

The normal gravity flame radiation power spectra for three locations, $x/d = 30, 90$, and 120 , respectively are shown in Fig. 7. At the lowest location, there is a strong peak at a frequency of approximately 14 Hz which may be related to the flame flicker observed at lower Reynolds numbers. Further downstream (e.g., $x/d = 90$), the spectra broaden out, and the spectral levels are higher at all of the frequencies. At $x/d = 120$, which is near the observed flame tip, the overall fluctuation amplitudes are larger and the frequency range of the turbulence is not reduced.

ACKNOWLEDGEMENT

This work was supported by NASA under cooperative agreement NCC3-544 and contract NAS3-98032. The assistance of Mr. Dennis Thompson, Zero-G Facility manager at NASA Glenn Research Center, in the conduct of the tests is greatly appreciated. Jonathan Sakai of the University of Dayton assisted with the numerical code computations during internships at NASA Glenn and NCMR.

REFERENCES

1. Hegde, U., Yuan, Z. G., Stocker, D. P., and Bahadori, M. Y. [1999] Characteristics of Non-Premixed Turbulent Flames in Microgravity, Fifth International Microgravity Combustion Workshop, Cleveland, OH.
2. Bahadori, M. Y., Stocker, D. P., Vaughan, D. F., Zhou, L., and Edelman, R. B. [1993] in Modern Developments in Energy, Combustion, and Spectroscopy (Williams, F. A., Oppenheim, A. K., Olfe, D. B., and Lapp, M., Eds.), Pergamon Press, Oxford, pp. 49-66.
3. Urban, D. L., Yuan, Z. G., Sunderland, P. B., Linteris, G. T., Voss, J. E., Lin, K. C., Dai, Z., Sun, K., and Faeth, G. M. [1998] *AIChE J.*, vol. 36, pp. 1346-1360.
4. Siegel, R., and Howell, J. [1981] *Thermal Radiation Heat Transfer*, Second Edition, McGraw-Hill.
5. Tennekes, H. and Lumley, J. L. (1977). *A First Course in Turbulence*. Fourth Printing, The MIT Press, Cambridge, Massachusetts.
6. Spalding, D. B. (1971) *Chem. Eng. Sci.*, vol. 26, pp. 95-114.



Fig 1 Narrow-view radiometer assembly

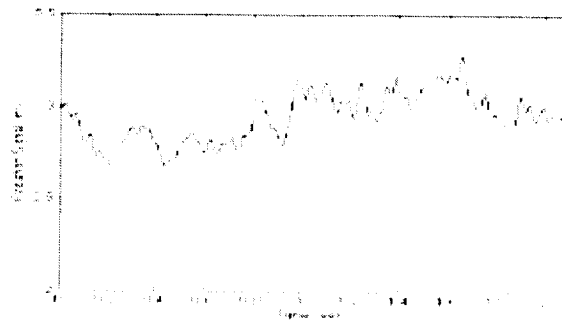


Fig 2 Typical measured radiometer signal during the final 2 seconds of the drop test

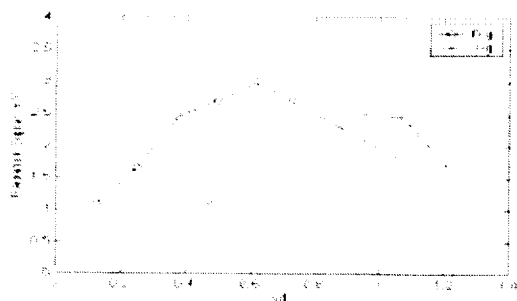


Fig 3 Measured radiation signal as a function of non-dimensional axial location

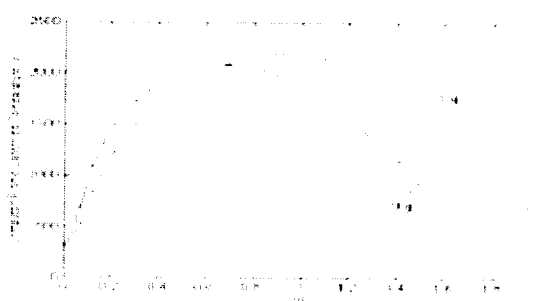


Fig 4 Computed centerline temperature distribution



Fig 5 Computed radial profile of axial velocity at an axial location corresponding to the normal gravity flame tip

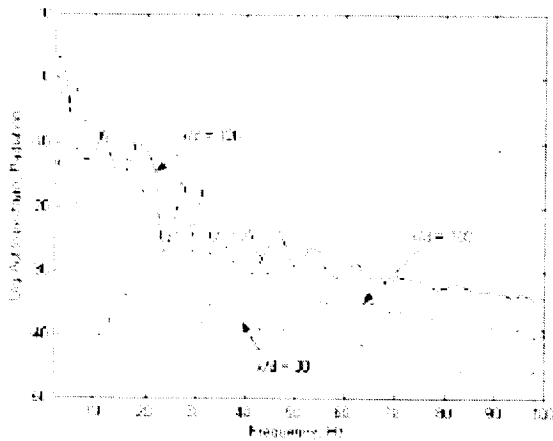


Fig 6 Measured log autospectra of microgravity flame radiation

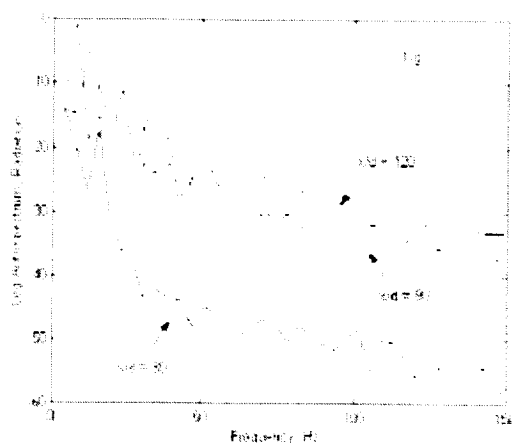


Fig 7 Measured log autospectra of normal gravity flame radiation

LARGE-SCALE FLOW STRUCTURE IN TURBULENT NONPREMIXED FLAMES UNDER NORMAL- AND LOW-GRAVITY CONDITIONS

N. T. Clemens, C. A. Idicheria and I. G. Boxx

Department of Aerospace Engineering & Engineering Mechanics, The University of Texas at Austin, Austin, TX 78712-1085

INTRODUCTION

It is well known that buoyancy has a major influence on the flow structure of turbulent nonpremixed jet flames. Buoyancy acts by inducing baroclinic torques, which generate large-scale vortical structures that can significantly modify the flow field. Furthermore, some suggest that buoyancy can substantially influence the large-scale structure of even nominally momentum-dominated flames, since the low velocity flow outside of the flame will be more susceptible to buoyancy effects.¹ Even subtle buoyancy effects may be important because changes in the large-scale structure affects the local entrainment and fluctuating strain rate, and hence the structure of the flame. Previous studies that have compared the structure of normal- and micro-gravity nonpremixed jet flames note that flames in microgravity are longer and wider than in normal-gravity.²⁻⁵ This trend was observed for jet flames ranging from laminar to turbulent regimes. Furthermore, imaging of the flames has shown possible evidence of helical instabilities and disturbances starting from the base of the flame in microgravity. In contrast, these characteristics were not observed in normal-gravity.

The objective of the present study is to further advance our knowledge of the effects of weak levels of buoyancy on the structure of transitional and turbulent nonpremixed jet flames. In later studies we will utilize the drop tower facilities at NASA Glenn Research Center (GRC), but the preliminary work described in this paper was conducted using the 1.25-second drop tower located at the University of Texas at Austin. A more detailed description of these experiments can be found in Idicheria *et al.*⁶

EXPERIMENTAL APPARATUS/CONDITIONS

The experiments were conducted using a newly constructed jet flame drop-rig (Fig. 1) that is housed in a standard GRC 2.2 second droptower frame (38"x36"x16"). Piloted ethylene jet flames were studied, which issued from a 1.75 mm straight tube into quiescent air within the drop box. A premixed methane-air pilot flame was used to ignite the flame and to further forestall flame liftoff. The ethylene and methane were stored in two onboard, 18.3 in³ stainless steel pressure vessels. Flow rates were controlled with line pressure regulators upstream of choked micro-metering valves. Line pressures were recorded using pressure transducers installed upstream of the micro-metering valves and read into the onboard computer. Solenoid valves, connected via solid-state relays to the digital I/O card of an onboard computer, were used to start and stop the flow. The onboard computer was a ruggedized Pentium Celeron based PC equipped with frame grabber and data acquisition cards. Flame luminosity was imaged using a progressive scan CCD camera (Pulnix TM-6710) operated at a resolution of 512x145 pixel² and 350 frames per second.

The preliminary data reported here were obtained with the 1.25-second drop tower at the University of Texas at Austin. The tower is 35 ft tall, with an 8 ft x 8 ft cross-section and provides a drop distance of 25 ft. The box is decelerated by falling into a 6 ft x 4 ft x 7 ft container filled with polyurethane foam cubes. Accelerometer data taken during the drops show

that low-gravity levels of 10-30 *mg* can be achieved. These relatively high *g*-levels result from the fact that no drag shield was used. The deceleration levels at impact were about 25*g*.

Jet flames at a range of Reynolds numbers were studied as shown in Table 1. The Reynolds number ($Re_D = U_0 D / \nu$) is based on the jet exit diameter *D*, jet exit velocity U_0 and the kinematic viscosity of ethylene at room temperature. Also shown in Table 1 is the parameter ξ_L , which was used by Becker and Yamazaki⁷ to quantify the effect of buoyancy on the mean entrainment of turbulent jet flames. This buoyancy parameter is defined as $\xi_L = Ri_s^{1/3} L_f / D_s$, where Ri_s is the source Richardson number ($Ri_s = g D_s / U_s^2$) based on the source diameter $D_s = D(\rho_0 / \rho_\infty)^{1/2}$, and source velocity $U_s = U_0$ for a top-hat velocity profile. L_f is the average visible flame length, *g* is the acceleration due to gravity, ρ_0 is the jet fluid density and ρ_∞ is the ambient density. Becker and Yamazaki⁸ suggest that flames with $\xi_L < 1$ are momentum dominated. Interestingly, this table shows that even under our milli-*g* conditions, the lower Reynolds number flames may exhibit some buoyancy effects.

Table 1. Flow conditions.					
Case	Fuel	U_0 (m/s)	Re_D	ξ_L (1 <i>g</i>)	ξ_L (20 <i>mg</i>)
1	Ethylene	12.4	2,500	8.5	2.4
2	Ethylene	24.8	5,000	6.6	1.5
3	Ethylene	37.2	7,500	4.6	1.3
4	Ethylene	52.2	10,500	3.7	1.0

RESULTS AND DISCUSSION

Figure 2 shows sample image sequences of the flame startup for low- and normal-gravity conditions at an exit Reynolds number of 7500. The jet was started only after the drop was initiated. The time to reach steady state was investigated quantitatively by analyzing the instantaneous flame tip location as a function of time. Figure 3 shows the flame length variation with time (as obtained from individual frames) for different Reynolds numbers. From these plots it is clearer that the low-gravity flame takes a longer time to reach steady state. Even in the low Reynolds number cases (2500 and 5000), the difference is only about 200 *ms*. At the higher Reynolds numbers, the startup transient is nearly the same for normal- and low-*g*, as the difference is about 100 *ms*. Also, in all cases the flame is seen to reach a steady state in less than 300 *ms*.

Figure 4 shows sample steady state sequences for a Reynolds number of 7500. The low-gravity sequence shows what appears to be evidence of a helical large-scale instability in agreement with Ref. 3, but a similar structure is not seen at 1*g*. The steady state sequences were used to compute mean emission images, as shown in Fig. 5, and from these the mean visible flame length (L_f) was measured. In all of the cases studied, there is little difference in the average visible flame lengths measured under normal- and low-gravity conditions, as shown in Figure 6. The maximum difference was of about 10% of the flame height at $Re_D = 5,000$. Any differences in length and width between flames in normal- and low-gravity conditions are seen to diminish as the flame becomes more momentum dominated.

We also investigated the evolution of the large-scale structures in the flames using volume rendering of image sequences. This technique, discussed by Mungal *et al.*⁸, gives good visual information on the structure evolution. In this technique a sequence of two-dimensional images (*x-y*) is stacked one behind the other along the *z*-axis (time, *t*) and a three dimensional volume (*x-y-t*) is generated. The surface of this 3-D model is an isocontour corresponding to the visible flame edge in each image. Volume rendering highlights features that are not immediately

apparent in the still images or movie sequences. Sample renderings at $Re_D=2500$ are shown in Figure 7. In these images, convection of large-scale structures appears as wrinkles traveling up and to the right on the surface of the volume. The slope of these wrinkles can be used as a qualitative estimate of the large-scale structure convection velocity. It can be seen that the flame tip in low-gravity (figure 7a) fluctuates at a lower frequency than in normal-gravity (figure 7b); however, in the higher Reynolds number case (figures not presented due to lack of space) we observed that the flame tip oscillations and large-scale structure convection velocities become comparable. All of these observations show the decreasing effect buoyancy has on flame characteristics and behavior, as ξ_L decreases.

FUTURE WORK

Our future work will be directed at investigating these observations further by utilizing the 2.2 second drop-tower at NASA GRC, which will provide us with purely momentum dominated flames in lower Reynolds numbers. We are also currently working on implementing laser-based diagnostics including Mie scattering and particle image velocimetry to further investigate the large-scale structures and strain-vorticity fields.

ACKNOWLEDGEMENTS

This work is supported by NASA under cooperative agreement NCC3-677. The authors also wish to thank Dr. Z. G. Yuan of NCMR and Andrew Jenkins of NASA Glenn for their invaluable input into the design and fabrication of the drop-rig.

REFERENCES

1. Roquemore, W.M., Chen, L.D., Goss, L.P. and Lynn, W.F., Lecture notes in Engineering Vol. 40, Springer-Verlag, pp. 49-63 (1989).
2. Bahadori, M.Y., Stocker, D.P., Vaughan, D.F., Zhou, L. and Edelman, R.B., Modern Developments in Energy, Combustion and Spectroscopy, Pergamon Press, pp. 49-66.
3. Hegde, U., Yuan, Z.G., Stocker, D.P. and Bahadori, M.Y., AIAA paper 2000-0697 (2000).
4. Hegde, U., Yuan, Z.G., Stocker, D.P. and Bahadori, M.Y., Fifth International Microgravity combustion Workshop, May (2000).
5. Hegde, U., Zhou, L., Bahadori, M. Y., Combustion Science & Technology, Vol. 102, pp. 95-113 (1994).
6. Idicheria, C.A., Boxx, I.G. and Clemens, N.T., AIAA paper 2001-0628 (2001).
7. Becker, H. A. and Yamazaki, S., Combustion and Flame, Vol. 33, pp. 123-149 (1978).
8. Mungal, M.G., Karasso, P.S. and Lozano, A., Combustion Science & Technology, Vol. 76, pp. 165-185 (1991).

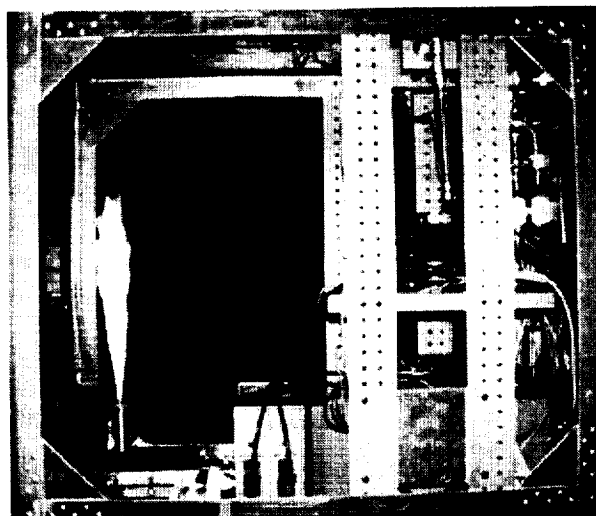
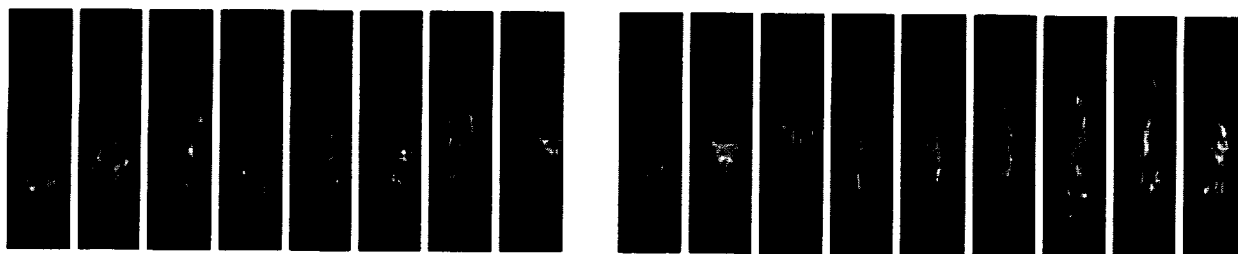


Figure 1. Photograph of the drop rig.



a) $Re_D=7500$, Low-gravity
b) $Re_D=7500$, Normal-gravity
Figure 2. Time resolved sequence of emission images showing jet-flame startup.

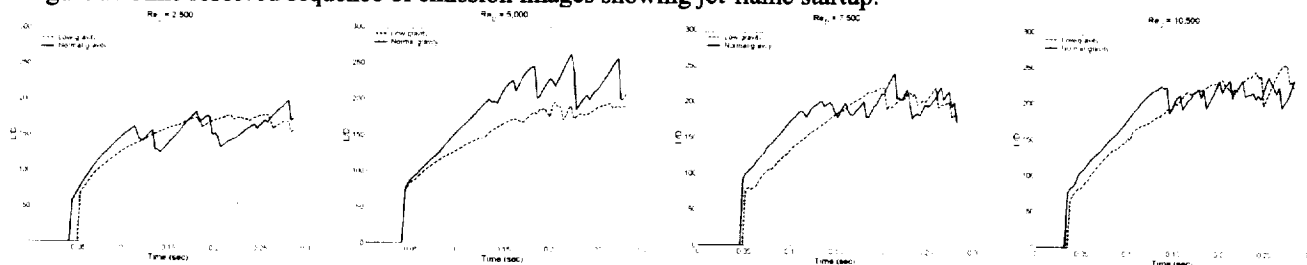


Figure 3. Flame tip variation with time for the various Reynolds numbers.



a) $Re_D=7500$, Low-gravity
b) $Re_D=7500$, Normal-gravity
Figure 4. Steady state sequences

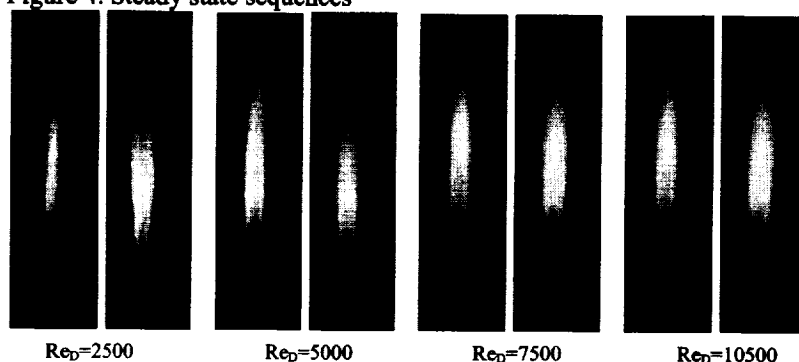


Figure 5. Average images obtained for different Reynolds numbers. In each pair normal-gravity image is to the left and low-gravity image is to the right.

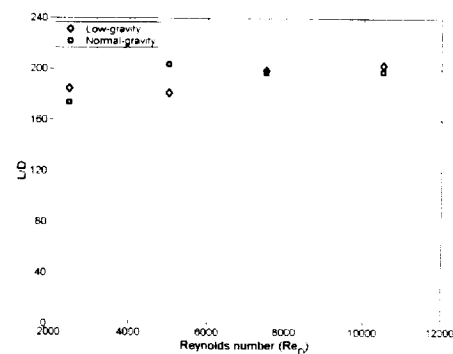


Figure 6. Variation of flame height with Reynolds number.

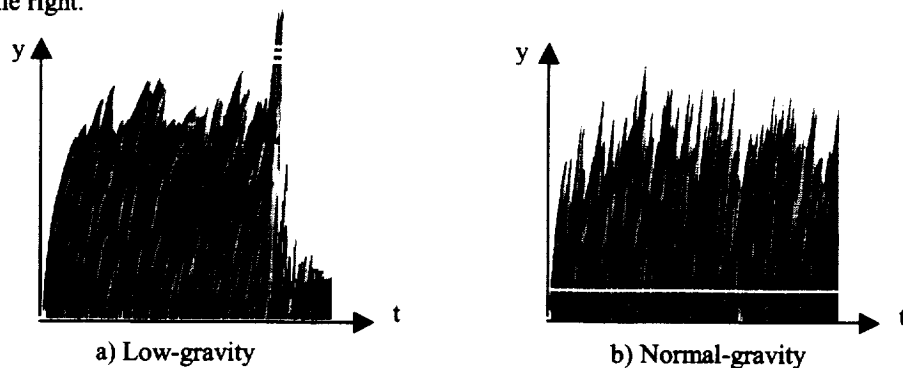


Figure 7. Sample volume renderings at $Re_D=2500$.

THE IMPACT OF BUOYANCY AND FLAME STRUCTURE ON SOOT IN A TURBULENT DIFFUSION FLAME

W. Kollmann*, R. L. Vander Wal and I. M. Kennedy*

*Mechanical and Aeronautical Engineering, UC Davis, CA 95616

NCMR at NASA-Glenn Research Center, Cleveland OH 44135

INTRODUCTION

Turbulence models generally rely on a single point closure of the appropriate time averaged equations. Hence, spatial information is lost and needs to be modeled using solution variables such as turbulence kinetic energy and dissipation rate, often with the assumption of isotropy. However, buoyancy can affect the physical structure of turbulent flames and can change the spatial extent of soot bearing regions. Experiments using laser induced incandescence and LES simulations can be applied to the investigation of buoyancy effects.

EXPERIMENTS

Experiments in an ethylene turbulent diffusion flame were undertaken using Laser Induced Incandescence (LII) with a coflowing stream of normal and vitiated air. The flame was supported on a 3.18 mm I.D. brass nozzle with the fuel flow rate adjusted to yield a Re number of 4000 based on cold gas density and viscosity at 298 K. An outer surrounding coflow of air, or air either diluted or enriched with N₂ or O₂ respectively, was maintained through a surrounding ceramic honeycomb of 9.5 inch diameter.

Light at 1064 nm from a pulsed Nd:YAG laser was expanded by a 6:1 telescope and formed into a sheet by a spherical/cylindrical lens combination. LII images were captured by a gated, intensified array camera and stored by a frame grabber in sets of 52 consecutive images. Results presented here are based on 156 images at each axial height.

Sequences of LII images were processed by custom code using commercial software. The code allowed for processing of individual images and generating radial intensity profiles and image statistics. Radial profile plots of LII intensity were extracted from LII images by selecting a horizontal swath of width 15 mm positioned at the image center and summing the intensity values in the rows contained within this swath. This procedure was performed for each image set collected at a given height. Averaging each radial profile obtained in this manner yielded the LII radial profiles for the different turbulent diffusion flames.

Figure 1 contains LII images produced by a single laser pulse for the turbulent ethylene air diffusion flame in ambients containing 15%, 21% and 27% O₂. Each image, selected as representative among the sequence collected, has been thresholded for reproduction purposes to illustrate the spatial structure of the soot containing regions. As suggested by the overall LII intensity, the spatially integrated f_v increases by over an order of magnitude for this range of ambient O₂ concentrations with the radiative heat loss correspondingly increasing. Similar large differences in soot loading and spatial extent were observed at other axial heights within these flames. A parallel observation, suggested by the LII images, is that the soot intermittency decreases.

Fig. 2 plots radial LII profiles at the indicated heights for the normal air case. The vertical markers reflect the spatially (radially) resolved root mean square (rms) variation in LII intensity. As such, the markers correspond to an absolute variation in f_v . Notably, the rms f_v varies markedly with radial position at each axial height.

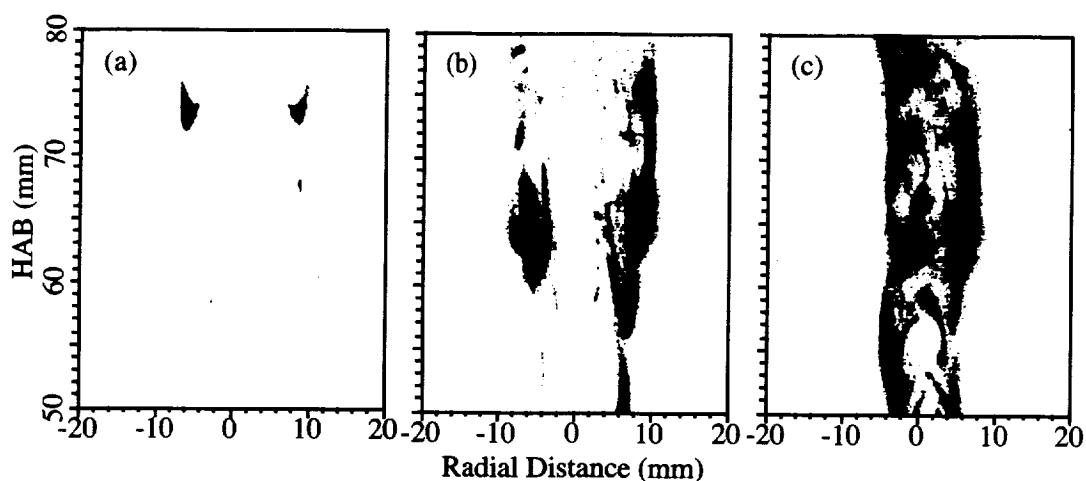


Fig. 1. LII images produced by a single laser pulse for (a) vitiated air, (b) normal air and (c) oxygen enriched air.

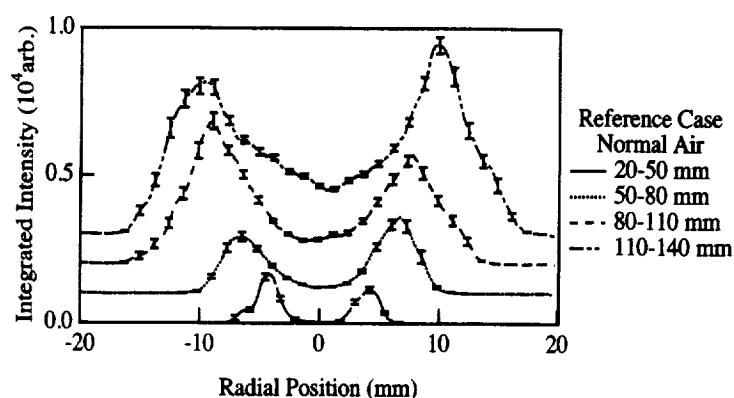


Fig. 2. Radial profiles of the integrated LII intensity at the indicated axial heights for the ethylene flame in normal air. The vertical marker bars represent twice the rms value of f_r .

MODELING

The compressible Navier-Stokes equations in cylindrical coordinates using the primitive variables were set up in dimensionless form consistent with the zero Mach number limit such that the incompressible equations are recovered without singularities. The full three-dimensional set of equations are discretized using a Fourier spectral method in azimuthal direction and high order finite difference methods in the other two spatial directions. However, the present results are obtained using the zero-mode version, i.e. axi-symmetric flows are simulated. The solver includes additional pdes for mixture fraction and soot volume fraction to deal with combustion and the formation and transport of soot.

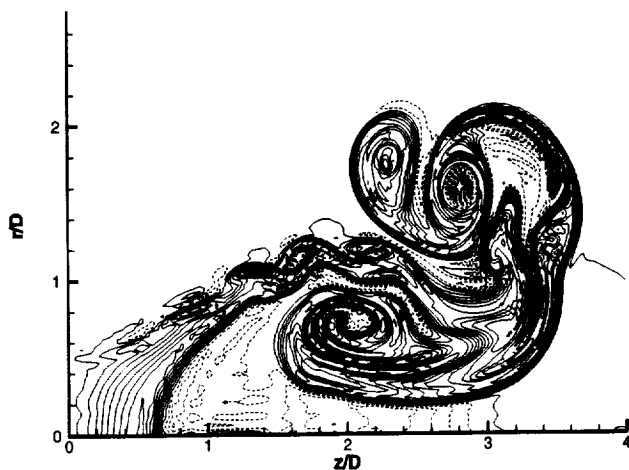


Fig. 3 Isotherms in non reacting compressible jet at $t = 11.17$, $Re = 1500$, $Ma = 0.4$, and $S = 1.41$

The present version of the solver allows the choice of second to eighth order for first and second derivatives as explicit central difference operators or third to ninth order upwind-biased differences for the convective terms in non-conservative formulation. If central difference operators are selected for the convective terms, high order filters are necessary to provide the numerical dissipation to stabilize the system. A fourth order Runge-Kutta type time integration method with an embedded third order scheme to monitor and control the time integration error and with minimal storage requirements was implemented. The simulation of turbulent flows requires the ability to prescribe time dependent boundary conditions for spatially evolving flows. Hence, the proper form of boundary conditions for compressible flows in domains with entrance and exit sections is required and the method developed by Poinso and Lele was used in the present solver.

The performance of the compressible flow solver is illustrated for three axi-symmetric flows: A compressible flow without combustion and two diffusion flames, one with the frozen-equilibrium flame sheet model and one using the equilibrium flame sheet model including radiative heat loss and soot formation, were considered. The flow field was the same in all cases: Swirling jets with a Reynolds number $Re = 1500$, Mach number $Ma = 0.4$, and swirl number $S = 1.41$, based on the conditions at the entrance boundary. The value of the swirl number was above the critical value for cold flows, i.e. a recirculation zone must be expected. Swirling round jets were considered as a test case, since they offer a significant advantage over non-swirling jets in being much shorter, hence allowing better resolution for a given number of grid points.

The semi-infinite flow domain (infinite in radial direction and eight diameters in axial direction) was mapped onto the image domain, which was a cylinder with unity radius and length, using two-parameter exponential maps to crowd the grid points in the region of interest. The number of grid points was $n_r \times n_z = 131 \times 261$ with uniform spacing in the image domain. The sixth order accurate spatial difference operators were used with eighth order explicit filters. The entrance boundary conditions were either ramped up smoothly to their asymptotic values within $\Delta t = 2$ dimensionless time units, or the simulation was started with the asymptotic entrance conditions extended throughout the flow field.

The isotherms for the compressible jet flow without combustion in Fig. 3 at time $t = 11.17$ show the properties of the cold compressible jet. The entrance conditions were ramped up in this case.

The second case was the simulation of the swirling jet with combustion modelled by the compressible, frozen-equilibrium flame sheet model for the reaction of ethylene with air; the

entrance conditions were ramped up as in case one. The local thermodynamic state in this model was determined by three scalar variables: mixture fraction, density and internal energy. The isotherms for the ethylene flame in Fig. 4 at the time $t = 18.44$ reflect the vortex structures generated in the flame. The reacting case shows a distinct difference to the cold flow in Fig. 3 as can be expected.

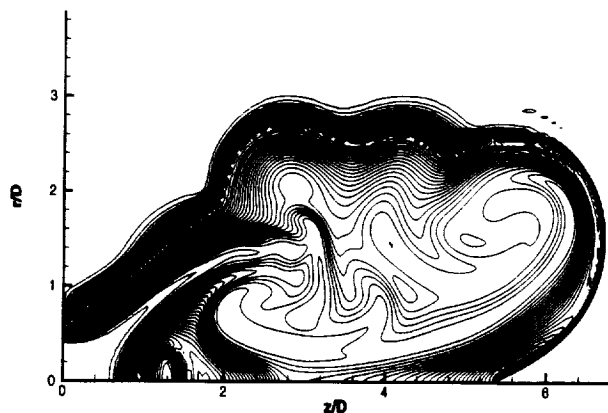


Fig. 4 Isotherms in the compressible flame for $t=18.44$ and $Re=1500$, $S=1.41$ using the frozen-equilibrium flame sheet model

The third case was the same ethylene-air diffusion flame as case two, except the chemical model was replaced by the equilibrium flame sheet model, the radiative sink term was added to the energy equation, and the transport pde for soot volume fraction was added to the Navier-Stokes system. The initial conditions were the asymptotic profiles extended throughout the flow field. The thermodynamic properties were computed by tri-linear interpolation in tables that were set-up before the solver was used.

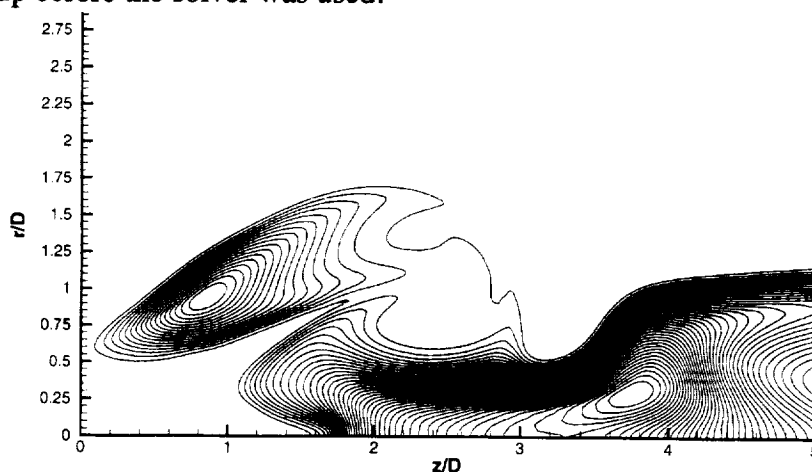


Fig. 5 Isolines of soot volume fraction in a compressible flame for $t=6.24$ and $Re=1500$, $S=1.41$

The soot volume fraction is shown in Fig. 5; it is small in the stretched region and large in the recirculation zone. The level of soot volume fraction at this early stage is, however, much smaller than in the fully developed flame.

AN INVESTIGATION OF FULLY-MODULATED, TURBULENT DIFFUSION FLAMES IN REDUCED GRAVITY

J.C. Hermanson,¹ H. Johari,¹ J.E. Usowicz,¹ R. Sangras,¹
D.P. Stocker,² U. G. Hegde,² T. Nagashima,³ and S. Obata.⁴

¹Mechanical Engineering Department, Worcester Polytechnic Institute, Worcester MA 01609 (jherm@wpi.edu), ²NASA Glenn Research Center, Cleveland, OH 44135, ³Department of Aeronautics and Astronautics, University of Tokyo, Tokyo, Japan, ⁴Aerospace Engineering Department, National Defense Academy, Yokosuka, Japan.

INTRODUCTION

Pulsed combustion appears to have the potential to provide for rapid fuel/air mixing, compact and economical combustors, and reduced exhaust emissions. The objective of this Flight-Definition experiment (PuFF, for Pulsed-Fully Flames) is to increase the fundamental understanding of the fuel/air mixing and combustion behavior of pulsed, turbulent diffusion flames by conducting experiments in microgravity. In this research the fuel jet is fully-modulated (i.e., completely shut off between pulses) by an externally controlled valve system. This gives rise to drastic modification of the combustion and flow characteristics of flames,[1-3] leading to enhanced fuel/air mixing mechanisms not operative for the case of acoustically excited or partially-modulated jets.[4] The fully-modulated injection approach also simplifies the combustion process by avoiding the acoustic forcing generally present in pulsed combustors. Relatively little is known about the behavior of turbulent flames in reduced-gravity conditions, even in the absence of pulsing. Fundamental issues addressed in this experiment include the impact of buoyancy on the fuel/air mixing and combustion characteristics of fully-modulated flames. It is also important for the planned space experiments to establish the effects of confinement and oxidizer co-flow on these flames.

EXPERIMENTAL APPROACH

As part of this program experiments are conducted both in the laboratory at WPI and in the GRC 2.2s Drop Tower. In both cases the combustor configuration consists of a single fuel nozzle with diameter $d = 2 \text{ mm}$ mounted on the centerline of a combustor $20 \times 20 \text{ cm}$ in cross section and 67 cm in height. The gaseous fuel jet flow is fully-modulated by a fast-response solenoid valve (Parker Hannifin Series 9) controlled by a Parker Hannifin Iota One control unit. The mean fuel velocity during injection, U_{jet} , gives Reynolds numbers from 3,000 to 10,000. A slow oxidizer co-flow (standard air for laboratory experiments; an oxygen/nitrogen mixture for the Drop Tower rig) is provided to properly ventilate the flame. An electrically heated *Kanthal* wire coil of 0.24 mm diameter situated at the nozzle exit serves as a continuous ignition source.

Four types of diagnostic techniques are employed in the experiments. First, video imaging is used to study the turbulent structure of the pulsed flames and to determine the corresponding flame lengths. Second, temperatures and radiant emissions are determined using fine-wire thermocouples and thermopile detectors. Particle Image Velocimetry (PIV) is employed to calculate the rate of air entrainment into the flame. Finally, the concentrations of stable gas species (CO , CO_2 , O_2 , NO_x , and unburned hydrocarbons) in the post-flame region are measured by gas sampling and standard emissions instruments. The emissions measurements and PIV are performed in the laboratory only; the thermal measurements and video imaging are performed both in the laboratory experiments and in the Drop Tower tests.

SELECTED EXPERIMENTAL RESULTS

Images of fully-modulated turbulent diffusion flames are shown in Fig. 1 for ethylene fuel. The results presented here were obtained in normal gravity in the laboratory. For the relatively long injection time of the flame in Fig. 1a ($\tau = 119$ ms), an elongated flame structure is produced, which is similar in appearance and in length to the steady-state flame. For shorter injection times, the flame length becomes noticeably shorter and a rounded vortex structure is generally apparent in the region of the flame near the flame tip, with a "tail" attached to the trailing portion of the burning fuel puff (Fig. 1b, $\tau = 46$ ms). For very short injection times (Fig. 1c, $\tau = 5.7$ ms), the puff-like structure typically exhibits a blue luminescence and appears to contain very little soot. The transition from compact, puff-like flame to elongated flame behavior can be characterized in terms of the injection parameter [1] $P \equiv [(4V_o/\pi d^2)/d]^{1/3}$, where V_o is the injected volume. Generally, puff-like behavior is seen for values of P less than approximately eight for ethylene/air flames.[1] The values of the parameter for the fully-modulated flames shown in Fig. 1 are $P = 11$, $P = 8$, and $P = 4$, respectively.

The mean flame lengths for fully-modulated flames are shown in Fig. 2 for several values of co-flow strength. In all cases shown the duty-cycle was sufficiently small ($\alpha < 0.1$) so that there was essentially no interaction between puffs. For the compact puffs ($P < 8$) the addition of co-flow generally increased the mean flame length. The effect of co-flow on the flame length of pulsed flames with longer injection times ($P \geq 11$), as well as steady flames, was less significant. Comparison with free (unducted) flames with the same injection conditions suggests that a co-flow strength of less than $U_{co}/U_{jet} = 0.005$ is sufficient to properly ventilate the flame in a space experiment.

In addition to the injected volume, the flame length in fully-modulated diffusion flames can be significantly impacted by the duty-cycle.[1,3] Increasing the duty-cycle results in closely-packed, interacting flame structures that show mixing and combustion characteristics similar to steady-state flames. The effects of duty-cycle are most apparent for the compact puffs ($P < 8$). The extent of interaction between neighboring structures for puff-like flames can be characterized in terms of a dimensionless interaction parameter $\Pi = V_o^{2/3}(1-\alpha)/A\alpha$, where A is the cross sectional area at the fuel nozzle exit.[1,3] This parameter collapses the mean flame length data, as shown in Fig. 3. The normalization used in the ordinate allows for variations in flame length arising solely from variations in injected volume. Thus the effects of duty-cycle on mean flame length appear to begin to become significant for a value of the interaction parameter less than approximately $\Pi = 80$.

The time-averaged concentration of unburned hydrocarbons measured on the combustor centerline are shown in Fig. 4. The sampling probe was positioned 3 cm downstream of the maximum flame length in all cases. For the most compact puffs ($P < 6$) the concentration of unburned hydrocarbons appears to exhibit an increase, attain a maximum and decrease with increasing duty-cycle. For larger values of P , the concentration of unburned hydrocarbons lies within the sensitivity of the detector. These results suggest that while $P = 8$ appears to represent an upper limit on compact behavior from a standpoint of flame length, the threshold value based on hydrocarbon emissions (hence combustion efficiency) is closer to $P = 6$. The emissions of CO follow a similar trend to the unburned hydrocarbons results presented here.

PARTICLE IMAGE VELOCIMETRY

It is hypothesized that the short flame length of the puffs with the shortest injection time is primarily due to the increased entrainment rate of the surrounding air. Preliminary experiments have been conducted to assess the feasibility of utilizing the PIV technique for quantifying the entrainment. These experiments were done at GRC using the same fuel injector described above.

The injector was placed in a 25-cm diameter chamber. The fuel used was ethylene and the flow was fully-modulated with an injection time of 20 ms and a duty-cycle of 0.05 ($P = 6$, compact puffs). Seed particles 2.5 μm in diameter were injected upstream of the nozzle exit in the chamber. The particles were illuminated by a dual pulsed Nd:YAG laser operating at a wavelength of 532 nm and imaged by a Kodak ES 1.0 CCD camera. The images were processed by a cross-correlation scheme using 64 \times 64 pixel windows and a 50% overlap. The image area was approximately 45 mm square resulting in a velocity vector grid spacing of 1.5 mm. The PIV system was synchronized with the solenoid valve.

A sample velocity field is shown in Fig. 5 for $\tau = 20$ ms. At the instant shown, the velocity field is recorded 40 ms after the flow initiation. The tail of the flame structure is clearly visible in this field, along with the ambient air being drawn into it. Integration of the velocity normal to specific contours in the flow provides a measure of the rate of air entrainment into the flame.

NUMERICAL MODELING

The numerical analysis of fully-modulated turbulent diffusion flames is performed (U. Tokyo/NDA) using gaseous hydrogen/oxygen combustion because of its simple reaction mechanism compared to hydrocarbon fuels. The governing equation set consists of the unsteady, 3-dimensional, Navier-Stokes equation, multi-species diffusion equations, and a 2-equation, q - ω turbulence model. These equations are solved by a finite-difference TVD formulation and LU-ADI implicit time integration. A duty-cycle of $\alpha=0.3$ was simulated for $1.6 < P < 2.8$. The axisymmetric calculation region (10 mm radius and 40 mm long) is divided into 53 \times 83 grid points, with the 2 mm diameter circular injection tube located on the center axis.

The concentration fields of hydrogen and water vapor are shown in Fig. 6 for $P = 2.2$. The entrainment of surrounding air into the jet appears to give rise to a mushroom-shaped region of unburned hydrogen, which resembles somewhat the puff-shape structures observed in the experiments. Similar structure is suggested by the water vapor concentration field. A mean flame length was defined based on the region where the centerline temperature decreases to a value of 2000 K. Based on this criterion, it is found that the flame length of the injected puffs is linearly proportional to the injection parameter P , as seen in the experiment.

ACKNOWLEDGEMENTS

The assistance of Drs. M. P. Wernet and P. S. Greenberg in conducting the PIV measurements, and the help of Ms. D. Bohman, is greatly appreciated. This work is sponsored by NASA Glenn Research Center under Agreement NCC3-673.

REFERENCES

- [1] Hermanson, J.C., Dugnani, R., and Johari, H., *Comb. Sci. Tech.* **155**, 203-225, 2000.
- [2] Hermanson, J.C., Usowicz, J., Johari, H., and Sangras, R., *AIAA J.*, submitted.
- [3] Johari, H. and Motevalli, V., *Comb. Sci. Tech.* **94** (1-6), 229-245, 1993.
- [4] Lovett, J.A. and Turns, S.R., *AIAA Journal* 28(1), 38-46, 1990.

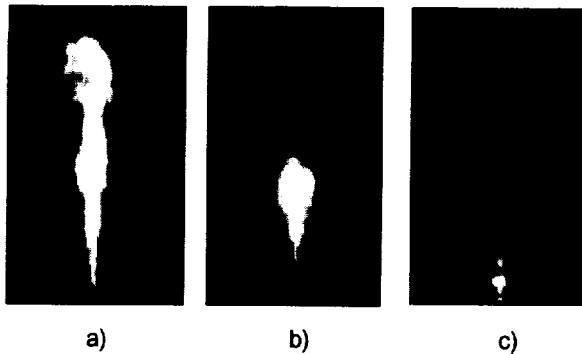


Fig. 1 Turbulent, fully-modulated ethylene/air flames. $U_{cof}/U_{jet} = 0.005$, $Re_{jet} = 5,000$. a) $\tau = 119$ ms, $V_0 = 8.4$ cm³; b) $\tau = 46$ ms, $V_0 = 3.2$ cm³; c) $\tau = 5.7$ ms, $V_0 = 0.40$ cm³. The image height is 43 cm.

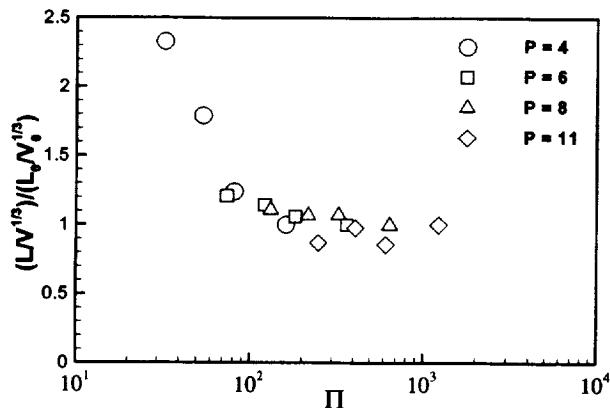


Fig. 3 Effect of duty-cycle on normalized flame length of fully-modulated flames.

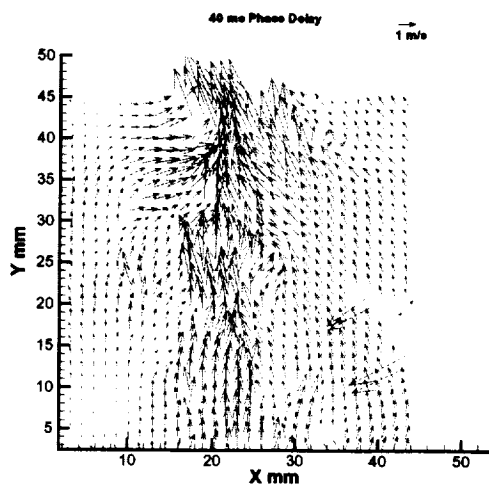


Fig. 5 Velocity field of a fully-modulated ethylene/air flame, $\tau = 20$ ms, $\alpha = 0.05$.

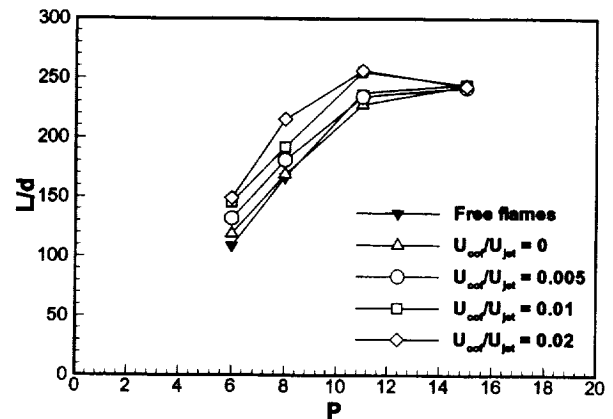


Fig. 2 Effect of co-flow on normalized flame length for isolated, fully-modulated flame puffs.

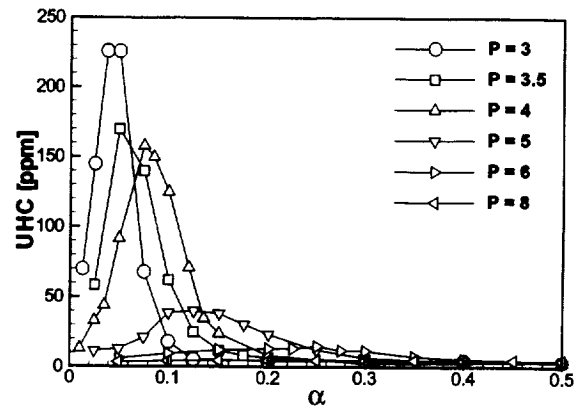


Fig. 4 Centerline unburned hydrocarbon emissions of fully-modulated flames.

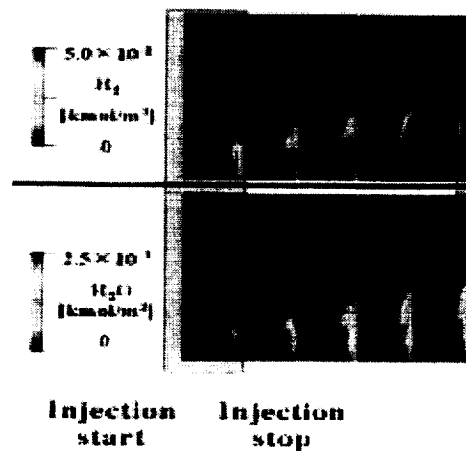


Fig. 6 Numerical simulation of a single fully-modulated flame puff, hydrogen/air chemistry, $P = 2.2$.

LARGE EDDY SIMULATION OF GRAVITATIONAL EFFECTS ON TRANSITIONAL AND TURBULENT GAS-JET DIFFUSION FLAMES

Peyman Givi, Department of Mechanical and Aerospace Engineering, University at Buffalo, SUNY, Buffalo, NY 14260-4400.

Farhad A. Jaber, Department of Mechanical Engineering, Michigan State University, East Lansing, MI 48824-1226.

OBJECTIVE

The basic objective of this work is to assess the influence of gravity on “the compositional and the spatial structures” of transitional and turbulent diffusion flames via large eddy simulation (LES), and direct numerical simulation (DNS). The DNS is conducted for appraisal of the various closures employed in LES, and to study the effect of buoyancy on the small scale flow features. The LES is based on our “filtered mass density function” (FMDf) model [1]. The novelty of the methodology is that it allows for reliable simulations with inclusion of “realistic physics.” It also allows for detailed analysis of the unsteady large scale flow evolution and compositional flame structure which is not usually possible via Reynolds averaged simulations.

FORMULATION

The flow field under investigation is that of a jet-flame in which a high speed fuel is injected into a low speed or stagnant coflowing stream of oxidizer. This flow is inherently time-dependent and three-dimensional (3D). Nevertheless, some 2D (planar) simulations (via both LES and DNS) are also conducted for validation of the numerical methods and for determining the range of parameters. We have primarily considered methane/air combustion because of the rich extent of literature on methane oxidation mechanism, and availability of significant data in such flames. The application of a spatially & temporally invariant and localized filter function to the fundamental transport equations of reacting flows yields:

$$\frac{\partial \langle \rho \rangle_\ell}{\partial t} + \frac{\partial \langle \rho \rangle_\ell \langle u_i \rangle_L}{\partial x_i} = 0 \quad (1)$$

$$\frac{\partial \langle \rho \rangle_\ell \langle u_j \rangle_L}{\partial t} + \frac{\partial \langle \rho \rangle_\ell \langle u_i \rangle_L \langle u_j \rangle_L}{\partial x_i} = -\frac{\partial \langle p \rangle_\ell}{\partial x_j} + \frac{\partial \langle \tau_{ij} \rangle_\ell}{\partial x_i} - \frac{\partial \mathcal{T}_{ij}}{\partial x_i} + \langle \rho \rangle_\ell g_j \quad (2)$$

$$\frac{\partial \langle \rho \rangle_\ell \langle \phi_\alpha \rangle_L}{\partial t} + \frac{\partial \langle \rho \rangle_\ell \langle u_i \rangle_L \langle \phi_\alpha \rangle_L}{\partial x_i} = -\frac{\partial \langle J_i^\alpha \rangle_\ell}{\partial x_i} - \frac{\partial \mathcal{M}_i^\alpha}{\partial x_i} + \langle \rho S_\alpha \rangle_\ell, \quad \alpha = 1, 2, \dots, \sigma \quad (3)$$

where filtered and Favre-filtered values of the transport variable $f(\mathbf{x}, t)$ are represented by $\langle f \rangle_\ell$ and $\langle f \rangle_L = \langle \rho f \rangle_\ell / \langle \rho \rangle_\ell$, respectively. In these equations u_i and ρ are the velocity vector and the density, p denotes the pressure, g_j denotes the gravity vector, and τ_{ij} , J_i^α are the molecular viscosity tensor and diffusivity vector, respectively. The scalars include mass fraction of chemical species, $\phi_\alpha \equiv Y_\alpha$, $\alpha = 1, 2, \dots, N_s$, and specific enthalpy, $\phi_\sigma \equiv h = \sum_{\alpha=1}^{N_s} h_\alpha \phi_\alpha$, in which $h_\alpha = h_\alpha^0 + \int_{T_0}^T c_{p\alpha}(T') dT'$ (T is the temperature). These equations are

closed by the constitutive relations. The hydrodynamic subgrid scale (SGS) closure problem is associated with $\mathcal{T}_{ij} = \langle \rho \rangle_\ell (\langle u_i u_j \rangle_L - \langle u_i \rangle_L \langle u_j \rangle_L)$ and $\mathcal{M}_i^\alpha = \langle \rho \rangle_\ell (\langle u_i \phi_\alpha \rangle_L - \langle u_i \rangle_L \langle \phi_\alpha \rangle_L)$ denoting the SGS stresses and the SGS scalar fluxes, respectively. The term $\langle \rho S_\alpha \rangle_\ell = \langle \rho \rangle_\ell \langle S_\alpha \rangle_L$ ($\alpha = 1, 2, \dots, N_s$) denoting the filtered reaction rates. The joint velocity-scalar FMDF is formally defined as:

$$\mathcal{F}_L(\mathbf{V}, \boldsymbol{\psi}, \mathbf{x}; t) \equiv \int_{-\infty}^{+\infty} \rho(\mathbf{x}', t) \xi[\mathbf{V}, \mathbf{U}(\mathbf{x}', t), \boldsymbol{\psi}, \boldsymbol{\phi}(\mathbf{x}', t)] H(\mathbf{x}' - \mathbf{x}) d\mathbf{x}' \quad (4)$$

where H is the filter function, $\boldsymbol{\psi}$ denotes the composition domain of the scalar array, $\boldsymbol{\phi}(\mathbf{x}, t)$, and \mathbf{V} denotes the probability domain of the random velocity vector, $\mathbf{U}(\mathbf{x}, t)$. The term $\xi[\mathbf{V}, \mathbf{U}(\mathbf{x}, t), \boldsymbol{\psi}, \boldsymbol{\phi}(\mathbf{x}, t)]$ is the fine-grained velocity-scalar density. Equation (4) implies that the FMDF is the *mass weighted spatially filtered* value of the fine-grained density. Starting from the original (unfiltered) transport equations of the velocity and the scalar variables, one may derive the transport equation for the joint velocity-scalar FMDF. By integrating the resulting equation over the velocity space, the transport equation for the joint filtered mass density function of the scalars, F_L is obtained:

$$\begin{aligned} \frac{\partial F_L}{\partial t} + \frac{\partial \langle u_i \rangle_L F_L}{\partial x_i} = & - \frac{\partial [\langle u_i | \boldsymbol{\psi} \rangle_\ell - \langle u_i \rangle_L] F_L}{\partial x_i} + \frac{\partial}{\partial x_i} \left\langle \rho D \frac{\partial \zeta}{\partial x_i} \right\rangle_\ell - \frac{\partial [\hat{S}_\alpha(\boldsymbol{\psi}) F_L]}{\partial \psi_\alpha} \\ & - \frac{\partial^2}{\partial \psi_\alpha \partial \psi_\beta} \left[\left\langle \rho D \frac{\partial \phi_\alpha}{\partial x_i} \frac{\partial \phi_\beta}{\partial x_i} | \boldsymbol{\psi} \right\rangle_\ell F_L / \hat{\rho} \right] \end{aligned} \quad (5)$$

where ζ represents the scalar fine-grained density, D is the molecular diffusion coefficient, $\langle \mathcal{A} | \mathcal{B} \rangle_\ell$ denotes the filtered value of the variable \mathcal{A} , “conditioned” on \mathcal{B} , and the hat is used to emphasize the quantities which are dependent only on the scalar field. It is noted that in this “exact” transport equation the terms associated with and chemical reaction is represented in a closed form.

PROGRESS TO DATE

Up to now, we have conducted several DNS and LES of 2D and 3D jet flames. Most of the LES are conducted via the scalar FMDF methodology; the use of the joint velocity-scalar FMDF is the subject of our ongoing investigation (please see next section). The SGS mixing term in this equation is modeled via the IEM closure as discussed in Ref. [1]. The finite-rate chemistry effects are explicitly included in this way since the chemistry is closed in the formulation. Numerical solution of the scalar FMDF is obtained with a hybrid Eulerian/Lagrangian scheme. The hydrodynamic field is obtained by solving the filtered continuity and momentum equations with a compact parameter finite-difference scheme. The scalar quantities include mass fraction of chemical species and enthalpy. The FMDF is represented by an ensemble of Lagrangian Monte Carlo [2] particles which are freely transported in the physical space by the combined actions of large scale convection and diffusion (molecular and subgrid). Transport in the composition space occurs due to chemical reaction and SGS mixing. Thus, the grid-free Lagrangian procedure considers “notional particles” whose evolution can be computed via a “stochastic process” to simulate motion in

physical space by convection and diffusion. The compositional values of particles are changed due to mixing and reaction. These are represented by the stochastic differential equations. The oxidation of methane is simulated via a one-step global mechanism [3].

The examination of the physical flame structure indicates that both the large and the small flow scales are significantly influenced by buoyancy. Expectedly, in cases with large values of the Froude number combustion has found to damp the jet growth due to adverse effects of chemical heat release on the growth of hydrodynamic instabilities. However, in cases with relatively low values of the Froude number, the combustion-generated density variations result in buoyancy induced instabilities and rapid jet growth (as compared to the non-reacting jet). This results in significant enhancement of turbulence at large and small scales, thus yields an increase in mixing and combustion. These results are consistent with experimental results on normal and microgravity jet flames [4], and suggest that there is a strong two-way coupling between turbulence and combustion in nonpremixed normal gravity jet flames which is very different from that in microgravity. These results also suggest that the models which are developed and tested at normal gravity flames may not work properly in microgravity, and vice versa. Our results also indicate that LES/FMDF is able to capture the large scale features of turbulence correctly. The effect of the buoyancy on the small scale flow quantities such as the SGS stresses and the closures used for these quantities needs to be studied further. Our preliminary results indicate that the magnitude of the SGS stresses, the SGS scalar fluxes and the SGS unmixedness enhance by the gravity.

Our investigation of the effects of gravity on the compositional structure of microgravity and normal gravity jet flames indicate that the gravity modifies significantly this structure. The finite rate chemistry effects, as portrayed by the scatter plots of the temperature in the mixture fraction space, are more significant in microgravity flame than those in normal gravity. This is attributed to the fact that mixing and combustion are intensified by buoyancy in normal gravity, and suggests that the ignition/extinction characteristics of the transitional/turbulent flames are dependent on the gravity at least at low to moderate values of the Froude number. An examination of the compositional flame structure for various flames also indicates that the gravity modifies the distribution of strain field, the major species in the flame zone, and the flame thickness.

The LES/FMDF predictions compare favorably with DNS data provided that the mixing frequency coefficient in the SGS mixing (IEM) model is assigned properly. This coefficient is somewhat dependent on the gravity level. The reason for this dependence is that the flow is not fully turbulent, specially near the inlet. Nevertheless, the values of the SGS scalar dissipation predicted by the model correlates very well with those obtained via DNS at all gravity levels. The large and the small scale flow structures are significantly modified by the gravity, resulting in variation in model coefficient at transitional jet region. In addition to DNS and LES/FMDF, we also simulated the jet flames via a conventional LES in which the SGS scalar correlations are ignored (this is labeled as LES-FD). A comparison between DNS and LES-FD indicates that in both zero- and normal-gravity environment the SGS scalar correlations have a strong influence on the large scale flow quantities; so if they are neglected the results would be erroneous.

WORK IN PROGRESS

Work is also in progress on the following issues which are of interest to this project:

- (1) We are considering the 12-step reduced kinetics mechanism of methane-air oxidation [5] in conjunction with the ISAT routine [6] in our scalar LES/FMDF. If this scheme proves to be computationally feasible, we will utilize it in our future simulations.
- (2) Under another project, we have recently developed a methodology, termed the velocity filtered density function (VFDF) which accounts for the PDF of the SGS velocity vector. At this point, the formulation is valid for constant density turbulent flow. We are currently extending the methodology to account for the joint PDF of the SGS velocity and scalars. If the outcome of this work is successful, the joint velocity-scalar FMDF will be constructed and will be used for the jet flame simulation.
- (3) We are conducting a feasibility assessment of a new computational methodology, termed the “Spectral/hp Element” method [7]. The advantage of this methodology is that it contains spectral accuracy and it also allows for utilization of “unstructured” grids. This assessment is being done for possible replacement of our current CFD mean flow solver with this methodology so that we can consider a larger computational domain for our jet flame LES and DNS.

ACKNOWLEDGMENT

This work is sponsored by the NASA Glenn Research Center under Grant NAG-3-225, with Dr. Uday Hegde of the National Center for Microgravity Research as the Technical Monitor. Computational resources are provided by the NCSA facilities at the University of Illinois at Urbana, and by the CCR at the University at Buffalo. We are indebted to Professor Stephen B. Pope (Cornell University) for his collaboration on various aspects of this work.

References

- [1] Jaber, F. A., Colucci, P. J., James, S., Givi, P., and Pope, S. B., *J. Fluid Mech.*, **401**:85-121 (1999).
- [2] Pope, S. B., *Prog. Energy Combust. Sci.*, **11**:119-192 (1985).
- [3] Bhui-Pham, M. N., Ph.D. Thesis, University of California, San Diego, CA, 1992.
- [4] Hegde, U., Zhou, L., and Bahadori, M. Y., *Combust. Sci. and Tech.*, **102**:95-113 (1994).
- [5] Sung, C. J., Law, C. K., and Chen, J.-Y., in *Proceedings of 27th Symp. (Int.) on Combustion*, pp. 295-303, The Combustion Institute, Pittsburgh, PA, 1998.
- [6] Pope, S. B., *Combust. Theo. Modelling*, **1**:41 (1997).
- [7] Karniadakis, G. E. and Sherwin, S. J., *Spectral/hp Element Methods for CFD*, Oxford University Press, New York, NY, 1999.

VORTEX/FLAME INTERACTIONS IN MICROGRAVITY PULSED JET DIFFUSION FLAMES

M. Y. Bahadori, Science and Technology Development Corporation; U. Hegde, National Center for Microgravity Research; and D. P. Stocker, NASA Glenn Research Center

INTRODUCTION

Significant differences have been observed between the structure of laminar, transitional, and turbulent flames under downward, upward, and microgravity conditions (Fig. 1). These include flame height, jet shear layer, flame instability, flicker, lift-off height, blow-off Reynolds number, and radiative properties [1-4]. The primary objective of this investigation is to identify the mechanisms involved in the generation and interaction of large-scale structures in microgravity flames. This involves a study of vortex/flame interactions in a space-flight experiment utilizing a controlled, well-defined set of disturbances imposed on a laminar diffusion flame. The results provide a better understanding of the naturally occurring structures that are an inherent part of microgravity turbulent flames. The paper presents the current progress in this program.

APPROACH

TGDF (Turbulent Gas Jet Diffusion Flames) is a self-contained, autonomous experiment which was flown in the cargo bay of the Space Shuttle *Columbia* during the STS-87 mission. Data on temperature field, radiative loss, and flame characteristics under pulsed conditions were obtained [5]. The imposed vortices were generated by periodically varying the open diameter of an iris located around the flame base. Figure 2 shows a comparison between smoke visualization of the vortex interacting with the flow field and the pulsed flame image in microgravity. A microgravity laminar propane diffusion flame burning in quiescent air was studied. The nozzle had an internal diameter of 1.65 mm, and the fuel was injected at $Re \cong 400$. The iris pulse frequency was in the 1-10 Hz range. Details of the experiment procedure are presented elsewhere [5]. A transient numerical model was developed to study the interaction of imposed vortices with the flame front. Figure 3 depicts the effects of disturbances on the temperature contour of the microgravity flame, and shows vortex-induced enhanced temperature zones. In addition, similar tests were conducted in normal gravity, and the effects of pressure were also studied.

RESULTS AND DISCUSSION

Analysis of the temperature-field oscillations provided insight into the vortex/flame interaction phenomenon. Figure 4 shows the normalized temperature oscillation for two locations inside the flame. It is seen that the phase difference is about 60° - 70° , i.e., oscillations are in-phase. In addition, it was found that for thermocouples located on both sides of the flame front, the flame movement causes the temperature oscillation to be almost 180° out of phase. As the flame gets closer to one thermocouple, its temperature rises, while the other thermocouple shows a drop in temperature. Therefore, oscillation phase-change occurs across the flame surface upon interaction of the vortex with the flame sheet. The axial variation of the temperature amplitude also shows some unique characteristics. Figure 5 compares the predicted and measured normalized centerline temperature for three axial locations. As the distance from the nozzle exit increases, the amplitude decreases. This is caused by oscillation decay and viscous dissipation. The observed phase lag for the locations along the centerline are related to the local convection velocity of the oscillations, and are shown to be in agreement with the computations[5]. As seen in Fig. 5, the predicted and measured centerline temperature oscillations, amplitude variation, and phase variation are in good agreement. Temporal variations of the velocity field have provided information on entrainment Figure 6 shows the

predicted instantaneous radial velocity field (i.e., $v = V + \hat{v}$) at three separate times during one cycle of the iris pulsing. In the lower part, near $x/d = 0$, the radial velocity is directed inward due to air entrainment, whereas in the upper part, the radial velocity is directed outward due to jet spreading. The dividing streamline, which represents the demarcation between these two regions, is also shown. In Fig. 6(b), the iris is moving inward towards its minimum open position, and the entrainment region becomes more dominant compared to that in Fig. 6(a) where the iris is near its maximum open position. The entrainment then reduces in the other part of the cycle, where the iris is moving outward in Fig. 6(c). The predicted field of the oscillatory component of radial velocity (i.e., \hat{v}) is shown in Fig. 7. The iris is moving in from its maximum open position in Fig. 7(a), and the inward velocity is dominant near the flame base, whereas outward radial-velocity component is present further downstream. Once the iris approaches its minimum open position in Fig. 7(b), the amplitude of \hat{v} increases in the flame lower part. In Fig. 7(c), the iris is moving outward, and the flame base shows an outward direction of \hat{v} .

The effects of nonlinear interactions between the imposed pulsations and the flame flicker were also studied. The axial variation of the temperature autospectrum with and without pulsing in normal gravity is shown in Fig. 8. The autospectra depicted in Fig. 8(a) show that the flicker amplitude increases up to the location x_2 (which is near the normal-gravity flame tip), and then begins to decay at further downstream locations x_3 and x_4 . In the presence of pulsing, as seen in Fig. 8(b) for $f = 3$ Hz, while the flicker amplitude increases up to the flame tip and then begins to decrease, the amplitude peak is considerably broadened. This shows the presence of nonlinear interaction between the imposed pulsations and the flame flicker. The flicker frequency in normal gravity has approximately a square-root dependence on both pressure and gravitational level (e.g., [4]). Hence, it was of interest to analyze a normal-gravity flame under reduced-pressure condition. Figure 9 shows the variation of the centerline temperature amplitude at the pulse frequency of 1.5 Hz for the three cases of (a) Microgravity flame at 1 atm, (b) normal-gravity flame at 1 atm, and (c) normal-gravity flame at 0.5 atm. The axial decay behavior in the three cases is significantly different. The relative amplitude of the normal-gravity oscillation at 1 atm decays initially, but then grows in the downstream regions in contrast to the microgravity case at 1 atm and the normal-gravity case at 0.5 atm. This different behavior is caused by a number of factors such as buoyant acceleration, effects of flicker, and nonlinear interactions between buoyant instabilities and imposed oscillations.

ACKNOWLEDGMENTS

This work was supported by the NASA John H. Glenn Research Center under Contract NAS3-98031 (with STDC) and Cooperative Agreement NCC3-544 (with NCMR).

REFERENCES

- [1] Bahadori, M. Y., Stocker, D. P., Vaughan, D. F., Zhou, L., and Edelman, R. B., "Effects of Buoyancy on Laminar, Transitional, and Turbulent Gas Jet Diffusion Flames," Modern Developments in Energy, Combustion, and Spectroscopy, pp. 49-66, (F.A. Williams, A.K. Oppenheim, D.B. Olfe, and M. Lapp, eds.), Pergamon Press, New York, 1993.
- [2] Hegde, U., Zhou, L., and Bahadori, M. Y., "The Transition to Turbulence of Microgravity Gas Jet Diffusion Flames," Combust. Sci. Tech., Vol. 102, pp. 95-113 (1994).
- [3] Bahadori, M. Y., Stocker, D. P., Zhou, L., and Hegde, U., "Radiative Loss from Non-Premixed Flames in Reduced-Gravity Environments," Combust. Sci. Tech., in press (2001).
- [4] Bahadori, M. Y., Zhou, L., Stocker, D. P., and Hegde, U., "Functional Dependence of Flame Flicker on Gravitational Level," AIAA Journal, in press (2001).
- [5] Hegde, U., Bahadori, M.Y., and Stocker, D.P., "Oscillatory Temperature Measurements in a Pulsed Microgravity Diffusion Flame," AIAA Journal, Vol. 38, pp. 1219-1229 (2000).

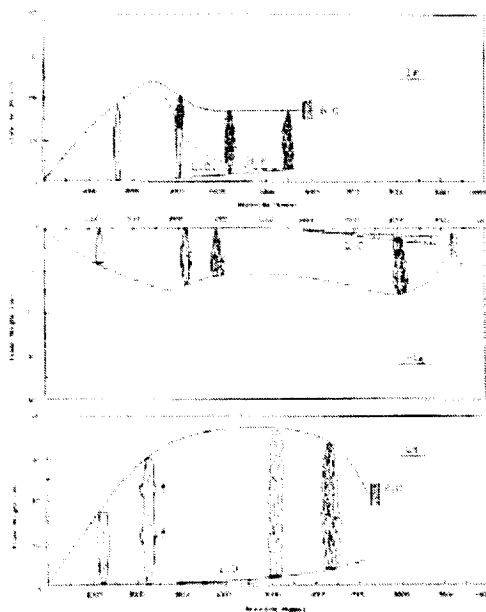


Fig. 4. Laminar, transitional, and turbulent premixed flame characteristics for the engine test. (a) laminar flame velocity; (b) turbulent flame velocity; and (c) flame height.



Fig. 5. Smoke visualization of the impaired vortex core and microgravity flame image (right).



Fig. 6. Predicted temperature contours (left) and flame surface (right). Note regions of vortex-induced enhanced temperature located in the flame surface.

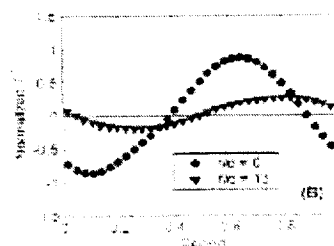
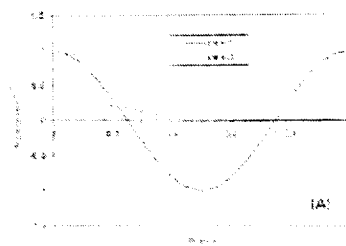


Fig. 7. Normalized temperature oscillations from (a) predictions and (b) flight experiment during one oscillation cycle at the same pulse frequencies. The data and predictions are presented for the same axial location $x/d = 38$. Both thermocouples are on the same side of the flame sheet.

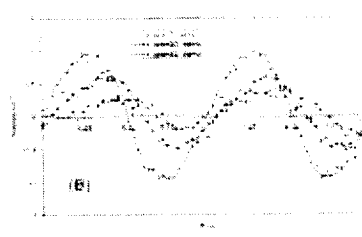
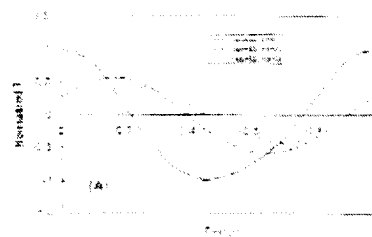


Fig. 8. Axial variation of the temperature amplitude along the flame centerline at the same oscillation frequency from (a) numerical model and (b) flight experiment. The normalized centerline temperatures are shown for three axial locations.

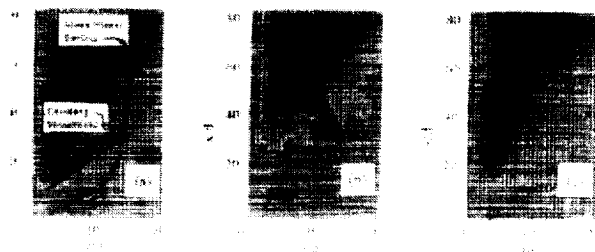


Fig. 6 Predicted instantaneous radial velocity distribution during one cycle of oscillation. Blue represents radially inward direction of velocity and red represents radially outward direction. The mean flame surface location and the dividing streamline are noted in (a); the iris is moving in from its maximum open position in (a), is moving inward in (b), and is moving outward in (c).

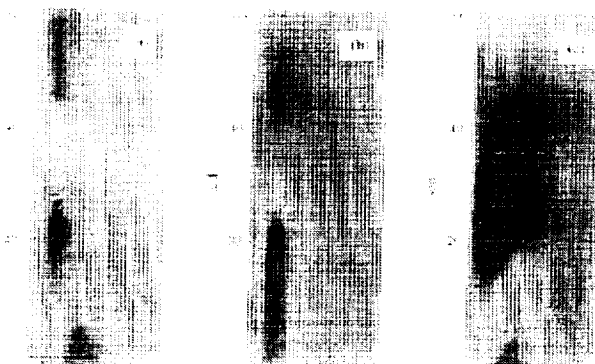


Fig. 7 Predicted flow structure during one cycle of pulsation obtained from the oscillatory component of the radial velocity. Blue indicates inward direction of radial velocity and red indicates outward direction. The iris is moving in from its maximum open position in (a), is approaching the minimum open position in (b), and is moving outward in (c).

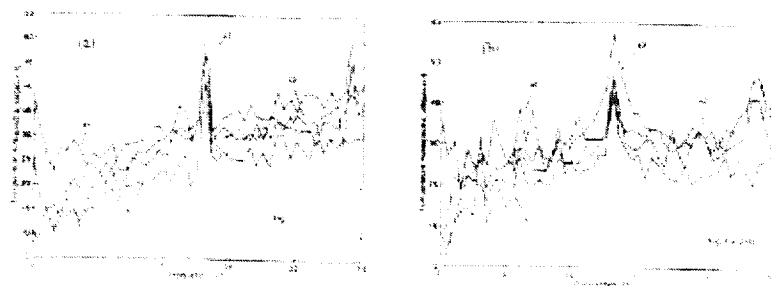


Fig. 8 Temperature autospectra in normal gravity at 1 atm for (a) unpuised flame, and (b) pulse frequency of 3 Hz. Four thermocouple locations along the flame centerline are shown. Here, x_1 , x_2 , x_3 , and x_4 correspond respectively to $x/d = 0, 30, 55$, and 91 , where x is the downstream distance and d is the nozzle diameter.

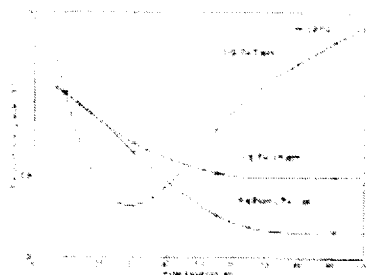


Fig. 9 Variation of temperature amplitude (pulse frequency of 1.5 Hz) for the flames in microgravity ($P = 1.0$ atm) and normal gravity ($P = 0.5$ atm and 1.0 atm). The data are shown for the thermocouple at $x/d = 9$, where x is the downstream distance along the flame centerline and d is the nozzle diameter.

Effects of Flame Structure and Hydrodynamics on Soot Particle Inception and Flame Extinction in Diffusion Flames

R. L. Axelbaum, R. Chen, *Washington University, St. Louis, MO USA*

P. B. Sunderland (NCMR), D. L. Urban, *NASA Glenn Research Center, Cleveland, OH USA*

S. Liu and B. H. Chao, *University of Hawaii, Hawaii, USA*

INTRODUCTION

This paper summarizes recent studies of the effects of stoichiometric mixture fraction (structure) and hydrodynamics on soot particle inception and flame extinction in diffusion flames. Microgravity experiments are uniquely suited for these studies because, unlike normal gravity experiments, they allow structural and hydrodynamic effects to be independently studied. As part of this recent flight definition program, microgravity studies have been performed in the 2.2 second drop tower. Normal gravity counterflow studies also have been employed and analytical and numerical models have been developed.

A goal of this program is to develop sufficient understanding of the effects of flame structure that flames can be “designed” to specifications – consequently, the program name *Flame Design*. In other words, if a soot-free, strong, low temperature flame is required, can one produce such a flame by designing its structure? Certainly, as in any design, there will be constraints imposed by the properties of the available “materials.” For hydrocarbon combustion, the base materials are fuel and air. Additives could be considered, but for this work only fuel, oxygen and nitrogen are considered. Also, the structure of these flames is “designed” by varying the stoichiometric mixture fraction. Following this line of reasoning, the studies described below are aimed at developing the understanding of flame structure that is needed to allow for optimum design.

SOOT INCEPTION

Recent experimental, numerical and analytical work has shown that the stoichiometric mixture fraction, Z_{st} , can have a profound effect on soot formation in diffusion flames [1-7]. This effect appears even at constant adiabatic flame temperature, T_{ad} , as demonstrated by Du and Axelbaum [1, 2]. An important finding of these works was that at sufficiently high Z_{st} the flames remain blue even when the strain rate approaches zero in counterflow flames, or as flame height and residence time approach infinity in coflowing flames. Lin and Faeth [4] coined the term *permanently blue* to describe such flames.

Flames considered in past studies involved counterflow and gas-jet configurations, which do not allow independent variation of flame structure and convection direction. Thus, it was not possible to assess the relative contributions of structure and hydrodynamics because both structure and hydrodynamics suppress soot formation at high Z_{st} in normal-gravity diffusion flames.

To better understand the mechanism responsible for permanently blue flames, the onset of luminous soot (the soot limit) was examined in spherical microgravity diffusion flames burning ethylene at atmospheric pressure. In a novel application of microgravity, spherical flames were employed to allow convection across the flame to be either from fuel-to-oxidizer or from oxidizer-to-fuel, while at the same time allowing Z_{st} to be independently varied. Stoichiometric mixture fraction was varied by changing

inert concentrations such that adiabatic flame temperature did not change [2]. Nitrogen was supplied with the oxidizer at low Z_{st} and with the fuel at high Z_{st} .

Thus motivated, we established four flames: (a) ethylene issuing into air, (b) diluted ethylene issuing into oxygen, (c) air issuing into ethylene, and (d) oxygen issuing into diluted ethylene. The stoichiometric mixture fraction for flames (a) and (c) is 0.064 and for flames (b) and (d) it is 0.78. Under the assumption of equal diffusivities of all species and heat, the stoichiometric contours of the flames have identical nitrogen concentrations and adiabatic temperatures.

The experiments were conducted in the NASA Glenn 2.2-second drop tower using a general-purpose combustion rig. The burner is a 6.4 mm diameter porous sphere consisting of sintered 10 micron stainless steel particles. Temperatures were measured using an uncoated Pt/Pt-Rh thermocouple and were corrected for radiation losses.

Since the drop tower provides only 2.2 seconds of microgravity time, a transient theoretical model was developed to evaluate the effects of unsteadiness and heat loss on the temperatures of the flames. The model adopts a simplified single-step, flame-sheet approximation for reaction chemistry and a detailed modeling of heat loss. Radiative heat losses from the gas and the burner surface are included. The optically thin model is adopted to formulate the gas radiation.

Figure 1 shows color images, captured just prior to drop termination, of representative flames for the four conditions considered. Each flame has an ethylene consumption rate of 1.5 mg/s and an adiabatic flame temperature of 2370 K. Figure 2 shows predicted flame and burner temperatures for the four flames of Fig. 1. The numerical results show that after ignition the flame temperature increases, approaching an asymptote in tens of seconds. None of the flames has reached steady state within the 2.2 seconds of drop time. Furthermore, although the adiabatic flame temperatures of all four flames are the same, the flame temperatures vary considerably. In particular, Flames (a) and (d) are substantially cooler and evolve more slowly than Flames (b) and (c). The agreement between theory and experiment is only fair, presumably due to the optically thin radiation assumption used in the model.

Structure is seen to have a significant effect on soot formation in the present flames, yielding permanently blue flames when Z_{st} is increased to 0.78. The permanently blue state is realized in Fig. 1d despite unfavorable hydrodynamics, where convection is towards the fuel. Flames (a) and (d) have almost identical measured temperatures and similar theoretical temperatures. Convection favors soot oxidation in Flame (a) and soot formation in Flame (d). Nonetheless, Flame (a) produces soot while Flame (d) does not, indicating that flame structure is responsible for the soot free conditions of Fig. 1d. Furthermore, the flame in Fig. 1b, which has $Z_{st} = 0.78$, is soot free.

The results of this study support the importance of flame structure on soot inception and permanently blue conditions. Nonetheless, the transient nature of the problem, as demonstrated by the numerical calculations, indicates that there are uncertainties. Microgravity tests in gas-jet flames indicate that steady soot concentrations require test times exceeding those of ground-based facilities. Furthermore, in the present brief tests, thermophoresis may cause soot formed during ignition to be trapped within the flame. Thus, longer microgravity test times are required and are being pursued.

FLAME EXTINCTION

The effects of Z_{st} on extinction of methane counterflow diffusion flames are shown in Figure 3, where numerical predictions of scalar dissipation rate at extinction (as characterized by $(\nabla Z)^2$ at Z_{st}) are plotted as a function of Z_{st} . Counterflow experiments have been performed to verify the model but are

not included here. The profound impact of Z_{st} is evident, with an almost 40 fold increase in scalar dissipation rate with Z_{st} . Furthermore, the flame temperature at extinction can be 140 °C lower when Z_{st} is increased from $Z_{st} = 0.055$ (methane/air) to 0.65. The minimum flame temperature at extinction occurs at the peak in scalar dissipation rate indicating that the flames at $Z_{st} = 0.65$ are very strong. This result is due to the shift in the oxygen profile into the high temperature region of the flame and the resulting increase in radical production, shown in Figs. 4 and 5. At $Z_{st} = 0.65$ the radical production region is coincident with the peak temperature, as seen in Fig. 5. For methane burning in air (Fig. 4) this is not the case and consequently much higher flame temperatures are required to sustain the flame. This interesting finding suggests that the $Z_{st} = 0.65$ flame is a better designed flame in that it more efficiently uses the high temperature of the flame for radical production.

This work was supported by NASA Grants NCC3-697, NAG3-1910, NCC3-696a, and NAG3-1912, with D. P. Stocker serving as Project Scientist. The assistance of S. A. Gokoglu, B. J. Goldstein, J. E. Pierce and H. D. Ross is duly appreciated.

REFERENCES

1. Du, J. and Axelbaum, R. L., *Combust. Flame* 100:367 (1995).
2. Du, J., and Axelbaum, R. L., *Proc. Combust. Inst.* 26:1137 (1996).
3. Chao, B. H., Liu, S. and Axelbaum, R. L., *Combust. Sci. Tech.* 138:105 (1998).
4. Lin, K. -C. and Faeth, G. M., *J. Prop. Power* 12:691 (1996).
5. Lin, K. -C. and Faeth, G. M., *J. Prop. Power* 12:10 (1996).
6. Lin, K. -C. and Faeth, G. M., *Combust. Flame* 115:468 (1998).
7. Sugiyama, G., *Proc. Combust. Inst.* 25:601 (1994).
8. Sunderland, P. B., Köylü, Ü. Ö., and Faeth, G. M., *Combust. Flame* 100:310 (1995).

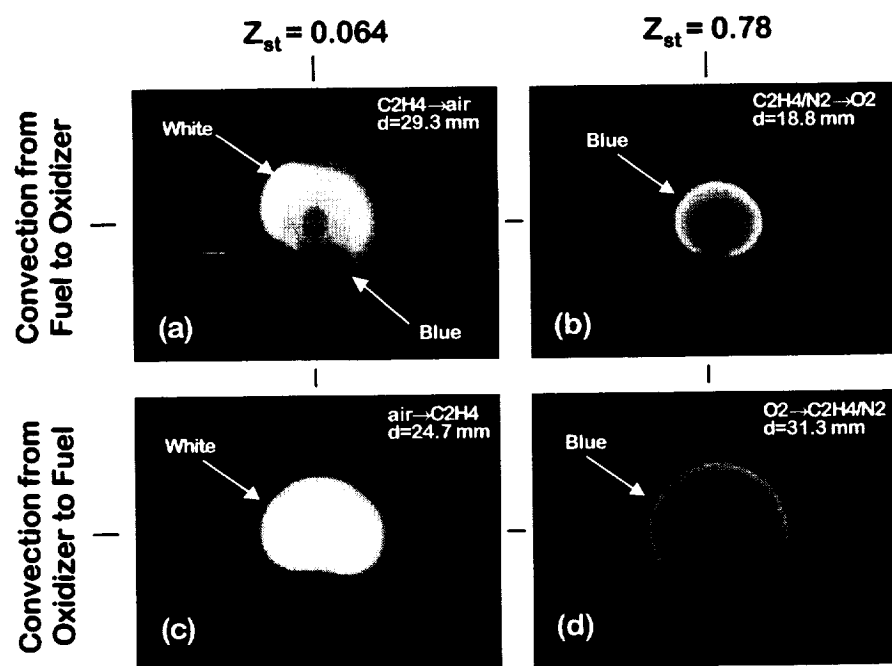


Fig. 1 Images of representative flames at the end of the 2.2 second drop: (a) ethylene (1.51 mg/s) issuing into air, fl.4; (b) diluted ethylene (19 mg/s) issuing into oxygen, fl.4; (c) air (22 mg/s) issuing into ethylene, fl.6; (d) oxygen (5.2 mg/s) issuing into diluted ethylene, fl.6. The scale is revealed by the 6.4 mm spherical burner. The ethylene consumption rate is 1.51 mg/s in all cases.

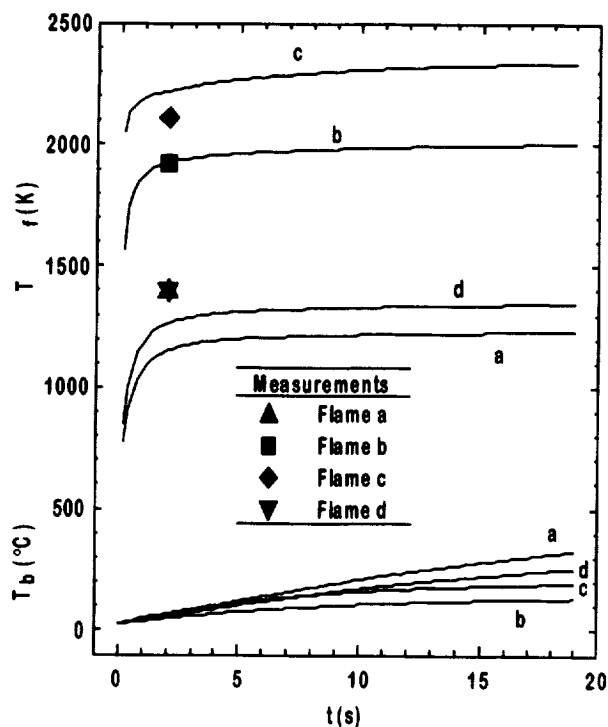


Fig. 2. Predicted flame temperature and burner temperature for flames (a) – (d). Also shown, by symbols, are measured peak temperatures after 2.2 s.

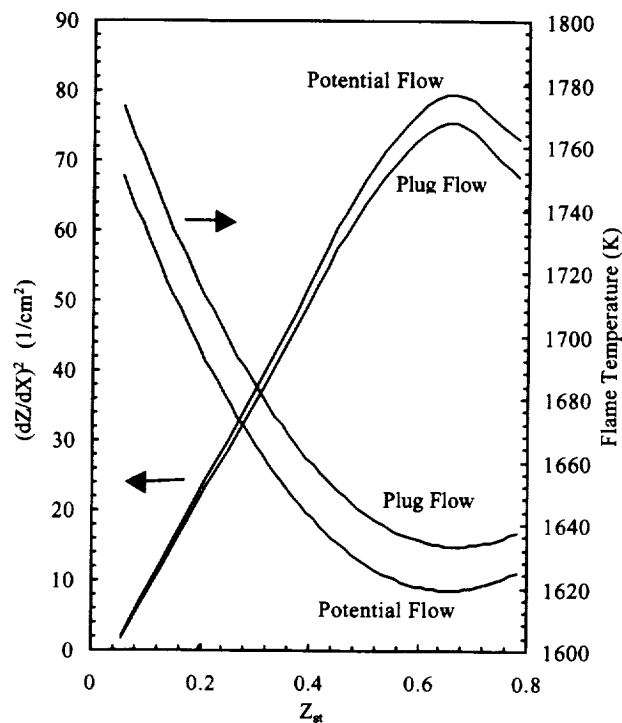


Fig. 3. Scalar dissipation rate (as characterized by $(\nabla Z)^2$ at Z_{st}) and flame temperature at extinction for methane.

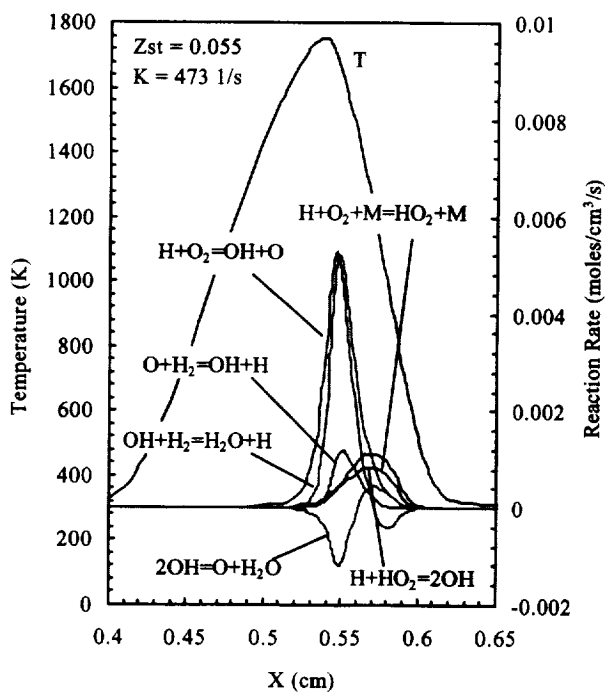


Fig. 4. Radical production rates and flame temperature distributions for a methane flame with $Z_{st} = 0.055$.

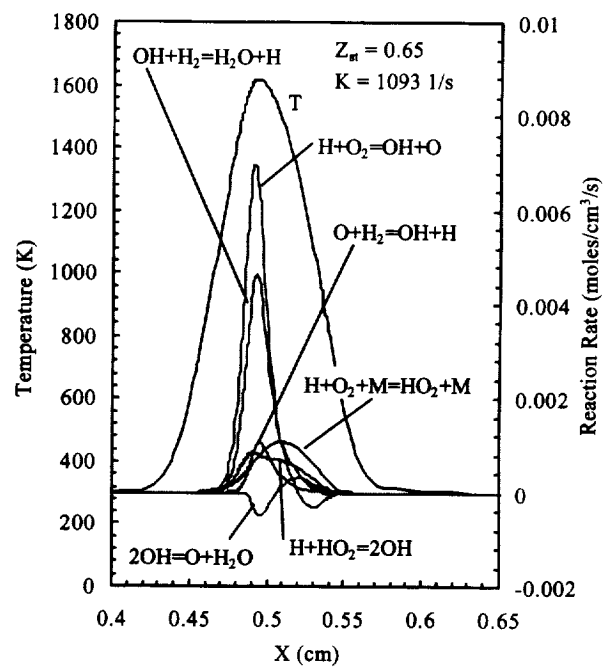


Fig. 5. Radical production rates and flame temperature distributions for a methane flame with $Z_{st} = 0.65$.

STRUCTURE AND STABILITY OF MICRO-BUOYANT SPHERICAL DIFFUSION FLAMES

C. K. Law¹, W. S. Yoo¹, E. W. Christiansen¹, and S. D. Tse²

¹Department of Mechanical and Aerospace Engineering
Princeton University, Princeton, NJ 08544

²Department of Mechanical and Aerospace Engineering
Rutgers, the State University of New Jersey, Piscataway, NJ 08854

ABSTRACT

The structure and stability of spherical diffusion flames were studied both experimentally and computationally. In order to observe a nearly-spherical flame under normal-gravity conditions, an "inverse" flame configuration at reduced pressures ($<0.25\text{atm}$) was used to minimize the density difference between the hot flame products and the surrounding ambient. This configuration produced stable low Grashof number (Gr) methane and hydrogen flames that were several centimeters in diameter. The resulting flames were imaged by an ultraviolet camera, with a narrow-band filter corresponding to electronically-excited OH (OH^*), and then deconvoluted to obtain the intensity profiles for chemiluminescent OH^* emission. For the weakly-buoyant methane flames, the flame structure was found to approximately scale as $Gr^{0.5}$. For the hydrogen flames, near-spherical flames were observed.

Near the extinction limits, flamefront instability was experimentally observed in the flames. However, it was not clear whether this instability was buoyancy induced or purely thermal-diffusive in nature. Thus, to better understand the mechanism for instability, the transient behavior of 1-D, spherical diffusion flames were computationally simulated using detailed chemistry and transport. Oscillatory instability was observed near both the high velocity induced limit (low mass flow rate) and the radiative induced limit (high mass flow rate) of the isola response of flame extinction. This oscillation typically grows in amplitude until it becomes large enough to extinguish the flame.

INTRODUCTION

The scaling for high Gr flames (based on boundary layer assumptions) is well established, with various combustion attributes proportional to $Gr^{0.25}$ [1,2], as verified by experiments, analytic methods, and computations. However, when Gr approaches unity, the problem becomes dramatically more difficult. Experimentally, either small or low-gravity systems, of sufficient size and duration, respectively, must be examined rigorously enough to ensure quality measurements. Analytically and computationally, the multi-dimensional, fully elliptical, and chemically reactive natures of the problem have, thus far, precluded solution for the physical scaling laws. Nonetheless, strong conceptual similarities do exist between the flame and the classical heat transfer problem (of a heated solid in a non-reactive field), as in the high Gr limit where both problems scale as $Gr^{0.25}$. For the classical heat transfer problem, at low Gr , the scaling goes as $Gr^{0.5}$ [3,4], and Law and Williams [5] have shown experimentally that in a combustion situation, low-buoyancy effects on the burning rate of droplets similarly scale as $Gr^{0.52}$. However, despite the favorable correlation and strong evidence that the scaling embodies

the underlying physics, additional experiments are needed to better resolve the issue, especially since it is not so obvious that the two problems should scale the same because, unlike the heated sphere case where the temperature profile is monotonic, the combustion case involves two distinct temperature profiles of opposite trend separated by the flame.

Furthermore, as extinction has been shown to occur in an oscillatory manner in $Le > 1$ premixed flames [6-8], it is not unreasonable to expect that extinction could occur in an unsteady manner for diffusion flames as well. Indeed, near-limit oscillations have been observed experimentally under microgravity conditions for both candle flames [9] and droplet flames [10]. Cheatham and Matalon [11] analytically investigated the unsteady behavior of diffusion flames with heat loss. They were able to identify an oscillatory regime which could be triggered by a sufficiently large Lewis number (even without heat loss) or in the presence of appreciable heat loss (even for $Le = 1$). In order to understand the dynamics of near-extinction limit diffusion flames, we have computationally simulated the unsteady behavior of the spherically-symmetric diffusion flame with radiative heat loss using detailed chemistry and transport.

EXPERIMENTAL RESULTS ON LOW GR FLAME SCALING

Flames were established by ejecting standard air (21%O₂/79%N₂) at four specific mass flow rates, $m = 0.063, 0.067, 0.070, 0.075$ g/s, into a pure methane environment at pressures ranging from 0.07atm to 0.3atm. Neglecting the dependence of flame temperature on pressure and gas composition, Gr becomes proportional to the square of the ambient pressure and to the volume of the flame. The flamefront position was assumed to correspond to the peaks of the OH* profiles obtained from the 2-D deconvoluted projections.

A typical methane OH* flame image and its deconvoluted image are shown in Fig. 1(a) and (b), respectively. Both the deconvoluted left (-) and right (+) images corresponding to the original "axisymmetric" projection are shown.

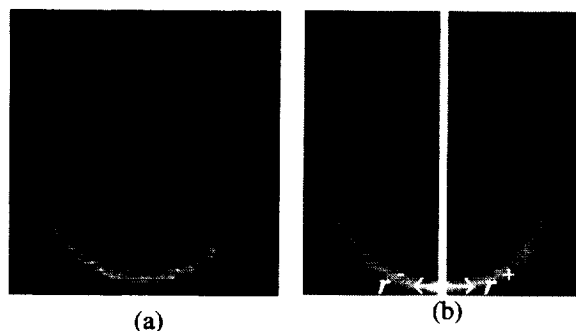


Figure 1: (a) Line-of-sight integral projection, (b) deconvoluted image of OH* emission for the methane flame. The gravity direction is ↓.

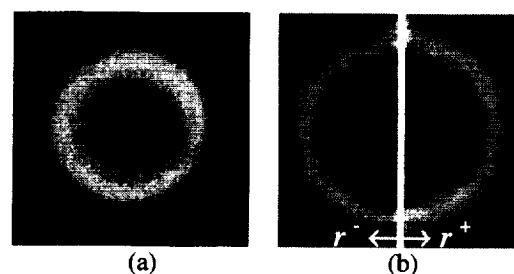


Figure 2: (a) Line-of-sight integral projection, (b) deconvoluted image of OH* for the hydrogen flame. The gravity direction is ↓.

A nearly-spherical hydrogen flame was formed by issuing a 9%O₂/91%N₂ mixture at a mass flow rate of 0.078g/s into a pure hydrogen environment at a chamber pressure of 0.079 atm. Figure 2(a) shows the OH* flame projection image, and Fig. 2(b) shows the deconvoluted image.

As in Ref. 1 for the boundary layer flame, Gr scaling was examined at the lateral and stagnation regions for the flamefront, where the lateral radius of the flame, R_l , was measured horizontally from the center of the burner to the side flamefront, while the stagnation radius, R_{st} , was measured vertically from the center of the burner to the bottom flamefront. In droplet burning [1], the instantaneous flame radius is scaled by the instantaneous droplet radius, which is

a natural length scale of the problem because the mass vaporization rate is proportional to the instantaneous surface area of the droplet. However, for the present problem, the mass flow rate is prescribed such that the natural length scale is the steady-state flame radius.

Flame deviation results from distortion by buoyant convection from its steady-state radius, the Gr dependence is hypothesized to follow $R_{l \text{ or } v}^{-1} = R_{ss}^{-1} + b Gr^c \approx R_{ss}^{-1} + b' (P^2 V)^c$.

To determine the exponent c , the experimental data were least-squared fit subject to the following constraints. For any given mass flow rate, the extrapolated steady-state radius (R_{ss}) at zero Gr is the same for R_l and R_v . Additionally, the extrapolated steady state radii for the different mass injection conditions must be proportional to the mass flow rate [12]. The volume (V) was taken to be the volume within the distribution of peak OH^* . Finally, the exponent c is constrained to be identical for all curve fits. A single fit collapses the experimental data, with the relevant flame dimensions scaling as Gr to 0.497 power.

COMPUTATIONAL RESULTS ON PULSATING INSTABILITY

To study the stability of spherical diffusion flames, we simulated a 50%CH₄/50%He into 21%O₂/79%He flame, employing helium as diluent in order to achieve larger than unity mixture Lewis numbers ($Le=2.3$ for the fuel and 1.9 for the oxidizer), thereby promoting the onset of instability. The spherically-symmetric unsteady diffusion flames were simulated using an appropriately modified version of the flame code developed by Kee *et al.* [13].

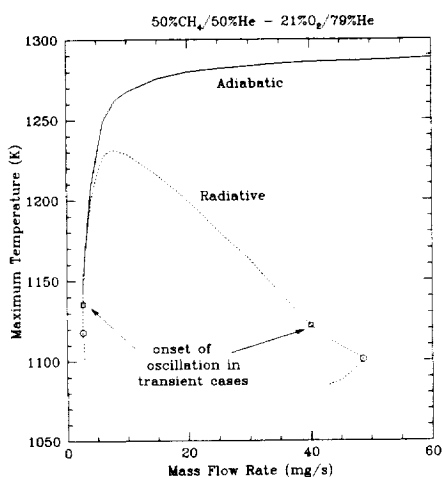


Figure 3: Maximum temperature in steady-state methane diffusion flames versus mass flow rate.

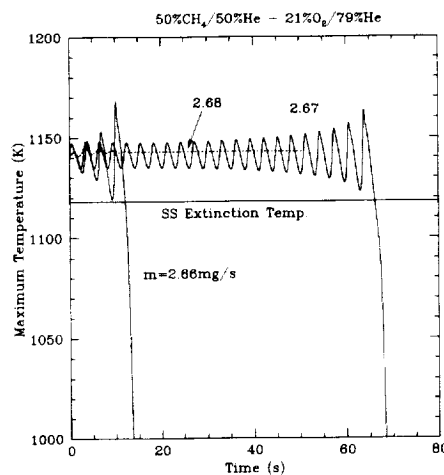


Figure 4: Maximum temperature as a function of time for methane diffusion flames.

The steady-state response curve for the mixture was first determined for both adiabatic flames and flames with radiative heat loss. The maximum flame temperature as a function of the mass flow rate is shown in Fig. 3. For the adiabatic flame, an extinction limit is reached as the mass flow rate (and hence Da) is decreased. The effect of radiative heat loss at low mass flow rates is negligible, and the two curves fall on top of one another, sharing the same turning point. However, at larger mass flow rates, the flame becomes larger in size, and the heat loss due to radiation becomes significant. Eventually, the heat loss due to radiation becomes sufficient to extinguish the flame. The square points on either end of the curve just before extinction mark the onset of oscillation discussed below.

Having determined the steady-state response of the methane diffusion flames, we then investigated the stability of these solutions by imposing a small (less than 1%) perturbation to the

temperature profile. Two distinct types of response were observed depending on the mass flow rate: 1) stable case where the perturbation is damped out and the flame approached the steady-state solution in an oscillatory manner, and 2) unstable case where the perturbation grows until the amplitude of oscillation became large enough to extinguish the flame. Figure 4 illustrates these two different types of behavior near the low mass flow rate extinction limit for the methane diffusion flame. The maximum temperature is plotted versus time for three mass flow rates: 2.68, 2.67 and 2.66mg/s. For the largest mass flow rate, the initial perturbation is damped out after a few oscillations. Reducing the mass flow rate results in an oscillation that grows in amplitude over several cycles until the flame eventually extinguishes. Finally, further reducing the mass flow rate prompts extinction after just a few cycles. Also shown in the figure is the maximum temperature of a flame at the steady-state turning point ($m=2.647\text{mg/s}$) as determined in Fig. 3. It appears that once the maximum flame temperature drops below this critical value during the course of oscillation, the flame cannot recover and extinction occurs.

CONCLUDING REMARKS

In the present study, weakly-buoyant flames generated by ejecting oxidizer mixture from a spherical porous burner into a pure methane/hydrogen environment at low pressures were analyzed using the OH* emission imaging system. The scaling of lateral and stagnation flamefront distances was determined to be $Gr^{0.50}$, similar to that of the heated sphere.

The steady-state and transient responses of spherically symmetric helium diluted methane diffusion flames were numerically simulated using detailed chemistry and transport, with and without radiative heat loss. Both the radiative and adiabatic steady-state results exhibited an extinction limit at small mass flow rates due to the short residence time through the small flames. At large mass flow rates, a radiative-induced extinction limit was observed that is not present in the adiabatic flames. Oscillatory behavior was observed near both limits and always led to extinction (no limit cycles were observed). However, the oscillations at some mass flow rates lasts longer than 320 cycles, suggesting this behavior could possibly be observed experimentally.

REFERENCES

- [1] Fernandez-Pello, A. C., and Law, C. K., *Combust. Flame*, 44:97-112 (1982).
- [2] Potter, J. M., and Riley, N., *Combust. Flame*, 39: 83-96 (1980).
- [3] Kurdyumov, V. N., and Liñán, A., *Int. J. Heat Mass Transfer*, 42:3849-3860 (1994).
- [4] Jia, H., and Gogos, G., *Int. J. Heat Mass Transfer*, 39: 1603-1615 (1999).
- [5] Law, C. K., and Williams, F. A., *Combust. Flame*, 19:393-405 (1972).
- [6] Dietrich, D. L., Ross, H. D., Frante, D. T., Tien, J. S., and Shu, Y., *4th Int. Microgravity Combustion Workshop*, NASA Conf. Publication 10194, (1997).
- [7] Nayagam, V. and Williams, F. A., *Seventh International Conference on Numerical Combustion*, York, England, (1998).
- [8] Cheatham, S., and Matalon, M., *Proc. Combust. Inst.*, 26:1063-1070, (1996).
- [9] Christiansen, E. C., Sung, C. J., and Law, C. K., *Proc. Combust. Inst.*, 27:555-562 (1999).
- [10] Christiansen, E. C., Law, C. K., and Sung, C. J., *Proc. Combust. Inst.*, 28 (2001), in press.
- [11] Christiansen, E. C., Sung, C. J., and Law, C. K., *Combust. Flame*, 124:35-49 (2001).
- [12] Tse, S. D., Zhu, D. L., Sung, C. J., and Law, C. K., AIAA-99-0585.
- [13] Kee, R. J., Grcar, J. F., Smooke, M. D., and Miller, J. A., *A Fortran Program for Modeling Steady Laminar One-Dimensional Premixed Flames*, Sandia Report SAND85-8240, 1985.

THE ONSET OF OSCILLATIONS IN NON-PREMIXED COMBUSTION

Moshe Matalon

McCormick School of Engineering and Applied Science,
Northwestern University, Evanston, IL 60208-3125
matalon@northwestern.edu

In a microgravity environment, molecular diffusion is the primary mechanism by which fuel and oxidizer that are initially separated are brought together to the reaction zone. Combustion systems in microgravity are therefore primed to diffusive-thermal instabilities. One such instability appears in the form of spontaneous oscillations. Oscillations were observed in condensed-phase fuels [1] and gas-jet diffusion flames [2], and in microgravity jet-flames [3], candle flames [4]-[5] and spherical flames surrounding large fiber-supported fuel droplets [6]. The nature of oscillations is quite different in each of these cases: the droplet flame exhibits radial oscillations, the edge of the candle flame is seen to move back and forth along the hemispherical flame surface and the jet-flame oscillations are primarily up and down along the axis. Despite these differences, associated mainly with the mode of oscillation, one may identify some common factors: in all cases the flame exhibits low-frequency oscillations, oscillations are only observed in special mixtures and their onset occur only at near-extinction conditions.

As in premixed systems, the disparity between the thermal diffusivity of the mixture and the molecular diffusivities of the fuel and oxidizer is responsible for the development of flame instabilities. While thermal diffusion tends to nullify temperature differences, and hence has a stabilizing influence, molecular diffusion may enhance these differences. It is known that a premixed system exhibits a cellular instability when the effective Lewis number¹ is below some critical value less than one, and a pulsating instability when the Lewis number is above a critical value larger than one. The situation in non-premixed systems, however, is more complex because there are now two effective Lewis numbers, associated with the fuel and oxidizer, and because the structure of a diffusion flame varies significantly with the Damköhler number D , representing the ratio of the diffusion to the chemical reaction times. When the Damköhler number is large, the reactants are completely consumed at a reaction sheet that separates a region of oxidant but no fuel from a region where there is only fuel. Since complete combustion dictated by the short chemical reaction time can only occur along the stoichiometric surface, any slight disturbance of the reaction sheet is obliterated and the flame is stable irrespective of the value of the Lewis numbers. For moderate values of the Damköhler number $D_{\text{ext}} < D < \infty$, with D_{ext} representing the extinction value, there is incomplete combustion with significant reactants leakage through the reaction zone. Preferential and differential diffusion, associated with non-unity and unequal Lewis numbers, may now lead to various forms of instability.

In this presentation, we summarize results based on a simple one-dimensional configuration in which one reactant (the fuel, say) is supplied in a uniform stream and the other (the oxidizer) is diffusing against the stream [8]. The objective has been to identify the basic mechanisms

¹ Based on the thermal diffusivity of the mixture, determined by the abundant component, and the molecular diffusivity of the deficient reactant.

responsible for the onset of oscillations. The simplicity of the model permits a comprehensive study that maps the entire range of parameters. In particular, we have examined the conditions for the onset of oscillations and their dependence on (i) the supply conditions, namely the mixture strength and the temperatures at which the fuel and oxidizer are introduced, (ii) the diffusion properties of the reactants represented by two distinct Lewis numbers, L_F and L_X , for the fuel and oxidizer, respectively and (iii) the dynamic properties lumped into a single parameter - the Damköhler number D .

An important auxiliary parameter that determines whether oscillations occur or not, is the heat transfer parameter γ , defined as the ratio of the excess heat conducted to one side of the reaction sheet to the total heat generated in the reaction zone. Generally, $-1 < \gamma < 1$ and when $\gamma = 0$ there are equal fluxes of heat directed away from the reaction sheet. More heat is transported to the fuel side when $\gamma < 0$ and to the oxidizer side when $\gamma > 0$. The degree of reactants leakage through the reaction sheet is determined by γ and the Lewis numbers; generally speaking, the fuel is the more completely consumed reactant when $\gamma < 0$ and the oxidizer is the more completely consumed reactant when $\gamma > 0$. For the planar flame considered here, the parameter γ takes a simple form when the fuel and oxidizer are supplied at the same temperature and the Lewis numbers are one. It then depends only on the mixture strength ϕ , defined as the ratio of the initial fuel to oxidizer mass fraction normalized by their stoichiometric proportions, and is given by $\gamma = (\phi - 1)/(\phi + 1)$. Thus, a fuel "rich" system corresponds to $\gamma > 0$; a fuel "lean" system to $\gamma < 0$. In general, γ depends on the Lewis numbers and on the supply-temperature differential ΔT .

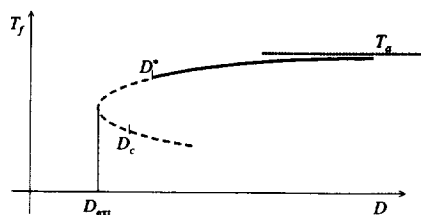


Figure 1

Our results indicate that oscillations occur when the reactant diffusing against the stream (the oxidizer in the present configuration) is the more completely consumed reactant, corresponding to a situation for which $\gamma > 0$, or a relatively "rich" system². Thus, for a given set of parameters corresponding to $\gamma > 0$ there exists a value of the Damköhler number $D^* > D_{ext}$ which identifies the onset of oscillations. The stable flames are

those extending from the Burke-Schumann solution with complete consumption ($D \rightarrow \infty$) down to the marginally stable state D^* , with the unstable states limited to $D_{ext} < D < D^*$. This is shown schematically in Fig. 1 where the dependence of the flame temperature T_f on the Damköhler number D is presented. Note that oscillations develop prior to but near extinction with the range of unstable states depending on the remaining parameters.

The primary mechanism responsible for oscillations appears to be the inability of the reactants to diffuse quickly enough to keep up with temperature fluctuations, namely when the Lewis numbers are sufficiently large (typically, but not necessarily larger than one). Neutral stability curves identifying regions of stable (above the curve) from unstable (below the curve) states, as a

² In "lean" systems, corresponding to $\gamma < 0$, another type of instability occurs; namely the development of cellular flames discussed in [7].

function of the Lewis numbers, are shown in Fig. 2 for $\phi = 1$ and $\Delta T = 0$. (The corresponding values of γ are in the range $0 < \gamma < 0.38$, depending on L_X). The figure shows, in particular, the range of unstable states expressed in terms of the Damköhler number relative to the extinction state. All states are stable when $D \rightarrow \infty$, as expected. For a given L_X , oscillations are possible only for a restricted range of L_F , and the range of unstable states grows as L_X increases.

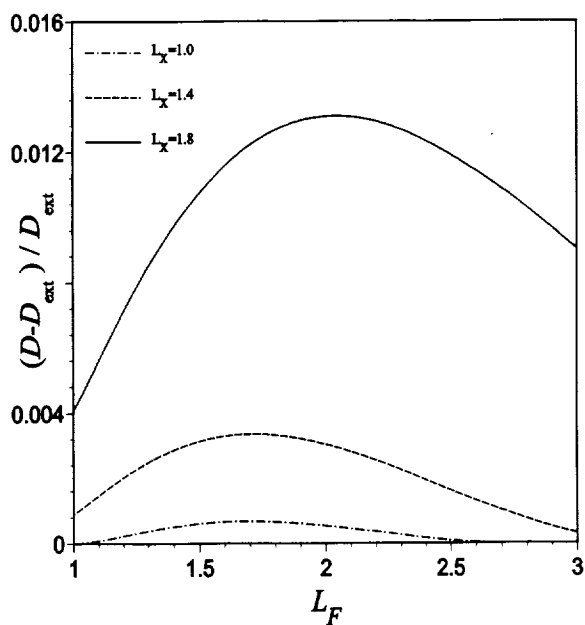


Figure 2

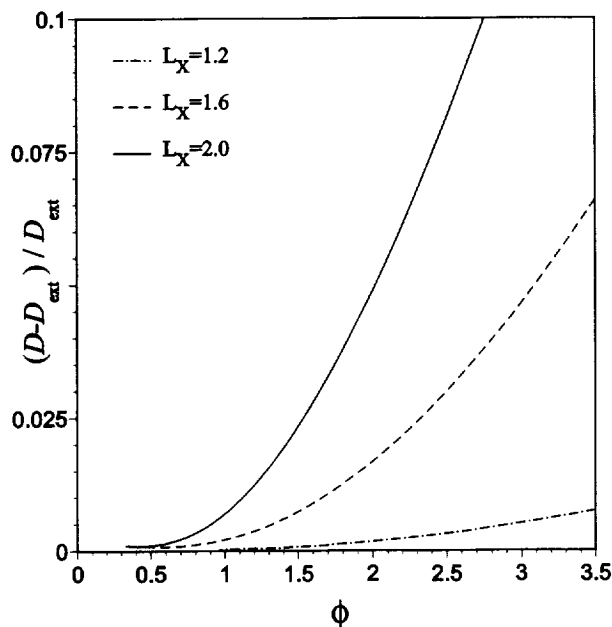


Figure 3

For conditions corresponding to $\gamma > 0$, the reaction sheet is located at a distance from the stoichiometric surface on the oxidizer side. If the reaction sheet is slightly perturbed toward the stoichiometric surface, the burning intensity increases with more heat generated. Due to the relatively large thermal diffusivity of the mixture, the temperature at the sheet drops at a faster rate than mass is being supplied to it, and for $\gamma > 0$ this imbalance is more pronounced on the oxidizer side. As a result, the reaction sheet tends to move back towards the stoichiometric surface, and possibly beyond its original location. Here the chemical reaction will be starving for fuel and the tendency, therefore, will be for the sheet to move back to the stoichiometric surface where again the burning intensity increases and the cycle continues. Heating the fuel relative to the temperature at which the oxidizer is supplied ($\Delta T < 0$) results in more heat transported to the oxidizer side and, according to the mechanism described, promotes the onset of oscillations. The reverse is expected when heating the oxidizer ($\Delta T > 0$). These tendencies are consistent with our predictions.

The predicted frequencies of oscillations at the onset of the instability are typically found in the range of 1-6 Hz, in accord with experiments. They grow larger when the onset occurs near the extinction limit ($D^* \approx D_{ext}$) and when the Lewis numbers are both near one.

An important conclusion from the present study is the importance of the mixture strength ϕ in promoting/suppressing the oscillations, as seen in Fig. 3. Stability curves, similar to the one presented in Fig. 2, show the effect of varying ϕ for selected values of L_X (drawn for $L_F = 1$ and $\Delta T = 0$). Similar to the experimental observations [2], it is seen that oscillations are more likely to occur ϕ is relatively large. It is evident from this figure that a small change in ϕ causes a much larger effect on promoting the oscillation, than any realistic variation in Lewis number would cause.

Experimental results [2] indicate that, for ϕ sufficiently large, oscillations will occur even if one of the Lewis numbers is slightly less than one. For example, oscillations were observed when pure methane was supplied in the fuel stream and the oxidizer stream was diluted with nitrogen, conditions corresponding to $\phi = 21.68$, $L_X = 1.11$ and $L_F = 0.81$. These results are not inconsistent with our theory; in fact, Fig. 1 clearly suggests that as L_X increases, for example, the range of unstable states will extend into regions where $L_F < 1$. We note that a similar behavior was also detected in [7] where the boundary for the cellular instability appears often to extend into a region of Lewis number bigger than one. A closer examination shows that this is indeed the case and that the critical fuel Lewis number, L_F^{cr} say, decreases with increasing L_X . This illustrates the importance of both Lewis numbers in identifying the conditions for the occurrence of oscillations.

The importance of heat losses in promoting flame oscillations has been previously recognized; see for example [9]-[11]. Indeed, our theory shows that a small amount of heat losses may induce oscillations under conditions where, in their absence, oscillations are not likely to occur. The effects of heat loss appear more pronounced especially when the mixture strength is relatively small, namely when the likelihood for oscillations is small.

ACKNOWLEDGMENTS

This work is being supported by the microgravity combustion program under NASA sponsorship; project NAG3-2511.

REFERENCES

1. Chan, W. & T'ien, J.S. 1978, *Combustion Science & Technology*, **18**, p. 139.
2. Furi, M., Papas, P., & Monkewitz, P.A. 2000, *Proceedings of the Combustion Institute*, **28**, p.
3. Hegde, U., Bahadori, M.Y. & Stocker, D.P. 1999, *AIAA Paper* 99-0582.
4. Dietrich D., Ross H. & Tien J.S. 1994, *AIAA Paper* 94-0429.
5. Ross, H.D., Sotos, R.G. & T'ien, J.S., 1991, *Combustion Science & Technology*, **75**, p. 155.
6. Nayagam, V. & Williams, F.A. 1998, Presented at the 7th Int. Conference on Numerical Combustion; York.
7. Cheatham S. & Matalon M. 2000, *J. Fluid Mechanics*, **414**, p. 105.
8. Kukuck S. & Matalon M. 2001, *Combustion Theory & Modeling*, to appear.
9. Kirkby, L.L. & Schmitz, R.A. 1966, *Combustion & Flame*, **10**, p. 205.
10. Cheatham S. & Matalon M. 1996, *Proceedings of the Combustion Institute*, **26**, p. 1063.
11. Golovanevsky, B., Levy Y., Greenberg J.B. & Matalon, M. 1999 *Combustion and Flame*, **117**(1/2), p. 373.

NUMERICAL SIMULATION OF AN ENCLOSED LAMINAR JET DIFFUSION FLAME IN MICROGRAVITY ENVIRONMENT: COMPARISON WITH ELF DATA

Kezhong Jia, Rajasekhar Venuturumilli, Brandon J. Ryan and Lea-Der Chen
Department of Mechanical Engineering, NADS, The University of Iowa, Iowa City, IA 52242

INTRODUCTION

Enclosed diffusion flames are commonly found in practical combustion systems, such as the power-plant combustor, gas turbine combustor, and jet engine after-burner. In these systems, fuel is injected into a duct with a co-flowing or cross-flowing air stream. The diffusion flame is found at the surface where the fuel jet and oxygen meet, react, and consume each other. In combustors, this flame is anchored at the burner (i.e., fuel jet inlet) unless adverse conditions cause the flame to lift off or blow out. Investigations of burner stability study the lift off, reattachment, and blow out of the flame.

Flame stability is strongly dependent on the fuel jet velocity. When the fuel jet velocity is sufficiently low, the diffusion flame anchors at the burner rim. When the fuel jet velocity is increased, the flame base gradually moves downstream. However, when the fuel jet velocity increases beyond a critical value, the flame base abruptly jumps downstream. When this "jump" occurs, the flame is said to have reached its lift-off condition and the critical fuel jet velocity is called the lift-off velocity. While lifted, the flame is not attached to the burner and it appears to float in mid-air. Flow conditions are such that the flame cannot be maintained at the burner rim despite the presence of both fuel and oxygen. When the fuel jet velocity is further increased, the flame will eventually extinguish at its blowout condition. In contrast, if the fuel jet velocity of a lifted flame is reduced, the flame base moves upstream and abruptly returns to anchor at the burner rim. The fuel jet velocity at reattachment can be much lower than that at lift off, illustrating the hysteresis effect present in flame stability, e.g., see Gollahalli et al. [2].

Although there have been numerous studies of flame stability [1-14], the controlling mechanisms are not well understood. This uncertainty is described by Pitts [3] in his review of various competing theories of lift off and blow out in turbulent jet diffusion flames. There has been some research on the stability of laminar flames [1,4-5], but most studies have focused on turbulent flames [2-3,6-14]. It is also well known that the airflow around the fuel jet can significantly alter the lift off, reattachment and blow out of the jet diffusion flame. Buoyant convection is sufficiently strong in 1-g flames that it can dominate the flow-field, even at the burner rim. In normal-gravity testing, it is very difficult to delineate the effects of the forced airflow from those of the buoyancy-induced flow. Comparison of normal-gravity and microgravity flames provides clear indication of the influence of forced and buoyant flows on the flame stability.

The overall goal of the Enclosed Laminar Flames (ELF) investigation (STS-87/USMP-4 Space Shuttle mission, November to December 1997) is to improve our understanding of the effects of buoyant convection on the structure and stability of co-flow diffusion flame, e.g., see <http://zeta.lerc.nasa.gov/expr/elf.htm>. The ELF hardware meets the experiment hardware limit of the 35-liter interior volume of the glovebox working area, and the 180x220-mm dimensions of the main

door. The ELF experiment module is a miniature, fan-driven wind tunnel, equipped with a gas supply system. A 1.5-mm diameter nozzle is located on the duct's flow axis. The cross section of the duct is nominally a 76-mm square with rounded corners. The forced air velocity can be varied from about 0.2 to 0.9 m/s. The fuel flow can be set as high as 3 std. cubic centimeter (cc) per second, which corresponds to a nozzle exit velocity of up to 1.70 m/s. The ELF hardware and experimental procedure are discussed in detail in Brooker et al. [20]. The 1-g test results are repeated in several experiments following the STS-87 Mission. The ELF study is also relevant to practical systems because the momentum-dominated behavior of turbulent flames can be achieved in laminar flames in microgravity. The specific objectives of this paper are to evaluate the use reduced model for simulation of flame lift-off and blowout.

NUMERICAL

The balance equations describing the transport of mass, momentum, energy, and individual species are solved using the computer program based on Sheu [16] and Sheu and Chen [17], as described in Jia [18]. The numerical scheme employs a control-volume discretization method, staggered, non-uniform grids, and semi-implicit fractional step time marching method. The flux corrected transport method is applied to convective flux, along with a Quadratic Upstream Interpolation for Convective Kinematics (QUICK) to produce monotonic results. The projection method is used to solve the pressure equation. The numerical scheme is of second-order accuracy in spatial discretization and first-order in temporal difference. A second-order time difference scheme is also used to test the first-order scheme. Essentially the same results of steady-state solution are obtained. Since steady-state solution is intended for the present study, the first-order scheme is used. An explicit scheme is used for the convection and an implicit scheme for the diffusive transport. A four-step reduced mechanism based on a fifty-step starting mechanism is used for calculation of the chemical reaction rate [16-18]. Seventeen species are considered: seven (CH_4 , H , H_2 , H_2O , CO , CO_2 and O_2) are independent reactive species and the remaining ten species (O , OH , C , CH , CH_2 , CH_3 , CHO , CH_2O , HO_2 and H_2O_2) are assumed to be steady-state species. Typical time step in the computation is set at 10 μs .

RESULTS AND DISCUSSION

The numerical simulation adopts a cylindrical enclosure of similar dimensions of the ELF hardware (70 mm in diameter and 166 mm in length): 35mm x 166mm. The simulation results discussed herein are focused at the prediction of ELF stability map. Numerical simulation successfully predicts stabilized, lifted and near blowout flames. For a fixed fuel jet velocity, the flame base moves to downstream locations when the co-flowing air velocity is increased. Further increase the co-flowing air velocity, the flame eventually reaches the blowout condition. Prior to the blowout, the flame length decreases, and a "tulip" like flame "tail" is predicted as well as a "disk" like flame shape just before the blowout condition is reached. It should be noted that the discussion of the flame shape is based on the simulation, as well as experimental, results obtained for the enclosed laminar flame studied.

Figure 1 shows the blowout map comparison between the numerical and the experimental results. Up to the fuel jet velocity of 1.0 m/s, the numerical prediction qualitatively agrees with the experiment results. However, the numerical calculation predicts a higher air velocity for the blowout to occur than that observed in the experiment. The numerical simulation predicts that, as shown in the experimental results,

lower air velocities can cause the flame blowout when the fuel jet velocity is sufficiently high. However, because the tremendous computation time is needed to complete a simulation, the data for higher fuel velocity (greater than 1.0 m/s), and simulation for the 1g conditions continues. An important experience we wish to share with the readers is that the simulation results defining the blowout are highly grid dependent. Specifically, numerical error results in an erroneous "nearly stationary" flame and a "second branch" in the combustion efficiency curve. Without careful examination of numerical error, the "nearly stationary" flame might have been identified as the solution describing the "nearly stationary flame" that was observed in some of the experimental condition prior to the blowout. To address the numerical error, a Local Uniform Grid Refinement (LUGR) method based on an algorithm suggested by Trompert is implemented to the flame code. A test case using three grid configurations is shown in Fig. 2. As an example, the calculated oxygen concentration along the centerline of the flow is shown in Fig. 3. The calculation is based on a reduced four-step mechanism. Encouraging results are obtained, and effort continues to study the flame stability in both 1-g and μ -g environments.

Acknowledgments

This work is supported by NASA Microgravity Science and Applications Division, Grant No. Grant No. NCC3-666, under the technical management of D.P. Stocker and M.K. King. The ELF investigation is carried out by Mission Specialists, Dr. Kalpana Chawla (NASA) and Dr. Takao Doi (NASDA) during the STS-87 mission. Members of ELF science teams are Dennis Stocker, John Brooker and L.D. Chen.

References

1. Chung, S.H. and Lee, B.J. Combust. Flame, 86:62-72 (1991).
2. Gollahalli, S.R., Savas, Ö. Huang, R.F., and Rodriguez Azara, J.L. Twenty-First Symposium (International) on Combustion, The Combustion Institute, Pittsburgh, 1986, pp. 1463-1471.
3. Pitts, W.M. Twenty-Second Symposium (International) on Combustion, The Combustion Institute, Pittsburgh, 1989, pp. 809-816.
4. Savas, Ö. and Gollahalli, S.R. J. Fluid Mech., 165:297-318 (1986).
5. Lee, B.J., Cha, M.S., and Chung, S.H. Combust. Sci. and Tech., 127:55-70 (1997).
6. Dahm, W.J.A. and Mayman, A.G., AIAA Journal, 28:7:1157-1162 (1990).
7. Feikema, D., Chen, R.-H. and Driscoll, J.F. Combust. Flame, 80:183-195 (1990).
8. Feikema, D., Chen, R.-H. and Driscoll, J.F. Combust. Flame, 86:347-358 (1991).
9. Whol, K. Kapp, N.M., and Gazley, C. Third Symposium on Combustion and Flame and Explosion Phenomena, The Williams & Wilkins Co., Baltimore, 1949, pp. 3-21.
10. Scholefield, D.A. and Garside, J.E. Third Symposium on Combustion and Flame and Explosion Phenomena, The Williams & Wilkins Co., Baltimore, 1949, pp. 102-110.
11. Kalghatgi, G.T. Combust. Sci. and Tech., 26:233-239 (1981).
12. Kalghatgi, G.T. Combust. Sci. and Tech., 41:17-29 (1984).
13. Takahashi, F., Mizomoto, M., Ikai, S., and Futaki, N. Twentieth Symposium (International) on Combustion, The Combustion Institute, Pittsburgh, 1984, pp. 295-302.

14. Eickhoff, H., Lenze, B., and Leuckel, W. Twentieth Symposium (International) on Combustion, The Combustion Institute, Pittsburgh, 1984, pp. 311-318.
15. Burke, S.P. and Schumann, T.E.W. Ind. Eng. Chem., 20:998-1004 (1928).
16. Sheu, J.C., "Numerical Simulation of Burke-Schumann Diffusion Flame Using Finite-Rate Chemical Kinetics," Ph. D. Dissertation, The University of Iowa, Iowa City, Iowa (1996).
17. Sheu, J.-C. and Chen, L.-D., AIAA J., Vol. 34, No. 10, pp. 2090-2098 (1996).
18. Jia, K., "The Structure and Stability of Enclosed Laminar Jet Diffusion Flame," Ph. D. Dissertation, The University of Iowa, Iowa City, Iowa (1999).
19. Sheu, J.-C. and Chen, L.-D., AIAA Paper 2000-690 (2000).
20. John E. Brooker, Dennis P. Stocker, K. Jia, L.-D., Chen, in Fifth International Microgravity Combustion Workshop, NASA/CP-1999-208917, pp. 97-100 (1999)

ACKNOWLEDGEMENTS

This work is supported by NASA Microgravity Science and Applications Division, Grant No. Grant No. NCC3-666, under the technical management of D.P. Stocker and M.K. King. The ELF investigation is carried out by Mission Specialists, Dr. Kalpana Chawla (NASA) and Dr. Takao Doi (NASDA) during the STS-87 mission. Members of ELF science teams are Dennis Stocker, John Brooker and L.D. Chen.

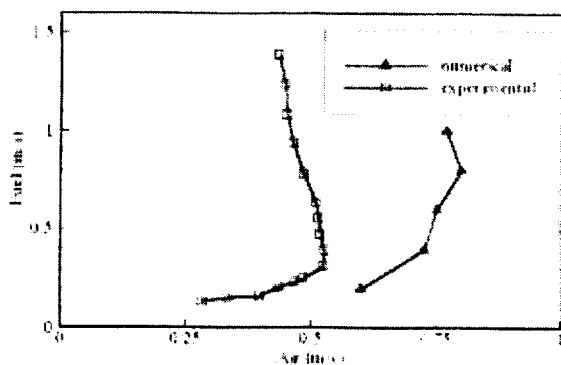


Figure 1. Comparison of blow-out conditions.

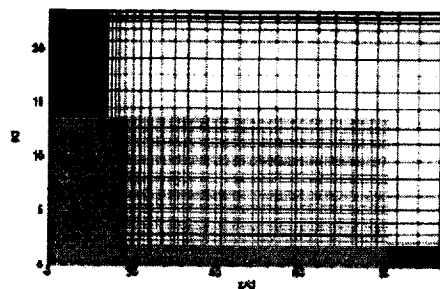


Figure 2. LUGR grid specification.

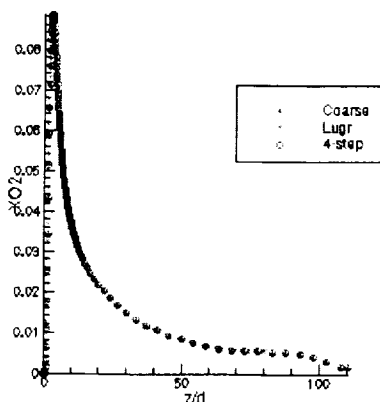


Figure 3. Comparison of calculated oxygen concentration along the centerline of the jet.

STRUCTURE AND EARLY SOOT OXIDATION PROPERTIES OF LAMINAR DIFFUSION FLAMES

A. M. El-Leathy, F. Xu and G. M. Faeth
Department of Aerospace Engineering
The University of Michigan
Ann Arbor, Michigan

INTRODUCTION

Soot is an important unsolved problem of combustion science because it is present in most hydrocarbon-fueled flames and current understanding of the reactive and physical properties of soot in flame environments is limited. This lack of understanding affects progress toward developing reliable predictions of flame radiation properties, reliable predictions of flame pollutant emission properties and reliable methods of computational combustion, among others. Motivated by these observations, the present investigation extended past studies of soot formation in this laboratory (refs. 1-12), to consider soot oxidation in laminar diffusion flames using similar methods, see ref. 13 for a detailed description of the study.

Early work showed that O_2 was responsible for soot oxidation in high temperature O_2 -rich environments (refs. 14-18). Subsequent work in high temperature flame environments having small O_2 concentrations (refs. 19 and 20), however, showed that soot oxidation rates substantially exceeded estimates based on the classical O_2 oxidation rates of Nagle and Strickland-Constable (ref. 14) and suggests that radicals such as O and OH might be strong contributors to soot oxidation for such conditions. Neoh et al. (refs. 20 and 21) subsequently made observations in premixed flames, supported by later work (refs. 22-25), that showed that OH was responsible for soot oxidation at these conditions with a very reasonable collision efficiency of 0.13. Subsequent studies in diffusion flames, however, were not in agreement with the premixed flame studies: they agreed that OH played a dominant role in soot oxidation in flames, but found collision efficiencies that varied with flame conditions and were not in good agreement with each other (refs. 26-30) or with Neoh et al. (refs. 20 and 21). One explanation for these discrepancies is that optical scattering and extinction properties were used to infer soot structure properties for the studies of refs. 26-30 that have not been very successful for representing the optical properties of soot, see refs. 2-4 and references cited therein. Whatever the source of the problem, however, these differences among observations of soot oxidation in premixed and diffusion flames clearly must be resolved. Motivated by these findings, the present study undertook measurements of soot and flame properties within the soot oxidation region of some typical laminar diffusion flames and exploited the new measurements to identify soot oxidation mechanisms for these conditions. Present considerations were limited to the early stages of soot oxidation (carbon consumption less than 70%) where reactions at the surface of primary soot particles dominate the process, rather than the later stages when particle porosity and internal particle oxidation become important as discussed by Neoh et al. (ref. 22).

EXPERIMENTAL METHODS

Measurements were obtained along the axes of nonpremixed laminar flames involving acetylene, ethylene, propylene and propane as the fuels burning in coflowing air at atmospheric pressure. The burner was directed vertically upward, to yield flames having luminous flame lengths of roughly 100 mm. The following measurements were made: soot volume fractions using deconvoluted laser extinction, flow temperatures using deconvoluted multilane emission, soot structure using thermophoretic sampling and TEM analysis, concentrations of major gas species using sampling and gas chromatography, concentrations of some radical species (H, OH and O) using the deconvoluted Li/LiOH atomic absorption technique and streamwise velocities using laser velocimetry.

RESULTS AND DISCUSSION

Soot and Flame Structure. All soot particles were the same as observed during earlier work in both laminar premixed and diffusion flames (refs. 1-12). They consisted of roughly spherical primary particles that were nearly monodisperse at each flame condition and collected into mass fractal aggregates having large variations of the number of primary particles per aggregate.

Present observations of flame structure were similar to earlier observations in laminar jet diffusion flames (refs. 2,3,11,12); a typical example is illustrated in Fig. 1. Flow velocities, u , increase with distance due to effects of buoyancy yielding a nonlinear variation of residence time with distance. Effects of radiant heat loss are substantial, yielding relatively flat temperature, T , distributions with maximum values well below adiabatic flame temperatures. Primary soot diameters, d_p , reach a maximum early in the soot formation region due to combined effects of soot nucleation, growth and oxidation. The original fuel disappears due to effects of decomposition, oxidation and soot formation (the last being relatively minor). Robust fuel-like species, however, persist throughout the soot formation region, e.g., C_2H_2 , C_2H_4 , CH_4 and H_2 . Concentrations of radicals, e.g., H , OH and O , increase as the flame sheet is approached. Unlike premixed flames where radical concentrations are nearly in thermodynamic equilibrium (ref. 10), however, radicals exhibit superequilibrium ratios generally in excess of 10 in the present diffusion flames.

Soot Surface Oxidation Rates. Measured soot surface oxidation rates were corrected for effects of soot growth using the expression based on the Colket and Hall (ref. 31) soot surface growth mechanism. No condition was considered, however, where the correction for soot growth was more than half the gross soot oxidation rate. Similar to Neoh et al. (refs. 21 and 22), present soot oxidation rates (corrected for soot growth) were converted into collision efficiencies (or reaction probabilities) based on kinetic theory estimates of the collision rates of a given gas species with the surface of primary soot particles, see refs. 13, 21 and 22 for detailed descriptions of computations of collision efficiencies.

Collision efficiencies for soot oxidation were found for O_2 , CO_2 , H_2O , O and OH , see ref. 13 for all these results; present results will be limited to collision efficiencies as a function of height for O_2 , CO_2 and OH as examples. The collision efficiencies of O_2 illustrated in Fig. 2 include the range of values measured by Neoh et al. (refs. 21 and 22) in premixed flames, the values found from the present experiments in diffusion flames, and values estimated from the predictions of Nagle and Strickland-Constable (ref. 14) for the conditions where present observations were made in diffusion flames. The Nagle and Strickland-Constable approach is known to be effective when soot oxidation is dominated by O_2 (i.e., when radical concentrations are small) and there are significant concentrations of O_2 along the present soot paths, see Fig. 1. Thus, the fact that Nagle and Strickland-Constable estimates of the O_2 collision efficiencies are 10-100 times smaller than present measurements strongly suggests that some other species is mainly responsible for soot oxidation in the present flames. The large scatter (nearly a range of 100) of the collision efficiencies for the flames illustrated in Fig. 2 also support the conclusion that O_2 is not the main oxidizing species of soot for the present flame environments.

The collision efficiencies of CO_2 for soot oxidation are plotted in Fig. 3. Results shown on the figure include the range of values observed by Neoh et al. (ref. 21) in premixed flames, and values from the present investigation in diffusion flames both considering and ignoring the contribution of O_2 (estimated using the correlation of ref. 14). Clearly, allowing for direct oxidation by O_2 has little effect on the collision efficiencies estimated in Fig. 3. In addition, the overall scatter of the CO_2 collision efficiencies approaches 1000 for the range of test conditions considered in Fig. 3. Taken together, these findings do not support CO_2 as a major contributor to soot oxidation in flames, either alone or in parallel with soot oxidation by O_2 . Similar considerations yielded the same finding for the collision efficiencies of H_2O and O .

Finally, the collision efficiencies of OH for soot oxidation are plotted in Fig. 4 in the same manner as the results for CO_2 in Fig. 3. Direct oxidation of soot by O_2 is not very

important for the present flames, as before. On the other hand, the combined results in premixed and diffusion flames exhibit rather small levels of scatter (roughly a factor of 3). Thus, the results in premixed and diffusion flames are in remarkably good agreement, e.g., the present mean OH collision efficiency in diffusion flames of 0.10 (with a standard deviation of 0.07) is not statistically different from the value of 0.13 measured by Neoh et al. (ref. 21) in premixed flames. These findings are helpful but the final stage of oxidation in diffusion flames (for carbon consumption larger than 70%), where primary particle porosity and internal particle oxidation become factors, must still be resolved.

ACKNOWLEDGMENTS

This research was sponsored by NASA Grant NAG3-1878 under the technical management of Z. G. Yuan of the National Center for Microgravity Research, NASA Glenn Research Center, Cleveland, Ohio.

REFERENCES

1. Sunderland, P.B., et al., *Combust. Flame* 96:97 (1994).
2. Sunderland, P.B., Köylü, Ü.Ö. and Faeth, G.M., *Combust. Flame* 100:310 (1995).
3. Sunderland, P.B. and Faeth, G.M., *Combust. Flame* 105:132 (1996).
4. Lin, K.-C., Sunderland, P.B. and Faeth, G.M., *Combust. Flame* 104:369 (1996).
5. Urban, D.L. et al., *AIAA J.* 36:1346 (1998).
6. Lin, K.-C. et al., *Combust. Flame* 116:415 (1999).
7. Lin, K.-C. and Faeth, G.M., *AIAA J.* 37:759 (1999).
8. Xu, F., Sunderland, P.B. and Faeth, G.M., *Combust. Flame* 108:1471 (1997).
9. Xu, F., Lin, K.-C. and Faeth, G.M., *Combust. Flame* 115:195 (1998).
10. Xu, F. and Faeth, G.M., *Combust. Flame* 121:640 (2000).
11. Xu, F. and Faeth, G.M., *Combust. Flame*, in press.
12. El-Leathy, A.M., Xu, F. and Faeth, G.M., *Combust. Flame*, in preparation.
13. Xu, F., El-Leathy, A.M. and Faeth, G.M., *Combust. Flame*, submitted.
14. Nagle, J. and Strickland-Constable, R.F., *Proc. Fifth Carbon Conf.* 1:154 (1962).
15. Rosner, D.E. and Allendorf, H.D., *AIAA J.* 6:658 (1968).
16. Wright, F.J., *Proc. Combust. Inst.* 15:1449 (1974).
17. Radcliffe, S.W. and Appleton, J.P., *Combust. Sci. Tech.* 4:171 (1971).
18. Park, C. and Appleton, J.P., *Combust. Flame* 20:369 (1973).
19. Fenimore, C.P. and Jones, C.W., *J. Phys. Chem.* 71:593 (1967).
20. Mulcahy, M.F.R. and Young, B.C., *Carbon* 13:115 (1975).
21. Neoh, K.G., Howard, J.B. and Sarofim, A.F., *Particulate Carbon* (D.C. Siegla and B.W. Smith, ed.), Plenum Press, New York, 1980, p. 261.
22. Neoh, K.G., Howard, J.B. and Sarofim, A.F., *Proc. Combust. Inst.* 20:951 (1984).
23. Wicke, B.C., Wong, C. and Grady, K.A., *Combust. Flame* 66:37 (1986).
24. Wicke, B.C. and Grady, K.A., *Combust. Flame* 69:185 (1987).
25. Roth, P., Brandt, O. and von Gersum, S., *Proc. Combust. Inst.* 23:1485 (1990).
26. Garo, A., Lahaye, J. and Prado, G., *Proc. Combust. Inst.* 21:1023 (1986).
27. Garo, A., Prado, G. and Lahaye, J., *Combust. Flame* 79:226 (1990).
28. Puri, R., Santoro, R.J. and Smyth, K.C., *Combust. Flame* 97:125 (1994).
29. Puri, R., Santoro, R.J. and Smyth, K.C., *Combust. Flame* 102:226 (1995).
30. Hardiquert, M. et al., *Combust. Flame* 111:338 (1997).
31. Colket, M.B. and Hall, R.J., *Soot Formation in Combustion* (H. Bockhorn, ed.), Springer-Verlag, Berlin, 1994, p. 442.

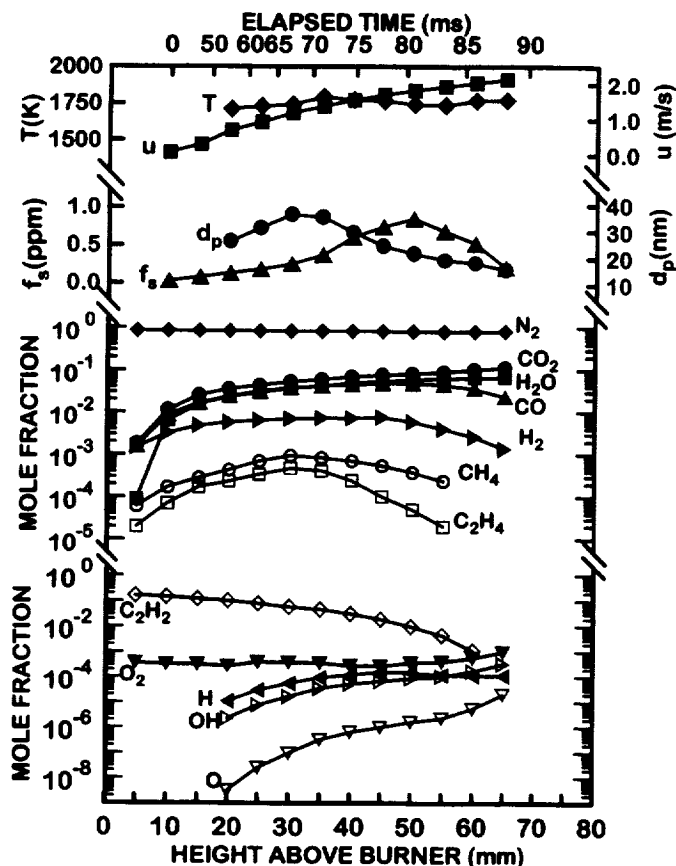


Fig. 1. Measured soot and flame properties along the axis of an acetylene/air laminar jet diffusion flame at atmospheric pressure.

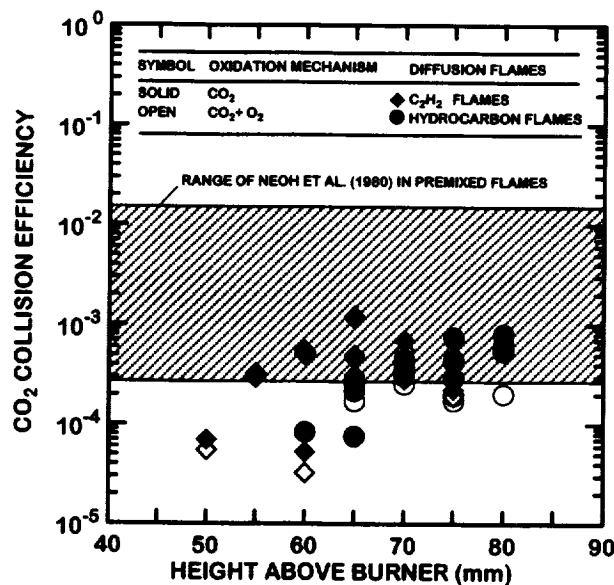


Fig. 3. Collision efficiencies assuming soot burnout due to attack by CO_2 . Found from refs. 13 and 21.

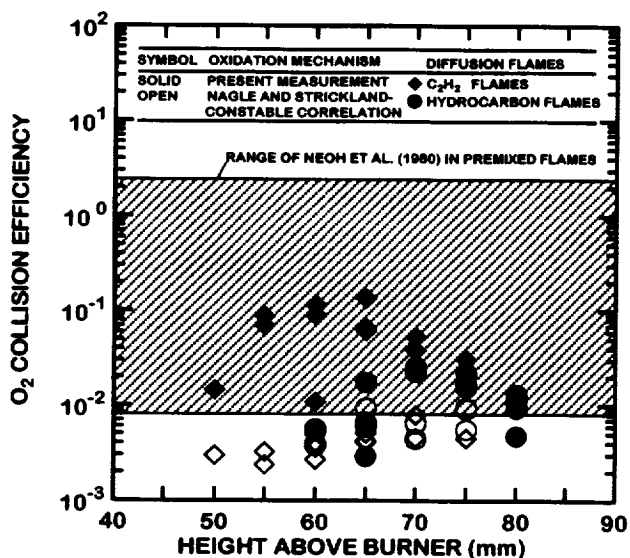


Fig. 2. Collision efficiencies assuming soot burnout due to attack by O_2 . Found from refs. 13, 14 and 21.

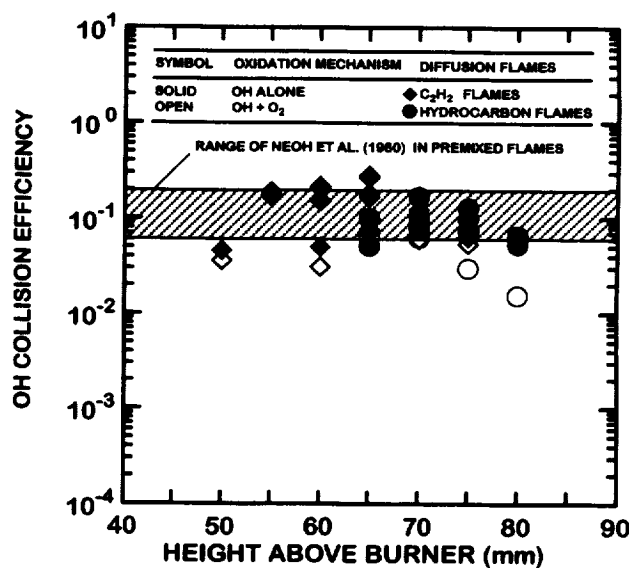


Fig. 4. Collision efficiencies assuming soot burnout due to attack by OH . Found from refs. 13 and 21.

SUPPRESSION OF SOOT FORMATION AND SHAPES OF LAMINAR JET DIFFUSION FLAMES

F. Xu, Z. Dai and G. M. Faeth
Department of Aerospace Engineering
The University of Michigan
Ann Arbor, Michigan

INTRODUCTION

Laminar nonpremixed (diffusion) flames are of interest because they provide model flame systems that are far more tractable for analysis and experiments than practical turbulent flames. In addition, many properties of laminar diffusion flames are directly relevant to turbulent diffusion flames using laminar flamelet concepts. Finally, laminar diffusion flame shapes have been of interest since the classical study of Burke and Schumann (ref. 1) because they involve a simple nonintrusive measurement that is convenient for evaluating flame shape predictions. Motivated by these observations, the shapes of round hydrocarbon-fueled laminar jet diffusion flames were considered, emphasizing conditions where effects of buoyancy are small because most practical flames are not buoyant.

Earlier studies of shapes of hydrocarbon-fueled nonbuoyant laminar jet diffusion flames considered combustion in still air and have shown that flames at the laminar smoke point are roughly twice as long as corresponding soot-free (blue) flames and have developed simple ways to estimate their shapes (refs. 2-5). Corresponding studies of hydrocarbon-fueled weakly-buoyant laminar jet diffusion flames in coflowing air have also been reported, see refs. 6 and 7 and references cited therein. These studies were limited to soot-containing flames at laminar smoke point conditions and also developed simple ways to estimate their shapes but the behavior of corresponding soot-free flames has not been addressed. This is unfortunate because ways of selecting flame flow properties to reduce soot concentrations are of great interest (refs. 8 and 9); in addition, soot-free flames are fundamentally important because they are much more computationally tractable than corresponding soot-containing flames. Thus, the objectives of the present investigation were to observe the shapes of weakly-buoyant laminar jet diffusion flames at both soot-free and smoke point conditions and to use the results to evaluate simplified flame shape models. The present discussion is brief, see refs. 9 and 10 for complete details.

SOOT FORMATION IN COFLOWING JET DIFFUSION FLAMES

Soot-free diffusion flames can be achieved by subjecting fuel jets to strong air coflow similar to air atomization processes (refs. 9 and 10). This can be seen from the sketch of a nonbuoyant coflowing laminar jet diffusion flame appearing in Fig. 1. The figure shows the flame sheet, the soot formation region at fuel-rich conditions, the soot oxidation region at fuel-lean conditions and flow streamlines. Later results will show that the length of the flame sheet is set by the fuel flow rate independent of coflow velocity at large coflows which implies that residence times for soot formation are inversely proportional to the air coflow velocity. Thus, increasing the coflow velocity inhibits soot formation and eventually leads to the soot-free flames that were sought during the present study.

EXPERIMENTAL METHODS

Measurements were carried out in a windowed chamber at low pressures to minimize effects of buoyancy. A coaxial tube burner was used, directed vertically upward, with fuel flow along the axis.

THEORETICAL METHODS

Simplified analysis of flame shapes for flames in still gases (ref. 4) was extended to treat coflow (ref. 7) assuming steady axisymmetric nonbuoyant flow, negligible radiation, thin flame sheet, equal mass diffusivities and specific heats of all species, boundary layer flow and constant properties. This yields the following expression for flame length, L_f , relative to a virtual origin, L_o (ref. 7):

$$(L_f - L_o)/d = C_f C_n \text{Re} Sc/Z_{st} \quad (1)$$

where d = burner diameter, Re = burner Reynolds number, Z_{st} = stoichiometric mixture fraction and $C_n = 3/32$ and $2/32$ for weak and strong coflow and $C_f = 1/2$ and 1 for soot-free and laminar smoke point flames. See ref. 7 for the formulation for flame shape and the algorithm for computing flame properties.

RESULTS AND DISCUSSION

Laminar Soot Points. The variation of the laminar soot-point and lift-off conditions, as a function of fuel and air flow rates and pressure, are illustrated in Fig. 2 for ethylene/air flames; results for other fuels were similar. The results show that increasing the air coflow velocity progressively increases the laminar soot-point fuel flow rate until the lift-off limit is reached. Increasing pressure, however, reduces the effect of coflow velocity because effects of buoyancy intrude and modifies the flow to enhance soot formation. Increasing pressure also increases the coflow velocity at lift off. Taken together, it is clear that coflow extends the range of soot-free operation, particularly when effects of buoyancy are small.

Luminous Flame Lengths. Measurements and predictions of luminous flame lengths for weakly-buoyant flames in strong coflow and for nonbuoyant flames in still air are illustrated in Fig. 3. Results are shown for both soot-free and smoke-point flames. It is clear that Eq. (1) provides excellent correlations of flame lengths conditions that are considered.

Shapes of Soot-Free Flames. Some measured and predicted luminous flame shapes in strong coflow are illustrated in Fig. 4. Two sets of measurements are shown: (1) colored photographs of the outer boundary of the strong blue reaction zone (involving CO_2 and OH emissions at fuel-lean condition), and (2) colored photographs taken with a filter for the CH line whose outer boundary should be close to the flame sheet. Both measurements yield similar results which are in remarkably good agreement with predictions. Similar results were obtained at other flame conditions, see ref. 10.

ACKNOWLEDGMENTS

This research was sponsored by NASA Grant No. NCC3-661 under the technical management of Z.-G. Yuan of the National Center for Microgravity Research, NASA Glenn Research Center, Cleveland, Ohio.

REFERENCES

1. Burke, S.P., and Schumann, T.E.W., *Ind. Engr. Chem.* 20:998 (1928).
2. Spalding, D.E., *Combustion and Mass Transfer*, Pergamon Press, New York, 1979, p. 185.
3. Sunderland, P.B. et al., *Combust. Flame* 116:376 (1999).
4. Lin, K.-C. et al., *Combust. Flame* 116:415 (1999).
5. Urban, D.L. et al., *AIAA J.* 36:1346 (1998).
6. Malingham, S. et al., *Combust. Flame* 82:231 (1994).

7. Lin, K.-C. and Faeth, G.M., *AIAA J.* 37:759 (1999).
8. Lin, K.-C. and Faeth, G.M., *J. Prop. Power* 12:691 (1996).
9. Dai, Z. and Faeth, G.M., *Proc. Combust. Inst.*, in press.
10. Xu, F., Dai, Z. and Faeth, G.M., *AIAA J.*, submitted.

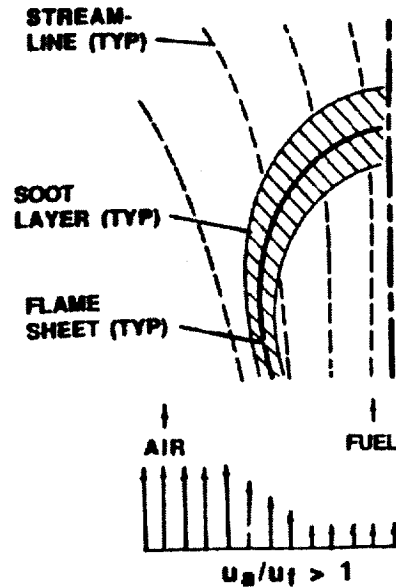


Fig. 1. Effect of reactant stream velocities on soot properties in laminar co-flowing jet diffusion flames having uniform initial air and fuel velocities.

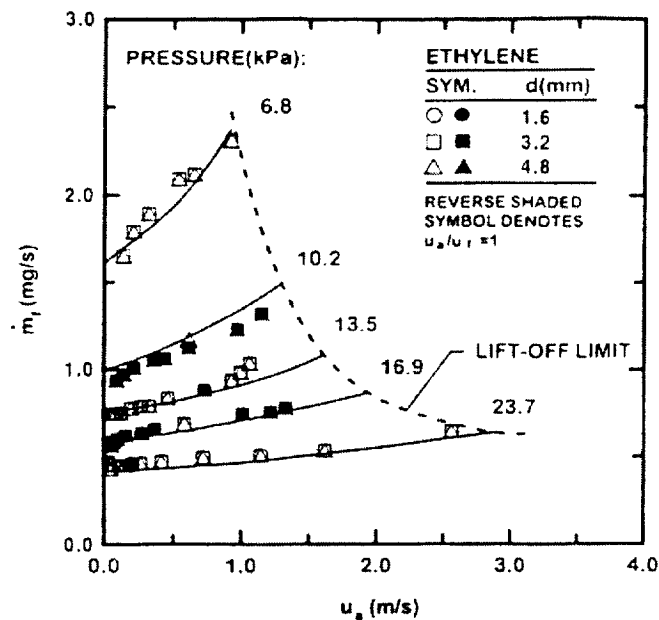


Fig. 2. Fuel flow rates at laminar soot-point and lift-off conditions for ethylene-fueled laminar jet diffusion flames in co-flowing air.

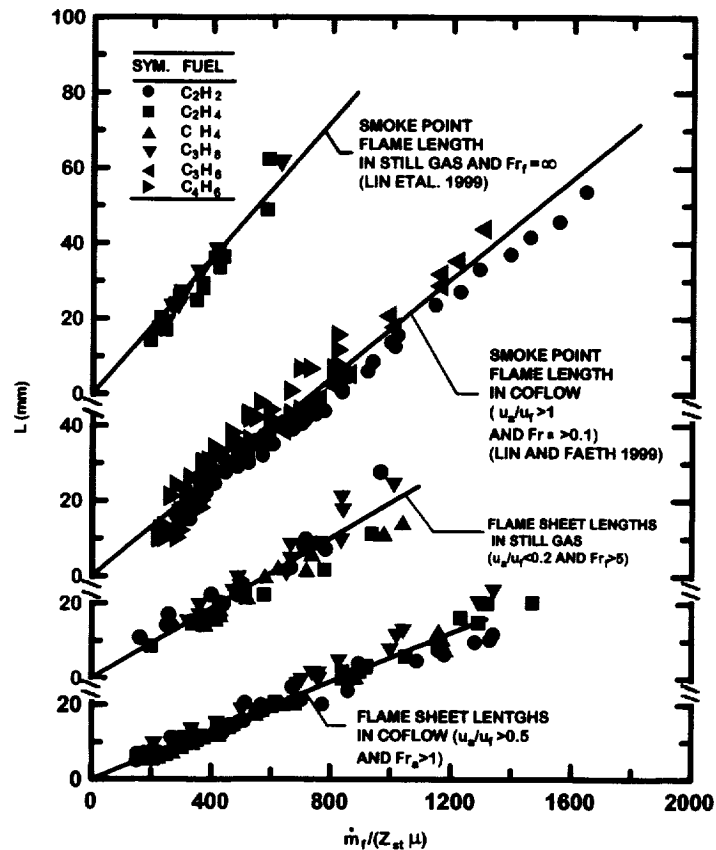


Fig. 3. Flame-sheet and luminous flame lengths (the latter at the laminar smoke point) of laminar jet diffusion flames in still air and in coflowing air.

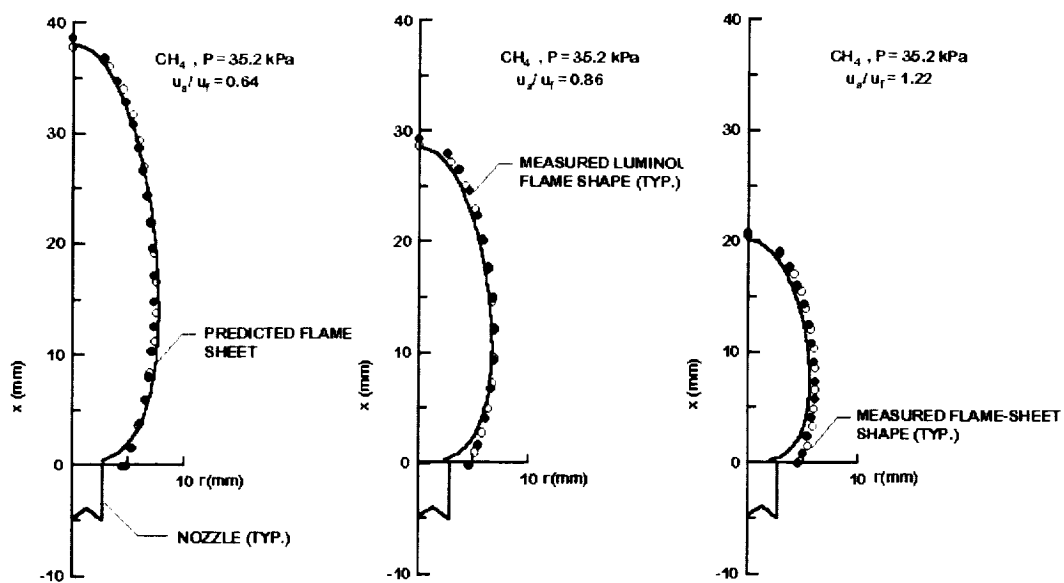


Fig. 4. Measured flame-sheet and luminous flame shapes and predicted flame-sheet shapes for soot-free methane-fueled laminar jet diffusion flames having a burner diameter of 4.3 mm for various air coflow velocity ratios.

COSMIC: CARBON MONOXIDE AND SOOT IN MICROGRAVITY INVERSE COMBUSTION

**L.G. Blevins¹, M.G. Fernandez², G.W. Mulholland²,
R.W. Davis³, E.F. Moore³, E.B. Steel³, and J.H.J. Scott³**

¹Combustion Research Facility, Sandia National Laboratories, Livermore, CA

²Building and Fire Research Laboratory, National Institute of Standards and Technology

³Chemical Science and Technology Laboratory, National Institute of Standards and Technology

INTRODUCTION

Almost seventy percent of deaths in accidental fires are caused by inhalation of toxins such as carbon monoxide (CO) and smoke (soot) that form during underventilated burning [1,2]. The COSMIC project examines the formation mechanisms of CO and soot during underventilated combustion, achieved presently using laminar, inverse diffusion flames (IDFs) formed between an air jet and surrounding fuel. A major hypothesis of the project is that the IDF mimics underventilated combustion because carbon-containing species that form on the fuel side of the flame (such as CO and soot) can escape without passing through an oxidizing flame tip. An IDF literature review was presented at the last microgravity workshop [3], and a few additional IDF papers have appeared since that meeting [4-6]. The COSMIC project is entering the third year of its four-year funding cycle. The first two years have been devoted to designing and constructing a rig for use in the NASA 2.2-second drop tower. A few computations and laboratory experiments have been performed. The goals of this paper are to discuss the use of numerical simulation during burner design, to present computational and experimental results that support the hypothesis that IDFs are similar to underventilated flames, and to delineate future plans.

COMPUTATIONAL AND EXPERIMENTAL METHODS

Computations of the effects of gravity on methane (CH₄) flame shapes were used to select an appropriate burner design and initial operating condition. Calculations were performed using direct numerical simulation (DNS) of the time-dependent Navier Stokes and conserved variable equations for an axisymmetric laminar flame [7]. The simulation employs assumptions of low Mach number, infinite-rate chemical kinetics (flame sheet), unity Lewis number, variable thermophysical properties, a semi-infinite surrounding fuel-stream, and negligible radiation heat transfer. Dilute-condition particle tracking incorporating the effects of inertial, thermophoretic, and gravitational forces is included [8]. Some particle tracking results are presented here to show basic IDF particle pathways. For the present results, particles are introduced at axial positions of 0 cm, 0.5 cm, 1 cm, 1.5 cm, and 2 cm from the burner and at radial locations corresponding to a characteristic soot formation temperature of 1250 K (see Ref. [9]). Detailed soot modeling is not performed; a recent paper discusses thorough soot modeling for IDFs [4].

For this project, it is desirable to achieve a broad variety of operating conditions that yield different flames in normal-gravity (1-g) and microgravity (0-g) conditions. Initial calculations and experiments were performed using a small (5 mm diameter air jet) co-flow burner chosen for its similarity in size to burners used in previous drop tower experiments [10]. Flame structures were computed for several possible CH₄ operating conditions, and several 1-g flames were stabilized in the laboratory. For all cases in the small burner, the computed IDFs were less than 1 mm long and were unaffected by gravity. In qualitative agreement with this result, laboratory flames were short and steady (similar to micro-flames [11]). Hence, the small burner was found

to be undesirable because a wide variety of IDF operating conditions could not be achieved. A larger burner was constructed after identification of desirable dimensions using computations.

The larger burner consists of a 1 cm diameter central air jet surrounded by a 3 cm diameter co-annular fuel tube. A nitrogen (N_2) curtain (6 slpm) flows through a 6.4 cm diameter tube surrounding the burner. The N_2 prevents secondary flames from forming between fuel and room air. Flow-straightening beads and honeycomb are present in the air and fuel passages, while the N_2 flow is smoothed with a fine-mesh screen. The air and fuel tubes are sharpened to knife-like edges to facilitate flame attachment. A propane flare was used downstream of the burner to prevent passage of unburned fuel into the laboratory exhaust duct. For the present paper, one CH_4 flame and one ethylene (C_2H_4) flame were studied. For CH_4 , a 46 mg/s (40 sccs or 50 cm/s average velocity) air flow and a 41 mg/s (64 sccs or 10 cm/s) fuel flow were used. For C_2H_4 , a 32 mg/s (27 sccs or 35 cm/s) air flow and a 49 mg/s (43 sccs or 7 cm/s) fuel flow were used. The air velocity was five times as large as the fuel velocity for both flames studied. Flame heights were estimated from digital photographs. For the C_2H_4 flame, soot particles were collected on a 3 mm, 400-mesh copper microscope grid coated with amorphous carbon film. The grid was secured to a thin metal spatula and inserted parallel to the flow in the center of the exhaust for five consecutive one-second intervals. The soot particles were analyzed using a Philips CM300FEG Scanning Transmission Electron Microscope (STEM) operating at 300 kV with a 1 nm probe.

RESULTS AND DISCUSSION

Figure 1 depicts temperature contours calculated for the 1-g and 0-g CH_4 flames. Representative particle pathways are shown in white. The 0-g flame length (defined by peak temperature) is about 2.2 cm, while the 1-g flame length is 2.1 cm. In

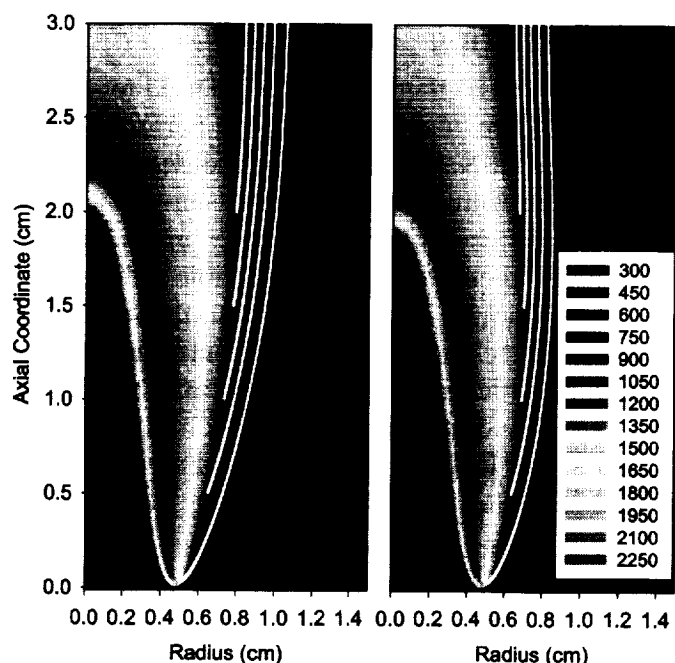


Fig. 1 Calculated absolute temperature (K) for 0-g (left) and 1-g (right) CH_4 IDFs. Half of the axisymmetric domain is shown. White streaks show particle pathways.

agreement with previous findings for laminar jet flames, the computed 0-g flame is longer and more rounded than the 1-g flame [12]. The particle paths shown in Fig. 1 demonstrate that soot particles formed low in the flame move away from the flame for IDFs and can escape with minimal oxidation for both gravity conditions. Figure 2 shows a digital photograph of the 1-g CH_4 flame. The blue flame with orange soot cap is similar to IDFs observed by others [13,14]. The blue portion of the flame is $2.2 \text{ cm} \pm 0.1 \text{ cm}$ long, in agreement with the predicted peak-temperature flame height. Despite the existence of the orange soot cap, the soot stream exiting the CH_4 IDF is invisible to the naked eye.

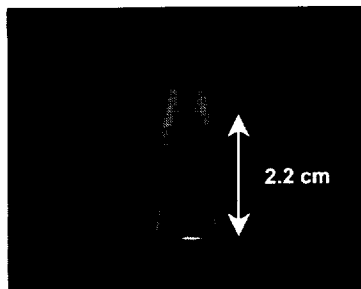


Fig. 2 Photo of 1-g CH_4 IDF.

Figure 3 portrays the calculated time-temperature histories of the particle paths shown in Fig. 1. Particles are tracked until they reach the end of the computational domain (3 cm above the burner). Longer cut-off times for the 0-g particles indicate the lack of buoyant acceleration. In both flames, particles move away from the high temperature region under the influence of thermophoretic forces. Particles in the 1-g flame spend less time at high temperatures than those in the 0-g flame. The implications of this predicted trend for soot structure will be studied in future COSMIC experiments.

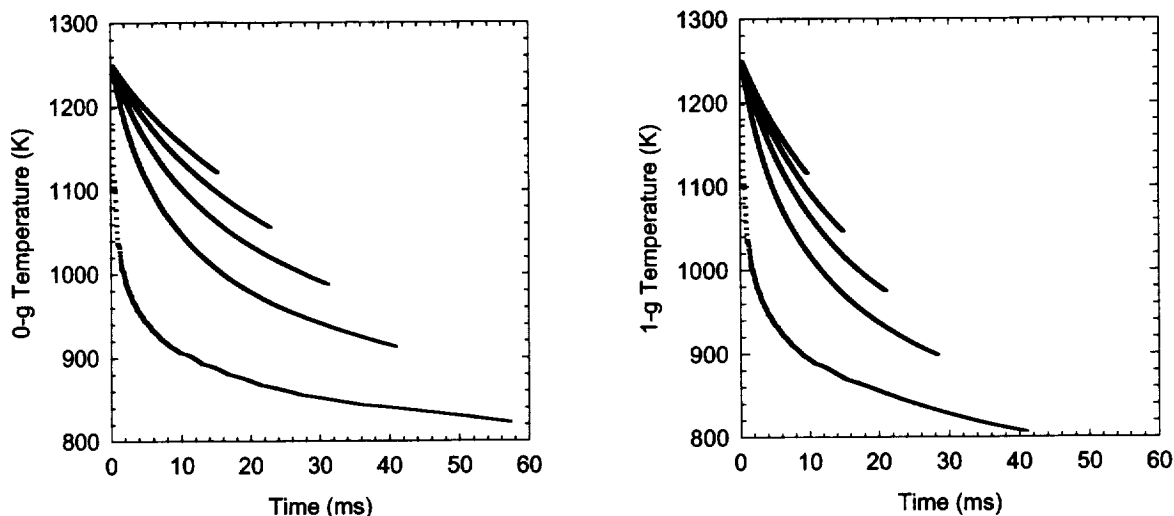


Fig. 3 Time/temperature history of particles in 0-g (left) and 1-g (right) CH_4 IDFs.

A digital photograph of the 1-g C_2H_4 IDF is shown in Fig. 4. The soot cap on the C_2H_4 flame constitutes 90 % of its visible height and its emission intensity saturates the digital camera. The blue portion of the flame is 0.35 cm long, while the total visible flame height is 3.5 cm. A soot stream exits the flame tip (not visible in the dark photograph). The asterisk on Fig. 4 shows the approximate location of soot sampling for the bright-field STEM soot micrograph shown in Fig. 5. The particles appear liquid-like, in agreement with early IDF studies where soot collected on metal targets was sticky and viscous [15-17]. The liquid structure is similar to soot collected in underventilated flame exhaust streams [18] and to soot precursors captured from diffusion flames [19]. The major difference between the Fig. 4 soot and that studied in Refs. [18] and [19] is that the present liquid-like structures

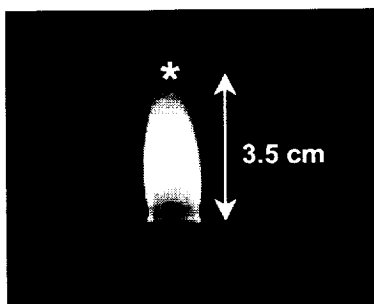


Fig. 4 Photo of 1-g C_2H_4 IDF. An asterisk marks the location of soot sampling.

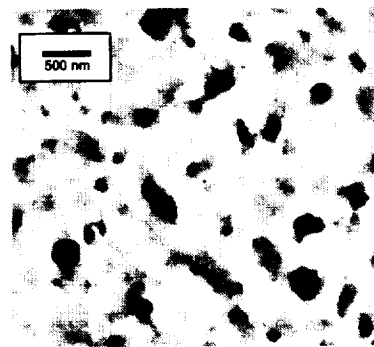


Fig. 5 STEM image of soot collected from 1-g C_2H_4 IDF.

are larger (~250 nm compared to about 20 nm), possibly a result of condensation and coagulation of organic vapors. Particle overlap on the heavily loaded grid could partially explain the large structures, or they may result from post-collection sample transformations. Ongoing efforts are aimed at refining the sampling technique and studying IDF soot structure further.

SUMMARY AND CONTINUING WORK

Direct numerical simulation has been used to guide the design of a burner—relatively large by 2.2-second drop tower standards—and to select initial operating conditions for 0-g and 1-g testing. Two burners were built and tested. Laboratory testing agreed qualitatively with predicted flame height and stability trends. Computed particle pathways revealed that IDF soot is likely to exit flame regions without being fully oxidized. Liquid-like soot samples collected above the flames corroborate this computed result. All of these findings support the major hypothesis that IDF soot (or CO) experiences conditions similar to those encountered by carbon-containing species in underventilated flames. Drop tower experiments employing CH₄ and C₂H₄ IDFs are planned for Summer 2001. Soot yields, CO yields, soot structure, and soot chemical makeup will be studied. The simulation method demonstrated here will be used to predict the paths traveled by soot and CO for the operating conditions studied. Results should provide insight into the formation mechanisms of undesirable CO and soot during underventilated fires.

This research is funded via NASA Contract No. C-32069-J. Dr. Peter Sunderland (technical contact) and Dr. Kurt Sacksteder (technical monitor) provide invaluable assistance.

REFERENCES

- [1] Hall, J. R. Jr., Burns, Toxic Gases, and Other Hazards Associated with Fires: Deaths and Injuries in Fire and Non-Fire Situations, National Fire Protection Association (NFPA), Quincy, MA, 1996.
- [2] Pitts, W. M., *Progress in Energy and Combustion Science*, 21:197, 1995.
- [3] Blevins, L. G., Mulholland, G. W., and Davis, R. W., *Proceedings of the Fifth International Microgravity Combustion Workshop*, NASA/CP-1999-208917, NASA, Cleveland, 1999, p.479.
- [4] Kaplan, C. R. and Kailasanath, K., *Combustion and Flame*, 124:275, 2001.
- [5] Sung, C. J., Zhu, D. L., and Law, C. K., *Twenty-Seventh Symposium (International) on Combustion*, The Combustion Institute, Pittsburgh, 1998, pp. 2559-2566.
- [6] Partridge, W. P., Reisel, J. R., and Laurendeau, N. M., *Combustion and Flame*, 116:282, 1999.
- [7] Davis, R. W., Moore, E. F., Chen, L. D., Roquemore, W. M., Vilimpoc, V., and Goss, L. P., *Theoretical and Computational Fluid Dynamics*, 6:113, 1994.
- [8] Davis, R. W., Moore, E. F., and Zachariah, M. R., *Journal of Crystal Growth*, 132:513, 1993.
- [9] Du, J. and Axelbaum, R. L., *Combustion and Flame*, 100:367, 1995.
- [10] Bahadori, M. Y., Edelman, R. B., Stocker, D. P., and Olson, S. L., *AIAA Journal*, 28:236, 1990.
- [11] Ban, H., Venkatesh, S., and Saito, K., *Journal of Heat Transfer*, 116:954, 1994.
- [12] Sunderland, P. B., Mendelson, B. J., Yuan, Z. G., and Urban, D. L., *Combustion and Flame*, 116:376, 1999.
- [13] Sidebotham, G. W. and Glassman, I., *Combustion and Flame*, 90:269, 1992.
- [14] Kent, J. H. and Wagner, H. G., *Zeitschrift Fur Physikalische Chemie-Wiesbaden*, 139 :59, 1984.
- [15] Arthur, J. R., Commins, B. T., Gilbert, A. S., Lindsey, A. J., and Napier, D. H., *Combustion and Flame*, 2:267, 1958.
- [16] Arthur, J. R. and Napier, D. H., *Fifth Symposium (International) on Combustion*, The Combustion Institute, Pittsburgh, 1955, pp. 303-316.
- [17] Arthur, J. R., Kapur, P. K., and Napier, D. H., *Nature*, 169:372, 1952.
- [18] Leonard, S., Mulholland, G. W., Puri, R., and Santoro, R. J., *Combustion and Flame*, 98:20, 1994.
- [19] Dobbins, R. A., Fletcher, R. A., and Chang, H. C., *Combustion and Flame*, 115:285, 1998.

Electrical Aspects of Microgravity Combustion

Derek Dunn-Rankin
Mech. and Aero. Engineering Department
University of California, Irvine

Felix J. Weinberg
Chemical Eng. and Chemical Tech.
Imperial College, London

The use of electric fields in zero gravity offers an intriguing opportunity to influence flames with a force analogous to buoyancy but in an environment in which this force is naturally absent. We are investigating three aspects of electric field application to microgravity combustion: (1) the cancellation of buoyancy at one-g to provide an earth-based microbuoyant environment for evaluating microgravity combustion phenomena on a terrestrially bound benchtop; (2) real-time control of zero-g flames via electric field induced forces; and (3) conveying fire extinguishment materials to a fire site with electric fields.

The phenomena associated with the electrical aspects of flames in microgravity derive from the combustion system's response to the imposition of an ion wind. The ion wind is the natural consequence of a high electric field placed across the flame since flame-generated ions are drawn from the flame and mobilized by the electric field in such a way as to produce a steady wind of the neutral molecules with which they collide. The ion wind thus produces a body-force on the gas proportional to the electric field strength and ion number density. We use this body force to manipulate the flame.

To demonstrate the ion-wind cancellation of buoyancy, we use a small capillary-fed methane diffusion flame. In earlier studies we attempted to duplicate microbuoyant conditions everywhere (i.e., to create a spherical flame), but we found this condition to be unstable (we were able to sustain the balance for only a few seconds). We have since modified the experimental configuration to simulate microgravity conditions directly below the capillary, and we find that the balance can be sustained for periods long enough to allow even point-by-point laser measurements. Figure 1 shows the experimental configuration. Figure 2 is a series of photographs showing the capillary methane/air diffusion flame under different applied fields. The methane flow rate is 10 cc/min and, as a scale, the capillary is 1.8 mm in diameter. For this configuration, the point of balance is between images (indicated by the arrow), occurring at approximately 2800V applied potential. Figure 3 shows the flame current and CH chemiluminescence of the flame as a function of applied potential. As expected, the current increases and then plateaus at the saturation value. Further increase of voltage beyond the plateau leads to additional current because secondary ionization begins to contribute to the electrical flow. Consistent with the images of Figure 2, the chemiluminescence decreases with increasing field through saturation where it again begins to increase. In this case, the point of balance occurs within the saturation plateau.

Instantaneous density interferograms of the flame under 1-g conditions near the point of balance show widely spaced fringes below the flame, indicating a significant reduction in the thermal gradients in that direction. The interferograms indicate that distinct gradients still exist on the sides of the flame, but not in the central region. To demonstrate both that the axial temperature profile in this central region matches that for a purely diffusive system and that the flame can be stably maintained in its balance condition, we measured the profile using coherent anti-Stokes Raman scattering (CARS), a point-by-point pulsed laser diagnostic technique. Figure 4 compares the measured temperatures at different applied potentials with the theoretical thermal profile of a diffusion-controlled flame. In addition, a tomographic analysis of our holographic interferograms agrees with the CARS results. Although these comparisons are persuasive evidence that we are canceling buoyancy at least along the bottom curve of the flame, we hope in future to also measure the velocity profile of this small flame. Further details of the foregoing results appear in Strayer et al. (2000a; 2000b).

The maintenance of microbuoyancy is a demonstration that electric fields can be used to control the flows near microgravity flames and thereby manipulate the combustion process to some degree. To take this concept to another level, we have developed a response model for the flame that matches the dynamic change in its heat release to fluctuations in the electric field. The approach uses standard tools of automatic control, and is implemented through the real-time

Matlab and Simulink environment. The system uses CH chemiluminescence as the sensor and the electric field as the actuator. Interestingly, the flame's chemiluminescence response is very similar to that of a simple second-order linear system. Figure 5 is a schematic of the control apparatus and Figure 6 is the flame's response to voltage impulses of different widths. The flame reaches its maximum response at impulse widths of approximately 40ms. By fitting a piecewise continuous model to the chemiluminescence one finds two characteristic timescales in the system; the first, on the order of tens of ms, is characteristic of the ion wind creation time. The second is much slower (of the order of seconds) and appears to result from capillary heating and cooling as the flame is buoyed up around or pulled off the capillary tip. With this fairly simple flame response model, it is then possible to create a suitable controller that will force the flame CH emission to respond to a desired target. Figure 7 shows that the relatively simple PID controller works very well, as the CH signal tracks very precisely the desired sinusoidal trajectory. Note that the voltage signal applied to the flame is not harmonic, showing that the actuator does not have a simple task to keep the system on track.

Our fire extinguishment activities explore the use of electric fields to produce and transport inert materials to a combustion site. Thus far, the electrostatic conveyance and fire extinguishment potential of liquid droplets and solid particles have been studied. Inert gas performance experiments are in process. Figure 8 shows the effectiveness of electrosprayed water for extinguishing a small flame and smolder front. The water flow rate was 0.035 cc/s and the flames were scaled to simulate the heat output per unit surface area of a flame nourished by the air flow typical in the microgravity environment. Details of this work were presented at the recent Combustion Symposium (Carleton, et al., 2000). Figure 9 shows the experimental apparatus used to charge and spray powder material (NaHCO_3). The particles are difficult to charge directly (each particle carries approximately $1/10^{\text{th}}$ the charge of a similar sized electrosprayed water droplet) and corona charging of the gas was not transferred to the particles. Nevertheless, Figure 10 demonstrates the powder's effectiveness. Unlike the water spray, the powder was ineffective against smolder, but the merest concentration (3--5 particles per second) is sufficient to extinguish the flame. To convey inert gases using an ion-wind, we can either use a corona discharge source to produce some electrically charged molecules, or we can use a flame to produce the ions and then use the combustion products as the inert gas. We are investigating both options.

In addition to measuring the fire suppression effectiveness of electro-sprayed liquids, we examined some of the fundamentals of creating electrohydrodynamic (EHD) sprays, including multiple capillary EHD sprays, air-assisted EHD atomization, and the efficiency of EHD spraying in terms of droplet surface area produced versus electrical power applied. Due to space limitations, this extended abstract cannot include results from these studies.

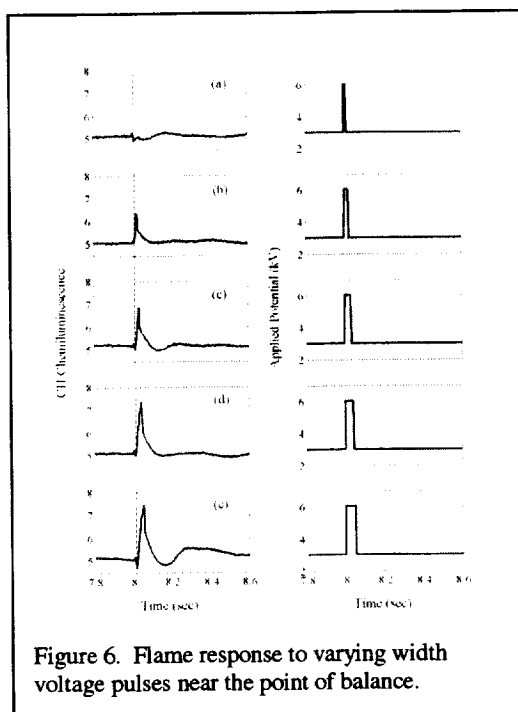
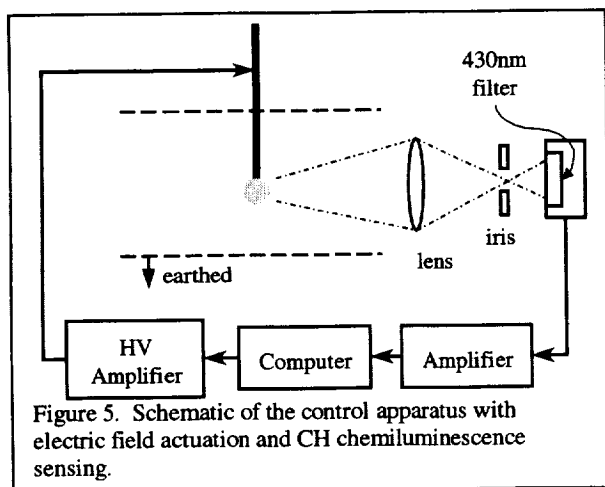
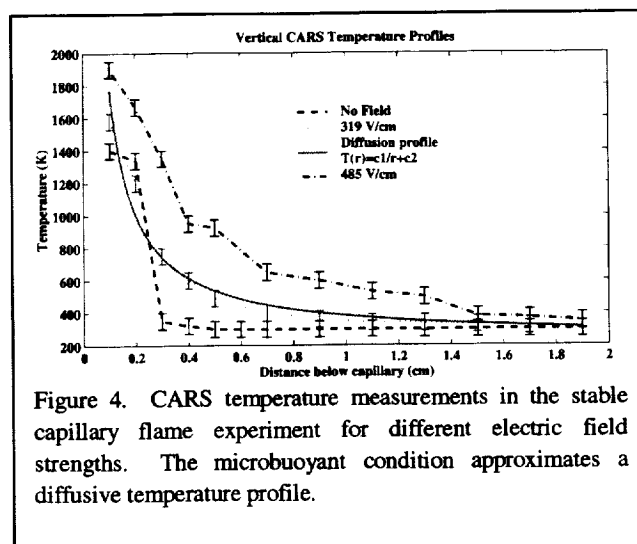
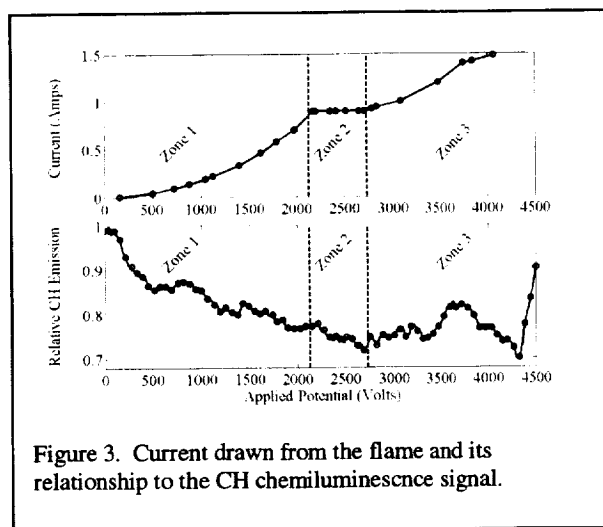
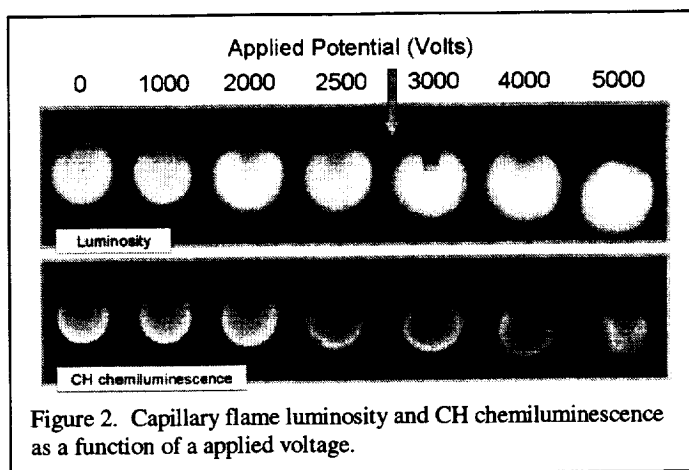
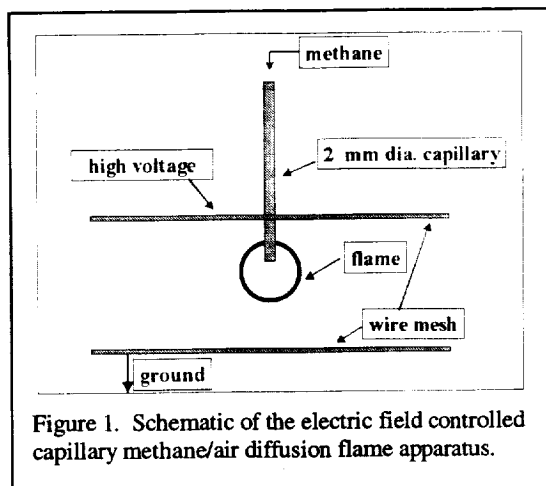
In summary, we have found electric field interactions with flames to have a variety of interesting possibilities for the microgravity combustion environment. When the obvious terrestrial transport mechanisms are compromised by space and weight restrictions, or by low-gravity itself, the body forces generated by electric fields acting on charged particles becomes useful for flame control.

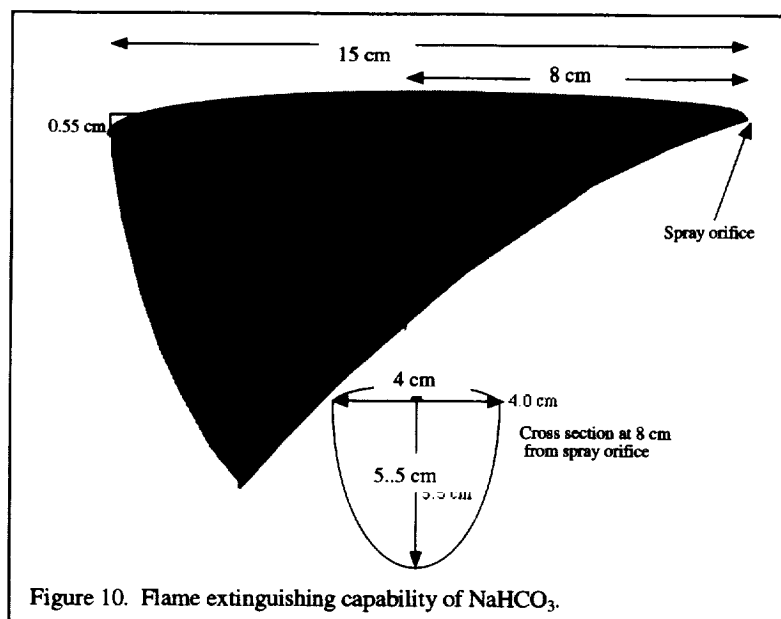
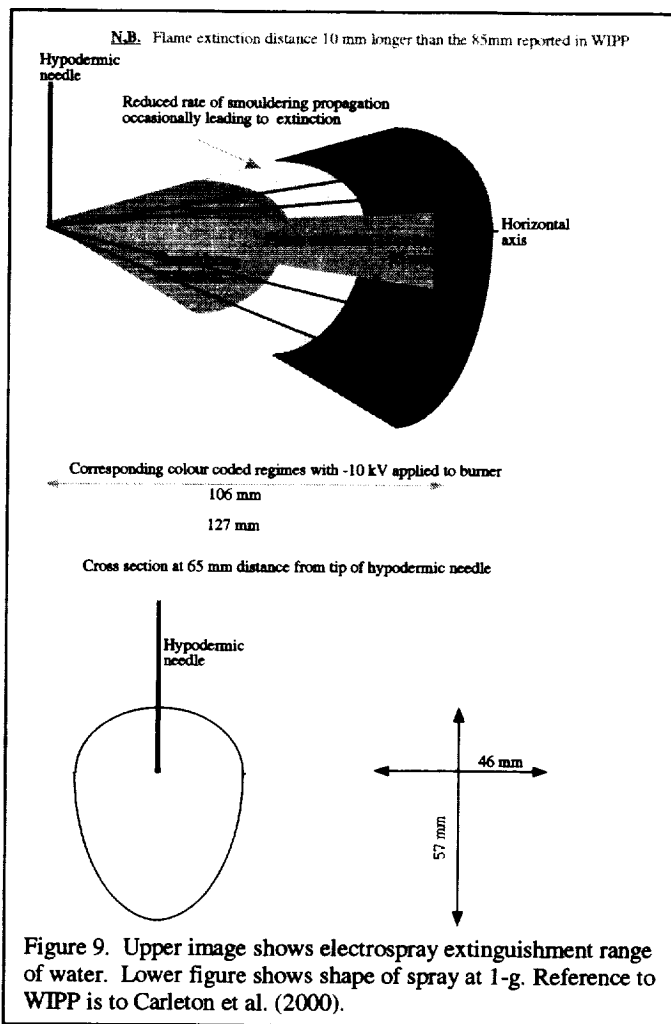
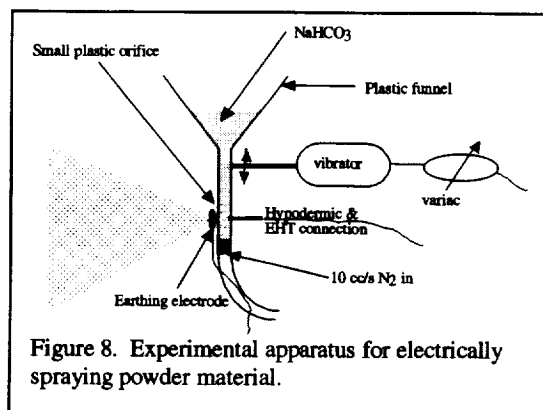
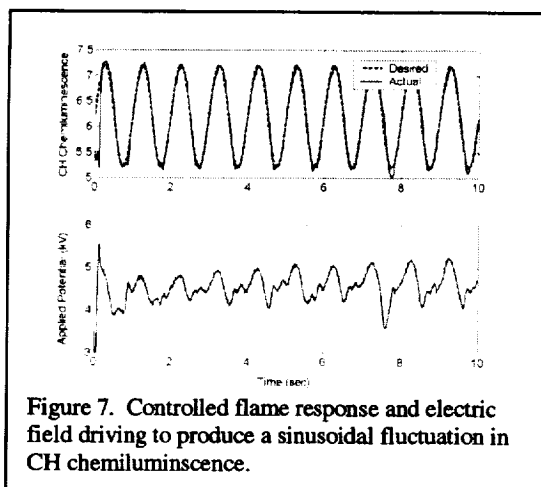
References:

Carleton, F., Dunn-Rankin, D., and Weinberg, F.J. "Electrical Spraying of Extinguishants for use in Microgravity," Poster Session, 28th International Symposium on Combustion, Edinburgh, July 30--August 4.

Strayer, B.A., Posner, J.D., and Dunn-Rankin, D. (2000a) "CARS Temperature Measurements of a Nonpremixed Flame under Electric Field Control," Western States Section/The Combustion Institute Spring Meeting, Colorado School of Mines, Golden, CO, March 13--14.

Strayer, B.A., Posner, J.D., Dunn-Rankin, D., and Weinberg, F.J. (2000b) "Further Studies on Simulating Microgravity Flames using Electric Fields," Poster Session, { \it 28th International Symposium on Combustion}, Edinburgh, July 30--August 4.





COUNTER-FLOW DIFFUSION FLAMES OF AMMONIUM PERCHLORATE WITH GASEOUS FUELS

M.D. Smooke

Department of Mechanical Engineering
Yale University
New Haven, Connecticut 06520-8284

R.A. Yetter

Department of Mechanical and Nuclear Engineering
The Pennsylvania State University
University Park, PA 16802

T.P. Parr and D.M. Hanson-Parr

Naval Air Warfare Center, Weapons Division
China Lake, CA 93555-6100
ParrTP@navair.navy.mil

INTRODUCTION

Many solid rocket propellants are based on a composite mixture of ammonium perchlorate (AP) oxidizer and polymeric binder fuels. In these propellants, complex three-dimensional diffusion flame structures between the AP and binder decomposition products, present on the length scales of the heterogeneous mixture, drive the combustion via heat feedback to the surface. Changing the AP crystal size changes the burn rate of such propellants. Large AP crystals are governed by the cooler AP self deflagration flame and burn more slowly while small AP crystals are governed more by the hot diffusion flame with the binder and burn faster. This allows control of composite propellant ballistic properties via particle size variation. Most composite propellants based on AP contain a bimodal or trimodal particle size distribution of AP. A typical formulation would contain 85% solids (AP) with 15% binder (eg. HTPB). The AP would consist of a mixture of coarse and fine AP (say 62% 200 μm and 38% 25 μm).

One method of studying diffusion flames of AP with fuel is using a counter-flow geometry. In a typical counter-flow diffusion flame experiment two laminar plug flow jets, one of fuel and one of oxidizer, are directed at each other so they impinge in the middle of the domain. Properly designed, this configuration leads to one-dimensional (1D) flames that can be modeled with the lower CPU demand of 1D codes. Here, the oxidizer side is not a jet but a solid pellet of AP (Fig. 1). AP does not normally self-deflagrate at pressures below about 200 to 800 PSIA (depending on purity)¹, but it was found that the flames self-sustained even at 0.92 atm, and nearly perfectly planar multi-flame structures have been imaged with fuel representatives of the HTPB

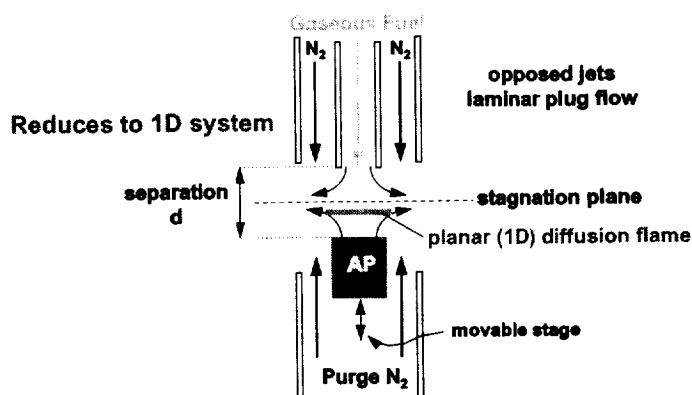


Fig. 1 Apparatus diagram for counter-flow diffusion flame experiments.

decomposition gases that would burn with the fine AP, namely methane and ethylene.² Varying the distance between the AP and fuel changes the flame strain rate. The behavior, and extinction, of flames as a function of strain rate is a sensitive probe of flame kinetics. However, in 1 g experiments it was found that only a very narrow range of strain rates could be studied before buoyancy affected the results. This prompted microgravity experiments in a program involving comparison of experimental results with modeling.

In the work presented here, the fuel is a mixture of H_2 and CO in the ratio of 52 mole% to 48 mole%, respectively. This simulates the chemistry of the combustion products from the binder (HTPB) and fine AP fraction of a composite propellant, which go on to react in a diffusion flame with the large diameter AP fraction. In the formulation example given, the neat AP flame (above large diameter AP crystals) would be 1377K, the fine AP / binder flame would be 1162K, and the final flame between the decomposition products from the large AP and the AP / binder flame products would be 2645K.

EXPERIMENTAL RESULTS

Using the techniques of planar laser-induced fluorescence (PLIF), spontaneous Raman spectroscopy, and ultraviolet/visible absorption spectroscopy (UV/vis absorption), quantitative species and temperature profiles were measured for the mixture of fuels, CO and H_2 .

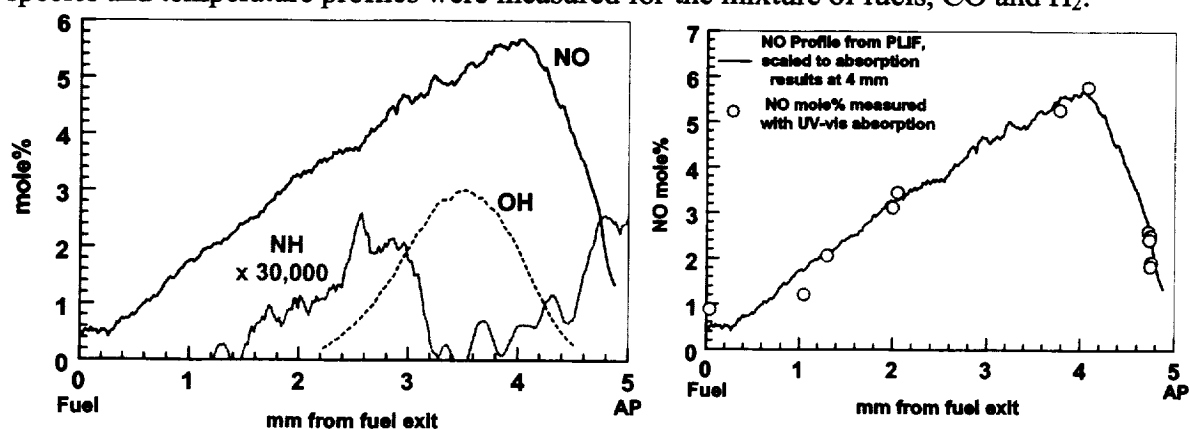


Fig. 2 NO, OH, and NH profiles the 5 mm AP / (H_2+CO) counter-flow diffusion flame. The mole% scale is absolute. The plot on the right is the NO PLIF profile showing corresponding UV-vis absorption results. The NO PLIF profile was scaled to UV-vis absorption results at 4mm.

Species measured included CN , NH , NO , OH , N_2 , O_2 , CO_2 , H_2 , CO , HCl , and H_2O . Temperature was measured using a thermocouple. OH rotational population distributions (PLIF), NO vibrational population distributions (UV/vis absorption), and spontaneous Raman spectroscopy. The burning rate of AP was also measured. Twelve scalars were therefore quantified in this flame system. The data will be helpful in validating models of AP diffusion flames based on detailed kinetics. Results for this system are shown in Figs. 2 and 3.

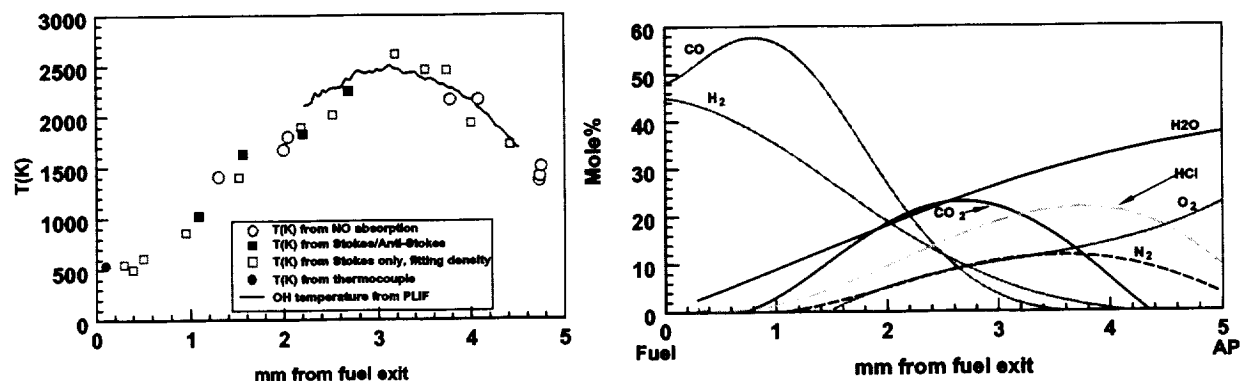


Fig. 3. (left) Temperature profile in the AP/(H₂ + CO) counter-flow diffusion flame with a 5 mm separation. (right) Species profile line fits to Raman data in the AP/(H₂ + CO) counter-flow diffusion flame with a 5 mm separation.

Measurements of the surface temperature at 0.92 atm were done to aid the modeling efforts. Since AP doesn't burn at this low a temperature without being preheated or without a little added fuel mixed into the sample, the surface temperature for pure AP at pressures near 1 atm has not been extensively determined. Powling and Smith³ used an infrared-emission method and measured surface temperatures at sub- and atmospheric pressures for both heated AP and AP mixed with paraformaldehyde. They saw little change of surface temperature with fuel concentration (at these low pressures, for 10 to 24% paraformaldehyde) even though the burning rate changed substantially. Preheating the AP also did not affect the surface temperature. They got a surface temperature of about 760K at 700 Torr for 10% paraformaldehyde (about 725K if they looked at a different wavelength). They also did measurements with a 50 micron wire thermocouple (so bead probably about 150 microns in diameter) and got a surface temperature of 698K at 100 Torr.

The AP samples for the current determination of surface temperature were pressed pellets of 200 micron AP. A thermocouple wire was stretched across the surface, holding it at a constant position (spring-loaded holder) and the temperature was monitored. These measurements were done for the AP/(H₂ + CO) counter-flow flame. There were some small fluctuations due to material being shed from the surface, but a very nice temperature plateau of 702K \pm 13K was observed. The 702K result agrees well with the aforementioned Powling and Smith surface temperature for AP burning at about the same rate as in the current experiments.

As a check on the modeling efforts, the AP burning rate as a function of strain rate was also measured for the methane/AP counter-flow flame, as shown in Fig. 5. The strain rate was calculated from the formula in a paper by K.-C. Lin and G.M. Faeth⁴:

$$\text{Strain rate (s}^{-1}\text{)} = 2v_{\text{Apgases}}((1+v_{\text{CH}_4}/v_{\text{Apgases}})(\rho_{\text{CH}_4}/\rho_{\text{Apgases}})^{0.5})/L,$$

where, v_{Apgases} is the speed of the AP combustion gases at the AP surface, v_{CH_4} is the speed of the CH₄ at the fuel exit, L is the separation, and ρ_{CH_4} , ρ_{Apgases} are the densities of the CH₄ and AP gases, respectively. The temperature of the CH₄ at the exit was taken to be 325K, and the AP gases were 1377K (flame temperature of AP). The density of AP gases was 2.24E-4 g/cm³ (based on a molecular weight of 27.52 g/mole and T of 1377, pressure of 0.92 atm). The density of CH₄ at the exit was 5.52E-4 g/cm³.

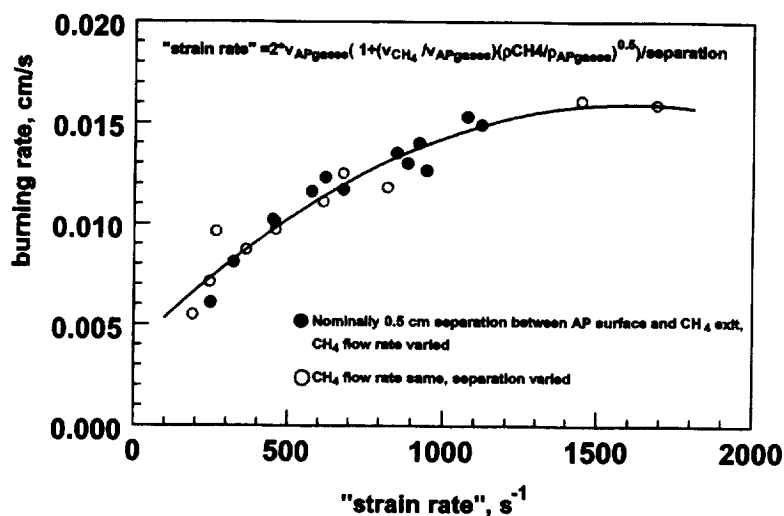


Fig. 4. AP burning rate as a function of the strain rate. Filled circles are experiments in which the methane flow rate was changed, keeping the separation between fuel exit and AP surface constant, and open circles are experiments where only the separation was varied.

VESSEL DESIGN

The pressure vessel to be used in the upcoming flight tests has been designed according to ASME specifications and fabrication is complete. The equipment rack to be used aboard the plane has been received.

FLIGHT TESTS

The engineer from China Lake chosen for the flight test has passed the Air Force physical and has completed all the paperwork necessary for the flight.

REFERENCES

- [1] "Response of Ammonium Perchlorate to Thermal and Mechanical Shock Stimuli", Ed. T. Boggs, NWC TP 7053 (1990).
- [2] T. P. Parr and D.M. Hanson-Parr, "AP Diffusion Flame Structure," *Proceedings of the 34th JANNAF Combustion Subcommittee Meeting*, CPIA publication 662, Vol. II, pp. 13-22, Oct. 1997.
- [3] Powling and Smith, *Combustion and Flame*, Vol. 7, pp. 269-275 (1963).
- [4] K.-C.Lin and G.M. Faeth, "Effects of Hydrodynamics on Soot Formation in Laminar Opposed-Jet Diffusion Flames", *Journal of Propulsion and Power*, Vol. 12, No. 4, pp. 691-698, July-August 1996.

STATUS REPORT ON MARS ISRU CO/O₂ HYBRID ENGINE DEVELOPMENT AND TESTING

**E.E. Rice, M.J. Chiaverini, M.M. Malecki, C.P. St.Clair, W.H. Knuth,
R.J. Gustafson, and D.J. Gramer**
Orbital Technologies Corporation (ORBITEC™)
Madison, WI 53717

INTRODUCTION

This article addresses the current status of a research and development effort in which ORBITEC has undertaken to test a new type of fuel/oxidizer system for ISRU-based propulsion systems on Mars. The Martian atmosphere (about 95.5% CO₂) provides a readily available supply of carbon dioxide (CO₂) to produce both CO and O₂, which can be used for hybrid rocket engine applications. Hybrid propulsion systems have several safety and operational features that make them attractive for space systems.¹ For Mars ISRU applications, CO gas can be frozen directly to form a solid fuel grain, then burned with liquid oxygen. The objectives of the program are to investigate the ignition, combustion, and fuel regression rate characteristics of SCO burning with oxygen in a hybrid engine, to demonstrate an end-to-end benchtop system of the total propellant manufacturing, grain freezing, and hot firing system, and to develop preliminary space system designs. This article presents recent results of the SCO combustion characterization efforts.

METHOD OF APPROACH

All of the experimental work discussed here was performed using ORBITEC's lab-scale Mark II cryogenic hybrid rocket engine and freezer. Figure 1 shows a section view of the engine assembly which consists of an outer vacuum chamber, a freezer core, and a grain chamber. The grain chamber is 12.7 cm long and has an inner diameter of 5.08 cm. The exit nozzle diameter 0.69 cm. A gaseous oxygen injector and hydrogen-oxygen igniter torch are situated in the injector plate, as is a camera for visual observations. The grain chamber was instrumented with several pressure transducers and thermocouples (T1, T2, and T3) for measuring the chamber pressure and local wall temperature during both freezing and firing operations.

The freezing point of CO is 68 K. Solid CO fuel grains were formed by freezing CO gas directly onto the inner wall of the grain chamber, which is kept cold by a surrounding bath of liquid helium (4 K). Formation of the liquid phase of CO was prevented by controlling the gaseous CO flow rate to maintain the gas pressure in the chamber below the triple point pressure of 119.1 Torr (2.3 psi). Typical freezing times for a 100-gram solid CO grain were about 20 minutes. For hot fire testing, gaseous oxygen was injected at the engine head-end to mix and burn with the CO fuel. Reference 2 provides a more thorough hardware description.

RESULTS AND DISCUSSION

Table 1 summarizes the operating conditions and average test results of the firings. All fuel grains were 100 g in size (4 cm initial internal diameter, 0.56 cm wall thickness 12.7 cm length). Only partial data is given for Test 4 due to an igniter failure. The characteristic exit velocity (C*) was determined as described in Reference 2. The combustion efficiency was calculated by comparing the experimental C*

values to the theoretical C^* that would be achieved assuming a 100% efficient chemical reaction process.

Table 1. Carbon Monoxide Hot Firing Tests in Mark II Engine

Parameter	Test 1	Test 2	Test 3	Test 4	Test 5	Test 6
CO gas delivery	Head-end	Nozzle	Nozzle	Nozzle	Nozzle	Nozzle
CO freez. press. (torr)	~ 1	9	9	9	90	90
Oxygen flow (g/s)	6.0	6.0	4.0	10.0	10.0	6.0
Avg. Reg. Rate, r (cm/s)	0.0576	0.0482	0.0430	—	0.0608	0.0438
Combustion Time (s)	9.7	11.6	13.0	—	9.2	12.8
Avg. O/F	0.57	0.70	0.51	—	0.92	0.76
Avg. pres., p_c (psia)	71	67	52	—	95	55.4
Igniter duration (s)	entire test	2	2	2	2	2
C^* (m/s)	1117	1176	1127	—	1166	1019
C^* efficiency	82%	87%	83%	—	88%	76%
Max temp on TC 1 (K)	310	260	270	—	300	540
Max temp on TC 2 (K)	710	720	430	—	810	180

Ignition and Combustion Behavior

Figure 2 presents a composite pressure trace summarizing all successful hot firing. The time defined as ' $t=0$ ' corresponds to the start of the main oxygen flow ramp (the igniter is activated at -0.5 s). At a time of 0.5 s, the oxygen ramp reaches its pre-programmed, constant plateau. The carbon dioxide grain burns until depleted. Oxygen continues to flow according to the pre-programmed profile, then is ramped down.

Based on the pressure trace, asymmetric grain formation was suspected for Test 1, resulting in premature grain burn-through in one location during the burn and a subsequent grain break-up. For Test 1, CO gas was introduced into the grain chamber through the igniter port, rather than through the exit nozzle. Room-temperature CO gas entering the grain chamber through the angled igniter port at high velocity could have warmed one area of the grain, resulting in a thin area prone to early burn-through. To reduce the chance of asymmetric grain formation, the location of the gas input was changed from the igniter port in the head end, which pointed into the chamber at an angle, to the nozzle at the aft end, which is directed straight up the axis of the chamber. In addition, the CO gas velocity and temperature were decreased to reduce convective warming of the grain chamber during the freezing process. As the Test 2 pressure profile illustrates, the second test had a lower pressure than the first, and a lower rise rate. Test 2 also displayed a smoother pressure tail-off, although some prominent pressure spikes appear near the end of the test. It is worth noting that Test 2 had a higher C^* efficiency than Test 1 (87%, vs. 82%), also suggesting a cleaner burn with less ejection of solid grain material.

Tests 1 – 3 and 5 exhibited the same overall pressure profile: a rapid rise at ignition, a gradual further increase for approximately 60%-70% of the test duration, and a concluding pressure tail-off which may or may not be marked with pressure spikes. The pressure spikes may be due to small pieces of solid fuel flaking off of the grain and passing through the exit nozzle. For a given test, the pressure increase and tail-off behavior may be due to both a non-uniform fuel regression rate profile along the length of the grain and also an increase in fuel surface area as combustion port radius increases due to fuel regression. Also, temperature data consistently indicated very hot temperatures near the aft end of the engine (T2) and very cold temperatures near the head end of the engine (T1). These data indicate that the most

intense burning was occurring near the aft end of the engine, suggesting that the injected oxygen flow was jetting past the head end of the grain and burning the grain away from the bottom up. This mode of burning is undesirable and could possibly contribute to grain break-up; ideally, the grain should regress evenly at the top and the bottom.

A conical spray injector was therefore designed for Test 6 with the intention of slowing the incoming oxygen gas and distributing it more uniformly to the head-end of the grain. Though the operating conditions are the same, the Test 6 pressure trace is generally lower than that of Test 2. This difference is also reflected in the relatively poor C* efficiency for Test 6: 76%, vs. 87% for Test 2. In general, Test 6 had fewer pressure spikes than Test 2, although the overall profile remained quite non-uniform. Thermocouple data indicated that temperatures in the head end of the grain chamber (T1) were much warmer than previously measured for Tests 1-3 and 5, while temperatures in the aft end of the engine (T2) were much cooler (see Table 1). This result indicates preferential head-end burning with the conical spray injector.

SCO Regression Rate Behavior

Figure 3 shows the average fuel regression rate behavior of SCO as a function of average oxygen mass flux for the test firings shown in Table 1. Data for additional fuels that ORBITEC has tested, such as methane (CH₄) and aluminized methane, are also shown. This type of plot is typical for illustrating regression rate dependence on operating conditions for conventional hybrids. Tests 2, 3, and 5 were used to obtain an SCO regression rate correlation of $r = 0.072 G_o^{0.38}$ with r in cm/s and G_o in g/cm²-s. The local, instantaneous regression rate will in general differ from this average. Test 1 was not included in the correlation because of the suspected asymmetric grain formation. Test 6 used the alternate conical GOX injector, and was also not used in obtaining the correlation. For comparison, Figure 3 also shows a regression rate correlation for conventional hybrid rocket engines burning oxygen and HTPB (hydroxyl-terminated polybutadiene) rubber. While this correlations from Ref. 3 has been extrapolated to the relatively low G_o levels used in the current study, it serves to illustrate that the cryogenic SCO regresses much faster than typical rubber-based hybrid fuels. Over the G_o range shown in Figure 3, the SCO regresses about 6.6 times faster than the correlation given in Ref. 3.

It is also worth noting that the power of 0.38 in Eq. (3) is significantly lower than those for the conventional hybrid correlations shown in Figure 3 (0.68). Fuel grains governed by convective heat transfer to the fuel surface in fully turbulent boundary layers have theoretical powers of 0.8.⁴ However, empirical correlations such as those shown in Figure 3 generally display somewhat lower values of 0.8 due to the influence of non-convective effects, such as thermal radiation, heterogeneous reactions on the fuel surface, or rate-limiting gas-phase reaction rates. Though the correlation $r = 0.072 G_o^{0.38}$ should be considered preliminary due to the small number of data points, it seems to suggest that the cryogenic SCO fuel regression behavior may differ significantly from that of classical hybrid fuel.

REFERENCES

1. Knuth, W. H., Chiaverini, M. J., Sauer, J. A., and Gramer, D. J., "Solid-Fuel Regression Rate and Combustion Behavior of Vortex Hybrid Rocket Engines," AIAA 99-2318, Los Angeles, 1999.
2. Rice, E. E., Chiaverini, M. J., St.Clair, C. P., Knuth, W. H., and Gustafson, R. J., "Mars ISRU CO/O₂ Hybrid Engine Development Status," AIAA 2000-1066, Reno, 2000.

3. Sutton, G., *Rocket Propulsion Elements: An introduction to the Engineering of Rockets*, Sixth Edition, John Wiley & Sons, 1992, pp. 513.
4. Marxman, G. A., Wooldridge, C. E., and Muzzy, R. J., "Fundamentals of Hybrid Boundary Layer Combustion," *Heterogeneous Combustion, Progress in Astronautics and Aeronautics*, Vol. 15, Academic Press, New York, 1964, p. 485-521.

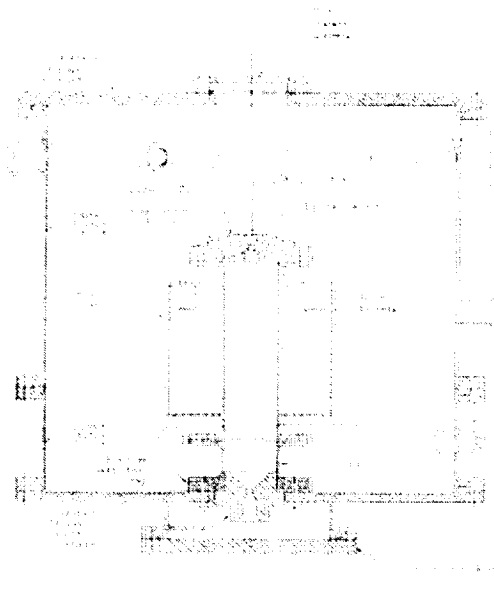


Figure 1. Mark II Engine Assembly

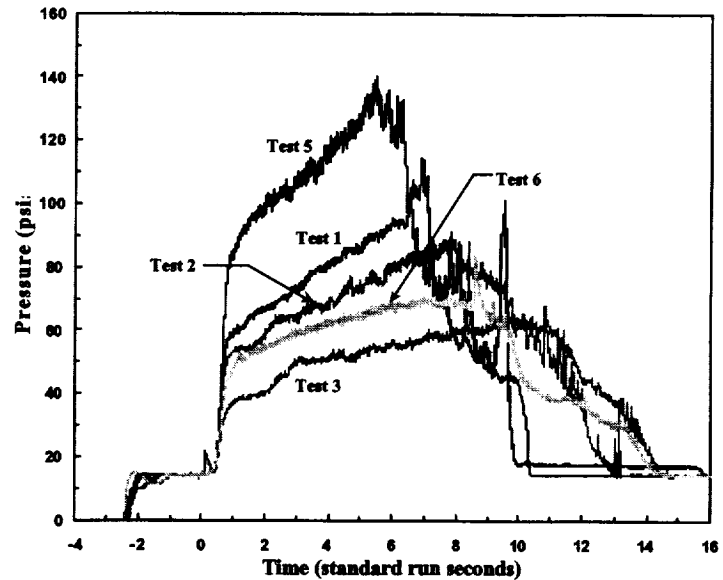


Figure 2. Pressure Summary

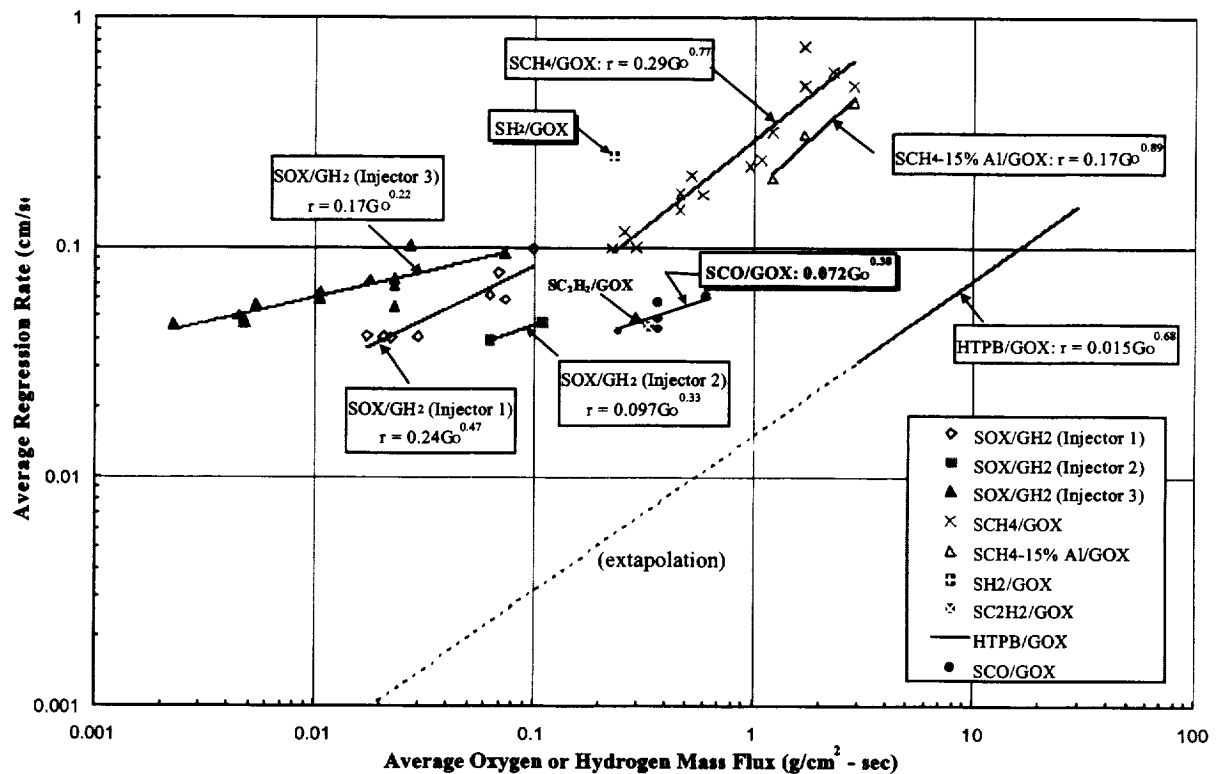


Figure 3. Average Regression Rate Data for SCO and Other Cryogenic Solid Propellants

Combustion of Interacting Droplet Arrays in a Microgravity Environment

D. L. Dietrich, NASA John H. Glenn Research Center

P. M. Struk, National Center for Microgravity Research

M. Ikegami, H. Nagaishi, S. Honma, K. Ikeda, Hokkaido National Industrial Research Institute

INTRODUCTION

Investigations into droplet interactions date back to Rex *et al.* [1]. Annamalai and Ryan [2] and Annamalai [3] published extensive reviews of droplet array and cloud combustion studies. In the majority of the reviewed studies, the authors examined the change in the burning rate constant, k , (relative to that of the single droplet) that results from interactions. More recently, Niioka and co-workers [4] have examined ignition and flame propagation along arrays of interacting droplets with the goal of relating these phenomena in this simplified geometry to the more practical spray configuration.

Our work has focussed on droplet interactions under conditions where flame extinction occurs at a finite droplet diameter. In our previous work [5], we reported that in normal gravity, reduced pressure conditions, droplet interactions improved flame stability and extended flammability limits (by inference). In our recent work, we examine droplet interactions under conditions where the flame extinguishes at a finite droplet diameter in microgravity. The microgravity experiments were in the NASA GRC 2.2 and 5.2 second drop towers, and the JAMIC (Japan Microgravity Center) 10 second drop tower. We also present progress on a numerical model of single droplet combustion that is in the process of being extended to model a binary droplet array.

EXPERIMENTAL HARDWARE AND DATA ANALYSIS

The experiments utilized the classical fiber-supported droplet combustion technique. A 125 or 230 μm (depending on the initial droplet size) fiber with a small bead (approximately 1.5-2.0 times the fiber diameter) supported the droplets. The fuel was n-decane for all of the tests. A small coiled hot-wire, withdrawn immediately after ignition, ignited the droplets.

The data for all of the experiments was from two orthogonally located video cameras. The first camera provided a magnified, backlit view of the droplet to obtain the droplet regression history. The second was an orthogonal view of the flame. For many of the tests, the flame was nearly invisible to the CCD camera. For these tests, we suspended a small 15 μm fiber across the droplet and flame to indicate the presence of the flame. The droplet diameter reported herein is an equivalent size obtained by equating the measured volume or the projected area of the droplet to that of the equivalent sphere or circle, respectively [6].

EXPERIMENTAL RESULTS

While the effects of buoyancy were minimized in the normal gravity testing, they were not altogether eliminated. Our first attempts to perform the same testing in microgravity involved testing in similar ambient conditions as the normal gravity tests. The initial testing [7] showed that the reduced pressure, air ambients that yield a finite extinction droplet diameter in normal gravity do not produce a finite extinction droplet diameter in microgravity. In fact, at pressures down to near the ignitable limit, the droplets burned to completion (or to a size smaller than the support fiber and bead). Thus in order to observe extinction at finite droplet sizes, we performed the microgravity experiments in reduced oxygen mole fraction, reduced pressure ambients.

Initial tests were in a 380 mm Hg, 0.17 oxygen mole fraction ambient. Flame extinction at a finite droplet diameter did not occur for either the single droplets or the binary droplet arrays. Consistent with earlier droplet array studies [8,9] the burning rate of the binary array was

lower than that of the single droplet. Additionally, the flame size of the array (measured normal to a line between the two droplets) is much larger (nearly 50 percent) than the flame of the single droplets. Finally, while the droplets in both tests burned to completion, the flame surrounding the binary array was much weaker (the intensity of the flame and the SiC fiber on the CCD camera) than the flame surrounding the single droplet.

The best ambient oxygen concentration for realizing extinction in microgravity was a 0.15 oxygen mole fraction ambient. Depending on the pressure, the flame did extinguish at a finite droplet diameter. Figure 1 shows the burning behavior as a function of time for a single droplet and a binary droplet array in a 380 mm Hg, 0.15 oxygen mole fraction (nitrogen diluted) ambient. Referring first to the single droplet tests, there are several noteworthy features of the burning behavior. First, this ambient condition was not flammable in normal gravity. In fact, droplets of this size could not sustain a flame in normal gravity regardless of the ambient pressure. Second, the burning behavior is non-linear. The burning rate is approximately $0.5 \text{ mm}^2/\text{s}$ immediately after ignition. It then increases throughout the test, reaching a final value nearly 40 percent higher than the value immediately after ignition.

The single droplet behavior presented in Figure 1 was typical over the range of pressures tested. At ambient pressures below 150 mm Hg, the flame extinguished at a finite droplet diameter for the single droplet tests. The extinction droplet diameter increased with decreasing ambient pressure, and at ambient pressures below 90 mm Hg, the flame extinguished almost immediately after ignition. While the extinction diameter was a strong function of pressure, the average burning rate constant was nearly independent of ambient pressure, consistent with the simplified theory for droplet combustion.

Finally, Figure 1 also presents the flame size and standoff ratio (normalized by the droplet diameter at that instant in time) for this droplet. The flame size initially grew with time. At some point in the middle of the burn, the flame size reached a maximum, remained constant for a time, then decreased with time until extinction. The flame standoff ratio, however increased nearly linearly with time throughout the burn. The flames were soot-free (visually) throughout the test, except for a brief period immediately after ignition for the higher pressure tests. Although not presented here, our testing in the 0.15 oxygen mole fraction ambient also examined droplet diameter effects, and ignition energy effects in addition to the pressure effects.

Figure 1, however, shows that the binary droplet array exhibited very different behavior. The flame surrounding the array extinguished quickly after igniter withdraw. The droplet diameter at flame extinction was approximately 1.1 mm for both droplets. The flame size (measured perpendicular to a line between the droplets), similar to the 0.17 oxygen mole fraction tests, was nearly 50 percent larger than the single droplet. In the binary array test, however, the flame size increased reached a maximum but then extinguished before decreasing. The flame standoff increased continuously and linearly until extinction. The above trends were consistent over a range of inter-droplet spacings and ambient pressures. In the 0.15 oxygen mole fraction ambient, in all cases tested, the flame surrounding the binary array always extinguished at a larger droplet size than the flame surrounding a single droplet.

The results cited above display an opposite trend to the normal gravity test results. That is, interactions diminished flame stability in the microgravity tests, whereas in the normal gravity tests, interactions promoted flame stability. This discrepancy may be in part due to the differing ambient oxygen mole fraction ambients in the two studies. Specifically, the large, weak flames in the microgravity tests were most likely strongly influenced by large radiative (spectral, due to

the lack of soot) losses from the flame zone. In fact, we believe that the extinction process was dominated by radiative loss [10].

Figure 2 shows the results of a single droplet and a binary droplet array, only in this case, the ambient was 0.25 oxygen mole fraction, 190 mm Hg and the diluent was helium as opposed to nitrogen. Typically, single droplets burning in helium, have high burning rates and lower flame temperatures because of the high gas-phase thermal conductivity than droplets burning in a nitrogen ambient (the same ambient oxygen mole fraction). The flames also have smaller standoff ratios. The result is flames that extinguish at finite-sized droplet diameters, in regions where radiative losses should be smaller than the flames in Fig. 1. Figure 2 shows that the flame surrounding the single droplet extinguished quickly after ignition. The burning rate constant before flame extinction was quite high, $1.0 \text{ mm}^2/\text{s}$. The flame standoff ratio was approximately 10, and was much smaller than in the nitrogen diluted tests (e.g. Fig. 1).

Figure 2 shows, in contrast to Fig. 1, that the binary droplet array ($L = 4 \text{ mm}$) burned for much longer, and extinguished at a smaller size than the single droplet. The trend is opposite to that displayed in Fig. 1, but in agreement with our previous normal gravity testing [5]. Interestingly, while the binary array had a smaller extinction droplet diameter, it also had a much smaller burning rate. The average burning rate constant was $0.75 \text{ mm}^2/\text{s}$, approximately 25 percent smaller than the single droplet. The flame size and standoff ratio, measured perpendicular to a line between the two droplets, for the binary array was larger than the flame size and standoff ratio for the single droplet. Also, while not presented in Fig. 2, we should note that the flames surrounding the binary droplet array at inter-droplet spacings of $L = 8$ and 12 mm (merged flames existed for both spacings) both extinguished at droplet diameters smaller than the single droplet. The extinction behavior at an inter-droplet spacing of 24 mm , however, was nearly identical to that of a single droplet. The flames surrounding the droplets (individual flames surrounded each droplet) extinguished nearly immediately after ignition.

The helium and nitrogen diluents clearly exhibit different extinction behavior for the binary arrays (when compared to the single droplets). We believe the difference is primarily a function of the importance of radiative loss from the flame zone. Specifically, the binary arrays in the nitrogen ambient have very large, weak flames, much larger than the flames surrounding the single droplet. These large flames are dominated by radiative loss, and the increase in flame size from the single droplet to the binary droplet array is enough to cause extinction of the binary droplet array. For a binary droplet array, if the inter-droplet spacing were to approach zero, this would create a single droplet whose size was 30 percent larger than each individual single droplet. This single, larger droplet could be larger than the radiative extinction droplet size.

A similar argument can be made to explain the behavior of the helium-diluted tests. In this case, extinction occurs when the residence time is smaller than the required chemical time. For the binary droplet array, if the inter-droplet spacing were zero, this would again create a larger single droplet. This single droplet would have a larger residence time, and thus would not extinguish.

We are also in the process of developing a numerical model of the single droplet and binary droplet array to quantitatively explain the experimentally observed extinction results. The model is based on an existing model of the candle flame. The model is transient, assumes constant properties and Lewis numbers (although each species can have a different Lewis number), and most importantly, includes radiative loss (purely loss using a Planck mean absorption coefficient). We are currently using the single droplet model to predict and explain some of our single droplet results, and are in the process of modifying the code to model the binary droplet array.

REFERENCES

1. Rex, J.F., Fuhs, A.E. and Penner, S.S. *Jet Propulsion* **26**, 179 (1956).
2. Annamalai, K. and Ryan, W. *Progress in Energy and Combustion Science* **18**, 221-295 (1992).
3. Annamalai, K. *Mechanics and Combustion of Droplets and Spray*, ed. H.H. Chiu and N. Chigier, Begell House Inc., New York, New York, 116-160 (1995).
4. Nohara, H., Maruta, K., Hasewage, S., Kobayashi, H., and Niioka, T., *Combustion Science and Technology* **153**, 169-178 (2000).
5. Struk, P.M., Dietrich, D.L., Sims, C., Picot, B., Kitano, K., Honma, S., Ikeda, K., Ikegami, M. "Interacting Droplet Combustion Under Conditions of Extinction," Joint Meeting of the United States Sections of the Combustion Institute (1999).
6. Struk, P., Ackerman, M., Nayagam, V. and Dietrich, D., *Microgravity Science and Technology* (1999).
7. Easton, J.E. "Large Diameter, Radiative Extinction Experiments with Decane Droplets in Microgravity," M.S. Thesis, Case Western Reserve University (1998).
8. Xiong, T.Y., C.K. Law, C.K. and K. Miyasaka *Twentieth Symposium (International) on Combustion* / The Combustion Institute, 1781-1787 (1984).
9. Mikami, M., Kato, H., Kono, M. and Sato, J. *Twenty-Fifth Symposium (International) on Combustion* / The Combustion Institute, 423-428 (1995).
10. Chao, B.H., Law, C.K., and T'ien, J.S., *Twenty-Third Symposium (International) on Combustion* / The Combustion Institute, 523-531 (1990).

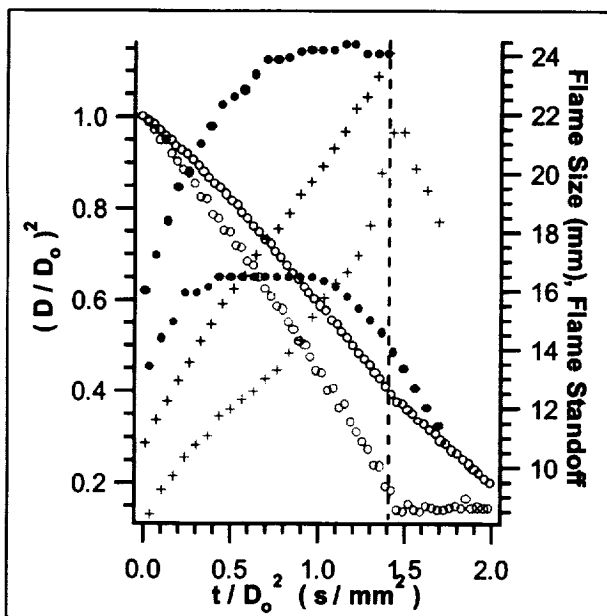


Figure 1. Droplet and flame histories for a Single droplet (red) and a binary array (blue). $P = 380$ mm Hg, $Y_{O_2} = 0.17$ (N_2 diluted). [for both figures: (o) droplet size; (●) flame size; (+) flame standoff ratio; and the dashed vertical line represents extinction.]

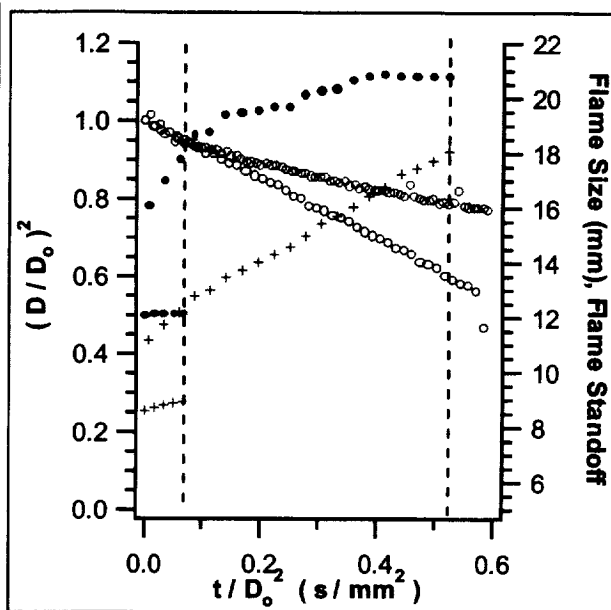


Figure 2. Droplet and flame histories for a single droplet (red) and a binary array (blue). $P = 190$ mm Hg, $Y_{O_2} = 0.25$ (He diluted).

HIGH-PRESSURE COMBUSTION OF BINARY FUEL SPRAYS

F.A. Williams, Center for Energy Research, Mechanical and Aerospace Engineering, University of California, San Diego, and **Daniel L. Dietrich**, NASA Glenn Research Center

INTRODUCTION

The research addressed here represents a small cooperative project between the US and Japan. The authors have now been involved in this project for a number of years. In previous workshops, the presentation has focused narrowly on the specific most recent accomplishment. If this tradition were followed again, then material about to be published [1] would form the basis of the present write-up. At the present stage, however, it may be of greater interest to step back and take a longer look at the overall character of the project and its history. The recent accomplishments therefore will be covered here only in an abbreviated manner.

SCIENTIFIC OBJECTIVE

The general scientific objective of this research, reflected in the title of this presentation, the current title of the US portion of the project, is to advance knowledge that can contribute to improvements in practical applications of spray combustion. Recognizing that practical interest centers mostly on high pressures and multicomponent fuels, the investigators chose to explore conditions up to critical pressures and to include binary liquid fuel mixtures as model systems with relevance to multicomponent fuels. Studies centered on single droplets, to the extent that their individual combustion characteristics were unknown, and on linear arrays of droplets, to obtain information on droplet-interaction effects having bearing on spray combustion. Intending to be fundamental, the investigation avoided the complexity of working with sprays themselves. It was never intended to go beyond arrays, and in fact most of the studies concerned droplet pairs and single droplets. In recent years, interest has progressed to the consideration of additional effects that might be employed to augment performance of spray combustion, namely effects of acoustic fields [1] and of electric fields. Embracing a wide range of physical phenomena, the work has explored a number of avenues for improving ideas about spray combustion.

ORGANIZATION

The project was organized in an attempt to establish, for the first time, a small-scale cooperative research program between Japan and the US in microgravity combustion. J. Sato of IHI was a prime mover in this organization. The universities involved are the University of Tokyo, where this research is led by M. Kono, and UCSD, where the research is led by F.A. Williams. The research includes experiments performed in the 2.2 second drop tower at NASA Glenn Research Center, with D.L. Dietrich overseeing the experiments. Graduate students from the University of Tokyo are involved in these drop-tower experiments and also perform experiments in a smaller drop tower at their own university. The graduate students who have (sequentially) participated in the project in this way are M. Mikami (now a professor at another university in Japan), O. Habara, K. Okai and, most recently, T. Ueda. The student typically visits Cleveland for about two months twice a year to perform experiments and then spends a week or two in San Diego analyzing the results with F.A. Williams before returning to Tokyo. The meanings of the experimental results, their theoretical interpretations and the associated new theoretical developments that are needed are then addressed by all of the investigators at their respective locations, with communications by mail, phone, fax and especially e-mail. These relatively recent advances in communications have been essential in making this cooperative program possible. The program is notably economical, with all of the work and travel of the Japanese investigators supported by Japan and of the US investigators by NASA.

HISTORY

The specific problems addressed in the research are determined jointly through discussions among the Japanese and US investigators. Following these discussions, first the combustion of single droplets of mixtures of heptane and hexadane was investigated in reduced-oxygen atmospheres at pressures up to 3 MPa [2]. The droplets studied are fiber-supported and

nominally of about 1 mm initial droplet diameter. Extending pressures to 6 MPa in air demonstrated the importance of accounting for three-component phase diagrams involving dissolution of inert gas in the liquid near the critical point if observed variations of minima of burning times are to be properly explained [3]

Having developed an understanding of single-droplet behavior, it was decided to investigate effects of interactions of droplets of these same fuels burning under these same atmospheric conditions. Closely spaced droplets were shown to exhibit increased burning lifetimes, there being a minimum in the lifetime at a critical interdroplet spacing [4]. For fuels that are mixtures of methanol and dodecanol, however, burning at pressures up to 9 MPa, the minimum is not present at any interdroplet spacing because the radiative augmentation of burning rates is insufficiently strong [5]. The most recent experiments in the 2.2 second tower employed single droplets with mirrors and other obstacles nearby to further clarify effects of radiation interactions [6]; these experiments showed significant influences of the obstacles on the flow fields under microgravity, with flow effects distorting flame shapes and generally outweighing radiation effects.

The work is thus seen to have progressed from studies of single droplets of pure fuels at pressures up to values in the vicinity of the critical pressure, to studies of single droplets of binary fuel mixtures at pressures up to critical (with staged and disruptive burning behaviors identified), to studies of interactions of arrays of pure-fuel and binary-mixture droplets, for different fuel pairs (alkanes and alcohols), again up to the vicinity of critical pressures. The information obtained in this way was judged to provide some understanding of droplet combustion behaviors relevant to high-pressure spray combustion, sufficient to proceed to investigate additional complicating effects that may be of benefit in spray-combustion applications. With this in mind, new apparatus was built for the purpose of measuring influences of acoustic and electric fields on the combustion of single droplets and of droplet pairs. Measurements have now been made of each of these effects separately, for both single droplets and droplet pairs, but as yet only for octane droplets burning in air at normal atmospheric pressure under normal and microgravity. The results are discussed in the following sections.

EFFECTS OF ELECTRIC FIELDS

To date, the experiments in the electric fields have been performed only in the small drop tower at the University of Tokyo. Initial droplet diameters were about 0.75 mm, and field strengths ranged up to 50,000 V/m. The effect of the field on the flame appears to be much stronger in microgravity than in normal gravity. The flame around a single droplet is attracted towards the negatively charged electrode, as anticipated from the belief that the ions and soot particles are predominantly positively charged. The burning rate of the droplet is slightly higher at the highest field strengths, as might be expected from the effect of the electric wind. At sufficiently high field strengths, there seems to be periodic emissions of burning soot particles through the flame, mainly towards the negatively charged electrode. These behaviors of single droplets may qualitatively be expected in advance.

For droplet pairs, the observed behaviors are more complex and in some ways counterintuitive. The experiments were performed with the electric field parallel to the axis between the centers of the droplets. For interdroplet separation distances small enough that the flame surrounds both droplets in the absence of the field, the electric field reduces the extent of droplet engulfment by the flame, tending to form separate flames around each droplet, and those two flames are asymmetrical, with the brighter flame located on the side towards the positive electrode, as if the flame on the side towards the negative electrode were subjected to a convective velocity from the electric wind that lengthens and narrows it, reducing its total luminosity. At larger interdroplet separation distances, the visible yellow flame around each droplet separately tends to be elongated towards the nearest electrode, which is unexpected for the flame near the positive electrode since it suggests that the electric wind is dominated by negatively charged particles there. The possible occurrence of negatively charged soot particles is supported by the observation that, although most burning soot particles are emitted in the direction of the negative

electrode, some are emitted in the direction of the positive electrode, even for single burning droplets if the electric field is sufficiently high. Visible flames thus are narrowed by the field and protrude not only in the direction of the negative electrode but also to some extent in the direction of the positive electrode, perhaps under the combined effects of positively and negatively charged particles in the flame.

EFFECTS OF ACOUSTIC FIELDS

Measurements of the influences of acoustic fields on the microgravity combustion of single droplets and of droplet pairs employed a loud speaker at the bottom of the chamber to produce the acoustic field [1]. Experimental results for single droplets showed that, at low frequency and small to moderate acoustic intensities, the evaporation rate increases with increasing acoustic field strength, with the burning-rate constant k nearly proportional to the product of frequency, f , and square of displacement, X^2 , that is,

$$k = k_0(1 + \alpha f X^2), \quad (1)$$

where k_0 denotes the burning-rate constant in the absence of the field, and α is a constant. At higher acoustic intensities, the burning-rate constant either remains constant or decreases, and, in some cases, flame extinction occurs at a finite flame diameter. The experimental results extending to these higher intensities can be fit by the formula

$$k = k_0 + A f X^2 [1 - f X^2 / (2D)], \quad (2)$$

with the value of the nondimensional constant A being about 0.03 and the critical acoustic diffusivity D at which the burning-rate constant is a maximum having a value of about $10 \text{ mm}^2/\text{s}$. Theoretical explanations for these experimentally observed values of the parameters are still under investigation.

Results of a representative experiment are shown in Fig. 1, where the acoustic velocity is defined a $V_a = 2\pi f X$, d denotes the droplet diameter, its initial value being d_0 , t is time, and the visible flame height H in the direction of the acoustic field and width W perpendicular to that direction are obtained from a CCD cameral. Experimental details are given elsewhere [1]. It is seen that H/d_0 and W/d_0 both plateau, with W/d_0 larger than H/d_0 as a consequence of the gas motions induced by the acoustic field.

Figure 2, where l denotes the interdroplet spacing, shows corresponding results for droplet pairs, at acoustic intensities giving X of order 0.1 mm. The acoustic field is applied here perpendicular to the axis between the two droplets and is seen to increase the burning-rate constant under the conditions of the experiment, and the flame height decreases with increasing frequency. The burning-rate constant for a droplet pair is consistently lower than that of the single droplets. At lower frequencies, the burning-rate constant reaches a maximum at an intermediate acoustic intensity for droplet pairs, and at higher frequencies it increases monotonically with increasing acoustic intensity. The flame size decreases as a result of interactions, as does the critical spacing for the formation of a merge flame around the droplet pair, rather than having individual flames surrounding the droplets. The results also show that interactions stabilize the flame, in that droplet pairs burn to completion under conditions where the flame surrounding a single droplet extinguishes at a finite droplet diameter. Figure 3 shows the variety of different shapes of flames around droplet pairs that can be produced by the acoustic field [1]; the droplet separations are all horizontal, and the arrows at the edges identify the direction of application of the acoustic field, which is parallel to the interdroplet axis in the third frame (c). Explanations of these results currently are undergoing further study.

FUTURE WORK

This program is planned to continue to study influences of electric and acoustic fields on the combustion of single droplets and droplet pairs. In addition to attempting to clarify better the physical reasons for the effects described above, it is intended to consider fuels other than octane and influences of pressures above atmospheric, to better ascertain how acoustic and

electric fields may affect spray combustion under conditions of greater practical interest. Many challenging questions clearly remain to be addressed.

REFERENCES

1. Okai, K., Moriue, O., Araki, M., Tsue, M., Kono, M., Sato, J., Dietrich, D.L. and Williams, F.A., "Combustion of Single Droplets and Droplet Pairs in a Vibrating Field under Microgravity," *Proceedings of the Combustion Institute*, Vol. 28, 2000, to appear.
2. Mikami, M., Kono, M., Sato, J., Dietrich, D.L. and Williams, F.A., "Combustion of Miscible Binary-Fuel Droplets at High Pressure Under Microgravity," *Combustion Science and Technology*, Vol. 90, 1993, pp. 111-123.
3. Mikami, M., Habara, O., Kono, M., Sato, J., Dietrich, D.L. and Williams, F.A., "Pressure Effects in Droplet Combustion of Miscible Binary Fuels," *Combustion Science and Technology*, Vol. 124, 1997, pp. 295-309.
4. Okai, K., Tsue, M., Kono, M., Mikami, M., Sato, J., Dietrich, D.L. and Williams, F.A., "Strongly Interacting Combustion of Two Miscible Binary-Fuel Droplets at High Pressure in Microgravity," *Proceedings of the Combustion Institute*, Vol. 27, 1998, pp. 2651-2657.
5. Okai, K., Moriue, O., Araki, M., Tsue, M., Kono, M., Sato, J., Dietrich, D.L. and Williams, F.A., "Pressure Effects on Combustion of Methanol and Methanol/Dodecanol Single Droplets and Droplet Pairs in Microgravity," *Combustion and Flame*, Vol. 121, 2000, pp. 501-512.
6. Okai, K., PhD Thesis, University of Tokyo, in preparation, 2001.

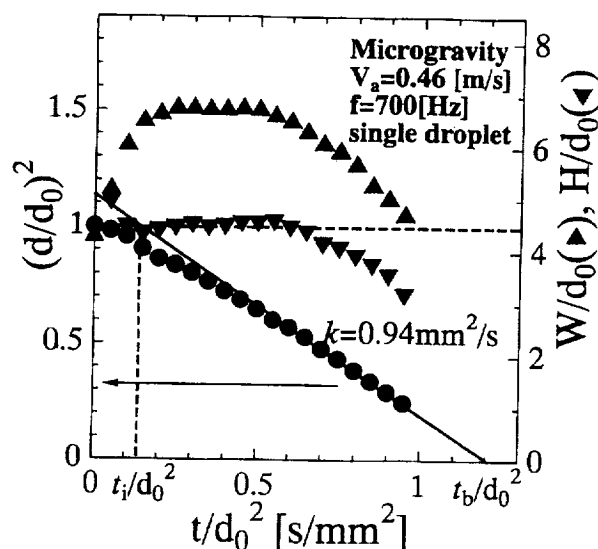


Figure 1: Histories of droplet diameters and flame characteristics for combustion of a single droplet in an acoustic field.

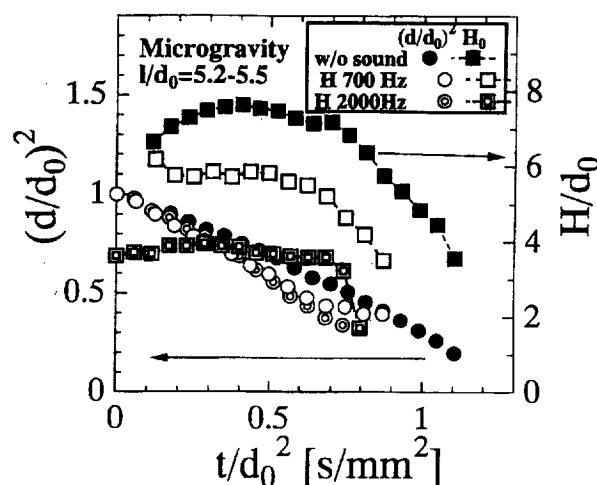


Figure 2: Histories of droplet diameters and flame characteristics for combustion of droplet pairs in acoustic field.

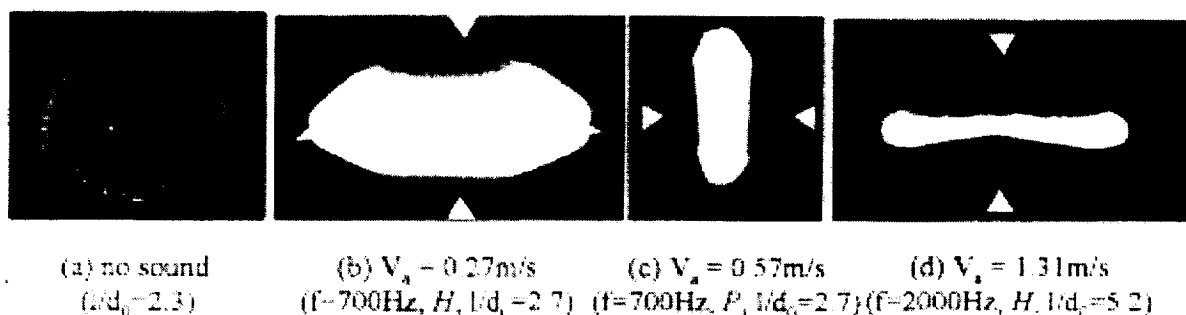


Figure 3: Typical direct photographs of flames for burning droplet pairs in acoustic fields.

MICROGRAVITY EXPERIMENT ON FLAME SPREAD OF A BLENDED-FUEL DROPLET ARRAY AT SUPERCRITICAL PRESSURE

Takeshi Iwahashi¹, Hideaki Kobayashi² and Takashi Niioka²

¹Toyota Motor Corporation, Toyota, Aichi 471-8572, Japan

²Institute of Fluid Science, Tohoku University, Sendai, Miyagi 980-8577, Japan

INTRODUCTION

Investigation of spray combustion in a high-pressure environment is important for improving control of practical high-loaded combustors and for developing sustainable combustion technology. The mechanism of spray combustion over the critical pressure is particularly interesting from a scientific point of view because the thermal and transport properties of liquid fuel drastically change in this pressure range.

Research using a model of flame spread of a fuel droplet array has been performed to simulate the fundamental flame propagation mechanism of fuel spray [1]. However, because the size of a flame is much larger than that of a single droplet, strong buoyancy is generated, especially at high pressure. Therefore, a microgravity environment is useful for conducting such experiments. Yoshida et al. performed flame spread experiments on droplet arrays of n-heptane, ethanol, and n-undecane using a drop facility and showed that the flame spread rate decreased monotonously with pressure [2]. The maximum pressure of their experiment was 0.5 MPa, which was lower than the critical pressure of the fuels. The present authors performed flame spread experiments on n-decane and n-hexadecane droplet arrays in normal gravity [3] and on n-decane in microgravity at pressures up to 5.0 MPa [4].

In the present study, we extended the flame spread experiments to those using 1-octadecene and blended fuel in microgravity, and herein discuss the effects of pressure and vaporization characteristics of the blended fuel on the flame spread phenomena.

EXPERIMENTAL APPARATUS

Microgravity experiments were performed using the drop-shaft facility of the Microgravity Laboratory of Japan (MGLAB) located in the city of Toki. The free-fall length, the test duration and the quality of microgravity of the facility are 100 m, 4.5 s, and $10^{-5}g$, respectively. Figure 1 shows the experimental setup installed in a payload rack of MGLAB's drop capsule. The apparatus consists of a high-pressure chamber, an image intensifier, a high-speed video system, a CCD video camera, optical mirrors, a note-book computer, and so on. A droplet array was arranged using the fiber suspension method. Each droplet was suspended at the end of a fine silica fiber $135 \pm 5 \mu\text{m}$ in diameter, the spherical end being $300 \pm 25 \mu\text{m}$ in diameter. In the present experiment, a maximum of 14 silica fibers was arranged with all spherical ends of the fibers on a line horizontally with equal spacing. Because the shape of each suspended droplet was ellipsoidal, the equivalent droplet diameter was calculated using the short and long diameters of the droplet. The droplet at the end of the array was ignited using a Kanthal wire coil.

The fuels used in this experiment were n-decane ($\text{C}_{10}\text{H}_{22}$, $T_b=447 \text{ K}$, $T_c=618 \text{ K}$, and $P_c=2.11 \text{ MPa}$, where T_b , T_c , P_c are standard boiling temperature, critical temperature, and critical pressure, respectively), 1-octadecene ($\text{C}_{18}\text{H}_{36}$, $T_b=558 \text{ K}$, $T_c=739 \text{ K}$, and $P_c=1.13 \text{ MPa}$), and blends of these fuels. Equivalent droplet diameter, D , and droplet spacing, S , were 1.0 mm and 2.0 mm, respectively. In the case of the blended fuel, the volume fractions of n-decane and 1-octadecene are 50% and 50%, respectively, corresponding to molar fractions of 62% and 38%. Estimated properties of the blended fuel were $T_b=467 \text{ K}$, $T_c=685 \text{ K}$, and $P_c=2.56 \text{ MPa}$.

Just after production of the droplet array, the capsule was released and then ignited. Recorded high-speed OH emission images of the spreading flame were analyzed after the capsule was recovered. The time history of the locus of the OH emission forehead of spreading flame was plotted and the flame spread rate was calculated from the gradient of the plot.

RESULTS AND DISCUSSION

OH Emission Images of Spreading Flame

Figure 2 shows the OH emission images of 1-octadecene and blended fuel. In the case of 1-octadecene (Fig. 2a), a relatively smooth flame spread was observed. On the other hand, in the case of blended fuel (Fig. 2b), zigzag and intermittent flame spread was often seen, similar to the case of the n-decane droplet array near and over the critical pressure [4]. In the case of the n-decane droplet array, it was previously found [4] that fuel vapor jets induced by Marangoni convection of droplet are issued from the unburned droplet in the pressure range near the critical pressure, causing the zigzag-like flame spread. Therefore, a fuel-vapor jet was also expected to occur in the case of the blended fuel droplet array.

Flame Spread Rates of Single and Blended Fuel Droplet Arrays

Figure 3 shows variations of the flame spread rate with pressure for n-decane, 1-octadecene and the blended fuel in microgravity. The flame spread rate of the 1-octadecene droplet array is smaller than that of n-decane, but its dependence on pressure appears to be similar to that of n-decane. For n-decane and 1-octadecene droplet arrays, it can be seen that the flame spread rates decrease with pressure and reach the minimum and then increase again with pressure. It has been explained that this variation is basically caused by enhancement of fuel transportation due to the generation of a fuel vapor jet from the unburned droplet mentioned above. The standard boiling temperature of 1-octadecene is about 140 K higher than that of n-decane and the molar latent heat of 1-octadecene is 40% greater than that of n-decane. This large latent heat and boiling temperature, which behave as large heat loss, lead to the low flame spread rate on the 1-octadecene droplet array because the unburned droplet is heated and ignited by the burning droplet, resulting in the flame spread phenomena.

Although data are not shown in this figure, the flame spread rate in normal gravity monotonously decreased with pressure and reached the flame spread limit at a certain pressure. This is due to the strong buoyancy effects at high pressure in normal gravity.

It is interesting to see in Fig. 3 that, for the blended fuel, the flame spread rate is large in the lower pressure range and the pressure dependence is very close to that of n-decane. However, when the pressure increases further and exceeds the critical pressure of the blended fuel (2.56 MPa), the flame spread rate decreases quickly and becomes almost equal to that of 1-octadecene. The mechanism of the pressure dependence of the flame spread rate for the blended fuel will be discussed in the next section.

Flame Spread Mechanism of a Blended Fuel Droplet Array

To clarify the mechanism of the pressure dependence of the flame spread rate for the blended fuel, the evaporation characteristics of the blended fuel should be considered. For flame spread of a fuel droplet array, the fuel is evaporated when the unburned droplet is heated by the flame of a burning droplet and the surface temperature reaches the boiling point. The change in the vapor composition during the heating can be estimated from the temperature-composition relations at various pressures. In this study, the equilibrium conditions of the gas and liquid phases for binary fuel were calculated. As for the calculation, the Peng-Robinson state equation was used at

pressures below 1.13 MPa, and the SKR state equation was used at pressures over 1.11 MPa. The equilibrium condition was determined so that the fugacity of the gas phase becomes equal to that of the liquid phase.

Figure 4 indicates the differences in the fuel vapor composition at 0.5 MPa and 2.3 MPa. In this figure, when temperature increases at of an n-decane molar fraction of 0.62, it reaches the liquid phase curve at both pressures. At 0.5 MPa, the equilibrium temperature is 560 K, corresponding to the boiling temperature at this pressure. The molar fraction of n-decane at the intersection point between the horizontal line of this equilibrium temperature and the gas phase curve corresponds to that of the n-decane molar fraction in the fuel vapor, which is 0.94 at this pressure. This means that when a blended fuel whose n-decane molar fraction is 0.62 is heated at 0.5 MPa, the boiling point becomes 50 K higher than that of n-decane and the n-decane molar fraction in the fuel vapor becomes 0.94. The variations of the n-decane molar fraction of fuel vapor with pressure estimated using the above-mentioned method indicated that the n-decane molar fraction in the fuel vapor decreases with a rise in pressure. On the other hand, the 1-octadecene molar fraction in the fuel vapor increases with pressure, reaching almost the same molar fraction as that of the liquid phase at pressures over 2.0 MPa.

Based on the above-mentioned pressure effects on the molar fractions of the fuel vapor, explanations of the mechanism of pressure dependence of the flame spread rate for the blended-fuel droplet array seen in Fig. 3 are possible. The pressure dependence of the flame spread rate is similar to that of n-decane at pressures up to about 2.5 MPa, although the flame spread rate is slightly smaller than that of n-decane. This is because the boiling temperature of the blended fuel is 50 K higher than that of n-decane but the most of the fuel vapor consists of n-decane. The velocity of the fuel-vapor jet is also expected to be smaller. When the pressure was increased further and exceeded 2.5 MPa, the flame spread rate decreased drastically and became almost equal to that of 1-octadecene. This is because the gas-phase molar fraction became almost equal to the liquid phase molar fraction and the effects of 1-octadecene on the ignition time became significant.

CONCLUSIONS

The flame spread rate of 1-octadecene was found to be smaller than that of n-decane over the whole pressure range in this experiment. The pressure dependence of the flame spread rate was dominated by n-decane in the pressure range from atmospheric pressure to a pressure near the critical pressure of the blended fuel. When the pressure increased further, 1-octadecene dominated the flame spread characteristics. These characteristics of the flame spread of the blended fuel were explained based on gas-liquid equilibrium states, that is, the fuel gas which evaporated from the droplet at ordinary pressure consists mostly of n-decane, whereas over the critical pressure, the composition of the fuel gas was almost the same as that of the liquid phase, resulting in a significant effect of 1-octadecene on ignition and flame spread at this higher pressure.

ACKNOWLEDGEMENTS

This research was supported by NASDA and the Japan Space Forum, under Ground Research Announcement for Space Utilization.

REFERENCES

1. Faeth, G. M., Dominicus, D. P., Tulpinsky, J. F., and Olson, D. R., *Proc. Combust. Inst.* 12: 9-18 (1969).

- [illegible]

Ambient pressure (MPa)	n-Decane (cm/s)	1-Octadecene (cm/s)	Blended fuel (cm/s)
0.1	4.0	1.1	2.9
0.5	3.3	0.8	2.4
1.0	3.0	0.9	2.1
1.5	3.2	0.9	2.5
2.0	3.4	1.0	2.4
2.5	3.3	1.1	2.7
3.0	2.9	1.1	1.4
3.5	3.3	1.2	1.3
4.0	2.9	1.2	1.3
4.5	2.7	1.1	1.3
5.0	2.5	1.1	1.3

Figure 1 is a phase diagram for n-decane showing Temperature (K) on the y-axis (ranging from 400 to 750) versus Mole fraction of n-Decane on the x-axis (ranging from 0 to 1). The diagram illustrates the phase boundaries for gas and liquid phases at two different pressures: 0.5 MPa and 2.3 MPa. The 0.5 MPa curves are shown as dotted lines, and the 2.3 MPa curves are shown as solid lines. The liquid phase boundary for 0.5 MPa starts at approximately 680 K at a mole fraction of 0 and decreases to about 520 K at a mole fraction of 1. The liquid phase boundary for 2.3 MPa starts at approximately 700 K at a mole fraction of 0.5 and decreases to about 520 K at a mole fraction of 1. The gas phase boundary for 0.5 MPa starts at approximately 680 K at a mole fraction of 0 and decreases to about 550 K at a mole fraction of 1. The gas phase boundary for 2.3 MPa starts at approximately 700 K at a mole fraction of 0.5 and decreases to about 550 K at a mole fraction of 1. A vertical line at a mole fraction of approximately 0.62 indicates the composition of the liquid fuel. A horizontal line at a temperature of approximately 420 K indicates the temperature of the evaporated fuel. The intersection of these two lines on the 2.3 MPa liquid phase boundary is labeled 'Liquid fuel'. The intersection of these two lines on the 0.5 MPa gas phase boundary is labeled 'Evaporated fuel'.

204

Auto-ignition and Flame Shapes of Geometrically Well-Controlled Group of Fuel Droplets in High Temperature Gaseous Environment under Micro-gravity

Hiroshi Enomoto, Hitoshi Nagata, Daisuke Segawa and Toshikazu Kadota

Department of Mechanical Engineering, Osaka Prefecture University
1-1, Gakuen-cho, Sakai, Osaka 599-8531 JAPAN

Phone: 81-722-54-9225

Fax: 81-722-54-9225

E-mail: enomoto@energy.osakafu-u.ac.jp

Introduction

The need to develop the advanced combustion technologies leading to the clean environments and the effective utilization of the fuel has resulted in the increased interest in the fundamental research on the combustion of fuel droplets. Most of the previous works has been toward the combustion of a single fuel droplet and an array of several number of fuel droplets. The knowledge of the fundamental aspects of the combustion phenomena of a group of fuel droplets, which is one of the key factors in the spray combustion, has been limited. In this paper, the new methodology to form a three-dimensional group of fuel droplets that are geometrically well controlled, Fine Wire Suspending (FWS) method is proposed. A net of SiC fibers supported by metal rings is available to suspend fuel droplets. Figure 1 shows the schematic of the group of fuel droplets.

On the other hand, the effect of gravitational forces impedes the combustion research more than most other fields of science since the combustion involves the production of high temperature burned gas, which results in the remarkable buoyant flow. The experiments are done at atmospheric pressure using the JAMIC drop shaft, which provides 10 seconds of effective

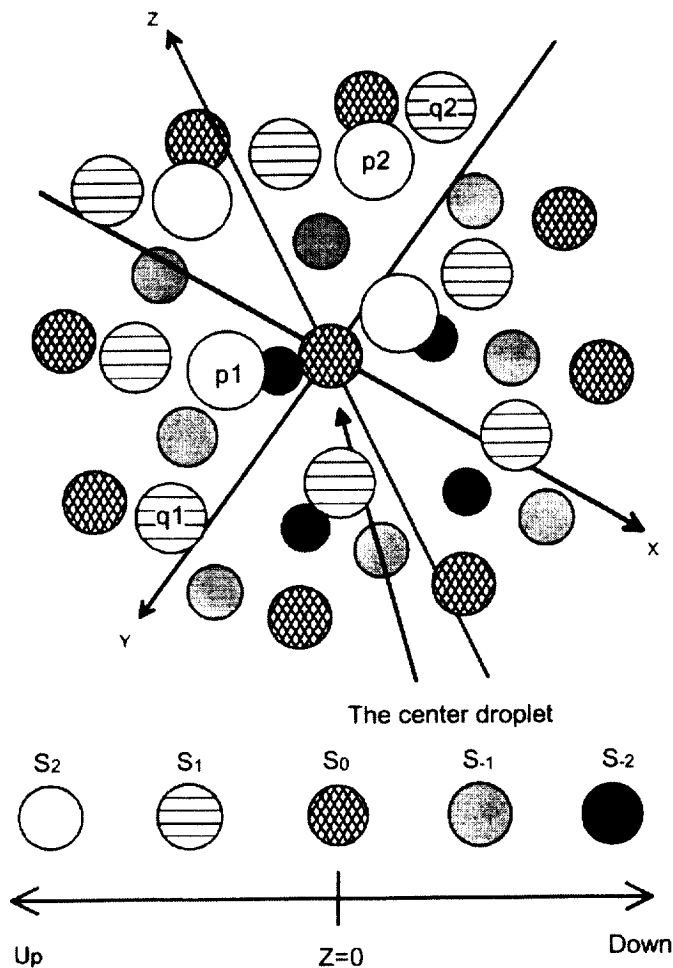


Fig. 1. Schematic of the well controlled group of fuel droplets.

period of time for the micro-gravity.

A group of fuel droplets arranged in symmetrically is subjected to the quiescent high temperature air in an electric furnace. A high speed video camera (250fps) is provided to observe the evaporation, auto-ignition and combustion of the group of fuel droplets. Figure 2 shows the typical flame shapes of the fuel droplets group under micro-gravity condition. The soot radiation could be observed. The time when the flame of the center droplet (see Fig. 1) could be recognized is the ignition time. Firstly, these droplets made the particle flames (at 4msec.). The duration that each particle flames could be distinguished is defined as the separated duration. These particle flames were integrated gradually (at 40msec.) and finally, the group flame could be observed (at 380msec.). The duration that the particle flames integrated to group flame is the integrated duration (see Fig. 2).

Experimental methodology

Figure 3 shows the experimental apparatus. The electric furnace had 127mm of inner diameter and 210mm inner height. The temperature was controlled by the computer and the wall temperature of the furnace was set at 1000K under atmospheric pressure. The sustaining ring was aluminum and 120mm of outer diameter and 114mm of inner diameter and 5mm of height. Five sustaining rings were used. The center ring was the stage 0 ring (S_0) and the upper rings (positive z-axis) were the stage 1 ring (S_1) and the stage 2 ring (S_2), respectively (see Fig. 1 and 3).

Fine wires were made of 3 SiC fibers, which diameter was $14\mu\text{m}$ ^(1, 2). n-eicosane was used for the droplet and the diameter was 0.55mm. The distance of droplet was the distance of the upper side between the sustaining rings. The ambient gas was air.

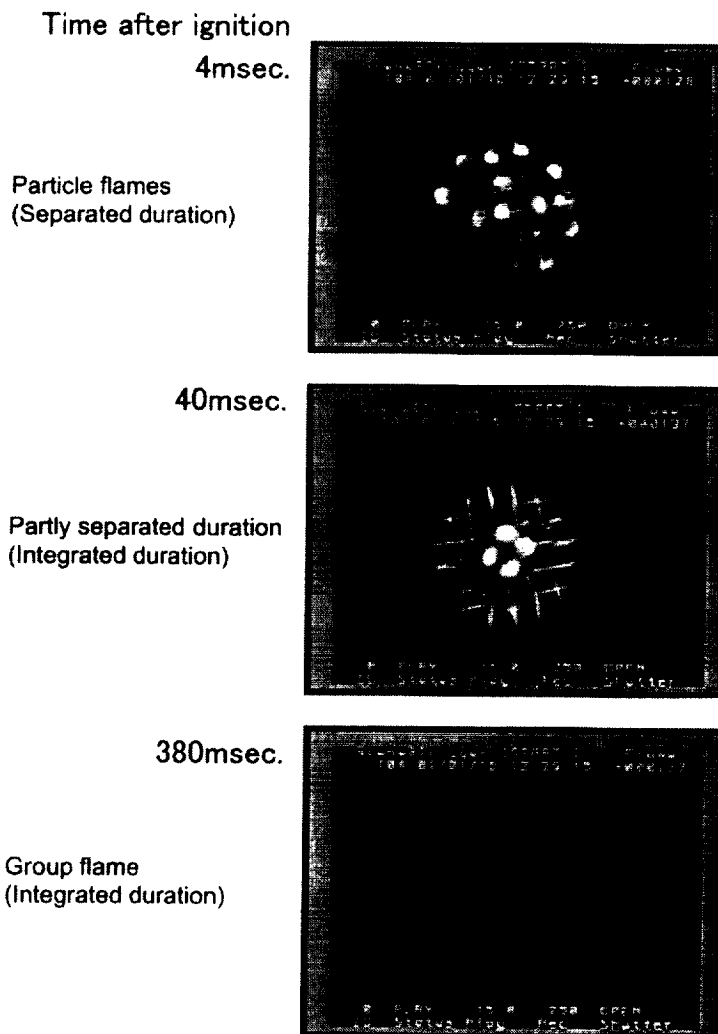


Fig. 2. Typical flame shapes.

Number of droplet: 33.
Diameter of droplet: 0.55mm
Distance of droplet: 10mm
Under micro-gravity condition.

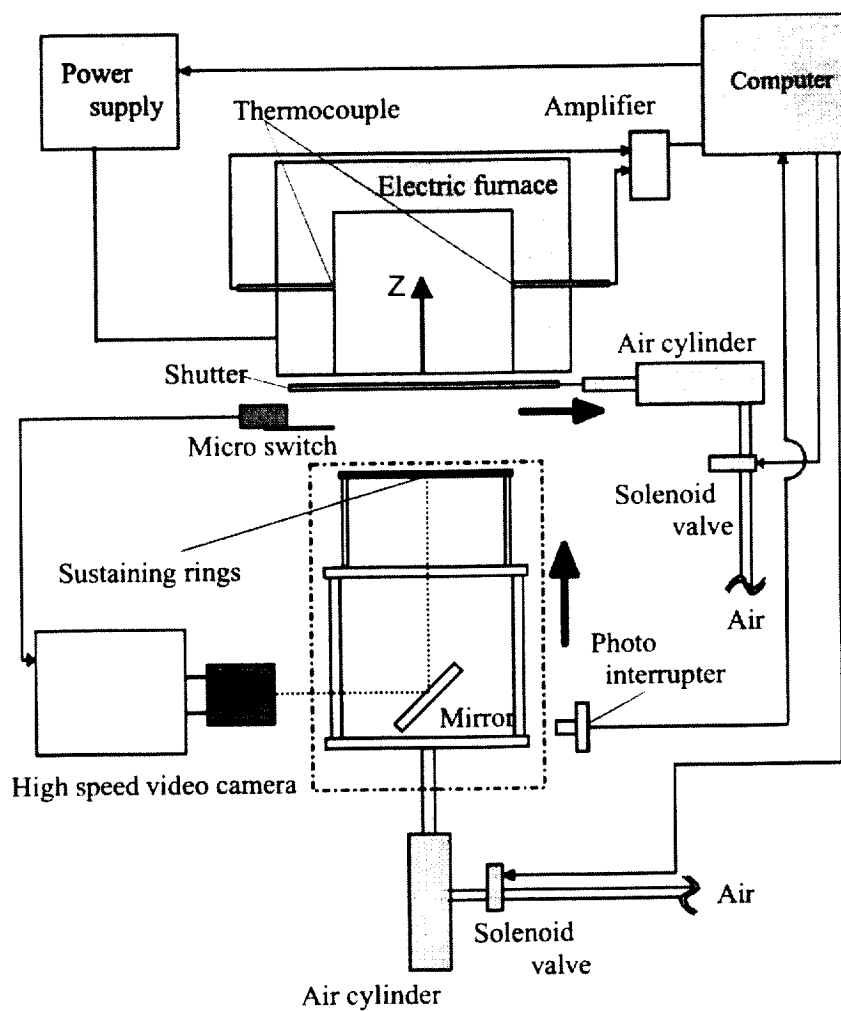


Fig. 3. Schematic of experimental apparatus.

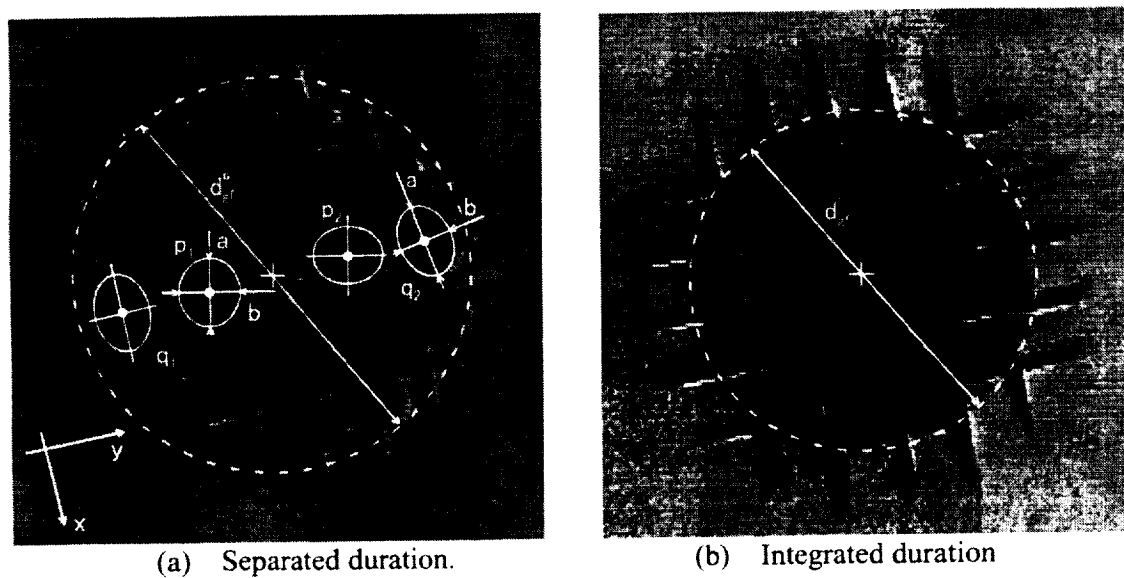


Fig. 4. Definitions of the diameters of the particle flames and the group flames.

The group of the droplets was set under the electric furnace and was lift into the furnace after 1sec. of the microgravity-start signal. Before that, the furnace was closed by the shutter. The shutter and the lifter were manipulated by the air cylinders. The lifting time was 0.25sec.

The definitions of the diameters of the particle flames and the group flame are shown in Fig. 4. Figure 4(a) is in the separated duration and 4(b) is in the integrated duration. In the separated duration, the particle flame diameter could be defined. As the particle flame shape is elliptic, the diameter is defined as the root of the product of the major and the minor axis. The group flame diameter in the separated duration is defined as the twice of the distance between the center of the group and the longest edge of the particle flame (Fig. 4(a), d_{gf}^s). In the integrated duration, the group flame diameter is twice of the distance between the center of the group and the longest edge of the group flame (Fig. 4(b), d_{gf}^i).

Results and Discussion

Figure 5 shows the time histories of the diameter of particle flame. The droplet p1 and q1 are on the stage 2 and stage 1, respectively (see Fig. 1 and 4). The flame diameter increased at first and decreased simply. The particle flame p1 and q1 could be verified for 90 msec. and 40 msec., respectively. After that, these particle flames were integrated into the one group flame. Figure 6 shows the time history of the diameter of the group flame. It shows a minimum at the change of the duration.

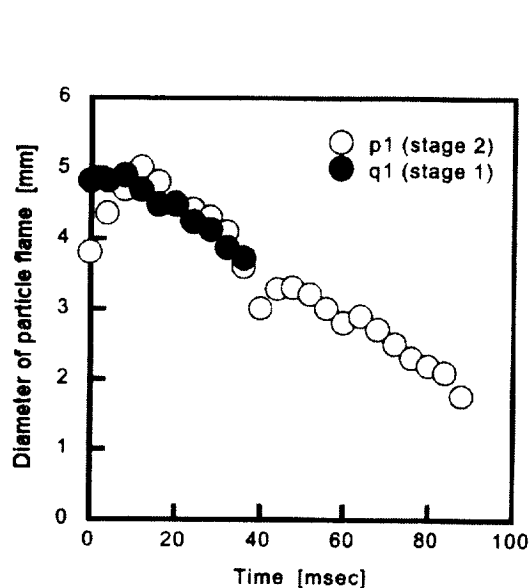


Fig. 5. Time histories of the diameter of the particle flame.

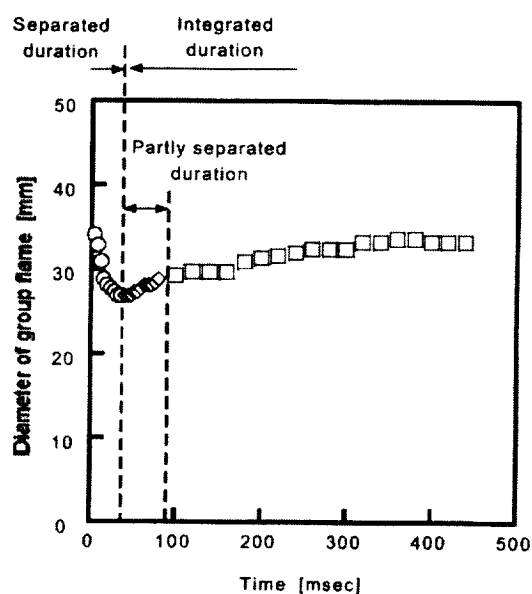


Fig. 6. Time history of the diameter of the group flame.

Reference

1. Ikegami, M. et al., Proc . Drop Tower Days 1998 in Hokkaido, (1998), 79-81.
2. Yahagi, Y. and Takeuchi, M., JSME (in Japanese), Vol. 65, No. 631, B, 1108-1114, (1999).

FROM A SINGLE DROP TO 2-D AND 3-D ARRAYS: ACOUSTO-ELECTRIC MANIPULATION OF DROPS AND PARTICLES

Robert E. Apfel and Yibing Zheng

Physical Acoustics Laboratory, Department of Mechanical Engineering, Yale University
New Haven, CT 08520-8286, USA

INTRODUCTION

Acoustic levitation techniques can be used to suspend liquid drops and solid particles without any physical contact. It has been applied to study drop dynamics and material processing in ground-based experiments related to those in microgravity. In the space shuttle, this technique helped to pre-squeeze a surfactant-bearing drop in the free drop oscillation experiment. A normal acoustic levitator uses only the acoustic standing field, and it can levitate a single drop or particle near the acoustic pressure node. An improved acousto-electric levitator is now developed to study not only a single drop or particle, but also the behavior of clusters and arrays of liquid drops and solid particles. This device utilizes an acoustic standing wave and an electric static field simultaneously to manipulate charged drop arrays in air. Near each acoustic pressure node, one two-dimensional drop array can be formed and stably suspended. When there are multiple pressure nodes in the levitator, several layers of these arrays can be levitated at the same time. If we use a high frequency transducer, and if we can control the spacing of the drops in each layer to be the same as the distance between layers, we can produce a quasi-3-D droplet cloud. Both these 2-D and 3-D arrays are promising in pre-positioning drops in the study of group combustion and evaporation. The future application of this system could be the control of aerosols and sprays in the energy and material sciences.

In this paper, the setup of the acousto-electric levitator and the generation of the drop clusters and arrays will be discussed first. The characteristics of this system and the levitation forces on particles and drops are analyzed numerically using the finite element method. The initial application of studying single and multiple component drop evaporation is presented.

ACOUSTO-ELECTRIC LEVITATOR

Fig. 1 shows the apparatus of the acousto-electric levitator [1]. It has an ultrasonic horn at the bottom and a concave reflector with a flat glass window on the top, just like a normal acoustic levitator. A strong vertical acoustic standing field can be generated between the horn and the reflector. When a drop or a particle is placed in this acoustic standing field, the acoustic radiation force will trap it at an acoustic pressure node so that it can be stably levitated. Unlike an ordinary levitator, an extra electric static field is applied to our acousto-electric levitator between the horn and the reflector, which can be used to charge droplets or particles and also provide an electric levitation force. This feature enables us to suspend charged drop and particle arrays.

When a liquid like ethanol is placed on the surface of the ultrasonic horn, it atomizes into fine droplets flying into the levitator due to the vibration of the horn. For ethanol, droplet diameters are around 25 to 50 μ m when the working frequency of the horn is 28KHz. These fine droplets

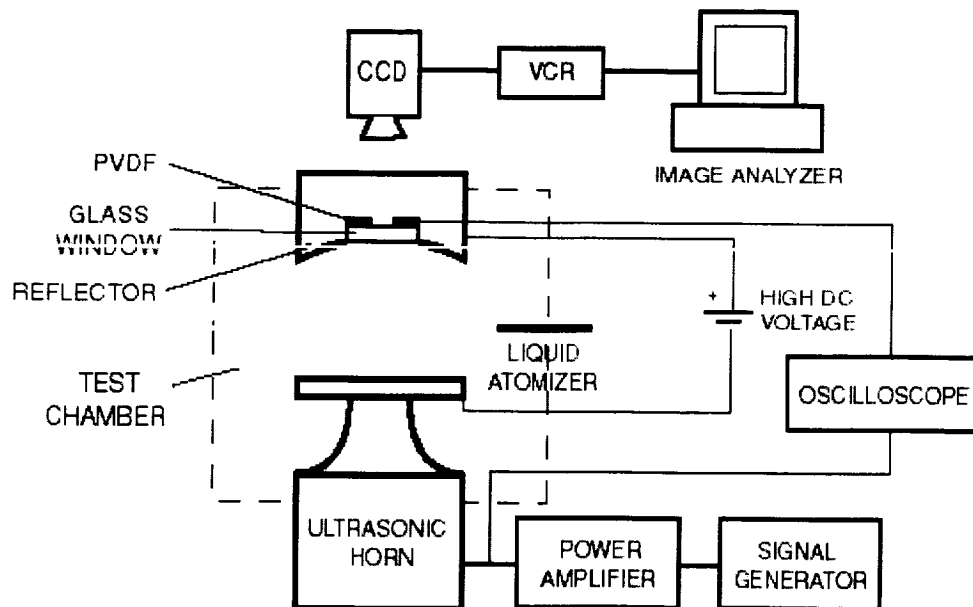


Figure 1 Acousto-Electric Levitator

are charged because of the electric field between the horn and the reflector. The lateral acoustic radiation force pushes the droplets together to form 2-D clusters, which are captured by vertical acoustic forces in the center of the levitator. Some of the flat clusters may contain a very large number of droplets, as many as 240. Droplets in a cluster will coalesce into a bigger drop when the acoustic field increases and the lateral force becomes larger. Many of these bigger drops will form a large drop array near an acoustic pressure node. Drops are separated from each other by the charges they are carrying. The size of the drops, the spacing between drops, and the total number of drops in one array can be controlled by varying the values of the voltage and the acoustic field intensity. Usually there are several acoustic pressure nodes in the levitator so that we are able to suspend several layers of such drop arrays in the same time. Fig. 2 is the top view of a liquid drop array, and Fig. 3 shows that two charged drop arrays are levitated in the levitator. The acousto-electric levitator can also levitate charged particles. If some conductive or metal-coated particles are placed on the surface of the horn, the vibration of the surface makes them jumping up into the levitator. They carry charges too and thus form 2-D arrays at acoustic pressure nodes.

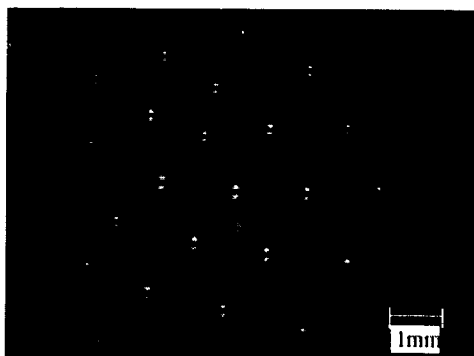


Figure 2 Top view of a drop array



Figure 3 Two layers of arrays levitated

Another method to charge and inject drops is to use an atomizer and a charger separated from the levitator. The drops are generated by the atomizer, such as a nozzle or a needle, and charged by an external electric field. The injected drops are captured by the acoustic radiation force and form arrays in the levitator. The advantage of this method is that the drop arrays can form quickly. However, the drop injection speed must be slow in order for the acoustic field to catch the drops.

We are making a high frequency acousto-electric levitator that works at 100KHz. The distance between two layers of drop arrays is reduced to 1.7mm. When the distance among drops in each layer is controlled to be about the same as 1.7mm, there forms a quasi-3-D array.

CHARACTERISTICS OF THE ACOUSTO-ELECTRIC LEVITATOR

In order to control and manipulate drop and particle arrays, it is important to know the characteristics of the levitator and the forces that hold drop arrays steady. Traditionally, the acoustic field in an acoustic levitator was considered to be one-dimensional. King in his paper analyzed the acoustic levitation force on a small sphere in one-dimensional field [2]. Since we have 2-D drop arrays, one-dimensional analysis is not sufficient. There are not only the vertical acoustic and electric levitation forces in the acousto-electric levitator, but also lateral acoustic forces and Coulombic forces that balance with each other to hold drop arrays. A numerical finite element method was employed in our study to calculate the acoustic field and acoustic radiation forces in this open-sided resonator with a concave reflector. The perfectly matched layer boundary condition [3] is used in the numerical calculation to absorb the outgoing acoustic waves. This method successfully estimates the characteristics of the resonator such as resonance frequencies and quality factors, etc. Fig. 4 shows the numerical result for the acoustic field we normally use to levitate drop arrays. The acoustic radiation forces on drops can also be calculated.

INITIAL APPLICATION IN DROP EVAPORATION

Acoustic levitation was used in the investigation of single drop evaporation because it can levitate drops without any contact. However, the evaporation speed of a drop levitated by an acoustic field is faster than expected. The reason is that the strong acoustic field always induces acoustic streaming around the drop, which carries away the vapor, thus enhancing the drop evaporation. Acoustic levitation also deforms the drop shape to some kind of a flat ellipse. That will cause measurement error too. Using the acousto-electric levitator, we are able to minimize these undesirable outcomes. We have utilized the acousto-electric levitation in the study of the evaporation of both single and multiple component drops.

The materials we chose in the evaporation study were heptane, octane and dodecane, which are the primary components of gasoline fuel. Since these materials themselves are nonconductive, it is not easy to charge them directly. An additive, Statis 450, was added into the fuel to increase the conductivity. Experiment results show that very small amounts of Statis 450 (0.3% by weight) do not have noticeable effect on the evaporation of alkanes. After a fuel drop was injected into the levitator, we decreased the acoustic field intensity as low as possible but still kept the drop levitated. With compensation of the electric levitation force, the acoustic field was small and the acoustic streaming was greatly reduced. During the drop evaporation, as drop became smaller and smaller, we controlled both the acoustic and electric fields to lower the

levitation forces so that the position of the drop always kept constant. As mentioned earlier, the minimum acoustic field also reduced the deformation of the drop shape so that the drop was almost perfectly spherical. We compared the evaporation results of three suspended octane drops: 1) one drop suspended by a glass fiber (the glass fiber can deform the drop shape too); 2) a drop levitated only by the acoustic radiation force and 3) another drop levitated by both the electric force and the minimum acoustic force. The results showed that the evaporation rates of Drop 1 and 3 were almost the same, but Drop 2 evaporated faster. For pure alkane drops, we found that their evaporations follow the d^2 law, which means that the diameter squared of the drop decreases linearly with time when the evaporation continues [4]. We also preformed an evaporation experiment on a multi-component drop: a mixture of octane and dodecane. In the theory of evaporation of a multi-component drop, both the equations of energy and continuity should be applied to each species. We also assumed fast mixing processes inside the drop and used Raoult's law for the vapor pressures around the drop. Since the temperature, liquid, and gas components change with time during evaporation, we had to solve several coupled differential equations numerically. Fig. 5 shows the experimental result of evaporation of the mixture drop (70% octane and 30% dodecane by mole) levitated in the acousto-electric levitator and the theoretical calculation. The agreement between the two results is good.

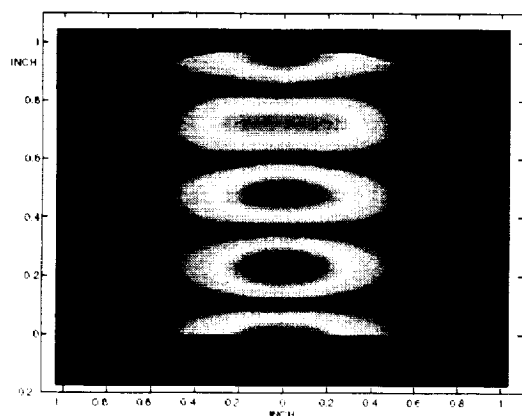


Figure 4 Numerical modeling of the acoustic field

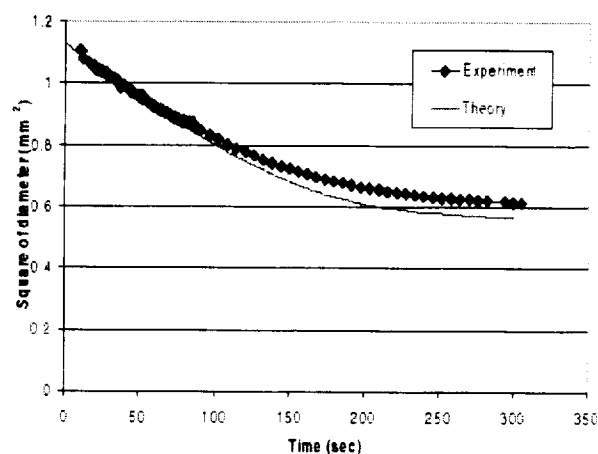


Figure 5 Evaporation of a drop of octane and dodecane mixture

REFERENCES

- [1] R. E. Apfel, Y. B. Zheng, and Y. R. Tian, "Studies of acousto-electrically levitated drop and particle clusters and arrays," *Journal of the Acoustical Society of America*, 105 (5), L1-L6 (1999).
- [2] L. V. King, "On the acoustic radiation pressure on spheres," *Proc. Roy. Soc. A*, 147, 212-240 (1934)
- [3] Z. S. Sacks, D. M. Kingsland, R. Lee, and J. F. Lee, "A perfectly matched anisotropic absorber for use as an absorbing boundary condition," *IEEE trans. Antennas Propagat.*, vol. 43, 1460-1463 (1995)
- [4] K. Annamalai, and W. Ryan, "Interactive processes in gasification and combustion .1. liquid-drop arrays and clouds," *Progress in Energy and Combustion Science*, 18 (3), 221-295 (1992).

HETEROGENEOUS COMBUSTION OF POROUS GRAPHITE PARTICLES IN NORMAL AND MICROGRAVITY¹

Harsha K. Chelliah,[†] Fletcher J. Miller,[‡] and Andrew J. Delisle,[†]

[†]Mechanical and Aerospace Engineering, University of Virginia, Charlottesville, VA 22903

[‡]National Center for Microgravity Research, MS 110-3, Cleveland, OH 44135-3191

OBJECTIVES: Combustion of solid fuel particles has many important applications, including power generation and space propulsion systems. The current models available for describing the combustion process of these particles, especially porous solid particles, include various simplifying approximations. One of the most limiting approximations is the lumping of the physical properties of the porous fuel with the heterogeneous chemical reaction rate constants [1]. The primary objective of the present work is to develop a rigorous model that could decouple such physical and chemical effects from the global heterogeneous reaction rates. For the purpose of validating this model, experiments with porous graphite particles of varying sizes and porosity are being performed. The details of this experimental and theoretical model development effort are described below.

EXPERIMENTAL APPROACH: As reported in previous Microgravity Workshops [2,3], the major experimental challenges of this project were particle deployment, ignition, and obtaining self-sustained combustion under normal and reduced gravity conditions. Four types of porous particles were considered in previous tests, but only results with glassy carbon spheres are reported here.

(i) *Methods of Enhancing Particle Oxidation:* Because of heat losses from the hot particle to room temperature air, and particle mounting techniques used, self-sustained combustion was never achieved in previous experiments. An external energy source in the form of a focused CO₂ laser beam, with a minimum heat flux of 88 W/mm² was needed to burn the particle in less than 25 secs. In order to attain self-sustained heterogeneous combustion, methods of enhancing the particle combustion were pursued recently, namely (a) using enriched air and (b) vitiated air. With the new enclosed chamber designed [4], under normal gravity and room temperature conditions, enriched air provided clear evidence of self-sustained combustion. Similar enriched conditions were used by Ubhayakar and Williams [5], in the context of combustion of a coal char particle (about 125 microns in diameter) under normal gravity conditions. The first microgravity experiments with the present setup, involving 1 mm size glassy carbon spheres in enriched air conditions are to be conducted in the KC135 aircraft in April/May, 2001, and a followup experiment is planned in June. As shown in Fig. 1, this modified experimental rig consists of an enclosed chamber, CO₂ laser and associated optics, camera, spectrometer, and oxygen sensor, all mounted on 4' × 2' optical bread board, with a separate equipment rack for power supply of the laser, image recording system, etc.

(ii) *Particle Deployment:* After considerable effort and testing of various particle mounting approaches, the challenge of keeping the particle in the camera field-of-view (FOV) during oxidation and minimization of heat losses was accomplished by using laser drilled particles, tethered with a 12 micron alumina (Al₂O₃) fiber. Because of the large aspect ratio (i.e. 1 mm sphere with a 15 micron diameter hole), the laser drilled holes were far from the desired 15 micron straight holes. Laser drilling of the particles were performed by several commercial vendors, as well as the NASA Glenn Research Center micromachining laboratory. In all these attempts, the drilled holes took an hour-glass shape (with 75

¹Work funded under NASA Grant NAG3-1928

micron at the ends and about 50 micron at the neck hole) because of the large aspect ratio involved. Nevertheless, these particles provided a viable approach of mounting particles for microgravity experiments. At very high particle temperatures and in an oxidizing environment, typically over 2500 K (especially in air enriched with oxygen), commonly used silicon carbide (SiC) fibers failed during the combustion tests. However, Al₂O₃ fibers with a lower melting temperature than the SiC fibers, survived oxidation and provided the only method of keeping the particle in the FOV.

For the KC135 aircraft experiments, which typically involves a sequence of 5-10 reduced gravity parabola's, a rotary table with five particle holding mechanisms was designed, as shown in Fig. 2. This table can be remotely indexed once the chamber is filled with enriched air; hence it can remain sealed during the sequence of parabola's providing 5 experimental data points.

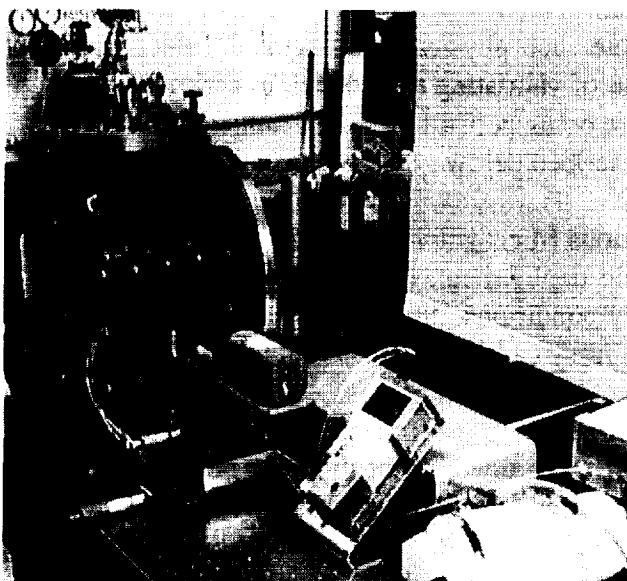


Figure 1: Photograph of the KC135 experimental setup, indicating the chamber, laser, camera, etc..

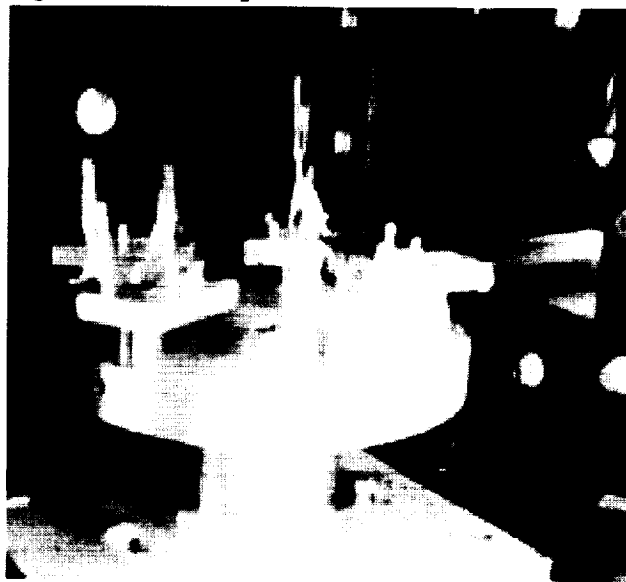


Figure 2: Rotary table with provision for holding 5 tethered particles.

(iii) *Ignition*: The ignition of the particle, roughly 1 mm in diameter was achieved by a 5W CO₂ laser. The laser was focussed to a 200 μ m diameter area and the beam intensity has been characterized previously [4]. A 10" focal length ZnSe lens held on a vertical xy-stage, with the entire assembly mounted outside the chamber allowed accurate focusing of the beam at the center of the particle. Unlike previous experiments where the particle was perched on a hypodermic needle with significant heat losses, in the present enriched air experiments with self-sustained combustion, the duration of exposure of the laser beam on the particle was very short (fraction of a second compared to combustion duration of the order of 10 secs).

(iv) *Regression Rate Surface Temperature Measurements*: The self-luminous particle during combustion was previously observed directly through the optical system, which consisted of a Cohu monochrome camera with an optem Zoom70 microscope lens, together with a VCR was used to record the particle size and shape. In the present enriched air experiments, the luminosity of the particle was overwhelming and a 410 ± 10 nm CO bandpass filter was used to record occurrence of heterogeneous combustion and the particle surface regression rate. As the combustion intensity changes, such a filtering scheme may not be ideal, especially during the initial transition stage, but here for convenience such filtered images were used to characterize the relative change in surface area

or particle size.

A miniature fiber-optic coupled spectrometer (Ocean Optics S2000) was used to acquire the emission spectrum from the particle in order to determine its temperature. This method requires only that the particle emissivity be constant over the spectral region measured, but not necessarily a black body. The recorded spectral emission in the range from 767 to 937 nm was considered, with fitting the resulting intensity vs. wavelength data to a blackbody curve to obtain the temperature. To obtain the spectrometer sensitivity function, it was used to measure a calibrated blackbody source at 1000°C [6].

(v) *Experimental Results:* The results presented in this report were obtained under normal gravity conditions with different levels of enriched air. The corresponding reduced gravity experiments are to be conducted in April/May in the KC135 aircraft.

Figure 3 shows a comparison between the present enriched air experiments (roughly 70% oxygen, 30% nitrogen in moist conditions) and the previously reported laser supported experiments of similar glassy carbon spheres. The enriched experiments show a counter-intuitive initial increase in particle size, followed by the expected D^2 -Law type reduction in its size. This perceived increase in size is perhaps due to combination of the initial increase in CO layer and the CO-bandpass filter used. Once the oxidation process is well established, the CO layer is expected to be rather narrow and adjacent to the surface and can be considered as a good marker of the measurement of surface regression rate. A close examination of the image intensity show that the edges of particle are not very sharp, indicating a somewhat broad CO oxidation layer (see Fig. 4). Such a broad CO layer may introduce uncertainties in the estimation of particle size, and methods for minimizing such errors must be developed.

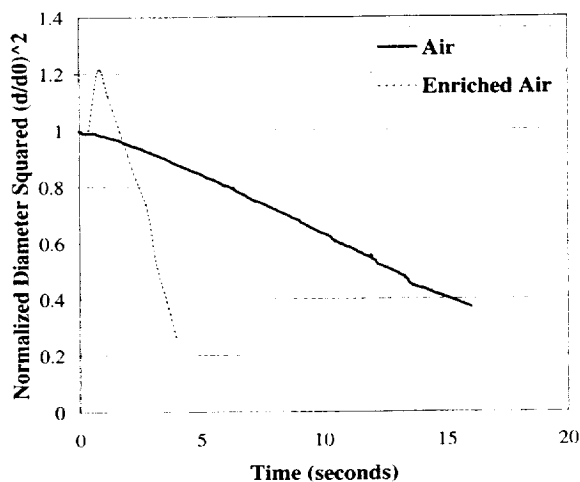


Figure 3: Comparison of the normalized equivalent particle diameter square vs. time, for normal air with laser heating and enriched air (self-sustained oxidation).

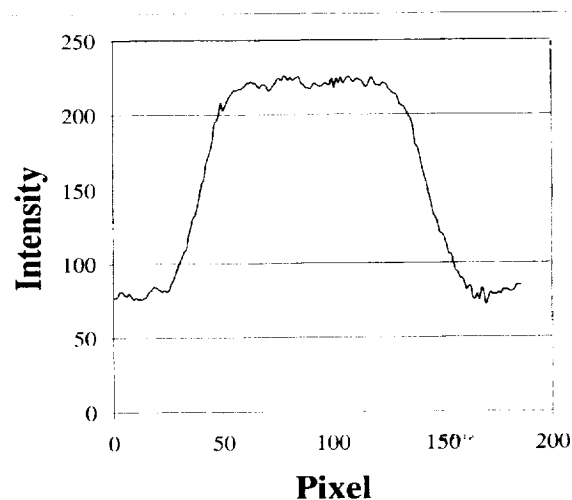


Figure 4: Recorded image intensity measurements across the particle in terms of pixels.

Clearly, the enriched self-sustaining combustion results shown in Fig. 3 indicate a much stronger oxidation of the particle, with the last image recorded indicating a particle size of about 450 microns. Whether this particle fell from the fiber support and moved out of the view of the camera or whether the combustion process extinguished must be examined carefully. The experiments by Ubhayakar

and Williams [5] describe the extinction of particle oxidation as the air enrichment level is reduced, essentially supporting the concept of the existence of a critical particle size for combustion, which is the ultimate goal of the present investigation.

NUMERICAL APPROACH: The details of the *unsteady* solid particle combustion model that is being developed were presented at the previous microgravity workshop [3]. The goal of this effort was to (a) couple the internal pore combustion to external homogeneous combustion, (b) develop a set of consistent inter-phase conditions for scalar variables, (c) investigate the transient effects, including extinction of particle oxidation, and (d) validate the model with experimental data.

Experimental data that were available for model validation at the last workshop were obtained by continuous laser heating of the particle to compensate for the significant heat losses through the hypodermic needle [3]. These experiments also indicated a particle temperature of about 2000K. In the corresponding simulations, the laser energy deposition of about 100 W/mm² was included, but heat loss through the hypodermic needle was ignored because of the uncertainty associated with modeling such a loss term. However, in simulations, if a maximum particle temperature is introduced to cap the uncontrolled increase in particle temperature, then the particle regression rate predictions obtained are consistent with the experimental data ($d(d^2)/dt = 0.04\text{mm}^2/\text{s}$). Figure 5 shows a plot of mass burning rate with the imposed temperature cap and Fig. 6 shows the corresponding variation of square of the particle radius vs. time, indicating the initial transient conditions, followed by quasi-steady oxidation. Simulations of particle oxidation under enriched air conditions are currently underway.

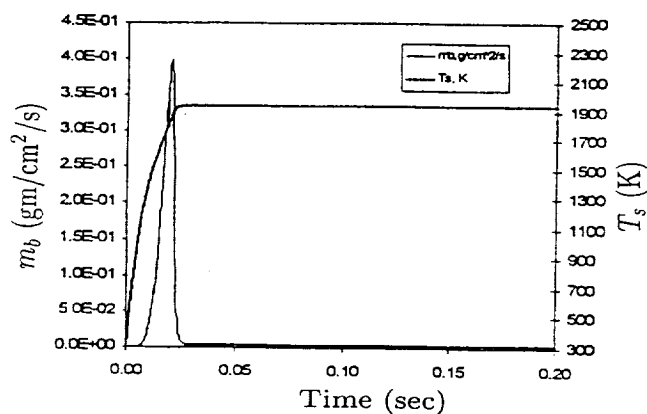


Figure 5: Variation of mass burning rate and surface temperature vs. time, with peak surface temperature around 2000 K.

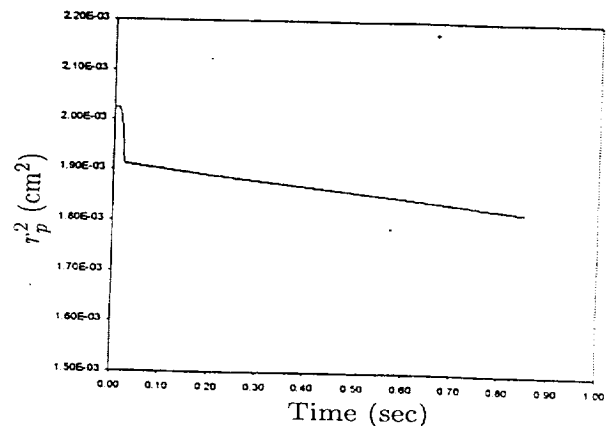


Figure 6: Corresponding square of the particle diameter vs. time, for the case in Fig. 5.

REFERENCES:

- [1] Laurendeau, N.M., *Prog. Energy Comb. Sci.* **4**:221 (1978).
- [2] Chelliah, H.K. and Miller, F.J., *Fourth Int. Microgravity Combustion Workshop*, Cleveland, OH, May 1997
- [3] Chelliah, H.K. Miller, F.J., Pantano, D., and Kasimov, A.K., *Fifth Int. Microgravity Combustion Workshop*, Cleveland, OH, May 1999
- [4] Ubhayakar and Williams, F.A., *J. Electrochem Soc.* **123**(4):747-756 (1976).
- [5] Pantano, D., MS Thesis, University of Virginia, May, 1999.
- [6] Miller, F.J., "Multi-wavelength Optical Pyrometry for Solid-Phase Temperature Measurements, WSS Meeting Paper, The Combustion Institute, Spring 2000.

REACTION MECHANISMS AND PARTICLE INTERACTION IN BURNING TWO-PHASE SYSTEMS

Edward L. Dreizin, Yuriy L. Shoshin, Ruslan S. Murdy
New Jersey Institute of Technology, Newark, NJ

and

Vern K. Hoffmann
AeroChem Research Laboratory, Titan Corporation, Princeton, NJ

INTRODUCTION

The main objective of this research is to understand the mechanisms by which particle interactions affect ignition and combustion in the two-phase systems. Combustion of metal aerosols representing the two-phase systems is carried out in the microgravity environment enabling one to avoid the buoyant flows that mask the particle motion due to the particle-particle interaction effects. In addition, relatively large, e.g., 100 μm diameter particles can be used, that remain aerosolized (i.e., do not fall down as they would at normal gravity) so that their behavior ahead, behind, and within the propagating flame can be resolved optically. An experimental apparatus exploiting this approach has been designed for the 2.2-s drop tower microgravity experiments [1]. A typical experiment includes fluidizing metal particles under microgravity in an acoustic field, turning off the acoustic exciter, and igniting the created aerosol at a constant pressure using a hot wire igniter [1,2]. The flame propagation and details of the individual particle combustion and particle interactions are studied using high-speed movie and video cameras coupled with microscope lenses to resolve individual particles. Recorded flame images are digitized and various image processing techniques including flame position tracking, color separation, and pixel by pixel image comparisons are employed to understand the processes occurring in the burning aerosols. Condensed combustion products are collected after each experiment for the phase, composition, and morphology analyses. New experiments described in this paper address combustion of Ti and Al particle clouds in air and combustion of Mg particle clouds in CO_2 . In addition, microgravity combustion experiments have been conducted with the particles of the newly produced Al-Mg mechanical alloys aerosolized in air.

MAGNESIUM AEROSOL COMBUSTION IN CO_2

Combustion of metal fuels in CO_2 is of interest for the design of atmosphere-breathing propulsion systems for Mars. The experiments were conducted with two size fractions of magnesium powders: particles in the size range of 150 – 180 μm , and particles of –325 mesh (< 44 μm). The combustion chamber and ballast vessel were purged with CO_2 prior to each experiment. For both particle sizes, reference experiments with the clouds of Mg particles burning in air were conducted. The magnesium mass loads were in the range of 0.1 – 0.7 g in the 0.5-liter chamber. The estimated equivalence ratios for the flames in CO_2 were in the range of 0.1 – 0.72 (for the flames in air, the respective equivalence ratios varied from 0.49 to 3.32). The flames readily ignited and propagated in the clouds of Mg particles in CO_2 , the velocities of the flame propagation were much higher than in air, e.g., 0.4 m/s in CO_2 versus 0.1 m/s in air for the 165 μm diameter particles. The products of combustion have been analyzed, only peaks of MgO were detected in addition to the peaks of unreacted Mg. Based on the qualitative comparison of the Mg/MgO peak intensities (cf. Fig. 1) for the products of Mg combustion in air and CO_2 , it could be concluded that the reaction was more complete in CO_2 .

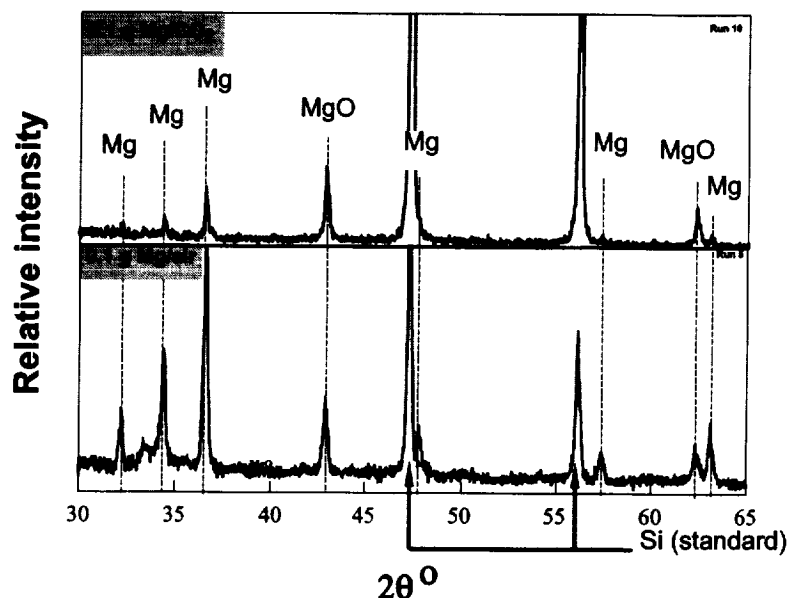


Fig. 1. X-ray diffraction patterns of combustion products of Mg powder in CO₂ and air.

TITANIUM AEROSOL COMBUSTION IN AIR

Titanium clouds in air were produced and ignited in microgravity. Two types of powder, 160 μm average diameter (by Wah Chang Company) and -325 Mesh ($< 44 \mu\text{m}$, by Alfa Aesar) were used. The flame velocity for the coarse particles varied in the range of 0.02 – 0.1 m/s, at equivalence ratios in the range of $4.8 < \phi < 6$. The fine particle flames propagated at a velocity of 0.3 m/s at $\phi = 2.2$ and 1.8 m/s at a higher particle loading, $\phi = 3.1$. The appearance of flames of clouds of titanium particles was qualitatively similar to those of zirconium. Individual particle flames could be clearly visible in all the runs. Particle explosions were observed in only one experiment with the fine particles and lower mass load (equivalence ratio of 2.2, cf. Fig. 2). The experiments have shown that the titanium combustion products do not agglomerate as much as the products of zirconium combustion as was observed in the earlier tests [3]. Instead, a large number of very fine particles were observed in the combustion products, indicative of significant vapor-phase reaction followed by the product condensation. The phase compositions of combustion products formed in experiments with finer Ti particles were analyzed and the results of these analyses are illustrated in Fig. 3. It is interesting that significant amounts of TiN are found in the products in addition to rutile and anatase, two modifications of Ti₂O₃. It can be noted that based on the relative peak intensities, more of the TiN (and less of Ti₂O₃) was formed in a run with the higher Ti powder load ($\phi = 3.1$), in which no particle explosions were observed. These observations are consistent with the earlier results [4] describing the process of Ti particle combustion. It has been suggested that during the initial combustion period, both oxygen and nitrogen are dissolved in molten titanium, with the initial rate of

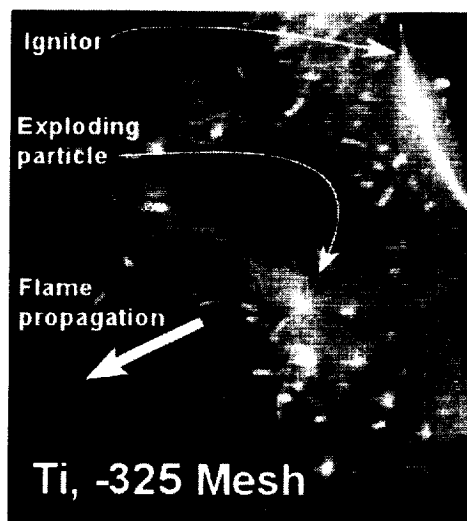


Fig. 2. Appearance of Ti flame in air (a high speed movie frame)

nitrogen dissolution being higher than that of oxygen. At the later stages of combustion, the rate of nitrogen dissolution decreases. At the end of combustion, when the particle temperature decreases, the solution becomes supersaturated, and nitrogen is released from the particles causing their explosions. Therefore, the interpretation of the current experiments is that in a fuel-rich mixture, the amount of oxygen available was not sufficient to produce the supersaturated solution and thus no explosions were observed. When the particles with large amounts of dissolved nitrogen cooled (relatively slowly in a cloud as compared to single particles), the phase of TiN formed.

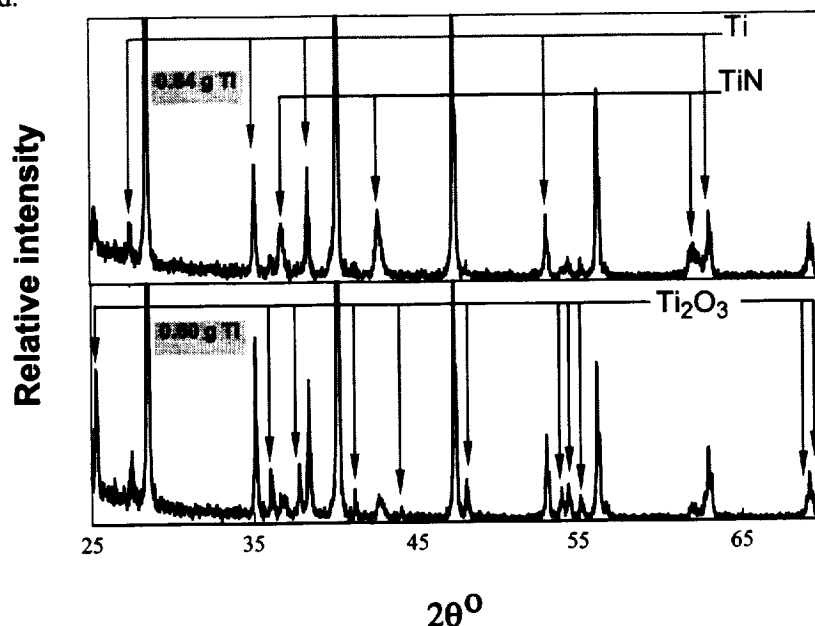


Fig. 3. X-ray diffraction patterns of Ti combustion products. Unmarked peaks are those of Si, used as an internal standard.

FLAMES OF ALUMINUM AND ALUMINUM-MAGNESIUM MECHANICAL ALLOY AEROSOLS

In an effort to develop new aluminum-based energetic materials for advanced metallized propellants, metastable Al-Mg mechanical alloys have been recently prepared and characterized [5]. In this work, the experimental setup and microgravity environment have been exploited to compare the flame propagation in the pure Al versus Al-Mg mechanical alloy aerosols. Two size fractions of the pure Al particles were used with the size ranges of 3 – 4.5 and 10 – 14 μm . The average sizes of the mechanical alloy particles were measured to be in the 7 – 10 μm range. Three compositions of the mechanical alloys with 10, 30, and 50 weight % of Mg were tested. It was found that the flame propagation velocities through the clouds of the alloy particles (around 0.5 m/s) exceeded noticeably the flame velocities in the same density aluminum particle cloud (~ 0.15 – 0.2 m/s). The flame structures of the alloy and aluminum particles are remarkably different, as illustrated in Fig. 4. The individual particles are well distinguished in the alloy flame but not in the aluminum flame, where only several large agglomerates are visible. The radiation intensity profiles measured across the flame zone are shown in Fig. 5. The flame front of the alloy aerosol flame is noticeably sharper as compared to the aluminum flame indicating a very narrow preheat zone. Such a difference has been expected based on the hypothesized mechanism of the alloy particle ignition at a specific phase transition temperature that is significantly lower than the Al_2O_3 melting point.

Combustion products have been collected after each microgravity experiment and the phase and elemental compositions of the products are being analyzed using electron microscopy coupled with the energy dispersive spectroscopy, and the x-ray diffraction.

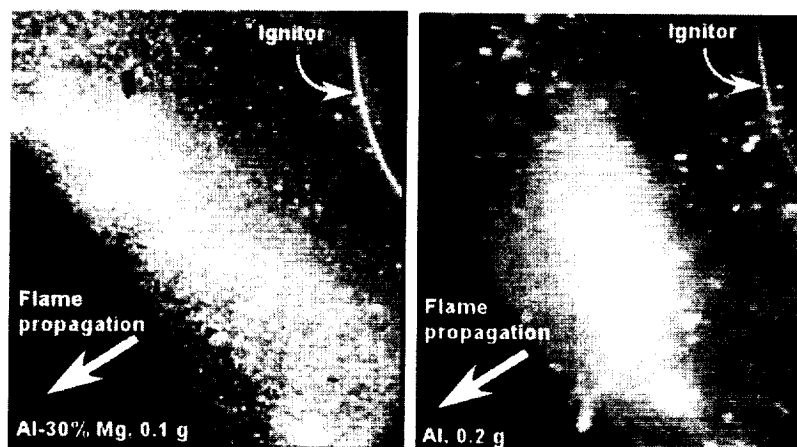


Fig. 4. High-speed movie images of flames propagating in the Al-30% Mg mechanical alloy and pure Al – air aerosols.

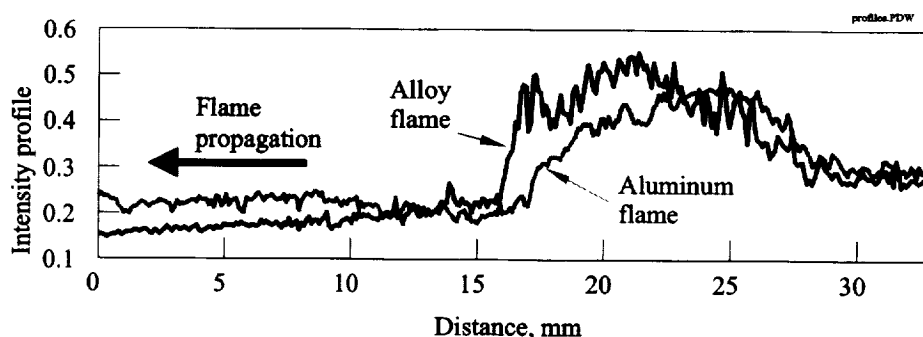


Fig. 5. Brightness profiles across images of the flames propagating in the Al-30% Mg mechanical alloy and pure Al – air aerosols.

ACKNOWLEDGEMENT

This research was supported by NASA Glenn Research Center, Cooperative Agreement NCC3-746. The help of Dr. Kurt Sacksteder in organizing the microgravity experiments is greatly appreciated. We also thank Mr. Hugh Aylward of NASA GRC for the assistance in image processing.

REFERENCES

1. Dreizin, E.L., Hoffmann V.K., "Constant Pressure Combustion of Aerosol of Coarse Magnesium Particles in Microgravity" *Combustion and Flame* 118:262-280 (1999)
2. Dreizin, E.L., and Hoffmann, V.K., "Experiments on magnesium aerosol combustion in microgravity" *Combustion and Flame* 122:20-29 (2000)
3. Dreizin, E.L., Hoffmann V.K., Vicenzi, E.P., "High Temperature Phases In Ternary Zr-O-N Systems" *Journal of Materials Research*, Vol. 14, No 10:3840-3842 (1999)
4. Molodetsky I.E., Dreizin, E.L., Vicenzi, E.P., and Law, C.K. "Phases of Titanium Combustion in Air" *Combustion and Flame* 112:522-532 (1998)
5. Shoshin, Y., Mudryy, R., and Dreizin E., "Preparation and characterization of energetic Al-Mg mechanical alloy powders" The Second Joint Meeting of the US Sections of the Combustion Institute. Oakland, CA, 2001

BURNING VELOCITY MEASUREMENTS IN ALUMINUM-AIR SUSPENSIONS USING BUNSEN-TYPE DUST FLAMES.

John Lee, Samuel Goroshin, Massimiliano Kolbe
McGill University, Montreal, Quebec, Canada

Introduction.

Laminar burning velocity (sometimes also referred in literature as fundamental or normal flame propagation speed) is probably the most important combustion characteristic of the premixed combustible mixture. The majority of experimental data on burning velocities in gaseous mixtures was obtained with the help of the Bunsen conical flame [1]. The Bunsen cone method was found to be sufficiently accurate for gaseous mixtures with burning velocities higher than 10-15 cm/s at normal pressure [1,2]. Hans Cassel [3] was the first to demonstrate that suspensions of micron-size solid fuel particles in a gaseous oxidizer can also form self-sustained Bunsen flames. He was able to stabilize Bunsen flames in a number of suspensions of different nonvolatile solid fuels (aluminum, carbon, and boron). Using the Bunsen cone method he estimated burning velocities in the premixed aluminum-air mixtures (particle size less than 10 microns) to be in the range of 30-40 cm/s. Cassel also found, that the burning velocity in dust clouds is a function of the burner diameter [4]. In our recent work [5], we have used the Bunsen cone method to investigate dependence of burning velocity on dust concentration in fuel-rich aluminum dust clouds. Burning velocities in stoichiometric and fuel-rich aluminum dust suspensions with average particle sizes of about 5 microns were found to be in the range of 20-25 cm/s and largely independent on dust concentration. These results raise the question to what degree burning velocities derived from Bunsen flame specifically and other dust flame configurations in general, are indeed fundamental characteristics of the mixture and to what degree are they apparatus dependent. Dust flames in comparison to gas combustion, are thicker, may be influenced by radiation heat transfer in the flame front, respond differently to heat losses [6], and are fundamentally influenced by the particular flow configuration due to the particles inertia. Since characteristic spatial scales of dust flames are larger, one can expect that they will also be more sensitive than homogeneous combustion to a particular experimental geometric configuration of the flame and the flow. With such sensitivity the introduction of the very concept of the fundamental flame speed may be problematic for dust combustion. With this in mind, the objective of the present work is to further investigate Bunsen dust flames and evaluate to what degree burning velocities derived from Bunsen cone depend on experimental conditions (i.e. flow rate and nozzle diameter).

Experimental Details.

Dust Burner.

The details of the experimental set-up and principles employed in the dust dispersion system are described in our previous works [5,6]. The following description only specifies modifications that were made to the apparatus in accordance with the objectives of the present work. A simple conical nozzle replaced the water-cooled detached ring that was used previously to stabilize dust flames [5]. The use of the flame stabilized directly on the nozzle, instead of the detached ring, eliminates the uncertainty in flow rate that might result from gas entrainment into the flame from the surrounding atmosphere. With the flame anchored on the nozzle the dust concentration is monitored directly within the dust supply tube by the redesigned laser light extinctions. In this modified design, the light emitted by the 3 mW laser diode is introduced into the dust tube through the airflow protected windows, it then passes through narrow channel and is focused by a long focal lens on a small aperture ($d = 0.25$ mm). The aperture plays the role of a spatial filter that cuts scattered laser light thus making deviation from the Bouguer's light attenuation law negligible even for optically thick dust clouds. A narrow bandwidth interference filter permits only the laser light to pass, protecting the photodetector from the light emitted by the flame and scattered by aluminum particles.

The gas dispersing flow is maintained constant throughout the duration of an experiment, and variation of the dust concentration is achieved by varying the dust feeding rate. In order to regulate the dust flow rate through the nozzle, an ejection system is used to eject part of the flow from the main stream into a bypass tube. Pure nitrogen is used as an ejecting gas. Thus the flow removed from the main stream by the ejector can be easily calculated by measuring the concentration of oxygen in the bypass tube. Oxygen concentration in the ejector flow is continuously monitored by an in-line electrolytic oxygen analyzer and is recorded by a computer data acquisition system.

Aluminum powder.

Atomized aluminum powder (Ampal 637, Ampal Inc., NJ) used in these experiments was from the same batch as in our previous works on flame quenching distance measurements [6] and flame speed measurements in rich mixtures [5]. The powder's aluminum content is no less than 99.5% and the aluminum particles are of a spheroidal or nodular shape. Differential distribution of particle sizes in the powder can be found in our previous work [6].

Dust concentration measurements.

The laser light extinctionmeter was calibrated by the complete aspiration of dust from the nozzle flow through a set of filters with a vacuum pump for a known time. Dust mass concentration in the flow is then determined by dividing total mass of the aspired dust by the volume of the gas passing through the nozzle during the same time. Mean particle Sauter diameter (d_{32}) in a suspension can be calculated from the data using Bouguer's light attenuation law. The calculations indicate an average particle diameter of about 6 μm (due to diffraction, light attenuation cross section for particles of this size is twice the size of the particle cross section [7]). This value practically coincides with the average Sauter diameter derived from the particle size distribution ($d_{32} = 5.8 \mu\text{m}$), which confirms that the particle agglomeration in the dust flow is negligible.

Photographic arrangement.

The flame image was split by a semitransparent mirror and simultaneously recorded by two single-lens Canon reflex cameras through two different narrow bandwidth interference filters. The bandwidth of one filter coincides with the sodium D-line (589 nm) and the bandwidth of the other coincides with the edge of the green band in the AlO molecular spectrum (508 nm). As the sodium concentration in flame remains constant, the maximum intensity in the sodium radiation might be associated with the maximum flame temperature, whereas the appearance of the AlO line indicates the ignition of aluminum particles. The flame images were digitized using a high-resolution slide scanner. The flame shapes and surface areas of the flame inner cones were determined with the help of image processing software.

Experimental Results.

General observations.

A photograph of the stoichiometric aluminum dust flame is shown in Fig. 1 along with a picture of a stoichiometric methane-air flame stabilized on the same nozzle at approximately the same flow rate (about 300 cm³/s). In comparison to the methane flame, the dust flame appears to be thicker and a bit larger. The flame base of the gas flame slightly overhangs the nozzle's rim, while the diameter of the base of the dust flame is closer to the inner diameter of the nozzle. The base of the dust flame is also lifted by about 2-3 mm above the nozzle exit while the distance from the nozzle to the base of the gas flame is less than 0.5 mm. The tip of the dust flame is more rounded and the inner boundary of the cone is usually better defined in comparison with the defused outer boundary. At very large dust concentrations the tip of the dust flame often opens up. The size of the opening is however relatively small (1-2 mm). Comparison of the inner flame cone contours derived from the photos taken through 508 nm and 589 nm filters show that they practically coincide with the exception of a small region close to the tip of the flame. The burning velocities derived from these pictures differ by less than 5%; thus only flames filmed through the 508 nm filter were used to measure burning velocity.

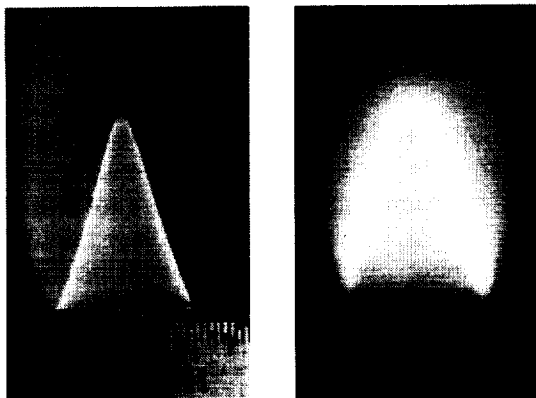


Figure 1. Photographs of the methane-air and aluminum-air stoichiometric flames stabilized on the same nozzle.

Burning Velocity Measurements.

Conical cylindrical brass nozzles with exit diameters 14, 18, and 22 mm were used to stabilize aluminum dust flames at different flow rates. All nozzles have the same base diameter (24.5 mm) and height (60 mm). The dependence of the burning velocity on dust concentration at two different flow rates is shown in Fig. 2 for 18 mm nozzle.

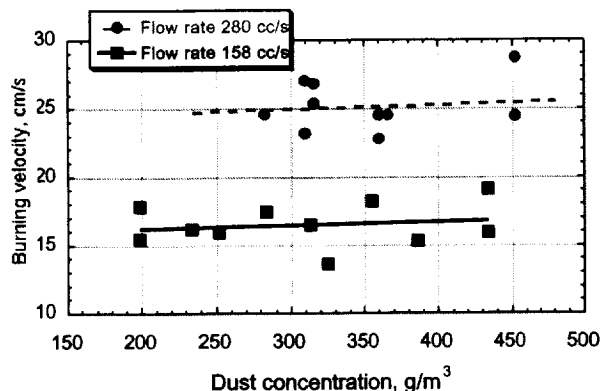


Figure 2. Dependence of burning velocity on dust concentration at two different flow rates (18 mm nozzle).

The derived dependence of the burning velocity on flow rate at approximately uniform dust concentration (350 g/m^3) is shown in Fig. 3. Maximum flow rate at which flame ceases to be completely anchored at the nozzle exit prior to blowoff, is about $300 \text{ cm}^3/\text{s}$, whereas at flow rate below $150 \text{ cm}^3/\text{s}$ the flame is prone to flashback for the 18-mm nozzle.

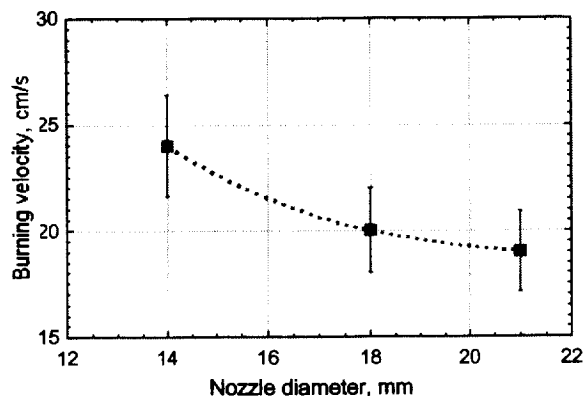
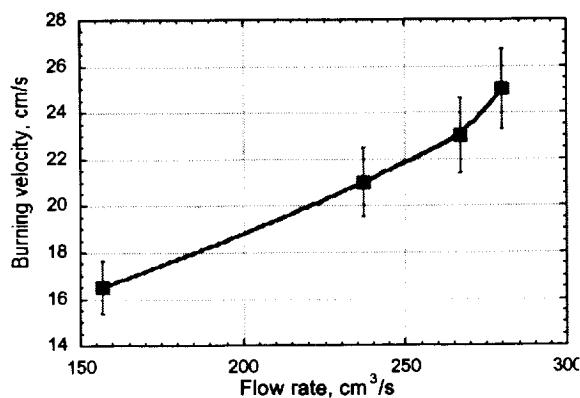


Figure 3. Dependence of the burning velocity on flow rate (18 mm nozzle, dust concentration is about 350 g/m^3).
Figure 4. Dependence of the burning velocity on the nozzle diameter.

The present experiments confirm the result of our previous work [5] which shows that flame speed in rich aluminum suspensions is insensitive to dust concentration. Surprisingly, the burning velocity demonstrates also no noticeable decline in the range of dust concentrations below stoichiometry (200-300 g/m³). The burning velocity shows clear tendency to increase with the increase in flow rate. In our experiments with different nozzle diameters, we were unable to stabilize flames on the large nozzle (22 mm) at the same flow rates as on 14 and 18 mm nozzles. Thus for the data shown in Fig. 4, the flow rates for two nozzles (14 mm and 18 mm) are the same (~ 280 cm³/s) whereas for the 22 mm nozzle the flow rate is higher (~ 400 cm³/s). Nevertheless, the results clearly show that burning velocity decreases with increase in the nozzle diameter. As was mentioned earlier, Cassel reported the same observation in his pioneering experiments with Bunsen dust flames [4].

Discussion.

Radiation effects, with their large characteristic spatial scales, which might be the reason for the strong sensitivity of the dust flame to geometric factor, can apparently be ruled out in explanation of the present experimental results. First of all, the absorption of radiation by a fresh dust mixture is negligible due to the small scale of the investigated flames. Direct measurement of the gas temperature ahead of the Bunsen flame front in our previous work [8], shows no substantial heating of the dust mixture beyond the usual preheat zone maintained by molecular heat conduction. The heat losses caused by radiation emitted by the combustion zone, regardless how substantial they might be, can only lead to decrease in the flame speed for flames stabilized on smaller nozzles or at larger flow rates as they are larger for smaller nozzles and for taller flames.

Cassel suggested [4] that the increase in the burning velocity for dust flames stabilized on smaller nozzles might be the result of the converging heat flux produced by flame curvature analogous to the known effect that increases the flame speed at the tip of the Bunsen gas flame [1]. He speculated that due to the larger thickness of a dust flame (?) the dust burning velocity might be effected even by relatively small (compared to gas) flame curvature as the curvature effect is proportional to $(1 + \delta/R)$ (where R is the radius of the flame). The curvature effect can not however explain the observed dependence of burning velocity on flow rate. In addition, our estimations show that the thickness of an aluminum dust flame is actually comparable to the thickness of the methane-air flame. Indeed, the quenching distance for the stoichiometric aluminum flame (measured with the same aluminum powder as in the present experiments) is about 5 mm compared with the methane-air flame which is about 2.5 mm [6]. Relatively small thickness of the aluminum flame can also explain why profiles of the flame cones formed by the sodium and AlO radiation appeared to be very similar. Thus it seems that other effects such as heat losses and (or) peculiarities of the two-phase flow dynamics might be responsible for the dependence of the burning velocity on flame scales observed in the present work.

Acknowledgment: This work is supported by the Canadian Space Agency under the Microgravity Science Program and by NASA under the CSA-NASA cooperation program.

References.

1. B. Lewis and G. von Elbe, *Combustion and explosion of Gases*, Academic Press, NY, 1987.
2. Andrews, G.E., and Bradley, D., *Comb. Flame* 18: 133-153, 1972.
3. Cassel, H. M., Das Gupta, A.K., Guruswamy, S., *Proc. Comb. Inst.* 3: 185-190, 1949.
4. Cassel, H.M., *Some Fundamental Aspects of Dust Flames*, Report of Investigation No. 6551, US Bureau of Mines, 1964.
5. Goroshin, S., Fomenko, I., and Lee, J.H.S., *Proc. Comb. Inst.* 26: 1961-1967, 1996.
6. Goroshin, S., Bidabadi, M., and Lee, G.H.S., *Comb. Flame* 105: 147-160, 1996.
7. Reist, P., *Aerosol Science and Technology*, McGraw-Hill, New York, 1993.
8. Goroshin, S., Shoshin, Yu., Ageyev, N., Poletayev, N., "The Structure of Premixed Aluminum Dust Flame", *Flame Structure*, V. 1, 213-218, Nauka, Novosibirsk, 1991.

COMBUSTION OF MAGNESIUM PARTICLES IN CARBON DIOXIDE UNDER MICROGRAVITY CONDITIONS

B. Legrand¹, C. Chauveau¹, E. Shafirovich², U. Goldshleger², E. Carrea³, C. Mounaim-Rousselle⁴, J.P. Rouan¹, and I. Gökalp¹

¹ *Laboratoire de Combustion et Systèmes Réactifs, Centre National de la Recherche Scientifique, 45071 Orléans cedex 2, France*

² *Institute of Structural Macrokinetics and Materials Science, Russian Academy of Sciences, Chernogolovka 142432, Russia*

³ *University of Genoa, Department of Environmental Engineering, 16146 Genoa, Italy*

⁴ *Laboratoire de Mécanique et d'Energétique, Université d'Orléans, 45072 Orléans cedex 2, France*

INTRODUCTION

It is proposed [1-5] to use combustion of magnesium in carbon dioxide for propulsion on Mars, the atmosphere of which consists of 95% CO₂. Ignition and combustion of single Mg particles in CO₂ and CO have been extensively studied in Refs. 6-10. The use of relatively large (1-3 mm) particles suspended on a thin wire has facilitated determination of combustion mechanisms and resulted in a number of interesting findings, such as pulsating combustion of Mg in carbon monoxide. Natural convection, however, could affect the combustion process in those experiments. Experiments under microgravity conditions are required to eliminate the disturbing effect of buoyancy on combustion of large particles.

Authors [11] employed the same method (a large particle suspended on a wire) in their experiments on combustion of Mg in CO₂ and CO under microgravity conditions generated during parabolic flights of the NASA KC-135 aircraft. Cylindrical Mg samples (2-4 mm in size) were heated to ignition by radiation of a xenon lamp. In a pure CO₂ atmosphere, a stable spherical flame was typically observed, perturbed by several "explosions" at the beginning of combustion. In CO a dim flame developed, which ceased after the xenon lamp was turned off.

In the present work, we study combustion of Mg particles (1-2 mm) in CO₂ under microgravity conditions onboard the CNES A300 ZERO-G aircraft, using heating by a hot wire. The developed technique ensures the use of every parabolic maneuver for conducting an experiment and allows normal gravity tests for comparison.

EXPERIMENTAL

Cylindrical Mg samples (99.99% purity) with equal diameter and length (1, 1.5 and 2 mm) and an axial hole (diameter 0.3-0.5 mm) are used in this work. The sample is installed on a wire in a cylindrical ampoule (inner diameter 45 mm, inner length 80 mm) made of quartz and optical glass (see Fig. 1). The ampoule has inlet and outlet for gas filling/evacuation and two opposite holes for installation of the wire. The wire consists of three sections connected with spot welding. The central section (20 mm) is a high-resistance wire; external sections are low-resistance wires. The diameter of the high-resistance wire is varied in the range 0.15-0.4 mm depending on the particle size to ensure sufficiently fast ignition during the microgravity period (which is typically equal to 22 s). The particle is installed on the central section of the wire before the welding. The wire with the particle is hermetically fixed in the ampoule with two ceramic insulators and glue.

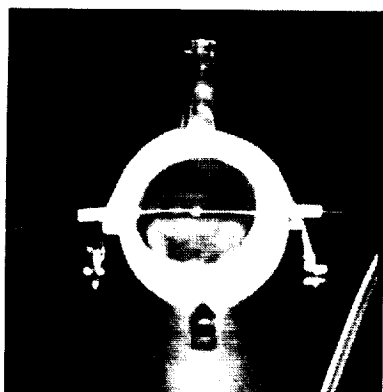


Figure 1. Ampoule with particle

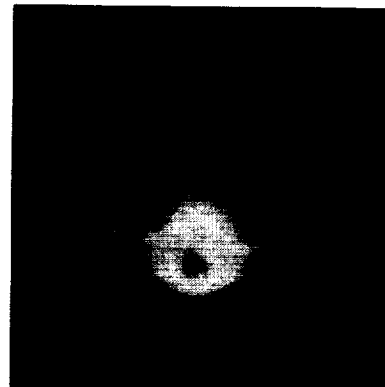


Figure 2. Flame in microgravity (left) and in normal gravity (right)

A set of 30 ampoules with particles is prepared for every flight, which includes 30 parabolic maneuvers. Before the experiment one ampoule is installed on a special pedestal inside a 70-l steel chamber with windows, which guarantees safety. A high-speed 16-mm film camera, a photo camera, and a photodiode are used for observations and measurements. During the experiment, the high-resistance wire is heated by electric current and ignites the particle. Note that after ignition the wire typically breaks in one point in the flame zone, thus electrical heating stops and cannot affect the combustion process. The described technique allows fast replacement of the used ampoule with the new one in the period between two parabolas. Condensed products of combustion inside the ampoules are analyzed after flights with SEM and X-ray diffraction methods. Experiments under normal gravity were also conducted for comparison; melting and ignition did not result in collapsing the particle. All experiments were conducted at pressure of 1 atm and room temperature.

RESULTS AND DISCUSSION

In about 50% of experiments we observed a stable flame, spherical in microgravity (see Figure 2). In the rest 50%, regardless of the gravity level, combustion was pulsating; after the initial phase of stable flame, the combustion process represented a series of flashes. Figure 3 shows typical normalized profiles of light emission intensity, obtained with the photodiode, for both stable and pulsating combustion.

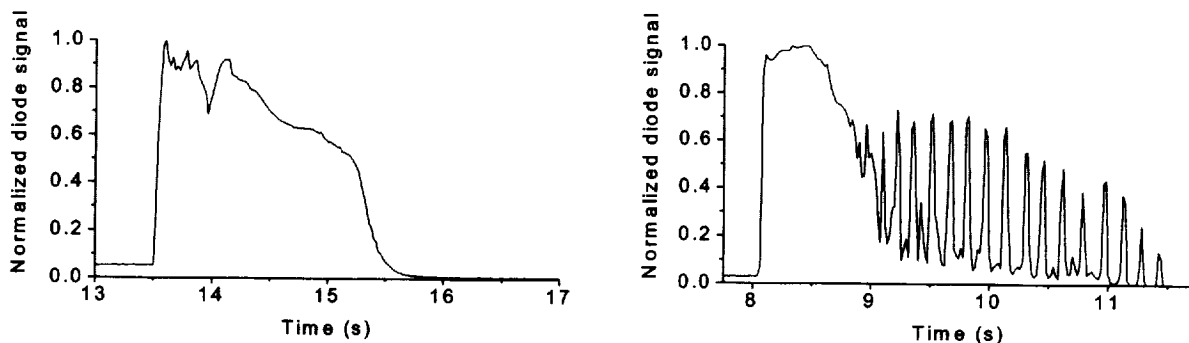


Figure 3. Light emission intensity profiles during combustion of 1.5-mm Mg particles in microgravity

In the experiments [6-10], pulsating combustion of the identical Mg particles was observed only in the atmosphere of CO; combustion in CO₂ was always stable despite superheating and fragment ejection at high pressures [6]. Pulsating combustion of 10-mm Mg disks ignited by a xenon lamp was observed in CO₂/CO mixtures [12]; note that the disks did not burn in pure CO. Authors [13] reported that combustion of Mg particles, 0.1-1 mm, in pure CO₂ was pulsating and explained the pulsations by formation of carbon, which plug pores in the surface oxide layer, hindering Mg vaporization. However, the above discrepancy in experiments conducted with different methods implies that the main reason for the instability is too large heat losses for the relatively small heat releases in such oxidizers as CO₂ and especially CO. The low level of heat losses in experiments [6-10], conducted with large particles on a thin wire in high-temperature environment, ensured stable combustion in CO₂ and pulsating combustion in CO. Higher heat losses in Refs. 12, 13 shifted the area of unstable combustion towards the higher concentrations of CO₂. Heat losses in the present experiments conducted at room temperature are obviously higher than in [6-10]; this results in the fact that the experiments are made in a border zone between areas of stable and unstable combustion. Recent experiments on combustion of Mg particles in diluted O₂/Ar mixtures revealed pulsating combustion at low O₂ concentrations [14]. This confirms the hypothesis that pulsating combustion of Mg particles in carbon oxides is associated with relatively low heat releases in these oxidizers.

Figure 4 compares the burning times in microgravity and normal gravity, measured as a function of equivalent diameter (diameter of spherical particles of the same volume). The accelerating effect of gravity on combustion of larger particles is caused by natural convection, which is significant for 2-mm particles ($Gr \approx 10^2$). The results obtained in experiments with stable combustion in microgravity are expressed by formula $t_b = 0.63 d^2$ where t_b is the burning time in seconds and d is the equivalent diameter in millimeters. The quadratic dependence means that combustion is controlled by diffusion in gas phase. The obtained rate constant 1.6 mm²/s is close to the value 1.8 mm²/s predicted by a quasi-steady diffusion model of Mg particle combustion in CO₂ [15].

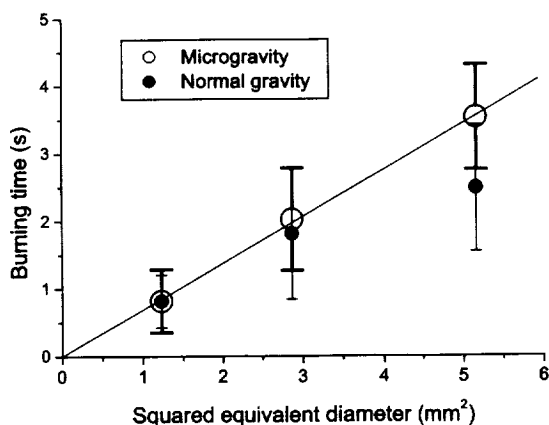


Figure 4. Burning time of Mg particles in CO₂ in microgravity and normal gravity

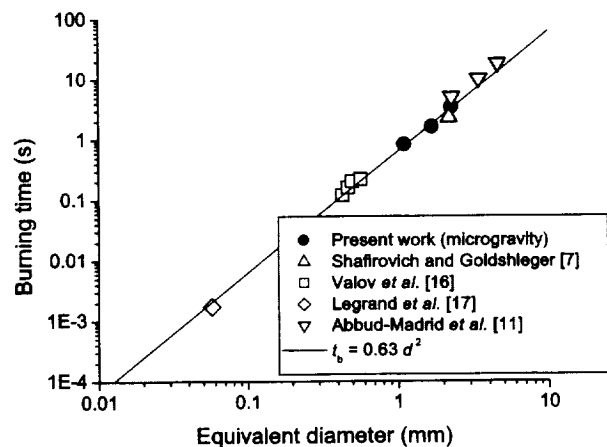


Figure 5. Comparison with results obtained for different particle sizes

Figure 5 compares the burning times in experiments with stable combustion under microgravity conditions with previous data obtained for Mg particles of different sizes in CO₂ [7, 11, 16, 17]. The previous data fit well the obtained dependence $t_b = 0.63 d^2$. This points to the identity of combustion mechanisms in the range of particle sizes 0.05-5 mm.

SUMMARY

Magnesium particles (1-2 mm) were ignited by a hot wire in room-temperature CO₂ environment under microgravity and normal gravity conditions. In about 50% of experiments, regardless of the gravity level, combustion was pulsating. The instability may be associated with the relatively low heat release in such oxidizer as CO₂ and high heat losses. For stable combustion, the burning times measured in microgravity fit a quadratic dependence on the particle size, which is typical for the diffusion-controlled combustion. Good quantitative agreement with previous data obtained for particles of different sizes indicates that combustion mechanisms of magnesium in CO₂ are identical in the range of particle sizes 0.05-5 mm.

ACKNOWLEDGEMENT

This work is supported by INTAS and ESA (Project INTAS-ESA 99-00138).

REFERENCES

1. Yuasa, S., and Isoda, H. AIAA Paper 89-2863.
2. Shafirovich, E. Ya., Shiryayev, A. A., and Goldshleger, U. I. *J. Prop. Power* 9(2): 197-203 (1993).
3. Shafirovich, E. Ya., and Goldshleger, U. I. *J. Prop. Power* 13(3): 395-397 (1997).
4. Goroshin, S., Higgins, A.J., and Lee, J.H.S. AIAA Paper 99-2408.
5. Wickman, J.H. AIAA Paper 99-2409.
6. Shafirovich, E. Ya., and Goldshleger, U. I. *Combust. Flame* 88: 425-432 (1992).
7. Shafirovich, E. Ya., and Goldshleger, U. I. *Combust. Sci. Tech.* 84: 33-43 (1992).
8. Shafirovich, E. Ya., and Goldshleger, U. I. *Combust. Sci. Tech.* 135: 241-254 (1998).
9. Goldshleger, U.I., and Shafirovich, E.Ya. *Comb., Expl., Shock Waves* 35(6): 637-644 (1999).
10. Goldshleger, U.I., and Shafirovich, E.Ya. *Comb., Expl., Shock Waves* 36(2): 220-226 (2000).
11. Abbud-Madrid, A., Omaly, P., Branch, M.C., and Daily, J.W. *Fifth Microgravity Combustion Workshop, May 18-20, 1999, Cleveland, Ohio*, NASA CP 1999-208917, pp. 211-214.
12. Yuasa, S., and Fukuchi, A. *Twenty-Fifth Symp. (International) on Combustion*, The Combustion Institute, Pittsburgh, 1994, pp. 1587-1594.
13. Maltsev, V. M., Maltsev, M. I., and Kashporov, L. Ya. *Main Characteristics of Combustion* (in Russian). Khimiya, Moscow, 1977.
14. Goldshleger, U.I., and Amosov, S.D. *Unsteady Combustion and Interior Ballistics, International Workshop, June 26-30, 2000, Saint Petersburg*, pp. 129-131.
15. Shafirovich, E. Ya., and Filonenko, A.K.. *Sov. J. Chem. Phys.* 2(9): 2115-2126 (1985).
16. Valov, A.E., Kustov, Yu.A., and Shevtsov, V.I. *Comb., Expl., Shock Waves* 30(4): 431-436 (1994).
17. Legrand, B., Shafirovich, E., Marion, M., Chauveau, C., and Gokalp, I. *Twenty-Seventh Symp. (International) on Combustion*, The Combustion Institute, Pittsburgh, 1998, pp. 2413-2419.

EXPERIMENTS ON DROPLET COMBUSTION IN SPACELAB AND SPACE STATION: PLANNING, DATA ANALYSIS AND THEORETICAL INTERPRETATIONS OF RESULTS

F.A. Williams, Center for Energy Research,
Mechanical and Aerospace Engineering, University of California, San Diego

INTRODUCTION

In a joint program among Prof. F.L. Dryer of Princeton University and Dr. V. Nayagam of the National Center for Microgravity Research on Combustion and Fluid Dynamics at the NASA Glenn Research Center, the combustion of liquid fuel droplets having initial diameters between about 1 mm and 6 mm is being studied, with the objective of improving fundamental knowledge of droplet combustion through microgravity experiments and through theoretical analyses. This research has involved experiments in both of the drop towers at the Glenn Research Center, as well as experiments in Spacelab during three different flights of the Space Shuttle. Plans are in progress for another Space-Shuttle experiment and for experiments to be performed in the Destiny module of the International Space Station. Some of the history of these experiments, as well as planning for future experiments are discussed here, as are analyses of the results from the latest free-droplet experiments in Spacelab.

FIBER-SUPPORTED DROPLET COMBUSTION

The principal focus of the present program concerns the combustion of single free fuel droplets in quiescent room-temperature atmospheres. Such experiments, however, for droplets in the size range addressed require relatively complicated experimental designs for the formation, deployment, ignition and data acquisition from droplets burning in microgravity. Significant experimental simplifications are provided if the droplets are suspended or "tethered" on a fiber to provide support, keeping them at fixed positions in the apparatus. The fiber-supported droplet combustion (FSDC) experiments were designed to achieve this kind of simplification, as a prelude to the free-droplet experiments in Spacelab. The FSDC experiments are, however, of interest in their own right for a number of reasons. First, they can provide information on influences of fiber supports on combustion, which are important since, for example, many droplet-combustion experiments are performed with fiber supports, and new physical phenomena of interest can be introduced by the fibers. Second, they afford the opportunity to investigate effects of phenomena that cannot readily be studied with free droplets, such as controlled forced convection and droplet interactions in the combustion of linear droplet arrays having fixed interdroplet spacings. The FSDC experiments have provided information on all of these phenomena.

FSDC is a "Glovebox" experiment, that is, one that does not require a full experiment rack of its own but instead can be run in the small multi-user Glovebox facility. It was first performed (FSDC-1) on the USML-2 mission in October, 1995 (STS-73) [1] and next (FSDC-2) on the second flight of the MSL-1 mission in July, 1997 (STS-94). FSDC-3 is currently scheduled to fly in the Space Shuttle as part of the R2 mission in April, 2002, in which 14 hours have been allotted to this experiment.

Because of the Glovebox restrictions, all FSDC experiments burn droplets in cabin air, but different experiments concern different fuels under different conditions. Different investigators are responsible for designing and analyzing the different experiments. Fuels for which data have been obtained include methanol, methanol-water mixtures, ethanol, ethanol-water mixtures, methanol-dodecanol mixtures, n-heptane, n-decane and heptane-hexadecane mixtures; in addition to studying single droplets in quiescent atmospheres, the FSDC work investigated single droplets in forced convective flow and droplet pairs. In total, in Spacelab there have now been more than 160 successful FSDC burns. Plans for FSDC-3 are to investigate droplet combustion of nonane-hexanol mixtures (T.C. Avadesian), sooting effects for nonane (M. Choi), ethanol-water mixtures (F.L. Dryer), forced-convective effects for decane-hexadecane and decane- α methylnaphthalene mixtures (V. Nayagam), quiescent decane-hexadecane mixtures (B.D. Shaw) and quiescent decane-

α methylnaphthalene mixtures (F.A. Williams), the last including the pure constituents and motivated by interest in diesel combustion.

The FSDC-2 experiments provided data on combustion of n-heptane, n-decane, mixtures of n-hexane and n-hexadecane, mixtures of methanol and water, ethanol and mixtures of ethanol and water for single droplets in quiescent atmospheres, on combustion of n-decane droplet pairs in quiescent atmospheres and on combustion of n-decane single droplets and droplet pairs in forced convective flow. Although results are reported in the L+1 Report for MSL-1 (the report presented one year after liftoff), co-authored by all of the FSDC-2 investigators (R. Colantonio, D. Dietrich, F.L. Dryer, J.B. Haggard, Jr., V. Nayagam, B.D. Shaw and F.A. Williams), the data obtained were so extensive that further analysis is still in progress. One notable finding of this research was the "Thomas twin effect" (so named because mission specialist D.A. Thomas was performing the experiment when it was observed), in which a pair of droplets anchored on the fiber by a bead moved apart at the moment of ignition but then drifted together after the flame was established around them; the anchor permitted some droplet motion along the wire but constrained the liquid, preventing its surface from passing over the bead. Various possible explanations of the phenomena were proposed, including the impulse from enhanced vaporization rates locally at the droplet surfaces nearest the flame. Payload specialist R.K. Crouch was the other crew member who performed the FSDC-2 experiments, while M.K. King and H.D. Ross offered notably helpful advice on the ground. Figure 1 includes recent results of analyses of FSDC-2 data on burning rates of heptane, showing that the burning rate decreases with increasing initial droplet diameter and that the presence of the fiber increases the burning rate. These results are explained, respectively, by increasing quantities of soot formation with increasing droplet size, leading to increased radiant energy loss, and by enhanced heat transfer into the droplet by heat conduction from the flame along the fiber support.

FREE DROPLET COMBUSTION

The experiments in Spacelab on the combustion of free droplets were carried out as the droplet combustion experiment (DCE), a two-rack experiment performed on the MSL-1 mission in both the April, 1997 flight (STS-83) [2] and STS-94. The DCE studies, thus far employing only heptane as the fuel, addressed mainly the combustion of free droplets, although two DCE tests also were made with fiber support for comparison with FSDC results. In the DCE tests the combustion occurred mainly in oxygen-helium atmospheres at pressures of 1.00 atm, 0.50 atm and (for 2 droplets) 0.25 atm, although 4 DCE data points from STS-94 involved combustion in normal Spacelab cabin air, 2 for free droplets and 2 for fiber-supported droplets. There were a total of 38 successful DCE tests for which combustion data were secured; these experiments were run by payload commander J.E. Voss and payload specialist G.T. Linteris. The principal types of data obtained were histories of droplet and flame diameters, as well as extinction diameters, as functions of atmospheric composition and pressure. In addition, information was acquired on soot-particle behavior, on droplet interactions, on flame elongation through convection, on droplet and flame oscillation phenomena, on staged combustion and on ignition and extinction characteristics. The main focus in the analysis of the results thus far has been on burning rates and flame-diameter histories, including identifying conditions and mechanisms of flame extinction. Efforts to explain the experimental results include computational investigations at Princeton and theoretical studies at UCSD. The Princeton contributions are identified by F.L. Dryer in a companion communication. The UCSD work is discussed here.

ANALYSIS OF DCE RESULTS

Our asymptotic theory of flame histories for heptane droplet combustion with the flame located in the outer transient zone has now appeared in print [3]. Our analysis and interpretation of the MSL-1 data on heptane droplet combustion, performed by Malissa Ackerman, should appear soon [4]. This analysis addresses both the DCE and the FSDC tests. Figure 1 summarizes the resulting burning-rate constants found at 1.00 atm (solid curves for helium-oxygen atmospheres and dotted curves for air) and at 0.50 atm in helium-oxygen atmospheres (dashed curves). The general trend of a decrease in the burning-rate constant with increasing

initial droplet diameter is evident in all of this data and is attributed to increasing influences of radiant energy loss. The burning-rate constant decreases with decreasing pressure and with increasing dilution, as expected, but the effect of dilution appears to be smaller at reduced pressures, an observation that requires further investigation. The two DCE tests in air with free droplets, identified by the symbol u, clearly give burning rates lower than those of the two DCE tethered-droplet tests, as well as lower than all of the FSDC tests, because of the roughly 10% enhancement of burning rate by the fiber support in these configurations.

Figure 2 shows dependences of the droplet diameter at extinction on the initial droplet diameter, measured in DCE experiments in helium-oxygen atmospheres. The symbol R identifies radiative extinction, while points without this symbol correspond to diffusive extinction, in which the flame contracts substantially prior to extinction. Relatively extensive results were obtained at 1.00 atm in 25% oxygen on a molar basis, showing the increase in extinction diameter with increasing initial diameter, attributed to increasing influences of radiant energy loss. The curve drawn in the figure illustrates this effect. The data point shown at this same pressure for 30% oxygen indicates that an increase in oxygen concentration results in an increase in the initial droplet diameter at which a given extinction diameter is observed, in accord with theoretical expectation from changes in stoichiometry and reaction rates. Similarly, the point at 0.50 atm and 25% oxygen shows that decreasing the pressure decreases the initial diameter at which a given extinction diameter occurs, likely because of decreased reaction rates. Since radiant loss rates associated with sooting should decrease with increasing dilution and decreasing pressure, this effect seems overbalanced by those indicated above.

Figure 3 shows DCE data in helium-oxygen atmospheres on the flame diameter at extinction as a function of the initial droplet diameter. The solid curves are for 1.00 atm and the dashed curves for 0.50 atm; different curves correspond to different oxygen concentrations. Data points without the symbol R again represent diffusive extinction. From the three solid curves it is evident that the final flame diameter increases as the oxygen mole fraction decreases, again expected from the stoichiometry and reaction rates. These curves also show that the final flame diameter increases with increasing initial droplet diameter but tends to level off at both small and large initial droplet diameters, as theory suggests for diffusive extinction at small diameters, and consistent with a radiation-dominated ignition limit at large diameters. At a given oxygen mole fraction, the final flame diameters are larger at lower pressures for chemical-kinetic reasons. The results in Fig. 3 are, in general, consistent with those in Fig. 2 but more extensive because of the greater ease with which final flame diameters can be measured.

Figure 4 is an attempt to extract boundaries between radiant and diffusive extinction in a parameter plane of the oxygen mole fraction of the atmosphere and the initial droplet diameter, from the DCE data in helium-oxygen atmospheres. In this figure, open symbols are tests that experienced diffusive extinction and solid symbols tests that experienced radiative extinction. The error bars indicate the range of uncertainty of the boundary location at 1.00 atm, and the curve is an estimate of where the boundary might lie. There are insufficient data to identify any differences in boundary location at 1.00 atm and 0.50 atm. Maps of this kind, which are challenging to generate experimentally, are helpful in testing theoretical predictions of effects of finite-rate chemistry in droplet combustion. The general increase in the initial droplet diameter with increasing oxygen mole fraction along the boundary is consistent with theoretical prediction, but quantitative comparisons remain to be made.

FUTURE DCE RESEARCH

In addition to continued theoretical analysis of the extensive heptane data now available, future DCE experiments (DCE-2) are being planned for the common, multi-investigator droplet-combustion facility in the International Space Station. In the DCE-2 experiments, droplets of methanol and methanol-water mixtures are to be burned in helium-oxygen-nitrogen atmospheres. The different diluents helium and nitrogen can lead to different combustion behavior, and effects of mixtures of these two diluents on the combustion have not previously been investigated. The experiments are intended to improve our understanding of methanol droplet combustion and of

the influences of different atmosphere mixtures on the burning. Comparisons of experimental results with calculations should help to determine the accuracy with which the calculations can be made and to refine the theoretical descriptions of droplet combustion, improving knowledge of basic thermodynamic, transport, radiative and chemical-kinetic parameters.

CONCLUSIONS

Much more theoretical work is needed on flame histories in droplet combustion if full understanding and quantitative prediction of experimental results such as those of FSDC and DCE are to be obtained. There are a number of qualitative agreements between prediction and observation, but there also are conditions under which no theory yet exists, such as flame extinction after droplet disappearance. It may be concluded that many outstanding research opportunities remain.

ACKNOWLEDGMENT

Besides those mentioned above, the DCE and FSDC engineering and data-acquisition teams deserve acknowledgment.

REFERENCES

1. Dietrich, D.L., Haggard, J.B., Jr., Dryer, F.L., Nayagam, V., Shaw, B.D., and Williams, F.A., "Droplet Combustion Experiments in Spacelab," *Twenty Sixth Symposium (International) on Combustion*, The Combustion Institute, Pittsburgh, PA, 1996, pp. 1201-1207.
2. Nayagam, V., Haggard, J.B., Jr., Colantonio, R.O., Marchese, A.J., Dryer, F.L., Zhang, B.L., and Williams, F.A., "Microgravity N-Heptane Droplet Combustion in Oxygen-Helium Mixtures at Atmospheric Pressure," *AIAA Journal*, Vol. 36, 1998, pp. 1369-1378.
3. Fachini, F.F., Liñán, A. and Williams, F.A., "Theory of Flame Histories in Droplet Combustion at Small Stoichiometric Air-Fuel Ratios," *AIAA Journal*, Vol. 27, 1999, pp. 1426-1435.
4. Ackerman, M., et al, "A Treatment of Measurements of Heptane Droplet Combustion Aboard MSL-1", *NASA TM*, to appear, 2001.

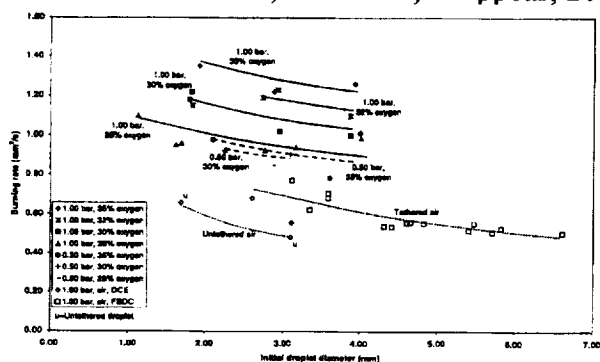


Figure 1: Burning-rate comparisons.

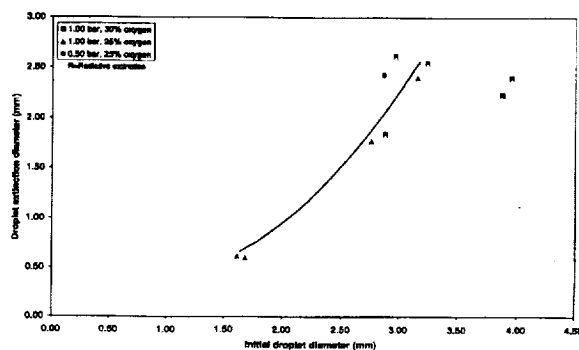


Figure 2: Droplet diameter at extinction.

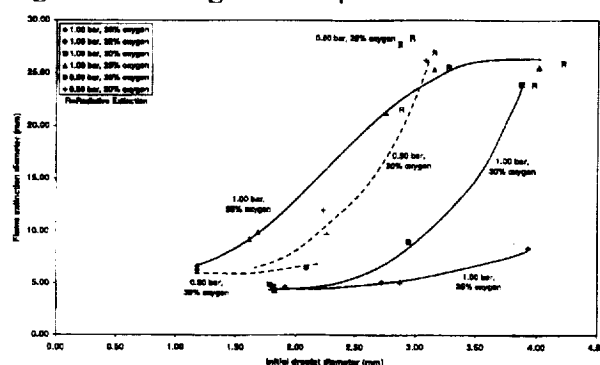


Figure 3: Final flame diameter.

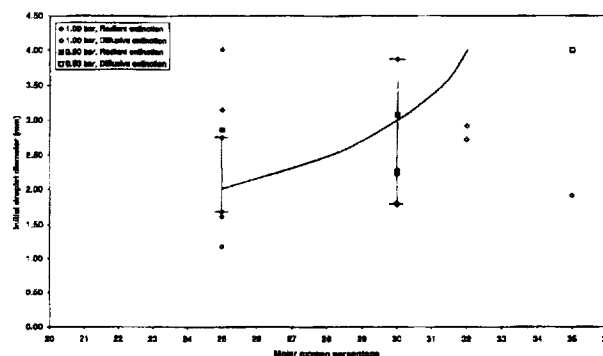


Figure 4: Boundary between radiant and diffusive extinction.

SOME RECENT OBSERVATIONS ON THE BURNING OF ISOLATED N-HEPTANE AND ALCOHOL DROPLETS

F. L. Dryer, A. Kazakov, and B.D. Urban

Mechanical and Aerospace Engineering, Princeton University, Princeton, NJ 08544-5263

INTRODUCTION

In a joint program involving Prof. F.A. Williams of the University of California, San Diego and Dr. V. Nayagam of the National Center for Microgravity Research on Combustion and Fluid Dynamics, the combustion of liquid fuel droplets of n-heptane, n-decane, methanol, methanol-water, ethanol and ethanol-water having initial diameters between about 1 mm and 6 mm continues to be studied. The objectives of the work are to improve fundamental knowledge of droplet combustion dynamics for pure fuels and fuel-water mixtures through microgravity experiments and theoretical analyses. The Princeton contributions to the collaborative program supports the engineering design, data analysis, and data interpretation requirements for the study of initially single component, spherically symmetric, isolated droplet combustion studies through experiments and numerical modeling. The complementary UCSD contributions apply asymptotic theoretical analyses and are described in the published literature and in a companion communication in this conference. The combined program continues to focus on analyses of results obtained from Fiber Supported Droplet Combustion (FSDC) experiments (FSDC-2, STS-94) conducted with the above fuels in shuttle cabin air and Droplet Combustion Experiment (DCE) data obtained for unsupported and fiber supported droplets of n-heptane in Helium-Oxygen mixtures and cabin air (STS-83, STS-94). The program is preparing for a second DCE experimental mission using methanol/methanol-water as fuels and helium-oxygen-nitrogen environments. DCE-2 is to be conducted aboard the International Space Station.

Emphases of recent Princeton work are on the study of simple alcohols (methanol, ethanol) and alcohol/water mixtures as fuels, with time-dependent measurements of drop size, flame-stand-off, liquid-phase composition, and finally, extinction. Ground based experiments have included bench-scale studies at Princeton and collaborative experimental studies in the 2.2 second drop tower at NASA-Glenn Research Center.

METHANOL

Methanol, an alternative fuel used in internal combustion systems as well as a hydrogen carrier for fuel cells, belongs to a class of fuels for which some of their combustion intermediates and products are highly soluble in the fuel itself. Methanol is unique because, for over-all equivalence ratios and pressures of interest in combustion systems, its oxidation kinetics leads to negligible formation of soot precursor species. The absence of soot, the relative simplicity of the detailed oxidation kinetics, and the substantial characterization of physical and thermophysical properties makes isolated methanol droplet combustion an ideal subject for developing and validating robust detailed models which test coupling effects of fundamental physical and chemical submodels on burning rate, flame structure, extinction, non-luminous radiation, product dissolution, and liquid phase mixing. Based upon a computational approach initially developed by Cho et al. [1], a time-dependent numerical model for isolated droplet combustion has been developed that includes temperature-dependent physical properties, detailed gas phase kinetics, multi-component gas phase diffusion, gas phase spectral radiative transport, water dissolution-vaporization, and mass/energy transport within the liquid phase [2].

It has been hypothesized that droplet formation processes, solutal and thermal Marangoni effects, and fiber tethers can generate liquid motions within isolated burning droplets, even when large relative gas/droplet motions are absent [3]. In order to maintain a tractable uni-dimensional

configuration, we estimate the effects of internal liquid phase motions as an increase in molecular transport properties in the liquid phase (increasing the "effective" liquid phase Peclet numbers for mass and energy transport). This approximation is reasonable for droplets at low gas/droplet relative velocity conditions because the Stefan flux velocity at the droplet surface is relatively large in comparison to the tangential surface velocity. As a result, while liquid phase motions have little influence on gas phase motions, the motions in the liquid phase strongly affect the liquid phase thermal and mass transport. The experimental observable with the most sensitivity to this effect is the integrated liquid phase water content as a function of time, and, in turn, its effect on droplet extinction. While this parameter has been measured in ground-based free fall droplet experiments [4], here, we report first data for drop tower experiments. The details of the experimental methodology will be described in the presentation. We have used experimental measurements to estimate the liquid phase mass Peclet number, i.e. the ratio of droplet surface regression velocity to liquid phase mass diffusive velocity, in various experiments including the new data, as well as those of Lee and Law [4]. Results for drop tower experiments, along with relevant calculations, are shown in Fig. 1.

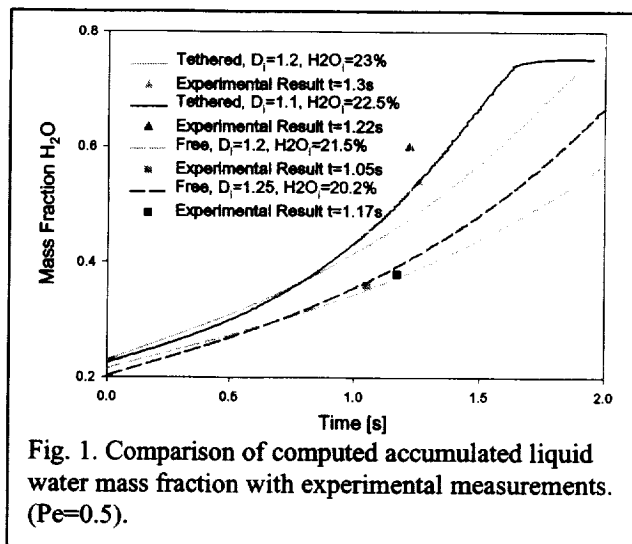


Fig. 1. Comparison of computed accumulated liquid water mass fraction with experimental measurements. ($Pe=0.5$).

Well-mixed "distillation limit" behavior [5] is observed for a Peclet number less than 0.005, while the "diffusion limit" is reached for Peclet numbers greater than 5, with best comparison for drop tower results with a free droplet at a Peclet number of approximately 0.5. However, drop tower experiments with tethered droplets appear to be in the well-mixed, distillation limit, indicating that the presence of the fiber accelerates liquid phase motions within the burning droplet. The chemically reacting flow model has also been applied to the experimental conditions of Lee and Law [4] conducted using small, free falling droplets (150-250 μ m). Comparisons with the model suggest that the droplets in these experiments experienced a high degree of internal liquid phase motions.

ETHANOL

Ethanol can be manufactured with high efficiency from bio-mass and is under use or consideration as a motor fuel, as a fuel additive in reformulated and oxygenated gasoline, and as a hydrogen carrier for fuel cells. From the fundamental point of view, ethanol represents one of the simplest liquid fuels. Its gas-phase oxidation chemistry is relatively simple, it is readily soluble in water and, like methanol, ethanol absorbs water vapor from the gas phase, but it exhibits azeotropic behavior. Ethanol is known to be a non-sooting fuel at ambient pressures in air. However, at elevated pressures (starting from as low as 2 atm of air), ethanol droplet flames have been shown to form soot profusely [6,7]. Ethanol is therefore an ideal pure fuel for studying sooting phenomenon in general, and the effect of pressure on soot formation during droplet combustion in particular.

Microgravity experiments have been performed using ethanol and ethanol/water mixtures in freely falling ground based experiments [4] in drop towers [9,10], and as part of the FSDC-2 experiments noted above [11]. In the latter, each droplet combustion test occurred at pressures 0.996–1.107 bar, oxygen mole fraction 0.204–0.222, and relative humidity 39–46% of the

Spacelab environment. Droplets of pure ethanol and 4% water in ethanol (near the azeotrope) were studied; initial droplet diameter ranged from about 2.5 to 6 mm. Here we present the first numerical modeling results of the above experiments.

Detailed gas-phase kinetics was described with the reaction mechanism of [12] that consists of 142 reversible reactions of 33 species. The gas-phase diffusion and heat conduction terms [13], and transport data [13, 14] were taken from the literature or evaluated. The vapor pressure at the surface of ethanol/water mixtures was calculated using vapor pressure data [15], temperature-dependent latent heats were taken from the literature [16], and mixture liquid density was computed [16,17]. The value of the effective liquid diffusivity (D_l) was assigned by analogy with methanol results, and comparisons of the model predictions with the experimental measurements of [4] were used to validate the choice of D_l .

Exemplar model comparisons with droptower [9] and FSDC-2 experimental data are presented in Figs 2 and 3. The model shows a reasonable agreement with the experimental burning rate data for the entire range of the droplet sizes. With the exception of where droplet motions became excessive or tethered droplet sizes approached the size of the filament tethering-bead. Analysis of the model predictions indicated that the observed decrease in the average droplet burning rate is primarily a result of the influence of non-luminous radiative heat losses which become more pronounced at larger droplet sizes. The predictions of simplified steady-state models [18,19] that do not consider radiative losses

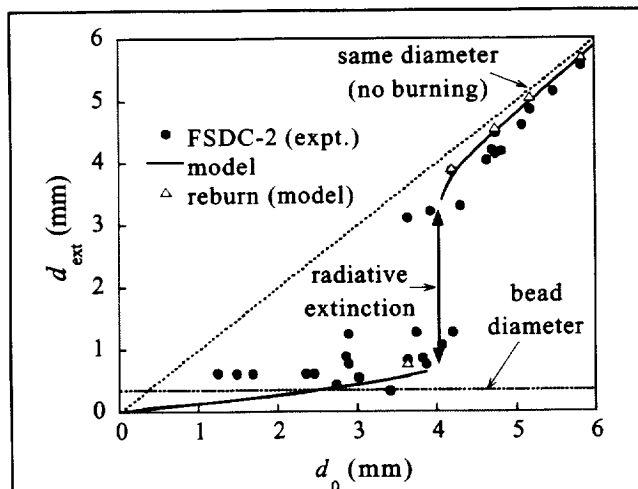


Figure 4. Droplet extinction diameter as a function of initial diameter for ethanol and ethanol/water mixtures burning in air at 1 atm.

burned and underwent extinction were subsequently re-ignited. This procedure was repeated until the droplet was fully consumed. Also shown in Fig. 3 is the sequence of re-ignition and extinction events calculated for the initially largest droplet in the data set (5.8 mm). The model closely follows the sequence of reburns reported in the experiments.

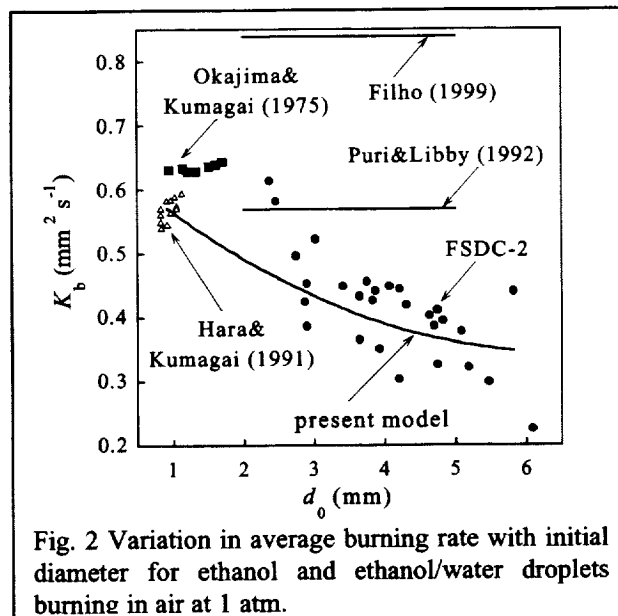


Fig. 2 Variation in average burning rate with initial diameter for ethanol and ethanol/water droplets burning in air at 1 atm.

(Fig. 2) are independent of initial drop size.

The model reproduced extinction diameter data obtained from FSDC-2 very well (Fig. 3). For droplets of less than 3 mm in diameter, extinction is mainly caused by water accumulation in the liquid phase, with experimental data compromised by the large tethering-bead. At $d_0 \sim 4$ mm, both the model and experimental data show a sharp, nearly discontinuous increase in the extinction diameter, indicative of radiative extinction. At larger values of d_0 , d_{ext} asymptotically approaches d_0 , based upon transient burning after ignition, a factor dependent on ignition criteria. During the FSDC-2 experiments, some of the large droplets that

ONGOING WORK

We expect further refinement and testing of the methanol numerical model to be benefited by a second DCE experiment devoted to the study of methanol and methanol/water combustion in helium/nitrogen/oxygen mixtures. The numerical model we have developed for n-heptane droplet burning is under modification to include an implicitly coupled description of processes related to droplet sooting. Results of DCE experiments will be compared with this model, initially, with further testing and validation of the model using data obtained in another program described at this work shop [20]. Finally n-heptane droplet ignition at elevated pressures and temperatures from 650 to 950 K [21,22,23] have exhibited "two-stage" ignition behavior. Others [24] have performed modeling of the higher temperature experiments (950 K) using a high temperature n-heptane semi-empirical kinetics [25]. We are presently conducting modeling studies of the lower temperature cases using a reduced mechanism that includes low temperature, cool flame, intermediate temperature, and high temperature kinetics.

This work was supported by NASA under COOP Nos. NCC3-487 and NCC3-735. We gratefully acknowledge discussions with Forman Williams, Vedha Nayagam, and contributions of Jordan Conley, Paul Michniewicz, Yolanda Stein, and Louis Ernst at Princeton and John Easton at NASA GRC.

References

1. Cho, S.Y., Yetter, R.A., and Dryer, F.L., J.Comput.Phys. 102:160 (1992).
2. Marchese, A.J., Dryer, F.L., and Colantonio, R., Proc.Combust.Inst. 27:2627 (1998).
3. Choi, M.Y. and Dryer, F.L., "Microgravity Droplet Combustion" to appear in a special volume on Microgravity Combustion", ed., H. Ross, in press, 2000.
4. Lee, A. and Law, C.K., Combust.Sci.Technol. 86:253 (1992)
5. Makino A. and Law, C.K., Combust.Flame 73:221 (1988).
6. Yap, L.T. Ph.D. thesis, Dept. of Mechanical and Aerospace Eng. Princeton University, 1986.
7. Ernst, L.F., Kroenlein, K., and Dryer, F.L. unpublished results, 2000.
8. Choi, M.Y. Ph.D. thesis, Dept. of Mechanical and Aerospace Eng., Princeton University, 1992.
9. Okajima,S., and Kumagai,S., Proc. Combust. Inst. 15:401-407 (1975); Hara,H., and Kumagai,S., Proc. Combust. Inst. 23:1605-1610 (1991)
10. Colantonio, R. O., and Nayagam, V., "Radiative Heat Loss Measurements During Microgravity Droplet Combustion," Proceedings of the 1997 Central States Section of the Combustion Institute, Paper No. 23, pp. 125-129 (1997).
11. Colantonio,R., Dietrich,D., Haggard,J.B., Jr. et al. Proceedings of the Microgravity Science Laboratory One Year Science Review Meeting, Huntsville, Alabama, 1998.
12. Norton,T.S., and Dryer,F.L., Int. J. Chem. Kinetics 24:319-344 (1992).
13. Kee,R.J., Dixon-Lewis,G., Warnatz,J., Coltrin,M.E., and Miller,J.A. A Fortran Computer Code Package for the Evaluation of Gas-Phase, Multicomponent Transport Properties, Sandia Report SAND86-8246, 1986.
14. Reid R.C., Prausnitz J.M., and Poling B.E. , The Properties of Gases and Liquids, Fourth ed., McGraw Hill, New York, 1987.
15. Kurihara,K., Minoura,T., Takeda,K., and Kojima,K., J. Chem. Eng. Data 40:679-684 (1995).
16. Daubert T.E., Danner R.P., Physical and Thermodynamic Properties of Pure Chemicals, Hemisphere, Washington, D.C., 1989.
17. Bai,T.-C., Yao,J., and Han,S.-J., J. Chem. Thermodynamics 30:1347-1361 (1998).
18. Puri,I.K., and Libby,P.A., Combust. Sci. Technol. 76:67-80 (1991).
19. Filho,F.F., Combust. Flame 116:302-306 (1999).
20. Choi, M.Y., Yozgatligil, A., Dryer, F.L., Kazakov, A., and Dobashi, R. This Work Shop.
21. Saitoh, T., Ishiguro, S., and Niiooka, T., Combust. Flame 48:27 (1982).
22. Takei, M., Tsukamoto, T., and Niioka, T., Combust. Flame 93:149 (1993).
23. Takei, M., Tsukamoto, T., and Niioka, T., Combust. Flame 93:149 (1993).
24. Saitoh, T. and Todoriki, H., Trans. Japan Soc. Mech. Eng. (B) 61:240 (1995) (In Japanese).
25. Müller, U.C., Peters, N., and Linan, A. Proc.Combust.Inst. 24:777 (1992).

Droplet Combustion in a Slow Convective Flow

V. Nayagam,¹ M. C. Hicks,² N. Kaib,¹ M. Ackerman,³ J. B. Haggard, Jr.,² and F. A. Williams³,

¹National Center for Microgravity Research, ²NASA Glenn Research Center
21000 Brookpark Road, Cleveland, OH 44135, email: v.nayagam@grc.nasa.gov

³Center for Energy Research
University of California, San Diego, La Jolla, CA 92093.

INTRODUCTION

The objective of the present flight experiment definition study is to investigate the effects of slow forced convective flows on the dynamics of isolated single droplet combustion and is designed to complement the quiescent, microgravity droplet combustion experiments (DCE-1 and DCE-2) of Williams and Dryer. The fuels selected for this study are the same as those of DCE, namely, a sooting alkane fuel (heptane) and a non-sooting alcohol (methanol), and imposed flow rates are chosen between 0 and 20 cm/s with varying ambient oxygen concentrations and pressures. Within this velocity range, both accelerating and decelerating flow effects will also be investigated. Two different approaches to generate the forced flow are currently under development in ground-based facilities; the first is a flow tunnel concept where the forced flow is imposed against a stationary droplet, and in the second a tethered droplet is translated at a specified velocity in a quiescent ambient medium. Depending upon the engineering feasibility a selection will be made between these two approaches so that the experiment can be accommodated in the Multiple Droplet Combustion Apparatus (MDCA) currently being designed for the International Space Station.

Recently, we have finished designing and fabricating the experimental rigs using both the above mentioned concepts. The flow tunnel concept is implemented in a 2.2 second drop tower rig. Preliminary experiments have been carried out using heptane and methanol in air at atmospheric pressure. The translating droplet apparatus is scheduled to be tested in the 5 second drop facility in the near future. This report presents some of the experimental results obtained for heptane.

EXPERIMENTS

Experiments were conducted in the NASA 2.2 second drop tower using the flow tunnel apparatus. The flow tunnel is capable of producing uniform forced flow velocities in the range of 0 to 20 cm/s within a cylindrical combustion chamber of cross sectional area 314 cm² and height 100 cm. Gas flow through the chamber is established by actuating a solenoid valve to open the gas line from a pressurized gas bottle to the chamber. A pressure regulator, located upstream of a sonic orifice, is used to control flow velocities inside the chamber. A specially designed droplet combustion insert was built to be accommodated within this flow tunnel. The insert consisted of 100 micron quartz fiber with a 200 micron bead at its tip, a stepper-motor-driven fuel syringe with a hypodermic needle to deposit the fuel droplet on the bead, and a solenoid-controlled hot-wire igniter. The time-synchronized operations of the flow tunnel, the fuel syringe motor, and the igniter are controlled by a programmable on-board microprocessor. The flow uniformity was checked with the insert in place using a hot-wire anemometer and was found to vary no more than ± 0.5 cm/s at a flow rate of 10 cm/s. Prior to each test the flow field

was allowed to reach steady conditions (a period of about 10 s), followed by the formation of a droplet of desired size on the support-fiber bead and then the experimental package was dropped. Ignition was achieved during the free fall in low gravity. During the drop back-lighted images of the droplet, also showing portions of the flame, were obtained using a color CCD camera at 30 frames per second. The back-lighting intensity was adjusted such that the soot-shells formed are visible in the droplet image. A flame camera with a larger field of view captured the flame shapes. Also, a wide-band (0.6 to 40 μm) and a narrow-band (5.1-7.5 μm) radiometers recorded the radiant emission from the burning droplet flame.

RESULTS AND DISCUSSIONS

Heptane droplets of initial diameter varying between 0.8 mm and 1.6 mm were burned in a forced flow of air at atmospheric pressure in microgravity. The flow velocities ranged from 2 cm/s to 10 cm/s. Nineteen successful tests were performed in the 2.2 second drop tower, and the results of these experiments are discussed below.

Flame Shapes:

Heptane droplets burning in air in a slow convective flow ($2 \text{ cm/s} \leq U_\infty \leq 10 \text{ cm/s}$) exhibited luminous, orange flames. As the flow velocity was increased from 2 cm/s to 10 cm/s the upstream leading-edge of the flame became dimmer and turned blue showing that the soot formation ceases there due to insufficient residence time. The flame tips downstream were found to be open. From the flame images various parameters can be identified and measured to characterize the flame geometry as shown in Fig. 1a. It should be noted that the downstream "flame length" corresponds to the visible flame length rather than the closed stoichiometric flame position (shown as the dotted curve in Fig. 1a). Dimensional analysis of this problem using a thin-flame approximation and constant thermophysical properties shows three dimensionless groups that are of relevance to the flame geometry, namely, the Reynolds number $Re (= U_\infty D / \nu_\infty)$, the stoichiometric coefficient S , and the dimensionless burning rate $M_b (= k / \nu_\infty)$; where k is the burning-rate constant [1]. The dimensionless parameters W/D , and H_2/D then should correlate with these three dimensionless groups. For the present set of experiments S is a constant and M_b varies over a small range. Figures (2b-2c) show the variations of the dimensionless flame width W/D , and the upstream flame standoff distance H_2/D , with Re (varying approximately as $\sim 1/Re$) for four different imposed velocities. The two sets of data corresponding to 5 cm/s are for two different initial droplet sizes (1.12 and 1.45 mm). The downstream "flame length" $(H_2 - H_1)/D$ cannot be correlated in similar fashion because of the fluctuations of the downstream yellow tip. Therefore we show the dimensional variation of H_1 against D in Fig. 2d. At 4 cm/s pulsation of opening and closing of the flame tip is reflected in the wiggle in Fig. 2d.

Soot-Shell Behavior:

Figure 2 shows a sequence of back-lit images of the droplet, starting shortly after ignition. A partial outline of the flame, the droplet, and the soot shell are visible. Initially, the soot shell takes a cup-shaped form with the open end facing downstream. Soon after, the perturbations to the temperature and the velocity fields caused by the fiber generate an effective thermophoretic force that draws a portion of the soot volume toward the droplet surface along the fiber. This impinging soot flow is eventually forced away from the droplet surface at a larger distances from the fiber by the Stefan-flow drag, thereby forming a soot ring downstream of the droplet. This

behavior is consistent with earlier discussions [2]. As the droplet burns, the soot ring remains trapped behind it, and at the end of the burn the soot ring is deposited on the support fiber. The soot rings were found to form only up to an imposed velocity of 8 cm/s for the range of droplet initial sizes examined in this study. At the highest velocity studied here, 10 cm/s, soot rings were not observed, and all of the soot escapes through the open flame tip downstream, similar to the condition shown in Fig. 2a. The maximum diameter of the soot ring during an experiment decreased with increasing flow velocity. Further studies are needed to address the occurrence and cessation of the soot rings. The planned translating droplet experiments with the fiber support perpendicular to the flow should also provide further insight into the soot-ring formation process.

Burning Rates:

Burning rate constants k , are obtained by fitting a linear curve to the D^2 versus time plots of the experimental data. The burning rates calculated for the quiescent conditions are slightly higher than the free-floated droplet results of DCE, but comparable to the fiber-supported droplet results of FSDC (Williams, this Volume). Figure 3 shows the variation of (k/k_0-1) as function of $Re^{1/2}$. Here k_0 is taken to be $0.75 \text{ mm}^2/\text{s}$ and the Re is calculated based on the initial droplet diameter with the properties evaluated at the mean temperature (850°K). Also shown in the figure for comparison is a correlation obtained earlier [3], namely, $(k/k_0-1)=0.3 Re^{1/2}$. Clearly, at higher Re values the well-known $Re^{1/2}$ relationship seems to hold. However, for Re smaller than one the trend is not linear, and more experimental data are needed to develop a firm correlation. The upcoming experiments with the translating droplet device should provide accurate data in this region.

CONCLUDING REMARKS

The current experiments in the ground-based facilities along with the theoretical models that are under development should provide tools for the development of the test matrix for the space experiments. With the limited microgravity time, acceleration/deceleration effects as well as extinction phenomena can not be studied in the ground-based facilities. Future space experiments should help address these issues.

ACKNOWLEDGEMENTS

The authors are grateful to Sandra Olsen for providing the flow tunnel facility. The NASA engineering team (M. Brace, H. F. Kacher, D. A. Robinson, and R. J. Slutz) helped with the design and fabrication of the hardware.

REFERENCES

- [1]. Wichman, I. S., and Baum, H. R., "A solution procedure for low Reynolds number combustion problems under microgravity conditions," ASME, Heat Transfer in Microgravity, HTD-Vol. 269, 1993, pp. 111-117.
- [2]. Avedisian, C. T., and Jackson, G. S., "Soot patterns around suspended n-heptane droplet flames in a convection-free environment," J. of Propulsion and Power, Vol. 16, No.6, 2000, pp. 974-979.
- [3]. Okajima, S., and Kumagai, S., "Experimental studies on combustion of fuel droplets in flowing air under zero- and high-gravity condition," Nineteenth Symposium (International) on Combustion, The Combustion Institute, Pittsburgh, 1982, pp. 1021-1027.

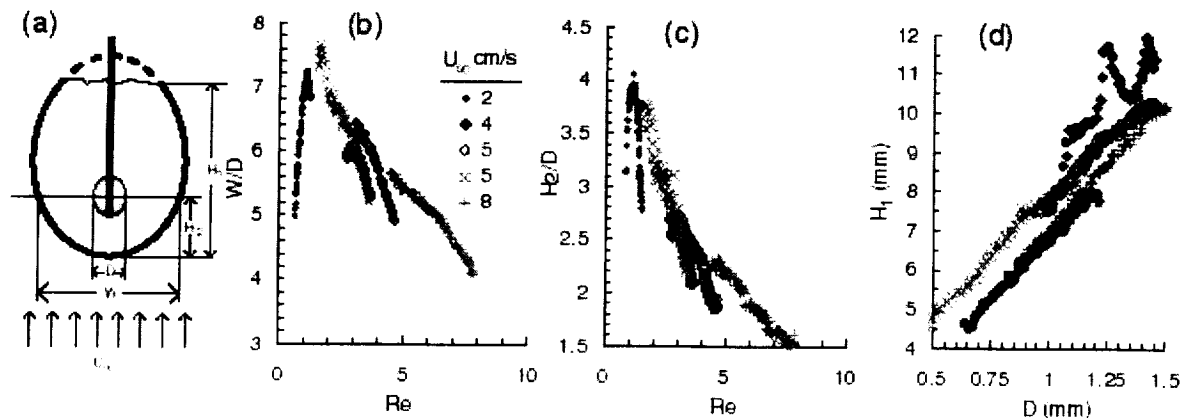


Figure 1. (a) Schematic illustration of the flame; (b) flame width, (c) upstream standoff distance, and (d) flame height variation.

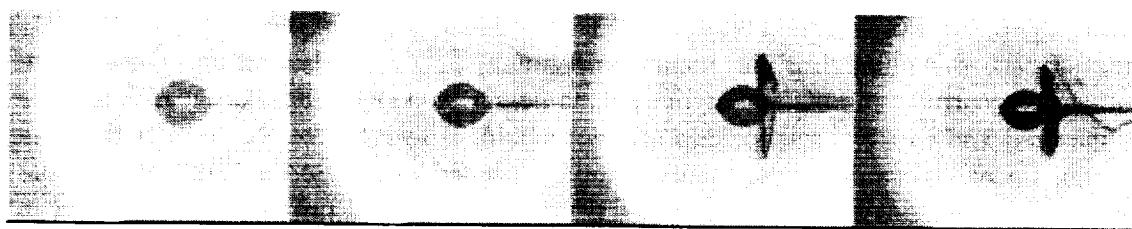


Figure 2. Soot-shell dynamics during n-heptane droplet combustion in air at atmospheric pressure with an imposed flow velocity of 3 cm/s (images are shown at 2/15 second intervals).

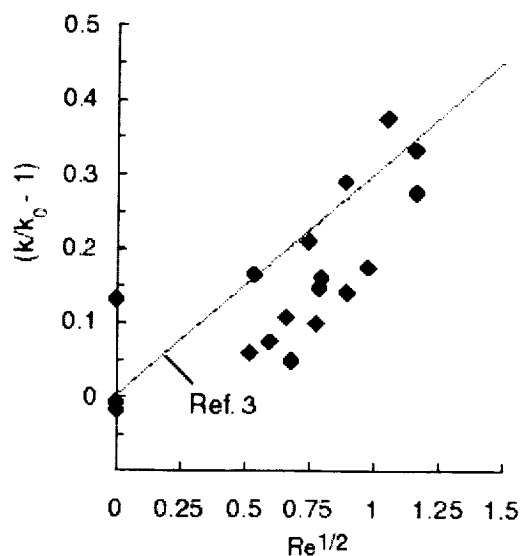


Figure 3. Heptane droplets burning in a forced flow in air at atmospheric pressure under microgravity.

CONTROL OF DROPLET COMBUSTION VIA ACOUSTICAL EXCITATION

O. I. Smith, A. R. Karagozian, C. Ghenai, R. Lobbia, and S. Dattarajan
Department of Mechanical and Aerospace Engineering, UCLA

ABSTRACT

This study focuses on quantifying and understanding the effects of external acoustical perturbations on condensed phase combustion processes. In the present configuration, a burning liquid methanol droplet is suspended within an essentially one-dimensional acoustic waveguide where standing waves of variable frequency and amplitude are generated by a loudspeaker placed at the end of the guide. Focus has been placed in normal gravity experiments on excitation conditions in which the droplet is situated at either: 1) a velocity antinode (pressure node), where the droplet experiences the greatest effects of velocity perturbations, or 2) at a velocity node (pressure antinode), where the droplet is exposed to minimal velocity fluctuations. The effects of the amplitude and frequency of excitation, the droplet position relative to pressure/velocity perturbation maxima, and conditions leading to increased burning rates are identified. Corresponding numerical simulations confirm these observations. Microgravity experiments on the acoustically excited, burning droplet are planned to take place in both NASA drop tower and parabolic flight facilities.

INTRODUCTION

This research program is designed to understand and quantify the effects of pressure oscillations on the combustion characteristics of condensed fuels under microgravity conditions. The issue of microgravity acoustic excitation of flames is especially pertinent to understanding the behavior of accidental fires which could occur in spacecraft crew quarters. The microgravity diffusion flames which could form are known to be very strongly affected by even small convective contributions [1]. Such disturbances could also be introduced by pressure and velocity perturbations within the crew quarters, e.g., as results from ventilation fans or engine vibrations.

In normal gravity, studies have shown that there can be an increase in fundamental transport processes from reactive surfaces with the imposition of an external acoustical field. These processes have been quantified for single droplet combustion to result in burning rate constants that can be significantly higher during acoustic excitation than without such excitation. Blaszczyk [2] measures up to a 14% increase in the burning rate constant K during acoustic excitation (as compared with no acoustic excitation) in the excitation frequency range 150-300 Hz and sound pressure level range 100-115 dB. Saito, et al. [3], on the other hand, find that when the fuel droplet is situated at a pressure node (corresponding to a velocity antinode), there can be as much as a two to three-fold increase in evaporative or combustion rate constants, but when the droplet is located at a pressure antinode (or velocity node), there is little appreciable change in the evaporation or combustion rates. Under reduced gravity, natural convection is no longer a dominant process, and the effect of acoustics could be even more pronounced.

CURRENT STUDIES

The normal gravity experiments conducted to date have examined single fuel droplet combustion within an essentially one-dimensional acoustic waveguide, in the absence of any mean (imposed) air flow. Microgravity experiments (in the NASA Glenn 2.2 sec drop tower) are anticipated

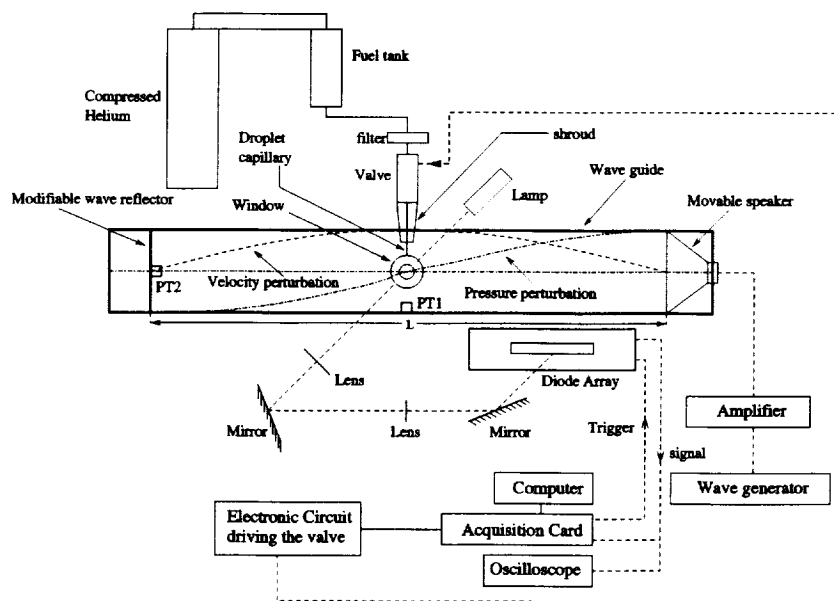


Figure 1: Schematic diagram of the acoustic waveguide with a fuel droplet situated in the center.

to take place during 2001. Standing waves are generated within the waveguide by a loudspeaker placed at one end. The speaker generates acoustic perturbations with varying frequency and amplitude via a function generator and amplifier. A detailed schematic diagram of the experimental apparatus is shown in Figure 1. The length of the acoustic waveguide is adjustable so as to maintain standing waves in the guide, depending on the applied frequency of excitation.

An unusual feature of the present experiments is that the fuel droplet here is suspended within the waveguide from a quartz capillary of approximately 0.3 mm OD, through which liquid methanol is continuously delivered during droplet combustion. Droplet diameters between 1.0 and 1.5 mm are explored in the present studies; in normal gravity the droplets are not spherical, and require correction to obtain effective burning rate constant (K) values. The methanol is metered to the capillary by a solenoid microvalve. The instantaneous fuel droplet side-to-side diameter may be determined by back-lighting the droplet and imaging the magnified droplet shadow onto a linear photodiode array. Thus, knowledge of the applied fuel volume flow rate Q_v and the instantaneous (effective) droplet diameter d may be used to determine the effective droplet burning rate constant K through application of mass continuity.

Experiments have been conducted here, with and without acoustic excitation, using two different methods of fuel delivery. In one method, the volume flow rate is maintained at a constant level, resulting in an effectively constant diameter, burning fuel droplet whose quasi-steady size depends on the fuel delivery rate. These results are described in [4]. Experiments have also been performed in which the droplet is controlled during burning at a pre-set diameter via closed loop control of fuel delivery through the microvalve; these results are described in [5]. An example of the performance of the droplet size controller is shown in Figure 2, demonstrating the ability of the controller to bring the burning droplet to the desired diameter set point within about one-half

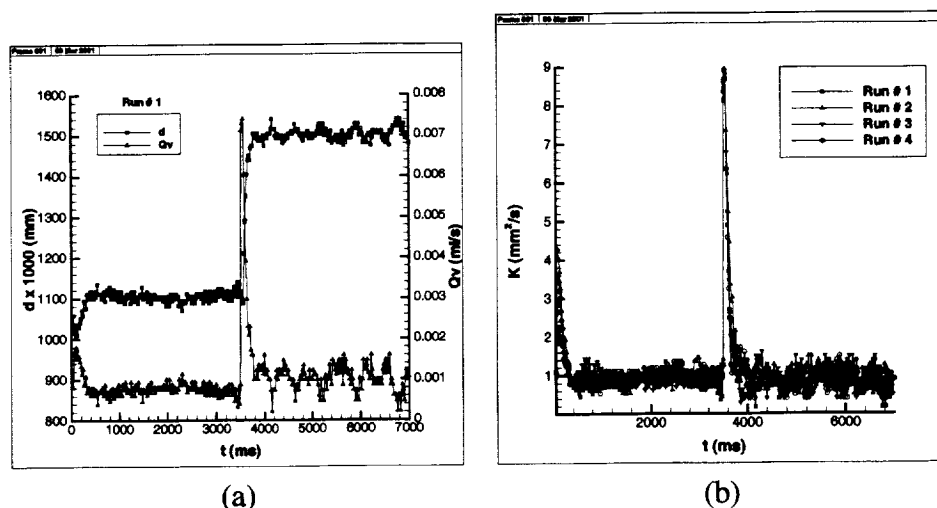


Figure 2: (a) Measured droplet diameter and fuel volume flow rate as a function of time during operation of the fuel flow controller, when the set point of the droplet diameter is abruptly changed from 1.1 mm to 1.5 mm at $t = 3.5$ sec [5]. (b) Corresponding time-dependent values of the effective burning rate constant K during this change in set point.

second. Both fuel delivery schemes yield similar results in terms of the net influence of acoustic excitation on droplet combustion processes, i.e., the average value of the burning rate constant K .

Corresponding computations are performed as well to further explore the effects of acoustic excitation on methanol droplet combustion [6]. A one-dimensional, axisymmetric representation of the essential diffusion and reaction processes occurring in the vicinity of the droplet stagnation point is used in order to isolate the effects of the imposed acoustic disturbance. The simulation is performed using a third order accurate, essentially-non-oscillatory (ENO) numerical scheme with a full methanol-air reaction mechanism [7].

The present experiments confirm the observations of Saito, et al. [3] which suggest that the effect of acoustic excitation on droplet burning rates can be substantial if the droplet is situated at a pressure node, where the velocity perturbations are large. In this instance, Figure 3a demonstrates that the average burning rate constant $\langle K \rangle$ can increase with acoustic intensity, particularly at sound pressure levels above 125 dB. At an SPL of 137 dB, the burning rate constant can be more than 20% above that for a non-forced, burning droplet. These results are qualitatively and quantitatively consistent with the corresponding computational studies of burning methanol droplets exposed to acoustic excitation [6]. In contrast, when the droplet is situated at a pressure antinode (velocity node), the negligibly small velocity perturbations cause the droplet burning rate constant to be essentially the same as that of the unforced burning droplet. These results are shown in Figure 3b. The large pressure oscillations appear to have little effect on droplet combustion characteristics, again consistent with prior observations [3, 6].

FUTURE STUDIES

Full testing of the acoustically excited, burning droplet will be conducted in both the Lewis 2.2 s drop tower (for concept testing) and in NASA low-g aircraft. Locations of the droplet's flame front and the soot shell are to be monitored by two intensified CCD cameras, and control of the

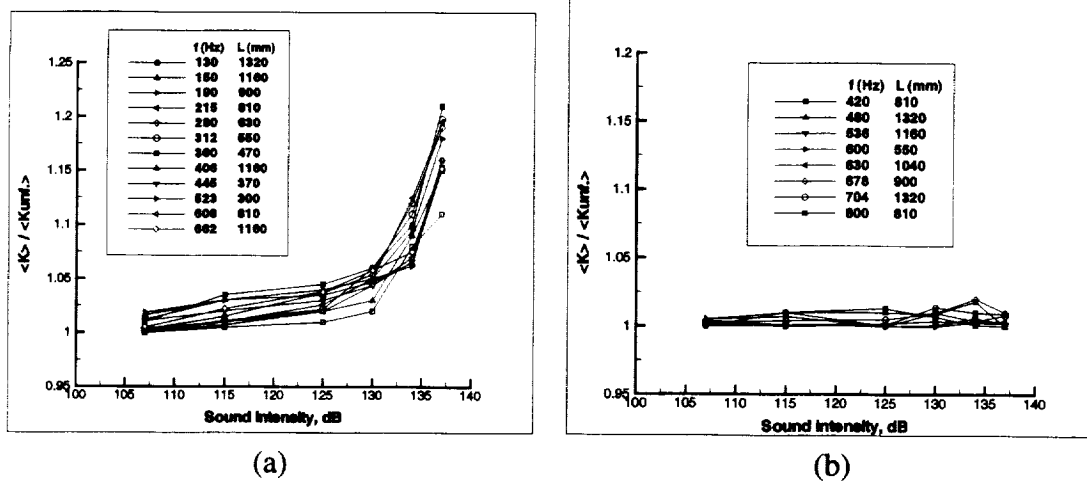


Figure 3: Effect of acoustic intensity (sound pressure level, in dB) on the droplet mean burning rate constant $\langle K \rangle$, normalized by the value of $\langle K \rangle$ in the absence of acoustic excitation. The droplet is situated at a **pressure node** in (a) and at a **pressure antinode** in (b), for various frequencies of acoustic excitation.

droplet diameter will proceed as described above for the normal gravity experiments. Alterations in the shape of the soot shell and flame (via chemiluminescence of OH) will be detected and compared for various conditions of acoustic excitation.

References

- [1] Friedman, R. and Urban, D., *NASA TM-101397*, 1989.
- [2] Blaszczyk, J., *Fuel*, 70, 1023-1025, 1991.
- [3] Saito, M., Sato, M., and Suzuki, I., *Fuel*, 73, 349, 1994.
- [4] Ghenai, C., Smith, O. I., and Karagozian, A. R., "Acoustical Excitation of Burning Fuel Droplets", AIAA Paper no. 2001-0328, 39th AIAA Aerospace Sciences Meeting, January, 2001.
- [5] Lobbia, R., Ghenai, C., Dattarajan, S., Smith, O. I., and Karagozian, A. R., "Control of Droplet Combustion via Acoustical Excitation", Paper 47, 2nd Joint Meeting of the U.S. Sections of the Combustion Institute, March, 2001.
- [6] Kim, H.-C., Karagozian, A. R., and Smith, O. I. "Numerical Simulations of Acoustically Driven, Burning Droplets", Paper 99F-50, Western States Section/The Combustion Institute Fall Meeting, October, 1999.
- [7] Marchese, A.J., Nayagam, N.V., Colantonio, R., and Dryer, F.L., *26th Symp. (Int.) on Comb.*, 1209, 1997.

Experiments and Model Development for the Investigation of Sooting and Radiation Effects in Microgravity Droplet Combustion

Mun Young Choi and Ahmet Yozgatligil
Department of Mechanical Engineering and Mechanics
Drexel University, Philadelphia, PA 19104

Frederick L. Dryer and Andrei Kazakov
Mechanical and Aerospace Engineering
Princeton University, Princeton, NJ 08544

Ritsu Dobashi
Department of Chemical Systems Engineering
University of Tokyo
Tokyo, Japan

INTRODUCTION

Today, despite efforts to develop and utilize natural gas and renewable energy sources, nearly 97% of the energy used for transportation is derived from combustion of liquid fuels, principally derived from petroleum. While society continues to rely on liquid petroleum-based fuels as a major energy source in spite of their finite supply, it is of paramount importance to maximize the efficiency and minimize the environmental impact of the devices that burn these fuels. The development of improved energy conversion systems, having higher efficiencies and lower emissions, is central to meeting both local and regional air quality standards. This development requires improvements in computational design tools for applied energy conversion systems, which in turn requires more robust sub-model components for combustion chemistry, transport, energy transport (including radiation), and pollutant emissions (soot formation and burnout). The study of isolated droplet burning as a unidimensional, time dependent model diffusion flame system facilitates extensions of these mechanisms to include fuel molecular sizes and pollutants typical of conventional and alternative liquid fuels used in the transportation sector. Because of the simplified geometry, sub-model components from the most detailed to those reduced to sizes compatible for use in multi-dimensional, time dependent applied models can be developed, compared and validated against experimental diffusion flame processes, and tested against one another.

Based on observations in microgravity experiments on droplet combustion, it appears that the formation and lingering presence of soot within the fuel-rich region of isolated droplets can modify the burning rate [Choi et al., 1990; Jackson and Avedisian, 1994], flame structure and extinction [Nayagam et al., 1998; Marchese et al., 1999], soot aerosol properties [Manzello and Choi, 2001], and the effective thermophysical properties [Choi et al., 1990; Jackson and Avedisian, 1994]. These observations led to the belief that "perhaps one of the most important outstanding contributions of microgravity droplet combustion is the observation that in the absence of asymmetrical forced and natural convection, a soot shell is formed between the droplet surface and the flame, exerting an influence on the droplet combustion response far greater than previously recognized" [Law and Faeth, 1994]. The effects of soot on droplet burning parameters, including burning rate, soot shell dynamics, flame structure, and extinction

phenomena provide significant testing parameters for studying the structure and coupling of soot models with other sub-model components.

OBJECTIVES OF STUDY

Microgravity droplet combustion is an ideal platform for advancing the understanding of diffusion flames of liquid hydrocarbon fuels and additives that are typically used in internal combustion engines and gas turbines. The burning of an isolated droplet is a robust problem that involves coupling of chemical reactions, multi-phase flow (liquid, gas, particulate) with phase change. The observations in previous microgravity investigations strongly suggest that a thorough interpretation of droplet burning behavior cannot be accomplished without examining and incorporating the influences of sooting and radiation. Experimental measurements will provide a robust test of the important interactions with burning rate, flame structure, flame extinction, and aerosol properties.

The development of detailed numerical modeling of spherically-symmetric droplet combustion provides opportunities to test and validate the chemical kinetic, transport, sooting, and radiation mechanisms for a realistic fuels under a variety of conditions that are unattainable by means other than those provided by microgravity. Improved mechanisms, especially the coupled gas-phase chemical kinetic and soot formation mechanisms for both n-heptane and ethanol fuels, are needed to integrate the influence of sooting in n-heptane combustion and to reconcile the recent discovery that ethanol flames produce significant soot under high pressures. Refinements of these models through comparison against well-characterized experiments performed in microgravity (for a wide range of residence times unattainable through any other geometrical configurations) can yield new and important understanding.

EXPERIMENT DESCRIPTION

The proposed experiments will consider two fuels: n-heptane, and ethanol. N-heptane is the simplest of liquid alkanes with properties similar to those found for conventional liquid fuels

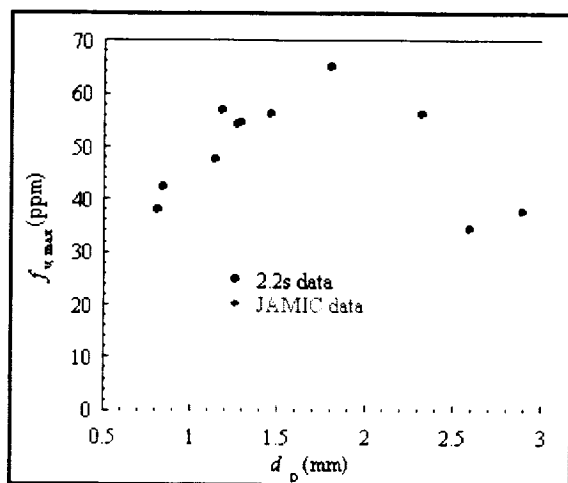


Figure 1

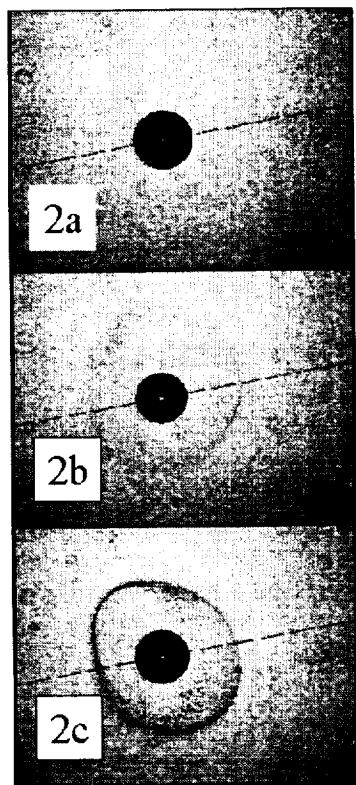
combustion studies and model validation that can ultimately lead to better understanding of practical liquid fuel combustion phenomena.

such as gasoline and distillates. Understanding of liquid ethanol combustion processes also has significant practical and fundamental implications. In recent years, the use of ethanol as a fuel additive has been stimulated by the Clean Air Act Amendments of 1990 [Vanderver, 1992] that require utilization of reformulated and oxygenated gasoline to reduce carbon monoxide and volatile organic compound emissions. With the phaseout of MTBE, ethanol remains one of the most favorable oxygenated additives. From the fundamental point of view, gas-phase oxidation chemistry for ethanol and n-heptane have been extensively studied. These factors make both valuable targets for fundamental droplet

In these experiments, soot volume fraction will be measured using full-field light extinction at 635 nm. In this method, line of sight extinction measurements are deconvoluted using tomographic inversion [Dasch, 1992]. Soot temperature will be measured using line of sight flame emission data at two separate wavelengths (700 nm and 900 nm) with subsequent tomographic inversion. The ratio of the spectral emission intensity at each radial position will then be used for the application of two-wavelength pyrometry. This technique is similar to that used successfully in Laminar Soot Processes (LSP) Shuttle experiments. As in the LSP experiments, it is expected that due to the small soot particle sizes, the difference between the gas-temperature and the soot temperature will be small. Radiation from the flame will be measured using a broadband radiometer (detection spectrum ranging from 0.5 to 5 microns). Soot agglomerates will be sampled using a thermophoretic technique and analyzed using transmission electron microscopy. Ultraviolet emission due to hydroxyl radical chemiluminescence (and the interference from soot emission) occurring within the flame will be imaged using a Xybion intensified array CCD camera with a narrowband filter with central wavelength of 310 nm and a FWHM of 10 nm. This approach yields the instantaneous location of maximum OH* emission which, in conjunction with detailed numerical modeling, will be used to define the transient flame structure.

RECENT PROGRESS

Soot volume fraction and radiative emission measurements for large droplet experiments



were performed at the JAMIC 10 sec facility in Hokkaido, Japan. The maximum soot volume fraction, f_{vmax} values measured for the 2.6 mm and 2.9 mm initial droplet diameter experiments are plotted in **Figure 1** along with previous measurements for smaller droplets [Lee *et al.* 1998]. The maximum soot volume fractions for the larger droplets exhibit a significant departure from the linear increase as a function of d_0 as it might be inferred from the small droplet experiments. The measured maximum soot volume fractions for the larger droplets are nearly 40% smaller than the values obtained at $d_0 = 1.8$ mm. This reduction in sooting is expected to have strong implications on many aspects of the burning process. It is believed that increases in initial droplet diameter will produce radiative losses (due to both soot and non-luminous component) that will reduce the temperatures to below threshold temperatures required for additional soot formation. Results were presented and published in the 28th *Symposium on Combustion* [Manzello *et al.*, 2001].

Characterization of soot morphological properties including the primary particle size, d_p , radius of gyration, R_g , fractal dimension, D_f , and mass fractal prefactor term, k_f are important for the analysis of soot processes including particle growth, soot agglomeration and oxidation processes. Measurements of primary particle size and fractal dimensions for soot sampled in n-hexane droplet flames burning in microgravity flames are shown in Table I.

Table I			
	d_p (nm)	D_f	k_f
Normal-Gravity Soot	25.9	1.61	6.6
μ g Soot at 0.5 sec	45.8	1.63	7.8

The increase in the primary particle dimensions with residence time is dramatic. The average primary particle size increased from 25.9 nm for soot collected in normal gravity to 45.8 nm for soot collected at 0.5s after ignition in microgravity. In the present experiments, the average k_f increased from 6.6 in normal gravity to 7.8 for the 0.5s microgravity experiment. D_f was nearly constant for normal-gravity and microgravity soot. Detailed results will appear in *the Int'l Journal of Heat and Mass Transfer* [Manzello and Choi, 2001].

As mentioned previously, ethanol has displayed unusual sooting characteristics that has not received much attention in the literature. As an oxygenate, ethanol is known to be essentially a non-sooting fuel at atmospheric pressures. At elevated pressures (starting from as low as 1.5 to 2 atm of air), however, an ethanol droplet flame has been shown to form soot [Yap, 1986]. High-pressure microgravity experiments using ethanol were performed at the JAMIC 10 sec. drop tower facilities. **Figure 2a** displays the back-lit view of an ethanol droplet burning in air at 1.8 atm. In **Figure 2b**, the pressure was increased to 2 atm and the oxygen concentration in nitrogen was increased to 0.25 mole fraction. The presence of the sootshell is clearly evident. In **Figure 2c**, the oxygen concentration was increased to 0.31 mole fraction while the pressure was maintained at 2 atm. The sootshell is more opaque (corresponding to higher soot concentration) and the luminosity of the flame was markedly brighter.

REFERENCES

1. Choi, M.Y., Dryer, F.L. and Haggard, Jr., J.B. *Proceedings of the Combustion Institute*, 23: 1597-1604, 1990.
2. Dasch, C.J., *Applied Optics*, 31:1146, 1992.
3. Faeth, G.M., *Prog. Energy and Comb. Sci.*, 3:191, 1977.
4. Jackson, G.S. and Avedisian, C.T. *Proc. R. Soc. Lond. A*. 446, 255-276, 1994
5. Law, C.K., *Prog. Energy Combust. Sci.*, 8:171, 1982.
6. Law, C.K. and Faeth, G.M., *Prog. Energy Combust. Sci.*, 20:65, 1994.
7. Lee, K.O., Manzello, S.L. and Choi, M.Y. *Combustion Sci. Tech.* 132, 139-156, 1998
8. Manzello, S.L. and Choi, M.Y., *Int'l Journal of Heat and Mass Transfer*, in press, 2001
9. Manzello, S.L., Choi, M.Y., Kazakov, A., Dryer, F.L., Dobashi, R., and Hirano, T., *Proc. Combust. Inst.* in press, 2001.
10. Marchese, A.J., Dryer, F.L. and Nayagam, V. *Combustion and Flame* 116, 432-459, 1999.
11. Nayagam, V., Haggard, J.B., Colantonio, R., Marchese, A.J., Zhang, B.L., and Williams, F.A. *AIAA Journal* 26, 1369-1378, 1998.
12. Vanderver T.A., Ed. *Clean Air Law and Regulation*. The Bureau of National Affairs, Washington, D.C., 1992.
13. Yap, L.T., Ph.D. Dissertation, Princeton University, MAE Department, 1986.

Acknowledgments: The authors wish to thank Dr. Paul Ferkul, project scientist, for helpful comments and suggestions. This work is supported by NASA through Grant NCC3-822. Support from JSUP (Mr. T. Sakuraya) and assistance in experiments from the JAMIC staff (Dr. M. Yamaoka, Director), Dr. S.L. Manzello (NIST), and Dr. K.O. Lee (Argonne) are gratefully acknowledged.

Combustion of Sooting Mixture Droplets at Low Gravity

C.T. Avedisian and J.H. Bae

Sibley School of Mechanical and Aerospace Engineering
Cornell University
Ithaca, New York 14853-7501

Introduction

This presentation concerns fuel droplets of miscible mixtures in which one of the components is heavily sooting. Low gravity is used to reduce the effects of convection and to make the burning process more spherically symmetric. It builds on prior experimental studies of mixture droplets performed in microgravity for both miscible and immiscible mixtures (Ahron and Shaw 1998; Okai et al. 1998; Dietrich et al. 1996; Jackson et al. 1991; Jackson and Avedisian 1998;). The results of such studies are the necessary validation tool for complex models of miscible and immiscible mixture effects for spherically symmetric burning processes that include detailed chemistry (e.g., Marchese et al. 1999; Jackson and Avedisian 1996). The following aspects are being studied: influence of initial droplet diameter on burning rate; soot shell development and the influence of a nonsooting miscible additive; and the effect of gravity on flame and soot shell structure.

Mixtures of nonane and hexanol are reported in this presentation. Concentrations included pure nonane and hexanol, and mixture concentrations of 10%, 25%, 40%, 60%, 80% by volume. These two hydrocarbons have some characteristics that make them ideal for study: they have almost identical boiling points; hexanol does not have a strong propensity for water vapor absorption; hexanol produces less soot than nonane so that mixtures of nonane and hexanol should show an effect of composition on soot formation; and thermophysical properties are readily calculated

Experiment

While we have done extensive testing on free droplets, in this particular effort we developed a fiber-supported design. It is similar to that of Lebedev and Marchenko (1979) and Dietrich and Haggard (1992). Two fibers are crossed at about 17° and a test droplet is mounted at the cross to prevent the droplet from sliding. Fiber supported D^2 progressions of nonane were found to be in excellent agreement with free droplets of nonane of the same initial diameter using the identical means of ignition, spark energy and duration. The D^2 history was measured for almost the entire burning and the evolution of soot shell diameter was recorded for the central 50% of the burning for reasons discussed later. Even for the very small fiber diameters we used, some soot was found on the fiber. For very large fibers, the fiber has a strong influence on the dynamics of soot shell development.

A drop tower equipped with a drag shield was used to create low gravity. The drag shield kept natural convection levels low enough so that the flames of the larger droplets remained reasonably spherical throughout. The total experimental time was 1.2s and the gravity (g_0) in the moving frame of reference was on the order of $10^{-4}g_0$ of Earth's normal gravity (g_0). Droplets were deposited on the fibers as described previously (Avedisian and Callahan 2000). Droplets were ignited 320ms after low gravity began by two sparks from four electrodes placed on opposite sides of the droplet to promote spherical symmetry. The spark duration ranged from 0.5ms to 0.75ms. Power to the tiny solenoids (home-built) was maintained for the duration of an experiment. Once ignited, the electrodes were rapidly retracted. Precise positioning of the electrodes after each experiment ensured repeatable D^2 progressions.

A LOCAM II 16mm movie camera operated at framing rates ranging from 10 frames/s to 200 frames/s recorded the droplet burning history. The camera was fitted with an Olympus 90mm Zuiko lens and extension bellows. Backlight was provided by one halogen lamp. This arrangement provided images with excellent clarity and sharpness for diameter measurements. Black and white, and color film was used. The 16mm color film proved effective to record the flame structure. A second camera (color CCD) was used to record the flame images to provide semi-quantitative measurement of the outer luminous zone diameter. The CCD image clarity was reduced from the 16mm color images. Individual movie frames were digitized by a Microtek scanner at 3900 dpi then imported into Image Pro-Plus 4.0 by Media Cybernetics. With Image Pro the area averaged droplet and soot shell diameters were obtained.

Results

Evolution of Droplet Diameter

The burning history of the nonane/hexanol mixtures showed a distinctly nonlinear process with the burning rate increasing with time. Figure 1 shows the evolution of burning rate for droplets that had essentially the same initial diameter (between 0.4mm to 0.5mm). The burning rates were calculated from the first derivative of each smoothed variation of $(D/D_0)^2$ with t/D_0^2 , which was then fitted by a logarithmic function. The two heavy lines are the bounds of

nonane and hexanol and the concentrations fall between these lines. As is evident, a single burning rate value does not describe the burning process. We believe that the increasing burning rate is due to a combination of droplet heating, even for the rather small droplet diameters examined, and soot formation.

Concerning droplet heating, we used an approach developed by Shaw and Williams (1990) to estimate its contribution. For properties typical of hexanol and nonane we found that droplet heating is a viable mechanism for nonlinear burning, even for the small D_0 values studied. Soot formation can also produce the curvature shown in figure 1. It has been previously shown that for small droplets, D_0 influences soot formation (Jackson et al. 1992; Jackson and Avedisian 1994, 1996) in that 'large' droplets produce proportionally more soot than 'small' droplets as originally inferred from photographs, and later from laser measurements (Lee et al. 1998). This trend holds as long as the droplet is not 'too' large that flame radiation is significant, which can then lower the flame temperature to where soot would not form during droplet burning (Dietrich et al. 1996). Increased soot formation translates into lower heat release at the flame, reduced heat transfer to the droplet and therefore a lower burning rate. The discovery of a D_0 influence on burning when convection is absent was made for burning processes on heptane that showed linear D^2 progressions to within the resolution of the experimental method. For the data of figure 1, D_0 is essentially constant. However, the continually changing droplet diameter could produce an influence of sooting that is similar to the effect of changing D_0 for a linear burning process. As the droplet then burns and becomes smaller, the residence time of fuel molecules which scales with D^2 (Jackson et al. 1992) decreases, less soot would form, and the droplet burns faster and the burning rate increases. This trend is shown in figure 1.

Even for hexanol nonlinear burning was observed (figure 1). This result is consistent with the above argument about soot because hexanol also produces soot. We illustrate this in figure 2, which shows a burning hexanol droplet at both low (a) and normal (b) gravity 0.16s and 0.2s after ignition, respectively. No backlighting was used and the droplet is not visible because of the low light intensity. The two white circular regions inside the flame are due to the fiber glow. Soot is not evident in figure 2a. We also recorded the burning process at normal gravity to promote soot visibility by aggregate transport into the wake and their subsequent oxidation. Figure 2b shows a typical flame structure. The plume in the wake reveals soot oxidation, which shows as 'yellow' in color (this image is reproduced in monochrome and soot shows up as the 'white' region of the wake plume in figure 2b). The yellow color is a marker for soot in diffusion flames (Glassman 1987). At low gravity, the soot shell is essentially encased by the flame and the aggregates are not oxidized unless they break free of the shell and are transported to the flame. Soot oxidation then shows up as white 'specks' in the (for black and white) photographic images. For comparison purposes, figures 3a and 3b show selected back-lighted pictures of burning nonane droplets at low and normal gravity, respectively ($D_0 \approx 0.74\text{mm}$). The intense backlighting clearly shows the droplet. A closed soot shell is visible in figure 3a. At normal gravity soot aggregates are transported into the flame in figure 3b by the strong natural convection and oxidize to produce the white plume shown. Between the two extremes of gravity shown in figure 3a and 3b, a soot shell must transition from closed and spherical to open and long following the wake flame.

Influence of Initial Droplet Diameter and Gravity

The motivation for performing experiments at normal gravity was to promote the visibility of soot by transport of aggregates to the flame and their subsequent oxidation and influence on the flame color. The photographic documentation of this process was analyzed to measure the evolution of droplet diameter. Figure 4 compares the normal and low gravity evolution of droplet diameter for nonane. Essentially two D_0 values were examined: nominal values of 0.73mm and 0.52mm. Several interesting points to note are the following.

The normal gravity burning process is faster than low gravity, which is expected because of the larger natural convection (higher Rayleigh number) at normal than low gravity; at normal gravity. Burning is nonlinear which can be due to the influences discussed previously. At normal gravity burning shows no influence of initial droplet diameter, at least the effect of D_0 is not measurable for the conditions of the present experiments. At low gravity there is a clear segregation of the burning patterns over the same range of D_0 which is most likely due to soot formation as discussed previously in connection with figure 1 and larger droplets burn slower than small droplets.

Luminous Zone Diameter and Soot Shell

The flame (luminous zone) diameter is defined by the position of peak flame temperature. Since our 'diagnostic' was emulsion film, we measured the outer luminous zone diameter for nonane/hexanol mixture droplets. Figure 5 shows the flame diameter normalized in the standard way as guided by the D^2 law for several mixture compositions. The repeatability of the measurements is good. The differences in initial diameter are not large enough to have an effect on soot formation (Jackson and Avedisian 1992, 1994). For quasi-steady burning, D_f/D should be constant. This is not the case at any time for the mixtures examined. Rather, the flame position continuously increases with time and the flame position moves progressively farther from the droplet (though becomes physically smaller) as burning proceeds. Flame contraction is not shown in figure 5. This is due to the similar volatilities and boiling points

of nonane and hexanol.

The soot shell diameter is shown in figure 6 for a 10% mixture for $D_0 \approx 0.53\text{mm}$. This is the highest hexanol loading where a shell could be seen in the films. The results are presented on the same coordinates as figure 5. The inset shows the same data on expanded coordinates. Only a limited portion of the burning history is indicated. This is the region where we were satisfied with measurement accuracy. The trends are consistent with those of pure components (Jackson and Avedisian 1994). Early in burning there is a delay time for soot formation and the shell cannot be seen. Later in burning after the shell has developed, any small disturbance in the surrounding gas causes the larger soot aggregates to break free and drift away, and measurements cannot be made. The shell diameter tracks with the flame position, qualitatively.

Droplet Levitation

We recently examined acoustic levitation to position a droplet in microgravity as an alternative to other free droplet methods (Avedisian (2000) reviews free droplet methods). The idea is to place the droplet in a pressure node of an acoustic levitator then turn off the levitator in low gravity and examine motion of the droplet. We mounted an acoustic levitator in a drop tower (with no drag shield) producing $g \approx 10^{-2}g_0$. In low gravity we then imposed linear and exponential voltage decay profiles on the levitator. The final levitator field strength expressed in terms of voltage (18V is full strength) was varied from zero (complete shut-off) to various minimum values. When the voltage was reduced to zero over the less than 1s ramp-down range examined, in all cases the droplet moved away from the pressure node. At low gravity the minimum voltage for levitation was about 2V while at normal gravity it was about 6V. The difference is due to the reduced weight of the droplet in low gravity.

Conclusions

The results show the very strong influence that soot formation can have on the droplet burning process when convection levels are low enough to produce spherical flames. For the initial droplet diameters examined (in the range of 0.4mm to 0.8mm) the influence includes nonlinear D^2 progressions and burning rates that increase with time. At normal gravity (in the presence of strong natural convection) the burning process was independent of D_0 for the range examined though burning was still nonlinear. Experiments are continuing on additional mixtures and more practical fuels such as various grades of Jet fuel and burning under high pressure conditions.

Acknowledgments

The authors are pleased to thank the following: Dr. Daniel Dietrich of NASA for supplying the fibers and monitoring the project; B.J. Callahan and N. Bishai for their help with the experimental work; Dr. Eugene Trinh of NASA for his valuable help with droplet levitation; and Prof. Fran McLeod for many conversations throughout.

References

- Aharon, I. and Shaw, B.D. Comb. Flame. 113, 507-518 (1998).
- Avedisian, C.T. AIAA J. Propulsion and Power, 16, 628-635 (2000).
- Avedisian, C.T. and Callahan, B.J. Proc. Comb. Inst., 28, in press (2001).
- Dietrich, D.L., and Haggard, J.B., Jr. NASA Conference Publication 10113, 317 (1992).
- Dietrich, D.L., Haggard, J.B., Jr., Dryer, F.L., Nayagam, V., Shaw, B.D., and Williams, F.A. Proc. Combust. Inst. 26: 1201-1207 (1996).
- Glassman, I. Combustion, San Diego, CA: Academic Press, (1987).
- Jackson, G.S., Avedisian, C.T., and Yang, J.C. Proc. Roy. Soc. London, A435, 359-68 (1991).
- Jackson, G.S., Avedisian, C.T., and Yang, J.C. Int. J. Heat Mass Trans. 35, 2017-2033 (1992).
- Jackson, G.S. and Avedisian, C.T. Proc. Roy. Soc. London, A446, 257-278 (1994).
- Jackson, G.S. and Avedisian, C.T. Comb. Sci. Tech. 115, 125-149 (1996).
- Jackson, G.S., and Avedisian, C.T. Int. J. Heat Mass Trans., 41, 2503-2515 (1998).
- Lebedev, O.N. and Marchenko, V.N. Heat Transf-Soviet Res. 11, 92-98 (1979).
- Lee, K.O., Manzello, S.L. and Choi, M.Y. Comb. Sci. Tech. 132, 139-156 (1998).
- Marchese, A.J., Dryer, F.L. and Nayagam, V. Comb. Flame, 116, 432-459 (1999).
- Okai, K., Tsue, M., Kono, M., Mikami, M., Sato, J. Dietrich, D.L. and Williams, F.A. Proc. Combust. Inst. 27, 2651-2657 (1998).
- Shaw, B.D. and Williams, F.A. Int. J. Heat Mass. Transf. 33, 301-317 (1990).

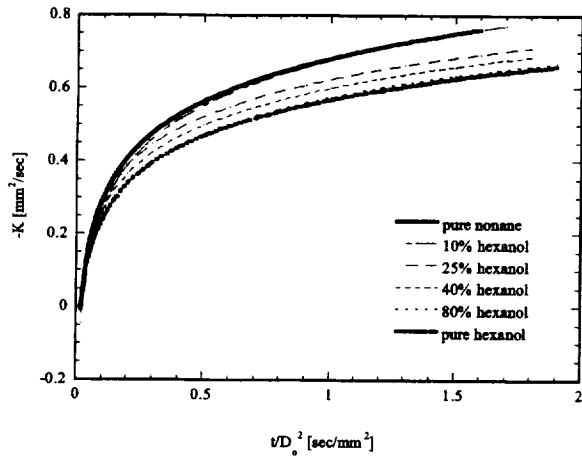


Figure 1 – Burning rate vs. scaled time in low gravity

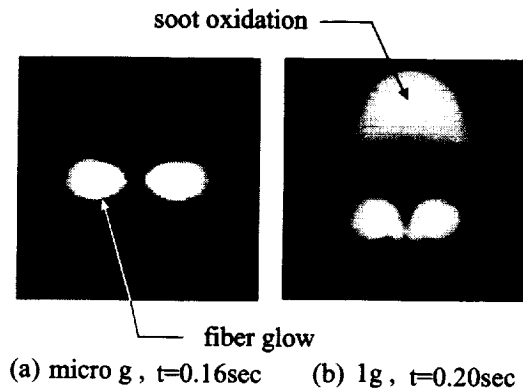


Figure 2 – Flame/soot structure for hexanol, $D_0 \approx 0.8\text{mm}$ (no backlighting)

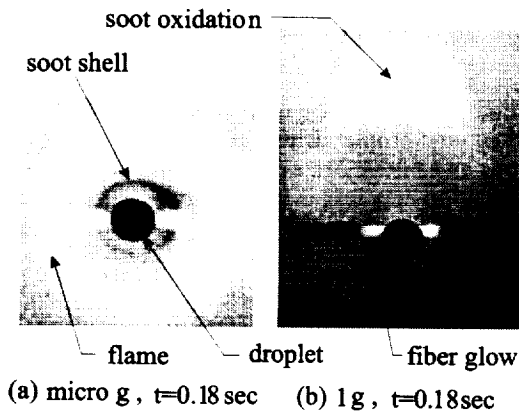


Figure 3 – Flame/soot structure for nonane, $D_0 \approx 0.74\text{mm}$ (backlighting photographs)

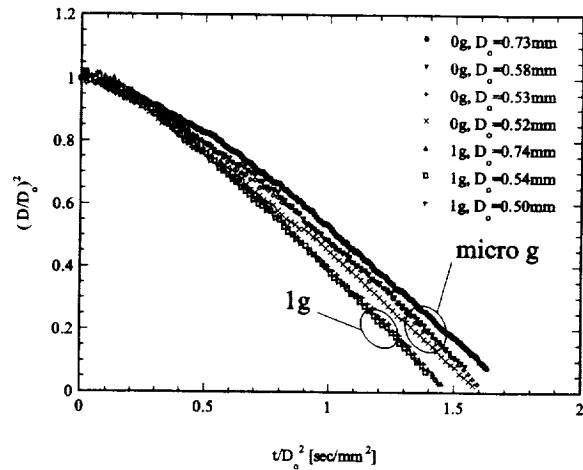


Figure 4 – D^2 profiles for nonane at 1g and micro g

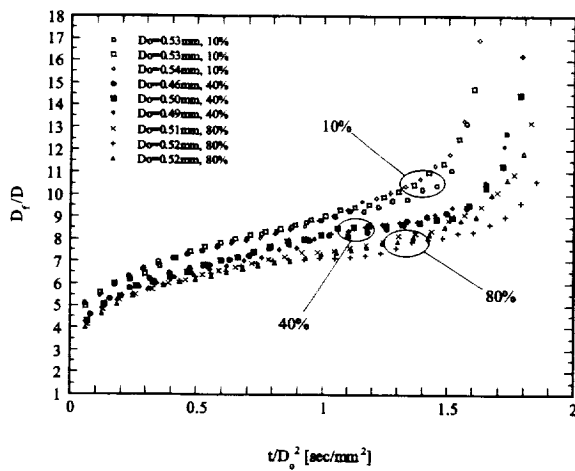


Figure 5 – Flame standoff ratio for the mixture of nonane/hexanol at low gravity

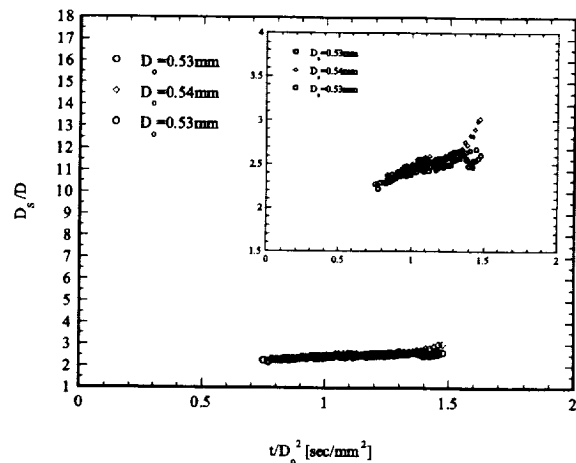


Figure 6 – Soot shell standoff ratio for 10% hexanol at low gravity

BI-COMPONENT DROPLET COMBUSTION IN REDUCED GRAVITY

B. D. Shaw, MAE Department, University of California, Davis, CA 95616

INTRODUCTION

This research deals with reduced-gravity combustion of bi-component droplets initially in the mm size range or larger. The primary objectives of the research are to study the effects of droplet internal flows, thermal and solutal Marangoni stresses, and species volatility differences on liquid species transport and overall combustion phenomena (e.g., gas-phase unsteadiness, burning rates, sooting, radiation, and extinction). The research program utilizes a reduced-gravity environment so that buoyancy effects are rendered negligible. Use of large droplets also facilitates visualization of droplet internal flows, which is important for this research.

In the experiments, droplets composed of low- and high-volatility species are burned. The low-volatility components are initially present in small amounts. As combustion of a droplet proceeds, the liquid surface mass fraction of the low-volatility component will increase with time, resulting in a sudden and temporary decrease in droplet burning rates as the droplet rapidly heats to temperatures close to the boiling point of the low-volatility component. This decrease in burning rates causes a sudden and temporary contraction of the flame. The decrease in burning rates and the flame contraction can be observed experimentally. Measurements of burning rates as well as the onset time for flame contraction allow effective liquid-phase species diffusivities to be calculated, e.g., using asymptotic theory [1]. It is planned that droplet internal flows will be visualized in future flight and ground-based experiments. In this way, effective liquid species diffusivities can be related to droplet internal flow characteristics.

This program is a continuation of extensive ground based experimental and theoretical research on bi-component droplet combustion that has been ongoing for several years. The focal point of this program is a flight experiment (Bi-Component Droplet Combustion Experiment, BCDCE). This flight experiment is under development. However, supporting studies have been performed. Because of space limitations, only some of the research performed over the last two years (since the 5th Microgravity Combustion Workshop) is summarized here (see below).

PROPANOL-GLYCEROL DROPLET COMBUSTION

In this research, reduced gravity experiments on combustion of propanol-glycerol mixture droplets were performed. Propanol-glycerol mixture droplets are of interest here because they are candidates for displaying Marangoni flows as a result of solutal capillary stresses. Droplets were initially in the mm size range with initial glycerol mass fractions of 0, 0.05 and 0.2. All experiments were in O_2/N_2 ambients at standard temperature and pressure. The ambient O_2 mole fraction was 0.21 (air) or 0.5. Use was made of a NASA-supplied drop rig, and the experiments were performed at the NASA Glenn Research Center 2.2 s Drop Tower.

In the experiments, droplets initially about 1 mm in diameter were deployed onto silicon-carbide support fibers (about 12 μm in diameter). The droplets were ignited via a hot-wire ignition system, and droplets and flames were imaged using onboard video cameras. Droplet and flame size data were obtained from the video records using digital image processing routines. The experiments showed clear indications of flame contraction. Representative data on flame and droplet size variations are shown in Fig. 1 (the discrete data points). Also shown are computational results for droplet size variations with time (the thick line).

For analysis of the data, a computational model was developed to predict the transient buildup of glycerol at the surface of a droplet. This model assumed the gas phase was quasi-

steady, which was apparently the case in the experiments since flame-to-droplet diameter ratios were nearly constant after ignition. The model allowed for variable transport properties in the liquid phase. In addition, spherical symmetry was assumed in both the liquid and gas phases. In employing this numerical model, the gas-phase thermal conductivities and liquid species diffusivities were varied so that the computational results on burning rates and onset times for flame contraction matched the experimental results closely. This allowed effective species diffusivities to be estimated. The numerical model, which was based on an explicit finite difference scheme, employed nonuniform gridding to allow fine resolution near the droplet surface. This provided substantial decreases in computation time while still maintaining accuracy. A schematic of the nonuniform gridding is shown in Fig. 2. For clarity, all grid points are not shown in this figure.

Comparison of the experiments with the numerical model, as well as with an asymptotic model [1], suggests that convective mixing was present in the droplets. The liquid species diffusivities in the numerical model needed to be increased by as much as an order-of-magnitude in order to match the experimental results. For example, liquid species diffusivities were increased by about a factor of four for the data in Fig. 1. In an actual droplet, increases in effective diffusivities are generally caused by liquid convection. Because of the large differences in surface tension between glycerol and propanol, such convection was likely the result of solutalcapillary instabilities. In addition, the experiments exhibited extinction after flame contraction, which was unexpected for droplets in this size range. Details on this research are available in Ref. [2].

NUMERICAL MODELING OF FIBER-SUPPORTED DROPLETS

Support fibers are commonly employed in microgravity droplet evaporation and combustion studies, and it is of interest to develop models of fiber-supported droplets. In this research, a numerical study of the Marangoni forces on a droplet supported by a fiber has been carried out for an evaporating methanol droplet in both dry air and humid air environments, with the focus being the development of instabilities that form early in the lifetime of a droplet. This modeling employed a finite-volume technique. A schematic of the fiber-supported droplet geometry considered here is shown in Fig. 3. The initial droplet-to-fiber diameter ratio was twenty for all cases considered.

The thermal Marangoni effect has a stabilizing effect, and it always drives the droplet surface toward an isothermal condition. The solutal Marangoni effect (from water absorption) is much larger in magnitude, and it tends to concentrate water on the surface. This tendency to concentrate water leads to surface waves and instabilities, which are relieved by diffusion of the water into the droplet interior. For 0.5 mm radius droplets (as measured from the fiber edge) the surface forces have generated liquid Reynolds numbers greater than one hundred. Figure 4 shows an instantaneous velocity field in a large droplet (the maximum velocity in Fig. 4 is about 20 cm/s). Also shown are water mass fraction profiles (y). At this instant in time, there are several vortices present in the droplet. These vortices are a result of the solutal Marangoni stresses.

Smaller droplets (initial radii of 0.005 mm) give qualitatively similar results, however the Reynolds numbers are reduced by size and diffusion damping influences. The numerical simulations are sensitive to droplet and supporting fiber size, and it appears that experimental verification and comprehensive numerical studies should be fully three-dimensional. It also appears that the solutal Marangoni flows are unstable to very small wavelengths, as suggested by previous linearized stability analyses [3]. Details on this research are available in Ref. [4].

MEASUREMENTS OF TRANSIENT DROPLET COMPOSITIONS VIA FIBER-OPTIC ABSORPTION SPECTROSCOPY

Experiments were performed to determine the time-dependent compositions of fiber-supported droplets initially in the mm size range. These experiments were performed to investigate mixing levels in bi-component droplets that are likely to have flows driven by solutalcapillary stresses. Droplets initially about 1 mm in diameter and composed of mixtures of methanol and acetone, or propanol and acetone, were investigated. Acetone was selected because its optical properties (i.e., absorption characteristics in the UV) are well characterized, while methanol and propanol are essentially transparent at a wavelength of about 270 nm, which is the peak wavelength in the spectral region where acetone absorbs strongly in the presence of polar liquids. The droplets evaporated in room air under normal gravity. The experiments employed thin optical fibers to carry light from a UV-Vis light source into and out of a droplet (Fig. 5). The time-dependent UV absorption spectrum of the liquid between the fibers was measured using a spectrometer coupled to one of the fibers, yielding the local transient acetone concentration.

Analysis of the experimental results [5] indicated that the droplets were well mixed while evaporating. This is likely a result of solutalcapillary flows that may have been induced as a result of water absorption into the droplets (the droplets evaporated in humid air). In addition, the data indicate that the more volatile component was preferentially evaporated. These trends are expected based on the relative vapor pressures of the components. Representative data are shown in Fig. 6 for a propanol-acetone droplet, where it is evident that the acetone concentration in the liquid decreased with time. Details on this research are available in Ref. [5].

FUTURE PLANS

Future ground-based research will include more drop tower experiments on reduced-gravity combustion of bi-component droplets initially about 0.8 - 1 mm in diameter. It is planned that these experiments will eventually employ flow-visualization so that droplet interior flowfields can be imaged during combustion. Experiments at UC Davis will include measuring local droplet interior compositions using absorption spectroscopy under conditions where Marangoni flows are both dominant as well as subdominant. A goal of these experiments is to provide data on mixing rates and liquid species fluctuations within droplets. Theoretical and computational studies will include development of a 3-d numerical model of fiber-supported droplet combustion, as well as further development of theory to predict effects of solutalcapillary stresses on droplet interior flows. Development of the BCDCE flight experiment will also continue.

ACKNOWLEDGEMENTS

The financial support of NASA is gratefully acknowledged. Dr. D. Dietrich is acknowledged for providing project supervision and technical support.

REFERENCES

1. Aharon, I. and Shaw, B. D., Combustion and Flame 113, 507 (1998).
2. Dee, V., and Shaw, B. D., AIAA paper 2001-0468.
3. Aharon, I., and Shaw, B. D., Physics of Fluids 8: 1820 (1996).
4. Dwyer, H. A., and Shaw, B. D., Combustion Science and Technology (in press).
5. Xiao, J. S., Wei, J. B., and Shaw, B. D., paper 43 presented at the 2nd Joint Meeting of the US Sections of the Combustion Institute, Oakland, CA (2001).

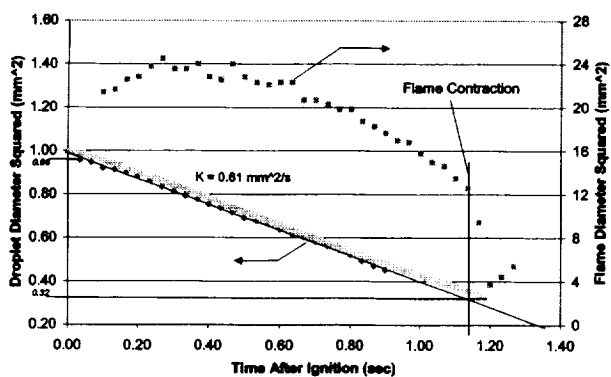


Figure 1. Propanol-glycerol droplet combustion data.

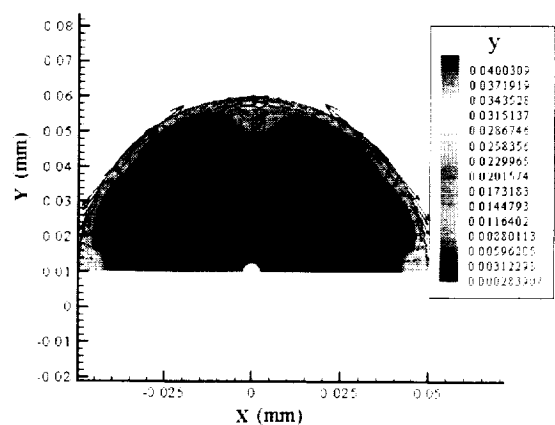


Figure 4. Water mass fraction (y) contours and velocity vectors (cm/s).

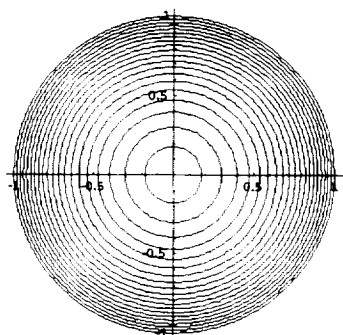


Figure 2. Nonuniform computational grid.

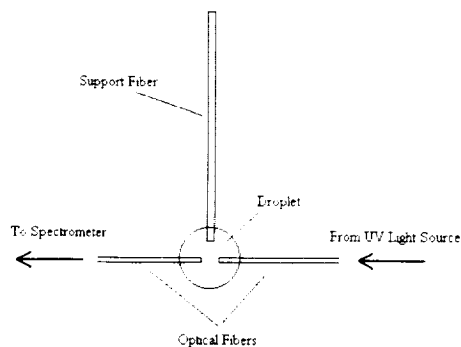


Figure 5. Schematic of the droplet spectroscopy setup.

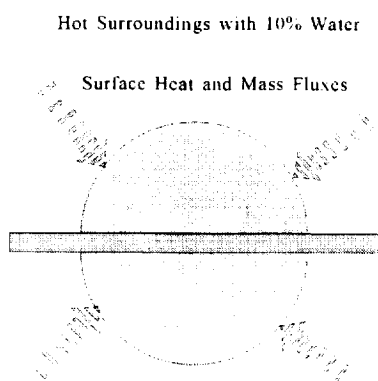


Figure 3. Schematic of a fiber supported droplet.

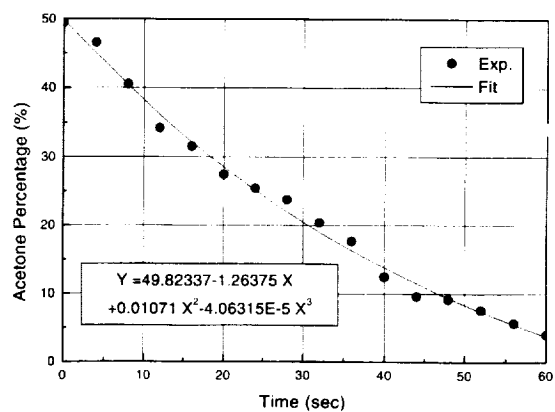


Figure 6. Acetone mass fraction vs. time.

COMBUSTION OF HAN-BASED MONOPROPELLANT DROPLETS IN REDUCED GRAVITY

B. D. Shaw, MAE Department, University of California, Davis, CA 95616

INTRODUCTION

Hydroxylammonium nitrate (HAN) is a major constituent in a class of liquid monopropellants that have many attractive characteristics and which display phenomena that differ significantly from other liquid monopropellants [1]. They are composed primarily of HAN, H_2O and a fuel species, often triethanolammonium nitrate (TEAN). HAN-based propellants have attracted attention as liquid gun propellants (e.g., [1]), and are attractive for NASA spacecraft propulsion applications [2]. A representative propellant is XM46. This mixture is 60.8% HAN, 19.2% TEAN and 20% H_2O by weight. Other HAN-based propellant mixtures are also of interest. For example, methanol and glycine have been investigated as potential fuel species for HAN-based monopropellants for thruster applications [3].

In the present research, experimental and theoretical studies are performed on combustion of HAN-based monopropellant droplets. The fuel species considered are TEAN, methanol and glycine. Droplets initially in the mm size range are studied at pressures up to 30 atm. These pressures are applicable to spacecraft thruster applications [2]. The droplets are placed in environments with various amounts of Ar, N_2 , O_2 , NO_2 and N_2O . Reduced gravity is employed to enable observations of burning rates and flame structures to be made without the complicating effects of buoyant and forced convection. Normal gravity experiments are also performed in this research program.

The experiment goals are to provide accurate fundamental data on deflagration rates, gas-phase temperature profiles, transient gas-phase flame behaviors, the onset of bubbling in droplets at lower pressures, and the low-pressure deflagration limit. Theoretical studies are performed to provide rational models of deflagration mechanisms of HAN-based liquid propellants. Besides advancing fundamental knowledge, this research should aid in applications (e.g., spacecraft thrusters and liquid propellant guns) of this unique class of monopropellants.

NORMAL GRAVITY EXPERIMENTS

Normal gravity experiments were performed: (1) to perform screening of the propellant formulations that might be investigated in microgravity; and (2) to provide baseline normal-gravity data to be compared with the reduced-gravity data. A summary of the results from these experiments is provided below. Details on these experiments are available elsewhere [4].

The normal-gravity experiments were performed at UC Davis using an available pressure vessel. This vessel was pressurized to as high as 10 atm with either N_2 or air. Individual droplets of various formulations (HAN-water, XM46, HAN-glycine, HAN-methanol, methanol, and TEAN-water) were deposited onto a quartz fiber using a computer-controlled assembly. A wire-loop heating element was used as an igniter, and a high-speed video camera was used to image droplet shape changes at frame rates as high as 1000 frame/s. In addition, droplet and flame behaviors were imaged using a conventional CCD camera as well as a Xybion intensified-array (ICCD) camera. The ICCD camera employed a 310 nm interference filter as well a UV lens system, thus allowing observation of UV emissions from OH radicals. A special UV-transmissive quartz window was utilized in the pressure vessel to allow clear imaging of OH emissions. Schematics of the experimental setup are shown in Figs. 1 and 2.

These experiments demonstrated that the different monopropellant combinations display very different behaviors. For example, HAN-water droplets (13 molar) did not produce a gas phase flame under any conditions. However, these droplets exhibited strong bubbling throughout their lifetimes. A representative image of a HAN-water droplet is shown in Fig. 3, where bubbles can be seen in the droplet. The bubbles are likely a result of liquid-phase chemical reactions as well as chemical stratification in the liquid. The igniter is visible in Fig. 3 (beneath the droplet).

In contrast, the XM46 droplets could be ignited in air (but not N_2). The flames were generally of very short duration relative to the droplet lifetime, with flames appearing towards the end of the droplet lifetime. Figure 4 shows droplet and flame lifetime data for XM46 droplets with initial diameters of about 1.6 mm (based on droplet volume). Flame durations, as sensed by the thermocouple, were about an order-of-magnitude shorter than the droplet lifetimes. These experiments were performed such that the temperature of the igniter-produced hot gas field around the droplets, as measured by a thermocouple, was nearly constant for all droplets and all pressures. The XM46 droplets generally exhibited bubbling throughout much of their lifetimes (droplet lifetimes were defined to be the time elapsed between energizing the igniter and the end of the flame lifetime, which generally coincided with the disappearance of the droplet).

Visible emissions from XM46 flames were yellowish in color, suggesting that soot was present, though the yellow coloration could be radiation from hot TEAN particles that might be produced during the combustion [5]. Imaging of UV emissions from the XM-46 flames indicated that the flame zones could be substantially larger than would be anticipated for simple diffusion flames. High-speed imaging of the XM46 droplets also showed that organized structures were sometimes present in the gas phase when the droplets were bubbling. For example, Fig. 5 shows a toroidal structure, which is likely a vortex, outside of a droplet. These structures appeared to form when material was locally ejected from the surface of a droplet. The gas-phase structures likely have aerosol particles in them, rendering them visible in the backlit images. The toroidal vortices were less common at high pressure because the gas flows became turbulent, disrupting the organized flows.

The 1-g experiments also showed that HAN-methanol droplets (with various amounts of HAN and water) could be ignited in air. An interesting characteristic of these experiments is that the flames displayed yellow coloration when HAN was initially present in the droplets. Methanol is a nonsooting fuel and as such the initially pure methanol droplets did not display yellow flames. The yellow coloration with the HAN-methanol droplet flames may have been from soot, though further experiments are needed to investigate this possibility. The HAN-methanol mixture droplets generally did not exhibit bubbling while flames were present. However, the flames around these droplets would extinguish prior to complete droplet gasification. The remaining liquid would then bubble intensely (because the igniter was still energized) until all the liquid was gone. The bubbling was likely a result of HAN decomposition in the liquid phase. Initially pure methanol droplets did not bubble at all, which was expected.

Other observations from these experiments are as follows. HAN-glycine droplets displayed luminous flames in air but not in N_2 . Also, HAN-glycine droplets left substantial residue behind and did not burn as completely as XM46. The XM46 flames were generally much larger than the HAN-glycine flames (as imaged by the ICCD camera). TEAN-water drops in air go through an evaporation stage followed by diffusion flame combustion of the condensed molten TEAN that remains after the water has evaporated. Finally, it is noted that these normal-gravity experiments clearly showed that buoyant flows were prevalent, e.g., from observations of flame shapes as well as the difficulties in igniting some of the droplets. Ignition difficulties were related to the buoyant flow produced by the igniter, which carried reactive species away from droplets.

REDUCED GRAVITY EXPERIMENTS

The reduced gravity research involves studying combustion characteristics of droplets initially in the mm size range. A drop rig is being constructed for use at the NASA Glenn 2.2 Sec Drop Tower. The design of this drop rig is primarily based upon the droplet combustion test rigs that are presently in use at the NASA Glenn Research Center. However, for these experiments, the pressure vessel has been modified to allow pressures up to 30 atm to be achieved. This vessel is mounted on a drop frame with imaging, electronic and fluid handling systems.

Orthogonal views will be used in these experiments. One view is used to image droplets and the other to image flames. The droplet view, which will be backlit, will utilize a high-speed camera to capture transient droplet behaviors. The flame view will not be backlit, and two cameras will be used to image flames. A 16 mm cine camera (or high-speed video camera) will be used to image visible gas-phase combustion behaviors, and an ICCD camera will be used to image OH emissions. The construction of the vessel is nearly complete. It is expected that microgravity experiments will commence shortly.

THEORETICAL RESEARCH

Theoretical efforts are focused upon providing theory to explain and interpret the results from the normal-gravity and reduced-gravity experiments. For example, it is clearly of interest to develop theory to provide interpretations of unexpected results such as the very large flames of XM46 droplets as well as the yellow coloring observed with the HAN-methanol droplets. The theoretical efforts are essentially divided into two efforts. In the first effort, rational theoretical models (based on existing HAN-based propellant deflagration theory [6] or new models to be developed) will be applied to the HAN-based liquid propellants. Theoretical models that are consistent with the experimental data will be selected or developed. Influences of phenomena such as nonequilibrium vaporization, two-phase flow, gas solubility in liquids, and the presence of a fuel species (e.g., TEAN) will be considered. The second effort is directed towards developing models of TEAN and glycine droplet/residue combustion, where it is evident from the experiments that condensed-phase pyrolysis may need to be accounted for. An emphasis of the theoretical work is to develop analytical models.

ACKNOWLEDGEMENTS

The financial support of NASA is gratefully acknowledged. The Technical Monitor for this research is Dr. D. Dietrich. Special thanks go to A. Birchenough for his efforts with the design and construction of the reduced gravity drop rig.

REFERENCES

1. Klein, N., Report ARBRL-02471, Ballistic Research Laboratory (1983).
2. Jankovsky, R. S., AIAA Paper 96-2863.
3. Wucherer, E. J., and Christofferson, S., AIAA Paper 2000-3872.
4. Farshchi, M., Vaezi, V., and Shaw, B. D., paper 223 presented at the 2nd Joint Meeting of the US Sections of the Combustion Institute, Oakland, CA (2001).
5. Beyer, R. A., CPIA Publication 557, Volume I, p. 605 (1990).
6. Shaw, B. D. and Williams, F. A., 24th Symposium (Int'l.) on Combustion, p. 1923 (1992).

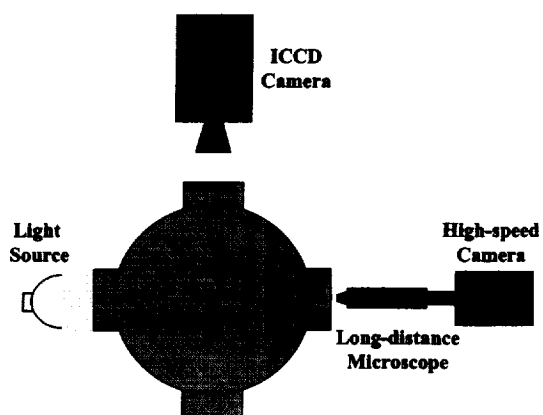


Figure 1. 1-g pressure vessel and cameras.

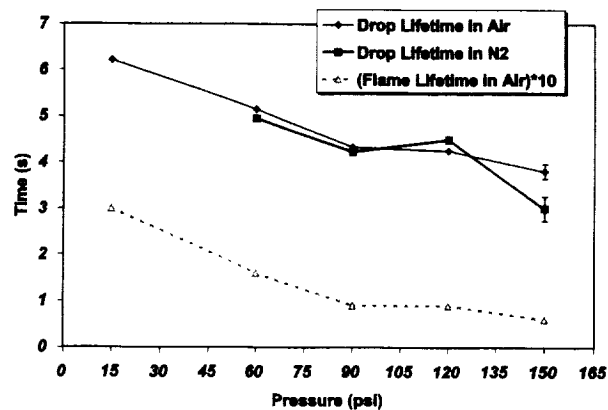


Figure 4. XM46 droplet and flame lifetimes.

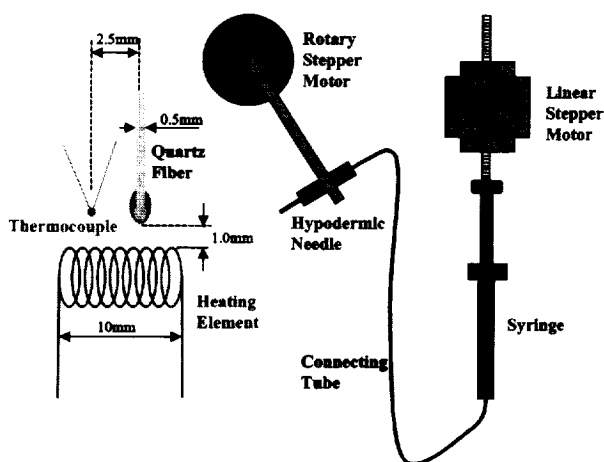


Figure 2. Droplet dispensation and gas temperature measurement systems.

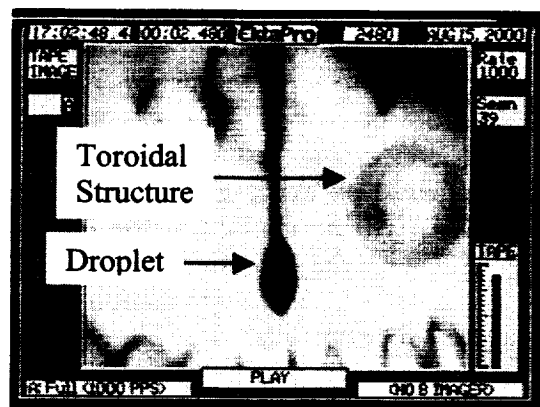


Figure 5. XM46 droplet in N₂ at 60 psi.



Figure 3. HAN-water droplet in air at 1 atm. Bubbles are present in the droplet.

Combustion Stages of a Single Heavy Oil Droplet in Microgravity

M. Ikegami, G. Xu, K. Ikeda, S. Honma, H. Nagaishi,
D. L. Dietrich*, P. M. Struk*, and Y. Takeshita**

National Institute of Advanced Industrial Sci. and Tech. (AIST), Sapporo 062-8517, Japan

*NASA John H. Glenn Research Center, Cleveland, OH 44135, USA

**Japan Space Utilization Promotion Center, Tokyo 169-8624, Japan

INTRODUCTION

Heavy oil is a common fuel for industrial furnaces, boilers, marines and diesel engines. Previous studies showed that the combustion of heavy oil involves not only the complete burning of volatile matters but also the burn-out of coke residues [1-3]. Detailed knowledge about heavy oil combustion therefore requires an understanding of the different burning stages of heavy oil droplets in the burner. This in turn, demands knowledge about the single droplet evaporation and combustion characteristics.

This study measured the temperature and size histories of heavy oil (C glass) droplets burning in microgravity to elucidate the various stages that occur during combustion. The elimination of the gravity-induced gas convection in microgravity allows the droplet combustion to be studied in greater detail. Noting that the compositions of heavy oil are various, we also tested the fuel blends of a diesel light oil (LO) and a heavy oil residue (HOR).

EXPERIMENTAL

The microgravity facility used was the drop shaft of Japan Microgravity Center (JAMIC) which can generate microgravity conditions better than $10^{-5} g_0$ ($g_0 = 9.81 \text{ mm/s}^2$) with a duration of 10 sec. Figure 1 shows a schematic of the experimental apparatus. Thermocouples made of platinum (Pt) and platinum-rhodium (Pt-Rh, 13 wt.% Rh) wires with diameters of 0.1 and 0.025 mm, respectively supported the droplets and also measured the temperature inside the droplet. The thermocouple was mounted on a metal arm that both rotated and translated up-and-down under the controls of two DC motors. Image data were taken using two orthogonally located video cameras that connected to two Hi 8 mm VCRs. One view was backlit to image the droplet and the other was a direct image of the flame. The backlight view provided a measure of the droplet size. The video images of both the views gave a framing rate of 30-Hz.

The test began with the formation of an oil droplet at about 1.0 min before microgravity started (dropping the capsule). To form a droplet, the thermocouple arm first rotated to a position

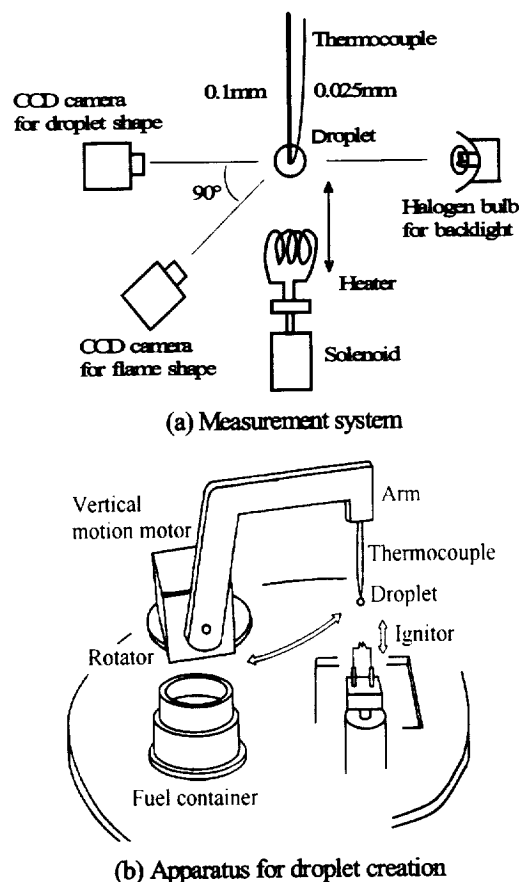


Fig. 1 Experimental apparatus

above a fuel container, and then moved down to immerse the thermocouple into the fuel reservoir. The arm and thermocouple then moved up, causing a fuel droplet to form on the thermocouple bead by the fuel viscosity. The arm finally rotated back to a position above the igniter and to have the droplet ready for burning. The record of the thermocouple data started at the onset of microgravity. One second later the igniter moved just beneath the droplet (1–2 mm) and turned on for a preset period of time, typically 1.6 sec. The actual time, however, varied slightly from test to test to ensure that the igniter withdrew shortly after ignition.

The stated droplet size in this report is an equivalent droplet size given as the cube root of the product of the droplet radius squared and the droplet length, $d = (\text{radius})^2 \times (\text{length})^{1/3}$. While the heavy oil (C class) used was bought commercially, the heavy oil residue (HOR) was made by fractionating the heavy oil at a fractional temperature of 563 K and a pressure of 35 mmHg. Three HOR-LO blends were tested. They were made by mixing the resultant HOR and a commercial diesel light oil (LO) at LO weight fractions of 45%, 35% and 17%.

RESULTS AND DISCUSSION

The combustion of the heavy oil droplets involves significant sooting, droplet swellings and contractions, and disruptive burning behavior, all of which were obvious from the video data. Figure 2 compares the droplet temperature and size histories of heavy oil (2a) and HOR (2b), showing clearly the following vaporization and combustion stages.

1. Pre-ignition heating and start-up Before ignition (event A), there is a pre-ignition stage where fuel vaporizes from the droplet surface, forming a vapor cloud surrounding the droplet. Figure 2 shows that the ignition of the HOR droplet occurred at a higher droplet temperature and at a later time (longer ignition delay time).

After ignition, a rapid increase in droplet temperature was obvious for both the fuels until event B in Fig. 2a and event D in Fig. 2b (events B and C did not occur for HOR). This increase of temperature was related to the lower droplet temperature at ignition and the enforced heating by the flame encircling the droplet. It in fact made the whole droplet reach high temperatures rapidly, and was essentially a start-up of the succeeding burning stage.

2. Inner evaporation For the heavy oil droplet in Fig. 2a, the start-up stage ended with the onset of inner fuel evaporation stage. This stage (event B) corresponds to a plateau in the droplet temperature history. We denote this plateau temperature as the evaporation temperature, T_e . After event B, the rate of temperature increase is much slower, as most of the energy transported

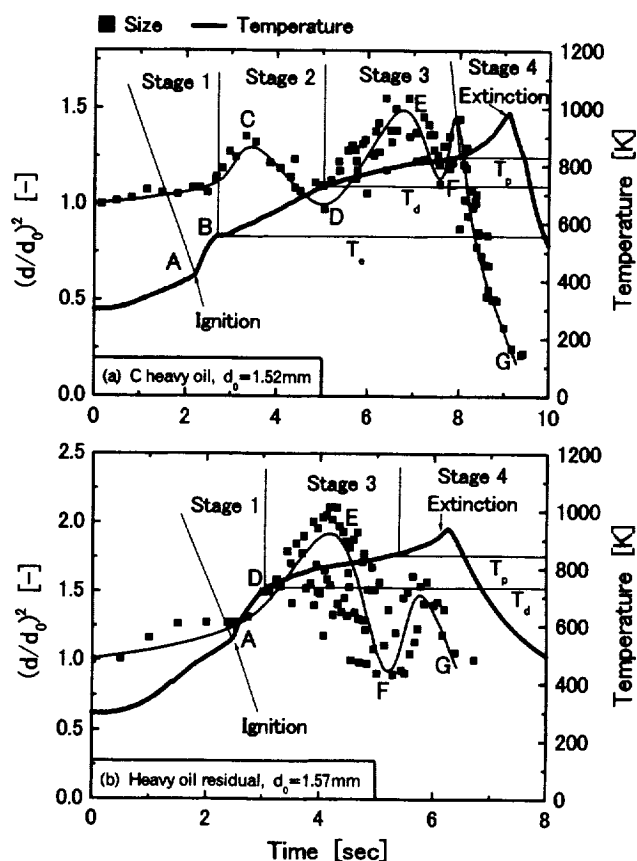


Fig. 2 Temperature and size histories for heavy oil and HOR droplets

from the flame to the droplet goes to vaporizing the fuel. The temperature increases as the higher volatility constituents begin to vaporize [2].

Rapid vapor generation within the droplet (probably at many positions) occurred during this stage. Those vapors near the droplet surface might escape from the droplet with only mild disruptions to the droplet and flame, causing the splashing phenomenon that occurred early in the stage. The other vapors that formed deep in the interior of the droplet could not reach the droplet surface. They tended to nucleate, combine and swell the droplet. Fig. 2a shows this as the increase in droplet size from events B to C. The droplet swelling ended at a sudden droplet contraction, usually as a microexplosion, at event C. After event C, the evaporation rate decreases with time, as a result of the depletion of most volatile species between events B and C. In response to this, Fig. 2a shows a decrease in droplet size and an increase in droplet temperature from events C to D. The burning then involved less splashing but more explosive behavior.

Figure 2a shows that the stage starts at approximately 560 K and ends at a temperature around 700 K. Baert [4] explained that the weakest chemical bonds in heavy oil do not begin to break below 625 K, and thermal cracking is not important until the temperature is over 700 K. Therefore, we can be reasonably certain that the stage between events B and D corresponds to vaporization of the light fuel components rather than thermal decomposition of the fuel. Therefore, one would not expect an HOR droplet to have an inner evaporation stage. Figure 2b shows that this is in fact the case. The figure, however, shows a start-up stage between events B and D for the HOR droplet where the droplet temperature increases rapidly. The fuel vaporized in the HOR droplet is certainly heavier than the lighter species of heavy oil. Thus, the droplet temperatures in Fig. 2b are higher than the corresponding temperatures in Fig. 2a during the start-up stage.

3. Thermal decomposition After the volatile components vaporize from the droplet, the remaining fuel begins an endothermic decomposition. At the beginning of this stage there is another plateau or an inflection point in the droplet temperature history, denoted by event D. In Fig. 2a, the onset of the decomposition stage is coincident with a local minimum in the droplet size history. This indicator is not present in Fig. 2b since such a decrease in droplet size is due to the inner vaporization of volatile constituents. The large energy required for thermal decomposition causes the inflection or plateau in the droplet temperature history, and also decreases the rate at which the droplet temperature increases. We identified the decomposition temperature, T_d , as the droplet temperature at this plateau or inflection. Figure 2 shows that this temperature is nearly the same for the heavy oil (2a) and HOR (2b) droplets, and is approximately equal to 740 K [4].

The thermal decomposition produced volatile gases, which made the droplet swell again. Figure 2 (a and b) shows this as an increase in the mean droplet size. The thermal decomposition stage can be further sub-divided into two periods. The fuel constituents that easily decompose produce volatile gases during the first period, between events D and E, and cause the gradual increase in droplet size. At event E, the droplet size reached a maximum, which corresponds to the most violent frothing of the droplet. Then, the production of the volatile gases decreases, as the more stable components begin to decompose. This leads the droplet to shrink gradually between events E and F. In comparison with the inner evaporation stage, microexplosions in the thermal decomposition stage were more intensive and frequent.

4. Polymerization After the thermal decomposition stage (event F), the rate of the droplet

temperature rise, the first derivative of droplet temperature with time, started to increase with time. The corresponding video images indicate that the droplet entered the last period of swellings and contractions, with each contraction resulting in a rough droplet surface. The droplet then began to look like a soft bituminous coal particle [4] until a coke particle formed at flame extinction. Therefore, the beginning of the polymerization stage is when the rate of droplet temperature rise begins to increase with time. The primary reason for the increase in the droplet temperature rise rate is that the droplet temperature is no longer controlled by the vaporization of fuel. The droplet temperature at event F is defined as the polymerization temperature, T_p . Figure 2 shows that this temperature is nearly identical for the heavy oil and HOR droplets, and equal to approximately 840 K.

Thermal decomposition takes place simultaneously with polymerization in this stage. The thermal decomposition produces radicals that are stable for further decomposition but active for re-combination. The volatile gases produced in the fuel decomposition continued to make the droplet swell and contract, resulting in the final parabolic size area in the droplet size history. Due to the rapid reactions of polymerization [1, 2], this area was much narrower than earlier ones for the other stages. In addition, Fig. 2 shows, as expected, that the final coke particle was much larger for HOR (2b) than for heavy oil (2a).

5. Mixture effects Figure 3 compares the droplet temperature histories for three different HOR-LO mixtures, with the LO mass fractions ranging from 0.17 to 0.45. The qualitative characteristics of temperature variation is obviously similar to that of the heavy oil droplets in Figs 2a. That is, the different burning stages can be separated by the three characteristic temperatures, T_e , T_d , and T_p . Further, Fig. 3 shows that T_d and T_p were almost independent of fuel composition, while T_e obviously decreased with increasing LO mass fraction. Also, the lower the initial LO mass fraction, the greater the rate of temperature increase during the start-up stage. The ignition delay time and the temperature at ignition decreased monotonically with the increase in the initial LO mass fraction. Finally, Fig. 3 identifies that the oil blends with higher initial LO mass fractions have longer inner evaporation stages but shorter thermal decomposition and polymerization stages. Conversely, the droplets with higher initial HOR mass fractions show longer thermal decomposition and polymerization stages.

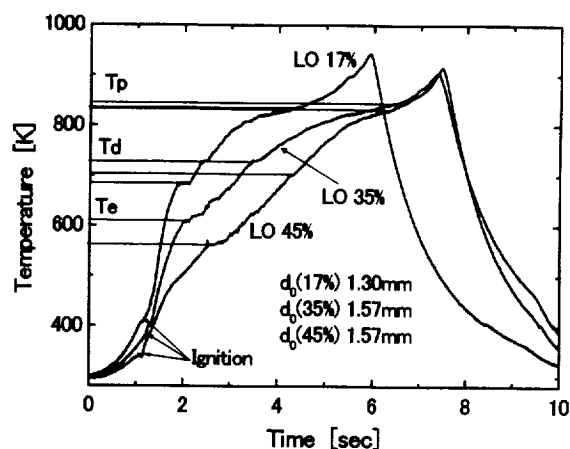


Fig.3 Droplet Temperature histories for different HOR-LO blends

ACKNOWLEDGEMENT

This work was sponsored by the Japan Space Utilization Promotion Center (JSUP), and was financed by the New Energy and Industrial Technology Development Organization (NEDO).

REFERENCES

- [1] E. G. Masdin & M. W. Thring, *J. Inst. Fuel*, **35**, 251-260 (1962).
- [2] M. I. Michael & M. W. El-wakil, 11th Symposium (Inter.) on Combustion, 1967, 1027-1035.
- [3] P. Lightman & P. J. Street, *J. Inst. Energy*, **56**, 3-11 (1983).
- [4] R. S. G. Baert, *Combust. Sci. Technol.*, **90**, 125-147 (1993).

COMBUSTION OF INDIVIDUAL BUBBLES AND SUBMERGED GAS JETS

Daniel E. Rosner, PI; Manuel Arias-Zugasti and Barbara La Mantia

Yale University, Department of Chemical Engineering, New Haven CT 06520-8286 USA

INTRODUCTION-BACKGROUND

Motivated by industrial "submerged flame" reactor experience, in which oxygen gas jets were ignited in liquid crude oil to synthesize acetylene and ethylene (Rosner, 1997), we are defining a sequence of fundamental micro-gravity and ground-based experiments, as well as carrying out ancillary theoretical studies, on the combustion of oxygen-containing *bubbles* in liquid fuels---especially transparent liquid hydrocarbons. Detailed studies of the combustion of large spherical bubbles are best carried out in a micro-gravity environment and useful single-bubble data *can* probably be obtained in existing drop-tower facilities.

The broad **objectives** of this research program may be summarized as follows:

- To exploit the micro-gravity environment and modern analytical/numerical/experimental techniques to carefully study a rather unexplored mode of *liquid fuel combustion*---ie., the transient combustion of an isolated spherical gaseous *oxidizer bubble*.
- To use micro-gravity-derived insights, ancillary theoretical/numerical studies and new ground-based laboratory studies of combustion in bubble columns and submerged jets to provide a more rational basis to ultimately design improved "*submerged gas jet combustors*" for use in ground-based synthesis-oriented chemical industry, especially when the liquid "fuel" (feedstock) is difficult to "atomize" (because of its viscosity or "chemical aggressiveness").
- To open up a relatively virgin branch of *bubble dynamics* dealing with *intra-bubble chemical reactions*. This can be later extended to more complex systems such as oxidizer bubbles in more energetic fuels (such as hydrazine or molten aluminum), or, conversely, *fuel vapor pockets* in non-cryogenic and cryogenic liquid *oxidizers*.

Ironically, fundamental studies of this until now neglected branch of combustion should, as byproducts, shed valuable new light on many apparently different modes of combustion or bubble-contacting devices, including, perhaps, the combustion of *foams* containing air.

MODEL PROBLEM FOR A PRE-MIXED GASEOUS BUBBLE

Since so little is known about the dynamics of *bubbles in which combustion occurs*, in the present communication we describe our initial work on the model problem of a centrally ignited reactive spherical bubble immersed in a viscous liquid which is inert, otherwise quiescent, incompressible, and non-volatile. No external forces or buoyancy are considered, so that the initial spherical symmetry of the system is preserved for all time. Such bubble evolution naturally separates into two qualitatively different stages: During Stage I a spherically symmetric premixed flame propagates from the bubble center, consuming the initial inventory of reactive gases initially present in the bubble and raising the internal pressure. This stage lasts until the flame approaches the bubble radius (to within one quenching distance). Because Stage I is so short, little heat or mass is transferred to the liquid phase during this period, moreover, since the characteristic diffusion time (for both, heat and mass) in the bubble is much larger than the time needed to complete this process, the temperature distribution inside the bubble can be approximated by a piecewise constant function (equal to the pressure-moderated initial

temperature outside of the flame radius, and the flame temperature for smaller radii. These approximations facilitate the computation of Stage I, with results shown in Figs. 1, 2 for the particular case of stoichiometric methane/air at $p = 1$ atm in a 1 cm. initial radius bubble in glycerol (98%) + 2% water. As may be seen, combustion produces a rise in both pressure and temperature inside the bubble, as well as an increase in bubble radius.

Flows of mass and heat *across the bubble interface*, neglected during Stage I, become important during the post-combustion Stage II. Here, some of the energy and products released during Stage I are transferred to the liquid by the relatively slow process of radial diffusion. During this process the abovementioned simplifications regarding the profiles of temperature and gas composition inside the bubble are no longer valid, and the complete PDEs governing mass and energy conservation must be solved in both phases. Moreover, one must simultaneously satisfy the boundary conditions (Rosner, 2000) of continuity of mass flux and heat flux across the interface, the condition of vapor/liquid equilibrium at the interface, and the condition of momentum conservation (Rayleigh-Plesset equation). This non-trivial task has been conveniently accomplished here using the Orthogonal Collocation Method (see, *eg.* Villadsen and Stewart, 1967). Our results show that Stage II is itself divisible in two sub-stages. The first is characterized by intense pressure and bubble radius oscillations, see Fig. 3 and Fig. 4. This sub-stage is followed by a longer period of slow heat and mass diffusion after the abovementioned bubble oscillations have been damped. The oscillations (first part of Stage II) are induced by the combustion-derived bubble overpressure. As may be inferred from the Fast Fourier Transform of the pressure and radius traces, the characteristic frequency of these oscillations is comparable to the Minnaert ("breathing") frequency (Leighton, T.G., 1994; *cf.* $\omega_M = 361.2/t_{ref}$ in the *isothermal* limit, $\omega_M = 427.3/t_{ref}$ in the *adiabatic* limit, for which $\omega_M = [3\gamma p_0/\rho_L]^{1/2}/R_0$).

During the oscillatory part of Stage II the higher temperature and concentration found in the bubble in the compressed half of each cycle tend to increase transfer rates from the bubble to the surrounding liquid. However, the bubble *surface area* is diminished and the boundary layers in the liquid are broadened. In contrast, during the over-expanded half of each cycle the bubble surface is enlarged and the gradients in the liquid are stronger, leading to an enhanced transport rate of mass and heat from the liquid to the bubble (Figs. 5, 6). To determine which effect dominates, the time-integral of the mass and heat flows across the bubble interface have also been calculated and compared to the analogous accumulated flows under the same conditions but in the absence of oscillations. Our preliminary results suggest that the first effect dominates over the second, leading a *modest enhancement of the rate of mass and heat transport from the (oscillating) bubble to the liquid*. However, we remark that the present results have been computed without taking into account the temperature dependence of the transport coefficients, or the Henry constant for CO₂ dissolving in glycerol.

The duration of the oscillatory part of Stage II is determined by damping. Because, in the present case, the kinematic viscosity (momentum-diffusivity; Rosner, 2000) of the liquid ($\nu = 5.09 \text{ cm}^2/\text{s}$) is much larger than the corresponding *heat* diffusivity of the liquid ($\alpha = 10^{-3} \text{ cm}^2/\text{s}$), the characteristic time for damping is dictated by the liquid's kinematic viscosity. At the end of this oscillatory substage we find that a thin boundary layer of liquid has been heated and saturated with dissolved gas. In the final substage of the process, mass and energy contained in this thin boundary layer diffuse to the liquid, as the concentration and temperature in the bubble approach their readily calculated final values. The characteristic evolution times for these last processes of heat/mass relaxation in the liquid are dictated by the liquid heat- and mass-diffusivities.

Summarizing, the present work clearly shows that, even in this deliberately simple system, we are dealing with no less than *five* characteristic times, the first of which is the time for a premixed flame to consume the pre-mixed reagents. Second, there is the characteristic time for rapid pressure oscillations, comparable to the inverse of the Minnaert frequency. Third, there is a much longer characteristic time in which these pressure oscillations are damped, at the same time that heat and mass are transferred from the bubble to a thin boundary layer in the liquid. Finally, there are the two characteristic diffusion times in the liquid, during which the temperature and concentration in the liquid boundary layer fall again until their values at infinity are attained. The recognition/use of several distinct time scales can, accordingly, improve our understanding of the dynamics of this class of systems, as well as increase the efficiency of such numerical calculations.

MODEL PROBLEM FOR AN OXYGEN GAS BUBBLE IN A LIQUID FUEL

The computational techniques exploited above lend themselves well to attacking the corresponding problem of a non-premixed *oxygen* bubble peripherally ignited in *liquid fuel*, at least in the $Le = 1$, diffusion-flame "sheet" level of approximation. In that case we must provide for not only the dissolution of a gaseous combustion product (as above), but also for the vaporization of the liquid (fuel) to sustain the inwardly propagating *diffusion* flame. Again, we expect a globally two-stage process, with Stage II (post-combustion) exhibiting interesting nonlinear dynamics. To guide the design of fruitful drop tower experiments, it will be important for us to identify the most instructive simple "observables", and anticipate as many of these dynamical features as possible.

PLANS

We are attempting to verify some of the most important predicted features of the abovementioned single bubble analyses, using simple demonstration premixed bubble experiments at Yale, and drop-tower experiments (on a single oxygen bubble in preheated alcohols) ultimately carried out at NASA-GRC. On the theoretical side, we plan to move toward multi-bubble (collective) phenomena, adopting multi-variate population-balance methods (analogous to a generalized "spray equation" approach; see, *eg.* Clause, A., 1997). Our long-range goal is to provide rational "tools" for designing "multi-bubble combustors" for future use in ground-based synthesis-oriented chemical industry. As part of this program it will probably be instructive to "retro-engineer" the (undoubtedly empirically optimized) BASF "submerged torch" ethylene + acetylene synthesis reactor (Bauer, 1969).

REFERENCES CITED

- [1] Arias-Zugasti, M., La Mantia, B. and Rosner, D.E. (2001) "The Dynamics of Pre-mixed Gas Combustion in a Centrally Ignited Spherical Bubble Contained in a Viscous Fluid", HTCRLab Publication (in preparation)
- [2] Bauer, K.G. (1969), "Acetylene From Crude Oil Makes Debut in Italy", *Chem. Eng.* Feb.10; p 82; see also, Bauer, K.G., and Taglieber, K., "Neuentwicklungen beim Tauchflammenverfahren", *Chemie-Ing. Techn.* 47 Jahrg. 1975, p. 385
- [3] Clause, A. (1997), "Bubble Population Models of Gas-Liquid Flows", in Vol. 3, **Trends in Heat and Mass Transfer**, pp 49-63
- [4] Leighton, T.G., (1994) **The Acoustic Bubble**, Academic Press, London

- [5] Rosner, D.E., (2000) **Transport Processes in Chemically Reacting Flow Systems**, Dover #0-486-41182-6, Mineola NY ; with 45p New Supplement
- [6] Rosner, D.E., Israel, R.S., and La Mantia, B., (2000) "'Heavy' Species Ludwig-Soret Transport Effects in Air-Breathing Combustion", *Combustion and Flame*, **123**, pp 547-560
- [7] Rosner, D.E. (Fall 1997) "Combustion Synthesis and Materials Processing", *Chem Eng. Educ.*, Amer. Soc. Engrg. Educ., pp 228-235
- [8] Villadsen, J.V. and Stewart, W.E. (1967) "Solution of Boundary-Value problems by Orthogonal Collocation", *Chemical Engineering Science* **22**, 1483-1501

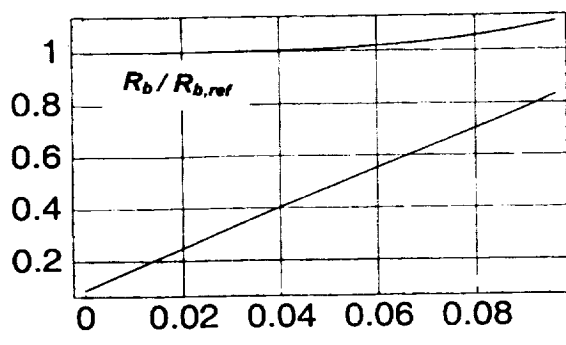


Fig. 1 Predicted bubble- and flame- radius (Stage I)

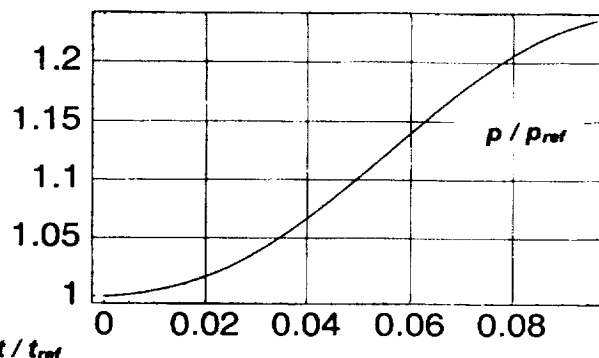


Fig. 2 Dependence of p/p_{ref} on t/t_{ref} ; Stage I

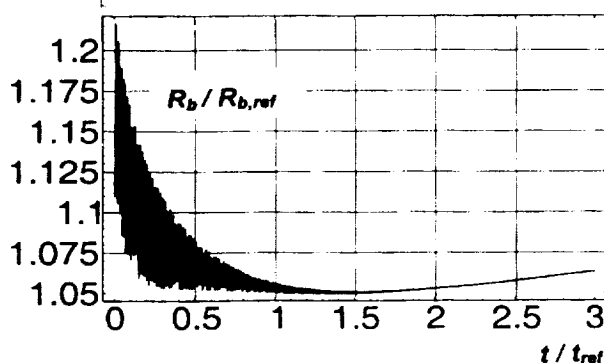


Fig. 3 $R_b/R_{b,ref}$ vs. t/t_{ref} ; Stage II

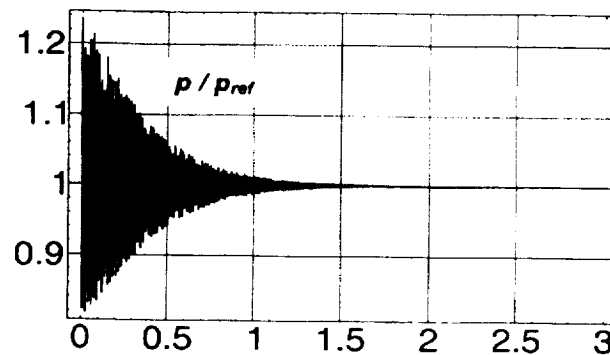


Fig. 4 p/p_{ref} vs. t/t_{ref} ; Stage II

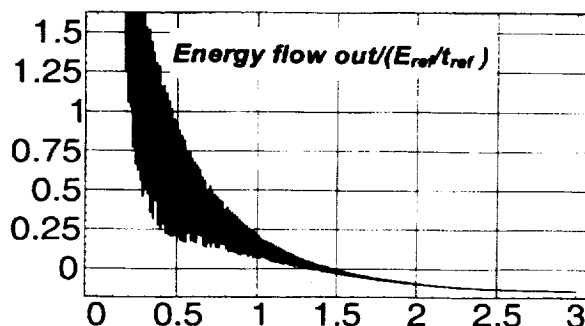


Fig. 5 Energy flow out / (E_{ref}/t_{ref}) vs. t/t_{ref} ; Stage II

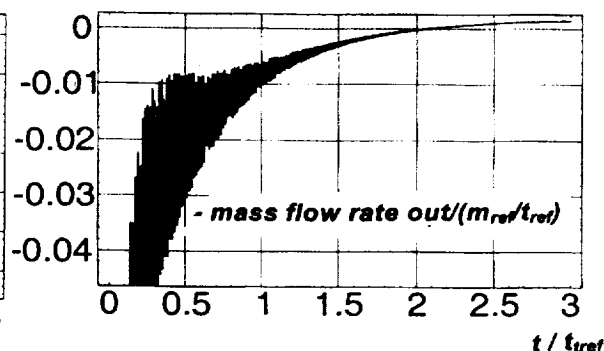


Fig. 6 -mass flow rate out / (m_{ref}/t_{ref}) vs. t/t_{ref} ; Stage II

For the figures presented above the reference quantities are as follows: $t_{ref} = 0.23$ s, $L_{ref} = 1$ cm, $p_{ref} = 1$ atm, $m_{ref} = 4.6$ mg, $E_{ref} = 0.239$ atm $\text{cm}^3 = 24.2$ G J. The convention used for the dimensionless flow rates are $q_d = \text{total instantaneous energy flow rate (in to out)} / (E_{ref}/t_{ref})$ and $md = \text{total instantaneous mass flow rate (out to in)} / (m_{ref}/t_{ref})$.

COMBUSTION OF METALS IN CARBON DIOXIDE AND REDUCED-GRAVITY ENVIRONMENTS

M. C. Branch, A. Abbud-Madrid, A. Modak, C. B. Dreyer, and J. W. Daily
Center for Combustion and Environmental Research
Department of Mechanical Engineering
University of Colorado at Boulder
Boulder, CO 80309-0427

INTRODUCTION

Ongoing exploration and future missions to Mars have given impetus to research on the use of natural resources of the planet. Since carbon dioxide (CO_2) constitutes approximately 95% of the Mars atmosphere and since it reacts directly and vigorously with several metals, this investigation focuses on metal- CO_2 reactions as a possible combination for rocket-propellant production and energy generation. Magnesium (Mg) has been initially selected as the metal fuel owing to its low ignition temperature and high specific impulse and burning rate in CO_2 .

Our studies in this field started with low gravity (g) combustion tests of Mg in O_2 , CO_2 , and CO [1]. Reduced gravity provided a clear picture of the burning phenomena by eliminating the intrusive buoyant flows in high-temperature metal reactions and by removing the destructive effect of gravity on the shape of molten metal samples. Suspended cylindrical metal samples of 2, 3, and 4-mm in diameter and length were radiatively ignited in low- g to generate free-floating samples exhibiting a spherically symmetric flame with increasing metal-oxide accumulation in an outer shell. For the Mg- CO_2 combination, burning times twice as long as in normal- g and five times longer than in Mg- O_2 flames were observed, revealing a diffusion-controlled reaction. The burning time is proportional to the square of the sample diameter. In tests conducted with pure CO, combustion was not possible without constant heating of the sample due to the formation of a thick carbon-containing coating around the Mg sample generated by surface reactions.

The following work presents two new studies that attempt to explain some of the low- g experimental observations. First, a simplified one-dimensional, quasi-steady numerical model is developed to obtain temperature, species concentrations, and burning rates of the spherically symmetric diffusion flame around the Mg sample burning in O_2 and CO_2 . Second, a Planar Laser Induced Fluorescence (PLIF) technique is implemented to provide spatially resolved measurements of magnesium oxide (MgO) in the reaction zone of Mg samples burning in O_2 and CO_2 . These experiments reveal fundamental differences between the two combustion systems.

NUMERICAL MODEL

A one-dimensional, quasi-steady numerical model of a spherically symmetric diffusion flame is developed to help in the interpretation of the low- g results and to serve as a preliminary effort for further development of a more complete model of Mg combustion. The model uses CHEMKIN [2] and a transport package for kinetics and transport calculations. Due to the lack of kinetic and thermophysical data for the heterogeneous reactions of Mg and the absence of a complete condensation mechanisms of MgO, the present model does not take into account surface reactions, radiation heat transfer, or complete condensation processes. Only vaporization of Mg from the sample surface is considered and MgO condensation is treated with an Arrhenius-type rate expression for the production rate of the liquid, MgO(l), and solid, MgO(s), oxides. These condensed products are treated like gas-phase species with a low diffusivity by

using a large value of the Lennard-Jones collision diameter in the transport property input. A collision diameter of 10 Å is chosen because is of the order of magnitude of the critical radius for condensation (3 Å) of MgO and small enough to avoid the treatment of a condensed phase. Equilibrium calculations are performed first to identify the most important species and to obtain the equilibrium temperature. The simulation is used to model the structure of Mg-O₂ and Mg-CO₂ flames. The Mg-CO₂ reaction mechanism contains the reactions of Mg with O, O₂, CO₂, and CO, and of CO and C with O₂ and O. Details of the model can be found in Ref. [1].

Figure 1a shows the flame structure of a 2-mm diameter Mg droplet burning in pure O₂ at 1 atm pressure and 300K temperature. Mg vapor diffuses out from the particle surface towards the counterdiffusing O₂. The surface temperature is only a few degrees below the boiling point of Mg (1366K). The temperature profile rises with a very steep gradient near the surface to a short plateau region where a maximum temperature of 3220K is reached. After the complete consumption of the Mg vapor, the slope of the temperature profile starts decreasing at a faster rate. The predicted maximum temperature of 3220K is slightly lower than the maximum equilibrium temperature of 3398K (vaporization-decomposition point of MgO). This difference in maximum temperature values may be attributed to the lack of an accurate liquid-to-solid condensation model, which may also be responsible for the absence of a large concentration of MgO(l) in the plateau region where the temperature exceeds the melting point of MgO (3105 K) and where the liquid oxide is the dominant species. As a result of the high flame temperature, a large amount of O is also present in the high temperature region. The significant concentration of O₂ at the surface indicates that heterogeneous reactions may play an important role.

The flame structure of a 2-mm diameter Mg droplet burning in a pure CO₂ atmosphere at 1 atm pressure is shown in Fig. 1b. In this case, the oxidizer ambient temperature is 1000 K since no convergence is obtained in the simulation for lower temperatures. This temperature is in agreement with experiments [1] where the Mg sample is ignited by heating the CO₂ gas around it. The maximum combustion temperature predicted by the simulation is 2645 K, which is lower than the equilibrium temperature of 3174 K. The cause of this discrepancy in maximum temperature values follows the same reasoning as in the Mg-O₂ case. The reaction zone observed in Fig. 1b is narrower than in the Mg-O₂ simulation, suggesting a slower molecular diffusion process in the case of CO₂ as the oxidizer. This result is in qualitative agreement with the low-g experiments where longer burning times are observed in Mg-CO₂ flames.

PLANAR LASER INDUCED FLUORESCENCE EXPERIMENTS

A PLIF technique has been developed to provide spatially resolved measurements of magnesium oxide (MgO) in the reaction zone of bulk samples of Mg burning in O₂ and CO₂ atmospheres. Mg cylinders (4-mm-diam and length) are radiatively ignited in normal-g with a xenon-arc lamp. Samples are positioned at the center of an alumina block. No forced flow of oxidizer is imposed on the samples, but a strong natural convection plume develops as a result of heating and combustion. A Nd:YAG pumped dye laser is used as the excitation source. Detection is accomplished using a gated intensified CCD camera fitted with a set of bandpass, shortpass, and neutral-density filters. This excitation/detection scheme enables PLIF measurements in the presence of significant laser scattering from combustion-generated solid MgO particles. Magnesium-oxide PLIF is accomplished by excitation of the MgO B¹Σ⁺ - A¹Π (0,0) transition, at approximately 601 nm, and observation of the resulting B¹Σ⁺ - X¹Σ⁺ fluorescence from 490 to 501 nm. Details of the experiment can be found in Ref. [3].

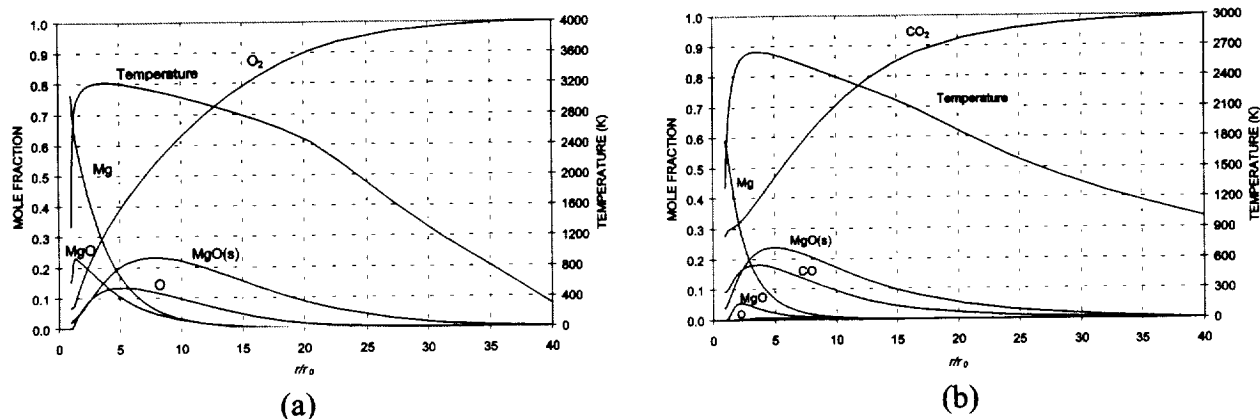


Figure 1. Numerical simulation of the flame structure of a 2-mm diameter Mg droplet burning in (a) O_2 and (b) CO_2 at 1 atm.

As indicated by the PLIF images of MgO, the combustion of Mg in 21% O_2 (balance Ar) at 1 atm is shown to be a predominately gas-phase reaction with quasi-steady combustion. The reaction zone is approximately 7-8 mm in width and the reaction time is 11.7 ± 1.5 seconds. Combustion exhibits a build-up period of approximately 1.5 seconds, followed by a quasi-steady period of approximately 5.2 seconds, and a burn-out period of 5.5 seconds with a rapid fall-off.

Combustion of Mg samples in pure CO_2 and in 80% CO_2 (balance Ar) at 1 atm reveals a more protective surface layer as compared to O_2 . This layer is seen to inhibit reaction at low partial pressures of CO_2 , while the gas-phase reaction is intermittent at high partial pressures. The reaction proceeds in an unsteady, pulsating manner, as opposed to the quasi-steady combustion in O_2 . Reaction times of approximately 5 seconds are shorter than in O_2 , but unburnt Mg remains on the base. A representative PLIF image from a reaction burst of Mg burning in 80% CO_2 is shown in Fig. 2a while Fig. 2b shows a surface plot of the PLIF signal vs. time and position along the vertical centerline of the sample melt. The surface of the melt is located at approximately 2.8 mm in Fig. 2b. As in combustion with O_2 , the large discontinuous signal seen at $t=0$ is due to scattered lamp light. Lamp shut-off occurs at $t=1$ second. Several rapid pulsations are evident that appear for only one frame. The pulse durations are shorter than the 10-Hz laser rate. No continuous gas phase reaction is observed. Analysis of the melt following reaction shows a core of unreacted Mg surrounded by a black carbon-containing layer with white MgO deposits on top. It appears that this layer inhibits the transport of Mg into the gas phase, while periodic fracturing of the surface releases Mg vapor that rapidly reacts with surrounding CO_2 . Gradual build-up of the carbon layer eventually extinguishes the reaction.

Analysis of the MgO PLIF signal strength reveals that the MgO mole fraction during combustion in 21% O_2 is slightly below the equilibrium value. In the case of Mg burning in 80% CO_2 , the MgO mole fraction is significantly below the equilibrium value. This discrepancy is not surprising considering the presence of heterogeneous reactions, incomplete reaction, and unsteady combustion.

CONCLUSIONS

A numerical model and PLIF measurements are conducted to support the low-g combustion experiments of Mg- CO_2 to assess the feasibility of using metal- CO_2 reactions as an in situ resource utilization technology on Mars. The flame structure predicted by the one-dimensional, spherically symmetric, quasi-steady model shows a maximum temperature close to the

vaporization-decomposition point of the metal oxide, as well as the coexistence of the gaseous and condensed phases of the oxide product. It also confirms the experimental results of a diffusion-controlled reaction and a slower burning rate of Mg in CO₂ as compared to O₂. The discrepancies between the numerical simulation and the experimental observations may be attributed to the absence of accurate condensation, radiation, and surface-reaction models.

The PLIF experiments provide confirmation of the pulsating nature of Mg-CO₂ combustion observed in the low-g tests and also prove the feasibility of using the PLIF technique to determine the spatial variation of particles and some species concentrations. Although this study indicates that Mg energetically reacts directly with CO₂ in the gas phase, further work is necessary to establish the ignition and steady-state combustion methods required for a successful operation of a Mg-CO₂ rocket on Mars.

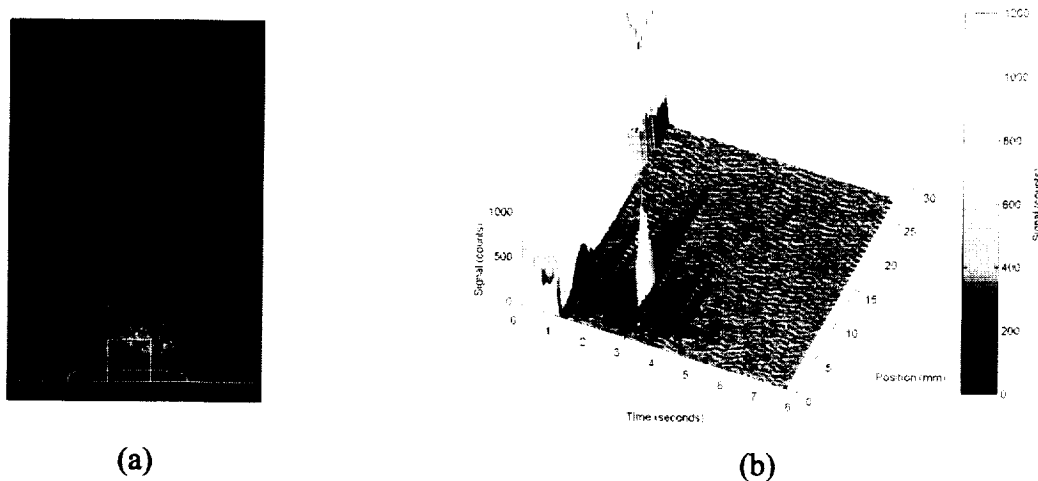


Figure 2. PLIF signal of MgO during combustion of Mg in 80% CO₂, 20% Ar. (a) PLIF image during a gas-phase reaction burst showing outlines of the original cylindrical sample and the disk-shaped melt just before lamp shut-off; (b) time and vertical distribution of the PLIF signal.

ACKNOWLEDGMENTS

This work is supported by NASA under Grant NAG3-2220. The authors gratefully acknowledge the technical supervision of Robert Friedman from NASA Glenn Research Center.

REFERENCES

1. Abbud-Madrid, A., Modak, A., Branch, M. C., and Daily, J. W., "Combustion Of Magnesium With Carbon Dioxide and Carbon Monoxide at Low Gravity," *Journal of Propulsion and Power*, to be published.
2. Kee, R. J., Miller, J. A., and Jefferson, T. H., "CHEMKIN: A General-Purpose, Problem-Independent, Transportable, Fortran Chemical Kinetics Code Package," Sandia National Laboratories, Report SAND80-8003, Livermore, CA, 1980.
3. Dreyer, C. B., Daily, J. W., Abbud-Madrid, A., and Branch, M. C., "PLIF Measurements of Magnesium Oxide During Combustion of Magnesium," Paper AIAA 2001-0788, 39th Aerospace Sciences Meeting & Exhibit, Reno, NV, January 8-11, 2001.

EFFECT OF GRAVITY ON THE COMBUSTION SYNTHESIS OF ENGINEERED POROUS COMPOSITE MATERIALS

John J. Moore, Franklin D. Schowengerdt, Reed Ayers, X. Zhang, M. Castillo
Center for the Commercial Applications of Combustion in Space (CCACS)
Colorado School of Mines

INTRODUCTION

Combustion synthesis (self-propagating, high temperature synthesis-SHS) is currently being used in the Center for the Commercial Applications of Combustion in Space (CCACS) at the Colorado School of Mines to produce a wide range of engineered composite materials. These advanced materials include ceramic, intermetallic, and metal-matrix composites that can be produced for applications that range from structural and oxidation/wear resistant materials, e.g., TiC-Al₂O₃, TiC-SiC, TiC-Cr₃C₂, TiB₂-TiC, MoS₂-SiC, NiAl-TiB₂, to engineered porous composites for ultra lightweight, catalyst support, high temperature filter and biomedical applications, e.g., B₄C-Al₂O₃, Ti-TiB_x, Ni-Ti, Ca₃(PO)₄ and glass ceramic composites. This paper will discuss the recent progress in the synthesis of porous Ti-TiB_x, Ni-Ti, and Ca₃(PO)₄ based materials for bone replacement applications.

The control parameters of a combustion synthesis reaction include green density, reaction stoichiometry, mode of combustion and heating rate, and reactant particle size. The level of porosity in the synthesized material can be engineered by the controlled release of a gasifying agent and the generation of a controlled amount of liquid at the reaction front through which the gas can permeate. As one would expect, the effect of gravity on the permeation of the gas through the liquid at the reaction front is significant, and strongly determines both the level and distribution of porosity as well as pore size. Materials to be used for bone replacement applications require typically 40-60% overall porosity with a pore size between 200-500 microns. Data will be presented of recent experiments conducted on the synthesis of porous materials in the NASA parabolic flight (KC-135 aircraft) facilities, and on the ability of these materials to perform as bone replacement materials using *in-vivo* experiments.

Ceramics and Metals have been used in various forms as implants. The biocompatibility (corrosion) of the implant material in the hostile body environment is of considerable concern. The consequence of corrosion is loss of material, which will weaken the implant, and probably more important, the corrosion products escape into the tissue resulting in undesirable effects on health. Titanium derives its resistance to corrosion by the formation of a solid oxidation layer of TiO₂. Under *in-vivo* conditions the TiO₂ is the only stable reaction product[1]. The oxidation layer forms a thin adherent film and passivates the material. Porous material has a certain open structure that provides a possibility for the bone ingrowth of bony tissue into the body of the implant, resulting in firm fixation to bone. Phosphate-based materials such as HA, TCP, based on Ca₃(PO₄)₂ are quite biocompatible. In addition, they promote the differentiation of the osteoblast phenotype from marrow stem cells and are thus osteoinductive [2]. These materials are also osteoconductive, promoting the direct attachment of osseous tissue to the implant surface [3]. An advantage of these phosphate-based materials over metals is their ability to degrade over time, allowing natural bone to fill in the implant space. The thesis project aims at using combustion synthesis or SHS (Self Propagating High Temperature Synthesis) to synthesize

advanced and engineered porous Ti-TiB, NiTi and $\text{Ca}_3(\text{PO}_4)_2$ replacements for bone defects, and bone tissue engineering, through the following SHS reaction systems: $(y+z)\text{Ti}+xz\text{B}=y\text{Ti}+z\text{TiB}_x$ (1), $\text{Ni}+\text{Ti}=\text{NiTi}$ (2), $3\text{CaO}+\text{P}_2\text{O}_5=\text{Ca}_3(\text{PO}_4)_2$ (3).

Reaction stoichiometry of the combustion synthesis reaction affects the exothermicity and therefore, the combustion temperature (T_c). Increasing the amount of boron in the reaction mixture resulted in the tendency for combustion temperature (T_c) to increase from 2700K to 3300K. The results indicate that increased amounts of boron in the reactant mixture yielded a product containing TiB_2 that is more porous than those containing TiB. The formation of Ti_3B_4 decreases the porosity of products in the both $\text{TiB}_2+\text{Ti}_3\text{B}_4$ and $\text{TiB}+\text{Ti}_3\text{B}_4$ phase regions. DTA provided information on the enthalpy and mass changes of the SHS reaction (3), Figure 1. The data indicate a large mass loss at the start of the reaction and a continual mass loss throughout the reaction as denoted by the peaks that do not match available thermodynamic data. The DTA shows two large exothermic peaks. The initial mass loss, caused probably by the boiling or sublimation of P_2O_5 , may give insight to the XRD pattern yielding phosphorus deficient calcium phosphate materials. The XRD analysis of the porous NiTi product (reaction 2) show that some Ni_3Ti and NiTi_2 , were also formed together with NiTi due to the narrow area of equiatomic NiTi phase in the Ni-Ti phase diagram. The equiatomic NiTi phase exhibits superelasticity and shape memory effects desired for certain implant applications. Increased control of the SHS reaction is being developed to ensure a greater amount of equiatomic NiTi is produced during the SHS reaction. Long term, high temperature annealing has been found to increase the NiTi content in that material. For reaction (3), the x-ray diffraction pattern shows that SHS produced calcium phosphate materials such as Ca_3P and Ca_5P_8 , but perhaps not the desired product ($\text{Ca}_3(\text{PO}_4)_2$) as expected. Fast cooling of the sample may be the cause for the large amount of amorphous product. There may exist metastable phases and the material may decompose or restructure over time. Further x-ray diffraction analysis of the aged material may confirm this hypothesis.

The green density of the reactant pellet can have a significant effect on the combustion synthesis reaction since, as the green density increases so will the thermal conductivity depending on the physical properties of the reactant[4]. Green density greatly affects the combustion velocity, combustion temperature, apparent porosity and pore size. As the green density is decreased in the Ti-TiB combustion synthesis reaction (1), the velocity significantly decreases, the combustion temperature decreases to approximately 1973 K, the apparent porosity increases and the average pore size increases from $50\mu\text{m}$ (65% relative green density) to $500\mu\text{m}$ (30% relative green density). A similar effect of green density on the pore size of the synthesized NiTi was also found, but the extent of porosity was less than in the Ti-TiB system. Decreasing the green density, only slightly increased the average pore size which also became more even. For reaction (3), it is not known as of yet if the green density affects the amount of amorphous to crystalline phases. A less dense material should have greater heat loss and therefore may form more crystalline phase. Green Density provides the SHS process with one additional degree of freedom to control the structural/chemical makeup of the biomaterial. For reaction (3), Figure 2 indicates that the material exhibits porosity similar to that of natural bone (100-400microns) together with some very large interconnected pores that might aid in vascularization. For samples that had a green density of $2.1\text{g}/\text{cm}^3$, the largest pores exhibited widths of approximately 0.5mm. Samples with green densities less than $2.1\text{g}/\text{cm}^3$ exhibited maximum pore widths of 1-2mm. All samples contained pores that ranged from 100-400 microns, similar to that of natural bone tissue. This pore morphology and structure increase the possibility of using this process and method for bone tissue infiltration.

The structure of the porous SHS product is highly sensitive to the internal and external forces which deform the sample. The internal forces develop due to the presence of volatile impurities or gasifying agent in the mixture. In the combustion wave, these components release the gas which expands the hot product of the synthesis reaction[5]. Recent results show that B_2O_3 is the best gasifying agent for the Ti-TiB system. With incorporation of B_2O_3 as a gasifying agent, gas is released at the propagating combustion front, and the apparent porosity increases to 60%. The pore size increases from $50\mu m$ to $300-500\mu m$, which is comparable to that of natural bone. Additionally, B_2O_3 helps to form a composite microstructure that more closely resembles natural bone.

The porous SHS product is also sensitive to the external forces present during the reaction. One of the external forces is gravity. The gravitational force retards the expansion of the porous SHS product. Brief exposure (20 sec) to variable gravity as provided by parabolic flights in the NASA KC-135 aircraft allows examination of these gravitational forces on the SHS reaction. As shown in Figure 3, the porosity of specimens reacted under low gravity condition is always higher than that conducted under high gravity conditions. Unfortunately, the maximum time of low gravity condition in parabolic flight is insufficient for the SHS reaction to be completed. As such the end of the solidification process is subjected to the 2g effect in the gravity cycle. It is therefore anticipated that longer exposure to low gravity conditions (shuttle or ISS), should show great difference in porosity compared with reacting under 1g condition.

The Ti-TiB porous sample was subjected to an air oxidation of ($900^\circ C$ for 12 hours) to establish a strong biocompatible TiO_2 layer in the surface prior to using these materials for *in-vitro* bone growth tests. Preliminary histological results of the Ti-TiB sample with the TiO_2 layer placed on the skull of Long-Evans rats indicated that there is some bone ingrowth when the implant is infiltrated with bovine collagen as shown in Figure 4.

The results presented here illustrate that composition, green density, gasifying agents, and gravity are important parameters for controlling the combustion synthesis of advanced porous material systems. These parameters greatly influence the SHS product porosity, pore size, microstructure and mechanical properties. Controlling the SHS reaction parameters, porous bodies of a variety of matrix combinations can be formed with a reproducible amount of porosity and microstructural features to engineer materials with desired mechanical properties (which are currently being evaluated). These composites can be further improved to meet consumer requirements.

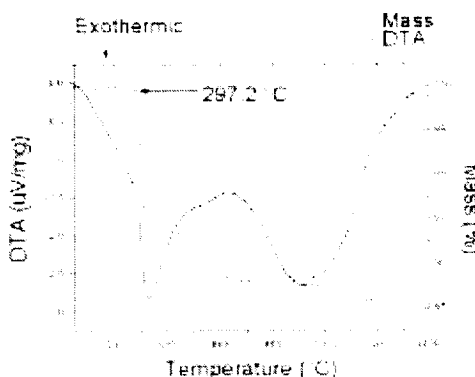


Figure 1. DTA and a mass change profiles of the SHS reaction (3) using a heating rate of $50^\circ/min$ in alumina crucibles under argon flowing at 30 ml/min .

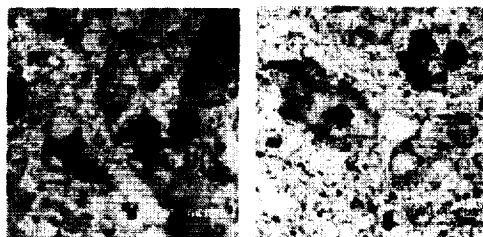


Figure 2. SEM photo micrographs of samples with a green density of $6 \times 10^{-4} \text{ g/cm}^3$ under 2 different magnifications.

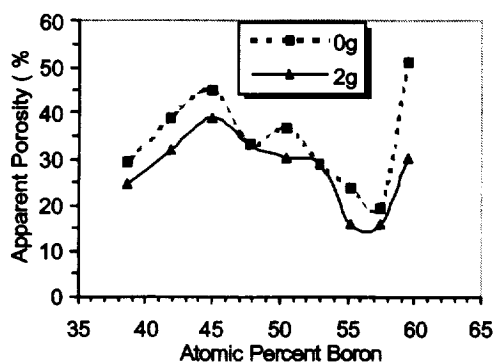


Figure 3. Gravity effect on porosity of Ti-TiB_x SHS products



Figure 4. Histological slide result of Ti-TiB-TiO₂ implant.

REFERENCE

- [1] Joon B. Park and Roderic S. Lakes. Biomaterials An Introduction Second Edition. 1992.
- [2] Kent JN, Zide MF (1984) Wound healing: bone and biomaterials. Otolaryngol Clin North Am 17:273-319
- [3] Black J, (1999) Biological Performance of Materials, Marcel Dekker, Inc., New York
- [4] Moore, J. J. An Examination of the Thermochemistry of Combustion Synthesis Reactions, Processing and Fabrication of Advanced Materials III, edited by V. A. Ravi, T. S. Srivatsan and J. J. Moore, The Minerals, Metals, and Materials Society, 1994; 817-831.
- [5] Merzhanov, A. G. Regularities and mechanism of Pyrotechnic Titanium-Boron Mixture, Proceedings of the Fourth Symposium on chemical Problems Connected with the Stability of Explosives, Mole, Sweden, 1975; 381-401.

MECHANISTIC STUDIES OF COMBUSTION AND STRUCTURE FORMATION DURING SYNTHESIS OF ADVANCED MATERIALS

A. Varma, C. Lau and A.S. Mukasyan

*Department of Chemical Engineering, and Center for Molecularly Engineered Materials
University of Notre Dame, Notre Dame, IN 46556, USA*

INTRODUCTION

Combustion in a variety of heterogeneous systems, leading to the synthesis of advanced materials [1-4], is characterized by high temperatures (2000-3500 K) and heating rates (up to 10^6 K/s) at and ahead of the reaction front. These high temperatures generate liquids and gases which are subject to gravity-driven flow. The removal of such gravitational effects is likely to provide increased control of the reaction front, with a consequent improvement in control of the microstructure of the synthesized products. Thus, microgravity (μ g) experiments lead to major advances in the understanding of fundamental aspects of *combustion* and *structure formation* under the extreme conditions of the combustion synthesis (CS) wave. In addition, the specific features of microgravity environment allow one to produce unique materials, which cannot be obtained under terrestrial conditions. The current research is a logic continuation of our previous work [cf.5, 6] on investigations of the fundamental phenomena of combustion and structure formation that occur at the high temperatures achieved in a CS wave.

Our research is being conducted in three main directions:

1. *Microstructural Transformations during Combustion Synthesis of Metal-Ceramic Composites.* The studies are devoted to the investigation of particle growth during CS of intermetallic-ceramic composites, synthesized from nickel, aluminum, titanium, and boron metal reactants. To determine the mechanisms of particle growth, the investigation varies the relative amount of components in the initial mixture to yield combustion wave products with different ratios of solid and liquid phases, under 1g and μ g conditions.
2. *Mechanisms of Heat Transfer during Reactions in Heterogeneous Media.* Specifically, new phenomena of gasless combustion wave propagation in heterogeneous media with porosity higher than that achievable in normal gravity conditions, are being studied. Two types of mixtures are investigated: clad powders, where contact between reactants occurs within each particle, and mixtures of elemental powders, where interparticle contacts are important for the reaction.
3. *Mechanistic Studies of Phase Separation in Combustion of Thermite Systems.* Studies are devoted to experiments on thermite systems (metal oxide-reducing metal) where phase separation processes occur to produce alloys with tailored compositions and properties. The separation may be either gravity-driven or due to surface forces, and systematic studies to elucidate the true mechanism are being conducted.

The knowledge obtained will be used to find the most promising ways of controlling the microstructure and properties of combustion-synthesized materials. Low-gravity experiments are essential to create idealized an environment for insights into the physics and chemistry of advanced material synthesis processes.

EXPERIMENTAL

The sample was placed in the reaction chamber, which was evacuated ($\sim 10^{-2}$ atm) and then filled with inert gas (high purity argon) up to 1 atm. An electrically heated tungsten coil initiated the combustion reaction, typically from bottom of the sample. A microcomputer (Tattletale) synchronized ignition and temperature measurements, with the experimental conditions (e.g. gravity). Combustion front propagation was recorded through a quartz window by using video camera (SONY CCD-IRIS). The velocity of combustion front propagation was determined by statistical analysis of the obtained video images (30 frames/s). A two-color infrared pyrometer (IRCON MIRAGE, MR-OR10-99C10) and thermocouples (W-Re 5/26) were used to measure the sample temperature-time history. The details of the experimental setup and procedure are described elsewhere [cf.5].

Quenching, which involves rapid cooling of the combustion front, was utilized to investigate the mechanisms of microstructural transformation taking place during CS. Different quenching methods have been reported and their intrinsic limitations have been discussed in the literature [cf.7]. In the present work, the most efficient method, i.e. quenching by massive copper block was used. After quenching, the phase composition and microstructures in different zones of the combustion wave were identified using layer-by-layer analysis of the sample from its tip (initial mixture) to the top (final product), to elucidate the evolution of material structure formation during CS. These microstructures were analyzed using scanning electron microscopy (SEM, JEOL 6400) along with energy dispersive X-ray spectrometry (EDXS, KEVEX) and advanced image analysis software (IMAGE PRO-PLUS 4.0).

All experiments were conducted identically in both terrestrial (1 g) and microgravity (10^{-2} g) conditions to make direct comparison and to identify the role of gravity on mechanism of combustion and microstructure formation. Microgravity experiments were conducted during parabolic flights of KC-135 aircraft in NASA Glenn Research Center, Cleveland, OH, providing microgravity environment ($\sim 10^{-2}$ g) for about 20 s.

RESULTS AND DISCUSSION

Microstructural Transformations during Combustion Synthesis of Metal-Ceramic Composites

Combustion synthesis of NiAl-based materials reinforced by TiB_2 particles was investigated under both 1g and μg conditions [8]. It was shown that the synthesized metal matrix composites (MMC) are characterized by fine ($<1 \mu\text{m}$) reinforced particulate, which have strong bonding along their entire surface with matrix (NiAl) and are distributed uniformly in it. It was also found that μg leads to a decrease in the average TiB_2 particle size, while higher volume fraction of NiAl component in the material leads to the formation of coarser reinforced particulates. The results of statistical analysis on average size, d , of TiB_2 grains for different compositions are presented in Table I.

Table I. Average grain size of TiB_2 after CS under different gravity conditions

Volume fraction of TiB_2 ; Mole ratio TiB_2/NiAl	Terrestrial		Microgravity	
	Average grain size, μm	σ μm	Average grain size, μm	σ μm
23 %; 1/4	0.65	0.32	0.50	0.27
26 %; 1/3.5	0.44	0.15	0.42	0.14
33 %; 1/2.5	0.38	0.14	0.38	0.13

It can be seen that d is generally smaller for materials synthesized under microgravity. The standard deviation σ , characterizing the uniformity of grain size distribution, is also somewhat smaller for materials formed under 10^{-2} g conditions. Thus *finer and more uniform* microstructures are obtained under reduced gravity. However, the influence of gravity is less pronounced for compositions with smaller volume fraction of NiAl matrix.

The mechanism of structure formation of different MMCs during CS was identified by using the quenching technique. Statistical analysis of typical microstructures and phase compositions in different cross-sections of quenched samples revealed that the process of microstructure formation during CS can in general be divided into four zones, which are characterized as follows:

- Zone 1:* reaction between Ni and Al with formation of primarily NiAl phase, while Ti and B remain essentially unreacted;
- Zone 2:* dissolution of Ti and B in NiAl phase with formation of complex Ni-Al-Ti-B solution;
- Zone 3:* crystallization of solid TiB₂ particles from the solution and their growth in NiAl-rich liquid matrix;
- Zone 4:* growth and uniform dispersion of TiB₂ particles in NiAl matrix, to yield the final product.

All zones described above were qualitatively present in all samples synthesized in both 1g and μ g conditions. However, the characteristic length of each zone in samples reacted under microgravity was *larger* as compared with terrestrial product (see Table II). Thus, an overall *decrease* of microstructural transformation rates was observed under μ g.

Table II. The length of characteristic microstructural zones (TiB₂/NiAl = 1/4)

Zone	Terrestrial	Microgravity
	L, μ m	L, μ m
1	300	400
2	4700	5850
3	3250	4250

Mechanisms of Heat Transfer during Reactions in Heterogeneous Media

It was shown that combustion of complex clad particles, where one metal forms the core (Al) while the other constitutes the shell (Ni), exhibits novel phenomena. It has been demonstrated by experiments conducted under weightless conditions in drop tower [5] and during parabolic flights on DC-9 aircraft [6], as well as confirmed by studies made in "MIR" space station [9], that it is possible to organize a so-called *contactless* combustion regime [10] with such particles, where radiation heat transfer controls the process. In this case, we showed [11] that by changing density of the reaction mixture, the mechanism of heat transfer which controls the reaction front propagation can be varied: radiation for low densities (in μ g conditions), gas heat conduction for intermediate values, and heat conduction through condensed skeleton for high sample densities (see Figure 1).

Further, the process of outer shell cracking plays an important role in the mechanism of combustion wave propagation. On one hand, more refractory shell (Ni) prevents the reaction medium from rapid agglomeration, while on the other hand, cracking of the shell followed by spreading of molten Al ahead of the front is important for combustion wave propagation in this system. The results suggest that combustion of complex particles with different initial densities including particle clouds) should be investigated under different oxidizing atmospheres, and this is planned for the near future.

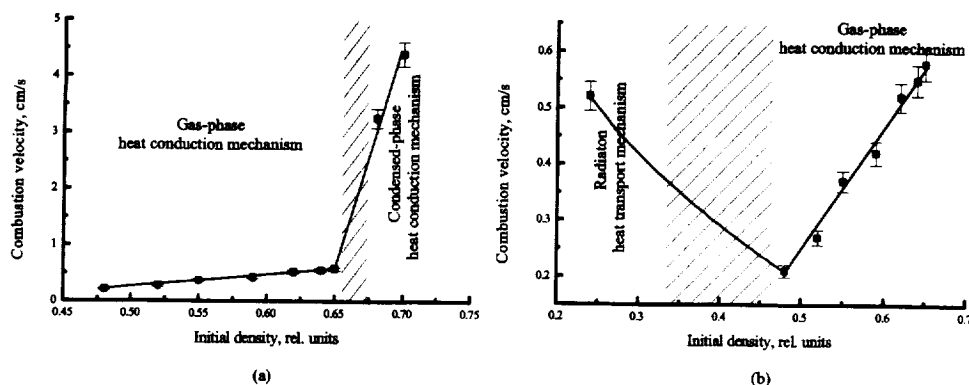


Figure 1. The dependence of combustion velocity on sample initial density.

Mechanistic Studies of Phase Separation in Combustion of Thermite Systems

Studies are devoted to experiments on thermite systems (metal oxide-reducing metal) where phase separation processes occur to produce alloys with tailored compositions and properties. Such reaction systems are important in various applications, including production of orthopedic implant materials. Due to high reaction exothermicity, the process results in a significant increase of temperature (up to 3000 °C) which is higher than melting points of all products. Since the products differ in density, phase separation may be a gravity-driven process: the heavy (metallic phase) settles while the light (slag) phase floats. However, our preliminary experiments demonstrate that a high degree of phase separation also occurs under μg conditions. Thus it is necessary to conduct more detailed research to elucidate the true mechanism of this phenomenon.

Three reaction systems (MoO_3-Al , Co_3O_4-Al and V_2O_5-Al) were selected for investigation, in which density differences between the products are different: compare $\rho_{Mo} = 10.22 \text{ g/cm}^3$, $\rho_{Co} = 8.92 \text{ g/cm}^3$, $\rho_V = 6.11 \text{ g/cm}^3$, $\rho_{Al_2O_3} = 2.8 \text{ g/cm}^3$. Both terrestrial and μg studies involving experiments under a wide range of conditions are currently in progress.

ACKNOWLEDGEMENTS

This work was supported by NASA grant NAG3-2213. We gratefully acknowledge the help of Mr. Robert Friedman and Peter Sunderland in managing the project.

REFERENCES

1. Merzhanov, A.G., and Borovinskaya, I.P., *Dokl. Chem.*, **204**: 429 (1972).
2. Moore, J.J., and Feng, H.J., *Prog. Mater. Sci.*, **39**: 243 (1995).
3. Varma, A., Rogachev, A., Mukasyan, A. and Hwang, *Adv. Chem. Eng.*, **24**: 79 (1998).
4. Varma, A., *Sci. Amer.* **283** (2): 58 (2000).
5. Mukasyan, A., Pelekh, A., Varma, A., Rogachev, A. & Jenkins, A. *AIAA J.*, **35**: 1821 (1997).
6. Mukasyan, A., Pelekh, A. and Varma, A. *J. Mater. Syn. Proc.* **5**: 391 (1997).
7. Mukasyan, A., and Borovinskaya I. P., *Intl. J. SHS.*, **1**: 55 (1992).
8. Lau, C., Mukasyan, A., Pelekh, A. and Varma, A., *J. Mat. Res.*, (2001, in press).
9. Merzhanov, A.G., *Proc. II Eur. Symp. on Fluids in Space*, Naples, Italy: 57 (1996).
10. Merzhanov, A.G., Rogachev, A.V., and Sytshev, A.E., *Dokl. Chem.*, **383**: 45 (1999).
11. Mukasyan, A.S., Lau, C. and Varma, A., *Comb. Sci. Tech.*, (2001, in review).

FILTRATION COMBUSTION IN SMOLDERING AND SHS ¹

BERNARD J. MATKOWSKY

Northwestern University
Evanston, Illinois

INTRODUCTION Smolder waves and SHS (self-propagating high-temperature synthesis) waves are both examples of filtration combustion waves propagating in porous media. Smoldering combustion is important for the study of fire safety. Smoldering itself can cause damage, its products are toxic and it can also lead to the more dangerous gas phase combustion which corresponds to faster propagation at higher temperatures. In SHS, a porous solid sample, consisting of a finely ground powder mixture of reactants, is ignited at one end. A high temperature thermal wave, having a frontal structure, then propagates through the sample converting reactants to products. The SHS technology appears to enjoy a number of advantages over the conventional technology, in which the sample is placed in a furnace and "baked" until it is "well done". The advantages include shorter synthesis times, greater economy, in that the internal energy of the reactions is employed rather than the costly external energy of the furnace, purer products, simpler equipment and no intrinsic limitation on the size of the sample to be synthesized, as exists in the conventional technology.

When delivery of reactants through the pores to the reaction site is an important aspect of the combustion process, it is referred to as filtration combustion. The two types of filtration combustion have a similar mathematical formulation, describing the ignition, propagation and extinction of combustion waves in porous media. The goal in each case, however, is different. In smoldering the desired goal is to prevent propagation, whereas in SHS the goal is to insure propagation of the combustion wave, leading to the synthesis of desired products. In addition, the scales in the two areas of application differ. Smoldering generally occurs at lower temperatures and propagation velocities than in SHS. Nevertheless, the two applications have much in common, so that what is learned in one application can be used to advantage in the other.

In porous media melting often occurs ahead of the propagating combustion wave. In certain cases there is so much melting that the porous solid structure is destroyed, e.g., by melting, and a suspension arises, consisting of a liquid bath containing solid particles and/or gas bubbles. The resulting combustion wave is referred to as a liquid flame.

We have considered a number of problems involving filtration combustion. Here, we describe four such studies: (A) **rapid buoyant filtration combustion waves**, (B) **diffusion driven combustion waves**, (C) **rapidly propagating liquid flames in gravitational fields**, (D) **gas-phase influence on liquid flames in gravitational fields**.

RAPID BUOYANT FILTRATION COMBUSTION WAVES In this investigation we describe a new type of FC wave, which arises due to the imbalance between the temperatures of the solid and gas phases. These waves can propagate much more rapidly than FC waves driven by diffusion of heat, and may be observed even in mixtures with very low thermal conductivity. Thus,

¹Work funded under NASA Grant NAG3-2209.

it poses a greater danger from the point of view of fire safety. From the point of view of SHS such waves may be desirable since products may be synthesized more rapidly.

We consider heterogeneous (solid/gas) combustion in a porous sample open to gas flow only at the top and the bottom. The reaction is initiated at the bottom of the sample and the combustion wave travels in the direction of gas filtration. There is a localized region of high temperature either ahead of or behind (depending on certain parameters) the combustion layer. Hot gas contained within this region rises due to gravity induced buoyant forces, thus drawing cool fresh gas containing oxidizer in through the bottom of the sample. A two-temperature model is employed to analyze upward buoyant filtration combustion (BFC) waves, with distinct temperatures for the solid and gas phases.

We focus on the reaction leading structure, in which the reaction occurs at the leading edge of the heated portion of the sample. The gas infiltrating through the hot product region significantly enhances the propagation of the combustion wave. For a relatively small gas flux, the infiltrating gas delivers heat from the hot product region to the reaction zone, thus increasing the maximum burning temperature, and hence, the combustion rate. This is referred to as the superadiabatic effect. The propagation of such waves is controlled by the diffusion of heat released in the reaction to the preheat zone. Diffusively driven BFC waves have been studied extensively using one-temperature models. One-temperature models assume a very large rate of interphase heat exchange between the solid and the gas, so that thermal equilibrium is attained almost immediately. However, if the gas flux is sufficiently large, the solid and the gas do not have sufficient time to equilibrate, and hence, the underlying assumption of one-temperature models is no longer valid. That is, one-temperature models are only appropriate for describing slowly propagating BFC waves in which the time of contact between the solid and the gas is sufficiently large for rapid thermal equilibrium to occur. However, not all BFC waves are slowly propagating. There can also be rapidly propagating BFC waves, in which case a two-temperature model, with the solid and the gas attaining distinct temperatures, is more appropriate.

For a relatively large gas flux, an alternative mechanism of enhancement occurs, in that the maximum combustion temperature is increased as a result of increasing the effective initial temperature of the solid. The propagation of such waves is controlled by the convection of heat stored in the product to the preheat zone. Convectively driven BFC waves depend on a pronounced temperature difference between the solid and the gas, and therefore, cannot be described with a one-temperature model. We employ a two-temperature model to study upward propagating BFC waves. In the appropriate limits, we consider both diffusively and convectively driven BFC waves, with the main interest lying in the latter, which requires that a two-temperature model be used. We analyze both modes of propagation and compare and contrast the results.

The filtration of gas may be driven by various mechanisms. A process which is simpler than, yet similar to, upward BFC is forced forward FC, in which the incoming gas flux is fixed by an external source. In BFC, gas flux is induced by the combustion process and must be determined, whereas in forced forward FC, the hydrodynamic description is reduced to prescribing the gas flux at the inlet of the sample. By comparing and contrasting convective upward BFC waves and convective forced forward FC waves, we determine the effects of a buoyancy driven gas flux, as opposed to a fixed gas flux, on convective FC waves.

DIFFUSION DRIVEN COMBUSTION WAVES Filtration of gas containing oxidizer, to the reaction zone in a porous medium, due, e.g., to a buoyancy force or to an external pressure gradient, leads to the propagation of filtration combustion (FC) waves. The exothermic reaction occurs between the fuel component of the solid matrix and the oxidizer. In this investigation, we analyze the ability of a reaction wave to propagate in a porous medium without the aid of filtration, as might occur in microgravity. One possible mechanism of propagation is that the wave is driven by diffusion of oxidizer from the environment. The solution of the combustion problem describing diffusion driven waves is similar to the solution of the Stefan problem describing the propagation

of phase transition waves. The difference is that in the combustion problem the temperature is not prescribed, but rather, is determined as part of the solution. The length of samples in which such self-sustained combustion waves can occur, must exceed a critical value which strongly depends on the combustion temperature T_b . Smaller values of T_b require longer sample lengths for diffusion driven combustion waves to exist. Because of their relatively small velocity, diffusion driven waves are considered to be relevant for the case of low heat losses, which occur for large diameter samples or in microgravity conditions.

Another possible mechanism of porous medium combustion describes waves which propagate by consuming the oxidizer initially stored in the pores of the sample. This occurs for abnormally high pressure and gas density. In this case, uniformly propagating planar waves, which are kinetically controlled, can propagate. Diffusion of oxidizer decreases the wave velocity. In addition to the reaction and diffusion layers, the uniformly propagating wave structure includes a layer with a pressure gradient, where the gas motion is induced by the production or consumption of the gas in the reaction as well as by thermal expansion of the gas. The width of this zone determines the scale of the combustion wave in the porous medium.

RAPIDLY PROPAGATING LIQUID FLAMES IN GRAVITATIONAL FIELDS We consider the combustion, in a gravitational field, of a porous solid, in which the high temperature ahead of the reaction zone destroys the solid, due, e.g. to melting of some of the solid components. Thus, a suspension is formed, consisting of a liquid bath containing solid or liquid particles. The resulting combustion wave is referred to as a liquid flame. Processes such as heat and mass transfer as well as chemical reactions in the suspension determine the structure of the liquid flame and its propagation velocity. Under the influence of gravitational forces there is the possibility of relative motion of the liquid and solid. Previous theoretical analyses considered the rate of heat transfer between the solid and liquid phases to be sufficiently large that their two distinct temperatures rapidly equilibrated to a single temperature. In addition to this case, we also consider the case when the rate of heat transfer is not so large and the model involves the separate temperatures of the solid and liquid phases. We find that multiplicity of traveling wave structures is possible. In particular, in addition to a low velocity structure, which is essentially the same as that obtained from the one temperature description, we find a high velocity structure, which does not exist in the one temperature description, but rather depends on the fact that the solid and fluid temperatures differ from each other. Both structures can exist for the same parameter values in a given range. We describe the dependence of the combustion characteristics of the two structures on gravitational forces and other factors. In particular, we compare the characteristics in gravity and microgravity environments.

GAS PHASE INFLUENCE ON LIQUID FLAMES IN GRAVITATIONAL FIELDS A porous solid is ignited at one end. A high temperature combustion wave then propagates through the sample. In this process, melting of some or all the components is often observed. Therefore, we study combustion waves propagating through a medium whose combustion temperature exceeds the melting temperatures of many components. The solid matrix is thus destroyed by the propagating combustion wave due to melting ahead of the reaction zone, and a liquid bath is formed which contains gaseous bubbles. The waves propagate in the presence of a gravitational field. Due to the effect of gravity, there is relative motion between the rising bubbles and the descending bath, which affects the composition of the medium, its thermophysical properties, the "liquid flame" structure, and the propagation velocity. To enhance our understanding of phenomena associated with the interaction of the relative motion with the propagating combustion wave we formulate and analyze a relatively simple mathematical model of liquid flames in a gravitational field. We describe the wave structure and combustion characteristics including the combustion velocity. We compare our results to existing experimental observations and suggest new experiments to be performed. We consider the effects of gravity and, in particular, examine both microgravity and large gravity conditions.

References

- [1] C.W. Wahle, B.J. Matkowsky, *Rapid, Upward Buoyant Filtration Combustion Waves Driven by Convection*, Comb. & Flame **124**, (2001), 14.
- [2] A.P. Aldushin, B.J. Matkowsky, *Diffusion Driven Combustion Waves in Porous Media*, Comb. Sci. & Tech. **156**, (2000), 221.
- [3] K.G. Shkadinsky, G.V. Shkadinskaya, B.J. Matkowsky, *Slowly and Rapidly Propagating "Liquid Flames" in Gravitational Fields*, Comb. Sci. & Tech. **157**, (2000), 21.
- [4] K.G. Shkadinsky, G.V. Shkadinskaya, B.J. Matkowsky, *Gas-Phase Influence on Quasisteady "Liquid Flames" in Gravitational Fields*, Comb. Sci. & Tech. **157**, (2000), 87.

EFFECT OF MICROGRAVITY ON HIGH-TEMPERATURE SELF-PROPAGATING REACTIONS

G. Cao*, R. Orrù*, E. Medda, A. Locci, A. Cincotti

Dipartimento di Ingegneria Chimica e Materiali, Centro Studi sulle Reazioni Autopropaganti (CESRA) and Unità di Ricerca del Consorzio Interuniversitario Nazionale di Scienza e Tecnologia dei Materiali, Università di Cagliari, Piazza d'Armi, 09123 Cagliari, Italy
tel.: +39-070-6755058, fax: +39-070-6755057, e-mail: cao@visnu.dicm.unica.it

ABSTRACT

The effects of gravity on the combustion characteristics and product microstructure of the metal ceramic composite Fe/TiC and the thermite system $\text{Cu}_2\text{O}/\text{Al}/\text{Al}_2\text{O}_3$ were studied under both normal and low gravity conditions. Under normal gravity conditions, pellets were ignited in the same orientation relative to the gravity vector. Low gravity self-propagating reactions were carried out aboard reduced gravity aircraft, specifically NASA's KC-135. For the system Ti/C/Fe finer and more uniform microstructures are obtained under reduced gravity. For the system $\text{Cu}_2\text{O}/\text{Al}/\text{Al}_2\text{O}_3$ finer size of the refractory phase is obtained under reduced gravity.

INTRODUCTION

Self-propagating High-temperature Synthesis (SHS) is a materials synthesis technique characterized by the fact that once the starting mixture is ignited by means of external thermal sources for relatively short times, highly exothermic reactions may propagate through the mixture in the form of a self-sustained combustion wave leading to final products progressively without requiring additional energy (cf. Merzhanov and Borovinskaya, 1972; Munir and Anselmi Tamburini, 1989; Merzhanov, 1995; Varma et al., 1998). SHS's main characteristics are process simplicity, short reaction time, easy-to-build equipments, low-energy requirements and the possibility of obtaining complex or metastable phases. SHS reactions and related structure formation mechanisms involve several stages, i.e. melting of reactants and products at, or ahead, of the reaction front, spreading of the melt, generation of gaseous species, droplet coalescence, diffusion and convection, buoyancy of solid particles and densification of liquid products, most of which are affected by gravity. In particular, generated liquid and gaseous species will be subject to gravity-driven fluid flow and vapor transport and convection, which are likely to significantly affect both SHS reaction stability and the morphology of product phases. It is then apparent the importance of investigating the effect of gravity on the above mentioned phenomena in order to identify the detailed mechanism of reaction evolution and structure formation. However, there has been only a limited amount of work conducted to investigate the effect of gravity on the SHS of advanced materials. Along these lines, interesting results have been obtained in the last decade using high gravity environment induced by centrifugal processing (cf. Karataskov et al., 1985; Merzhanov and Yuxhvid, 1990; Odawara, 1990; Kachin and Yuxhvid, 1992; Orrù et al., 1995; Yuxhvid et al., 1997; Rogachev et al., 2000a; Rogachev et al., 2000b). The possibility of obtaining layered and functionally graded materials, ceramic-lined pipes, compact materials, metal-matrix composites, alloys, etc. has been demonstrated. It was shown that the microstructure of products strongly depends on centrifugal overloads. In particular, the effect of gravity is mainly related to the volume fraction of liquid formed and its corresponding lifetime. On the other hand, low gravity experiments are able to permit the general mechanism of combustion and structure formation to be revealed without disturbing effects of gravity (cf. Medda et al., 2000, and references therein). The experimental results, which may be classified into two main groups, i.e. the synthesis of highly porous materials and the influence of gravity on the microstructure of final

products, clearly demonstrate that gravity may significantly affect the process of structure formation during SHS. In particular, it was shown that products with finer and more uniform microstructure are obtained under low gravity conditions with respect to normal ones.

In this work the effect of gravity on the SHS of the metal-ceramic composite Fe/TiC and the thermite system $\text{Cu}_2\text{O}/\text{Al}/\text{Al}_2\text{O}_3$ is studied under both normal and low gravity conditions. The selection of these two systems was made based on the fact that the former one is particularly suitable for thermal spraying application and thus requires specific investigation to eventually optimize its synthesis, while the latter one might become of great interest for welding processes aboard the International Space Station (ISS).

It should be noted that this work represents the first experimental investigation on the SHS technique conducted under low gravity conditions by a European team, while previous works have been performed by research groups from Russia, USA, Japan and Canada, (cf. Medda et al., 2000, and references therein).

RESULTS AND DISCUSSION

The starting mixture were prepared by mixing the reactants according to the following reactions: $\text{Ti}+\text{C}+\text{Fe}\rightarrow\text{TiC}+\text{Fe}$, for the metal-ceramic composite Fe/TiC, and $3\text{Cu}_2\text{O}+6\text{Al}\rightarrow2\text{Cu}_3\text{Al}_2+\text{Al}_2\text{O}_3$, for the thermite system $\text{Cu}_2\text{O}/\text{Al}/\text{Al}_2\text{O}_3$. Details on the experimental set-up and procedure are reported elsewhere (cf. Medda et al., 2000) for sake of brevity. However, it is worth noting that the experiments were conducted using the Guigné International's COSYMTM facility under normal gravity as well as low gravity aboard reduced gravity aircraft, specifically NASA's KC-135. In the Ti/C/Fe and $\text{Cu}_2\text{O}/\text{Al}/\text{Al}_2\text{O}_3$ systems, the amount of Fe and Al_2O_3 in the initial mixture was varied to obtain final products suitable for thermal spraying application and welding processes, respectively. The maximum combustion temperature measured for the samples related to the system Ti/C/Fe are reported in Table 1 for the case of terrestrial and microgravity conditions.

Table 1. Measured combustion temperatures.

Sample	Temperature (°C)	
	Normal gravity	Microgravity
Ti/C/10wt.%Fe	1933	1733
Ti/C/20wt.%Fe	1866	1805
Ti/C/30wt.%Fe	1888	1833

It can be seen that the temperature values are lower under microgravity as compared with terrestrial conditions in accordance with previous investigations (cf. Medda et al., 2000, and references therein). On the other hand, the measurement of the temperatures for the system $\text{Cu}_2\text{O}/\text{Al}/\text{Al}_2\text{O}_3$ was somehow difficult and therefore the corresponding values are not reported. It is worth mentioning that the values of the velocity of front propagation measured for the two systems investigated in this work are within the range of typical levels of SHS processes.

From the characterization of the obtained product by XRD, it results that, for the case of TiC/Fe system, apart from the expected TiC and Fe, Fe_3C is also formed. This is due to the presence of the C obtained as a combustion product of the organic binder added to the starting mixture. On the other hand, for the case of the system $\text{Cu}_2\text{O}/\text{Al}/\text{Al}_2\text{O}_3$, non reacted Cu is present in the combustion products, together with corundum (Al_2O_3) and the intermetallic phase (Cu_9Al_4). Typical microstructures of the composite Fe/TiC under terrestrial and microgravity conditions are shown in Figures 1a and 1b, respectively. Both are characterized by fine grains of TiC (dark

phase) dispersed in Fe (light phase) matrix. It may be seen that finer and more uniform microstructures are obtained under reduced gravity. In addition, it is worth noting that the results shown in Figure 1 are also representative of compositions with smaller amount of Fe, i.e. samples Ti/C/10wt.%Fe and Ti/C/20wt.%Fe.

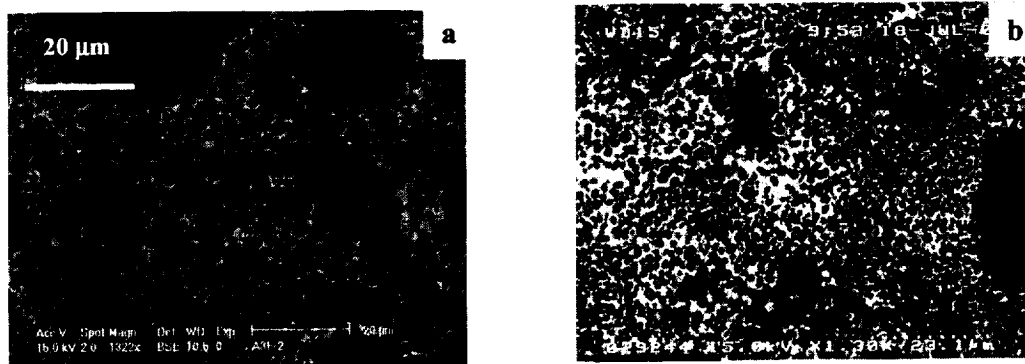


Figure 1. Back Scattered Electron images of the microstructure of the composite obtained when reacting the system Ti/C/30wt.%Fe under different gravity conditions: (a) terrestrial; (b) microgravity.

For the case of the $\text{Cu}_2\text{O}/\text{Al}/\text{Al}_2\text{O}_3$ system, whose results are not reported here for sake of brevity, the SEM investigation revealed that the intermetallic species Cu_9Al_4 is surrounded by the refractory compound Al_2O_3 . In addition, it was found that finer size of the refractory phase Al_2O_3 is obtained under reduced gravity, in accordance with previous results available in the literature (cf. Mukasyan, 1997). While for the system $\text{Cu}_2\text{O}/\text{Al}/\text{Al}_2\text{O}_3$ is difficult at this stage to provide additional results, further considerations are made in the sequel for the system Ti/C/Fe. Specifically, since the combustion temperatures measured are above the melting point of Ti (1668°C) and Fe (1358°C), metals in the samples during the combustion reaction should exist in molten state (cf. Choi and Rhee, 1993). In our Ti/C/Fe system there are two fluids: Ar gas and the molten metal matrix phase ahead or at the combustion front. While convective flow of Ar plays an important role when the pellet is ignited from the bottom under normal gravity conditions, its effect is almost negligible under microgravity conditions (cf. Yi et al., 1998). Therefore the amount of the liquid phase present ahead or at the combustion front plays the most important role in process evolution and may influence the mechanism of microstructure formation as postulated by several authors (cf. Mukasyan, 1997; Yi et al., 1998). In addition, in our case solid and liquid phases coexist for some period thus giving rise to the microstructure of the final products. Although the mechanism of the structure formation of TiC/Fe has never been investigated under microgravity conditions, from the results obtained under terrestrial gravity (cf. Choi and Rhee, 1993), it may be postulated that after the dissolution and diffusion of C into the liquid mixture of Ti and Fe, the formation of TiC and its subsequent grain growth occur. Thus two main mechanisms can be responsible of the product microstructure obtained under different gravity conditions: Ostwald ripening and buoyancy enhanced coalescence. Due to first mechanism, larger particles growth at the expense of smaller ones so as to lower the free energy of the system. On the other hand, buoyancy, due to the difference in density of liquids (Fe and Ti) and solids (TiC), is likely to increase the number of collisions between the solid particles, accelerating the particle coarsening by coalescence. However, since no experiments using the combustion front quenching technique (cf. Mukasyan and Borovinskaya, 1992; Rogachev et al., 2000) to investigate the mechanism of microstructure formation under reduced gravity have been performed up to date, it

is difficult at this stage to identify which is the governing mechanism responsible for the microstructural changes occurring under different gravity conditions. This important topic is currently under investigation in the framework of the Topical Team on "Combustion Synthesis and Microgravity" sponsored by the European Space Agency.

ACKNOWLEDGEMENTS

The financial support of Agenzia Spaziale Italiana (ASI) and European Space Agency (ESA) is gratefully acknowledged.

REFERENCES

- Choi, Y. and Rhee S.W. *J. Mater. Res.*, 8(12), 1993, 3202-3209.
- Kachin, A.R. and Yuhvid V.I. *Int. J. of SHS*, 1(1), 1992, 168-171.
- Karataskov, S.A., Yuhvid V.I. and Merzhanov A.G. *Fizika gorenia i vzriva*, 6, 1985, 41-43
- Medda E., Orrù R., Cao G., Fry J., Guignè J. Y. and Zell M. *Proc. First Intern. Symp. on Microgravity Res. & Appl. in Physical Sciences & Biotechnology - Sorrento, Italy*, (2000) in press.
- Merzhanov, A.G. and Borovinskaya I.P. *Dokl. Akad. Nauk.*, 204(2), 1972, 366-369.
- Merzhanov, A.G. and Yuhvid V.I. *Proc. First US-Japanese Workshop on Combustion Synthesis*, Tokyo, Japan, 1990, 1-22.
- Merzhanov, A.G. *Ceramics International*, 21, 1995, 371-379.
- Mukasyan, A. S. and Borovinskaya I.P. *Int. J. SHS*, 1, 1992, 55-63.
- Mukasyan, A.S., Pelekh A., Varma A. and Rogachev A. *AIAA Journal*, 35(12), 1997, 1821-1828.
- Munir, Z.A. and Anselmi-Tamburini U. *Mater. Sci. Rept.*, 3, 1989, 277-365.
- Odawara, O. *J. Amer. Ceram. Soc.*, 73(3), 1990, 629-638.
- Orrù, R., Simoncini B., Viridis P. and Cao G. *Inter. J. Self-Prop. High-Temp. Synth.*, 4, 1995, 137-147.
- Orrù, R., Sannia M., Cincotti A. and Cao G. *Chemical Engineering Science*, 54(15-16), 1999, 3053-3061.
- Rogachev, A. S., Sanin V.N., Sytshev A.E., Yuhvid V.I., Medda E., Orrù R. and Cao G. *Proc. Centrifugal Materials Processing IV, Kluwer Academic/Plenum Publisher*, 2000a, in press.
- Rogachev, A. S., Sanin V.N., Sytshev A.E., Yuhvid V.I., Medda E., Orrù R. and Cao G. *Proc. of 33rd COSPAR Scientific Assembly, Advances in Space Research*, 2000b, in press.
- Varma, A., Rogachev A.S., Mukasyan A.S. and Hwang S. *Adv. Chem. Eng.*, 24, 1998, 79-226.
- Yi, H.C., Woodger T.C., Moore J.J., and Guignè J.Y. *Metall. And Mater. Trans. B*, 29B, 1998, 889-897.
- Yuhvid, V.I., Silyakov S.L., Sanin V.N. and Merzhanov A.G. *Proceedings of the Joint Xth European and VIth Russian Symposium on Physical Sciences in Microgravity*, 1997, 397-400.

KISS: KINETICS AND STRUCTURE OF SUPERAGGLOMERATES PRODUCED BY SILANE AND ACETYLENE

G. W. Mulholland J. C. Yang, and J. H. Scott, National Institute of Standards and Technology, Gaithersburg, MD, 20899; Y. Sivithanu, En'Urga, Inc., 1291-A, Cumberland Ave., West Lafayette, IN 47906.

INTRODUCTION

The objective of this study is to understand the process of gas phase agglomeration leading to superagglomerates and a gel-like structure for microgravity (0-g) silane and acetylene flames. Ultimately one would apply this understanding to predicting flame conditions that could lead to the gas phase production of an aero-gel. The approach is to burn acetylene and silane and to analyze the evolution of the soot and silica agglomerates. Acetylene is chosen because it has one of the highest soot volume fractions and there is evidence of super agglomerates being formed in laminar acetylene flames¹. Silane has the advantage that silica particles are the major combustion product resulting in a particle volume fraction a factor of ten greater than that for a carbonaceous smoke.

COMBUSTION FACILITY

The condition of autoignition for silane gas coming in contact with air poses a safety challenge different from those faced by previous drop tower experiments. Another safety issue for silane is its production of fine silica particles, which contaminate gas lines and prevent check valves from operating. In collaboration with contacts from the semiconductor industry and the gas handling staff at NIST, a system has been designed to ensure the safe burning of silane. Key design features are the use of metallic pneumatic and metering valves, butt-weld plumbing to minimize contaminants and dead volume, both vacuum and nitrogen purge, and the use of a minimum amount of silane (about 1 g). This small amount of silane assures that even if all of it were released to the combustion chamber, the pressure would remain below the maximum allowable value of about 0.41 MPa gauge(60 psig). A filter collection system has been assembled to prevent personnel exposure to silica particles during testing in the laboratory. The facility has passed NIST safety inspection for use in a chemical fume hood and results for normal gravity (1-g) experiments involving silane and acetylene will be described below.

IMAGING MEASUREMENTS

Acetylene was burned in the standard NASA cylindrical combustion chamber with a diameter of 25 cm and a height of 53 cm. The burner consisted of a 4.52 mm diameter stainless steel tube positioned along the centerline about 15 cm from the base of the chamber. A digital camera with backlighting through a diffuser was used to photograph both the flame and smoke plume as illustrated in the lower portion of the Fig. 1. The photographs show the flame and plume just past the onset of sooting at a fuel flow rate of 0.66 cm³/s and the intense sooting condition with superagglomerates appearing as specks for a fuel flow of 2.10 cm³/s.

The upper series of photographs was taken at a location about 9 cm from the burner exit with the digital camera and a Xenon flash lamp with a pulse duration of 1.3 μ s and a pulse energy of 0.35 J to "freeze" the motion of the soot agglomerates. The shutter speed of the camera was synchronized with the flash lamp, and the lens was selected to provide a long working distance of 15 cm and a magnification of 1:4.4. At the lower flow rate the soot appears as a relatively

gray background while at the larger flow, individual $50\text{ }\mu\text{m}$ to $100\text{ }\mu\text{m}$ particles appear to be connected across much of the plume. Other noteworthy features are the increasing plume width with increasing fuel flow rate and the sharpness of the smoke boundary. A comparison between these observations and plume calculations will be given below.

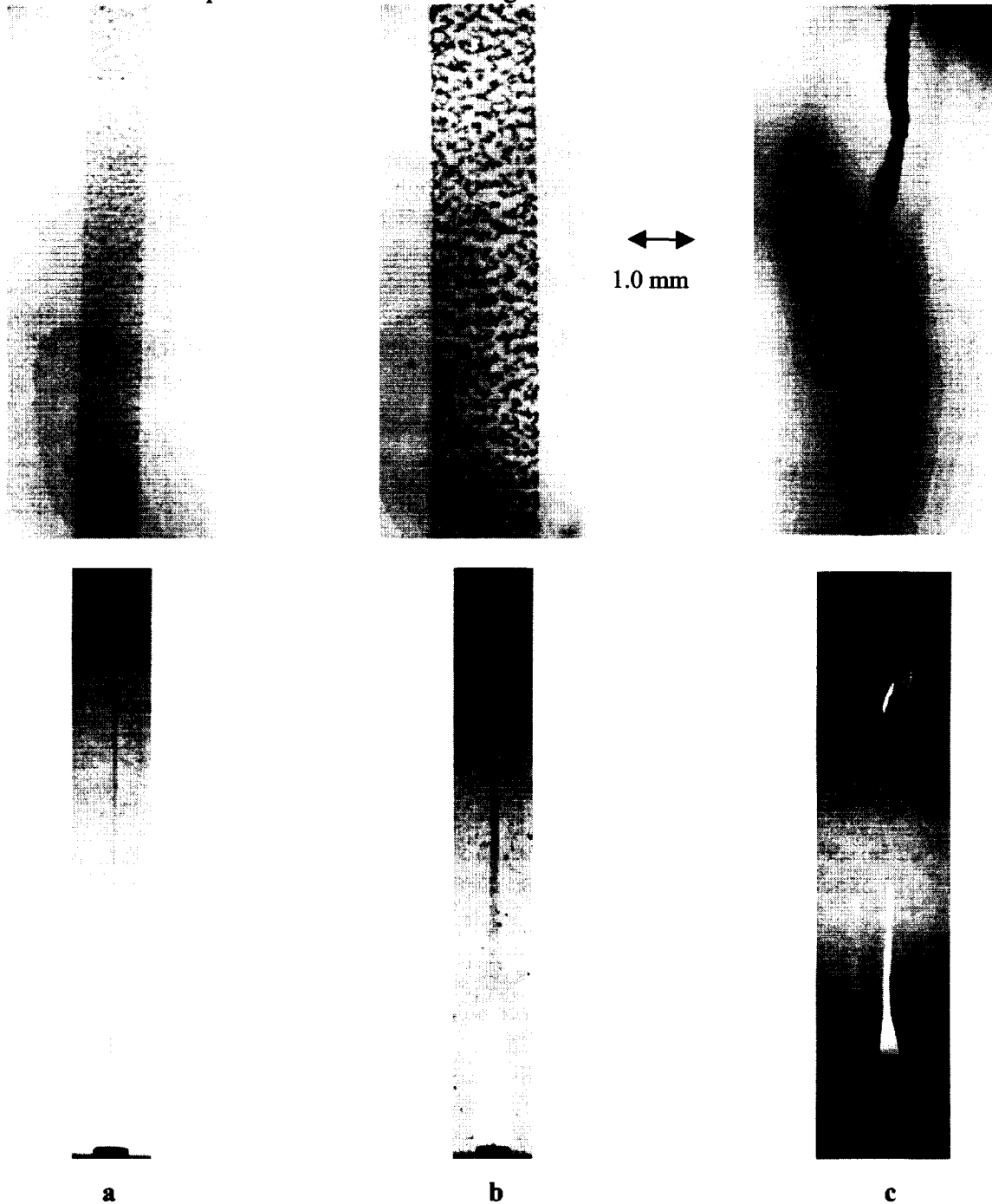


Fig. 1 Photographs of low flow (a) and high flow (b) acetylene flames, and a low flow silane flame (c). Flash photos of the plume are taken 9 cm above the burner .

For the silane experiment, the flow was controlled/monitored with a metering valve and analog pressure gauge. One difficulty with silane is that an SiO_2 "crust" coats the burner tube and forms a conical deposit at the burner exit as indicated by the restriction of the flame in Figure 1. Even over a period of 10 s there is a noticeable decrease in the visible flame height. We were surprised to observe filaments leaving the flame zone rather than superagglomerates such as for acetylene. The photograph of the silane flame in Fig. 1 shows one fiber that has broken off and another forming in the flame. A μs flash photograph of a filament 9 cm above the flame is shown in Fig. 1. Thermophoretic sampling from the plume indicates a high concentration of particles smaller than $10\text{ }\mu\text{m}$ in addition to the fibrous particles.

Fibrous particles were examined with a stereomicroscope and a field emission scanning electron microscope. The digital image (Fig. 2) obtained with a video camera attached to the stereomicroscope indicates a complex filament structure. The scanning microscope images are for fragments from the original fiber, since most of the fiber attached with double stick carbon pads was lost when the chromium deposition chamber was evacuated. The SEM micrograph shows evidence of partially fused spherule structures with diameters as small as about 150 nm . It is possible that the original structures started as agglomerates that coalesced as a result of the flame temperature exceeding the melting point of SiO_2 .

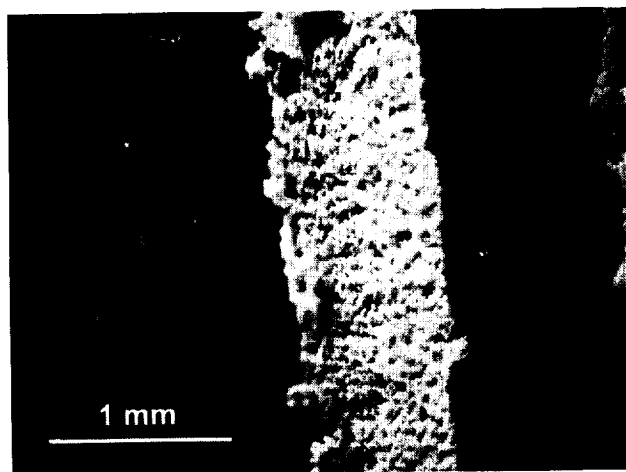


Fig. 2a. Optical micrograph of silica fiber.

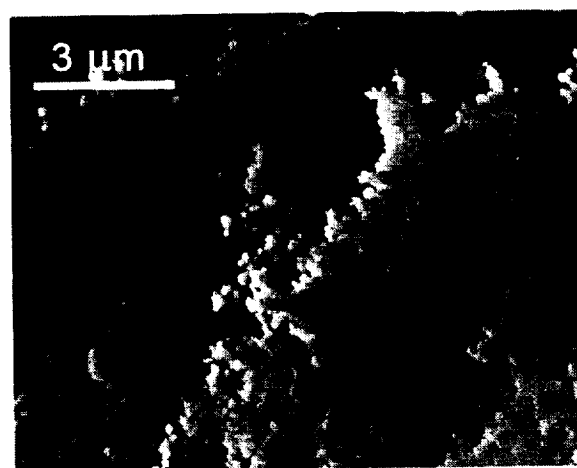


Fig. 2b. SEM of fiber residue coated with a few nm of Cr.

MODEL CALCULATIONS

It is important to compute the profiles for particle volume fraction, temperature, species, and velocity to establish the environment for the computer simulations of the agglomeration process. The calculation method by Sivathanu and Gore², which is based on a boundary layer jet flow, a chemical kinetics model by Lueng *et al.*³, and radiation loss and gain was used for computing these quantities for acetylene. The trend of an increasing width of the soot volume fraction profile with flow rate follows the same trend as measured experimentally. The 0-g condition leads to a broadening of the concentration profile almost a hundred fold; however, the predicted peak soot volume fraction is almost the same for both cases. The much broader profile and the shifting of the peak concentration to a downstream location at 0-g conditions will require a broader field of view and lower magnification for the flame imaging and the microsecond flash photography compared to the 1-g imaging.

For silane, a global reaction model based on state relationships is used. Essentially, the model assumes that any time oxygen and silane comes into contact, silicon dioxide particulate is formed. The availability of silane and oxygen at any location is obtained from the local gas phase mixture fraction. The silicon dioxide formed is then convected with a low diffusion coefficient (1000 times lower than gas). The predicted width of the SiO_2 particulate profile is about half the width of the acetylene profile because the oxygen requirement for silane combustion is less than for acetylene combustion (2 O_2 molecules compared to 3 O_2 molecules for acetylene) and because every silicon atom forms SiO_2 compared to about 10 % of the carbon atoms becoming soot. The other difference is that the peak SiO_2 particulate volume fraction is about 100 fold larger than for soot for 1-g and decreases to about 30 fold larger for 0-g conditions.

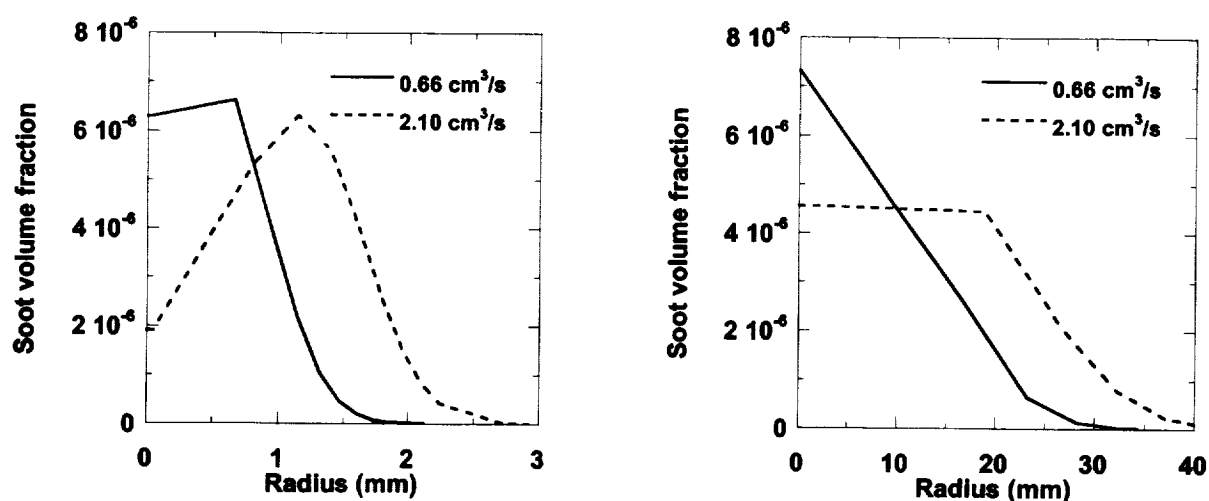


Fig. 3 The predicted soot volume fraction profile 90 mm downstream from the burner for 1-g (left plot) and for 0-g (right plot).

DISCUSSION

The apparently interconnected structure of soot observed in this study at high fuel flow rate is similar to that reported in the study of Sorensen *et al.*¹ We expected that the much larger particulate volume fraction for the silane flame would lead to a totally interconnected gel-like structure and were surprised to observe a fibrous material. It is likely that the combination of the higher flame temperature for silane combustion together with the lower melting point of SiO_2 particulate has resulted in the formation of the filaments. Our original plan to vary the flame temperature by varying the oxygen concentration will likely be important in controlling the morphology – gel-like or fiber – of the silica particles.

ACKNOWLEDGEMENT: This work is funded by NASA Microgravity Combustion Program with Suleyman Gokoglu as technical monitor.

REFERENCES

- ¹ Sorensen, C.M., Hageman, W.B., Rush, T.J., Huang, H., and Oh, C., *Phys. Rev. Lett.*, 80: 1782 (1998).
- ² Sivathanu, Y.R. and Gore, J.P. *Combust. Flame*, 97: 161 (1994).
- ³ Leung, K.M., Lindsted, and Jones, W.P., *Combust. Flame*, 87:289 (1991)

Formation of Carbon Nanotubes in a Microgravity Environment

J. M. Alford¹, G.R. Mason², and D.A. Feikema³

^{1,2}TDA Research, Inc., 12345 W.52 Ave., Wheat Ridge, CO 80033

³NASA Glenn Research Center

Introduction

Because of their potential as new materials, there is currently a large interest in the synthesis and characterization of carbon nanotubes. Carbon nanotubes were first discovered in 1991 by Iijima¹ who observed the presence of nanometer sized multi-walled carbon nanotubes (MWNTs) on the graphite electrodes used for fullerene production. Addition of a transition metal catalyst was subsequently shown to produce single-walled nanotubes² (SWNTs) such as the C₆₀ sized nanotube illustrated in Figure 1. Unlike conventional carbon fibers, the SWNT structure is atomically perfect, thus producing defect free fibers that have many unique electronic and physical properties³. For example, with a predicted Young's modulus of ~1 Tera-Pascal, SWNTs represent the strongest known type of carbon fiber and form the ideal basis for new composite materials. Calculations show that a carbon nanotube-based cable could have one hundred times the strength of steel while having just one-sixth of the weight. Carbon fiber composites made from nanotubes would save significant weight in spacecraft and aircraft structures. In addition to their mechanical properties, nanotubes also have interesting electronic properties, which are dependent upon the tubes morphology. Some tubes have conducting electronic structures and can be envisioned as molecular "quantum" wires, while others are semiconducting and can be used to fabricate the world's smallest "single molecule" transistors. The development of field effect transistors and memory elements made from SWNTs has been demonstrated. Other promising uses for SWNTs include tips for atomic force microscopy (AFM) and hydrogen storage.

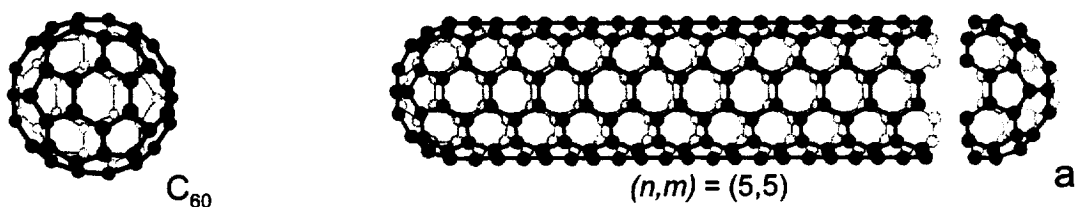


Figure 1. Comparison of C₆₀ fullerene and its single-walled nanotube analogue.

To date, most investigations have concentrated on determining the physical properties of the tubes, and very little is known about the fundamental processes involved in nanotube formation. The current nanotube synthesis processes are poorly understood and can only produce small quantities of nanotubes that are less than ~100 microns in length. These sizes and quantities have enabled the successful investigation of electronic devices, but meaningful composite materials research has been severely hindered. If industrial amounts of tubes 10-100 times longer, 1-10mm, could be efficiently produced, then commercial applications in new composite materials would become much more favorable. The key to developing better production processes is to gain a better understanding of the nanotube formation process. Thus, the goal of this investigation is to use microgravity processing to improve our understanding of the nanotube formation process and allow us to produce superior single-walled carbon nanotubes (SWNTs).

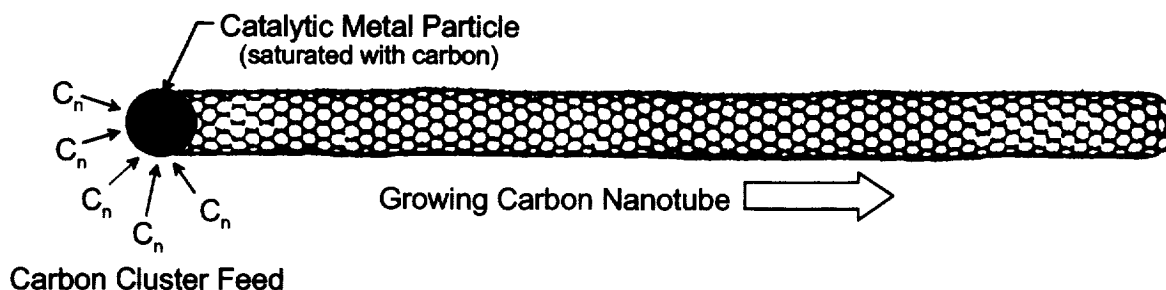


Figure 2. Catalytic growth of a SWNT.

There are currently several methods for the production of single-walled carbon nanotubes, including: the carbon arc⁶, laser vaporization of graphite⁷, chemical vapor decomposition⁸ (CVD), high pressure disproportionation of CO⁹, and flame synthesis¹⁰. All rely on catalytic growth of the nanotube from either carbon or hydrocarbon vapor in the presence Co/Ni or other transition metal catalysts as shown in Figure 2. As vaporized carbon (or hydrocarbon) and metal catalyst atoms cool, they condense into small nanometer sized clusters that continually collide and grow. When the metal carbide clusters produced from the transition metal catalyst become super-saturated with carbon, the carbon re-crystallizes as a nanotubes. The metal particle remains on the head of the tube and channels the remaining carbon it encounters into the tube. Studies performed on the vapor plume produced during laser ablation of graphite suggest that nanotube growth can continue as long as the catalyst particle remains saturated with carbon and the temperature remains high enough for carbon to efficiently diffuse through the particle¹¹.

The two most common and well-characterized processes for nanotube production are the carbon arc and laser ablation method. Both are gas phase processes that resemble the formation of soot during combustion processes. Buoyancy is known to have a large effect on soot formation, and we hypothesize that the same is also true for nanotube formation. Both processes vaporize carbon in a high temperature (5000-10000 °C) plasma that induces strong convective flows. In arc reactors, large convection currents are readily observed and explain the wide variation in reported operating conditions¹² and why the quality of nanotube deposits varies greatly depending on their position in the apparatus. The formation of a nanotube is undoubtedly a strong function of the time/temperature/concentration history of the growing tube and its precursors, and buoyancy produces an uncontrolled environment that makes estimation and optimization of these critical factors difficult. Microgravity conditions provide a much more controlled environment for measurement, modeling, and optimization of these parameters.

Experimental

The carbon arc method was selected as the basis of our microgravity apparatus because it is simpler and provides a greater amount of carbon vapor than the laser method. However, several challenges were presented in moving the carbon arc from the production lab to the drop tower. The typical carbon arc apparatus^{6,12} employs large 6-12 mm diameter electrodes and consumes several kilowatts (or more) of power that is supplied continuously from a large welding power supply. The metal catalyst required to produce SWNTs is introduced by simply drilling holes in the electrodes and packing them with metal powder. During operation, the arc gap is usually adjusted manually while observing the arc through a viewport. Substantial innovation was required to adapt this configuration to a drop tower rig while maintaining a production rate high enough to produce meaningful quantities of nanotubes.

A schematic of the mini arc we developed is shown in Figure 3. The carbon electrodes are now downsized to ~ 0.5 mm while the absolute power was decreased to about 1 KW for the 2.2 second drop time. Note however, that the power density for the cross-sectional area of the electrode is now much higher than the larger arc machines, and this “mini-arc” actually produces more nanotubes per second than its bigger brethren. A new impregnation method was developed to dope the rod with Ni/Y metal catalyst, and the arc gap is now continuously adjusted with a spring-loaded electrode. Power for the arc is supplied by a large (0.5 F) capacitor bank that is charged to 60 volts prior to each drop. Before producing nanotubes, the reaction chamber is purged of air by pumping to vacuum and then filled with Ar at 600 torr. The arc vaporizes ~ 10 mg of carbon during each 2.2 second run, and the resulting SWNTs agglomerate into web like fibers that are easily observed and collected for analysis.

The results of our initial tests now allow a comparison of the arc plasma at normal gravity and microgravity, Figure 3. The observed behavior is remarkably similar to a sooting flame. At 1g, the development of a convective jet that carries the resulting nanotube soot to the top of the chamber is readily apparent. Under microgravity, the behavior of the plasma resembles a weightless sooting flame and the nanotubes form at the spherical boundary of the reaction zone.

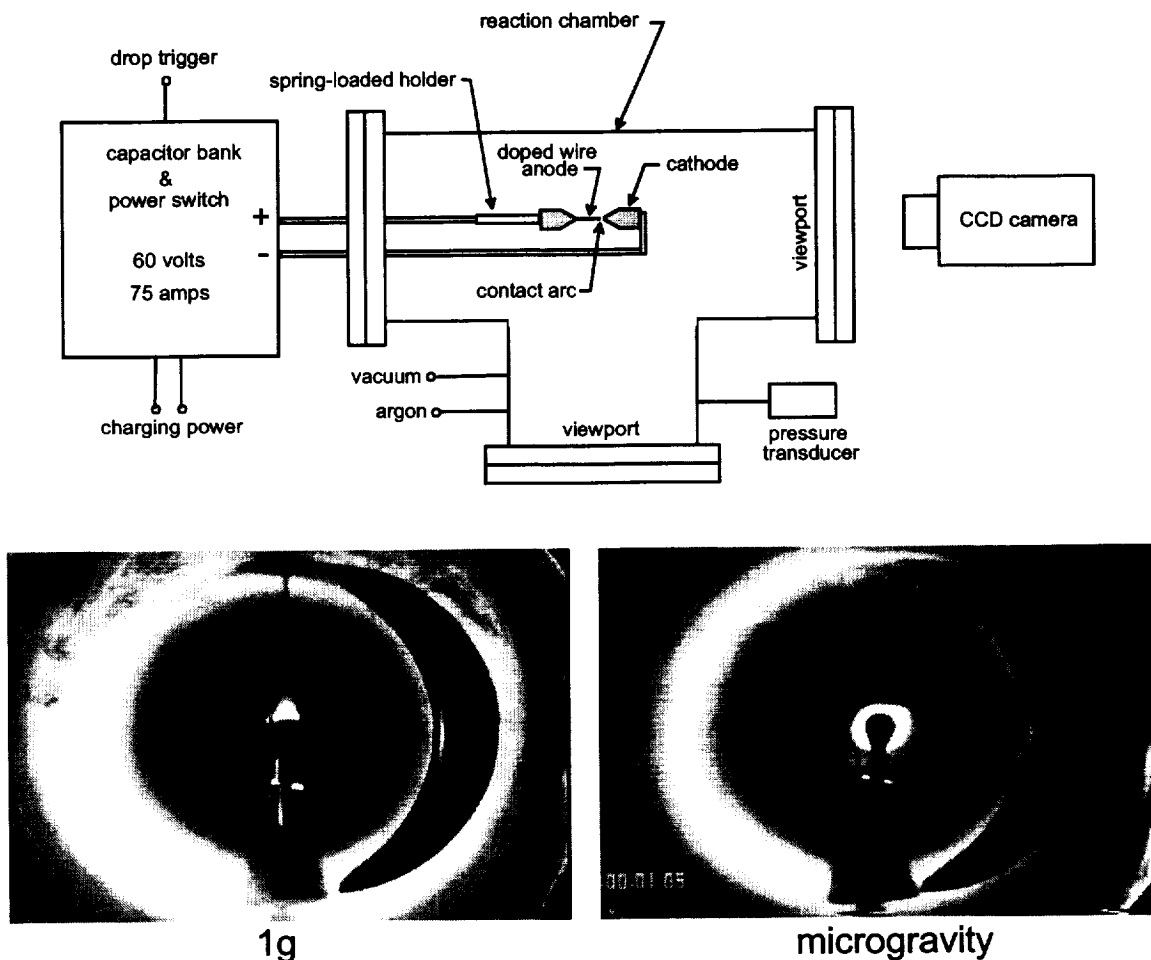


Figure 3. Apparatus schematic and video stills illustrating the difference between the 1g arc and the microgravity arc.

microscopy. When this testing is completed, the production process will be optimized. The ultimate goal is to obtain a controlled, spherically uniform reaction zone in which rapid nanotube growth can be sustained undisturbed for the entire drop time of 2.2 and eventually 5 seconds.

Summary

Even though nanotube science has become one of the worlds most rapidly advancing areas of research, very little is known about the processes involved in nanotube synthesis. To study the formation of carbon nanotubes in an environment unhindered by the buoyancy induced flows generated by the high temperatures necessary to vaporize carbon and grow nanotubes, we have designed a miniature carbon arc apparatus that can produce carbon nanotubes under microgravity conditions. During the first phase of this project, we designed, built, and successfully tested the mini carbon arc in both 1g and 2.2 sec drop tower microgravity conditions. We have demonstrated that microgravity can eliminate the strong convective flows from the carbon arc and we have successfully produced single-walled carbon nanotubes in microgravity. We believe that microgravity processing will allow us to better understand the nanotube formation process and eventually allow us to grow nanotubes that are superior to ground-based production.

References

- (1) S. Iijima, *Nature* **354** (1991) 56.
- (2) (a) S. Iijima and T. Ichihashi, *Nature* **363** (2000) 603. (b) D.S. Bethune, C.H. Kiang, M.S. de Vries, G. Gorman, R. Savoy, J. Vazquez, and R. Beyers, *Nature*, **363** (2000) 605.
- (3) The following reviews and references therein provide a good introduction into the current issues in carbon nanotube production, their physical properties, and applications. (a) P. Ajayan, *Chem. Rev.* **99** (1999) 1787. (b) T.W. Ebbeson (Ed.) *Carbon Nanotubes, their Preparation and Properties*, CRC Press, Boca Raton, FL, 1997. (c) R. Satio, M. Dresselhaus, G. Dresselhaus *Physical Properties of Carbon Nanotubes*, Imperial College Press, London, 1998. (d) B.I. Yakobson and R.E. Smalley, *American Scientist* **85**, (1997) 324.
- (6) Journet, C., W.K. Maser, P. Bernier, A. Loiseau, M. Lamy de la Chapelle, S. Lefrants, P. Deniard, R. Lee, and J.E. Fischer, *Nature* **388** (1997) 756.
- (7) T. Guo, P. Nikoleav, A. Thess, D.T. Colbert, and R.E. Smalley, *Chem. Phys. Lett.* **236** (1995) 419.
- (8) J.F. Colomer, C. Stephan, S. Lefrant, G. Van Tendeloo, I. Willems, Z. Konya, A.Fonseca, Ch. Laurent, and J.B. Nagy, *Chem. Phys. Lett.* **317** (2000) 83.
- (9) R. Dagani, *Chem. Eng. News* **78** (2000) 78.
- (10) (a) R.L. Vander Wal, T.M. Tichich, and V.E. Curtis, *Chem. Phys. Lett.* **323** (2000) 217. (b) M.D. Diener, N. Nicholson, and J.M. Alford, *J. Phys. Chem. B* **104** (2000) 9615.
- (11) (a) A.A. Puzoskey, D.B. Geohegan, X. Fan, and S.J. Pennycook, *Appl. Phys. A.* **70** (2000) 153. (b) F. Kokai, K. Takahashi, M. Yudasaka, and S. Iijima, *J. Phys Chem B* **104** (2000) 6777.
- (12) (a) Z. Shi, Y. Lian, F.H. Liao, X. Zhou, Z.Gu, Y. Zhang, S. Iijima, H. Li, K.T. Yue, and S. Zhang, *J. Phys. Chem. Solids.* **61** (2000) 1031. (b) Y. Ando, X. Zhao, K. Hirahara, K. Suenaga, S. Bandow, and S. Iijima, *Chem. Phys. Lett.* **323** (2000) 580. (c) A. Huczko, H. Lange, and T. Sogabe, *J. Phys. Chem. A* **104** (2000) 10708.

GAS-PHASE COMBUSTION SYNTHESIS OF NONOXIDE NANOPARTICLES IN MICROGRAVITY

R. L. Axelbaum, B. M. Kumfer, Z. Sun, and B.H. Chao*

Department of Mechanical Engineering, Washington University, St. Louis, Missouri

*Department of Mechanical Engineering, University of Hawaii, Hawaii

INTRODUCTION

Gas-phase combustion synthesis is a promising process for creating nanoparticles for the growing nanostructure materials industry. The challenges that must be addressed are controlling particle size, preventing hard agglomerates, maintaining purity, and, if nonoxides are synthesized, protecting the particles from oxidation and/or hydrolysis during post-processing. Sodium-halide Flame Encapsulation (SFE) is a unique methodology for producing nonoxide nanoparticles that addresses these challenges [1,2]. This flame synthesis process incorporates sodium and metal-halide chemistry, resulting in nanoparticles that are encapsulated in salt during the early stages of their growth in the flame (Fig. 1). Salt encapsulation has been shown to allow control of particle size and morphology, while serving as an effective protective coating for preserving the purity of the core particles. Metals and compounds that have been produced using this technology include Al, W, Ti, TiB_2 , AlN, and composites of W-Ti and Al-AlN [2,3]. Oxygen content in SFE synthesized nano-AlN has been measured by neutron activation analysis to be as low as 0.54wt.% [4], as compared to over 5wt.% for unprotected AlN of comparable size [5].

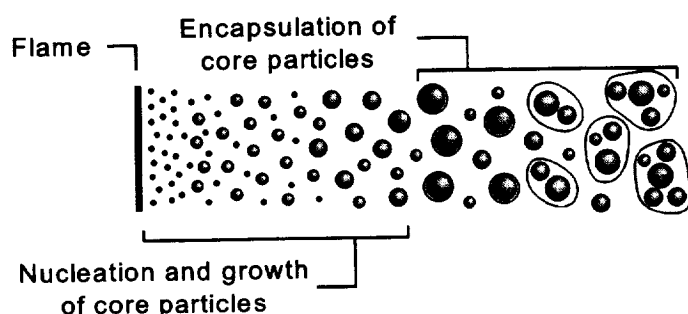


Fig. 1 - Schematic of Particle Encapsulation

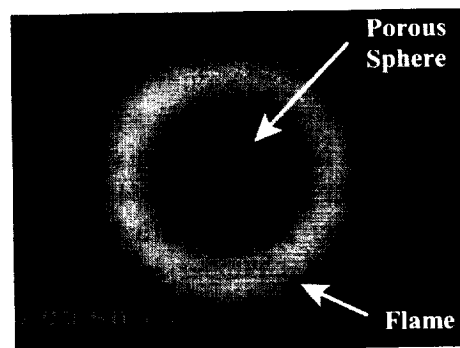


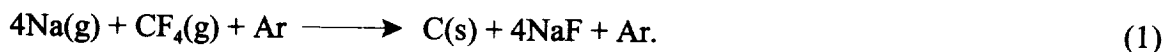
Fig. 2 - Sodium-Halide Flame in μg

The overall objective of this work is to study the SFE process and nano-encapsulation so that they can be used to produce novel and superior materials. SFE experiments in microgravity allow the study of flame and particle dynamics without the influence of buoyancy forces. Spherical sodium-halide flames (Fig. 2) are produced in microgravity by ejecting the halide from a spherical porous burner into a quiescent atmosphere of sodium vapor and argon. Experiments are performed in the 2.2 sec Drop Tower at the NASA-Glenn Research Center. Numerical models of the flame and particle dynamics were developed and are compared with the experimental results.

EXPERIMENT SETUP

The metal halide chosen for the microgravity experiments was carbontetrafluoride (CF_4). CF_4 is an attractive precursor because it is nonhazardous and exists as a gas at standard conditions, unlike many of the metal-halides used to produce the materials previously mentioned. Furthermore,

the characteristics of the encapsulation process are not a strong function of the choice of metal-halide. Therefore, information gained from studying synthesis and encapsulation of carbon can be applied to the synthesis of other materials. An additional reason for using CF_4 is that nano-carbon particles are not reactive in air. Since particles will be extracted from the flames and examined by electron microscopy to determine their morphology, it is important that unencapsulated core particles be nonreactive. Nanometer-sized metal and nonoxide ceramic particles would react rapidly when exposed to air. The reaction for the production of carbon is given by



A stainless-steel combustion chamber was constructed for the drop tower experiments (Fig. 3). To maintain sufficient sodium vapor concentration, the chamber walls are heated to temperatures ranging from 600 to 700 °C using resistive heat tapes. Sodium is stored in a reservoir located near the base of the chamber. By keeping the top surface of the chamber slightly cooler than the rest of the chamber, sodium condenses on the top surface during charging, and a saturation condition is achieved. The partial pressure of sodium in the chamber is then known from vapor pressure data. Argon is added to achieve the desired sodium concentrations and the chamber is operated at subatmospheric pressure.

The halide/argon mixture is delivered to the chamber through a 1/4" spherical porous stainless-steel burner with a pore size of 10 micron. The chamber is equipped with two access ports, both of which can be used as windows for video recording. A pneumatic piston-actuating assembly may also be installed at the top port for particle sampling or temperature probing.

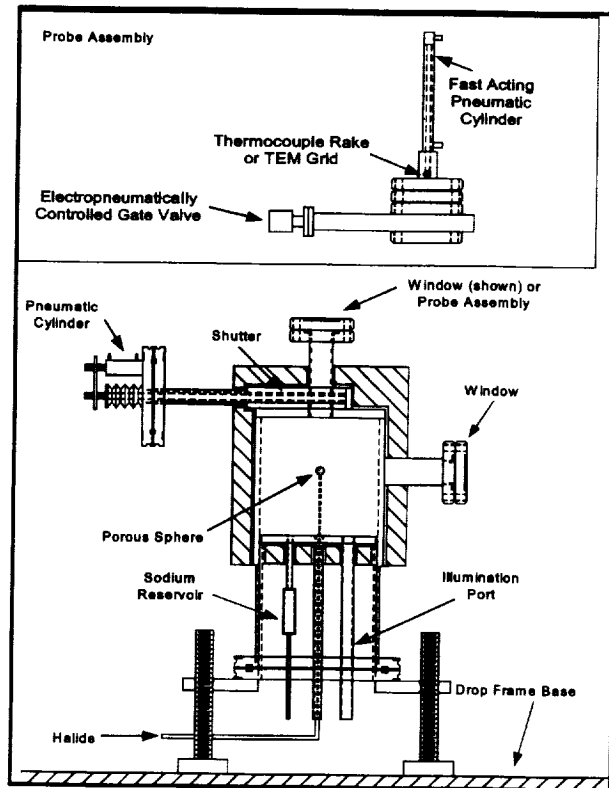


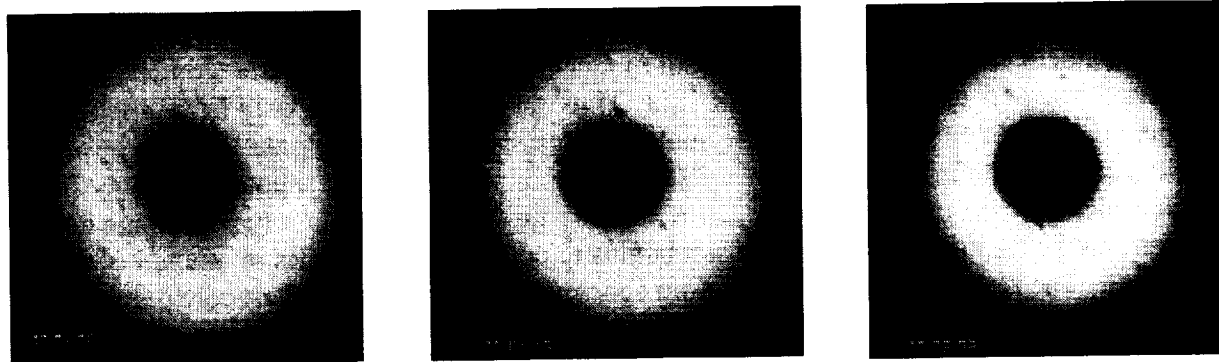
Fig. 3 - Microgravity Combustion Chamber Schematic

RESULTS

Figure 4 shows a series of images of a sodium-halide flame during a 2.2 second drop. The flame was produced with an initial sodium mole fraction of 0.33. The CF_4 /argon mixture was 20% CF_4 by volume, and was delivered through the porous sphere at a rate of 32.9 mg/min.

The sodium-halide reaction is hypergolic. Therefore, no ignition source is required, but controlling the exact time of ignition is challenging because the time for delivery of the halide varies with run conditions. The flame in Fig. 4 was ignited in 1g, and dropped immediately after visual evidence of ignition.

There are significant differences between the characteristics of flames that are obtained in microgravity and those produced in 1g. In normal gravity, a blueish flame with a much narrower



t = 1.17 sec t = 1.50 sec t = 2.07 sec
Fig. 4 - Video-frame sequence of encapsulated-carbon synthesis in μg

flame thickness was produced. For chamber pressures in the range of 300-500 mmHg, microgravity flames were too dim to easily distinguish from the background, and appeared to grow much larger than their 1g counterparts. Enhanced mixing due to buoyant flows in normal gravity reduces flame size and increases flame intensity. Indeed, the flame in Fig. 4 transformed to a smaller, thin blue flame immediately after impact at the bottom of the tower.

The video of the flame shown in Fig. 4 clearly revealed the existence of a uniformly dispersed field of large particles (on the order of 1 mm) emitting from the flame. After performing a series of runs in microgravity, which included this case, a sample of the large particles that had impacted on the base of the chamber was collected. A scanning electron micrograph of the surface of this sample reveals a monodisperse distribution of spherical NaF particles (Fig. 5a). The characteristic size of these salt particles is $1.9 \mu\text{m}$ (Fig. 5b). In this sample there is no evidence of unencapsulated carbon particles. This is consistent with results from laminar and turbulent jet flames [1,3,4] in which the core particles were found to be encapsulated in salt, and it implies that the carbon particles in the sample are indeed embedded in the salt spheres.

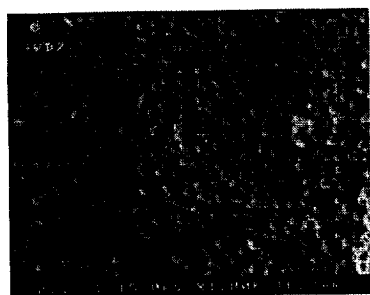


Fig. 5a - Monodisperse distribution of NaF particles

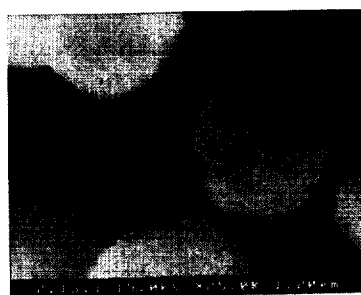


Fig. 5b - Typical NaF sphere

NUMERICAL MODELING

A numerical code was developed to model a 1-D spherical diffusion flame in the absence of buoyancy. This program employs the SANDIA packages for evaluating kinetics and gas-phase thermal and mass transport properties [6]. The code uses a two-point boundary value solver to solve the partial differential equations by the modified Newton-Raphson iteration method [7]. The flame in Fig. 4 was modeled with this program. At steady state, the model predicted a flame radius of 0.74 cm (Fig. 6). This is consistent with the region of the bright zone shown in Fig. 4, where the total radius in the last frame is approximately 0.85 cm. The flame code predicted a maximum flame

temperature of 2023 K.

A numerical multi-component aerosol model employing a Monte Carlo simulation (MCS) has been developed under this program [8]. Thus far the model has only been applied to a homogenous closed system. However, the qualitative results for salt condensation and encapsulation are relevant to this study. The salt is initially in the vapor phase, and the simulation shows that the core particles that are produced in the flame initially grow as they do in a typical flame aerosol. However, as the temperature drops, the salt begins to condense on particles in the tail of the size distribution. The Kelvin effect keeps salt from condensing on all but the largest core particles. The heterogenous condensation of salt rapidly leads to large salt particles having a narrow size distribution. These large salt particles then scavenge the remaining core particles. The experimental results represented in Fig. 5a support this description of the aerosol evolution. In the future, the MCS will be incorporated into the 1-D flame code in order to study nano-encapsulation within the flame.

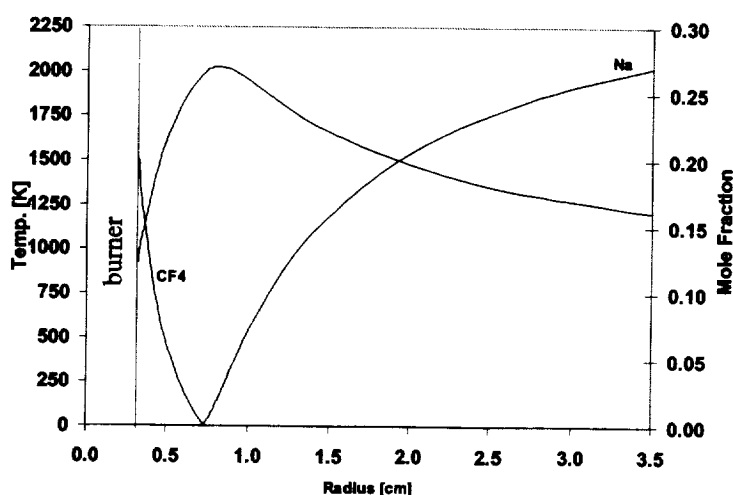


Fig. 6 - Results from 1-D flame code, $m = 32.9$ mg/min

ACKNOWLEDGEMENTS

This work was supported under NASA Grant NAG-1910, under the technical monitoring of Dr. Suleyman Gokoglu. The authors gratefully acknowledge Johnathan Barr, provider of SEM imaging, and Aleksey Pelekh, Frank Myhr, Lee Rosen, and Doug DuFaux for assistance with this project.

REFERENCES

- [1] Axelbaum, R.L., DuFaux, D.P., Frey, C.A., and Sastry, S.M.L., *Metallurgical and Materials Transactions B*, 28B:1199-1211 (1997).
- [2] Axelbaum, R.L., Lottes, C.R., Huertas, J.I., and Rosen L.J., *Twenty-Sixth Symposium (International) on Combustion*, The Combustion Institute, pp. 1891-1897 (1997).
- [3] DuFaux, D.P. and Axelbaum, R.L., *Combustion and Flame*, 100:350-358 (1995).
- [4] Rosen, L.J., Lottes, C.R., DuFaux, D.P. and Axelbaum, R.L., To be published.
- [5] Baba, K., Shohota, N., and Yonezawa, M., *Proceedings of the 8th International Conference on Plasma Chemistry*, ed. By Akashi, K. and Kinbara, A., ISPC-8, pp. 2034-2039 (1987).
- [6] Kee, R.J., Rupley, F.M., and Miller, J.A., "Chemkin-II: A Fortran Chemical Kinetics Package for the Analysis of Gas-Phase Chemical Kinetics," SAND89-8009B (1993).
- [7] Grcar, J.F., "The Twopnt Program for Boundary Value Problems," SAND91-8230 (1992).
- [8] Sun, Z., Huertas, J.I., and Axelbaum, R.L., *Fifth International Microgravity Combustion Workshop*, Cleveland, OH (1999).

FLAME SYNTHESIS OF SINGLE- AND MULTI-WALLED CARBON NANOTUBES AND NANOFIBERS

R.L. Vander Wal

The National Center for Microgravity Research at NASA Glenn Research Center
and

Thomas M. Ticich

Centenary College of Louisiana

INTRODUCTION

Metal-catalyzed carbon nanotubes are highly sought for a diverse range of applications that include nanoelectronics [1], battery electrode material [2], catalysis [3], hydrogen storage media [4] and reinforcing agents in polymer composites [5]. These latter applications will require vast quantities of nanotubes at competitive prices to be economically feasible. Moreover, reinforcing applications may not require ultra-high purity nanotubes. Indeed, functionalization of nanotubes to facilitate interfacial bonding within composites will naturally introduce defects into the tube walls, lessening their tensile strength [6].

Current methods of aerosol synthesis of carbon nanotubes include laser ablation of composite targets of carbon and catalyst metal within high temperature furnaces [7] and decomposition of organometallics in hydrocarbons mixtures within a tube furnace [8]. Common to each approach is the generation of particles in the presence of the reactive hydrocarbon species at elevated temperatures. In the laser-ablation approach, the situation is even more dynamic in that particles and nanotubes are borne during the transient cooling phase of the laser-induced plasma for which the temperature far exceeds that of the surrounding hot gases within the furnace process tube [9]. A shared limitation is that more efficient methods of nanoparticle synthesis are not readily incorporated into these approaches.

In contrast, combustion can quite naturally create nanomaterials such as carbon black [10]. Flame synthesis is well known for its commercial scalability and energy efficiency [11]. However, flames do present a complex chemical environment with steep gradients in temperature and species concentrations [12,13]. Moreover, reaction times are limited within buoyant driven flows to tens of milliseconds [14]. Therein microgravity can greatly lessen temperature and spatial gradients while allowing independent control of flame residence times. In preparation for defining the microgravity experiments, the work presented here focuses on the effect of catalyst particle size and reactant gas in 1g.

EXPERIMENTAL

Catalyst nanoparticles were generated by means of the well known gas evaporation technique. During resistive heating, an inert gas flow of argon was directed across a boat that contained melted iron, thereby entraining evaporated metal. Scatter from a laser beam intersecting the gas flow downstream of the evaporator provided a visual guide of the vaporization rate and thus a means of feedback control. The resulting catalyst aerosol was then directed to the fuel inlet tube of the burner supporting the pyrolysis flame.

The flame was established on a 0.8-cm outer diameter brass fuel tube running through the center of a McKenna burner. Metal nanoparticles and reactant gases were mixed prior to introduction to this fuel tube so as to establish a uniform mixture. Upon emerging from the fuel tube, the aerosol mixture was heated by the surrounding post-flame gases from a rich, premixed flame supported on the sintered metal surface of the McKenna burner. The premixed flame was fueled by 11.0 slpm air and 1.5 slpm C_2H_2 . A 15.2-cm long, 2.5-cm outer diameter steel chimney placed 1 cm above the burner served to stabilize the flame.

Material samples from the flame were obtained by thermophoretic sampling 0.5-cm above the chimney. Transmission electron microscopy (TEM) grids were attached to the probe by a sandwich grid holder consisting of a 0.075-mm thick brass shim with a 2 mm diameter hole exposing both sides of a holey TEM grid, as described previously [15]. Probe dwell times within the flow were kept short (250 ms), thus minimizing probe heating. For the dwell times used here, previous measurements have registered a probe temperature elevation of less than 200 C [16].

RESULTS AND DISCUSSION

Single-walled nanotubes (SWNTs) were produced by Fe particles with CO/H₂ gas mixtures in the flame. We observed a strong dependence of the relative yield with total gas flow within the pyrolysis flame and with the relative concentrations of CO and H₂. Figure 1 shows a HRTEM image of a Fe-catalyzed SWNT. As observed with CO/H₂ mixtures within a high temperature furnace, there was a lack of amorphous carbon coverage on the SWNT walls, indicative of an absence of pyrolysis products within the reacting flow.

In contrast to the SWNTs produced with CO/H₂ mixtures, C₂H₂/H₂ mixtures resulted in amorphous carbon nanotubes (more appropriately considered as nanofibers) composed of nongraphitic walls. Figure 2 shows that the nanotube walls contain short, discontinuous, randomly-oriented graphene segments or short stacks of graphitic lamella. The degree of disorder varies among the multi-walled nanotubes (MWNTs) but in no instance did the nanotubes possess the graphitic quality observed when using CO/H₂ mixtures.

Other structures occasionally observed included short MWNTs grouped in clusters embedded within amorphous carbon. Figure 3 shows an outcrop of such a cluster. These graphitic structures always appeared in groups, never individually. This suggests that either a cluster of particles led to their simultaneous formation or that the clustering reflects their coalescence within the gas flow. Lower carbon concentrations did not significantly decrease the amorphous coating but generally led to disappearance of the clusters altogether. Thus, there appears to be a threshold gas-phase carbon concentration necessary for their growth.

In summary, the following results have been observed; a) SWNTs produced with CO/H₂/He mixtures, b) predominantly nongraphitic MWNTs produced with C₂H₂/H₂/He mixtures, albeit in vastly fewer quantities than the SWNTs produced with CO as carbon containing gas. Given that the flame environments fueled by both CO or C₂H₂ possess similar temperatures and residence times, these factors clearly do not account for the observed differences in reactivity and nanotube structure. Therein a combination of both physical and/or chemical factors likely are responsible. While there is a clear physical size difference between the SWNTs and MWNTs, reflecting that of the catalyst particle, this likely reflects a size dependent chemistry/reactivity.

The very different nanotubes and the strong reactivity difference of the Fe particles towards CO and not C₂H₂ are a manifestation of different nanotube growth mechanisms. To describe SWNT growth by pre-formed catalyst particles, Dai et al. have proposed a *yarmulke* mechanism whereby a hemispherical cap of carbon forms on the metal catalyst particle [17]. With additional carbon supplied by dissociative adsorption of carbon containing gases, the cap lifts off, forming the closed end of the lengthening nanotube. Growth continues provided favorable temperature and carbon supply are maintained. In this mechanism, the carbon migrates to the growing nanotube by surface diffusion. Thus the particle diameter must closely match those quantized sizes allowed for SWNTs. Notably this mechanism does not account for the formation of nongraphitic MWNTs.

In contrast, the nongraphitic nanotubes reflect a well-established mechanism used to describe carbon filament growth. In this model, carbon containing gases dissociate on the catalyst particle, producing surface carbon. Subsequent carbon atom solvation, diffusion through the particle followed by dissolution (precipitation) from the rear of the particle leads to nanotube (filament) growth [18].

Common to both mechanisms is that the catalyst particle determines the size of the nanotube. A second commonality is that the particle provides the carbon by catalyzing dissociative adsorption of reactant gases. Contrasting the two mechanisms, in the yarmulke mechanism the catalyst particle determines only the nanotube diameter, not its structure which is constrained by energetics to be a single graphitic layer parallel to the growth axis. In the latter mechanism, the catalyst particle not only determines the nanotube diameter but also its morphology. As the carbon is supplied by interstitial lattice sites in the particle, the particle rear facets determine the orientation and pattern of the carbon layers forming the nanotube. Notably in this mechanism, the catalyst particle crystal structure is equated to that of the bulk material.

A critical question to be answered by these mechanisms pertains to the relative reactivities of Fe particles towards the different reactant gases. Similar size particles are exposed to the two reactant gases at similar temperatures. Therein the observed differences likely reflect a size dependent reactivity. The electron density and density of electronic states is a strong function of particle size on the nanometer scale. From bulk single crystal studies, CO and C_2H_2 are known to readily undergo dissociative adsorption upon transition metal surfaces, but by very different mechanisms [19]. After end-on adsorption, dissociation of CO proceeds by donation of electron density from the highest bonding orbital, the 5s M.O. to the metal with concurrent back donation into the 1st antibonding orbital, the 2p M.O. In contrast, C_2H_2 adsorbs parallel to the surface, bridging lattice sites. Direct donation of electron density from the sp orbitals lowers the C-C bond order. Dissociation can occur directly or by insertion of other surface adsorbed species into the weakened C-C bond, thereby "gasifying" one of the carbon atoms. We note that other factors may act independently or synergistically. For example, particle surface restructuring could occur upon CO adsorption as known from bulk single crystal studies [19].

Within this framework, the absence of SWNTs produced by small Fe particles within C_2H_2 mixtures reflects an electronic structure incommensurate with electron density acceptance compared to donation to adsorbed CO. In contrast, the predominance of SWNTs produced by CO and relative lack of MWNTs (some highly graphitic structures were observed) reflects the very high reactivity of small (nanometer or subnanometer) Fe particles towards CO. Their high reactivity selects that portion of the particle size distribution suitable for SWNT formation. With increasing particle size, the electronic structure changes, approaching that of the bulk material. As their properties become more similar to the bulk material, they can catalyze dissociative adsorption in a similar manner as the bulk material. Thus larger Fe particles are able to catalyze C_2H_2 dissociation giving rise to MWNTs.

That larger particles are necessary for nanotube growth in C_2H_2 gas mixtures accounts for their much lower relative yield compared to SWNTs using CO gas mixtures. First, they are not the dominant size class produced by the evaporation source. Secondly, MWNT growth may proceed more slowly than SWNT growth as carbon diffusion through the particle will necessarily possess a higher activation energy than carbon diffusion over a smaller particle surface and likely possess a higher temperature dependence.

ACKNOWLEDGMENTS

This work was supported by a NASA NRA 97-HEDs-01 combustion award (Dr. vander wal), administered through NASA cooperative agreement NAC3-544 with The National Center for Microgravity Research on Fluids and Combustion (NCMR) at The NASA-Glenn Research Center. Prof. Ticich acknowledges support through the Ohio Aerospace Institute ASEE faculty fellowship program.

REFERENCES

- [1] Tans, S.J., Devoret, M.H., Dai, H., Thess, A., Smalley, R.E., Geerligs, L.J., and Dekker, C., *Nature* 386, 474-477 (1997).

- [2] Gao, B. Kleinhammes, A., Tang, X.P., Bower, C., Fleming, L., Wu, Y., and Zhou, O., Chem. Phys. Lett. 307:153–157 (1999).
- [3] Rodriguez, N.M., Kim, M.-S., and Baker, R.T.K., J. Phys. Chem., 98:13108–13111 (1994).
- [4] Pinkerton, F.E., Wicke, B.G., Olk, C.H., Tibbetts, G.G., Meisner, G.P., Meyer, M.S., and Herbst, J.F., J. Phys. Chem. B104:9460–9467 (2000).
- [5] Ajayan, P.M., Stephan, O., Colliex, C. and Trauth, D., Science 265:1212–1214 (1994).
- [6] Garg, A., and Sinnott, S.B., Chem. Phys. Lett. 295:273–278 (1998).
- [7] Kokai, F., Takahashi, K. Yudasaka, M., Yamada, R., Ichihashi, T. and Iijima, S., J. Phys. Chem. 103:4346–4352 (1999).
- [8] Andrews, R., Jacques, D., Rao, A.M., Derbyshire, F., Qian, D., Fan, X., Dickey, E.C. and Chen, J., Chem. Phys. Lett. 303:467–473 (1999).
- [9] Arepalli, S., and Scott, C.D., Chem. Phys. Lett. 302:139–145 (1999).
- [10] Pratsinis, S.E., AIChE Symp. Ser., Vol. 85 (#270), 1980, 57–68
- [11] Ulrich, G.D., Combust. Sci. and Technol. 4:45–57 (1971).
- [12] Santoro, R.J., Yeh, T.T., Horvath, J.J. and Semerjian, H.G., Combust. Sci. and Technol. 53:89–115 (1987).
- [13] Smyth, K.C., Miller, J.H., Dorfman, R.C., Mallard, W.G., and Santoro, R.J., Comb. and Flame 62: 157–181 (1985).
- [14] Roper, F.G., Comb. and Flame 29:219–226 (1977).
- [15] Vander Wal, R.L., Choi, M.Y. and Lee, K.-O., Comb. and Flame 102:200–204 (1995).
- [16] Vander Wal, R.L., Householder, P.A. and Wright, T.W. III, Appl. Spectrosc. 53:1251–1257 (1999).
- [17] Dai, H., Rinzler, A.G., Nikolaev, P., Thess, A., Colbert, D.T. and Smalley, R.E., Chem. Phys. Lett. 260:471–474 (1996).
- [18] Rodriguez, N.M., Chambers, A. and Baker, R.T.K., Langmuir 11:3862–3866 (1995).
- [19] The Chemical Physics of Solid Surfaces and Heterogeneous Catalysis, (D.A. King and D.P. Woodruff eds.) Elsevier 1990 Part A.

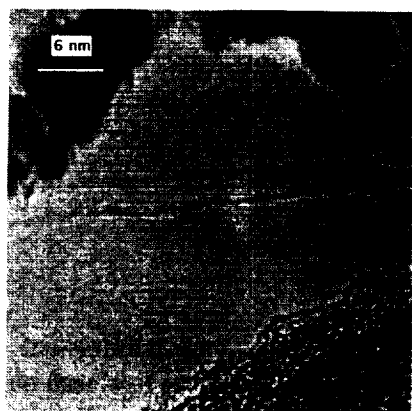


Fig. 1 A HRTEM image of a Fe-catalyzed SWNT produced within the pyrolysis flame with a CO/H₂/Ar mixture. The flow rates were 0.5, 0.5 and 0.5 slm respectively.

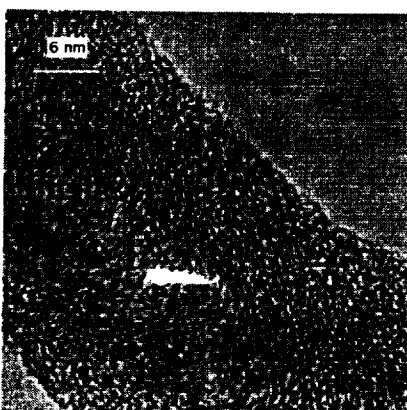


Fig. 2 A HRTEM image of a non-graphitic Fe-catalyzed MWNT produced within the pyrolysis flame using a C₂H₂/H₂/Ar mixture. The flow rates were 0.25, 0.25 and 0.5 slm respectively.



Fig. 3 A HRTEM image of graphitic MWNT clusters, catalyzed by Fe, produced within the pyrolysis flame using C₂H₂/H₂/Ar mixtures.

OUTWARDLY PROPAGATING FLAMES AT ELEVATED PRESSURES

C. K. Law,¹ G. Rozenchan,¹ S. D. Tse² and D. L. Zhu¹

¹Department of Mechanical and Aerospace Engineering
Princeton University, Princeton, NJ 08544

²Department of Mechanical and Aerospace Engineering
Rutgers, The State University of New Jersey, Piscataway, NJ 08854

ABSTRACT

Spherical, outwardly-propagating flames of CH₄-O₂-inert and H₂-O₂-inert mixtures were experimentally studied in a high pressure apparatus. Stretch-free flame speeds and Markstein lengths were extracted for a wide range of pressures and equivalence ratios for spherically-symmetric, smooth flamefronts and compared to numerical computations with detailed chemistry and transport, as well as existing data in the literature.

Wrinkle development was examined for propagating flames that were unstable under our experimental conditions. Hydrodynamic cells developed for most H₂-air and CH₄-air flames at elevated pressures, while thermal-diffusive instabilities were also observed for lean and near-stoichiometric hydrogen flames at pressures above atmospheric. Strategies in suppressing or delaying the onset of cell formation have been assessed. Buoyancy effects affected sufficiently off-stoichiometric CH₄ mixtures at high pressures.

INTRODUCTION

For the present work, we adopted a recently-developed novel experimental apparatus for the investigation of elevated pressure H₂ and CH₄ flames [1-3], capable of conducting experiments up to 60 atm, and that allows for the direct imaging of a near-constant-pressure outwardly propagating flame. Using this apparatus, the laminar burning rates and downstream Markstein lengths of H₂-O₂-inert and CH₄-O₂-inert mixtures were experimentally and computationally obtained. The laminar flame speed, s_u^0 , is a fundamental thermochemical parameter of the flame, embodying information about the diffusive and reactive aspects of a combustible mixture, and has been extensively used to validate detailed reaction mechanisms. The Markstein length, which characterizes and quantifies the flame response to stretch, is an indicator of the effective Lewis number of the combustible mixture, as it embodies the accelerating/decelerating tendency of the flame as it propagates, subject to positive/negative stretch, as well as the nonequidiffusive nature of the flame. The occurrence (or absence) of thermal-diffusional instabilities over the flame gives this reasoning further support.

EXPERIMENTAL AND COMPUTATIONAL METHODS

Apparatus and Instrumentation - The experimental apparatus consists of two coaxial cylindrical chambers. The inner chamber has quartz discs on both ends for optical access, and is initially filled with the combustible mixture. The outer chamber has quartz windows mounted in the end caps, and is initially filled with an inert mixture. There are matching rows of holes on the lateral

wall of the inner chamber and on its encasing sleeve which allow for continuity between the two chambers, when aligned; once offset, these holes are isolated via O-rings.

The reactants were mixed by a jet-stirring apparatus. The mixtures were ignited by a spark discharge and the flame propagation was optically recorded using Schlieren cinematography and a high-speed camera. Both chambers are equipped with digital pressure gages, used for filling the mixtures. Operational details, error analysis and system specifications can be found in Refs. 1-4.

Filling and Ignition Procedures - The individual components were introduced to the inner chamber according to the partial pressure method. Mixing and rest periods took place for ~10 minutes each. Homogeneity of the mixture could be visually inspected through the Schlieren system. The encasing sleeve was then translated, establishing continuity between the chambers, and the quiescent mixture was simultaneously ignited. Flame propagation was terminated when the flame reached the walls of the inner chamber, with the total pressure buildup attenuated due to the volume ratio between the two chambers. Therefore, a near-constant-pressure flame was established.

The temperature of the initial combustible mixture was kept at $298 \pm 3\text{K}$, and the ignition energy was adjusted to be close to its minimum value to achieve ignition, reducing its influence of initial flame acceleration.

Data Reduction - Measurements were restricted to spherical, smooth flames having diameters between 10 and 40 mm to avoid spark and wall effects. Results were averaged over 3-4 measurements for each point. Linear extrapolation [5,6] was chosen to obtain the unstretched flame speed (s_b^0) and the Markstein length (L_b), according to the relation $s_b = R = s_b^0 - L_b \kappa$, where κ is the stretch rate given by $\kappa = 2\dot{R}/R$. Substituting κ in the expression for \dot{R} and integrating, we get the final correlation [7]: $R + 2L_b \ln R = s_b^0 t + C$, where, by measuring the flame radius (R) versus time, one can obtain L_b and s_b^0 by linear regression, after filtering the data for high-frequency noise. The unburned flame speed (s_u^0) is obtained by dividing s_b^0 by the density ratio of the planar flame through continuity.

From the concept of a one-step overall reaction, overall reaction orders (n) were extracted from both the experimental and computational data on the s_u^0 vs. pressure plots, according to the relation $n = 2 + 2[\partial \ln s_u^0 / \partial \ln p]$ that comes from dimensional analysis [8,9].

Numerical computations - The experimentally determined laminar flame speeds were compared to those of planar, adiabatic, one-dimensional premixed flames calculated by the Sandia PREMIX code [10]. H_2 flames were simulated using a detailed reaction mechanism including 9 species and 21 elementary reactions [11], CH_4/air flames with 53 species and 325 reactions (GRI-Mech 3.0) [12], and $\text{CH}_4/\text{O}_2/\text{He}$ flames with 35 species and 217 reactions (GRI-Mech 3.0 without N-containing species and reactions). Third-body efficiency factors for Ar were used for He, and Soret effects were included. Adaptive gridding was used to map the flame structure. Radiative heat loss was not included. The unburned mixture temperature at the cold boundary was set at 298K, and zero gradients were imposed at the burned boundary.

RESULTS AND DISCUSSION

Experimental data on H_2 -air and CH_4 -air mixtures at 1 atm as a function of equivalence ratio has been compared with results from existing literature, and the good agreement provides a benchmark of accuracy for the present setup. These comparisons, along with plots of H_2 and CH_4 flame speeds as a function of equivalence ratio for different pressures can be found in Refs. 2-4. Figure 1 presents laminar flame speeds, Markstein lengths and overall reaction orders as a function of pressure for different H_2 - O_2 -inert mixtures. Discrepancies between experiments and com-

putations can be attributed to little validation of the mechanism used for the rich branch, uncertainties on H-atom diffusion properties and on the third body efficiency of He.

Figure 2 shows laminar flame speeds and Markstein lengths as a function of pressure for different CH₄-O₂-He mixtures. In general, for both H₂ and CH₄ mixtures, laminar flame speeds and Markstein lengths decrease with pressure, while L_b increases with equivalence ratio for a given pressure. The decrease in L_b with pressure is due to the decrease in flame thickness, while the decrease in s_u^0 follows from the fact that $n < 2$ for most of the mixtures studied (see exception for low pressures in Figs. 1a and 1c), meaning that the overall density increase outweighs the increase in concentration in the Arrhenius rate expression. Third-body termination reactions, such as $H+O_2+M \leftrightarrow HO_2+M$ are also favored at high pressures, contributing to this outcome by lowering n . Overall reaction orders decrease with pressure for H₂-air, H₂-O₂-He and CH₄-air mixtures, and increase with pressure for CH₄-O₂-He mixtures.

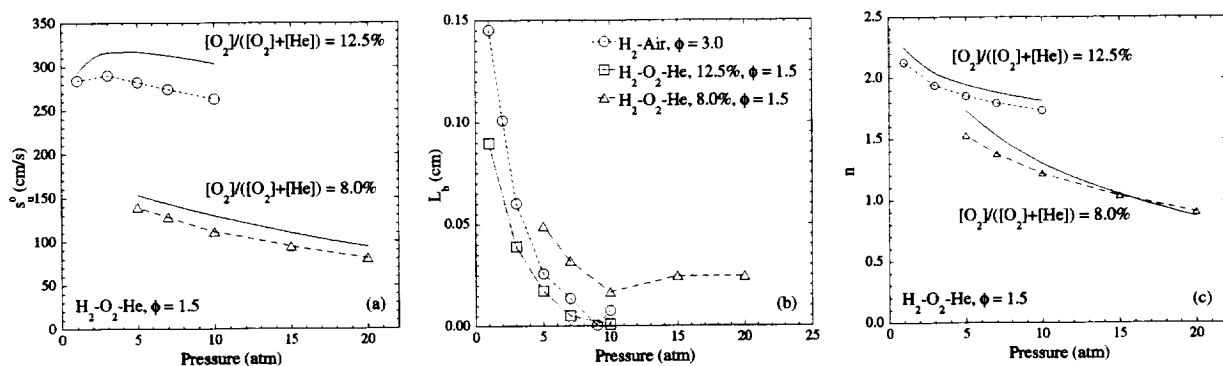


Fig. 1. Variation of flame properties of H₂-O₂-inert mixtures at fixed equivalence ratios with pressure: (a) laminar flame speed, (b) Markstein length and (c) overall reaction order. Symbols represent experimental data; lines represent simulation.

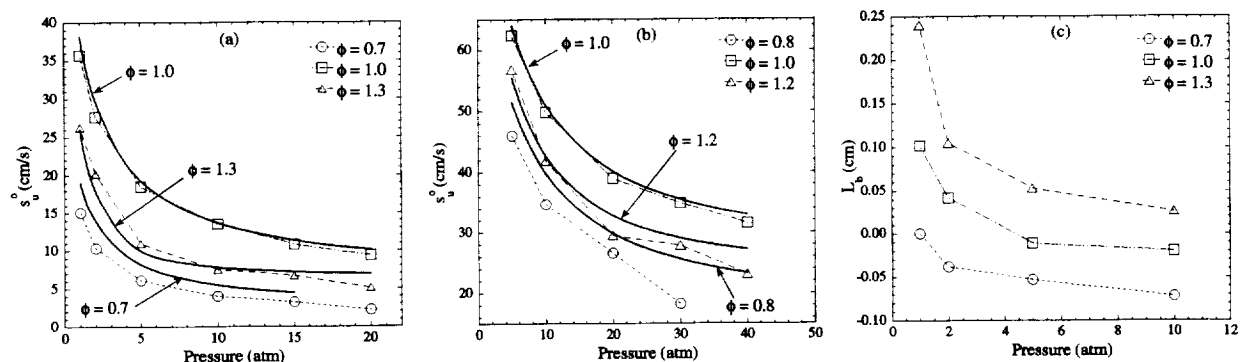


Fig. 2. Variation of laminar flame speed of (a) CH₄-air and (b) CH₄-O₂-He, O₂/(He+O₂) = 17% mixtures at fixed equivalence ratios with pressure; (c) variation Markstein length of CH₄-air mixtures with pressure. Symbols represent experimental data; lines represent simulation.

Smooth flame speeds could only be measured for H₂-air flames at 1 atm (for all ϕ) or at very high ϕ (for higher pressures). At 2 atm, most lean and near-stoichiometric H₂-air flames are already unstable to hydrodynamic and thermal-diffusive instabilities, as seen in Fig. 3. Flames 3a and 3b have the same adiabatic flame temperature, but the former has $L_b > 0$ (and hence $Le > 1$, which makes it stable to thermal-diffusive cells [9]), while the latter has $L_b < 0$ ($Le < 1$). Fig. 3a also shows that large wrinkles, characterizing hydrodynamic cells, are formed first, while the thermal-diffusive cells (of smaller size and evenly distributed throughout the flame surface) have their onset at a later stage of propagation. CH₄-air flames do not manifest any thermal-diffusive

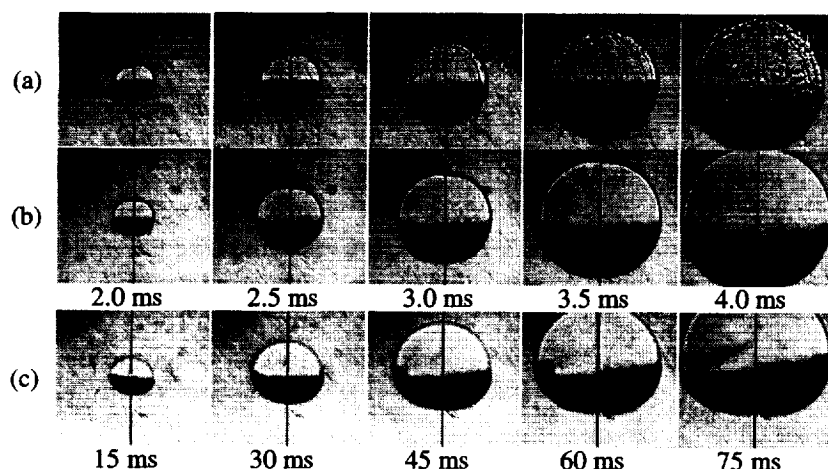


Fig. 3. Schlieren pictures of H_2 -air flames at 2 atm: (a) $\phi = 0.56$, (b) $\phi = 3.00$. In (c) CH_4 -air, 2 atm, $\phi = 0.60$.

cells up to 40 atm (even for negative L_b), being unstable only to hydrodynamic wrinkles above 10 atm. Part of this phenomenon might be due to the stabilizing effect of positive stretch in the outwardly-propagating flame [13], and part due to the size of the chamber used. Thermal-diffusive instabilities have been reported for CH_4 -air flames at such pressures [14], but their onset is delayed until a critical radius is

reached. Two strategies were devised to delay the onset of instabilities: higher O_2 dilution with inert in the oxidizer, weakening the flame and therefore reducing the effect of thermal expansion; and replacement of N_2 with He as inert, thereby increasing the mixture's Le . Both strategies also increase the flame thickness, hence damping the baroclinic torque across the flame that supports hydrodynamic instabilities. They have extended the smooth flame propagation regime up to 20 atm for H_2 and 30 atm for CH_4 .

Figure 3 also shows that, for sufficiently off-stoichiometric CH_4 mixtures at high pressures, the low flame speed in conjunction with the increased density differential between the unburned and the burned gas enhance the buoyancy and thereby promote flame shape distortion. Fundamental flame speeds could not be extracted for these near-limit flames which are of great practical interest, e.g. in lean natural gas combustion for energy efficiency and pollution control.

REFERENCES

- [1] Tse, S.D., Zhu, D.L., and Law, C.K. *A High-Pressure Combustion Apparatus* (2000), in preparation.
- [2] Tse, S.D., Zhu, D.L. and Law, C.K. *Proc. Combust. Inst.* 28 (2000), in press.
- [3] Rozenchan, G., Tse, S.D., Zhu, D.L. and Law, C.K. *AIAA* 2001-1080 (2001).
- [4] Rozenchan, G. *M.S.E. Thesis*, Princeton University (2001), in preparation.
- [5] Davis, S.G. and Law, C.K. *Combust. Sci. and Tech.* 140:427-449 (1998).
- [6] Vagelopoulos, C.M., Egolfopoulos, F.N. and Law, C.K. *Proc. Combust. Inst.* 25:1341 (1994).
- [7] Taylor, S.C. *Ph.D. Thesis*, University of Leeds (1991).
- [8] Sun, C.J., Sung, C.J., He, L. and Law, C.K. *Combust. Flame* 118:108-128 (1999).
- [9] Law, C.K. and Sung, C.J. *Prog. Energy Combust. Sci.* 26:459-505 (2000).
- [10] Kee, R.J., Grcar, J.F., Smooke, M.D. and Miller, J.A. SAND85-8240 (1985).
- [11] Mueller, M.A., Kim, T.J., Yetter, R.A., Dryer, F.L. *Int. J. Chem. Kinet.* 31:113-125 (1999).
- [12] Smith, G.P., Golden, D.M., Frenklach, M., Moriarty, N.W., Eiteneer, B., Goldenberg, M., Bowman, C.T., Hanson, R.K., Song, S., Gardiner Jr., W.C., Lissianski, V.V. and Qin, Z. http://www.me.berkeley.edu/gri_mech/
- [13] Bechtold, J.K. and Matalon, M. *Combust. Flame* 67:77-90 (1987).
- [14] Manton, J., Von Elbe, G. and Lewis, B. *J. Chem. Phys.* 20:153-157 (1952).

STUDIES OF PREMIXED LAMINAR AND TURBULENT FLAMES AT MICROGRAVITY

(NASA Grant No. NAG3-2124)

M. Abid, K. Aung, C. Kaiser, J.-B. Liu, P. D. Ronney, J. Sharif
Department of Aerospace and Mechanical Engineering
University of Southern California, Los Angeles, CA 90089-1453

INTRODUCTION

Several topics relating to premixed flame behavior at reduced gravity have been studied. These topics include: (1) flame balls; (2) flame structure and stability at low Lewis number; (3) experimental simulation of buoyancy effects in premixed flames using aqueous autocatalytic reactions; and (4) premixed flame propagation in Hele-Shaw cells.

STRUCTURE OF FLAME BALLS AT LOW LEWIS-NUMBER (SOFBALL)

The SOFBALL space flight experiments on STS-83 and STS-94 in 1997 showed that spherical, stable, stationary flame structures ("flame balls") could be observed in long-duration microgravity experiments in low Lewis number premixed gases near extinction limits. The resulting data provided the opportunity to study the interactions of the two most important processes necessary for combustion (chemical reaction and heat and mass transport) in the simplest possible configuration.

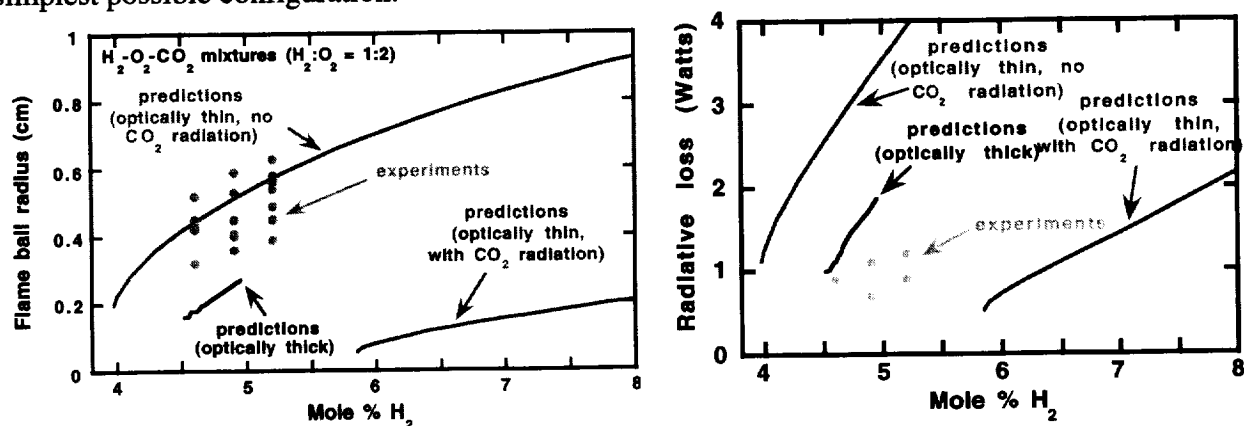


Figure 1. Predicted and measured flame ball properties as a function of fuel concentration for $H_2 - O_2 - CO_2$ mixtures at 1 atm. Left: radii. Right: radiant power.

Despite their simplicity, flame balls presents a number of interesting challenges to the computationalist. In particular, prior computations comparing results obtained assuming optically thin vs. optically opaque (no transmission) CO_2 radiation suggest that reabsorption of emitted radiation is probably a dominant effect in flame ball mixtures diluted with CO_2 . Consequently, an investigation of the effects of reabsorption of emitted radiation on flame balls was conducted using a numerical code with detailed chemical, transport, and radiative emission-absorption models. A Statistical Narrow Band—Discrete Ordinates method was used to model radiative transport. It was found that reabsorption effects were moderate in H_2 -air mixtures but dominant in H_2 - O_2 - CO_2 mixtures, due to the fact that in the former case the ambient mixture contains only radiatively inert gases whereas in the latter case CO_2 , a strong absorber, is present in the unburned gas. It was found that reabsorption of emitted radiation led to substantially larger flame ball sizes and wider extinction limits than calculations using optically-thin radiation models (Fig. 1). It was found that for H_2 - O_2 - CO_2 mixtures, the agreement between model predictions and experimental results was much closer when reabsorption effects were incorporated (Fig. 1). It is concluded that fundamental flammability limits of flame balls can exist

due to radiative heat loss, but these limits are strongly dependent on the emission-absorption spectra of the reactant and product gases and their temperature dependence, and cannot be predicted using gray-gas or optically-thin model parameters.

FLAME STRUCTURE AND STABILITY AT LOW LEWIS NUMBER

Recent theoretical work on premixed flames by Linan and by Buckmaster and nonpremixed flames by Dold indicate that at low Lewis number, a transition in the structure of stretched premixed flames in a counterflow from smooth or moderately cellular flames to flame tubes may occur near extinction, which enables the flame to survive in the presence of strain that would cause it to extinguish were it forced to remain planar and continuous. This behavior is somewhat analogous to spherically-symmetric flame balls observed in microgravity experiments where in that case radiative transfer rather than extensional strain is the prevailing loss mechanism, but in both cases the Lewis number enhancement of flame temperature causes the curved flame to survive where a plane flame could not. With this motivation, flames in strained H_2 - O_2 - N_2 mixtures were studied using a counterflow slot-jet apparatus (Fig. 2). Three configurations were examined: single premixed, twin premixed and nonpremixed flames. For all three configurations a wide variety of nonplanar flame structures were observed. Two extinction limits, one at very high strain (corresponding to a residence time limitation) and one at low strain (corresponding to a heat loss extinction) were found (Fig. 3). It was found that as the fuel concentration was decreased for a fixed value of strain rate, the following sequence of behavior was observed (Figs. 3 and 4) —(1) twin wrinkled flames, (2) twin flames with some portions of the two flames merged, a structure which we have termed bridged tubes, (3) isolated tubes which are inevitably travelling in the direction parallel to the stagnation plane, (4) two isolated, stationary tubes, (5) one isolated, stationary tube and (6) complete flame quenching. Both strain-induced and heat-loss induced quenching was observed. At high flow velocities transition to turbulent flow was noted. For nonpremixed flames (not shown), nonplanar flame structures were observed only for near-extinction conditions, but the resulting flame shapes were quite similar to those of premixed flames.

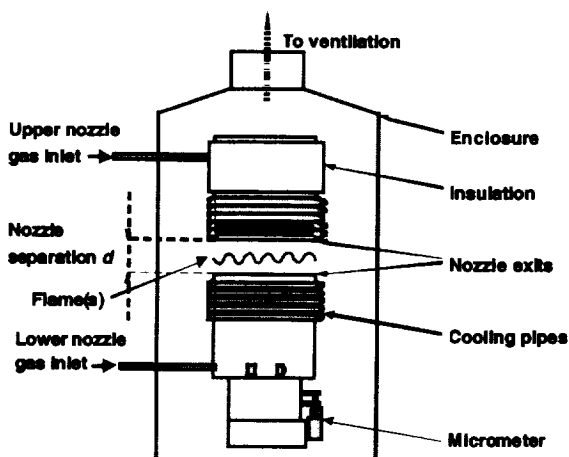


Figure 2. Schematic diagram of counterflow slot-jet burner.

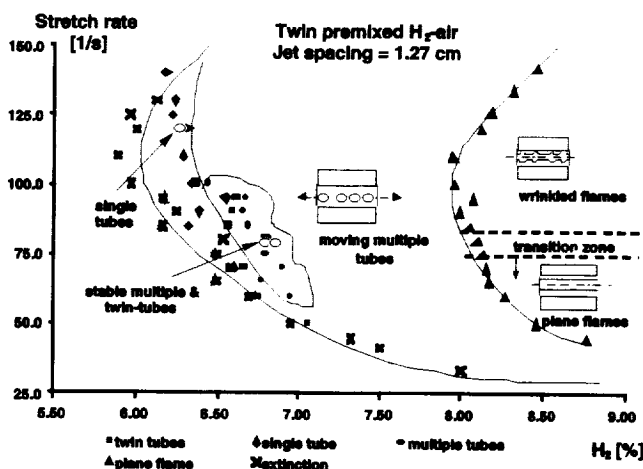


Figure 3. Stability and extinction limits for twin H_2 -air premixed flames.



Figure 4. Shadowgraph images of twin premixed flames. Except where noted, jet spacing is 1.27 cm. (a). Plane flames, 8.26% H_2 , strain rate $60\ s^{-1}$.



Figure 4.(b) Wrinkled flames, $H_2 = 8.10\%$, stretch rate $110\ s^{-1}$.

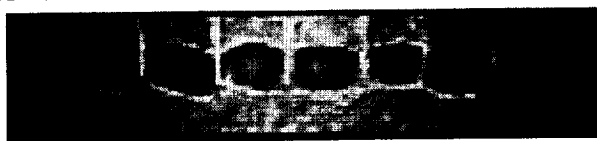


Figure 4.(c) Moving tubes front view, 6.96% H_2 , strain rate $60\ s^{-1}$.

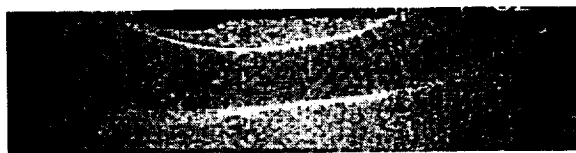


Figure 4. (d) Moving tubes side view, jet spacing 1.35 cm, 6.96% H_2 , strain rate $56\ s^{-1}$.



Figure 4.(e) Twin tubes, 6.68% H_2 , strain rate $60\ s^{-1}$.

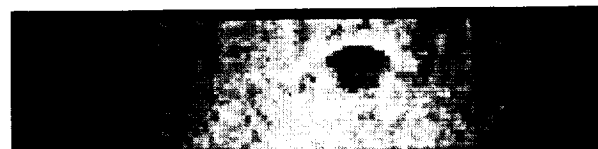


Figure 4. (f) Single tube in center, 6.64% H_2 , strain rate $60\ s^{-1}$.

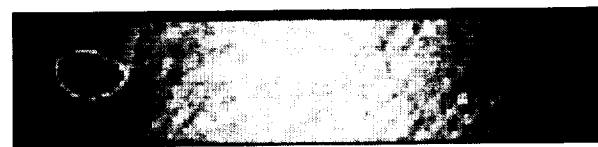


Figure 4. (g) Single tube near wall,, 6.11% H_2 , strain rate $100\ s^{-1}$.



Figure 4. (h). Turbulent flame structure, 6.9% H_2 , strain rate $158\ s^{-1}$.

LIQUID FLAMES

The PI has introduced the use of aqueous autocatalytic chemical reaction fronts for the experimental simulation of combustion processes. These fronts exhibit little density change across the front, have simple chemistry, are unaffected by heat losses and have high Schmidt numbers, allowing the front to remain flamelet-like even in the presence of very strong flow disturbances or turbulence. Thus, such fronts are useful for experimental study of combustion under conditions more readily simulated by available theoretical and numerical models. Hele-Shaw cells are frequently employed to study buoyancy effects in fluid systems in a simple quasi-two-dimensional geometry where the flow is governed by a linear equation (Darcy's law). Thus, autocatalytic reactions in Hele-Shaw cells represent the simplest possible experimental realization of the interaction of a propagating front with buoyancy-induced convection. We have conducted experiments buoyantly unstable upward-propagating autocatalytic reaction-diffusion fronts and non-reacting displacement fronts in Hele-Shaw cells and found a fingering-type instability (Fig. 5) whose wavelengths (λ^*) are consistent with an interfacial tension (Σ) at the front caused by the change in chemical composition, despite the fact that in both cases the solutions are miscible in all proportions. Using the Saffman-Taylor model for the maximum wavelength of disturbances at an interface in a Hele-Shaw cell, the relation $\Sigma \cong K/\tau$, where τ is the interface thickness and $K \cong 4 - 2 \times 10^{-6}$ dyne for weak ionic solutions, is shown to enable prediction of the observed values of λ^* for both types of fronts as well as results of several prior experiments on miscible fronts. This value of K typically yields tensions on the order of 0.005

dyne/cm, which is more than 10,000 times smaller than that of a water-air interface at room temperature, yet this tension has a dominant effect on the observed flow and fingering patterns.

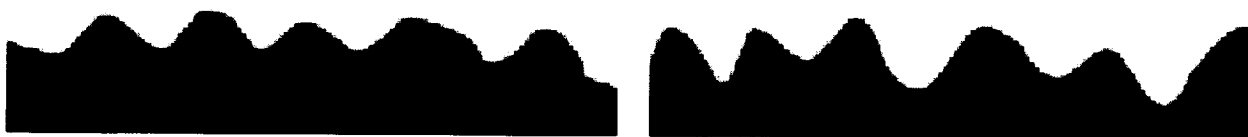


Figure 5. Contrast-enhanced images of interfaces in Hele-Shaw cells. Left: upward propagating reaction-diffusion front with $s = 0.0038$ cm/s, $w = 1.0$ mm, $\delta = 0.00032$, $Pe = 63$, field of view 5.0 cm wide. Right: non-reacting displacement front of water over water/ethanol solution with $KMnO_4$ dye, $w = 0.80$ mm, $\delta = -0.00036$, $\theta = 180^\circ$, $Pe = 85$, field of view 5.4 cm wide.

PREMIXED-GAS FLAME PROPAGATION IN HELE-SHAW CELLS

Premixed gas flame fronts are subject to a number of instability mechanisms that affect their propagation rates and shapes via wrinkling. To obtain a more detailed understanding of these instabilities in a simple geometry, experiments were performed in a 600 mm x 400 mm x 13 mm Hele-Shaw cell using methane and propane as fuel and N_2 or CO_2 as diluents. Upward, downward and horizontal propagation configurations were tested. In this way the effects of buoyancy, thermal expansion and Lewis number were studied. Fronts with a variety of burning velocities (S_L) and Lewis numbers were examined. Wrinkling was observed for all flames examined. The burning rates of these flames are quite different from their laminar, unwrinkled values. Values of S_T/S_L in the quasi-steady stage were higher for upward vs. downward propagation, but only weakly dependent on Lewis and Peclet numbers (Figure 6). These results show that even for mixtures with high Lewis number (stable to diffusive-thermal effects) at microgravity, thermal expansion and viscosity changes across the front will lead to flame instabilities. These results also indicate that the behavior of flame propagation in narrow channels such as crevice volumes in premixed-charge internal combustion engines may be quite different from that inferred from simple laminar flame experiments. This behavior is noteworthy because flame quenching in crevice volumes is an important source of unburned hydrocarbon emissions in these engines.

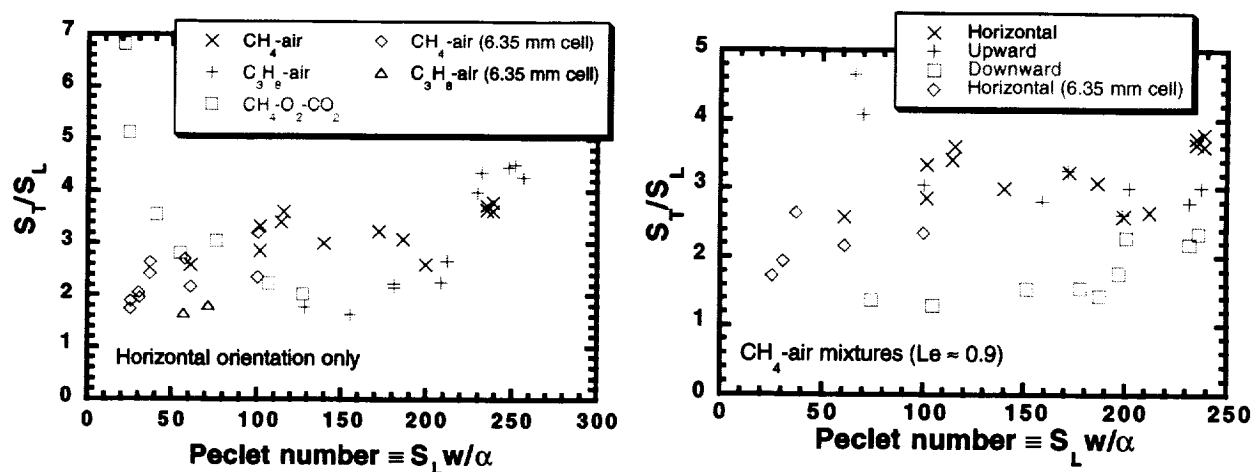


Figure 6. Effect of Peclet number on steady flame propagation speeds (relative to laminar burning velocity). Left: Varying fuel- O_2 -diluent combinations having varying Lewis numbers. Right: Varying propagation direction relative to gravity.

THE COOL FLAMES EXPERIMENT

Howard Pearlman[†]
University of Southern California
Department of Aerospace and Mechanical Engineering
Los Angeles, CA 90089
howard.pearlman@grc.nasa.gov

Richard Chapek, Donna Neville, William Sheredy
NASA GRC, Cleveland, OH 44135

Ming-Shin Wu
NCMR, Cleveland, OH 44135

Robert Tornabene
ZIN Technologies, Brook Park, OH 44142

INTRODUCTION

A space-based experiment is currently under development to study diffusion-controlled, gas-phase, low temperature oxidation reactions, cool flames and auto-ignition in an unstirred, static reactor. At Earth's gravity (1g), natural convection due to self-heating during the course of slow reaction dominates diffusive transport and produces spatio-temporal variations in the thermal and thus species concentration profiles via the Arrhenius temperature dependence of the reaction rates. Natural convection is important in all terrestrial cool flame and auto-ignition studies, except for select low pressure, highly dilute (small temperature excess) studies in small vessels (i.e., small Rayleigh number).

On Earth, natural convection occurs when the Rayleigh number (Ra) exceeds a critical value of approximately 600 (Tyler, 1966; Fine, et. al., 1970; Barnard and Harwood, 1974). Typical values of the Ra, associated with cool flames and auto-ignitions, range from 10^4 - 10^5 (or larger), a regime where both natural convection and conduction heat transport are important. When natural convection occurs, it alters the temperature, hydrodynamic, and species concentration fields, thus generating a multi-dimensional field that is extremely difficult, if not impossible, to be modeled analytically (Griffiths, et. al., 1971; Melvin, 1969). This point has been emphasized recently by Kagan and co-workers (Kagan, et. al., 1997; Volpert, et. al., 2000) who have shown that explosion limits can shift depending on the characteristic length scale associated with the natural convection. Moreover, natural convection in unstirred reactors is never "sufficiently strong to generate a spatially uniform temperature distribution throughout the reacting gas (Griffiths et. al., 1974)." Thus, an unstirred, nonisothermal reaction on Earth does not reduce to that generated in a mechanically, well-stirred system.

Interestingly, however, thermal ignition theories (Semenov, 1958; Frank-Kamenetskii, 1939, 1940) and thermokinetic models (Yang, 1969) neglect natural convection and assume a heat transfer correlation of the form: $q = h(S/V)(\bar{T} - T_w)$ where q is the heat loss per unit volume, h is

[†] Corresponding Author

the heat transfer coefficient, S/V is the surface to volume ratio, and $(\bar{T} - T_w)$ is the spatially averaged temperature excess. This Newtonian form has been validated in spatially-uniform, well-stirred reactors, provided the effective heat transfer coefficient associated with the unsteady process is properly evaluated (Griffiths, et.al., 1974; Gray, et.al., 1974). Unfortunately, it is not a valid assumption for spatially-nonuniform temperature distributions induced by natural convection in unstirred reactors. "This is why the analysis of such a system is so difficult (Griffiths, et. al., 1974)."

Historically, the complexities associated with natural convection were perhaps recognized as early as 1938 (Frank-Kamenetskii, 1939) when thermal ignition theory was first developed. In the 1955 text *Diffusion and Heat Exchange in Chemical Kinetics*, Frank- Kamenetskii recognized that "the purely conductive theory can be applied at sufficiently low pressure and small dimensions of the vessel when the influence of natural convection can be disregarded." This was reiterated by Tyler in 1966 (Tyler, 1966) and further emphasized by Barnard and Harwood in 1974. Specifically, they state: "It is generally assumed that heat losses are purely conductive. While this may be valid for certain low pressure slow combustion regimes, it is unlikely to be true for the cool flame and ignition regimes (Barnard and Harwood, 1974)." While this statement is true for terrestrial experiments, the purely conductive heat transport assumption is *valid* at microgravity (μg).

Specifically, buoyant complexities are suppressed at μg and the reaction-diffusion structure associated with low temperature oxidation reactions, cool flames and auto-ignitions can be studied (Pearlman, 1999, 2000). Without natural convection, the system is simpler, does not require determination of the effective heat transfer coefficient, and is a testbed for analytic and numerical models that assume pure diffusive transport. In addition, μg experiments will provide baseline data that will improve our understanding of the effects of natural convection on Earth.

GROUND-BASED COOL FLAME AND AUTO-IGNITION STUDIES

Laboratory (1g) and KC-135 aircraft experiments are actively being conducted in preparation for the space flight. These tests are performed in a spherical, quartz reactor, housed in a preheated furnace. The vessel is filled with a fuel-oxidizer premixture and the ensuing reaction is monitored. Details of the hardware are discussed in the references 10 and 11.

Cool Flames

Representative cool flame images obtained in the lab and aboard the KC-135 aircraft are shown in figures 1a and 1b. Note that the cool flame at μg starts in the center of the spherical reactor and propagates radially outward.



Fig.1: Sequential cool flames images obtained using a 50v%n-C₄H₁₀-50v%O₂ premixture at 310°C and 3.2psia in a 10cm i.d. spherical quartz reactor in the (a) 1g and (b) KC-135 μg aircraft.

Multiple Cool Flames

Multiple cool flames are also observed at 1g for a select range of test parameters. To date, however, only one cool flame has been observed in the butane-oxygen system at μg , within the available 23s test time. To determine if the absence of multiple cool flames at μg is due to insufficient test time for thermal relaxation, an equimolar mixture of $\text{n-C}_4\text{H}_{10}\text{-O}_2$ was diluted with equal volumes of helium or argon to vary the thermal diffusivity of the mixture ($\alpha_{\text{He-mix}} \sim 4\alpha_{\text{Ar-mix}}$), thus, adjust the thermal relaxation time ($t_{\text{th}} \sim L^2/\alpha$).

The pressure histories associated with the reaction in the (a) Ar and the (b) He - diluted mixtures at μg are shown in figures 2a and 2b, respectively. The first pressure peak in the Ar-diluted trace and all pressure peaks in the He-diluted trace correspond to cool flames, as verified with the video record. As many as five sequential cool flames have been observed at μg !

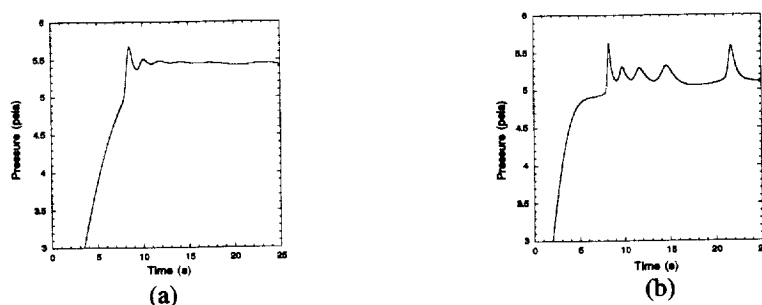


Fig. 2: Pressure traces at μg for a 25% $\text{n-C}_4\text{H}_{10}\text{-25\%O}_2$ mixture diluted with (a) 50% Ar, (b) 50% He in an aged 10.2cm i.d. spherical vessel, $T_{\text{vessel}}=310^\circ\text{C}$, $P_{\text{initial}}=4.95\text{psia}$.

Interestingly, the magnitude of the pressure excursions associated with successive cool flames in the He-diluted mixture at μg do not vary monotonically. As one might also expect, the intensity (integrated spectral emission) also varies. This is shown in figure 3, which corresponds to four successive cool flames in a He-diluted mixture at μg .

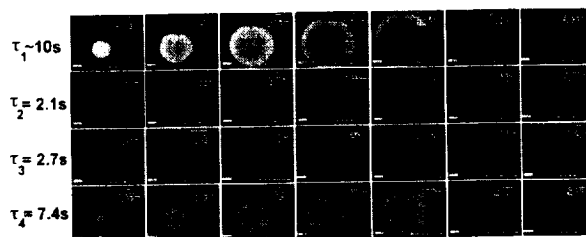


Fig.3: Multiple cool flames at μg ; τ_i ($i=1,2,3,4$) are the induction times; premixture: 25% $\text{n-C}_4\text{H}_{10}\text{-25\%O}_2\text{-50\%He}$ in an aged 10.2cm i.d. spherical vessel, $T_{\text{vessel}}=310^\circ\text{C}$, $P_{\text{initial}}=4.2\text{psia}$.

Multi-Stage Ignition

Multi-stage ignition, one (or more) cool flames followed by a hot ignition, has also observed at 1g and μg . Representative side-view images, depicting the development and progression of a representative two-stage ignition are shown in figures 4a and 4b, at 1g and μg , respectively. Similar to the cool flames shown in figure 1, both the cool flame and hot flame associated with the two-stage process originate near the top of the vessel at 1g and near the center at μg . Note that the second induction period (the time between the cool flame and the hot flame) is also shorter at μg than at 1g, perhaps due to the shorter

transport times at μg (diffusion times $\sim L^2/\alpha$ and L^2/D , where α is the mixture thermal diffusivity and D is species diffusion coefficient) compared to 1g (buoyant rise time $\sim (gL)^{1/2}$).

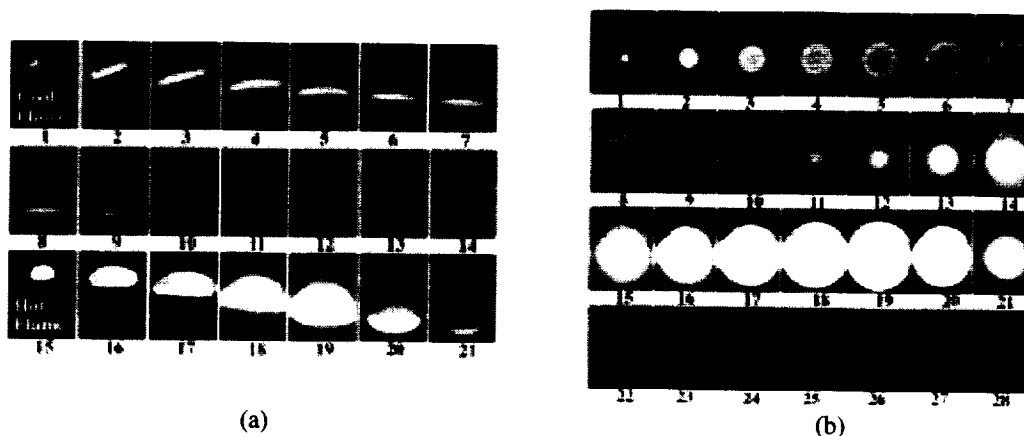


Fig.4: Two-Stage Ignition in 50v% $\text{n-C}_4\text{H}_{10}$ -50v% O_2 mixture, $P_{\text{initial}}=4.9\text{psia}$, $T=310^\circ\text{C}$, Vessel i.d.=10.2cm, (a) 1g , Time between sequential frames is $1/10\text{s}$, (b) μg ; Time between sequential frames is $1/30\text{s}$.

Single-stage ignition at μg has also been observed. Future effort aims to quantify the flame structure, evolution, and stability and map the ignition diagrams for different hydrocarbons.

ACKNOWLEDGMENTS

Special thanks to Professor John Griffiths for helpful discussions. This work is supported by NASA under NCC3-871.

REFERENCES

1. Barnard, J.A. and Harwood, B.A. (1974) *Combustion and Flame* **22** 35-42.
2. Fine, D.H., Gray, P. and MacKinven, R. (1970) *Royal Society of London* **A316** 223-240.
3. Frank-Kamenetskii, D.A. (1939) *Zh. Fiz. Khim.* **13** 738.
4. Frank-Kamenetskii, D.A. Diffusion and Heat Exchange in Chemical Kinetics, Princeton University Press, 1955.
5. Gray, P., Griffiths, J.F., and Moule, R.J. (1974) *Faraday Symposia of the Chemical Society* **9** 103-113.
6. Griffiths, J.F., Gray, B.F., and P. Gray (1971) *13th Symposium (Int.) on Comb.*, 239-248.
7. Griffiths, J.F., Gray, P., and Kishore, K. (1974) *Combustion and Flame* **22** 197-207.
8. Kagan, L., Beresyski, H., Joulin, G. and Sivashinsky, G. (1997) *CTM* **1** 97-111.
9. Melvin, A. (1969) *Combustion and Flame* **13** 438-9.
10. Pearlman, H. (1999) *Combustion and Flame* **121** (1-2) 390-3.
11. Pearlman, H. *The 3rd International Seminar on Fire and Explosion Hazards of Substances*, Lake Windermere, UK, April 10-14, 2000.
12. Semenov, N. N. Some Problems of Chemical Kinetics and Reactivity, Vol. 1, Pergamon Press, New York, 1958.
13. Tyler, B.J. (1966) *Combustion and Flame* **10** 90-91.
14. Volpert, V., Barillon, C., Dumont, T., Genieys, S., and Massot, M, *The Fire and Explosion Conf. hosted by the Univ. of Central Lancashire, Windermere, UK, August 10-14, 2000.*
15. Yang, C.H. and Gray, B.F. (1969) *Journal of Physical Chemistry* **73** (10) 3395-3406.

THE BEHAVIOR OF METHANE-AIR PARTIALLY PREMIXED FLAMES UNDER NORMAL- AND ZERO-G CONDITIONS

Ishwar K. Puri*, Suresh K. Aggarwal*, Chun Wai Choi*, and Uday Hegde†

*University of Illinois at Chicago, Chicago, Illinois

and

†National Center for Microgravity Research, Cleveland, Ohio

Introduction

Partially premixed flames (PPFs) represent a class of hybrid flames containing multiple reaction zones. These flames are established when less than stoichiometric quantity of oxidizer is molecularly mixed with the fuel stream before entering the reaction zone where additional oxidizer is available for complete combustion. This mode of combustion can be used to exploit the advantages of both nonpremixed and premixed flames regarding operational safety, lower pollutant emissions and flame stabilization. A double flame containing a fuel-rich premixed reaction zone, which is anchored by a nonpremixed reaction zone, is one example of a partially premixed flame[1]. A triple flame is also a PPF that contains three reaction zones, namely, a fuel-rich premixed zone, a fuel-lean premixed zone, and a nonpremixed reaction zone [2].

Herein we focus on two aspects of our investigation, one involving the development of optical diagnostics that can be used on a microgravity rig, which has been recently fabricated, and the other on the numerically predicted differences between normal- and zero-gravity PPFs. Both the measurements and simulations examine the detailed structure of methane-air PPFs stabilized on a Wolfhard-Parker slot burner.

Experimental Results

Optical diagnostic techniques have proved very useful for nonintrusive temperature and

composition measurements in flames, since they provide detailed data with high spatial and temporal resolution. Temperature measurement methods include Rayleigh and Raman scattering, laser-induced fluorescence, and higher-order light-scattering methods such as coherent anti-Stokes Raman spectroscopy. These techniques are used for both point and planar measurements, but do not readily yield quantitative information and cannot be easily used in microgravity applications due to both power and size restrictions. Alternatively, path-integrated or line-of-sight measurement techniques based on the change in the optical phase of a light beam, such as interferometry [3,4,5] and deflectometry [6], can be used to reconstruct the refractive index in flames and thereby infer the temperature distribution. These techniques are well suited to the available

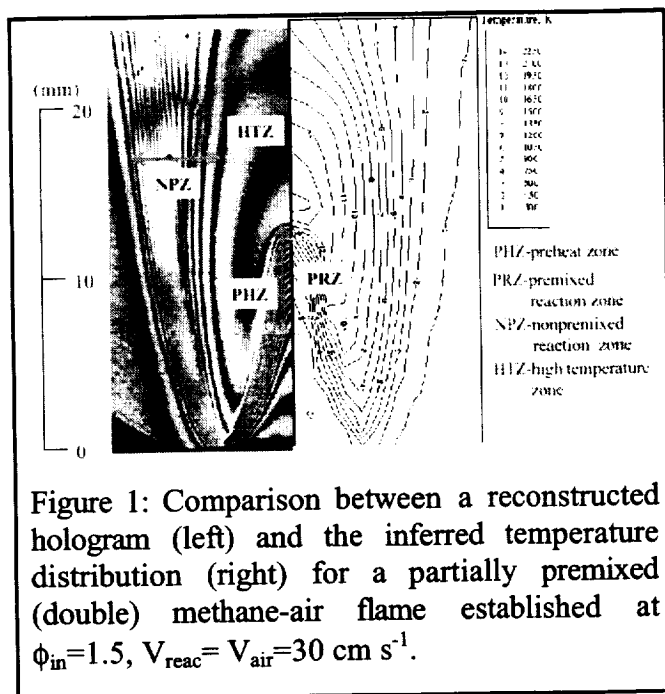


Figure 1: Comparison between a reconstructed hologram (left) and the inferred temperature distribution (right) for a partially premixed (double) methane-air flame established at $\phi_{in}=1.5$, $V_{reac}=V_{air}=30 \text{ cm s}^{-1}$.

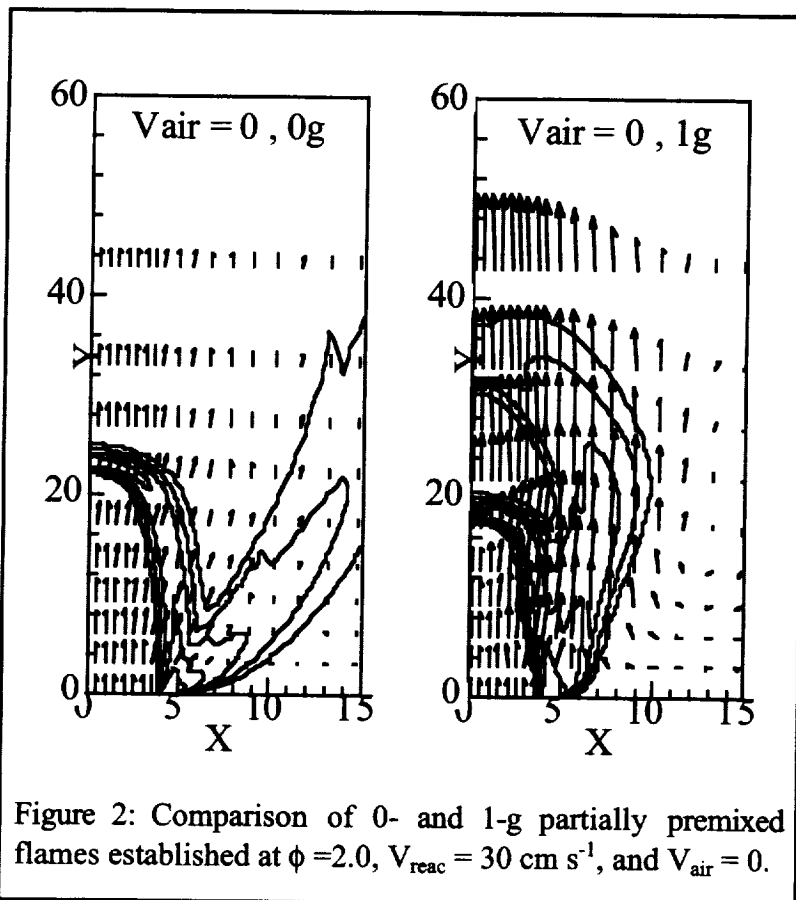


Figure 2: Comparison of 0- and 1-g partially premixed flames established at $\phi = 2.0$, $V_{\text{reac}} = 30 \text{ cm s}^{-1}$, and $V_{\text{air}} = 0$.

microgravity facilities.

We have developed an application of holographic interferometry that is appropriate for partially premixed flames. We have refined a double-exposure laser image plane holographic technique to measuring the temperature profiles of steady two-dimensional partially premixed flames [4,5]. An example of the fringe pattern that is formed is presented in Figure 1. We have shown that the refractive index in PPFs can be modeled by a relation that contains relatively minor errors, which depend upon the rich-side equivalence ratio. Larger errors arise in the case of nonpremixed flames. The maximum error in determining the local temperature lies in the range 6.3-34% (its value being $\approx 50 \text{ K}$ for

PPFs) for $1.5 \leq \phi_r \leq \infty$, while the corresponding average error lies in the range 2.4-12.3%. The temperature distributions determined by using holographic interferometry were found to correlate with the heat release in the various reaction zones.

Numerical Predictions

Although oscillating flames and flame-vortex interactions have been studied extensively, previous investigations have generally examined these phenomena in the context of either nonpremixed or premixed flames, but not with respect to a partially premixed flame (PPF) containing both premixed and nonpremixed reaction zones. Compared to either a premixed flame or a nonpremixed flame, the response of a PPF to perturbations or to a vortex may be significantly different due to thermochemical and transport interactions between the two reaction zones. We have examined the structure of unsteady partially premixed flames focusing on interactions between the two reaction zones and the existence of state relationships for oscillating partially premixed flames. Details of the computational model are to be found in the literature [2,7].

Figure 2 presents a comparison of the 0- and 1-g partially premixed flames established at $\phi = 2.0$, $V_{\text{reac}} = 30 \text{ cm s}^{-1}$, and without any coflow. The flame structure is depicted in terms of heat release rates and velocity vectors. For both cases, the flame structure is characterized by the presence of two reaction zones, one a rich premixed zone and the other a nonpremixed zone. These reaction zones are spatially separated, but involve strong interactions due to the

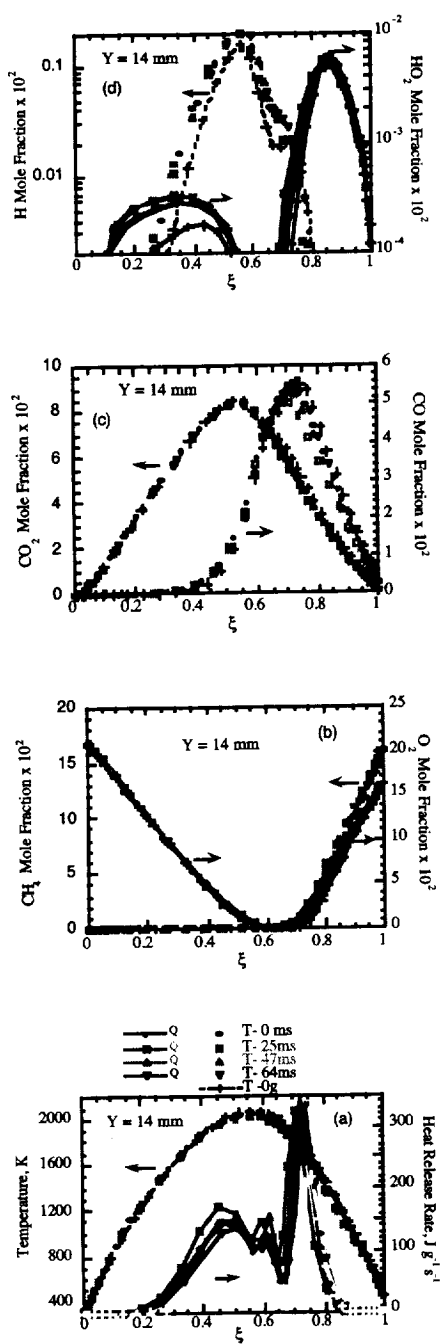


Figure 3: Comparison of 1- and 0-g flames in modified mixture fraction (ξ) space for the 1-g and 0-g PPFs established at $\phi=2.0$, $V_{\text{reac}}=30 \text{ cm s}^{-1}$, and $V_{\text{air}}=0$. State relationships are shown in terms of (a) temperature, (b) mole fractions of CH_4 and O_2 , (c) CO_2 and CO , and (d) H and HO_2 plotted versus ξ .

thermochemistry and scalar transport. The fuel is mostly consumed in the premixed zone to produce CO and H_2 , which are transported to and consumed in the nonpremixed zone. The nonpremixed zone in turn provides heat and H atoms to the premixed zone.

Under 1-g conditions, the flame heat release produces both flow dilatation and buoyant convection. Flow dilatation or gas expansion due to the heating causes downstream motion normal to the flamefront, which is quite evident in the region downstream of the inner premixed reaction zone for both 1- and 0-g flames. The buoyant gases accelerate the flow in an opposite direction to the gravity vector, causing air entrainment that enhances the fuel-air mixing and, consequently, influences the upstream region. The effect of flow dilatation is to push the outer nonpremixed reaction zone away from the central plane, while the buoyant convection has the opposite effect. For the 1-g flame, in the absence of coflow, the latter effect dominates. Consequently, the outer nonpremixed reaction zones differ distinctly for the 0- and 1-g flames. For the latter, this reaction zone is more compact and closer to the inner premixed zone, and has a closed tip. Thus, the effect of gravity on a partially premixed flame is to reduce the spatial separation, and, thereby, enhance interactions between the two reaction zones.

Figure 3 presents state relationships for the temperature and species mole fractions with respect to ξ for the 0- and 1-g flames at an axial location $Y=14 \text{ mm}$ above the burner exit. The species include the reactant species (CH_4 and O_2), an intermediate fuel species (CO), a major product species (CO_2), and two radical species (H and HO_2). In order to identify locations of the two reaction zones, the heat release rate profiles are also shown in Fig. 4a. Since the 1-g flame for these conditions is unsteady, the profiles for this flame are shown at four different times during one oscillation period. The profiles depict both the reaction zones. The rich premixed reaction zone for both 1- and 0-g flames lies between 0.72

$< \xi < 0.8$, and the nonpremixed zones between $0.47 < \xi < 0.55$. Although the 1- and 0-g flames have markedly different spatio-temporal characteristics, the temperature as well as the major and minor species profiles follow similar state relationships in terms of ξ for the two flames. Thus, an important observation is that the modified mixture fraction is effective in characterizing the structure of both steady and unsteady partially premixed flames.

The minor species (H and HO₂) profiles also exhibit remarkable similarity for the two flames in the modified mixture fraction space. The maximum in the H atom concentration occurs in the nonpremixed zone, implying that this zone represents a region of higher chemical activity from which H radicals are transported to the premixed reaction zone. HO₂ radicals are produced through the reaction $H + O_2 + M \rightleftharpoons HO_2 + M$ and mainly consumed through the reaction $HO_2 + H \rightleftharpoons OH + OH$ both in the premixed and nonpremixed reaction zones. This is confirmed by the HO₂ profiles presented in Figure 3d. These profiles also indicate that the chemical activity involving HO₂ is much higher in the premixed zone compared to that in the nonpremixed zone, and the production of HO₂ occurs upstream of the premixed reaction zone ($\xi > 0.9$), and outside of the nonpremixed reaction zone ($\xi < 0.3$).

Acknowledgment

This research was supported the NASA Microgravity Research Division through Grant No. NCC3-688.

References

1. Shu, Z., Choi, C. W., Aggarwal, S. K., Katta, V. R., and Puri, I. K., *Combust. Flame* 118:91-107 (1999).
2. Azzoni, R., Ratti, S., Aggarwal, S. K., and Puri, I. K., *Combust. Flame* 119: 23-40 (1999).
3. Hertz, H. M., *Optics Communications* 1:131-136 (1985).
4. Xiao, X., Choi, C. W., and Puri, I. K., *Combust. Flame* 120:318-332 (2000).
5. Xiao, X. and Puri, I. K., *Applied Optics* 40:731-740 (2001).
6. Faris, G. W. and Byer, R. L., *Applied Optics* 27:5202-5212 (1988).
7. Puri, I. K., Aggarwal, S. K., Ratti, S., and Azzoni, R., *Combust. Flame* 124:311-325 (2001).

GRAVITATIONAL INFLUENCES ON FLAME PROPAGATION THROUGH NON-UNIFORM, PREMIXED GAS SYSTEMS

Fletcher J. Miller and John Easton, National Center for Microgravity Research, MS 110-3, Cleveland, OH, 44135-3191, fletcher@grc.nasa.gov
Howard D. Ross, NASA Glenn Research Center, MS 500-115, Cleveland, OH 44135.
Anthony Marchese, Rowan University, Glassboro, NJ, 08028-1701
David Perry and Michael Kulis, Univ. of Akron, Akron, OH 44325-3601

INTRODUCTION

Flame propagation through non-uniformly premixed (or layered) gases has importance both in useful combustion systems and in unintentional fires. As summarized previously [1,2,3], *non-uniform* premixed gas combustion receives scant attention compared to the more usual limiting cases of diffusion or *uniformly* premixed flames, especially regarding the role gravity plays. This paper summarizes our progress on furthering the knowledge of layered combustion, in which a fuel concentration gradient exists normal to the direction of flame spread. We present experimental and numerical results for flame spread through propanol-air layers formed near the flash point temperature (25 °C) or near the stoichiometric temperature (33 °C). Both the model and experimental results show that the removal of gravity results in a faster spreading flame, by as much as 80% depending on conditions. This is exactly the opposite effect as that predicted by an earlier model reported in [4]. We also found that having a gallery lid results in faster flame spread, an effect more pronounced at normal gravity, demonstrating the importance of enclosure geometry. Also reported here is the beginning of our spectroscopic measurements of fuel vapor.

EXPERIMENTAL APPARATUS

The experimental rig, described more fully in earlier papers [1,2,3], consists of a porous bronze fuel holder 76 cm long by 10 cm wide by 3.2 mm deep, inside a thermally controlled tray that is covered by a stainless steel lid and Lexan gallery. The gallery has a 10 cm square cross section and can have either open or closed ends and top (one or the other is always open). The lid retracts automatically, and after a predetermined time for fuel vapor to diffuse and form a stratified, flammable boundary layer, a flame is ignited at one end and spreads to the opposite end of the gallery. We use the same rig for the microgravity experiments in the NASA Glenn 2.2s Drop Tower, with ignition and flame spread after release. A separate, but similar apparatus is used in normal gravity along with a Michelson interferometer to measure the fuel vapor concentration before and during flame spread [5].

In newly initiated research we have begun to measure the infrared spectrum of methanol as part of adopting a spectroscopic technique for its detection that is suitable for drop tower tests. A Fourier Transform Infrared (FTIR) spectrometer records training spectra in a range of conditions including temperature, methanol concentrations, and water concentrations. We designed and built a heated sample cell that allows temperatures of 500 °C to be achieved. A chemometric analysis will be used to correlate the spectral data with concentrations and temperature and to identify the optimal spectral window of a few wavenumbers.

NUMERICAL MODEL

The model used in this work was originally developed for studying flame spread across sub-flash liquids, primarily 1-propanol and 1-butanol [6]. Previous references give much more

detail; here only a summary is given. The numerical model uses the SIMPLE algorithm [7] and a hybrid-differencing scheme to solve the gas-phase continuity, species, energy, x-y momentum equations and the liquid phase energy and x-y momentum equations. To simulate the experiments, the model initially runs for a specified time period (e.g. 60 seconds) without introducing the ignition source. During this period, a time step of 5 ms is used. This allows the fuel to vaporize at the pool surface and diffuse into the gas phase, setting up initial conditions consistent with the experiments. The output from the non-reacting case becomes an input to the reacting case. Reference [3] contains a diagram and further description of the model.

For the work reported here, we made three primary changes to the model. One, we changed the gallery dimensions to closely match the experiment. Two, modifications to the temperature-vapor pressure relationship produced better agreement with both the literature's vapor pressure data and our experimental flame spread results at temperatures above the flashpoint. Three, the effect of the porous bronze fuel holder was accounted for by modifying the liquid phase density, specific heat and thermal conductivity to be closer to that of bronze using a weighting formula.

RESULTS

Figure 1 shows the flame position as a function of time, as determined from the video record for representative cases of 1-propanol at 27 °C. The slope of the experimental data yields the flame spread rate. As can be seen, the flame spread rates are steady, with the microgravity flame spreading faster. Also shown on the graph are the results for the numerical model, which are obtained until a steady flame spread rate is achieved. These data also show a difference between 1g and μ g spread rates, but further work needs to be done to obtain better agreement with the experiments, and to check the spread rate for longer times.

Figure 2 contains a summary of our experimental propanol data for various diffusion times at 27 °C, in normal and microgravity both with and without a lid. As can be seen, there is some variation in the data (the uncertainty is similar to that found in the literature), and therefore several—usually four—nominally identical tests were conducted at each condition to achieve a good average. Once averaged, the results clearly show an effect of gravity level, with the flame spreading faster in microgravity, especially at longer pre-ignition diffusion times. This is true regardless of the presence of a lid on the gallery, which has the effect of increasing the flame spread rate. For a 60 s diffusion time, the μ g flame spread 81% faster with the lid off, and 63% faster with it on, compared to 1g. At 35 °C (not shown) the 1g/ μ g flame spread rates were much closer, varying by about 15% with the lid off, and being essentially identical with the lid on.

Prior to ignition, the predicted mole fraction contours are essentially horizontal lines (except near the ends of the gallery where vapor spill-over occurs). In Figure 3 we show the predicted fuel mole fraction after ignition for a 1g case. As can be seen, the flame pushes the fuel vapor upwards as it approaches, increasing the effective flammable layer thickness. The work of [8] reports a similar displacement of fuel for methane layers along ceilings. This plot also shows the nature of the predicted double flame (a triple flame with the lowest branch quenched), with the premixed flame along the front and top, a non-combustible region in the middle, and a diffusion flame burning along the fuel surface where excess oxygen meets evaporating fuel vapor.

Figure 4 shows a similar plot as deduced from interferometric measurements in normal gravity at the same conditions as Figure 3. The molar refractivity of 1-propanol was not available to us, but we used a value of 18 based on comparisons of methanol/methane and ethanol/ethane values reported in [9] for the calculations. The agreement is good between model and experiment, with both showing roughly the same flammable layer thickness and the effect of fuel layer displacement by the flame. What is not as well predicted is the flame thickness (as deduced from the contour lines becoming disrupted), which is clearly larger in the experiment.

As part of the solution procedure the numerical code calculates the pressure; Figure 5 reports these results for both 1g and μ g. The contours have been color coded for ease of interpretation, with darker (blue) regions being lower pressure, and lighter (redder) regions being higher. It is clear that one major difference between the 1g and 0g flame, as predicted by the model, is that in the μ g case the flame is spreading into a region of lower pressure, while just the opposite is true in 1g. The difference between the highest and lowest pressure is about 47 Pa in both cases; this difference may contribute to the higher flame spread rate in μ g.

For the spectroscopic measurements, a preliminary spectrum in Figure 6 shows two possible candidate intervals for methanol detection; one in the 7191 cm^{-1} region; the other in the 7195 cm^{-1} region as measured by our FTIR. The two methanol peaks are relatively large compared to the water peaks and relatively sharp compared to other methanol peaks in this region. The 7195 cm^{-1} region is most preferable since it contains both methanol and water information.

CONCLUSIONS

We have shown flame spread through non-homogeneous gas layers can be up to 80% faster in μ g as compared to 1g. Both experiments and a numerical model have demonstrated this phenomenon. Further work needs to be done on obtaining quantitative agreement between the model and experimental flame spread rates; in particular we have initiated changes in the vapor pressure model and added heat loss to a bronze fuel holder. We obtained good agreement in the fuel vapor mole fraction predictions and measurements in 1g, and numerical results showed little difference in μ g. Therefore, the faster flame spread rate in μ g may be due to another effect, that of pressure, which we have begun to explore via the model and planned measurements. To make fuel vapor measurements in μ g, we have also begun methanol spectrum measurements.

ACKNOWLEDGEMENTS

We wish to acknowledge Ron Mileto and Frank Zaccaro for help on the drop rig, Dr. Nancy Piltch for valuable discussions of the spectroscopic technique, and Jennifer Akers at Rowan University for help with plotting some of the preliminary numerical data.

REFERENCES

- [1] F. J. Miller, E. B. White, and H. D. Ross, "Gravitational Influences on Flame Propagation Through Non-Uniform Premixed Gas Systems," NASA CP-10194, 343-348, 1997.
- [2] F. J. Miller, J. Easton, H. D. Ross, and A. Marchese, "Gravitational Influences on Flame Propagation Through Non-Uniform Premixed Gas Systems," NASA/CP-1999-208917, 57-60, 1999.
- [3] F. J. Miller, J. Easton, A. Marchese, and H. D. Ross, "Flame Spread Through Non-Homogeneous Gas Layers," presented at the Western States Section of the Combustion Institute Spring 2000 Meeting, Golden, CO, March 2000. Paper number 13-4.
- [4] M. Kaptein and C. E. Hermance, "Horizontal Propagation of Laminar Flames Through Vertically Diffusing Mixtures Above a Ground Plane," 16th Symposium (Int'l) on Combustion, 1295-1305, 1976.
- [5] E. B. White, "Flame Propagation Through Fuel Vapor Concentration Gradients," Master's Thesis, Case Western Reserve University, Dept. of Mechanical and Aerospace Engineering, 1997.
- [6] D. N. Schiller, H. D. Ross, and W. A. Sirignano, "Computational Analysis of Flame Spread Across Alcohol Pools," *Combust. Sci. Technol.*, vol. 118, pp. 205, 1996.
- [7] S. V. Patankar, *Numerical Heat Transfer and Fluid Flow*, Hemisphere Publishing Corporation, NY, 1980.
- [8] J. Liebman, J. Corry, and H. Perlee, "Dynamics of Flame Propagation through Layered Methane-Air Mixtures," *Combustion Science and Technology*, Vol. 2, pp. 365-375, 1971.
- [9] W. C. Gardiner, Y. Hidaka, and T. Tanzawa, "Refractivity of Combustion Gases," *Combustion and Flame*, Vol. 40, 213-219, 1981.

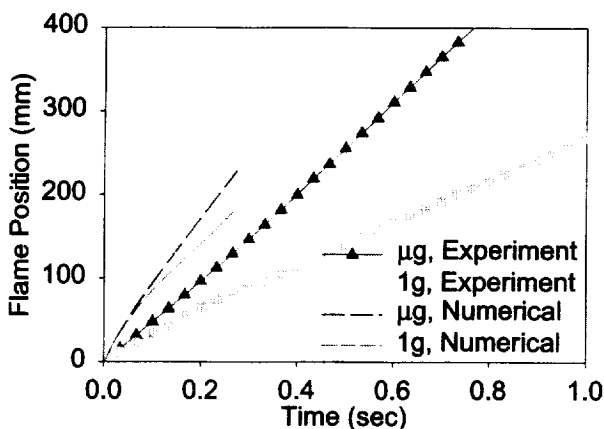


Figure 1. Flame position vs. time with a 60 s diffusion time for propanol in normal and microgravity, with the gallery lid off. Initial fuel temperature is 27 °C.

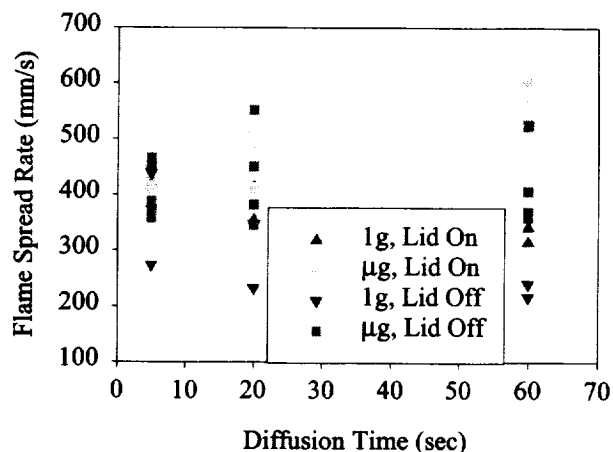


Figure 2. Summary of propanol tests with the gallery lid on or off. The data symbols represent the results of individual experiments.

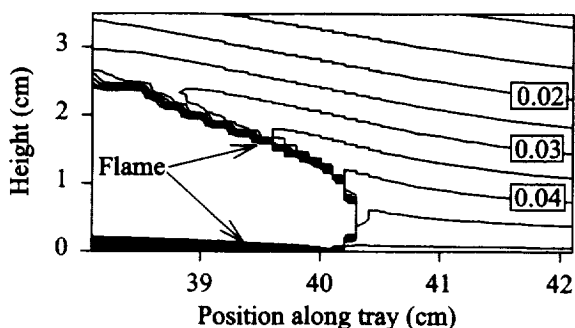


Figure 3. Numerical results of fuel vapor mole fraction at 35 °C and 60 second diffusion time.

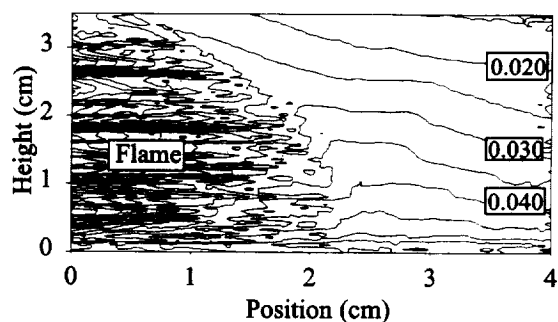


Figure 4. Experimental results for fuel vapor mole fraction at 35 °C and 60 s diffusion time.

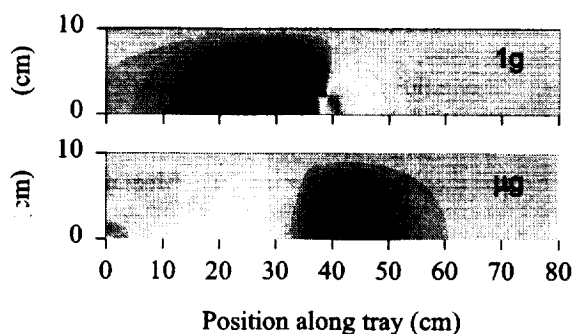


Figure 5. Pressure field in 1g and μ g, 35 °C, 60 s diffusion time. Darker regions are lower pressure. Flame is at 40 cm in 1g, 43 cm in μ g.

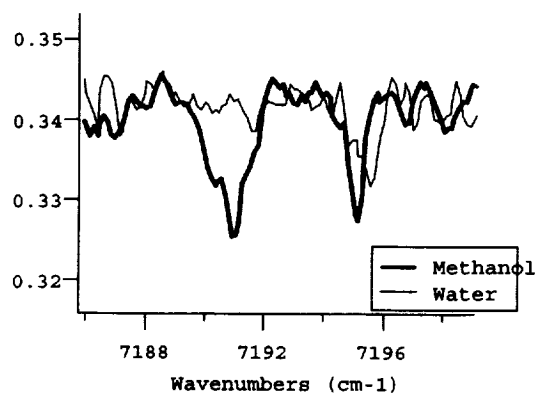


Figure 6. Methanol and water spectra. Vertical axis is proportional to transmission.

STRUCTURE AND SOOT FORMATION PROPERTIES OF LAMINAR FLAMES

A. M. El-Leathy, F. Xu and G. M. Faeth
Department of Aerospace Engineering
The University of Michigan
Ann Arbor, Michigan

INTRODUCTION

Soot formation within hydrocarbon-fueled flames is an important unresolved problem of combustion science for several reasons: soot emissions are responsible for more deaths than any other combustion-generated pollutant, thermal loads due to continuum radiation from soot limit the durability of combustors, thermal radiation from soot is mainly responsible for the growth and spread of unwanted fires, carbon monoxide emissions associated with soot emissions are responsible for most fire deaths, and limited understanding of soot processes in flames is a major impediment to the development of computational combustion. Motivated by these observations, soot processes within laminar premixed and nonpremixed (diffusion) flames are being studied during this investigation. The study is limited to laminar flames due to their experimental and computational tractability, noting the relevance of these results to practical flames through laminar flamelet concepts. Nonbuoyant flames are emphasized because buoyancy affects soot processes in laminar diffusion flames whereas effects of buoyancy are small for most practical flames (refs. 1-7).

This study involves both ground- and space-based experiments, however, the following discussion will be limited to ground-based experiments because no space-based experiments were carried out during the report period. The objective of this work was to complete measurements in both premixed (refs. 8-10) and nonpremixed (refs. 11-13) flames in order to gain a better understanding of the structure of the soot-containing region and processes of soot nucleation and surface growth in these environments, with the latter information to be used to develop reliable ways of predicting soot properties in practical flames. The present discussion is brief, more details about the portions of the investigation considered here can be found in refs. 8-13.

EXPERIMENTAL METHODS

Measurements in premixed flames were completed along the axis of a 60 mm diameter water-cooled porous-plug flat flame burner directed vertically upward, involving a total of twelve different fuel-rich ethylene/air and methane/oxygen flames at atmospheric pressure. Measurements in nonpremixed flames were completed along the axis of flames produced by a coflowing jet burner directed vertically upward with a 35 mm fuel port and a 60 mm inner diameter air port operating at atmospheric pressure. A total of six nonpremixed flames were studied, involving acetylene, ethylene, propylene and propane as fuels.

Measurements in both premixed and nonpremixed flames were as follows: soot volume functions using deconvoluted laser extinction, flow temperatures using deconvoluted multiline emission, soot structure using thermophoretic sampling and TEM analysis, concentrations of major gas species using sampling and gas chromatography, concentrations of some radical species (H, OH and O) using the deconvoluted Li/LiOH atomic absorption technique and streamwise velocities using laser velocimetry.

RESULTS AND DISCUSSION

Soot and Flame Structure. All soot particles were the same as observed in earlier work in diffusion flames (refs. 1-7). They consisted of roughly spherical primary particles that were monodisperse at each flame condition and collected into mass fractal aggregates having large variations of the number of primary particles per aggregate.

Samples of premixed flame structure can be found in refs. 8-10, present considerations will be limited to properties along the axis of a typical diffusion flame as illustrated in Fig. 1 for an ethylene-fueled flame. Flow velocities increase with distance due to effects of buoyancy, yielding a nonlinear variation of residence time with distance. Effects of radiant heat loss are substantial yielding a relatively flat temperature distribution with maximum values well below adiabatic flame temperatures. Primary soot particle diameters reach a maximum early in the soot formation region due to combined effects of soot nucleation, growth and oxidation. The original fuel eventually disappears due to effects of decomposition, oxidation and soot formation (the last being relatively minor). Robust fuel-like species, however, persist throughout the soot formation region, e.g., C_2H_2 , C_2H_4 , CH_4 and H_2 . Concentrations of radicals, e.g., H , OH and O , increase as the flame sheet is approached. The soot formation region does not approach equilibrium concentrations similar to premixed flames (refs. 8-10), however, but exhibits superequilibrium ratios generally in excess of 10.

Soot Surface Growth. Measured soot surface growth rates were corrected for effects of soot oxidation, similar to past studies of soot growth in this laboratory (refs. 2-4,6,7). Reported values of corrected soot growth, however, were limited to conditions where estimated soot oxidation rates never exceeded half the gross soot surface growth rate. Soot surface growth rates, w_g , were interpreted using the Hydrogen-Abstraction-Carbon-Addition (HACA) soot growth mechanisms of Frenklach and coworkers (refs. 14-16) and Colket and Hall (ref. 17).

To a first approximation $w_g \sim [H][C_2H_2]$, where $[i]$ denotes the concentration of the species i , for the HACA soot growth mechanisms of refs. 14-17. This behavior is illustrated in Fig. 2 in order to provide a direct test of the main features of the HACA soot growth mechanisms, without the intrusion of uncertainties due to the numerous empirical parameters of the detailed HACA mechanisms of refs. 14-17, based on measurements in premixed and diffusion flames (refs. 8-12). The correlation for the various flame conditions is quite good, and improves when actual HACA mechanisms are used, which is encouraging.

The corresponding evaluation of the HACA mechanism of soot surface growth due to Colket and Hall (ref. 17) is illustrated in Fig. 3, where R_{CH} denotes the value of reaction rate expression of this approach (and unknown steric factor in the model has a very reasonable value of 0.9). The overall correlation illustrated in Fig. 3 is seen to be reasonably effective for both premixed and diffusion flames. Results using the HACA mechanism of Frenklach and coworkers (refs. 14-17) were similar, see ref. 17.

Soot Nucleation. Soot nucleation is complex but a reasonable hypothesis is that it is dominated by the rate of formation of large molecular weight soot precursor species whose rates of formation should be somewhat similar to rates of soot surface growth, leading to a potential soot nucleation rate correlation $w_n = k_n(T)[C_2H_2][H]$, where the rate constant k_n was sought as an Arrhenius expression in terms of the temperature T . Available measurements of soot primary particle nucleation rates measured in premixed and diffusion flames (refs. 8-12) are illustrated in Fig. 4. This yields a scattered correlation with results for premixed and diffusion flames behaving in similar manner. Improved methods that achieve less scattered results are needed, however, that properly account for the detailed chemical and physical processes responsible for soot nucleation.

ACKNOWLEDGMENTS

This research was sponsored by NASA Grants NAG3-2048 and -2404, under the technical management of D. L. Urban of the Glenn Research Center, Cleveland, Ohio.

REFERENCES

1. Sunderland, P.B., Mortazavi, S., et al., *Combust. Flame* 96:97 (1994).
2. Sunderland, P.B., Köylü, Ü.Ö. and Faeth, G.M., *Combust. Flame* 100:310 (1995),
3. Sunderland, P.B. and Faeth, G.M., *Combust. Flame* 105:132 (1996),
4. Lin, K.-C., Sunderland, P.B. and Faeth, G.M., *Combust. Flame* 104:369 (1996).
5. Urban, D.L. et al., *AIAA J.* 36:1346 (1998).
6. Lin, K.-C. et al., *Combust. Flame* 116:415 (1999),
7. Lin, K.-C. and Faeth, G.M., *AIAA J.* 37:759 (1999).
8. Xu, F., Sunderland, P.B. and Faeth, G.M., *Combust. Flame* 108:1471 (1997),
9. Xu, F., Lin, K.-C. and Faeth, G.M., *Combust. Flame* 115:195 (1998),
10. Xu, F. and Faeth, G.M., *Combust. Flame* 121:640 (2000),
11. Xu, F. and Faeth, G.M., *Combust. Flame*, in press.
12. El-Leathy, A.M., Xu, F. and Faeth, G.M., *Combust. Flame*, in preparation.
13. Xu, F., El-Leathy, A.M. and Faeth, G.M., *Combust. Flame*, submitted.
14. Frenklach, M. and Wang, H., *Proc. Combust. Inst.* 23:1589 (1990).
15. Frenklach, M. and Wang, H., *Soot Formation in Combustion* (H. Bockhorn, ed.), Springer-Verlag, Berlin, 1994, p. 165.
16. Kazakov, A., Wang, H. and Frenklach, M., *Combust. Flame* 100:111 (1995).
17. Colket, M.B. and Hall, R.J., *Soot Formation in Combustion* (H. Bockhorn, ed.), Springer-Verlag, Berlin, 1994, p. 442.

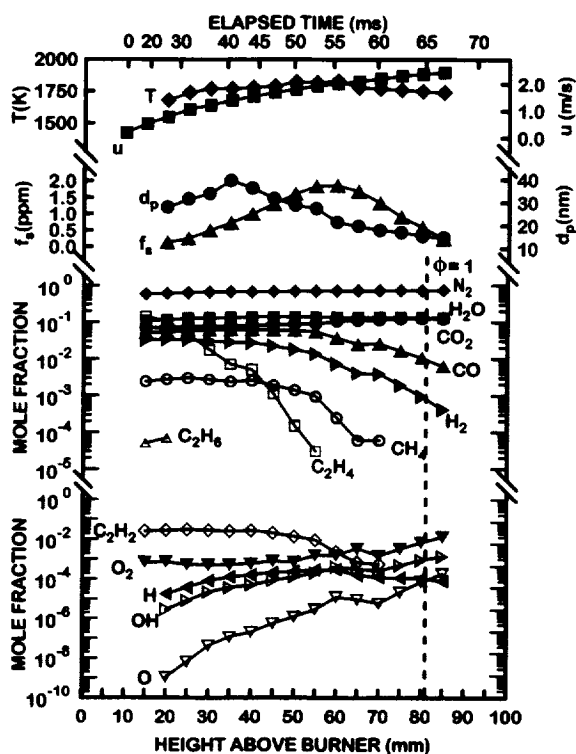


Fig. 1. Measured soot and flame properties along the axis of an ethylene/air laminar jet diffusion flame at atmospheric pressure.

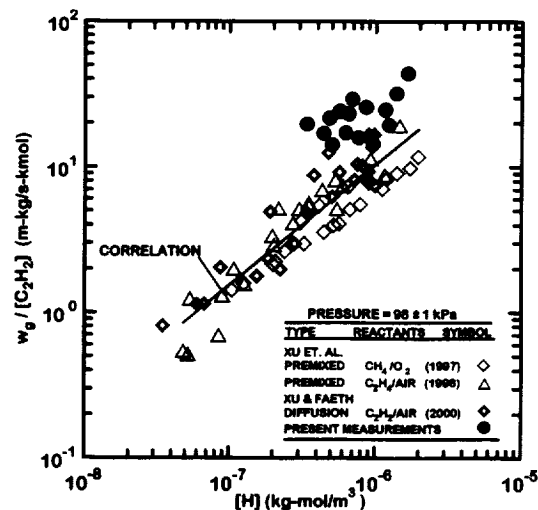


Fig. 2. Soot surface growth rates (corrected for soot oxidation) as a function of acetylene and hydrogen-atom concentrations for laminar premixed and diffusion flames at atmospheric pressure. Measurements from refs. 8-12.

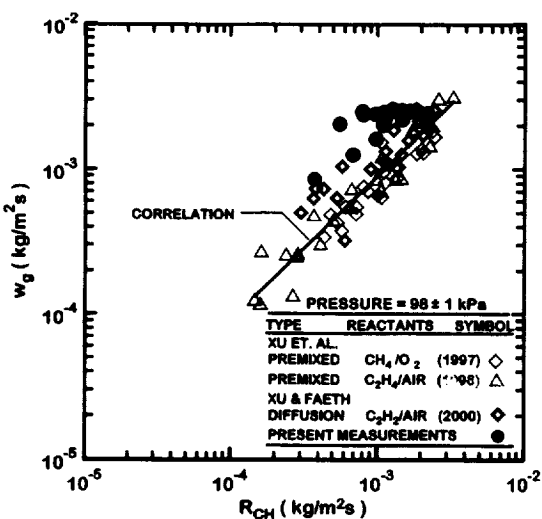


Fig. 3. Soot surface growth rates (corrected for soot oxidation) in terms of the HACA mechanism of Colket and Hall (ref. 17) for laminar premixed and diffusion flames at atmospheric pressure. Measurements from refs. 8-12.

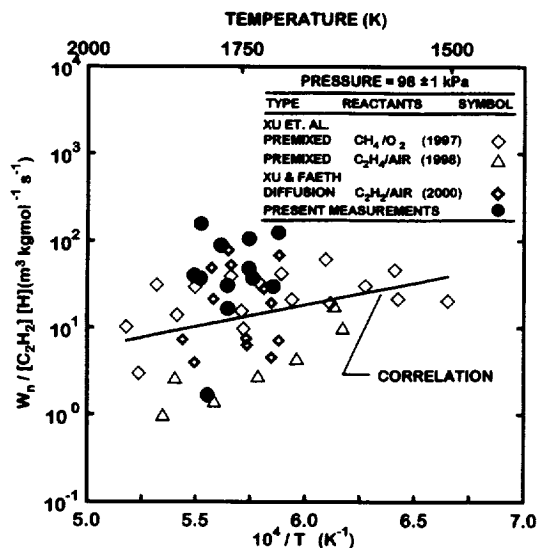


Fig. 4. Soot nucleation rates as a function of acetylene concentrations, hydrogen-atom concentrations and temperatures for laminar premixed and diffusion flames at atmospheric pressure. Measurements from refs. 8-12.

Candle Flames in Microgravity

D.L. Dietrich, H.D. Ross, NASA Glenn Research Center
P.Chang, J.S. T'ien, Case Western Reserve University

Introduction

The goal of this work is to study both experimentally and numerically, the behavior of a candle flame burning in a microgravity environment. Two space experiments (Shuttle and Mir) have shown the candle flame in microgravity to be small (~ 1.5 cm diameter), dim blue and hemispherical. Near steady flames with very long flame lifetimes (up to 45 minutes in some tests) existed for many of the tests. Most of the flames spontaneously oscillated with a period of approximately 1 Hz just prior to extinction (summarized in ref. 1).

In a previous model of candle flame in microgravity, a porous sphere wetted with liquid fuel [1] simulated the evaporating wick. The sphere, with a temperature equal to the boiling temperature of the fuel, was at the end of an inert cone that had a prescribed temperature. This inert cone produces the quenching effect of the candle wax in the real configuration. Although the computed flame shape resembled that observed in the microgravity experiment, the model was not able to differentiate the effect of wick geometry, e.g., a long vs. a short wick. This paper presents recent developments in the numerical model of the candle flame. The primary focus has been to more realistically account for the actual shape of the candle.

Model Formulation

We have reformulated the candle flame problem in microgravity using cylindrical coordinates and transformed the set of governing partial differential equations using body-fitted coordinate transformation [2]. This transformation includes a better, more detailed wick and candle geometry description. Fig. 1 shows one of the candle configurations (wick length = 9.6 mm) and the numerical grid distribution.

The model is identical to the previous model [1] except that the current formulation uses an alternating direction implicit scheme for the unsteady terms (the original model used an explicit formulation). This increases the allowed time step and reduces the total amount of computer time required for the flame to reach steady state (by a factor of 70). With these changes, it is more practical to test the near-limit flame oscillation phenomena. The wick is coated with liquid fuel at a prescribed temperature. The model assumes finite-rate, one-step gas phase chemical reaction. The flow from the wick is treated by the potential flow formulation of Baum [3]. The model further assumes constant properties, and Lewis numbers, although each species can have a different (constant) Lewis number. Surface radiative loss is assumed to be black. Gas radiation from CO_2 and H_2O are computed using the local Planck-mean absorption coefficient multiplied by a factor of 0.4. This factor is based on previous one-dimensional comparisons and the anticipated flame thickness. This gas radiation is assumed to be a pure heat loss. Flame radiation heat feedback to the wick is not treated in this work (ref. 4 provides information on radiative heat feedback effects).

Model Results

Effect of wick length

Fig. 2 shows the temperature contours of three candle flames with different lengths (3.6, 6.6, and 9.6 mm) at an oxygen mass fraction $Y_{\text{O}_2}=0.254$. A longer wick produces a larger flame

and a slightly larger aspect ratio; the flame standoff distance along the wick direction (y-axis) is larger and so is the lateral standoff distance. A longer wick produces a flame with a lower maximum flame temperature. This is due to the larger radiative loss for the larger flames. With no gas-phase radiative loss in the model, the opposite trend prevails (the longer wick produces a flame with a higher temperature).

Effect of ambient oxygen percentage

Fig. 3 shows the reaction-rate contours for three steady flames. Decreased oxygen increases the quenching distance at the base of the flame and decreases the flame aspect ratio. This trend is in agreement with previous experimental results [1], and was also predicted with the previous model. The more realistic cylindrical wick, however, appears to give a better quantitative comparison with the experiment.

Simulation of near-limit flame oscillation

The candle flame extinction in the space experiment occurs because of the gradual depletion of oxygen inside the closed volume of the glovebox. We used the numerical model to study both flame extinction and the oscillations that occur near extinction. For small containers, the boundary conditions at the outer edge of the domain change to a zero flux boundary condition. For outer boundaries greater than 8 cm, the computational time from a steady flame to extinction is too long, so we prescribe a rate of ambient oxygen mole fraction decrease at a fixed location from the flame. The starting oxygen mole fraction at the outer boundary for both computations is $Y_{O_2} = 0.1813$. At this oxygen mole fraction, a steady solution exists, but it is very close to the lowest ambient oxygen mole fraction that will support a steady flame. The steady profiles at this oxygen percentage are the initial condition for the transient calculations.

Transient computations were performed on spherical containers with radii of 6.5, 7.0, 7.5, and 8.0 cm. The wick is near the center of the sphere. For all the cases, the flame temperature decreases monotonically to extinction without any detectable oscillation. The largest container (8.0 cm) is larger than the perforated candle box but is substantially smaller than the glovebox. The equivalent volume of the candle box – glovebox combination is difficult to estimate.

To better approximate the experimental situation, while making the problem computationally tractable, the rate of oxygen decrease is prescribed at $r = 6.5$ cm, the outer radius of the computation domain. Large values of dY_{O_2}/dt correspond to smaller containers, and smaller values correspond to larger containers. Qualitatively, large values of dY_{O_2}/dt give a monotonic decrease of flame temperature, similar to the closed container cases investigated. When dY_{O_2}/dt becomes small enough, a near-limit oscillation occurs prior to extinction. Figure 4 shows that the number of cycles before extinction increases as dY_{O_2}/dt decreases. The period of oscillation is essentially independent of dY_{O_2}/dt , but the amplification rate decreases with decreasing dY_{O_2}/dt . The numerical experiments indicate that near-limit oscillations require a very gradual approach to extinction.

References

1. Dietrich, D.L., Ross, H.D., Shu, Y., Chang, P and T'ien, J.S.: *Combust. Sci. and Tech.*: 156, 1-24 (2000)
2. Joe F. Thompson, Z.U.A. Warsi, and C. Wayne Mastin, Numerical Grid Generation, Elsevier Science Publishing Co., Inc. 1985.
3. Baum, H.R. Modeling in Combustion Science, Springer, 1994.
4. Rhatigan, J.L., Bedir, H. and T'ien, J.S.: *Combust. Flame* 112:231-241 (1998).

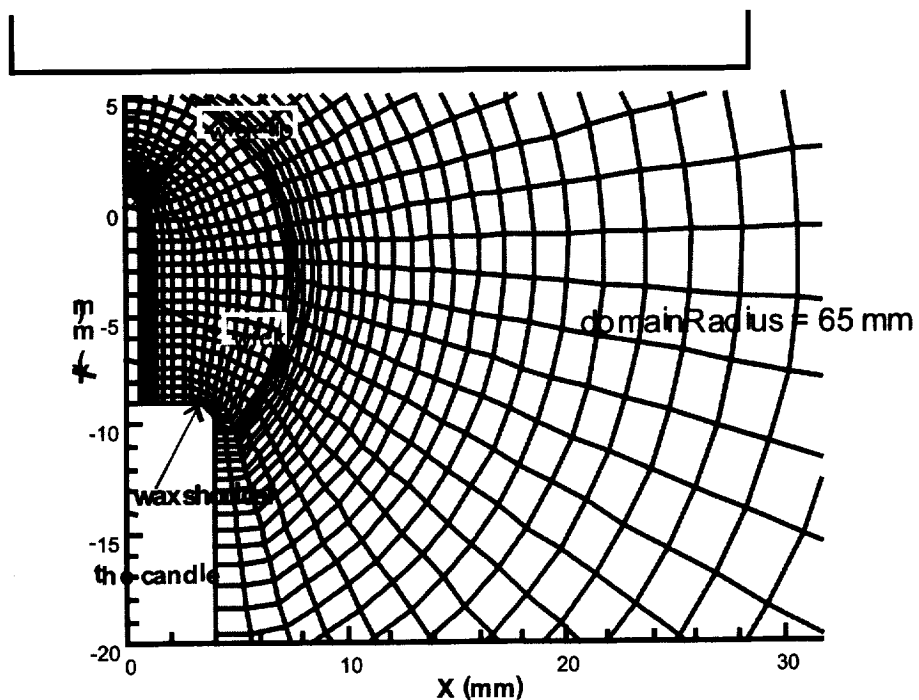


Figure 1. Candle configuration and grid distribution.

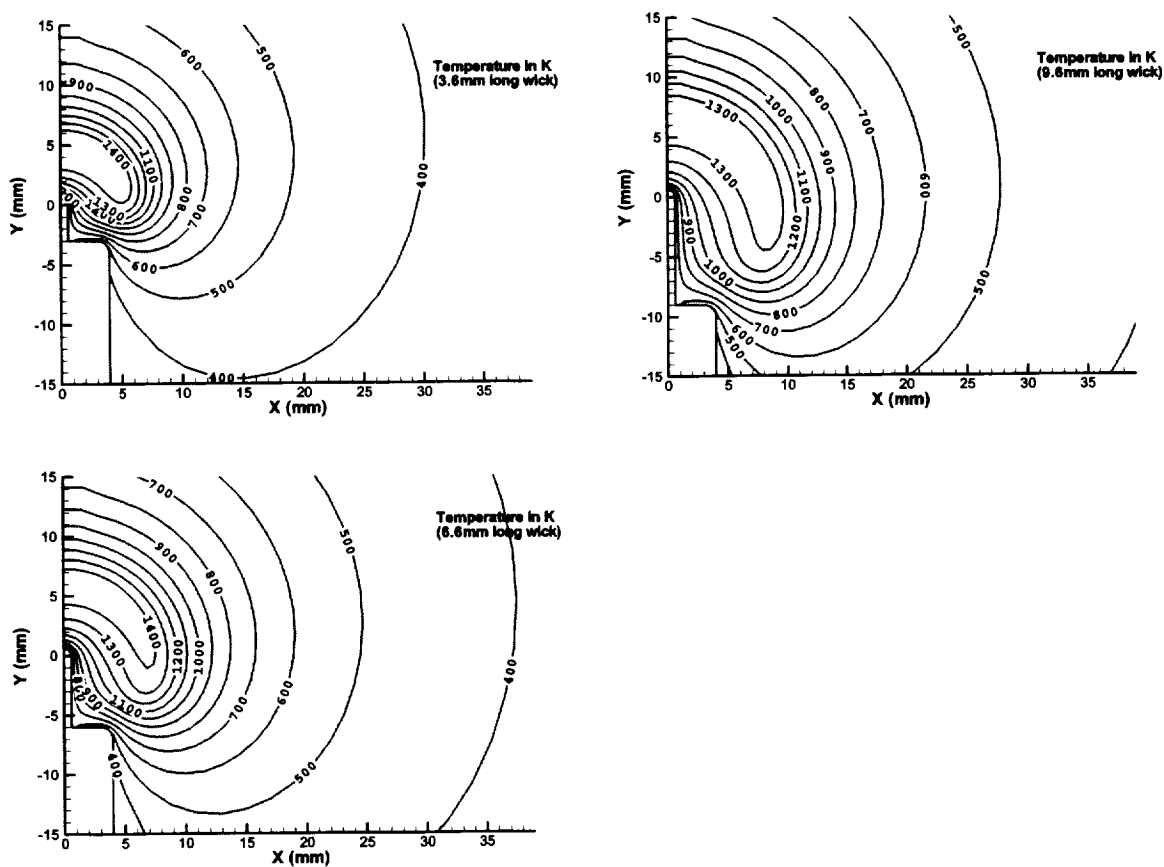


Figure 2. Temperature contours for three candles with different wick lengths.

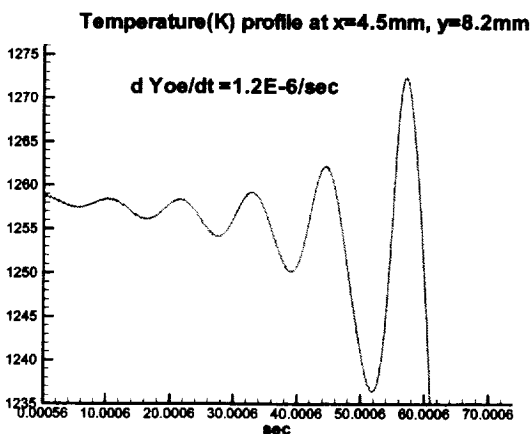
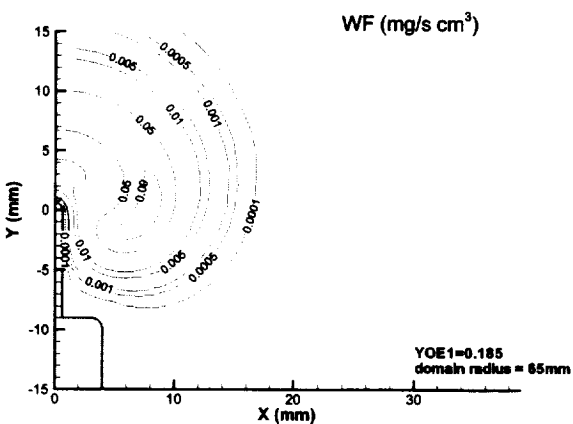
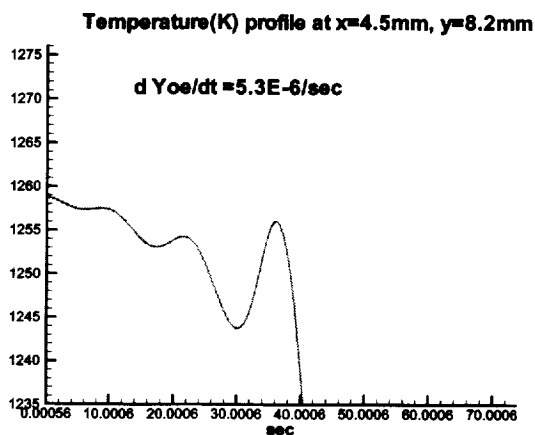
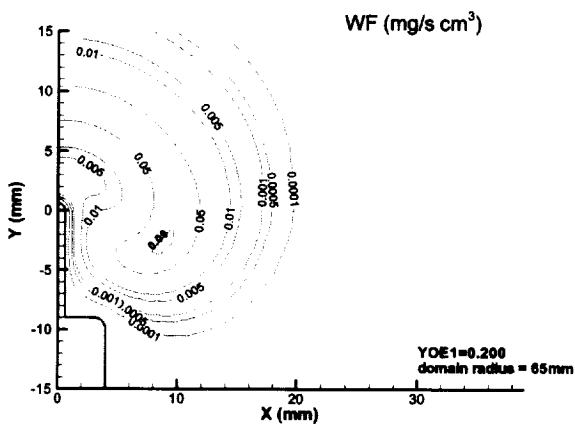
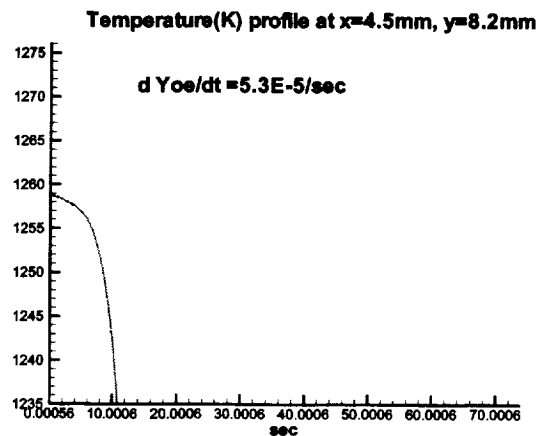
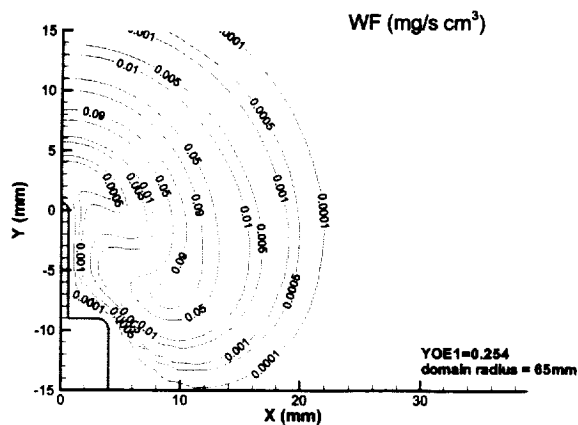


Figure 3. Reaction rate contours for three steady candle flames in different oxygen mole fraction ambients.

Figure 4. Near-limit flame oscillations for three candle flames with different rates of oxygen depletion.

SIMULATION OF COMBUSTION SYSTEMS WITH REALISTIC g-JITTER

W. E. Mell¹, K.B. McGrattan², Y. Nakamura², H.R. Baum²

¹ Mechanical Engineering, University of Utah, Salt Lake City, UT 84112

² Mail Stop 8640, NIST, Gaithersburg, MD 20899

INTRODUCTION

A number of facilities are available for microgravity combustion experiments: aircraft, drop towers, sounding rockets, the space shuttle and, in the future, the international space station (ISS). Acceleration disturbances or g-jitter about the background level of reduced gravity exist in all these microgravity facilities. While g-jitter is routinely measured, a quantitative comparison of the quality of g-jitter among the different microgravity facilities, in terms of its effects on combustion experiments, has not been compiled. Low frequency g-jitter (< 1 Hz) has been repeatedly observed to disturb a number of combustion systems [1]. Guidelines regarding tolerable levels of acceleration disturbances for combustion experiments have been developed for use in the design of ISS experiments. The validity of these guidelines, however, remains unknown.

In this project a transient, 3-D numerical model is under development to simulate the effects of realistic g-jitter on a number of combustion systems. The measured acceleration vector or some representation of it can be used as input to the simulation.

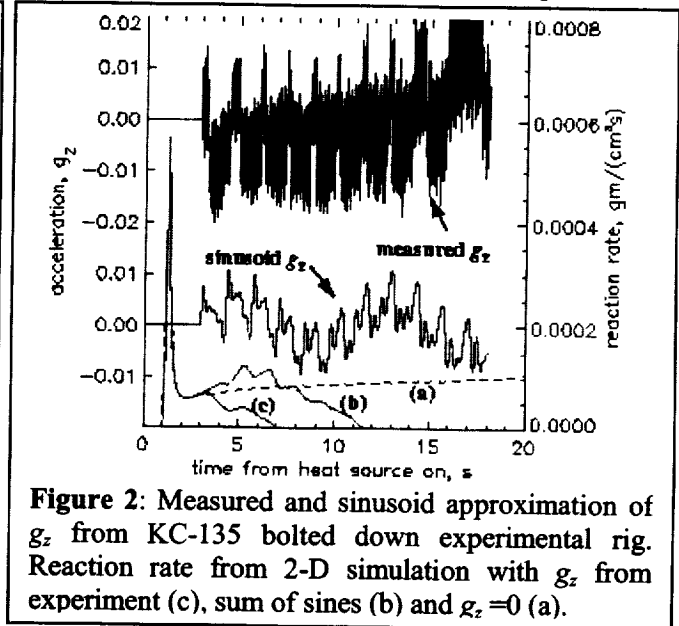
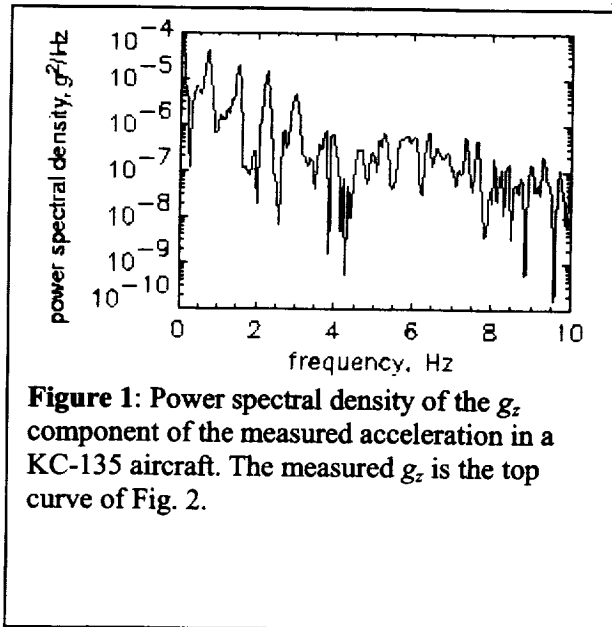
BACKGROUND AND TECHNICAL APPROACH

Only a few quantitative studies have considered the effects of g-jitter on combustion (e.g., [2,3,4]). Also, the numerical studies to date are limited in the sense that they are not 3-D and can not account for the complex orientation of realistic g-jitter. Often time series acceleration data are analyzed through band pass filters and power spectral densities. These techniques are very useful in identifying environmental contributions to g-jitter (e.g., crew activity, or thruster use in the space shuttle). But further work is needed to determine the character (e.g., orientation, frequency, magnitude) of g-jitter that will not adversely affect a given combustion experiment. The goal of this project is to develop a simulation tool that can be used by experimental investigators to a-priori assess the potential effects of g-jitter on their combustion system.

The simulation code, when finished, will be capable of performing both direct numerical simulations (DNS) and large eddy simulations (LES) of combustion. This code is the result of combining two proven codes developed at NIST: a fully 3-D NIST large eddy simulation fire code and a microgravity flame spread code that has some symmetry assumptions. The low Mach number approximation to the conservation equations is used. For the sake of computational efficiency, the gas phase chemical kinetics scheme is either one-step, finite rate reaction or an infinite rate reaction (mixture fraction). The radiation transport equation for a gray gas is solved using a finite volume method. Explicit second-order time stepping with a second order spatial discretization scheme with partial upwinding on a staggered grid is used.

RESULTS

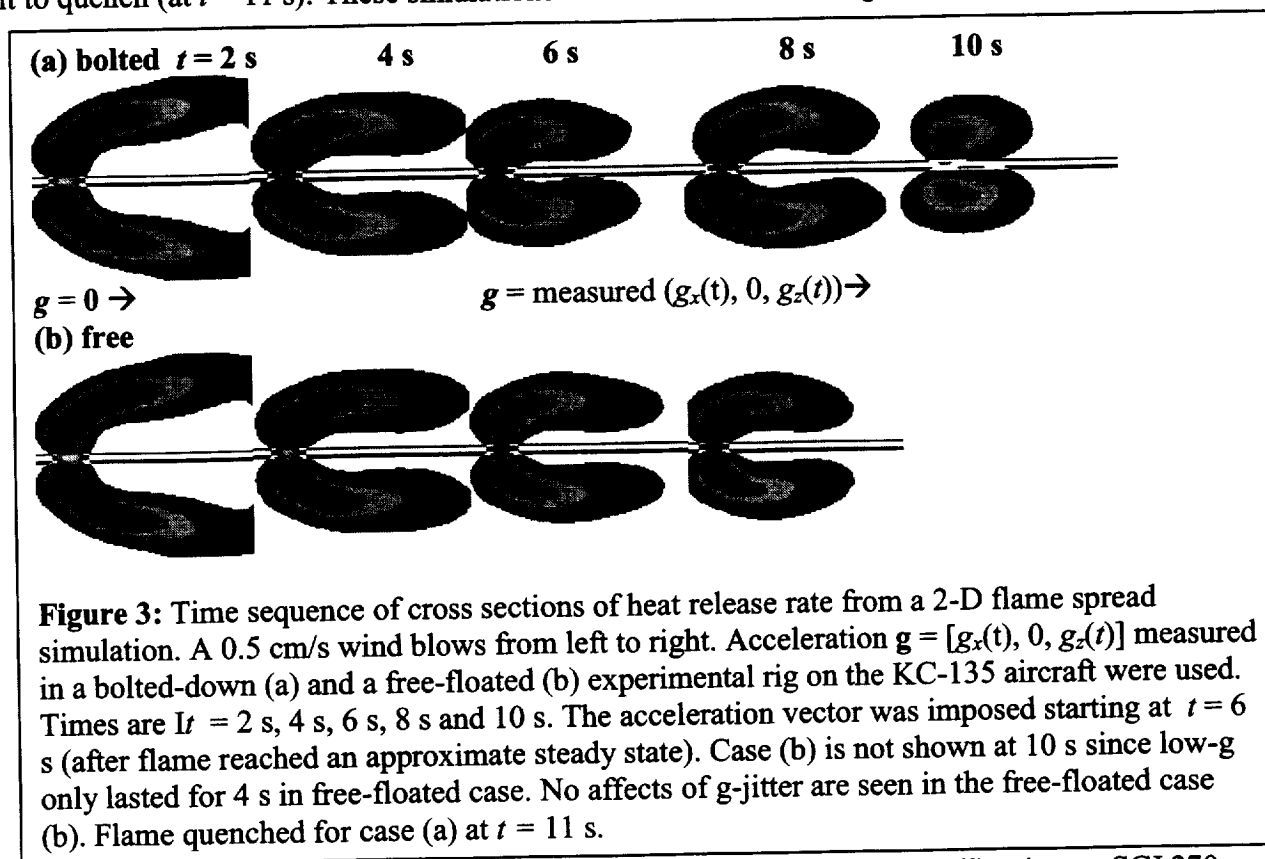
Figure 1 shows the power spectral density (PSD) of the g_z component of the acceleration vector associated with an experimental rig bolted to the frame of NASA's KC-135 aircraft. The measured time trace of g_z is the top curve in Fig. 2. A possible approximate representation of g_z is a sum of sine functions. To obtain such a representation the first five peaks in the PSD were used to determine the frequencies and amplitudes of five sine functions. The amplitude associated with a given peak was found by integrating the PSD over a frequency band containing the peak. Two-dimensional simulations of upwind flame spread over a cellulosic sample were



performed using three representations of the acceleration vector $\mathbf{g} = [0, 0, g_z(t)]$: the measured g_z , sum of five sinusoids (see Fig. 2), or $g_z = 0$. Negative g_z pointed in the direction of flame spread. Note that the onset of nonzero g_z was delayed until the flame was established. In both cases with nonzero g_z the flame extinguished, but sooner for the measured g_z case. Clearly, the low frequency or transient behavior in the measured g_z was not adequately represented by the sum of sines.

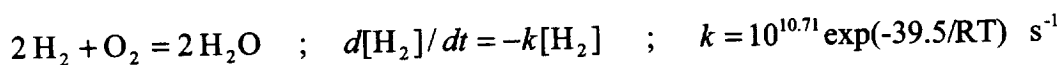
The simulation results shown in Fig. 2 were obtained from the preexisting 2-D flame spread code which assumes the cellulosic sample is a plane of symmetry. Barring the effects of holes in the sample, this assumption is reasonable in zero gravity or when g -jitter occurs only parallel to the direction of flame spread. Flame spread results from the 2-D version of the code under development are shown in Figs. 3 and 4. In these figures, the acceleration vector, $\mathbf{g} = [g_x(t), 0, g_z(t)]$, is from measured acceleration levels in the KC-135 aircraft with the experimental rig bolted down (Fig. 3) and free floated (Fig. 4). In both figures an ambient 0.5 cm/s wind blows from left to right. Acceleration levels in the free floated experiments are approximately two orders of magnitude lower ($\sim 5 \times 10^{-4} g_e$, where g_e is normal gravity) than for the bolted down experiments. As a result, the flame is unaffected by the g -jitter in the free floated experiment. It should be noted that if the investigators wanted to measure steady state flame spread they may not choose the free-floated platform since reduced gravity lasts for only about 7 s – approximately to the time it takes for the simulated flame to reach steady state. Reduced gravity levels in the bolted down experiments last for 18 s to 20 s. But, as seen in Fig. 3a, g -jitter associated with the bolted down experiments affected the simulated flame and eventually caused

it to quench (at $t = 11$ s). These simulations were made on uniform grids 12 cm horizontal and 41



cm vertical of 2/3 mm resolution and cost about 80 μ s/(time step x grid cell) using an SGI 270 MHz R12000 (single processor).

A preliminary analysis of spherical flames has begun. A very challenging simulation is a flame ball. In the simplest form of the experiment, air and hydrogen are mixed in a combustion chamber. For a certain range of equivalence ratio, stable spherical flames that are 5 to 10 mm in diameter will form [8]. The aim of the numerical simulation in this case is not necessarily to produce a detailed picture of the chemistry within the ball, but rather to evaluate the effect of g-jitter on its formation and stability. The goal is to model the combustion process as a single-step, finite rate reaction or some reduced mechanism involving a few reaction steps. Since the calculations need to be done in three dimensions to account for the g-jitter, the number of transport equations to solve must be held to a minimum. Sawyer and Glassman [7] proposed a single-step reaction for hydrogen mixed with air



Calculations are underway to determine if this reaction mechanism will yield stable flame balls. Thus, far a stable flame ball has not been produced, but it may not necessarily be due to the simplicity of the reaction scheme. Boundary conditions are of concern simply because one dimensional calculations of flame balls have used very fine numerical grids extending more than 10 cm from the center of the ball [8]. We will need comparable domain size in three dimensions to accommodate far-field boundary conditions plus flame ball drift due to g-jitter. To address these issues, simpler calculations are being performed based on infinite rate chemistry along a

flame sheet. From these calculations we obtain temperature fields comparable to that of a flame ball, but without the need to stabilize the flame. Sample temperature fields for a flame ball held in one position under the effect of g-jitter typical of the KC-135 aircraft are shown in Fig. 4.

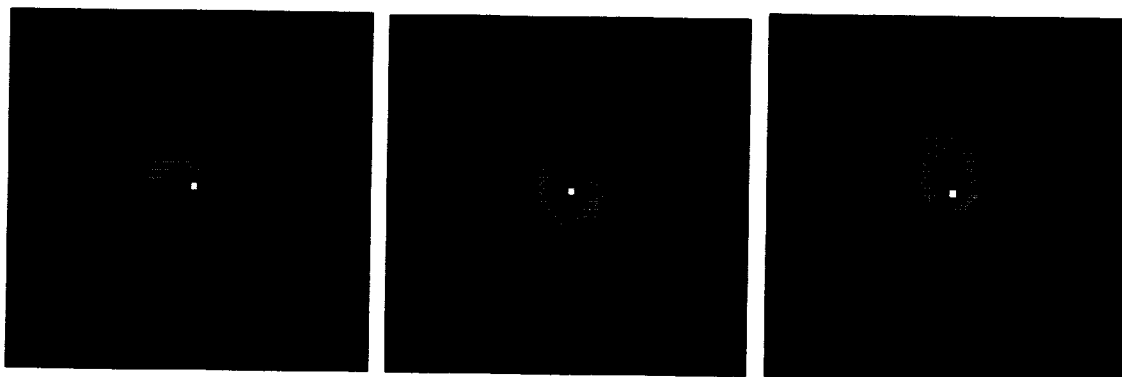


Figure 4: Three snapshots of a simulated flame ball under g-jitter characteristic of a rig bolted down in the KC-35 aircraft. Shown are contours of temperature surrounding a small fixed ignition point.

ACKNOWLEDGMENTS

This study is supported by the NASA Microgravity Science Program under the Inter-Agency Agreement No. C-32070-J.

REFERENCES

- [1] Howard Ross, NASA Lewis Research Center, personal communication.
- [2] Kaplan, C.R., Oran, E.S., Kailasanath, K. and Ross, H.D., "Gravitational Effect on Sooting Diffusion Flames," *26th Intl. Symp. on Comb.*, Combustion Institute, New York, 1996, pp. 1301–1309.
- [3] Struk, P.M., Dietrich, D.L. and T'ien, J.S., "Large Droplet Combustion Experiment Using Porous Spheres Conducted in Reduced Gravity Aboard an Aircraft – Extinction and the Effects of g-jitter," *Microgravity Sci. Technol.*, Vol. 9, No. 2, 1996, pp. 106–116.
- [4] Long, M., Walsh, K. and Smooke, M., "Computational and Experimental Study of Laminar Diffusion Flames in a Microgravity Environment," NASA Conference Publication 10194, *Proceedings of the Fourth International Microgravity Combustion Workshop*, Cleveland, OH, May 19–21, 1997, pp. 123–128.
- [5] DeLombard, R., "Compendium of Information of Interpreting the Microgravity Environment of the Orbiter Spacecraft," *NASA Technical Memorandum 107032*, Lewis Research Center, Cleveland, OH, August, 1996.
- [6] DeLombard, R., McPherson, K., Moskowitz, M. and Hrovat, K., "Comparison Tools for Assessing the Microgravity Environment of Missions, Carriers and Conditions," *NASA Technical Memorandum 107446*, Lewis Research Center, Cleveland, OH, April, 1997.
- [7] Sawyer, R.F. and Glassman, I., "The Reactions of Hydrogen with Nitrogen Dioxide, Oxygen, Mixtures of Oxygen and Nitric Oxide," *12th Intl. Symp. on Comb.*, Combustion Institute, New York, 1969, pp. 469–479.
- [8] Ronney, P. D., Wu, M. S., Weiland, K. J. and Pearlman, H. G., "Flame Ball Experiments in Space: Preliminary Results from STS-83," *AIAA Journal*, Vol. 36, pp. 1361–1368 (1998)..

HYDRODYNAMIC STABILITY OF LIQUID-PROPELLANT COMBUSTION: LANDAU'S PROBLEM REVISITED

S. B. Margolis, Combustion Research Facility, MS 9052, Sandia National Laboratories,
Livermore, California 94551-0969 / margoli@sandia.gov

EXTENDED ABSTRACT

Hydrodynamic, or Landau, instability in combustion is typically associated with the onset of wrinkling of a flame surface, corresponding to the formation of steady cellular structures as the stability threshold is crossed. As its name suggests, it stems from hydrodynamic effects connected with thermal expansion across the reaction region. In the context of liquid-propellant combustion, the classical models that originally predicted this phenomenon have been extended to include the important effects that arise from a dynamic dependence of the burning rate on the local pressure and temperature fields. Thus, the onset of Landau instability has now been shown to occur for sufficiently small negative values of the pressure sensitivity of the burning rate, significantly generalizing previous classical results for this problem that assumed a constant normal burning rate. It has also been shown that the onset of instability occurs for decreasing values of the disturbance wavenumber as the gravitational-acceleration parameter decreases. Consequently, in an appropriate weak-gravity limit, Landau instability becomes a long-wave phenomena associated with the formation of large cells on the liquid-propellant surface. Additionally, a pulsating form of hydrodynamic instability has been shown to occur as well, corresponding to the onset of temporal oscillations in the location of the liquid/gas interface. This instability occurs for sufficiently large negative values of the pressure sensitivity, and is enhanced by increasing values of the burning-rate temperature sensitivity. It is further shown that for sufficiently small values of this parameter, there exists a stable range of pressure sensitivities for steady, planar burning such that the classical cellular form of hydrodynamic instability and the more recent pulsating form of hydrodynamic instability can each occur as the corresponding stability threshold is crossed. For larger thermal sensitivities, however, the pulsating stability boundary evolves into a C-shaped curve in the (disturbance-wavenumber, pressure-sensitivity) plane, indicating loss of stability to pulsating perturbations for all sufficiently large disturbance wavelengths. It is thus concluded, based on characteristic parameter values, that an equally likely form of hydrodynamic instability in liquid-propellant combustion is of a nonsteady, long-wave nature, distinct from the steady, cellular form originally predicted by Landau.

The notion of hydrodynamic instability in combustion originated with Landau's seminal study of premixed flame propagation.¹ In that work, it was postulated that a flame could be represented by a surface of discontinuity propagating normal to itself with constant speed. It was then determined that a premixed gaseous flame was intrinsically unstable to steady (cellular) disturbances. This specific form of hydrodynamic instability, generally referred to as Landau instability, also occurs in the combustion of liquids, and was briefly addressed at the end of Landau's original study. In that problem, the unburned mixture is a liquid propellant and the burned region consists of gaseous products. The physical existence of a liquid/gas interface led to the inclusion of additional physics in the model, namely surface tension and gravitational acceleration (downward propagation was assumed). Consequently, a stability criterion was derived such that the liquid/gas interface was either hydrodynamically stable or unstable in the Landau (cellular) sense, depending on the product of gravitational acceleration and surface-tension coefficient being greater or less than a critical value. This result was later extended by Levich,² who considered the effects of (liquid) viscosity in lieu of surface tension and obtained a similar result. Thus, in the limit of sufficiently reduced gravity, these results suggest that liquid-propellant deflagration is intrinsically unstable to hydrodynamic

perturbations. However, while the notion of a thin reaction region or sheet is often a valid asymptotic limit, the assumption of a constant normal burning rate is now generally regarded as an oversimplification when applied to the problem of combustion instability.

Early attempts at modifying the assumption of a constant burning rate consisted of postulating a linear relationship between burning rate and flame curvature,³ while more recent approaches have employed asymptotic methods to analyze the flame structure and derive locally-dependent expressions for the burning rate.⁴⁻⁷ In propellant combustion, on the other hand, it has long been customary to experimentally measure the pressure response, or pressure sensitivity, of the burning rate, as well as (to a lesser extent) its temperature sensitivity. Although asymptotic models that resolve the combustion-wave structure can be developed,⁸⁻¹⁰ the representation of combustion as a surface that propagates according to a prescribed locally-dependent burning-rate law allows one to circumvent the intricacies of the combustion region and to impose fewer restrictions on the hydrodynamic model. Thus, for liquid-propellant combustion, the Landau/Levich hydrodynamic models have been combined and extended to account for a dynamic dependence of the burning rate on the local pressure and temperature fields.^{11,12} Analysis of these extended models is greatly facilitated by exploiting the realistic smallness of the gas-to-liquid density ratio ρ , the ratio of the gas-to-liquid viscosity ratio μ , and, in the reduced-gravity limit, the smallness of the inverse Froude number Fr^{-1} . Assuming only pressure-coupling effects (in which case the burning rate is functionally dependent only on the local pressure field), an asymptotic expression may be derived for the cellular stability boundary $A_p(k)$, where A_p is the pressure sensitivity of the burning rate and k is the disturbance wavenumber.¹³ In particular, we obtain the result

$$A_p \sim -\rho + \frac{2\rho\mu P [1 + k(\rho\gamma + 2\mu P + 2\rho P)]}{4\mu P(1 + k\rho P) - (\rho\gamma + 2\mu P)[1 - (1 + 4\mu^2 P^2 k^2)^{1/2}]} + \frac{\rho^2}{2k} Fr^{-1}, \quad (1)$$

where P is the liquid Prandtl number and γ is the surface-tension coefficient. The cellular stability boundaries given by Eq. (1) are shown in Fig. 1 in terms of scaled quantities $A_p^* = \epsilon^{-1} A_p$, $\rho^* = \epsilon^{-1} \rho$ and $\mu^* = \epsilon^{-1} \mu$, where $\epsilon \sim \rho$ is the small expansion parameter (typical values of ρ are on the order of 10^{-3} or 10^{-4}).

Since Eq. (1) is in fact a uniform composite approximation that is valid over the wavenumber regime $\epsilon^2 \lesssim k \lesssim \epsilon^{-1}$, it is clear from both the analysis and Fig. 1 that surface tension and viscosity are stabilizing for large-wavenumber disturbances, whereas gravity is stabilizing only at small wavenumbers. Since the minimum in the stability boundary occurs for negative values of A_p , it is also apparent that in the realistic case $\rho \ll 1$, $O(\epsilon)$ negative pressure sensitivities, which often occur in a number of HAN-based formulations over certain pressure ranges, are required for hydrodynamic stability in the Landau (cellular) sense. The two distinct sets of curves that are exhibited in Fig. 1 correspond to $Fr^{-1} \sim O(1)$ (normal gravity) and $Fr^{-1} \sim O(\epsilon)$ (reduced gravity). Thus, it is readily seen that the essential qualitative difference between the normal and reduced-gravity curves is the location of the critical wavenumber for instability. Specifically, the minimum in the neutral stability boundaries occurs for $O(1)$ values of k under normal gravity, and at $k \sim O(\epsilon^{1/2})$ in the reduced-gravity limit considered here. It is also clear from Fig. 3 that increasing the values of any of the parameters P , μ or γ serves to shrink the size of the unstable domain through damping of short-wave perturbations. The non-negligible effects of gas-phase viscosity represents, aside from the incorporation of a local pressure dependence on the burning rate, an important correction to Levich's original treatment [3] in which these effects were simply assumed to be small. The present formulation thus synthesizes and significantly extends the classical Landau/Levich results [1,3], not only

in allowing for a dynamic dependence of the burning rate on local conditions in the vicinity of the liquid/gas interface, but also in its formal treatment of those processes (surface tension, liquid and gas-phase viscosity) that affect damping of large-wavenumber disturbances. For $A_p = 0$, the Landau/Levich results are recovered in appropriate limiting cases, although as discussed above, this generally corresponds to a hydrodynamically unstable parameter regime for $\rho \ll 1$.^{1,2,13}

Aside from the classical cellular form of hydrodynamic instability, there also exists a pulsating form of instability corresponding to the loss of stability of steady, planar burning to time-dependent perturbations.¹⁴ This occurs for negative values of the parameter A_p that lie below the boundaries shown in Fig. 1, and is thus absent from the original Landau/Levich models. Consequently, in the extended model discussed thus far, there exists a stable band of negative pressure sensitivities bounded above by the Landau type of instability, and below by this pulsating form of hydrodynamic instability, where the latter is given explicitly by $A_p^* \sim -\rho^*(1 + 2Pk)^{1/2}$. Indeed, nonsteady modes of combustion have been observed at low pressures in hydroxylammonium nitrate (HAN)-based liquid propellants, which often exhibit negative pressure sensitivities.¹⁵ While nonsteady combustion may correspond to secondary and higher-order bifurcations above the cellular boundary,¹⁶ it may also be a manifestation of this pulsating type of hydrodynamic instability.

In addition to the pressure-coupling parameter A_p introduced thus far, the present generalized model has been extended further by incorporating a nonzero temperature sensitivity into the asymptotic analysis.^{13,14,17,18} This entails a coupling of the energy equation to the previous purely hydrodynamic problem, and leads to a significant modification of the pulsating boundary such that, for sufficiently large values of a temperature-sensitivity parameter, liquid-propellant combustion can become intrinsically unstable to this alternative form of hydrodynamic instability. Thus, in addition to the pressure-coupling parameter A_p , we also introduce, in an analogous fashion, the temperature-sensitivity parameter A_Θ . In the parameter regime of interest here, the appropriate scale for A_Θ that describes the fully developed effects of thermal coupling is $A_\Theta = A_\Theta^* \epsilon^{1/4}$, although the first effects that lead to the development of the C-shaped stability boundary exhibited in Fig. 2 below occur on the smaller scale $A_\Theta \sim O(\epsilon^{1/2})$. Thus the first effects of thermal sensitivity occur for $A_\Theta/A_p \sim O(\epsilon^{-1/2}) \gtrsim 30$, which is a typical nondimensional value of the overall Arrhenius activation energy.

Referring to Figure 2, it is seen that for $A_\Theta^* > 0$, the pulsating boundary becomes C-shaped, the upper branch approaching the cellular boundary as $k \rightarrow \infty$, and the lower branch approaching the original ($A_\Theta^* = 0$) pulsating boundary. The region within the C-shaped curve is stable, and thus not only is steady, planar burning intrinsically unstable for sufficiently small wavenumbers, but also, for larger k , any crossing of the C-shaped boundary from the stable to the unstable region corresponds to the onset of a pulsating instability. As A_Θ^* increases, the turning point of the pulsating boundary shifts to the right; as A_Θ^* becomes small, the turning point shifts to small values of k that ultimately lie outside the $O(1)$ wavenumber region. Thus, in the outer wavenumber regime corresponding to sufficiently large wavenumbers, the original pulsating and cellular boundaries are recovered as A_Θ^* decreases, but for A_Θ^* sufficiently large, the original cellular boundary lies within the unstable region and the basic solution becomes intrinsically unstable to oscillatory disturbances. Thus, the lower branch of the composite boundary is a pulsating boundary for all wavenumbers, whereas the upper branch transitions from a pulsating boundary for $O(1)$ wavenumbers to a cellular boundary for $O(\epsilon^{-1})$ wavenumbers. The nature of the evolution, as A_Θ^* decreases, of the pulsating stability boundary depicted in Fig. 2 to the separate pulsating and cellular boundaries described above in the limit $A_\Theta = 0$ may be determined by analyzing the dispersion relation for smaller order-of-magnitude wavenumbers and appropriately rescaled values of A_Θ . In particular, it turns

out that this transition occurs as A_Θ decreases through $O(\epsilon^{1/2})$ values,¹⁷ thereby recovering a region of stability in which the classical form of Landau (cellular) instability occurs as A_p^* increases through small negative values.

ACKNOWLEDGEMENTS

This work was supported by the U.S. Dept. of Energy (contract DE-AC04-94AL85000) and by the NASA Microgravity Science Research Program (contract C-32031-E).

REFERENCES

- [1] Landau, L. D., *Acta Physicochimica URSS* 19:77–85 (1944).
- [2] Levich, V. G., *Dokl. Akad. Nauk SSSR* 109:975–978 (1956).
- [3] Markstein, G. H., *Non-Steady Flame Propagation*, Pergamon Press, Oxford, 1964.
- [4] Sivashinsky, G. I., *Combust. Sci. Tech.* 15:137–146 (1977).
- [5] Pelcé, P., & Clavin, P., *J. Fluid Mech.* 124:219–238 (1982).
- [6] Matalon, M., & Matkowsky, B. J., *J. Fluid Mech.* 124:239–259 (1982).
- [7] Margolis, S. B., *Prog. Energy Combust. Sci.* 17:135–162 (1991).
- [8] Margolis, S. B., & Williams, F. A., *Combust. Sci. Tech.* 59:27–84 (1988).
- [9] Margolis, S. B., & Williams, F. A., *SIAM J. Appl. Math.* 49:1390–1420 (1989).
- [10] Bechtold, J. K., & Margolis, S. B., *Combust. Sci. Tech.* 68:49–84 (1989).
- [11] Armstrong, R., & Margolis, S., *22nd Symp. (Int'l) on Combustion*, 1807–1815 (1989).
- [12] Armstrong, R. C., & Margolis, S. B., *Combust. Flame* 77:123–138, (1989).
- [13] Margolis, S. B., *Combust. Flame* 113:406–423 (1998).
- [14] Margolis, S. B., *Twenty-Seventh Symposium (Int'l) on Combustion*, 2375–2386 (1998).
- [15] Vosen, S. R., *Twenty-Second Symposium (Int'l) on Combustion*, 1817–1825 (1989).
- [16] Bechtold, J. K., & Margolis, S. B., *SIAM J. Appl. Math.* 51:1356–1379 (1991).
- [17] Margolis, S. B., *Combust. Theory Modelling*, 613–635 (1999).
- [18] Margolis, S. B., *AIAA Journal*, to appear (2001).

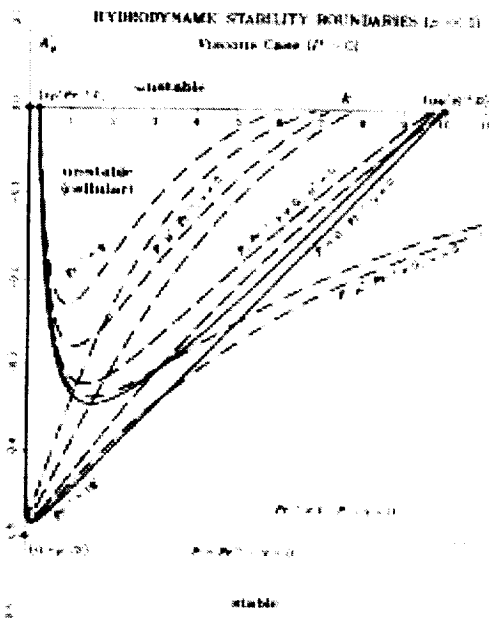


Figure 1

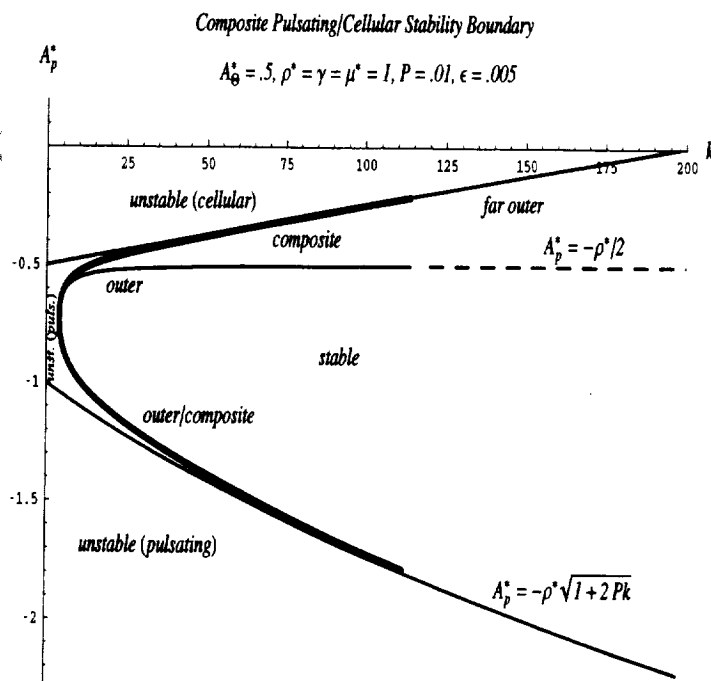


Figure 2

LARGE LEWIS NO. EDGE-FLAME INSTABILITIES

J.Buckmaster

University of Illinois at Urbana-Champaign

INTRODUCTION

Edge-flames play an important role in a number of microgravity investigations, and in the general study of flames. Examples include the candle-flame experiments carried out on board both the Space-Shuttle and the Mir Space Station, e.g.[1]; the flame-spread-over-liquid work carried out by H.Ross and W.Sirignano, amongst others, e.g. [2,3]; and lifted turbulent diffusion flames. In all of these configurations a local two-dimensional flame structure can be identified which looks like a flame-sheet with an edge, and these structures exhibit dynamical behavior which characterizes them and distinguishes them from *ad hoc* 2D flame structures.

Edge-flames can exist in both a non-premixed context (edges of diffusion flames) and in a premixed context (edges of deflagrations), but the work reported here deals with the edges of diffusion flames. It is particularly relevant, we believe, to oscillations that have been seen in both the candle-flame context, and the flame-spread-over-liquid context. These oscillations are periodic edge-oscillations (in an appropriate reference frame), *sans* oscillation of the trailing diffusion flame.

References [4,5] examine a simple model of an anchored edge-flame, and construct solutions using DNS. It is shown that if the Lewis number of the fuel is sufficiently large (the Lewis number of the oxidizer is taken to be 1), and the Damköhler number is sufficiently small, oscillating-edge solutions can be found. Oscillations are encouraged by an on-edge convective flow and the insertion of a cold probe, discouraged by an off-edge convective flow.

In the present work, the nature of these oscillations is examined in more depth, using a variety of numerical strategies.

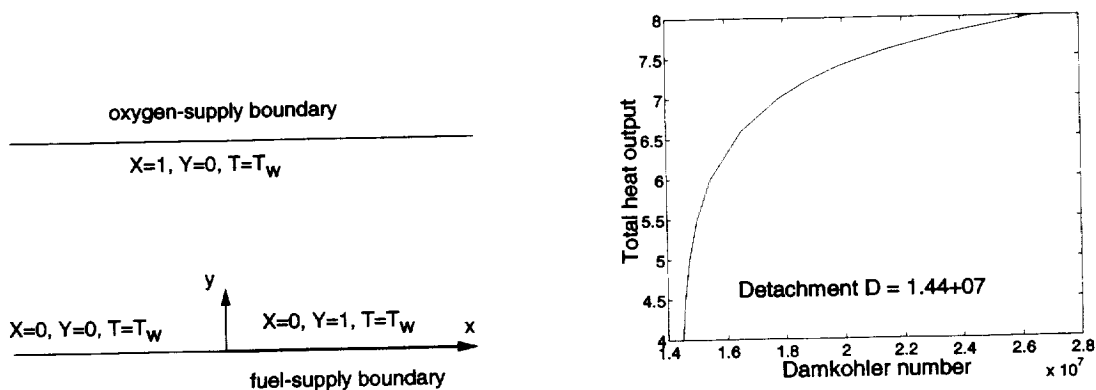


Figure 1: (i) The model configuration (the lower and upper boundaries are at $y = 0$, $y = 1$); (ii) Response diagram for the steady 2D solutions.

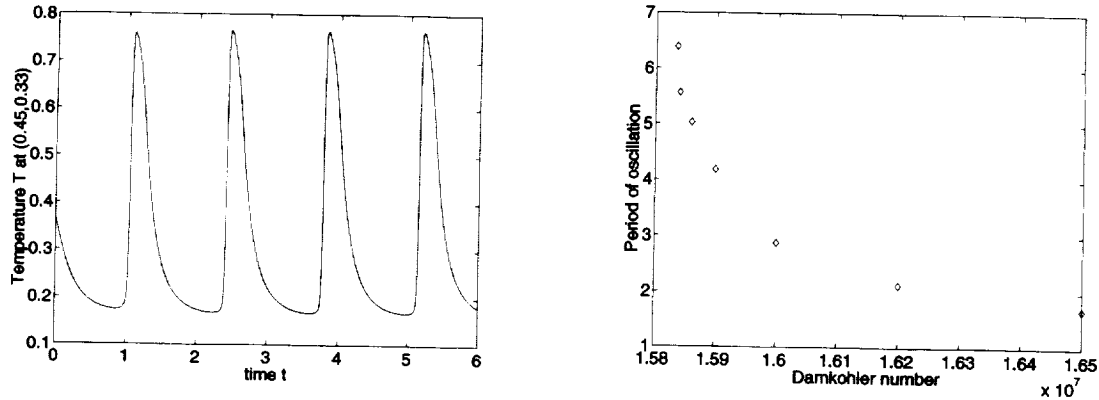


Figure 2: (i) Unstable solution for $D = 1.7 \times 10^7$; (ii) Variations of the period of oscillation with Damköhler number.

THE CONFIGURATION AND STEADY SOLUTIONS.

The model configuration, first introduced in [4], is sketched in Figure 1(i). The discontinuity in data at the fuel-supply boundary introduces a weak anchor for an edge-flame nominally located in the region $x > 0$. The field equations are

$$\frac{\partial}{\partial t} (T, X, Y) = \nabla^2 \left(T, \frac{1}{Le_X} X, \frac{1}{Le_Y} Y \right) + (q, -\alpha_X, -\alpha_Y) DXY e^{-\theta/T}, \quad (1)$$

and these describe a 1D frozen solution at $x \rightarrow -\infty$, a 1D diffusion flame solution at $x \rightarrow +\infty$. The latter is characterized by the familiar S-shaped response of diffusion flames, with an upper strong-burning branch when $D > D_{min}$. When

$$\alpha_X = \frac{1}{2}, \quad \alpha_Y = \frac{1}{2}, \quad Le_X = 1, \quad Le_Y = 2, \quad q = 1, \quad \theta = 6, \quad T_w = \frac{2}{13}$$

(values that we shall use throughout), we find $D_{min} = 0.79 \times 10^7$.

Solutions of the 2D problem defined by (1) are constructed using 4th-order spatial differencing and Runge-Kutta time integration. For some values of D , stationary solutions are unstable. To calculate these using the unsteady code we fix the integral

$$I_\Omega = \int_{x_{min}}^{x_{max}} dx \int_0^1 dy DXY e^{-\theta/T}. \quad (2)$$

Then at each fractional time step in the R-K integration in which X , Y , and T are adjusted, D is also adjusted to fix I_Ω . The solutions constructed in this way are characterized by the response of Figure 1(ii) where the total heat output (ordinate) is I_Ω , since here $q = 1$. This reveals a detachment Damköhler number, $D_{det} = 1.44 \times 10^7$, below which 2D solutions do not exist.

Unsteady DNS at fixed D identifies stable steady solutions at late time if $D > D_{ns}$, and oscillating solutions for some range of D in $D < D_{ns}$. Figure 2(i) shows temperature variations at a fixed point when $D = 1.7 \times 10^7$, a value less than D_{ns} ; indeed D_{ns} lies somewhere between 1.9273×10^7 and 1.9580×10^7 .

At this point we have identified three significant Damköhler numbers: the 1D quenching value $D_{min} = 0.79 \times 10^7$; the 2D stationary-edge detachment value $D_{det} = 1.44 \times 10^7$; and the 2D neutral stability value $D_{ns} \approx 1.94 \times 10^7$. A fourth significant number is the minimum value for

which oscillating (non-detached, non-quenched) solutions can be obtained. This is approximately $D = 1.583 \times 10^7$, a value greater than D_{det} . As $D \searrow 1.583 \times 10^7$, the amplitude of the oscillations increases, so that the maximum distance between the edge and the anchor point at $(0, 0)$ increases. Apparently both the amplitude and the period of the oscillations approach infinity, albeit slowly. Thus Figure 2(ii) shows the period for various D . The minimum D here is 1.5835×10^7 and x_{max} for the computational domain is 8, to prevent failure due to disappearance of the flame from the domain.

LINEAR STABILITY

We have seen how steady 2D edge-flame solutions can be constructed for all D greater than a critical detachment value, whether they are stable or unstable. These solutions can be used as the foundation of a linear stability analysis.

If we include z derivatives in the description (1) and linearize about the steady-state solution by writing

$$T = T_s + T', \quad \text{etc.}, \quad (3)$$

the perturbation variables satisfy the linear system

$$\frac{\partial}{\partial t} (X', Y', T') = \left(\frac{\partial^2}{\partial x^2} + \frac{\partial^2}{\partial y^2} - k^2 \right) \left(\frac{1}{Le_X} X', \frac{1}{Le_Y} Y', T' \right) + (-\alpha_X, -\alpha_Y, q) D [XY e^{-\theta/T}]', \quad (4)$$

where we have assumed that the perturbations are proportional to e^{ikz} , corresponding to corrugations in the z direction of specified wave-number. The boundary conditions are

$$T' = X' = Y' = 0 \quad \text{at} \quad y = 0, 1; \quad \frac{\partial}{\partial x}(\cdot)' \rightarrow 0 \quad \text{as} \quad |x| \rightarrow \infty. \quad (5)$$

For the parameter values examined here, the relevant 1D solution is stable for all D greater than the 1D quenching value.

A common strategy for discussing the solutions to systems such as (4), (5) is to make the replacement $\frac{\partial}{\partial t} \rightarrow \lambda$ and solve the eigenvalue problem by finite differencing and matrix methods. But an alternative is to use the unsteady solver that we have used for all of the other numerical components of the problem. Time integration of (4), (5) with arbitrarily chosen initial conditions leads to an ever-growing solution if D lies to the left of D_{ns} . This growth can be monitored for one of the field variables, at a single point. Provided there is only a single unstable mode, both the growth rate $\mathcal{Re}(\lambda)$ and the frequency $\mathcal{Im}(\lambda)$ can be deduced from this output. At the same time, a late-time snapshot of the field variables identifies the eigenfunction, e.g. Figure 3(i). The dipole nature of the reaction-rate eigenfunction, Figure 3(i), is simply a reflection of the oscillating nature of the disturbance. When the reaction center, the core of the edge, moves to the left, the reaction rate is augmented at points on the left, diminished at points on the right, as here. Note that the perturbation is confined to the edge, and does not affect the trailing diffusion flame.

Figure 3(ii) shows variations in the growth rate $\mathcal{Re}(\lambda)$ with wave-number k when $D = 1.777 \times 10^7$. Variations of frequency with k are modest, and we do not show them. These results are typical of those that we have found when D is in the unstable range. Further details and 3D DNS calculations that we have carried out will be reported elsewhere, but we note that the growth rate is a maximum when $k = 0$ and, consistent with this, the 3D DNS calculations show that 3D disturbances are suppressed in favor of 2D disturbances.

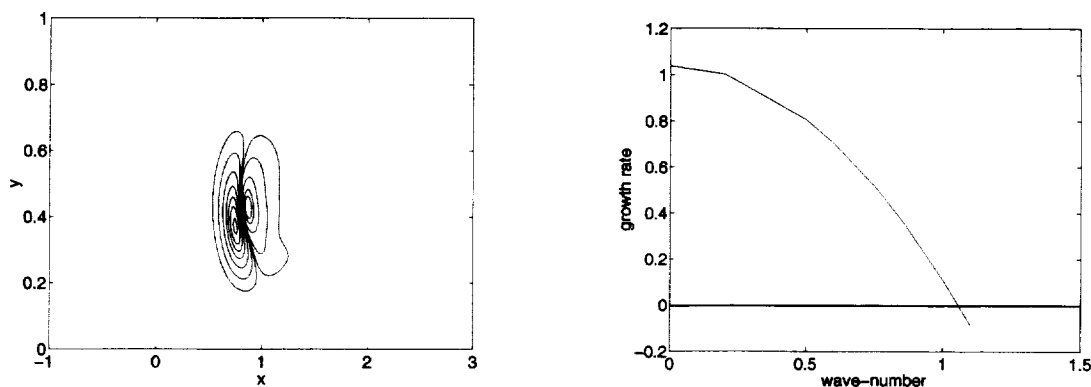


Figure 3: (i) Perturbation reaction-rate contours: the left group are positive, values 10 50 150 300 450 600 750; the right group are negative, values -10 -50 -150 -250 -300; (ii) Variation of growth rate with wave-number. $D = 1.777 \times 10^7$.

CONCLUDING REMARKS

In this study we have gained further insight into the nature of oscillating edge-flame solutions. But of greater interest, perhaps, is the demonstration that unsteady DNS can be used to construct unstable steady solutions and to solve the corresponding linear stability problem. The numerical examination of stability problems is commonplace in the fluid mechanics literature, but rare in the combustion literature, and perhaps the results presented here will encourage others to pursue this strategy in a variety of applications.

ACKNOWLEDGEMENTS

This work was supported by NASA-GLEN and by AFOSR.

REFERENCES

- [1] D.L.Dietrich, H.D.Ross, D.T.Frate, J.S.T'ien, Y.Shu, "Candle flames in microgravity", *Fourth International Microgravity Combustion Workshop*, NASA Conference Publication 10194 p.237 (1997).
- [2] H.D.Ross, F.J.Miller, "Flame spread across liquids", *Fifth International Microgravity Combustion Workshop*, NASA Conference Publication 1999-208917 p.321 (1999).
- [3] I.Kim, H.Li, W.A.Sirignano, "Flame spread across liquids: numerical modeling", *Fifth International Microgravity Combustion Workshop*, NASA Conference Publication 1999-208917 p.325 (1999).
- [4] J.Buckmaster and Yi Zhang, "A theory of oscillating edge-flames", *Combustion Theory and Modelling* **3** 547 (1999).
- [5] J.Buckmaster, A.Hegab, and T.L.Jackson, "More results on oscillating edge-flames", *Physics of Fluids* **12** 1592 (2000).

DESIGN AND FABRICATION OF A HELE-SHAW APPARATUS FOR OBSERVING INSTABILITIES OF DIFFUSION FLAMES

I. S. Wichman, L. Oravec-Simpkins, S. Olson

Department of Mechanical Engineering

Michigan State University

East Lansing, MI 48843

Email : wichman@egr.msu.edu , oraveczl@egr.msu.edu, Sandra.Olson@lerc.nasa.gov

1. INTRODUCTION

Examinations of flame fronts spreading over solid fuels in an opposed flow of oxidizer have shown that the flame front fragments into smaller (*cellular*) flames. These "flamelets" will oscillate, recombine, or extinguish, indicating that they are in the near extinction limit regime (i.e., to one side of the quenching branch of the *flammability map*). Onset of unstable cellular flamelet formation for flame spread over thin fuels occurs when a heat-sink substrate is placed a small distance from the underside of the fuel. This heat-sink substrate (or *backing*) displaces the quenching branch of the flammability map in a direction that causes the instabilities to occur at higher air velocities. Similar near-limit behavior has been observed in other works [1-3] using different fuels, thus suggesting that these dynamic mechanisms are fuel-independent and therefore fundamental attributes of flames in this near-limit flame spread regime. The objective of this project is to determine the contributions of the *hydrodynamic and thermodiffusive mechanisms* to the observed formation of flame instabilities. From this, a model of diffusion flame instabilities shall be generated.

Previously, experiments were conducted in NASA drop towers [4], thereby limiting observation time to O(1-5 sec). The NASA tests exhibited flamelet survival for the entire drop time, suggesting that flamelets (i.e., small cellular flames) might exist, if permitted, for longer time periods. By necessity, experiments were limited to thermally thin cellulose fuels (~.001 in thick): instabilities could form by virtue of faster spread rates over thin fuels. Unstable behavior was unlikely in the short drop time for thicker fuels. In the International Space Station (ISS), μg time is unlimited, so both thin and thick fuels can be tested.

1.1 The Hele-Shaw Apparatus for Normal Gravity Simulation of Low-g Flow:

Hele-Shaw (HS) apparatuses have been used as flow visualization devices for irrotational fluid flow. For the HS geometry, buoyant flow between the two closely separated plates is suppressed. In essence, flame spread experiments in the HS apparatus are simulations of microgravity flames because the influence of gravity is minimized. Although the drop towers provide valuable information for flame instabilities, the Hele-Shaw is advantageous to this project because test times are unconstrained.

EXPERIMENT

Schematics of the test section and flow system of the HS apparatus, which in this project is called the "MSU Rig", are shown in **Figures 1 and 2**. The overall (outer) height of the apparatus was constant, however, spacer plates allowed test section (inner) heights to vary between 0.2-1.2 cm. The very narrow gap along which the air flowed prevented the appearance of buoyant cells arising from the heated lower sample, caused by the flame spreading over it. For initial testing, thin cellulose fuels were used with a copper substrate backing in order to compare with prior NASA experiments. A high resistance wire ignited the sample. A quartz plate formed the

transparent top of the test section. The flow above the sample (between sample and top of test section) was subsequently exhausted to the downstream ambient atmosphere.

The flow system provided low flow velocities from 1-30 cm/s in the test section. The bulk velocities in the test section could be estimated during the course of each test. This was possible due to the O-ring system used to seal the MSU Rig. Preliminary testing indicated that higher flow velocities than those used in the thin fuel NASA drop tower tests (above ~ 6 cm/s) were needed to generate a flat uniform flame front. In addition, plenum fill times for low flow rates were in excess of ~ ½ hour, so our needle valve arrangement provided near-instantaneous flows in the test section.

At the beginning of each test, the needle valve flushed the test section with oxidizer at a higher flowrate than the test condition for instabilities. Higher flow rates were needed because the top of the test section acts as a heat sink for the flame. When an even flame front was established, the needle valve was closed until the flame front became corrugated or broke apart into cellular flames. Usually, this occurred when the needle valve was fully closed and most of the air was directed through the channel containing the flow orifice.

A ramp inside the contraction increased the velocity of the air before it entered a sintered porous plate. Since the cross sectional area of the test section was changed for different tests, a contraction nozzle-type geometry---often used in wind tunnels---could not be used to produce uniform flow. This was due to the fact that the rigid apparatus materials could not flex with varying test section heights. Instead, a porous plate (5 micron pores) was used to diffuse vortices and/or flow irregularities from the plenum and ramp. Plates on either side of the porous plate prevented air losses from under the test section or from under the ramp. In other words, the ramp led to an opening that was as large as the test section on both sides of the porous plate. See **Figure 1**.

DEVICE PARAMETERS AND PRELIMINARY RESULTS

Each section of the MSU Rig was carefully constructed based on conservative estimations of the flow field. The porous plate was chosen based on the supplied pressure drop. When the pressure drop across the porous plate was at least two orders of magnitude higher than the dynamic pressure, any effects from vortices, etc. would not be felt in the test section.

Boundary layer calculations were made using extreme flow conditions in order to determine maximum test section entrance lengths. This ensures proper placement of the sample: no part of it should be located in the side-wall boundary layer. This calculation was used to decide the maximum sample width and length. It was sought to test with the widest possible samples, since repeating instabilities will occur across the entire fuel surface and a large width allows adequate resolution.

Preliminary tests of the MSU Rig showed that for test section heights from 0.3-0.9cm, and substrate distances of 0.5cm and 0.7 cm flat flame fronts result as shown in **Figure 3.a**. The uniform flame fragmented into cellular flames that created a fingering pattern like the one in **Figure 3.b**, which was very comparable to smoldering flames in the experiment of [2]. In many tests, upon decreasing the oxidizer flow, the entire flame front would begin to slowly oscillate resembling the motion of a standing wave produced by a string with fixed end nodes. A sine wave flame front would ensue, and the flame would abruptly change from sooty yellow color to a much thinner blue flame that was only a few millimeters across. In many cases, a very rapid pulse would travel across the length of the sooty flame front. Further decreases in the airflow caused the blue flame to corrugate and begin its fingering motion. Tiny cellular flames would

meander down the sample, sometimes oscillating or extinguishing. The corrugation and oscillations resembled the flamelets seen in the drop tower experiments, however, the flamelets were often yellow in color and the oscillation frequencies were larger than in the NASA tests. Often the yellow flamelets would transform into bright blue crescent flames in which the curvature was in the direction of flame spread. These flame shapes were very stable, rarely oscillating, and they resembled the very stable oval flamelets with blue leading edges in the NASA tests. In some runs, after the flamelets extinguished, pulses and oscillations would occur and the entire front would re-ignite. *It is very important to observe that this series of events always occurred in the same sequence.*

All of these preliminary tests indicated very complex flame dynamics near the extinction limit, which were qualitatively similar to previous drop tower tests. Future testing will include surface thermocouple measurements. An energy balance will be evaluated for the flame spread process and compared with previous drop tower evaluations. Thicker fuels such as PMMA will be tested, as well as other thin fuels. A hotwire will be used to calibrate the variable area flowmeter, so transient air velocities can be measured *in situ*. The hotwire will also be used to determine turbulence (i.e., fluctuation) intensities downstream of the porous plate. Flamelet spacing and dynamics will be observed for various test conditions, and incorporated into the theoretical model.

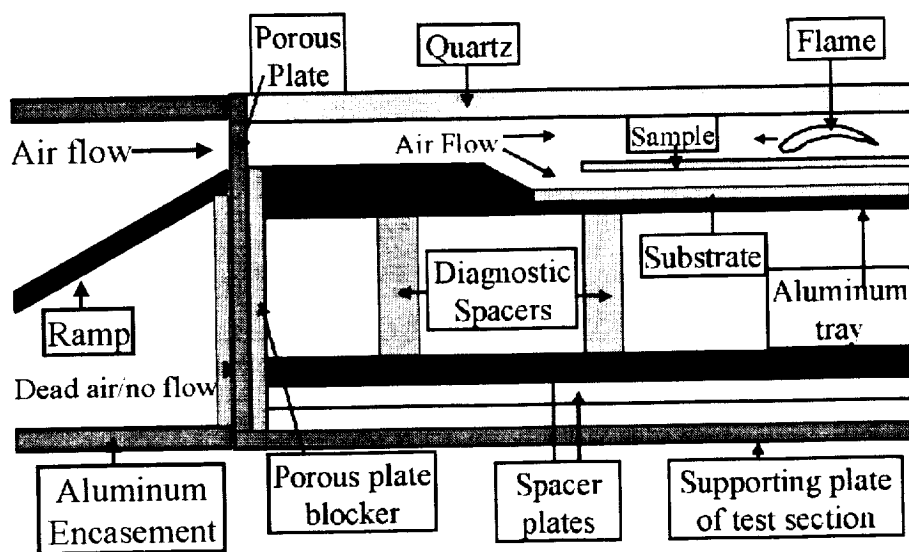


Figure 1. Schematic of MSU Rig test section.

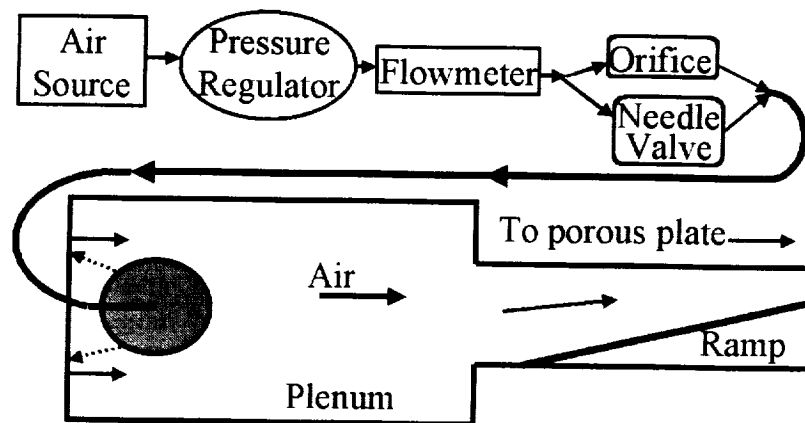


Figure 2. Schematic of MSU Rig flow system.

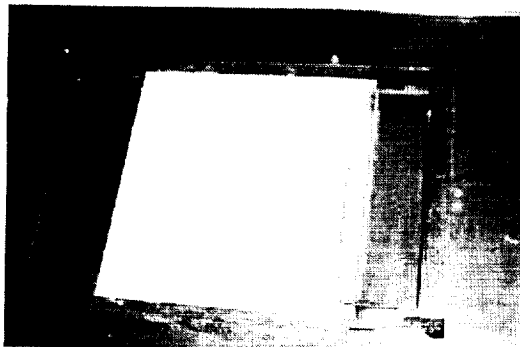


Figure 3.a. Uniform flame front



Figure 3.b. Fingering instabilities

ACKNOWLEDGMENTS

This work was performed under NASA Contract NCC3-662. Dr. Fletcher Miller served as project monitor.

REFERENCES

1. Chen, R., Bradley-Mitchell, G., Ronney, P., "Diffusive-Thermal Instability and Flame Extinction in Nonpremixed Combustion," Twenty-Fourth Symp. (Int) on Comb., The Combustion Institute, 1992, pp. 213-221.
2. Zik, O., Olami, Z., Moses, E., "Fingering Instability in Combustion," Phys. Rev. Lett. **81**, 3868, Nov., 1998.
3. Dietrich, D., Ross, H., Frate, D., T'ien, J., and Shu, T., "Candle Flames in Microgravity," Fourth International Microgravity Combustion Workshop, NASA Conf. Pub. No. 10194, May, 1997, pp. 237-242.
4. Oravec, L., Wichman, I. S., Olson, S., "Instability of Flame Spread in Microgravity," ASME Int. Mech. Eng. Cong. and Exp. HTD, ISSN: 0272-5673, Nov. 1999, pp. 183-187.

EFFECTS OF GRAVITY ON TRIPLE FLAME PROPAGATION AND STABILITY

J.-Y. Chen¹, Tarek Echekki², and Uday Hegde³, ¹6163 Etcheverry Hall, University of California at Berkeley, Berkeley, CA 94720-1740, jychen@newton.me.berkeley.edu, ²Combustion Research Facility, MS 9051, Sandia National Laboratories, Livermore, CA 94551-0969, techekk@ca.sandia.gov, ³National Center for Microgravity Research, NASA Glenn Research Center, Cleveland, OH 44135, uday.hegde@grc.nasa.gov

INTRODUCTION

Numerical simulations of 2-D triple flames under gravity force have been implemented to identify the effects of gravity on triple flame structure and propagation properties and to understand the mechanisms of instabilities resulting from both heat release and buoyancy effects. A wide range of gravity conditions, heat release and mixing widths for a scalar mixing layer are computed for downward-propagating (in the same direction with the gravity vector) and upward-propagating (in the opposite direction of the gravity vector) triple flames.

TRIPLE FLAME PROPAGATION

Simulations of planar triple flames in a scalar-mixing layer are implemented [1,2]. A single fuel and oxidizer are considered with unity Lewis numbers and a simple irreversible reaction with unitary stoichiometric coefficients. The compressible Navier-Stokes equations along with the conservation equations for species and energy are solved in a two-dimensional domain. Spatial derivatives are approximated with a sixth-order compact finite-difference algorithm. Temporal integration is performed using a low-storage third-order Runge-Kutta scheme. Boundary conditions are specified using the Navier-Stokes Characteristic Boundary Conditions (NSCBC) [3]. The flame is stabilized using a procedure similar to the one implemented by Ruetsch *et al* [4]. A correction is applied to the streamwise component of the velocity field such that temperature contours in the leading edge of the reaction zone are fixed at the same location. The inlet velocity is adjusted accordingly; while, the mass fraction at the inlet is specified with an error function profile. The solutions are allowed to evolve until steady-state of the flame structure is reached.

Figure 1 presents the computed contours of fuel consumption rate in a two-dimensional domain. The mixture enters the domain from the left side of the boundary. As seen in the reaction rate contour, the triple flame structure is delineated by its three branches. The two “wings” correspond to the lean and rich premixed flames. The “tail” trailing the premixed branches corresponds to the diffusion flame where excess fuel and oxidizer from the premixed branches are burned. As the triple flame propagates upstream, the flow ahead of the triple flame tip is decelerated as streamlines diverge. Near the reaction zone, heat release causes the flow to accelerate. Further downstream of the triple flame tip, the flow gradually decelerates as the flow behind the flame tip continues to expand laterally.

The propagation speed of the triple flame is computed by tracking an interface corresponding to a fixed fuel mass fraction along the centerline. The corresponding displacement speed, S_D , of this interface along the centerline in the streamwise is related to the triple flame propagation speed, S_p , using the following relation:

$$S_p = (S_D - u) + u_0, \quad (1)$$

where u is the streamwise velocity component at the interface and u_0 is the inlet velocity, both evaluated at the centerline. A series of simulations have been conducted to explore the relation between the triple flame propagation speed and the Froude number, $Fr_{Lf} = S_L^2/gL_f$, based on the flame thickness, L_f . S_L is the laminar flame speed and g is the gravity acceleration. The value of g , and accordingly the value of the Froude number, is positive in downward-propagating flames and negative in upward-propagating flames. The run conditions are summarized in Table 1.

Case	α	W/L_f	$S_L/S_L(A)$	ρ_0/ρ_∞	$1/Fr_{Lf}$
A	0.85	2	1	6.67	(-1.0→0.5)
B	0.85	4	1	6.67	(-0.5→0.5)
C	0.85	8	1	6.67	(-1.0→0.625)
D	0.70	4	1	3.34	(-1.0→0.5)
E	0.85	3.2	0.8	6.67	(-0.938→0.547)
F	0.85	4.8	1.2	6.67	(-0.417→0.365)

Table 1. Simulation conditions. Under all conditions, the Zel'dovich number is 8. α is the heat release parameter that corresponds to the ratio between the flame temperature to the difference between the flame temperature (denoted with subscripts ∞) and unburnt gas temperature (denoted with subscripts 0) at stoichiometric conditions. W is the scalar mixing layer width. All flame speeds shown are normalized with the value in case A. ($a \rightarrow b$) corresponds to a range of values between a and b .

Comparisons of the contributions of the local gas velocity and the displacement speed to S_p shows that the enhancement of S_p due to buoyancy effects may be attributed primarily to buoyancy-induced flow acceleration. A simple analytical model for the triple flame speed, which accounts for both buoyancy and heat release, is developed [1]. The model formulation yields the following relation between the triple flame speed and gravity in the limit of small gravity force:

$$\frac{S_p}{S_{p,g=0}} \approx \left(1 - C_0 \frac{\rho_\infty}{\rho_0} \frac{1}{Fr_{Lf}} \right)^{1/2} \equiv \sqrt{1 - X}, \quad (2)$$

where C_0 is a constant to be determined and $X \equiv C_0 (\rho_\infty/\rho_0)(1/Fr_{Lf})$. Although this correlation is limited to small values of the parameter, X , its predictions of the general trends of the triple flame propagation speed may extend beyond its underlying assumptions. First, the relation predicts the behavior of the flame at the limiting conditions of zero gravity. The expression also shows that the triple flame speed is enhanced by gravity in upward-propagating flames and reduced in downward propagating flames. As in the original analysis of Ruetsch *et al* [4], lateral flow expansion is the primary mechanism for triple flame speed enhancement, and through which heat release (expressed here in terms of the density ration, ρ_∞/ρ_0) appears in the expression for the triple flame speed. Buoyancy, then, acts to modulate this expansion by fluid acceleration or deceleration through the flame. Finally, the above equation suggests the existence of a critical value for Fr_{Lf} in downward propagating flames for which the triple flame propagation speed approaches zero:

$$Fr_{L_f, critical} \approx C_0 \frac{\rho_\infty}{\rho_0}, \quad \text{or} \quad g_{critical} \approx \frac{\rho_0}{\rho_\infty} \frac{S_L^2}{L_f}. \quad (3)$$

Results of the analysis are compared to the simulations summarized in Table 1. Figure 2 presents a comparison of computed triple flame propagation speeds and the simplified model with $C_0 = 10$. The agreement is good except for large values of X where the assumption of small gravity force is not valid. Also indicated in the figure are the estimated ranges for stoichiometric methane-air combustion and those with a fuel mixture of 77% N_2 and 23% H_2 by volume. The latter has the same laminar flame speed as methane-air premixed flame but with a thickness about four times larger. These estimates are seen to fall into the regions where Equation 2 is accurate. Consequently, Equation 2 may be used as a semi-empirical correlation for estimating the effect of buoyancy on triple flames with practical fuels at gravity conditions ranging from 0 to earth gravity.

TRIPLE FLAME STABILITY

Downward-propagating triple flames at relatively strong gravity conditions have exhibited instabilities. These instabilities are generated without any artificial forcing of the flow. Instead, disturbances are initiated by minute round-off errors in the numerical simulations, and subsequently amplified by instabilities. Figure 3 shows samples of time sequence of unstable triple flames superposed on vorticity iso-contours. The figure shows that vortices originating behind the premixed branches travel downstream and consequently alter the shape of the diffusion branch.

An inviscid linear stability analysis is implemented on the steady-state triple flame solutions obtained using the formulation described above. The eigenfunction equations from the linearized disturbance equations are solved using a shooting method. The contribution of buoyancy and viscous terms are neglected in the eigenfunction analysis. The computed results for the negative imaginary part of wave number, $-\alpha_i$, versus frequency are presented in Figure 4. These results are based on velocity and temperature profiles at $3\frac{1}{2}$ scalar mixing layer widths downstream of the triple flame tip with two different values of Fr_{L_f} and zero gravity. The results show that increasing the contribution of gravity in downward-propagating triple flames promotes the onset of instability, a trend that is consistent with computational observations. The most amplified frequency from stability analysis is within 15 % of the estimated value from computations. The magnitude of the frequency is lower further downstream of the premixed branches, further suggesting that instabilities originate just downstream of the premixed branches.

ACKNOWLEDGMENTS

This work is currently supported by NASA Glenn Center for Microgravity Combustion Science.

REFERENCES

1. Chen, J.-Y. and Echehki, T., Numerical Study of Buoyancy Effects on the Structure and Propagation of Triple Flames, to appear, *Combust. Theory Modelling*, 2001.
2. Chen, J.-Y. and Echehki, T., Proc. 5th Int. Microgravity Combustion Workshop, NASA/CP report 1999-208917 (1999).
3. Poinsot, T. and Lele, S., *J. Comput. Physics*, 101: 104-129 (1992).
4. Ruetsch, G.R., Vervisch, L. and Lifãn, A., *Phys. Fluids* 7(6): 1447-1454 (1995).

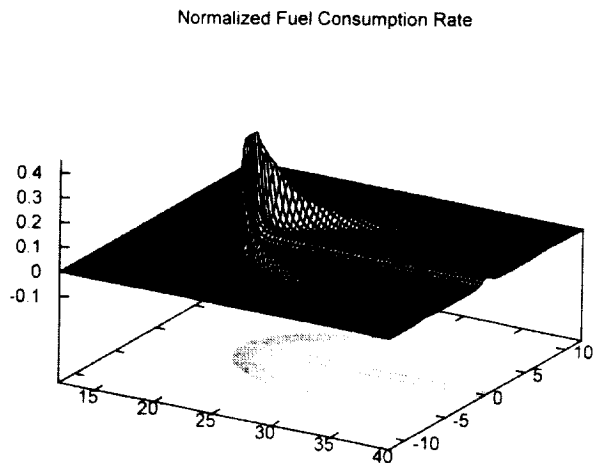


Figure 1 Computed fuel consumption rate of triple flame.

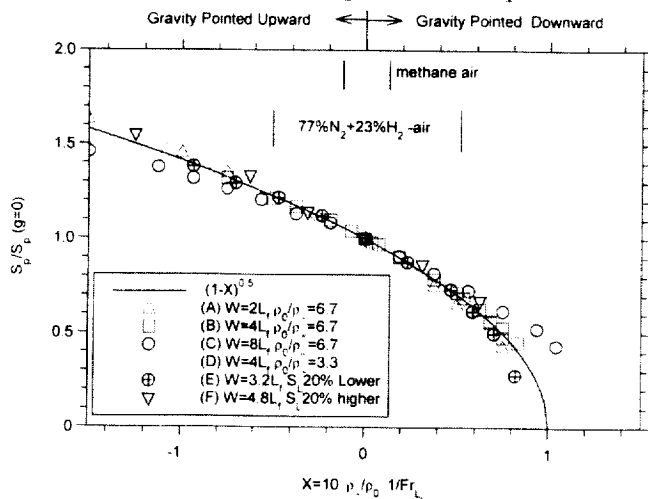


Figure 2 Correlation of flame propagation with buoyancy.

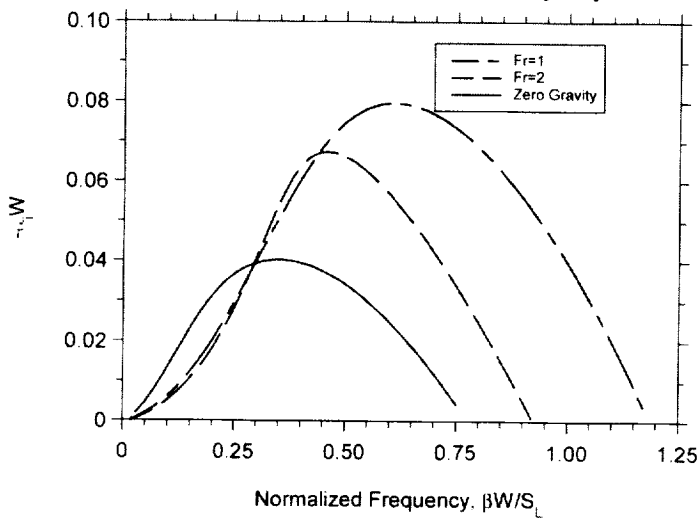


Figure 4 Linear instability analysis of triple flames.

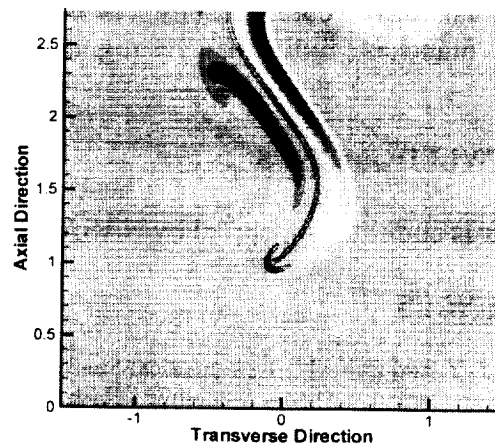
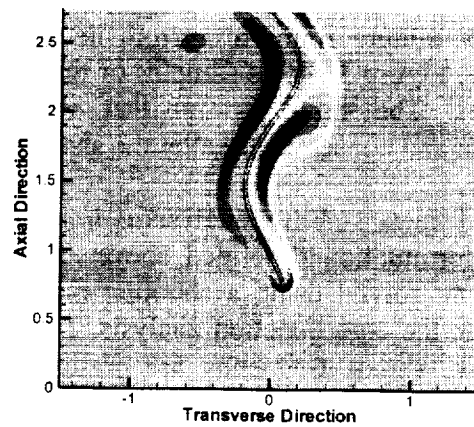
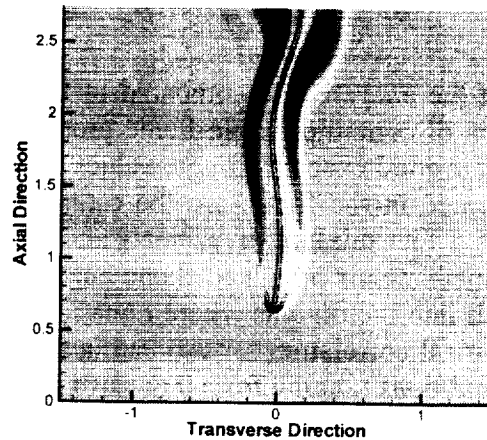


Figure 3 Unstable Triple Flames.

ESA - INSERT FOR NASA'S CIR: ENVIRONMENT FOR COMBUSTION EXPERIMENTS UNDER ELEVATED TEMPERATURE AND PRESSURE

Eigenbrod, Ch.*, König, J.*, Rath, H.J.*, Kufner, E.**

Center of Applied Space Technology and Microgravity, ZARM; Am Fallturm,

D-28359 Bremen, Germany, eigen@zarm.uni-bremen.de

** ESA/ESTEC, Noordwijk, The Netherlands, Ewald.Kufner@esa.int

Abstract

Within the course of DLR's DROP-COS (Development and Research Program on Pollutant-Reduced Combustion Systems) project and ESA's CPS-MAP (Combustion Properties of Partially Premixed Spray Systems – Microgravity Applications Promotion Program) project, a drop tower facility for droplet autoignition investigations at elevated pressure and temperature was developed. This facility shall be adopted as an insert for NASA's CIR in order to enable combustion experiments at elevated pressure and temperature. This insert can complement existing (or planned) inserts delivering a furnace equipped diagnostible combustion chamber applicable to droplet- and particles investigations as well as for gaseous combustion to take place at various ambient temperature conditions. An ongoing phase A study shall verify the feasibility of the implementation into the CIR as well as reflect on the optimal flexibility in order to serve different users demands.

Project description

Investigations of the selfignition process of fuel froplets and sprays at elevated temperature and pressure at sub- and supercritical conditions are ongoing in Europe since many years. The technical background is to aim for a fundamental understanding of the physical and chemical processes finally leading to the autoignition of fuel sprays. This is required to enable the development of numerical simulations of the process predicting the behaviour of reactors that either need controled autoignition for a proper operation (diesel-engines) or have to avoid unwanted autoignition (internal combustion engines, gas-turbines). As the LPP-concept (lean-prevaporized-premixed) has been proven as the most promising method to lower local combustion temperatures below the onset temperature of thermal NO_x formation, it might be possible to apply this method also to aero-engines supplemeting the RQL process actually be in use. Knowledge in detail is therefore needed the more as aero-engines are difficult to design flashback-safe on one hand and rising inlet temperatures and pressures limit the time available for vaporization and turbulent mixing on the other hand.

Microgravity environment is needed as the physical and chemical processes must be basically examined without the masking effects of natural convection of a flow field. In normal gravity more dense fuel vapour drops off the droplet and exothermal precursor reactions reduce the local density in the viscinity of a droplet. As a specific advantage of this issue, the micron-sized droplets of a technical spray do not strongly interact with the turbulent flow field and natural convection plays a minor role during the milliseconds lifetime of such droplets. Therefore, the transformation of results from microgravity experiments on comparably large droplets (easy to handle, easy to diagnost) to technical applications has to bridge only small gaps.

Experiments in high pressure and high temperature have been performed utilizing the Bremen drop tower. As the microgravity time needed for a single experiment is short, drop towers are well suited to develop the experiment in all aspects. As the parameter field of interest is wide and the number of drop experiments is naturally limited, an orbital facility delivers the ideal environment to answer the questions in a reasonable time period. During drop tower experiments it was found that due to branched chain reactions only slight changes in fuel- and mixture-composition or pressure or temperature can lead to significantly changing induction times.

Facility description

The existing drop tower insert (Fig. 1) mainly consists of a pressurizable vessel with optical access through four windows (Fig. 2).

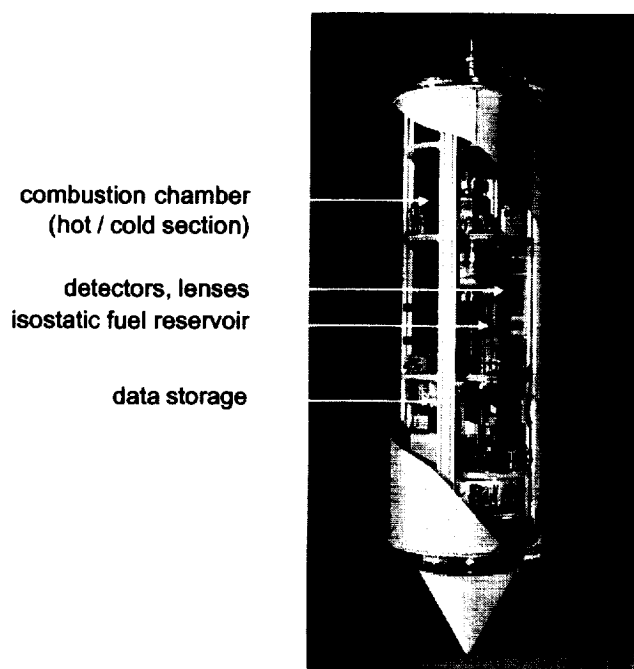


Fig. 1 Drop Capsule with Combustion Chamber



Fig. 2 Combustion Chamber

The interior of the vessel (Fig. 3) contains an insulated resistance heated furnace in the upper section and the fuel management system in the lower cold section. The vessel can be opened at the main flange allowing for maintenance of the furnace and the fuel supply system. The mid part of the three folded main flange can bear a cooled separating plate (heat exchanger) to prevent from furnace heat losses to affect the fuel supply. At both ends of the vessel, flanges for experiment specific feethroughs are available. In the depicted case the lower flange is used to support the droplet elevation system for rapid insertion of the suspended droplets into the hot section. An on-chip CCD-camera with LED-illumination is installed within the vessel to enable monitoring of the remote controlled fuelling process.

Tab. 1 nominates the technical data of the existing drop tower facility. It is noted, that these data might undergo changes in terms to match the CIR interface and safety requirements.

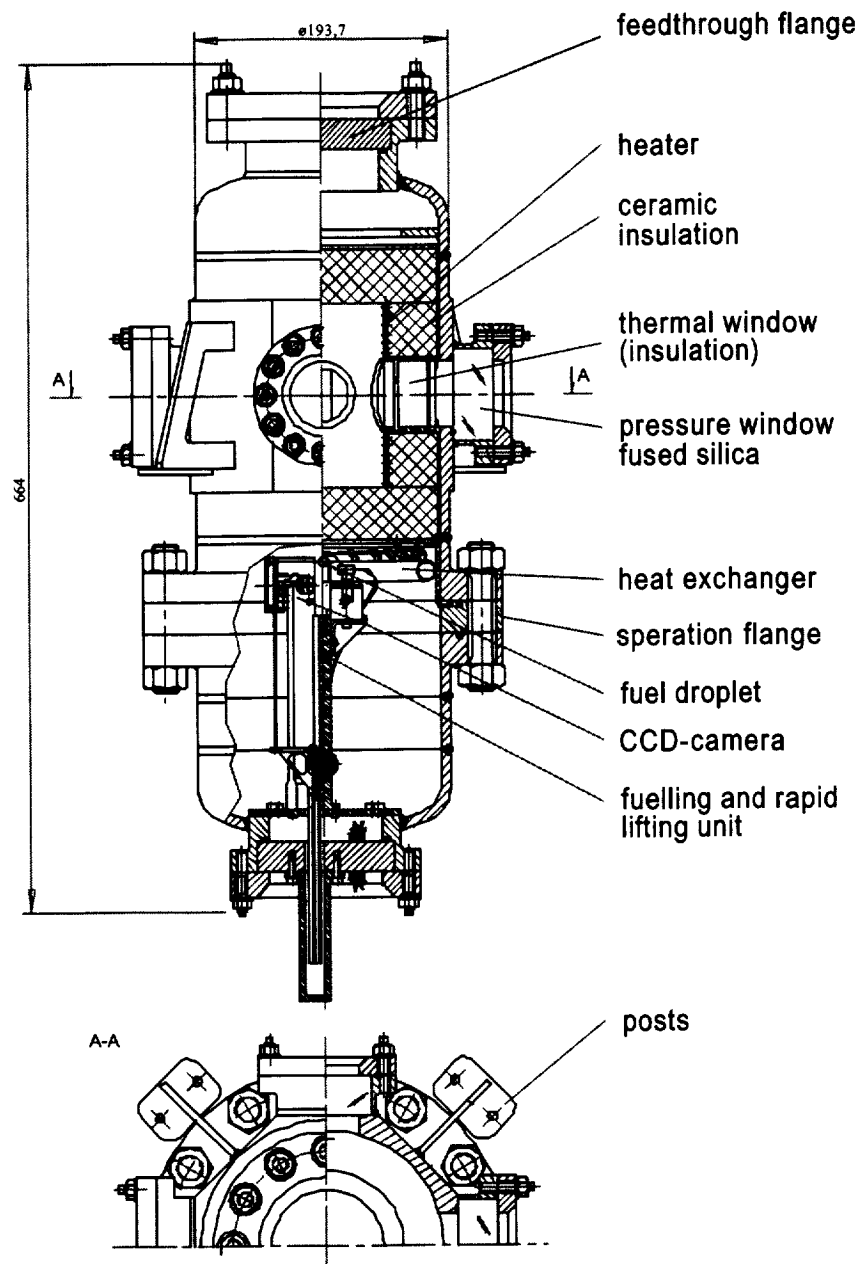


Fig. 3 Interior of the Pressurized Vessel

Tab. 1 Technical data of the depicted drop tower insert

Vessel Volume	12 liters
Mass	60 kg
Max. Operating Pressure	8.0 Mpa
Window Aperture	50 mm
Window Material	Fused Silica
Furnace Diameter	90 mm
Furnace Height	140 mm
Max Temperature	1000 K (at 0.5 Mpa)
Max Power Consumption	0.6 kW (34 VDC)

Diagnostics

Besides the application of DLR's ADL laser diagnostic system that is currently under development (see there) it is foreseen to equip the CPS facility with the DOAS-system

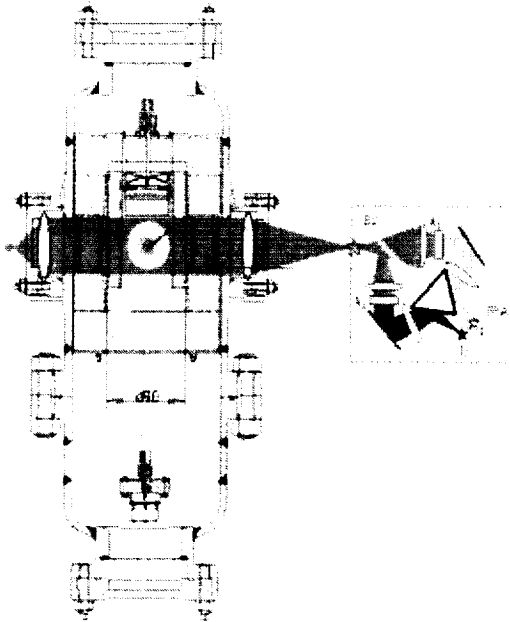


Fig. 4: Optical pathway of DOAS for supercritical droplet evaporation diagnostics

The same equipment can be used for 2D-thermography of solid particles or surfaces. In this case the lenses focus on the area of interest and the IR-backlit illumination is exchanged to the radiating object itself. Advantage of this thermographic method is, that the

calibration efforts to gain accurate temperature data is minimized as all disturbing effects (black-body difference, optical pathway effects) are eliminated due to the differential method. Fig. 5 explains how the intensities of the two filtered signals from the grey-body radiation are calculated. Tab. 2 gives the technical data of the IR-camera that is used (with LN2 cooling) at the drop tower Bremen.

Tab. 2: Technical data of Indigo's Phoenix™ IR-camera

$$I = A \epsilon \frac{c_1}{\lambda^5 (e^{c_2/(\lambda T)} - 1)}$$

$$\frac{I_1}{I_2} = \frac{\lambda_2^5 (e^{c_2/(\lambda_2 T)} - 1)}{\lambda_1^5 (e^{c_2/(\lambda_1 T)} - 1)}$$

Fig. 5: Differentiation of the filtered grey-body radiation signals

Mid IR	2 – 5 μm
Stirling-Cooled	
Frame Rate	100 Hz (640x512)
	340 Hz (320x256)
Shock Proof	20g<11ms
Acceleration	12g
Power Consumption	15 W

Space-DRUMS™ - CONTAINER AND CONTAINERLESS PROCESSING ON THE ISS

Mr. Ron Davidson, Dr. Jacques Guigné, Mr. Peter Everett, Guigné Technologies Ltd.,
447 Kenmount Road, St. John's, NF, CANADA A1B 3P9
rdavidson@guigne.com

Guigné Space Systems Inc. (GSSI) announces the availability of Space-DRUMS™ to conduct experiments, science and processing on the International Space Station (ISS) as early as 2002.

Guigné will provide Space-DRUMS™, a whole rack research and processing facility on USER LOGISTIC FLIGHT #1 (ULF1) in 2002. The facility will be available for 3-5 years (up to 20 increments) on the US Laboratory Module "Destiny" for conducting experiments, science and processing through contract leasing.

Space-DRUMS™ is a flexible and modifiable experimental platform, within which a wide range of research and processing can be conducted.

Space-DRUMS™ was developed to be responsive to the user community to minimize cost and schedule demands on a broad range of areas. Space-DRUMS™ also fits the NASA objective to promote the infusion of innovative new technology for ISS research. Space-DRUMS™ is the first containerless facility that can control large objects while in microgravity. Solid objects up to three inches (7.62 cm) and liquid objects up to 5.5 inches (14 cm) can be controlled inside the 12.5 inch (30cm) chamber.

SPACE-DRUMS™

In 1994 Guigné recognized the commercial opportunities of the ISS and developed a flexible facility, capable of conducting a wide range of science that is also re-configurable on orbit. The facility is the first commercial science and experiment processing facility built specifically for Space Station. NASA is supporting this initiative through their Space Product Development (SPD) Office, based in Marshall Space Flight Center. Leases have been signed with the Colorado School of Mines through the NASA Center for Commercial Applications of Combustion in Space (CCACS), to process advanced glass, porous ceramic and glass ceramic materials.

Currently, negotiations are under way for three further Space-DRUMS™ Agreements for porous bone replacement tissue growth, Methane Catalytic Combustion and Fluid Physics. Other projects regarding electric field induced combustion synthesis, granules and protein crystal growth have been initiated.

Core Technology:

The core technology is a 30-cm stainless steel processing chamber that can accommodate solid, liquid or gaseous materials in triple containment.

To assist this core technology a robotic system (the Material Handling System - MHS) is employed for retrieving samples from a samples storage system (SSS), placing these samples within the processing chamber and returning the samples to storage after processing. Both the MHS and SSS are placed within the triple containment volume. Samples can also be introduced manually via a 13cm front entry port.

Sometimes it is necessary to process materials in a containerless mode, containers producing unwanted artifacts in high temperature samples and fluids processing. When this is required, samples are placed at the center of the chamber by the Material Handling Robotic System (MHRS) and maintained inside a control zone by the Guigné patented DRUMS™ system. This consists of 20 projectors, activated by function generators/power amplifiers and monitored by visible light and infra red edge detection and controlled by positional and restoring algorithms. By this means fluid and solid samples of up to 14-cm diameter and 1.4+-KG mass can be controlled in a free fall position. Additionally, the chamber is rated to heat reject samples of 6cm diameter at 2000 degrees centigrade.

The Space-DRUMS™ facility uses a full rack and draws its power (1035 watts) from the ISS 28VDC system. It also takes advantage of the ISS provided avionics air and moderate temperature cooling loops to provide 2KW of heat rejection. The facility software interfaces with ISS for up and down links, (data and commanding) and the ISS vacuum resource is used, in conjunction with Space-DRUMS™ Gas and Vacuum System, for purging of the processing chamber.

Space-DRUMS Configuration: Processing Module : Housed in a quad sized middeck locker, the Processing Module consists of a 30-cm stainless steel chamber with 32 ports accommodating 20 acoustic projectors, arranged in dodecahedron configuration. These projectors are used in the containerless processing mode to maintain samples at the center of the processing chamber.

The additional ports are used as follows:

- ◆ Two 13cm ports at each end of the chamber, housing the Material Handling Robotic System and the Sample Storage System.
- ◆ A front mounted 13cm port to allow for samples to be manually inserted. The chamber and its MHS/SSS form a level of containment to sustain a pressure of 2 atmospheres.
- ◆ Six 6cm ports accommodating six cameras, providing edge detection of samples in both visible light and infrared spectra. The visible light cameras also provide an internal inspection capability during and after processing.
- ◆ The final three ports are for the introduction of gases and the venting of gases and debris and to mount instrumentation.

Also housed in the Processing Module are the Material Handling Controller (MHC) and the Thermal Control System.

Payload Computer Electronics Module (PCEM): The PCEM, housed in a middeck locker, contains the payload 500Mhz Pentium computer and 60GHZ hard storage disk. All boards containing CMOS devices are Orbital Replaceable Units (ORUs) and are carried as spares in the event of damage by radiation bursts. The Hard Drive is also an ORU. The computer operating system is Windows NT and code for command and telemetry is written using a self-testing compiler program. Proprietary algorithms are used to determine and maintain positional control over the sample during processing. The software configuration supports all ISS and Shuttle protocols.

Experimenters can monitor the progress of their science both visually and electronically in near real time modes. Data can also be loaded to the hard drive and transmitted to the operations center at a later time. Links can be established from the operations center to the experimenter's home base. Command and telemetry software is up link re-configurable and down link verifiable to accommodate different science and processing. Finally, the system conducts health and safety checks during start up, shut down and while processing, with near real time display of critical functional steps. Being developed from Commercial-Off-The-Shelf (COTS) components, the PCEM is an inexpensive, robust, space qualified computer that is also available to other facility (payload) developers.

Argon Gas and Vacuum Module (AGVS): The module, housed in a middeck locker, can deliver a wide range of gases to the processing chamber and provide the controls to vent or filter expended gases and collect any solid or gaseous debris using the ISS vacuum resource. In developing the AGVS, Guigné found that existing space approved gas bottles were not only very expensive but were not sized to meet ISS packaging requirements. Using a COTS approach, new gas bottles were developed and space qualified for less than 25% of then available products. These bottles are available from Guigné.

Ignition Power Module (IPM): The IPM is an energy storage device, with easy on orbit re-configuration to provide power profiles of up to 2kW for 30seconds or 1kW for 60 seconds etc. Many experiments and processes require high peak electrical power and with the total ISS power resource (both average and peak combined) being limited to 2kW per EXPRESS rack, two problems are addressed; a. A need for up to 2 kW short term peak power; and, b. A limitation of power resources on ISS means facilities with lower power resource requirements will be favored.

The IPM provides power to tungsten filaments that ignite the combustion synthesis pellets and reduces the power requirements for Space-DRUMS™ to 1035 watts This COTS derived space qualified IPM can also be obtained from Guigné.

Acoustic Positioning Electronics Module (APEM): The APEM, housed in a middeck locker, contains the heart of the space vision system, with phase locked loop function generators and class B power amplifiers. These electronics drive the acoustic projectors in banks of five. It also interfaces with the PCEM, which having received telemetry feed back from the infra red and visible light cameras, sends commands derived from the restoring algorithms back to the projectors to maintain sample positional control at a rate of 30 frames per second. This module

is only employed in the containerless processing mode or when measuring free drift of an object with relation to the chamber vibration.

Some Experiment examples

- A. **Glass Ceramics and Porous Glass Ceramics** – Using a motorized carousel, housed in the Sample Storage System, pellet samples are retrieved by the robotic MHS and placed in the center of the chamber. The AGVS floods the chamber with high purity argon and the MHS retrieves a tungsten igniter from the carousel and inserts it into the pellet recess and the IPM having been programmed applies a specified power for a specified time. As soon as the pellet ignites, the MHS releases the pellet and positional control is maintained by the Space Vision System (SVS). When the pellet has cooled, it is retrieved from the chamber center and re-inserted into the carousel. The AGVS then purges the chamber of argon and any debris.
- B. **Catalytic Combustion** – Noble metal coated lollipops are inserted through the 13cm front port, along with power and telemetry cables. The Sample Storage Carousel is removed and the measuring laser is introduced through the 13cm MHSS port. The gaseous mixture is also introduced via this port. Burn gases are expelled through the vacuum port and collected in the filter trap. The filter trap is replaceable on-orbit.
- C. **Fluid Physics Ripple Turbulence** – The Carousel is removed and a water delivery system placed into the MHS. The Space Vision System is activated and water sphere is injected to the center of the chamber. Illumination of the sphere is provided using a xenon flash powered by the IPM Module. Using an acoustic projector, turbulence is imparted to the surface of the sphere and monitored by a CCD camera.
- D. **Protein Crystal Growth** – Using a similar fluid delivery system to case C above, , a protein nutrient solution is grown at the center of the chamber. A series of low power turbulent projector are used to stir the nutrient solution and eliminate the depletion zone effect that limits crystal size
- E. **Low Resistance Glasses** – a “coke can” module is inserted through the front panel. This can contains a low resistant glass rod; around which is wrapped a platinum sheath and encase in steal. Spiraled around this casing are both heating and cooling elements. The IPM Module delivers power to the heaters and the glass rod liquefies and is cry-cooled by gases.

HOLOGRAPHIC INTERFEROMETRY AND LAMINAR JET DIFFUSION FLAMES IN THE PRESENCE OF NON-UNIFORM MAGNETIC FIELDS

J. Baker¹, M. E. Calvert¹, K. Saito², and R. Vander Wal³

¹University of Alabama at Birmingham, Birmingham, AL 35294

²University of Kentucky, Lexington, KY 40506

³NASA Glenn Research Center, Cleveland, OH 44135

INTRODUCTION

Magnetic fields impact combustion processes in a manner analogous to that of buoyancy i.e., as a body force. It is well known that in a terrestrial environment buoyancy is one of the principal transport mechanisms associated with diffusion flame behavior. Unfortunately, in a terrestrial environment it is difficult if not impossible to isolate flame behavior due magnetic fields from the behavior associated with buoyancy. A micro-, or reduced, gravity environment is ideally suited for studying the impact of magnetic fields on diffusion flames due to the decreased impact of buoyancy on flame behavior.

For over one hundred years now it has been recognized that magnetic fields can be used to affect the behavior of diffusion flames [1]. While early efforts considered this interaction to be due to the interaction between magnetic fields and ions in the flame, it is now accepted that the principal interaction is due to the paramagnetic and diamagnetic behavior of the constituent gases [2]. Atoms with no permanent magnetic dipole moment exhibit diamagnetic behavior i.e., the interaction between the atomic magnetic dipole moments within an atom results in a zero net magnetic dipole moment. When a magnetic field is applied, the orbital behavior of the electrons is changed such that a net magnetic dipole moment exists. As a result of Lenz' law, the resulting net dipole moment opposes the applied field and thus a diamagnetic materials exhibits a weak repulsion to an applied magnetic field. Note that diamagnetic behavior is present in all materials but is weak compared to paramagnetic behavior. Materials such as oxygen, whose atoms possess permanent magnetic dipole moments, exhibit paramagnetic behavior. For paramagnetic materials, the magnetic dipole moments are randomly oriented when not in the presence of a magnetic field. When a magnetic field is applied, the dipoles line up with the magnetic field and thus a weak attraction to an applied magnetic field is produced. This attraction must compete with the randomizing effect of thermal motion. The magnetic susceptibility, χ , defined as the ratio of the magnetization vector to the magnetic field strength, for a paramagnetic gas is given by the Curie-Weiss law. The Curie-Weiss law is $\chi = C/(T - \theta)$ where C and θ are material dependent constants and T is the temperature. For a diamagnetic gas, the susceptibility is independent of temperature. The magnetic susceptibility is $O(10^{-6})$ and $O(-10^{-9})$ for paramagnetic and diamagnetic gases, respectively. The force per unit volume, F , exerted on a paramagnetic or diamagnetic gas by the applied magnetic field is

$$F = \mu_0 \chi H \frac{\partial H}{\partial z} \quad (1)$$

where μ_0 is the permeability of free space and H is the magnetic field strength. An order of magnitude analysis shows that, under certain conditions, the forces associated with an applied magnetic field can be comparable to those associated with buoyancy [3].

The purpose of this investigation is to better understand the behavior of laminar diffusion flames in the presence of non-uniform magnetic fields and the impact that paramagnetism and

diamagnetism have with regard to transport phenomena in the vicinity of such flames. This will be accomplished by experimentally observing, in an environment where buoyant forces are negligible, the effect of non-uniform magnetic fields on diffusion flame characteristics and on the associated temperature fields. A significant aspect of the experimental effort is the development of holographic interferometry as a microgravity combustion diagnostics tool.

MAGNETOCOMBUSTION

From a thermodynamic point of view, early work involving chemical reactions and magnetic fields predicted that prohibitively large magnetic field strengths would be required to produce a significant interaction [4,5]. These conclusions were based upon order-of-magnitude estimates and did not account for the highly nonlinear nature of chemical reactions. Recently there has been a renewed effort to develop the equations needed to analyze the thermodynamic interaction between chemical reactions and magnetic fields [6-9]. Using a chemical equilibrium model that included a magnetic field contribution, Baker and Saito [10] were able to show that a uniform magnetic field can affect equilibrium combustion behavior at extremely elevated temperatures. In prior experimental investigations of magnetocombustion behavior, the temperature of the flames has not been large enough to produce a significant magnetic field interaction for uniform magnetic fields. Non-uniform fields have been shown to produce significant magnetic field/flame interaction for several cases [11-24].

HOLOGRAPHIC INTERFEROMETRY

Holographic interferometry (HI) is non-intrusive visualization technique that can be used to detect changes in velocity, density, temperature, or species concentration. HI has already been successfully used to examine combustion behavior and a few of the papers involving HI are presented in the Reference section of this paper [25-28]. HI possesses several desirable characteristics that make it ideally suited to micro-, or reduced, gravity combustion research. Because HI measures only relative changes in the object wave, high quality optics such as those used in traditional interferometry are not needed thus decreasing the cost of the experimental apparatus. Holographic interferometry also does not have the power requirements of techniques such as laser-induced fluorescence. For the investigation discussed here, holographic interferometry measurements will use the fact that the refractive index of a gas is temperature dependent. Once a relation between the refractive index and the temperature is developed, the temperature at any given location near the flame can be determined by examining the fringe pattern in relation to a point of known temperature. The difficulty in obtaining quantitative temperature measurements of magnetocombustion phenomena is that the system does not consist of a homogeneous mixture of gases. In the planned effort, holographic interferometry will be used to qualitatively examine the temperature distribution of the gases surrounding the flame.

TECHNICAL APPROACH

An experimental test cell is being built that will be capable of producing both optical images and holographic interferograms of laminar jet diffusion flames in the presence of non-uniform magnetic fields. At the time of writing, the holographic interferometer is being constructed. Optical images have been obtained of slot diffusion flames and this data has been used to examine the impact of non-uniform magnetic fields on laminar flame height. Figure 1 is an example of the typical results obtained during the initial investigation. Note that the flames produced during this initial investigation have inner burner port widths of $O(0.5mm)$. A non-

uniform magnetic field was produced using cast iron prisms attached to a neodymium iron boron (NdFeB) magnet. For the current experimental configuration, a maximum magnetic induction of 1.00 Tesla and a maximum magnetic induction gradient of approximately 100 Tesla/m was used. When such a non-uniform magnetic field was applied to the diffusion flame; the flame does not attach to the wall, the flame height was decreased, and the sooting characteristics of the flame were changed.

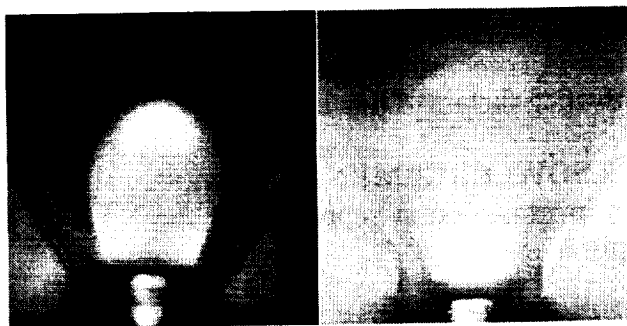


Figure 1: Slot diffusion flame in the presence of a magnetic field (left) and with no applied magnetic field (right).

Once the holographic interferometer is fully operational, temperature data will be gathered in the vicinity of the flame both with and without an applied magnetic field. The temperature data will be examined to determine if oxygen is being concentrated in the vicinity of the flame. As one would expect, if oxygen is being concentrated in the vicinity of the flame, the flame temperature will increase. After the data from the terrestrial investigation has been fully analyzed, a test cell will be designed for use in a reduced-gravity carrier. As with the terrestrial investigation, the reduced-gravity test cell will employ both holographic interferometry and optical images. The reduced-gravity investigation will examine the behavior of laminar jet diffusion flames as a function of the type of fuel, the fuel flow rate, the burner port geometry, peak magnetic field strength, and the magnetic field gradient. Empirical correlations will be developed for flame height as a function of the above-mentioned variables and these correlations will be compared to mathematical models of magnetocombustion behavior. The effectiveness of holographic interferometry as a microgravity combustion diagnostic tool will also be evaluated. If the results of this investigation show that holographic interferometry is a viable tool for microgravity combustion research, a preliminary effort will be undertaken to examine the use of holographic interferometry for species measurements in a reduced gravity. Such quantitative information would significantly enhance magnetocombustion research as well as microgravity combustion research in general.

CONCLUDING REMARKS

Magnetic fields are known to affect combustion behavior and in a terrestrial environment buoyancy effects cannot be fully isolated from the effects of magnetic fields. Initial results indicate that non-uniform magnetic fields produced using permanent magnets do change diffusion flame characteristics even in a terrestrial gravitational field. The planned investigation will attempt to isolate magnetic field effects by examining the behavior in a reduced gravity environment. Holographic interferometry will be used to examine temperature behavior in the vicinity of the flames. Examining the temperature field is important because it is believed that magnetic fields can be used as a means of achieving an oxygen-enhanced combustion environment. For the flames being considered, oxygen is the only major constituent gas that is paramagnetic. Recall that paramagnetic gases are attracted to a magnetic field. For specific magnetic field configurations, it should be possible to concentrate oxygen in the vicinity of the flame. Oxygen-enhanced combustion has many desirable characteristics. For example, oxygen-enhanced combustion is known to produce increased flame temperatures, flammability limits,

thermal efficiency, and flame stability. This list is only a partial listing of the effects of increased oxygen concentration on combustion. The potential for the development of oxygen-enhanced combustion technologies through the use of magnetic fields is one of the primary motivating factors of this investigation.

ACKNOWLEDGEMENTS

This investigation is supported by the NASA's Office of Life and Microgravity Science and Applications.

REFERENCES

1. Faraday, M., *The London, Edinburgh and Dublin Philosophical Magazine and Journal of Science* 31(S.3):401 (1847).
2. von Engle, A. and Cozens, J.R., *Advances in Electronics and Electron Physics* 20:99 (1964).
3. Baker, J. and Calvert, M.E., Paper No. OOS-037, Spring Meeting of the Western States Section of the Combustion Institute, Golden, CO, 2000.
4. Delhez, R., *Bulletin de la Société Royale des Sciences de Liège* 26(4):161 (1957).
5. Delhez, R., *Bulletin de la Société Royale des Sciences de Liège* 26(2):83 (1957).
6. Zimmels, Y., *Physical Review E* 52(2):1452 (1995).
7. Zimmels, Y., *Physical Review E* 53(4):3173 (1996).
8. Zimmels, Y., *Physical Review E* 54(5):4924 (1996).
9. Zimmels, Y., *Physical Review E* 55(5):5102 (1997).
10. Baker, J. and Saito, K., *Journal of Propulsion & Power*, 16(2):263 (2000).
11. Hayashi, H., *Chemical Physics Letters* 87(2):113 (1982).
12. Wakayama, N.I., Ogasawara, I., and Hayashi, H., *Chemical Physics Letters* 105(2):209 (1984).
13. Ueno, S., Esaki, H., and Harada, K., *IEEE Transactions on Magnetics* 21(5):2077 (1985).
14. Ueno, S., Esaki, H., and Harada, K., *IEEE Translation Journal on Magnetics in Japan TJMJ-2*(9):861 (1985).
15. Ueno, S. and Harada, K., *IEEE Transactions on Magnets* 22(5):868 (1986).
16. Ueno, S. and Harada, K., *IEEE Transactions on Magnets* 23(5):2752 (1987).
17. Ueno, S., *Journal of Applied Physics* 65(Feb. 1):1243 (1989).
18. Aoki, T., *Japanese Journal of Applied Physics* 28(5):776 (1989).
19. Aoki, T., *Japanese Journal of Applied Physics* 29(5):952 (1990).
20. Aoki, T., *Japanese Journal of Physics* 29(1):181 (1990).
21. Aoki, T., *Japanese Journal of Applied Physics* 29(5):864 (1990).
22. Wakayama, N.I., *Chemical Physics Letters* 188(3,4):279 (1992).
23. Wakayama, N.I., *Combustion and Flame* 93:207 (1993).
24. Wakayama, N.I., Ito, H., Kuroda, Y., Fujita, O., and Ito, K., *Combustion and Flame* 107:187 (1996).
25. Xiao, X., Choi, C.W., and Puri, I.K., *Combustion and Flame*, 120:318 (2000).
26. Ito, A., Narumi, A., Konishi, T., Tashtoush, G., Saito, K., and Cremers, C.J., *Journal of Heat Transfer*, 121:413 (1999).
27. Tzannis, A.-P., Beaud, P., Frey, H.-M., and Gerber, *Applied Optics*, 36(30):7978 (1997).
28. Vovchuk, J.I. and Poletaev, N.I., *Combustion and Flame*, 99:706 (1994).

RETRIEVAL OF TEMPERATURE AND SPECIES DISTRIBUTIONS FROM MULTISPECTRAL IMAGE DATA OF SURFACE FLAME SPREAD IN MICROGRAVITY

K.D. Annen and John A. Conant, Aerodyne Research, Inc.
and
Karen J. Weiland, NASA Glenn Research Center

INTRODUCTION

Weight, size, and power constraints severely limit the ability of researchers to fully characterize temperature and species distributions in microgravity combustion experiments. A powerful diagnostic technique, infrared imaging spectrometry, has the potential to address the need for temperature and species distribution measurements in microgravity experiments. An infrared spectrum imaged along a line-of-sight contains information on the temperature and species distribution in the imaged path. With multiple lines-of-sight and approximate knowledge of the geometry of the combustion flowfield, a three-dimensional distribution of temperature and species can be obtained from one hyperspectral image of a flame. While infrared imaging spectrometers exist for collecting hyperspectral imagery, the remaining challenge is retrieving the temperature and species information from this data.

An initial version of an infrared analysis software package, called CAMEO (Combustion Analysis Model et Optimizer), has been developed for retrieving temperature and species distributions from hyperspectral imaging data of combustion flowfields. CAMEO has been applied to the analysis of multispectral imaging data of flame spread over a PMMA surface in microgravity that was acquired in the DARTFire program. In the next section of this paper, a description of CAMEO and its operation is presented, followed by the results of the analysis of microgravity flame spread data.

CAMEO ANALYSIS METHODOLOGY

CAMEO uses a nonlinear model matching approach to analyze imaging spectrometer data. This approach, as shown in Figure 1, consists of two main parts. The first part is a numerical model of the measured data. This model must treat both the physical process that produces the infrared signal, such as the PMMA surface combustion modeled in this work, and the measurement process that produces the hyperspectral or multispectral image data. In general, the numerical model requires inputs to describe both the physical process and the measurement process. The second part of the nonlinear model matching approach is an optimizer that iteratively modifies the inputs to the model to produce a predicted data set that matches the measured data.

The analysis procedure, as indicated in Figure 1, starts with the initial input parameter estimates being read by the optimizer and then passed to the model to generate a set of predicted measurements, i.e., a predicted hyperspectral or multispectral image data set. The optimizer then compares the predicted data set with the measured data set, calculates an objective function value that represents the overall difference between the measured and predicted data sets, and then generates a new set of parameter estimates that are passed to the model. The model generates an updated predicted data set from these new parameters and passes the updated set to the optimizer for

evaluation. This process is repeated until the optimizer determines that it has found the set of input parameter estimates that provides the best match between the predicted and measured data sets.

The numerical model component of CAMEO consists of subroutines for two separate models, one to model the physical process producing the infrared signal, and a second to model the generation and measurement of the infrared signal. At the heart of this second model is a three-dimensional radiation transport code, RAD3D, developed by

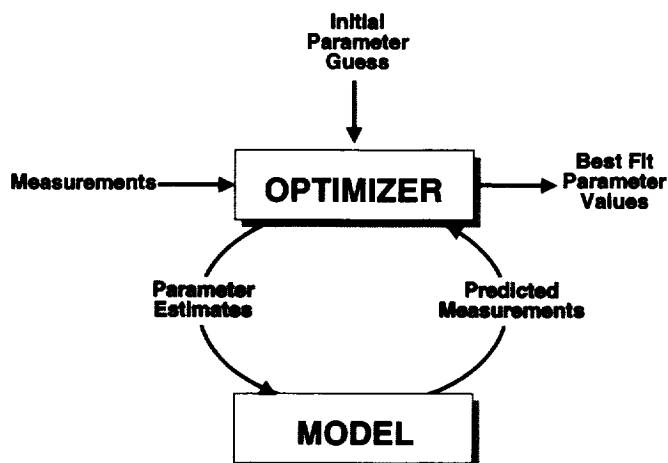


Figure 1 Nonlinear Model Matching Methodology

Aerodyne. RAD3D computes the spatially and spectrally resolved infrared signal from a three-dimensional distribution of temperature and species. RAD3D uses band models to calculate the infrared emission and absorption by the infrared-active species in the combustion flowfield. Additional routines then convert the hyperspectral image computed by RAD3D to a form that allows a comparison with the measured data.

In the present version of CAMEO, the model of the physical process that produces the infrared signal must be supplied by the user for each class of combustion process, or other physical process, to be analyzed. This model must generate a flowfield description, i.e., distributions of temperature and species concentrations, as a function of model input parameters. The complexity of this model can range from empirical to detailed. An empirical model, for example, may use a prescribed shape of the flame front and determine the distribution of species and temperatures based on functional forms for temperature and species in various regions of the combustion flowfield. The inputs to this model are typically the parameters used in the functional form descriptions of the species and temperature distributions. This type of model was used in analyzing the PMMA flame spread data. A detailed model may use a “first principles” approach, with inputs perhaps being turbulence intensity, thermal and mass diffusivities, and characteristic lengths and velocities.

The optimizer used in CAMEO is a general constrained optimization package, NPSOL, using a sequential nonlinear programming algorithm[1]. In an initial study of optimizers, NPSOL was found to use the fewest number of function evaluations (iterations) to achieve a good match between measured data and predictions[2]. The sum of squared residuals was used as the objective function that was minimized by NPSOL to obtain the best match between data and prediction. While use of this normal Least Squares criterion is most common, NPSOL can also use objective functions based on Bayesian or Maximum Likelihood approaches to uncertainty in the measured data.

CAMEO ANALYSIS OF MICROGRAVITY FLAME SPREAD DATA

While CAMEO has been designed for the general application of analyzing hyperspectral image data, it also can analyze multispectral imagery, such as collected in the DARTFire program[3]. The DARTFire data consist of a set of six images, each for a different bandpass filter. The filters covered the 1.88 μm H_2O band, CO_2 bands at 2.7 and 4.3 μm , MMA band at 3.4 μm , and CO band at 4.8 μm . For this data analysis, the hyperspectral image computed by RAD3D is integrated over modified

filter transmission curves to obtain six images for comparison with the data. The modified filter curves account for the variation in detector response over the filter bandpass regions. For analysis with CAMEO, the raw DARTFire images containing eight-bit detector intensity information were converted to images containing radiance values. This conversion also introduced "flag" values for locations where the measured radiance was below the detector sensitivity limit. These regions are used in calculating the objective function if the predicted radiances are greater than this low limit value. As mentioned above, an empirical approach was used to model the PMMA flame spread combustion flowfield. A flame front location is defined by the user by specifying a number of points to which a spline curve is fit. Profiles for temperature and species are defined for two regions: the fuel rich region between the flame front and pyrolyzing PMMA surface, and the fuel lean region outside the flame front.

Analysis of the multispectral flame spread imagery has posed a number of challenges, primarily due to the three-dimensional character of the actual combustion flowfield, the relatively simple nature of the empirical model of the flowfield, and the low spectral resolution of the data. Initial attempts to analyze the data using a two-dimensional empirical model failed to closely reproduce the radiance images. After the empirical model was extended to account for flame height variation in the transverse direction, an improved agreement with the radiance images was obtained. The figure plate on the following page shows the data images for five bands in the top row, the "optimized solution" model images in the middle row, and the objective function (proportional to the square of the residual) on the bottom row. The band for each column is given at the bottom of the plate. Differences in the radiance spatial distributions between the data and model clearly exist, though considering that a single distribution of temperature and species concentrations produces the different distributions for the five filter bands shown in the plate, the agreement is reasonable. The agreement between the data and model on the peak radiances in each filter band is generally quite good. The peak radiances agree exactly for Filter 3 (MMA), within 5% for Filter 5 (CO_2 -4.3 μm), 12% for Filter 1 (CO_2 -2.7 μm), and 25% for Filter 6 (CO). The only substantial mismatch is Filter 4 where the model intensity is low by almost a factor of two. This mismatch could possibly be caused by inaccuracies in the band model for H_2O , since a detailed model for this band was not available.

The objective function images in the figure plate show where the major regions of difference between the data and model exist for each band. With the exception of the H_2O band, the regions of greatest difference are near the PMMA surface at the leading or trailing edge of the flame. Thus, the inability of the simple empirical model to represent the details of the flowfield in this region accounts for the largest discrepancies. In the center region near the flame zone, the agreement is quite good, as indicated by the agreement of the peak radiances cited above. While improvements in CAMEO to reduce run time and improve its geometric flexibility are desirable, CAMEO has produced encouraging results on this difficult analysis problem.

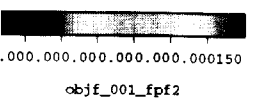
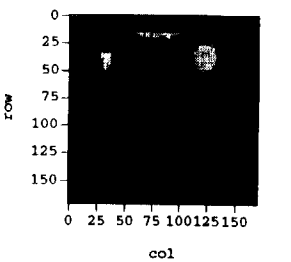
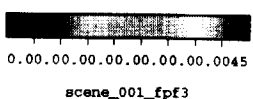
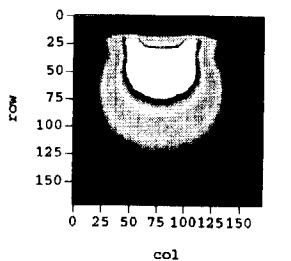
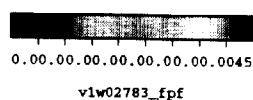
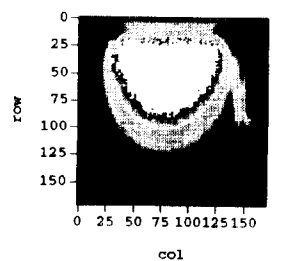
1. P.E. Gill, et al., NPSOL (Version 4.0): A Fortran Package for Nonlinear Programming, Systems Optimization Laboratory Report SOL 86-2, Dept. Operations Research, Stanford Univ., 1986.
2. E.R. Niple, K.D. Annen, and J.C. Wormhoudt, "Analysis Tools for Spectrally-Resolved and Broadband IR Imaging Data," Final Report, NASA LeRC Contract No NAS3-27267, July 1995.
3. S.L. Olson, et al., "Diffusive and Radiative Transport in Fires Experiment: DARTFire," Fourth International Microgravity Combustion Workshop, NASA CP-10194, p.393, May 1997.

Data

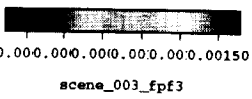
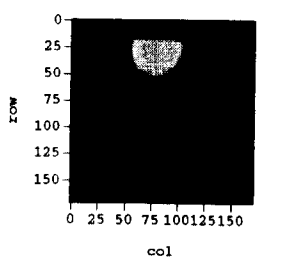
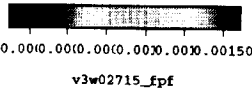
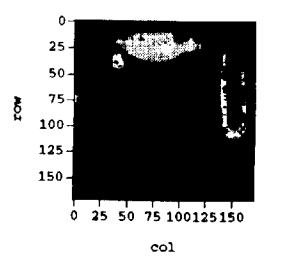
Model

Objective

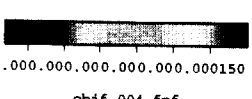
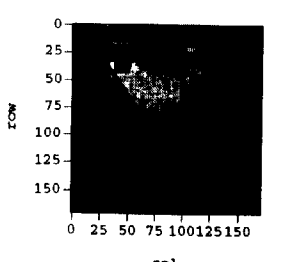
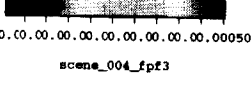
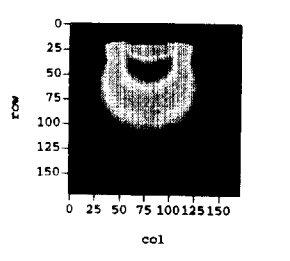
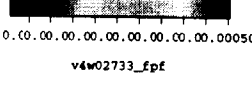
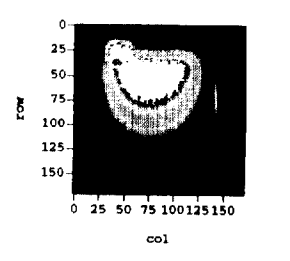
Function



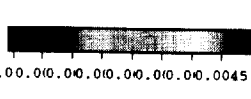
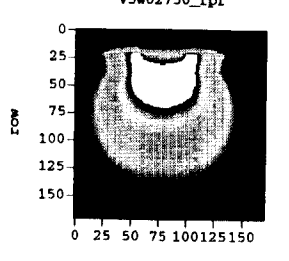
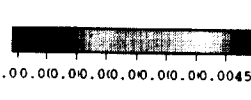
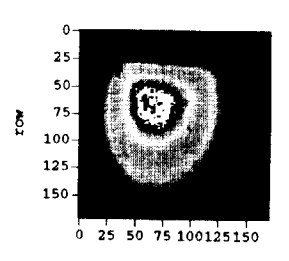
Filter 1, CO2(2.7um)



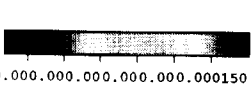
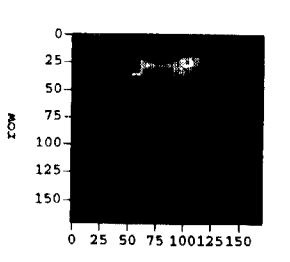
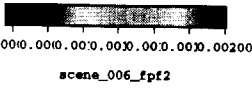
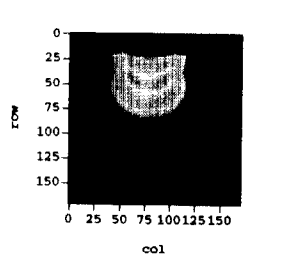
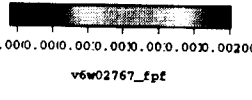
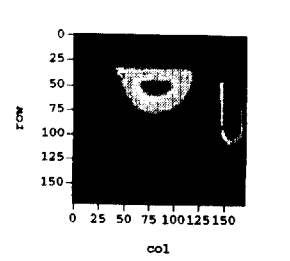
Filter 3, MMA



Filter 4, H2O (1.88um)



Filter 5, CO2 (4.3 um)



Filter 6, CO

FAN BEAM EMISSION TOMOGRAPHY FOR TRANSIENT FIRES

Yudaya Sivathanu, Jongmook Lim, Vinoo Narayanan and Rony Joseph
En'Urga Inc.
1291-A Cumberland Avenue
West Lafayette, IN 47906

Introduction

Radiation signatures can be utilized to maximum advantage for determining structural information in turbulent flows (Sivathanu and Faeth, 1990, Sivathanu and Gore, 1991, Sivathanu et al., 1991). Emission spectroscopy does not require a light source, and alignment and data collection are relatively straightforward. Emission spectroscopy is most advantageous in the infrared regions of the spectra, principally because these emission lines arise from transitions in the fundamental bands of stable species such as CO_2 and H_2O . Emission spectroscopy also currently offers the most accurate method of temperature determination (Zhu et al., 1997). However, emission spectroscopy is a line of sight method and deconvolution of measurements has to be addressed with all emission spectroscopy methods.

In laminar combusting flows, tomography has been used both with absorption (Chen and Goulard, 1976; Santaro et al., 1981), emission (Tourin, 1983, Uchimaya et al., 1985) and simultaneous absorption/emission (Best et al., 1991) spectroscopy to retrieve local properties in axisymmetric and non-axisymmetric laminar flows.

One of the most exciting developments in tomography is the advent of statistical deconvolution algorithms. It has been recently shown (Vardi and Lee, 1993) for systems with strict positivity constraints (i.e. absorption and emission are always greater than one and never negative), that a Maximum Likelihood Estimation (MLE) approach provides convergent solutions. Strict convergence can be proved for a wide array of physical systems ranging from image deblurring to optimal investments (Vardi and Lee, 1993).

The MLE method has been used for the non-intrusive measurement of soot volume fraction and temperature PDFs in turbulent flames (Sivathanu et al., 1995) using emission tomography. The iterative algorithm is based on the MLE method (Vardi and Lee, 1993). In addition, statistical deconvolution for the retrieval of mean and fluctuating components in turbulent flows have been recently developed by the PI in collaboration with others (Nyden et al., 1996).

Based on the above, the objective of the present work is to develop Fan Beam Emission tomography methods for the transient fires that are currently being supported by the NASA microgravity program. It is anticipated that a robust technique for obtaining local temperature and gas species concentrations for a wide variety of transient fires will be made available for possible inclusion into the Combustion Integrated Rack for the International Space Station.

Experimental methods

A high speed spectrometer system (Spectraline ES100) is designed to collect radiation from a flame source located up to 1 meter from its entrance port. The radiation from the source enters the input port of the enclosure and is incident upon a 0.5 mm wide slit. The light passing through the slit is chopped at 390 Hz and is dispersed into its spectral components using two CaF_2 prisms. The dispersed light is focused onto a PbSe detector array with 160 elements. The imaging spectrometer was developed under a prior NASA Phase I project and provides a spectral resolution of approximately 20 nm from 1.3 to 4.8 microns. The imaging spectrometer has an outer dimension of 27 x 24 x 11 cm, and weighs 6.4 kg. The numerical aperture of the system is $\pm 0.25^\circ$. Therefore, a very tight collimation of the source being imaged is possible with the spectrometer. The spectrometer has been used in JAMIC drop tower experiments and successfully obtained single view angle emission intensity data. The spectrometer is currently marketed by En'Urga Inc. under the brand name Spectraline.

A schematic diagram of the FBET system is shown in Fig. 1. The FBET system consists of three imaging spectrometers, with scanning mirrors in front of them. Each imaging spectrometer with a scanner in front of it is positioned 120 degrees from each other. The spectrometers collect path-integrated intensities from a fan angle of 80 degrees, with an angular resolution of $\pm 0.25^\circ$ and a discretization of four degrees. Therefore, the three scanners provide simultaneous emission intensity data at a rate of 30 Hz (20 separate angles per scanner at 625 Hz per angle) for a total of sixty angles. This speed is sufficient for most pool and solid fire experiments currently studied in the microgravity combustion program

The spatial resolution of the system will be $1/20^{\text{th}}$ of the flow area being scanned. If the total flow area is 1 cm, the spatial resolution of the system will be approximately 0.5 mm. This is sufficient to validate combustion models in laminar and transient flames.

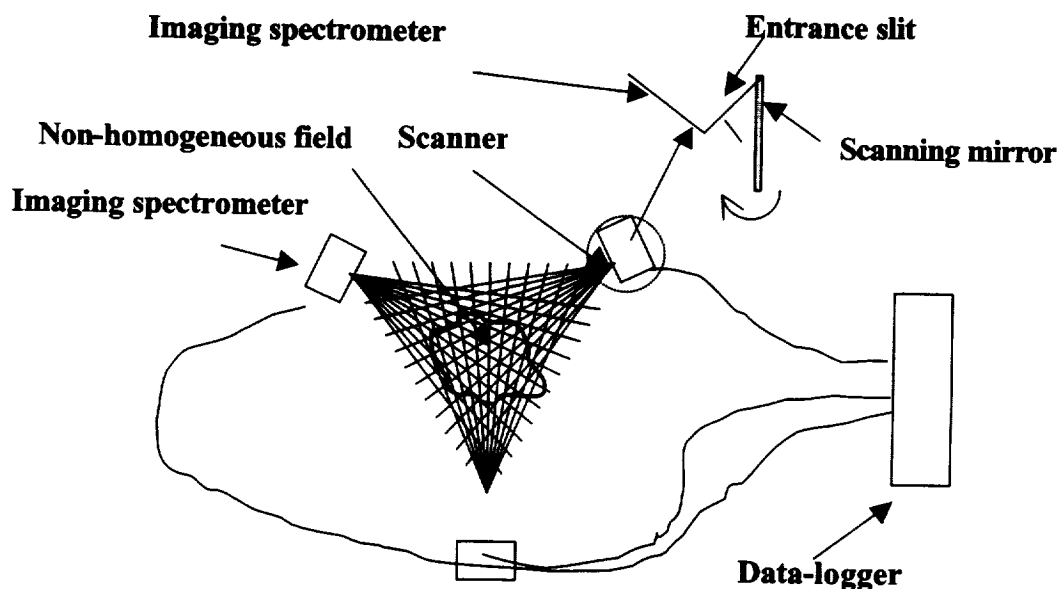


Figure 1. Schematic diagram of the FBET system.

Numerical Method

Fan beam absorption tomography has been utilized in the past to investigate turbulent structures in reacting flows. Previous studies show that with as little as 20 projections, RMS errors of less than 5% are possible. The feasibility of obtaining very high quality reconstruction data with the proposed 60 projections (20 projections per spectrometer) will be explored during the first year of the study using synthetically generated data.

The reconstruction algorithm that will be used to deconvolute the path-integrated data is based on maximum likelihood solutions for positive linear inverse problems. The reconstruction is obtained one wavelength at a time. The maximum likelihood solution is obtained iteratively, and the iterative algorithm for any wavelength λ is briefly discussed below.

For the triangular grid shown in Fig. 5, let the spectral emission intensity at each of the nodal values be X_{ikm} , where i represents the number of nodal points along the beam k that falls on spectrometer m . Let the number of beams in the fan be K , the number of spectrometers be M , and the number of nodal points along the beam k for spectrometer m be I . The total spectral intensity incident on spectrometer m from beam k (designated T_{km}) is obtained from the summation of the intensities along all the nodes, X_{ikm} that fall on the beam, modified by the transmittance of the segments τ_{ikm} . T_{km} can be represented as:

$$T_{km} = \sum_{i=1}^I \tau_{ikm} X_{ikm} \quad (1)$$

The unknown values in equation (1) are the local intensities X_{ikm} and transmittances τ_{ikm} .

The deconvolution algorithm is iterative, and the update value for the intensity at the n^{th} iterate is obtained as:

$$X_{ikm}^n = X_{ikm}^{n-1} * \sum_{k=1}^K \sum_{m=1}^M \tau_{ikm}^{n-1} (T_{km} / T_{km}^{n-1}) \quad (2)$$

where τ_{ikm} is the contribution of the intensity from the node to the path integrated intensity defined as:

$$\tau_{ikm} = X_{ikm} \sum_{j=1}^I \tau_{jkm} \quad (3)$$

The iterative deconvolution converges to the maximum likelihood value in as little as 20 iterations. The deconvolution is performed one wavelength at a time. During the first iteration, the transmittances are set to 1 and the local intensities are set to the total intensity measured divided by the number of nodes (uniform field). After the local intensities have been obtained, they are used in conjunction with a narrow band model such as the RADCAL to obtain the local gas species concentrations and temperatures. The local transmittances are obtained from the local properties and re-introduced into the iterative deconvolution program.

The gas species concentrations (CO_2 and H_2O) needed for the calculations were obtained from the predicted reaction progress variable. Narrow-band radiation models are accurate to within 10 % provided the temperature is specified accurately and species concentrations predicted within 30% along the path are specified correctly. For the FBET system, 60 such spectra (20 beams at each spectrometer) will be obtained theoretically, and deconvoluted to provide the local gas species concentrations and temperatures. In addition, the aberration caused by transmission of radiation through the sapphire window has to be accounted for by the algorithm.

Conclusion

Initial studies show that the proposed FBET system is a promising method for obtaining temperatures and major gas species concentrations in transient fires.

References

- Best, P. E., Chien, P. L., Carangelo, R. M., Solomon, P. R., Danchak, M. and Ilovici, I 1991, Combust. Flame, vol. 85, pp. 309-318.
- Nyden, M. R., Vallikul, P., and Sivathanu, Y. R., 1996, JQSRT, vol. 55, pp. 345-356.
- Ravichandran, M., and Gouldin, F. C., 1988, Appl. Opt., vol. 27, pp. 4084.
- Sivathanu, Y. R., and Faeth, G. M., 1990, Combust. Flame, vol. 89, pp. 150-165.
- Sivathanu, Y. R., and Gore, J. P., 1991, Combust. Sci. & Tech., vol. 80, pp. 1-21
- Sivathanu, Y. R., Hamins, A., Hagwood, C., and Kashiwagi, T., 1995, Proceedings of the Joint Technical Meeting of the Central and Western States Sections and the Mexican National Section of the International Combustion Institute and American Flame Research Committee, pp. 92-97.
- Sivathanu, Y. R., Gore, J. P., and Dollinar, J., 1991, Combust. Sci. Tech., vol. 76, pp. 45-66.
- Sivathanu, Y. R., and Gore, J. P., 1993, JQSRT, vol. 50, pp. 483-492.
- Solomon, P. R., Philip, E. B., Carangelo, R. M., Markham, J. R., Chien, P. L., Santoro, R. J., and Semerjian, H. G., 1986, Twenty-First Symposium (International) on Combustion, The Combustion Institute, Pittsburgh, PA, pp. 1763-1771.
- Vardi, Y., and Lee, D., 1993, J. R. Statist. Soc. B, vol. 55, pp. 569-612.
- Zhu, Y.J., Sivathanu, Y. R., and Gore, J. P., 1997, *Heat Transfer in Combustion and Fire*, HTD-vol. 310, pp. 120-127, ASME, New York, NY.

FULL NAVIER-STOKES MODELING OF A BOUNDARY-LAYER DIFFUSION FLAME OVER A POROUS FLAT PLATE

Ramagopal Ananth*, Chuka C. Ndubizu¹, and P.A. Tatem
Navy Technology Center for Safety & Survivability, Chemistry Division
Gopal Patnaik and K. Kailasanath
Laboratory for Computational Physics and Fluid Dynamics
Naval Research Laboratory, Washington, DC 20375

INTRODUCTION

Boundary layer flames form naturally on burning solid surfaces, which are of significant interest in microgravity. Most existing models [1-5] consider combustion near the leading edge or make boundary layer approximations, which are valid far downstream. Here, we present a fully transient model and describe suppression dynamics for uniform injection of fuel gas through a porous plate burner, a configuration similar to that used in the recent microgravity experiments [6].

APPROACH

Solutions of unsteady, full Navier-Stokes equations are obtained using Barely Implicit Correction to Flux Corrected Transport (BIC-FCT) algorithms [7]. The smallest (0.2x0.4 mm) cells are placed near the leading edge and are stretched in both directions on 150x200 grid. Single step combustion kinetics [8] is integrated using Burlich-Stoer method with Rhombberg interpolation. The transport properties are evaluated as functions of temperature and composition based on the kinetic theory of gases. Comparisons with the literature data [5] have shown quantitative agreement for the steady state temperature and axial velocity distributions for the dry air case.

DISCUSSION

Transient solutions of the Navier-Stokes equations for temperature, heat release rate (HRR), and iso-concentration contours are shown in Figure 1 for three cases; (1) dry air, (2) air with 20 wt% steam, (3) air with 20 wt% water droplets. The abscissa in each figure consists of a leading non-porous plate (5 cm), followed by a the porous plate (5 cm), and a non-porous end plate (8 cm). The leading plate is adiabatic while the other two sections were kept at room temperature. The ordinate represents distance perpendicular to the surface, y . Initially air containing the additives flows (30.0 cm/sec) past the solid plate from left to right. At time zero, ethane gas is injected (0.25 cm/sec) through the porous burner and is ignited near the leading edge by adding external heat for a short period of time (20 msec). Figure 1a shows isotherms (red broken lines) and a single HRR contour (black solid line) at the end of ignition. During this time fuel is ejected uniformly along the plate forming a fuel-air mixture ahead of the flame front as shown by the iso-concentration (mole fraction, X_i) contours for fuel (blue solid line) and oxygen (green broken line) in Figure 1b.

As time progresses, the flame front propagates forward into the partially mixed gas forming a triple flame structure as shown by the HRR contour for the dry air case in Figure 1c at 170 msec. The triple flame consists of a main stem, a long right arm and a half-formed left arm. There is a partially mixed fuel-air to the right of the triple flame and a fuel rich gas to the left of the left arm of the triple flame. The region between the main stem and the right arm contains oxygen rich gas.

These can be seen in Figure 1d. The region between the fuel and oxygen contours in Figure 1d represents partially mixed gas and the region inside the oxygen contour represents oxygen lean gas. Also, the region outside of the fuel contour represents the oxygen rich gas. The main stem of the HRR contour in Figure 1c is anchored firmly to the adiabatic leading plate on the left. There is little fuel leakage upstream behind the flame due to the presence of adiabatic leading plate, which results in a high surface temperature. This can be seen clearly in Figure 1c and 1d by the isotherms and the fuel contour, which run perpendicular to the adiabatic leading edge. Therefore, a triple flame structure is formed only on the propagating arm of the HRR contour in Figure 1c. The isotherms in Figure 1c appear to follow the general shape of the HRR contour. But, the isotherms are not necessarily parallel to the HRR contour, since reaction rates depend both on temperature and composition. The isotherms corresponding to the maximum flame temperature appear to lay within the HRR contour. Clearly, the temperature gradients are much smaller on the fuel side of the HRR contour than on the air side.

In the presence of steam, a triple flame similar to that in dry air case is displayed in Figures 1c and 1d. However, the maximum temperature is significantly lower than that in dry air case due to oxygen dilution and higher specific heat of water vapor than air. In the presence of water droplets, the flame structure is found to be dramatically different from the dry air and steam cases as shown in Figures 1c and 1d. Very small water droplets are considered and are modeled as heat sinks independent of droplet size. The latent heat effect seems to destabilize the flame near the leading edge causing the flame to lift up and completely detach from the solid surface. Figure 1c shows the formation of a closed flame pocket despite continued presence of fuel-air mixture as displayed in Figure 1d. As time progresses, the flame pocket is simply transported downstream (blowout) as shown in Figures 1e and 1g, as the fuel gas is continuously ejected from the porous plate forming fuel-air mixture behind the flame as shown by the fuel and air contours in Figures 1f and 1h. In the cases of dry air and steam, the triple flame continues to spread and finally transform to a boundary layer structure at steady state as shown in Figures 1d through 1h.

CONCLUSIONS

The transient solutions describe formation of triple flame structure, dynamics of flame suppression with the addition of steam, dynamics of flame destabilization near the leading edge and blow-off due to the latent heat absorption of water droplets. As the forced convection velocity is decreased, gravity and radiation effects become significant. The model can be extended to include the microgravity effects on boundary layer flames and on the dynamics of flame suppression.

REFERENCES

- [1] Mao, C-P., Kodama, H., and Fernandez-Pello, A.C., *Comb. & Flame*, **57**, 209(1984)
- [2] Chen, C-H. and Tien, J., *Comb. Sci. Tech.*, **50**, 283(1986)
- [3] Di Blasi, C., Crescitelli, S., and Russo, G., *Comb. & Flame*, **72**, 205(1988)
- [4] Kikkawa, S. and Yoshikawa, K., *Int. J. Heat Mass Transfer*, **16**, 1215(1973)
- [5] Ramachandra, A. and Raghunandan, B.N., *Comb. Sci. Tech.*, **33**, 309(1983)
- [6] Brahmi, L., Vietoris, T., Joulain, P., David, L., and Torero, J.L., 37th AIAA Aerospace Sciences Meeting, Reno, Nevada, paper AIAA-99-0581, January 11-14, 1999
- [7] Patnaik, G., Laskey, K.J., Kailasanath, K., Oran, E.S., and Brun, T.A., NRL Memo Report 6555, Naval Research Laboratory, Washington DC, September 27, (1989)
- [8] Westbrook, C.K. and Dryer, F.L., *Prog. Energy Combust. Sci.*, **10**, 1(1984)

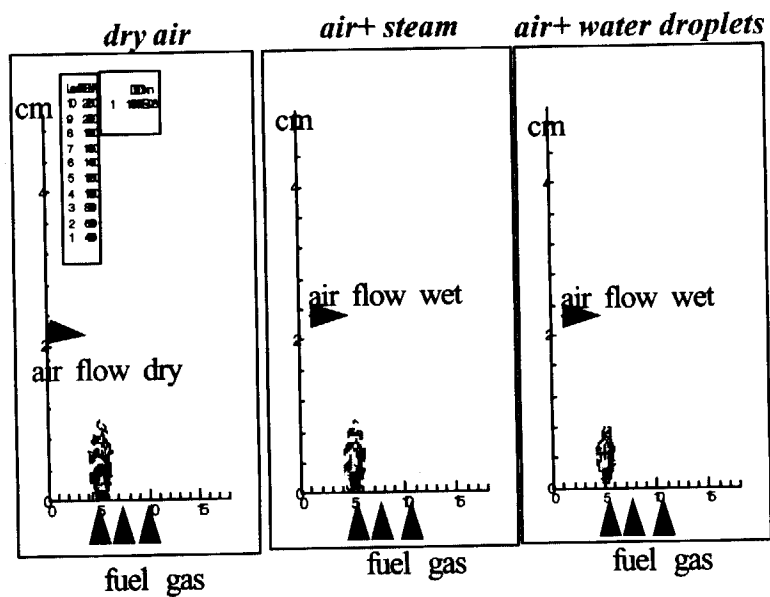


Figure 1a. Isotherms and HRR Contour at 20 msec

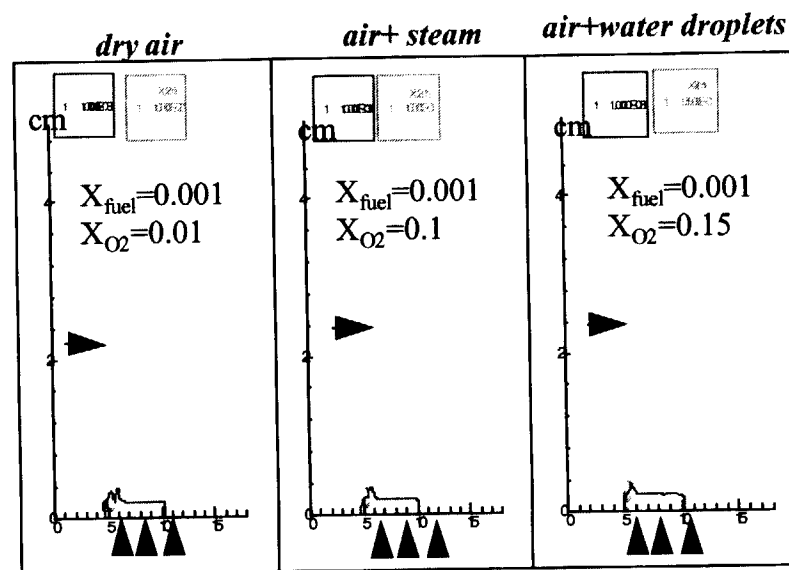


Figure 1b. Contours for fuel and oxygen at 20 msec

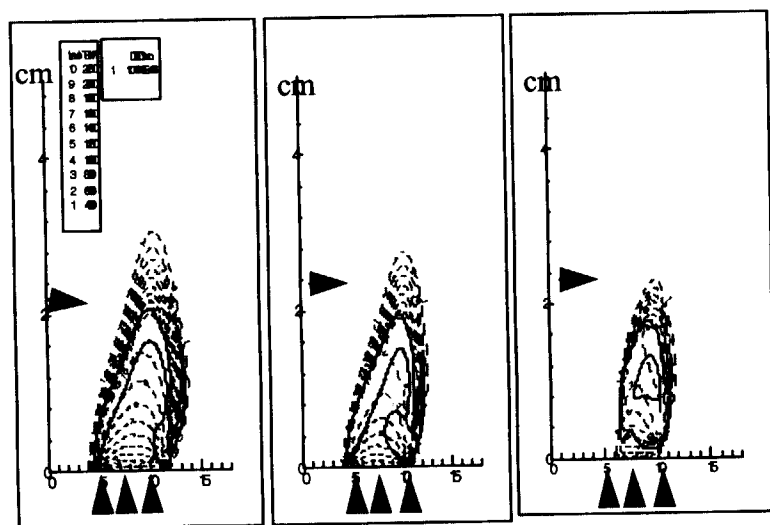


Figure 1c. Isotherms and HRR Contour at 170 msec

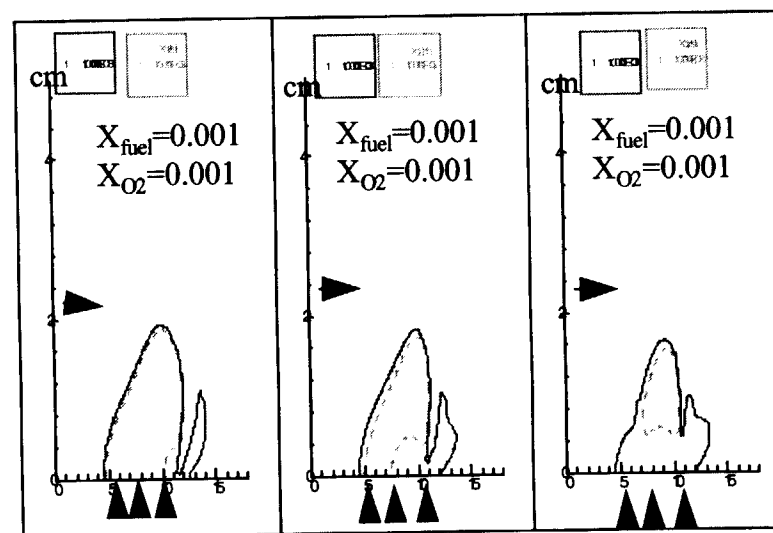


Figure 1d. Contours for fuel and oxygen at 170 msec

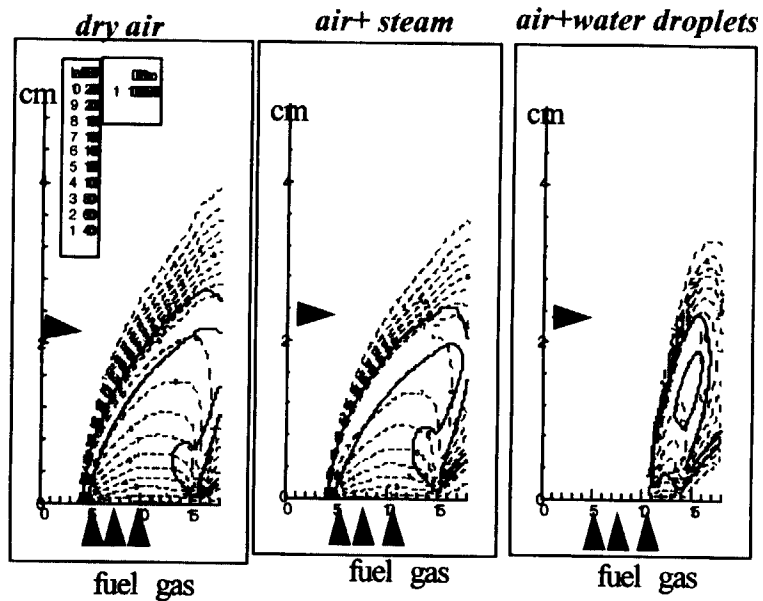


Figure 1e. Isotherms and HRR Contour at 420 msec

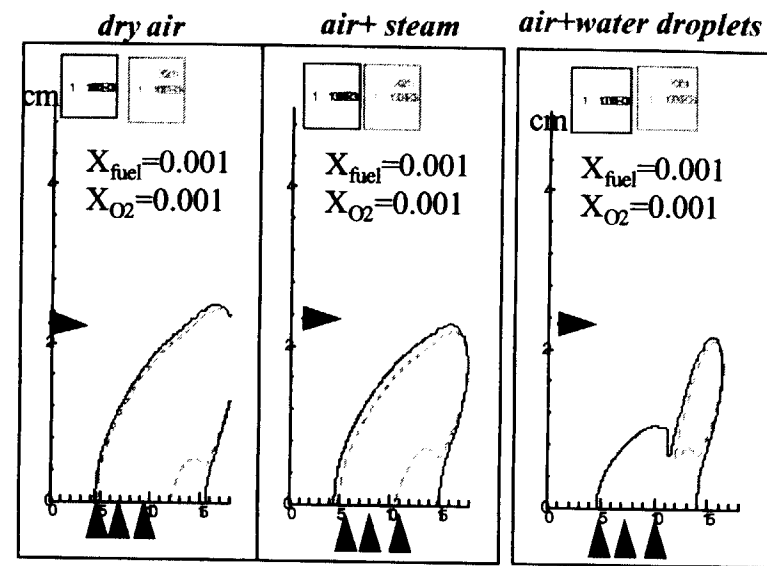


Figure 1f. Contours for fuel and oxygen at 420 msec

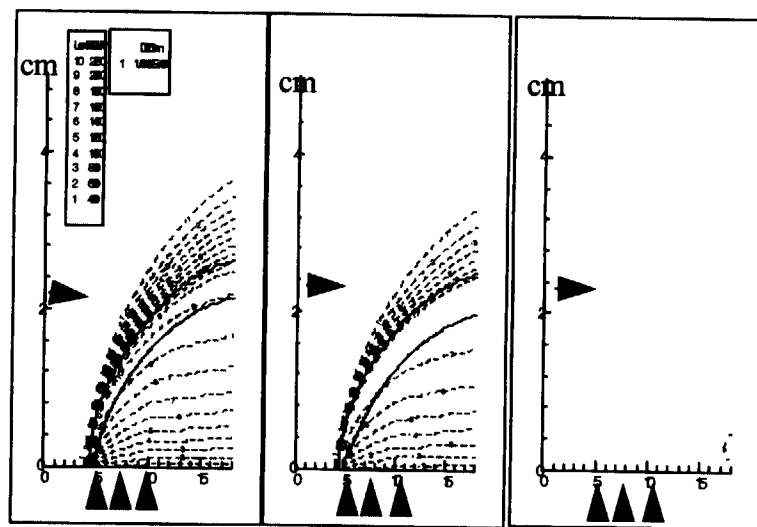


Figure 1g. Isotherms and HRR Contour at 1420 msec

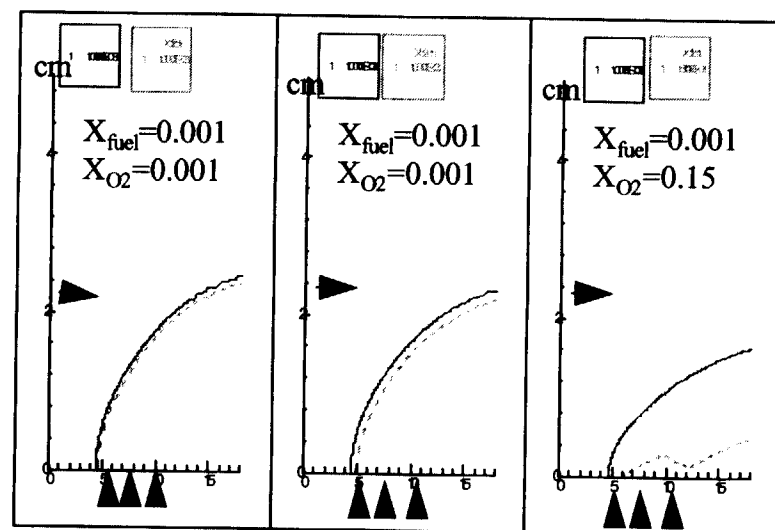


Figure 1h. Contours for fuel and oxygen at 1420 msec

Combustion of Gaseous Fuels with High Temperature Air in Normal- and Micro-gravity Conditions

Y. Wang and A. K. Gupta*

University of Maryland, Dept. of Mechanical Engineering, College Park, MD 20742

*Tel.: 301-405-5276; e-mail: ak Gupta@eng.umd.edu

Summary

The objective of this study is determine the effect of air preheat temperature on flame characteristics in normal and microgravity conditions. We have obtained qualitative (global flame features) and some quantitative information on the features of flames using high temperature combustion air under normal gravity conditions with propane and methane as the fuels. This data will be compared with the data under microgravity conditions. The specific focus under normal gravity conditions has been on determining the global flame features as well as the spatial distribution of OH, CH and C_2 from flames using high temperature combustion air at different equivalence ratio.

Introduction

The highly preheated air combustion is a new concept on combustion and heat transfer technology, and its application is enormous including furnaces for various industrial purposes and combustion engines. In furnaces it can reduce the fuel consumption by up to about 50%, reduce the size of the equipment or increase the throughput for the same size of the equipment, and reduce the emission of pollutants by about 30% (including CO_2) without any adverse effort on thermal loading or performance of the system. In this method low oxygen concentration air is used for the combustion of fuels. In order to explore the potential of highly preheated air combustion, we examine the basic differences in the combustion behavior of theses flames under normal and microgravity conditions. The flame characteristics have been found to be significantly different using high temperature combustion air as compared to the results obtained with normal temperature combustion air.

Normal Gravity Studies

In the normal gravity experiments, the combustion air is preheated to temperatures from 900 °C to 1100 °C. The oxygen concentration in the combustion air is varied from 21% to about 2% to produce ultra-lean mixtures. Under normal temperature conditions it is normally not possible to stabilize the flame at such fuel-lean mixtures. The results have been obtained with methane and propane as the fuels. The results showed that as the air preheat temperature is increased, the flame color as well as the flame volume changes significantly. The flame volume is significantly larger at reduced oxygen concentration of oxygen in air. The flame color changes from yellow to blue to bluish-green to green with propane as the fuel over the range of conditions examined (see Fig.1). In contrast, with methane as the fuel colorless or flameless oxidation of the fuel was observed (see Fig. 2). The flame volume is much larger at low O_2 and high air-preheat temperatures. These unique features of the flames with high temperature combustion air have not been reported before. The distribution of C_2 in flames at different air preheats temperature and O_2 concentration in air is presented in Fig. 3. The results show that the gradients of C_2 at low O_2 concentration air and high air preheat temperatures are much less as compared to its counterpart. The spectral characteristics showed significant peak at the swan band for C_2 (at 516.5 nm, see Fig. 4) at high temperatures for the propane flame. This peak is directly responsible for the observed green color flame of propane flame. The experiments

conducted under normal gravity conditions provide guidelines for the design and experiments under microgravity conditions. The usual philosophy is that with an increase in combustion air temperature the formation of NO_x will be higher. However if the oxygen concentration in air is reduced the NO_x emission can be reduced significantly under high temperature air conditions. The experiment performed under normal gravity has shown that the use of high temperature combustion air provides uniform distribution of temperature in the flame and hence a uniform heat flux distribution in the combustion zone.

Microgravity Combustion Studies

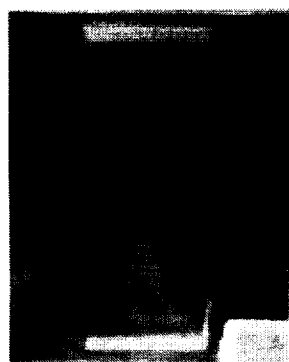
The experimental facility for use in microgravity combustion conditions has been designed. Various parts for the facility have been assembled. The burner assembly consists of a cylindrical burner in which the fuel is injected on the central axis surrounding which high temperature combustion air is injected. The high temperature is produced by electrically heating the air. The tests conducted showed that the temperature air could be raised to about 1100°C using electrical heating elements. This raised the issue of touch temperature of the other parts in the facility. Calculations revealed that the one can run the facility in excess of 10 minutes before the temperature in the drop rig can be 40°C . Therefore one can run the tests in the drop tower and aircraft for several seconds without having concern on the touch temperature rise in the experimental rig. The oxygen concentration in the combustion air will be varied using bottled gas having desired composition of the O_2 and N_2 mixture. This procedure will also allow us to easily change the N_2 in the air with CO_2 . The reason for changing the N_2 with CO_2 is that in our normal gravity experiments significant differences were found in the flame combustion characteristics between the two gases. The flame global features will be observed using an CCD and digital cameras. The data will be stored on a computer in the rig and then transferred to an external computer after the tests for further processing the data. Tests will be conducted with combustion air preheat temperatures in the range of approximately 900 to 1100°C . The O_2 concentration in the combustion air would be varied from 21% down to 2% in discreet steps at any air preheat temperature. Nitrogen or CO_2 will be used as the dilution gas to reduce the concentration of oxygen in the combustion air.

The microgravity studies will be conducted first in the NASA 2.2 second drop tower facility and then in the KC 135 for longer duration tests. The drop rig would consist of an air preheater, burner, combustion chamber, gas cylinders, CCD and digital cameras and associated lens, filters and associated optical mounts, battery packs and a computer. An electrical heater will be used to preheat the air to the desired temperature. A schematic diagram of the preheater used for microgravity studies is presented in Fig.5. The flame obtained is given in Figure 6. The combustion chamber shown in Figure 7 is used for the microgravity studies.

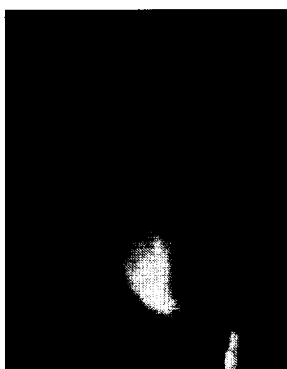
Specify measurements to be made at microgravity will include measurements similar to those conducted under normal gravity conditions, namely, flame size and shape, and time resolved spatial distribution of OH, CH and C_2 from the flames. These data will then be analyzed to determine the role of microgravity on the flame behavior. Our studies will further provide means of controlling the flame signatures and flame radiation in addition to providing a database for model validation and model development.

Acknowledgements

NASA supported this research under contract number NCC3686. We gratefully acknowledge the contributions and collaborations of several NASA Glenn Research staff members in the microgravity division.



2% ($\Phi=0.83$)
EGR=949%
1100 °C

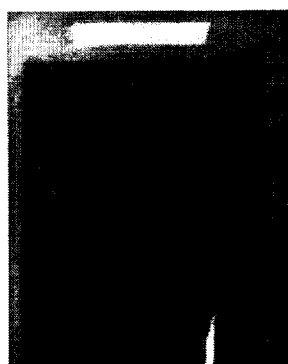


8% ($\Phi=0.21$)
EGR=163%
950 °C

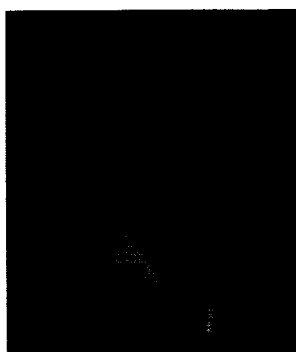


21% ($\Phi=0.079$)
EGR=0%
900 °C

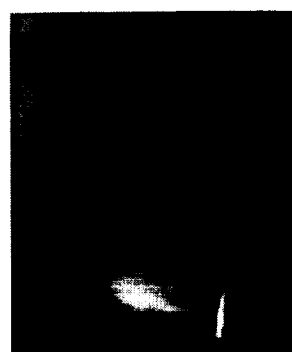
Figure 1: Propane Flame (note the green color at low O_2 concentration in air)



2% ($\Phi=0.3$)
1100°C

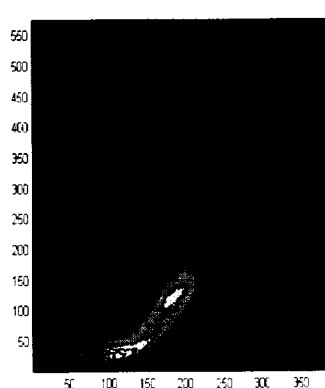


8% ($\Phi=0.08$)
950°C

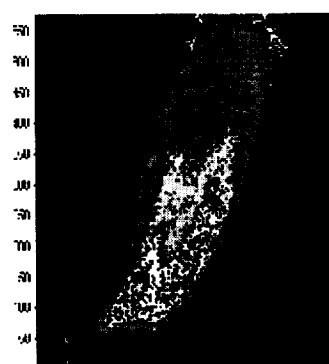


21% ($\Phi=0.031$)
900° C

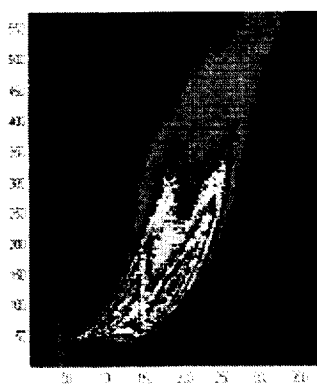
Figure 2: Methane Flame (Note the flameless/colorless oxidation of fuel at low O_2 conc. in air)



C2 (15%) 980 °C



C2 (15%) 1070 °C



C2 (15%) 1160 °C

Figure3. Effect of Air Preheat Temperature on the Distribution of C_2 in Flames

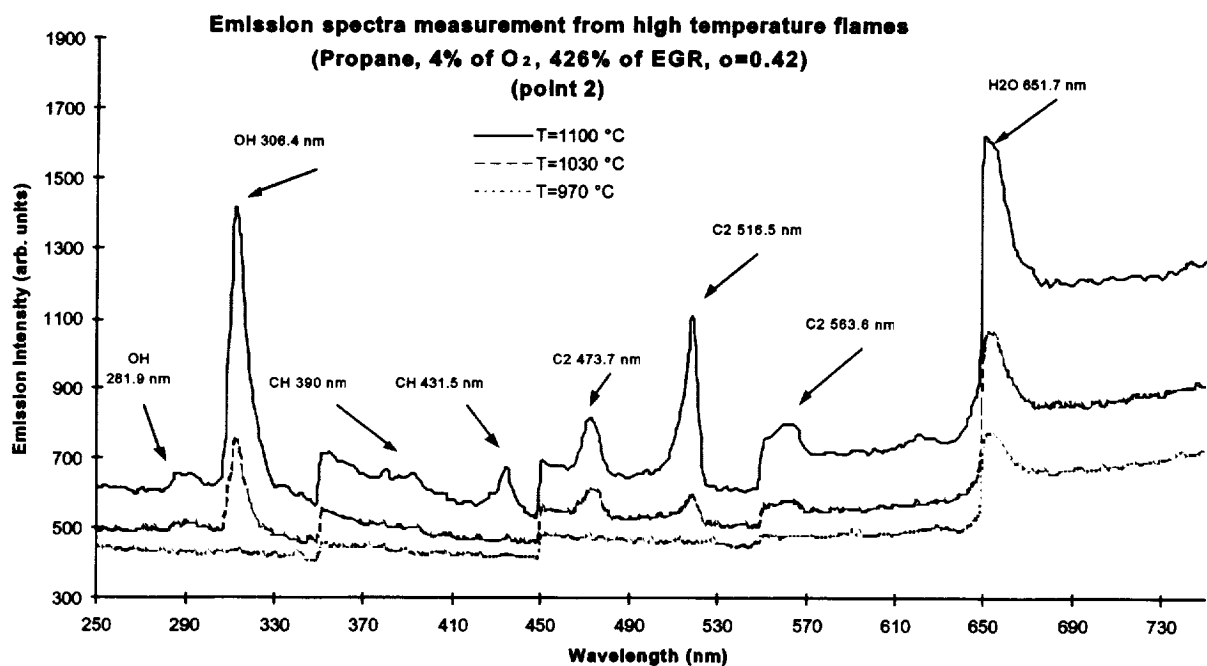


Figure 4. Emission Spectra of Propane Flame at Normal Gravity

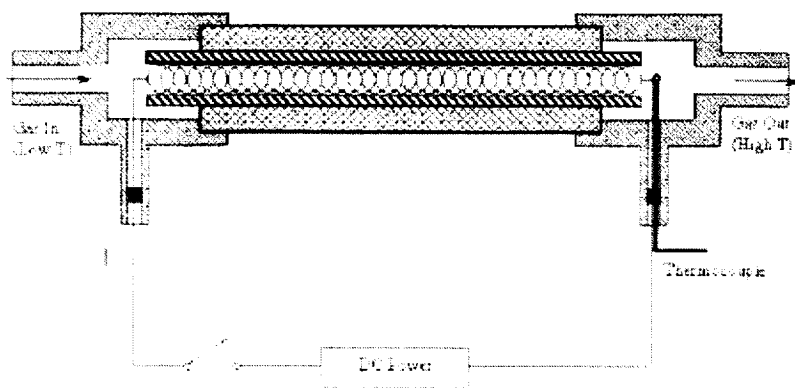


Figure 5. Air Preheater Assembly

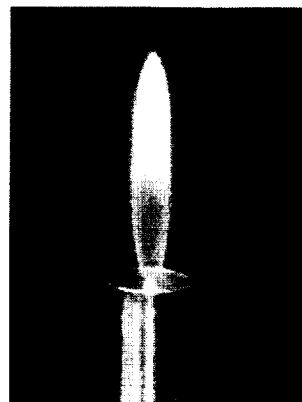


Figure 6. Flame at 1g

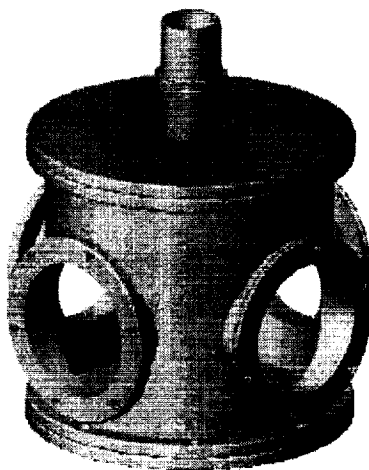


Figure 7. Combustion Chamber for the μ g Rig

AN ANALYTICAL MODEL FOR NON-UNIFORM MAGNETIC FIELD EFFECTS ON TWO-DIMENSIONAL LAMINAR JET DIFFUSION FLAMES

M. E. Calvert¹, J. Baker¹, K. Saito², and R. L. Vander Wal³

¹University of Alabama at Birmingham, Birmingham, AL 35294

²University of Kentucky, Lexington, KY 40506

³NASA-Glenn Research Center, Cleveland, OH 44135

INTRODUCTION

In 1846, Michael Faraday found that permanent magnets could cause candle flames to deform into equatorial disks [1]. He believed that the change in flame shape was caused by the presence of charged particles within the flames interacting with the magnetic fields. Later researchers found that the interaction between the flame ions and the magnetic fields were much too small to cause the flame deflection. Through a force analysis, von Engel and Cozens [2] showed that the change in the flame shape could be attributed to the diamagnetic flame gases in the paramagnetic atmosphere. Paramagnetism occurs in materials composed of atoms with permanent magnetic dipole moments. In the presence of magnetic field gradients, the atoms align with the magnetic field and are drawn into the direction of increasing magnetic field. Diamagnetism occurs when atoms have no net magnetic dipole moment. In the presence of magnetic gradient fields, diamagnetic substances are repelled towards areas of decreasing magnetism. Oxygen is an example of a paramagnetic substance. Nitrogen, carbon monoxide and dioxide, and most hydrocarbon fuels are examples of diamagnetic substances.

Over the past twenty years, there has been an increase in the interest in the ability to control combustion behavior. Much research on the relation between combustion and magnetic fields has taken place in Japan. These researchers have found that the presence of magnetic fields caused significant changes in diffusion flame behavior, such as changes in radiative emissions from the flames [3], changes in flame shape and sizes [4-8], and changes in the extinction points [8]. However, this research has typically involved the use of electromagnets to supply the magnetic fields. One possible problem with this approach has been the interaction between the flames and the electric fields surrounding the coils used to generate the magnetic field [9]. As is known from research in magnetohydrodynamics, electric fields can interact with charged particles in fluids, causing physical changes in the fluid's behavior. The conclusions of the previous research have used order of magnitude analysis to argue that the electrical field interactions were insignificant when compared to the para- and diamagnetic behavior of the fluids involved in the combustion process [4]. Little research has been done on interactions between flames and the "pure" magnetic fields produced by permanent magnets to quantify this behavior without the presence of electric fields. This has primarily resulted from the lack of permanent magnets of strength comparable to that of electromagnets. Recent advances in material science have allowed for the commercial manufacture of rare earth permanent magnets with strengths on the order of 1 Tesla. In order to evaluate the usefulness of these magnets in altering flame behavior, a study has been undertaken to develop an analytical model to describe the change in the flame length of a laminar diffusion jet in the presence of a nonuniform magnetic field.

The analytical model derived for this study is an extension of the model derived by Roper for the investigation of slot diffusion flames in the presence of a gravity field [10]. In the cited reference, Roper derived expressions for the flame lengths from different types of burner geometries. His analysis showed that the length of flames from square and circular burners was independent of buoyancy effect. His analysis of slot burners revealed that buoyancy effects could not be neglected for this type of burner geometry. Using the Froude number, Roper identified three flow regimes for this geometry of burner; momentum controlled, buoyancy controlled, and transitional. Due to the nature of magnetic fields, the slot burner geometry lends itself well to an analysis of magnetic fields effects on diffusion flames.

By its nature, the para- and diamagnetic properties of matter make magnetocombustion behavior research an ideal choice for microgravity environments. Microgravity is useful for studying combustion behavior because the absence of buoyant forces simplifies the physical processes occurring during combustion. Within a microgravity environment, the interaction between the magnetic fields and the flames could be optimized, and greater understanding of the physical processes could be gained. However, the cost of designing and carrying out such an experiment requires that some type of initial analysis be performed to optimize the experiment design to obtain the greatest amount of meaningful data from the experiment. This analytical analysis represents the first step in this process.

ANALYSIS

As stated previously, magnetic gradient fields exert a body force on para- and dia-magnetic materials. This induced body force is given by Kelvin's law:

$$\mathbf{F}_{MAG} = \frac{1}{2} \frac{\chi_i}{\mu_0} \nabla \mathbf{B}^2 \quad (1)$$

where μ_0 is the permeability of free space, χ_i is the volumetric susceptibility of material i , and \mathbf{B} is the magnetic field. The volumetric susceptibility is $O(10^{-9})$ for diamagnetic gases and of $O(10^{-6})$ for paramagnetic materials. When a material is placed in another material of differing susceptibility within a magnetic gradient field, Kelvin's law causes a body force to be exerted, similar to that exerted by gravity on two materials of differing densities. This body force is given by

$$\mathbf{F}_{MAG} = \frac{1}{2} \frac{\chi - \chi_\infty}{\mu_0} \nabla \mathbf{B}^2 \quad (2)$$

where some gas of susceptibility χ is in an atmosphere of susceptibility χ_∞ . Assuming that the magnetic field is a function of z coordinate only, and that momentum and buoyancy forces are negligible, the conservation of momentum equation for the z direction may be integrated to give

$$v_z = v_{f0} \left[-Pm \left(\left(\frac{B}{B_0} \right)^2 - 1 \right) \right]^{1/2} \quad (3)$$

where the magnetic pressure number is defined as

$$Pm = - \frac{(\chi - \chi_\infty) B_0^2 / \mu_0}{\rho_f v_{f0}^2} \quad (4)$$

where the subscript 0 on B defines the point at the burner exit, and all other notation is as used by Roper. [10] In order to obtain an expression for flame length as a function of magnetic gradient, it is necessary to assume the variation of magnetic field as a function of z . For the purposes of this study, a linear relation was defined as

$$B = B_0 - \Delta B z \quad (5)$$

where ΔB represents the magnetic field gradient. Following Roper's method to obtain flame length expressions, the following expression is obtained:

$$\left[\left(\frac{\Delta B}{B_0} L_{f,MAG} - 1 \right) \left(2 \frac{\Delta B}{B_0} L_{f,MAG} - \left(\frac{\Delta B}{B_0} L_{f,MAG} \right)^2 \right)^{1/2} + \arccos \left(1 - \frac{\Delta B}{B_0} L_{f,MAG} \right) \right] \\ = \frac{2}{Pm^{1/2}} \frac{\Delta B}{B_0} L_{f,MOM} \quad (6)$$

which implicitly defines the magnetic-controlled flame length, $L_{f,MAG}$. $L_{f,MOM}$ is defined as the momentum controlled flame length as defined by Roper [10].

RESULTS AND CONCLUSIONS

Figure 1 shows plots for three different values of $B \cdot dB/dz$ for four burner ports of differing aspect ratios. The values for the port dimensions used in the calculations are shown on the plots in figure 1. The values for B and ΔB are given in table 1. The fuel used for this study was propane in quiescent air. The flame temperature was taken as the adiabatic flame temperature of propane [11]. The volumetric susceptibility of air (χ_∞) was calculated as 3.74×10^{-7} , and the value for propane was calculated as -3.21×10^{-9} . The initial values for susceptibilities were obtained from [12], and were converted from molar value in cgs-emu system of units. It should be noted that the volumetric susceptibility for propane was corrected for the difference in density between the value given in [12] and the fuel density at the flame temperature.

From the plots in figure 1, it may be observed that changes in the product $B \cdot dB/dz$ did not result in linear changes in the flame length as a function of flow rate Q . Instead, the flame length seemed to approach an asymptotic value for increasing $B \cdot dB/dz$. The rate of approach to this asymptote decreases with increasing $B \cdot dB/dz$. Roper showed that the flame length for a buoyancy induced slot flame would asymptotically collapse onto the burner with increasing gravitational field. It would be expected that the same phenomena would occur here with increasing $B \cdot dB/dz$. It may also be noted that the flame height is slightly influenced by the geometry of the burner port. These results show that non-uniform magnet fields can significantly alter the flame lengths of laminar diffusion flame. Further research is warranted to observe how different fuel and oxidizers affect this phenomenon, as well as how this affect compares to buoyancy effects and initial momentum effects.

REFERENCES

- [1] M. Faraday, "On the Diamagnetic conditions of Flame and Gases," *The London, Edinburgh and Dublin Philosophical Magazine and Journal of Science*, vol. 31, pp. 401-421, 1847.

- [2] A. von Engle and J. R. Cozens, "Flame plasmas," *Advances in Electronics and Electron Physics*, vol. 20, pp. 99-146, 1964.
- [3] N. I. Wakayama, I. Ogasawara, and H. Hayashi, "The External Magnetic Field Effect on the Emission Intensity of the Na D Line in Hydrogen-Oxygen Flames," *Chemical Physics Letters*, vol. 105, pp. 209-213, 1984.
- [4] T. Aoki, "Radicals' Emissions and Butane Diffusion Flames Exposed to Upward Decreasing Magnetic Fields," *Japanese Journal of Applied Physics*, vol. 28, pp. 776-785, 1989.
- [5] T. Aoki, "Radical Emissions and Butane Diffusion Flames Exposed to Uniform Magnetic Fields Encircled by Magnetic Gradient Fields," *Japanese Journal of Applied Physics*, vol. 29, pp. 952-957, 1990.
- [6] T. Aoki, "Radical Emissions and Anomalous Reverse Flames Appearing in Upward-Increasing Magnetic Fields," *Japanese Journal of Physics*, vol. 29, pp. 181-190, 1990.
- [7] T. Aoki, "A Magnetically Induced Anomalous Ring Flame and Quenching Characteristics of Butane Flames," *Japanese Journal of Applied Physics*, vol. 29, pp. 864-867, 1990.
- [8] S. Ueno, "Quenching of Flames by Magnetic Fields," *Journal of Applied Physics*, vol. 65, pp. 1243-5, 1989.
- [9] J. R. Carruthers and R. Wolfe, "Magnetothermal Convection in Insulating Paramagnetic Fluids," *Journal of Applied Physics*, vol. 39, pp. 5718-5722, 1968.
- [10] F. G. Roper, "The Prediction of Laminar Jet Diffusion Flame Sizes: Part I. Theoretical Model," *Combustion and Flame*, vol. 29, pp. 219-226, 1977.
- [11] S. R. Turns, *An Introduction to Combustion: Concepts and Applications*. New York: McGraw-Hill, 1996.
- [12] R. C. Weast, "CRC Handbook of Chemistry and Physics," 67 ed. Cleveland: CRC Press, Inc., 1986.

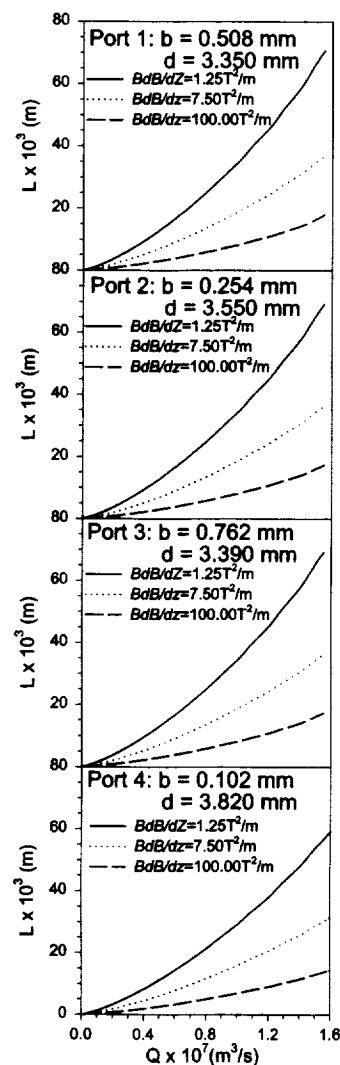


Figure 1: Predicted flame height as a function of flow rate and magnetic field.

Trioxane-Air Counterflow Diffusion Flames in Normal and Microgravity¹

Gregory T. Linteris (Fire Research Div., NIST Gaithersburg, MD); Marc D. Rumminger, (Ceryx, Inc., Santa Paula, CA); and David L. Urban (NASA-GRC, Cleveland, OH)

Introduction

Trioxane, a weakly bound polymer of formaldehyde ($C_3H_6O_3$, m.p. 61 °C, b.p. 115 °C), is a uniquely suited compound for studying material flammability. Like many of the more commonly used materials for such tests (e.g. delrin, polyethylene, acrylic sheet, wood, and paper), it displays relevant phenomena (internal heat conduction, melting, vaporization, thermal decomposition, and gas phase reaction of the decomposition products). Unlike the other materials, however, it is non-sooting and has simple and well-known chemical kinetic pathways for its combustion. Hence it should prove to be much more useful for numerical modeling of surface combustion than the complex fuels typically used.

We have performed the first exploratory tests of trioxane combustion in the counterflow configuration to determine its potential as a surrogate solid fuel which allows detailed modeling. The experiments were performed in the spring and summer of 1998 at the National Institute of Standards and Technology in Gaithersburg, MD, and at NASA-GRC in Cleveland. Using counterflow flames at 1-g, we measured the fuel consumption rate and the extinction conditions with added N_2 in the air; at μg conditions, we observed the ignition characteristics and flame shape from video images. We have performed numerical calculations of the flame structure, but these are not described here due to space limitations. This paper summarizes some burning characteristics of trioxane relevant to its use for studying flame spread and fire suppression.

Experiment

A stagnation flow of air (with optional N_2 diluent) against a horizontal, planar surface of trioxane was used to establish a counterflow diffusion flame. The oxidizer was supplied from above via a stainless steel jet (2.27 cm I.D. with three 60 mesh/cm screens to provide uniform laminar flow), which was located 1 cm above the trioxane, while a concentric stainless steel tube (5.35 cm I.D.) provided a co-flow of nitrogen [1]. The trioxane was supplied in two separate ways. In the first, a small puck of solid trioxane was formed in the counter-bored region of an aluminum alloy plate (56 mm x 78 mm, 6.28 mm thick, with a 24.1 mm diameter, 3.1 mm deep hole in the center). The trioxane was melted and poured into the hole, overfilling it by about 1 mm, and allowed to solidify at the laboratory temperature (21.0 ± 1.5) °C. The airflow was set to the desired value, and the flame was established, causing the trioxane to melt, vaporize, and burn. The fuel surface regressed during the test, but data were only used for trioxane levels within ± 1.5 mm of the edge of the Al plate. To obtain the fuel consumption rate, the Al plate and trioxane puck were positioned on a scale (Mettler², model PE360), and the weight as a function of time was recorded by a computer.

¹ Official contribution of NIST, not subject to copyright in the United States.

² Certain commercial equipment, instruments, or materials are identified in this paper to adequately specify the procedure. Such identification does not imply recommendation or endorsement by the NIST, nor does it imply that the materials or equipment are necessarily the best available for the intended use.

In the second apparatus, a high-pressure syringe pump (Isco, model 314, insulated and heated to $(70 \pm 5)^\circ\text{C}$) injected liquid trioxane continuously [2] to a small pool (formed by a 2.54 cm O.D. stainless steel tube with 1.64 mm walls, and 12 mm deep). The transfer lines and fuel cup were held at $(100 \pm 5)^\circ\text{C}$. A concentric stainless steel tube (47.8 cm I.D.) filled with glass beads allowed for co-flowing N_2 gas. The trioxane level was held flush with the top of the fuel cup through manual control of the piston pump rate (which varied with the strain rate and N_2 mole fraction). The global strain rate in the flame is estimated using the formulation of Seshadri and Williams [3] as $2V_{\text{air}} / L$. Here, V_{air} is the gas exit velocity from the air jet, and L is the spacing between the air jet exit nozzle and the fuel surface.

Gas flows were measured with digitally-controlled mass flow controllers (Sierra Model 860) with a quoted repeatability of 0.2% and accuracy of 1% of full-scale flow, which were calibrated with bubble (Gillian Gilibrator) and dry (American Meter Co. DTM-200A) flow meters so that their accuracy was 2% of the indicated flow. House compressed air (filtered and dried) was used after it was additionally cleaned by passing it through an $0.01\ \mu\text{m}$ filter, a carbon filter, and a desiccant bed to remove small aerosols, organic vapors, and water vapor. The 1,3,5 trioxane was from Aldrich (99+%), and the added nitrogen was boil-off from liquid N_2 .

All uncertainties are reported as *expanded uncertainties*: $X \pm U$, where U is ku_c , and is determined from a combined standard uncertainty (estimated standard deviation) u_c , and a coverage factor $k = 2$ (level of confidence approximately 95%) [4]. Likewise, when reported, the relative uncertainty is $U / X \cdot 100\%$, or $ku_c / X \cdot 100\%$. The expanded relative uncertainties for the experimentally determined quantities in this study are indicated on the figures.

Exploratory tests of the behavior of trioxane-air flames in μg were conducted in the GRC 2.2-second drop tower. The multi-purpose combustion rig was used. Melted trioxane was poured into a counter-bored region of a 51 mm x 51 mm x 6.4 mm thick Teflon holder and allowed to solidify and reach laboratory temperature. The recessed trioxane sample in the holder was 25.4 mm in diameter 3.2 mm thick; however, the trioxane was typically overfilled by about 1 mm. The Teflon fuel holder was screwed to an aluminum standoff 50 mm above the base of the combustion chamber. Provisions were made for supplying ambient air from a 12.2 mm diameter nozzle located 21 mm from the sample surface, so the flame could be tested with and without imposed flow. The trioxane was ignited with a 6 cm length of 0.255 mm diameter Kanthal wire just touching the trioxane surface. Video images were obtained with a fiber-coupled camera.

Results and Discussion

For strains above $100\ \text{s}^{-1}$, the counterflow trioxane flames were bright blue and non-sooting, and planar and parallel to the fuel surface. As the strain decreased, or the added N_2 was increased, the intensity of the blue flame emission decreased, but the color was unchanged. We could not extinguish flames of trioxane and pure air by increasing the air flow since for those conditions, the strong air jet (strain $> 1000\ \text{s}^{-1}$) blew the liquid trioxane out of the fuel cup. Flames in 1-g supported by natural convection were also stable.

Figure 1 shows the trioxane fuel consumption rate for both burners (solid puck of trioxane and the liquid feed system). Both indicate an approximately linear relationship between strain (i.e. imposed air velocity) and fuel consumption rate, with a fuel consumption rate of about 0.5

g/cm²/min at $a=300\text{ s}^{-1}$. It is somewhat surprising that the two different techniques show approximately the same fuel consumption rate. It is likely that the puck method is influenced by transient thermal effects, while the liquid feed system would require careful balancing of the heat flows for accurate measurement of fuel consumption rate. Great pains were not taken in these preliminary tests to account for or control either of these influences.

The effect of nitrogen added to the air stream on the fuel consumption rate is shown in Figure 2. Data are presented for 0, 10, 20, 30, and 40% added nitrogen mole fraction in air. To first order, the effect of added nitrogen is approximately linear, with nitrogen addition decreasing the fuel consumption rate proportionately. The extinction condition of the continuous feed trioxane burner with added N₂ is shown in Figure 3. The mole fraction of added N₂ required for extinction decreases from 41% at a strain of 150 s^{-1} to 25% at $a=550\text{ s}^{-1}$. A linear extrapolation implies an extinction condition of 48% added N₂ at zero strain, and an extinction strain rate of 1100 s^{-1} with pure air.

Trioxane-air flames in the drop-rig (trioxane puck in a Teflon holder) are shown in Figure 4. The top image is in 1-g, with no imposed flow. The second through fourth images are all in μg , with increasing imposed flows of 0, 640, and 1100 sccm. All fuel reservoirs are 25.4 mm in diameter except the bottom one, which is 22.2 mm. Remnants of the igniter wire are visible in each image for the μg flames.

Conclusions

Trioxane is an easy fuel to work with for combustion studies of material flammability. Flames can be established over a wide range of strain rate and oxygen mole fraction in the air, in both normal and microgravity. Trioxane is easily ignited in μg , and the flame is stable in both 1-g and μg with no imposed flow. The intensity of the flame emission (and presumably the temperature and heat release rate) increases as the imposed airflow increases. The fuel consumption rate and the intensity of visible flame emission are amenable to straightforward laboratory experiments. The kinetic studies (not discussed in the present work) show the decomposition pathway of trioxane to be simple, proceeding through $\text{CH}_2\text{O} \rightarrow \text{HCO} \rightarrow \text{CO} \rightarrow \text{CO}_2$ mostly via H-atom attack on CH_2O , thermal decomposition of HCO, and OH attack on CO. With trioxane, it should be possible in models of material flammability to include realistic fuel decomposition kinetics to describe the gas-phase chemistry. Since we are interested in studying the effect of physical and chemical inhibitors on condensed-phase flames in microgravity, trioxane may be a useful fuel for this purpose.

The authors thank Peter Sunderland for assistance with the drop-tower experiments. This work was supported by the Office of Biological and Physical Research at NASA.

References

- [1]. Puri, I.K. and Seshadri, K., *Combust. Flame* 65:137 (1986).
- [2]. Hochgreb, S. and Dryer, F.L., *J. Phys. Chem.* 96:295 (1992).
- [3]. Seshadri, K. and Williams, F.A., *Int. J. of Heat and Mass Transfer* 21:137 (1978).
- [4]. Taylor, B. N. and Kuyatt, C. E., *Guidelines for Evaluating and Expressing the Uncertainty of NIST Measurement Results*, National Institute of Standards and Technology, NIST Technical Note 1297, 1994.

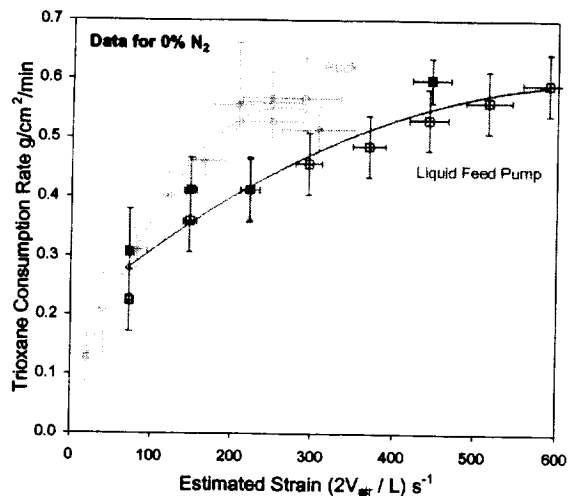


Figure 1 – Trioxane consumption rate vs. strain; puck and and continuous feed systems.

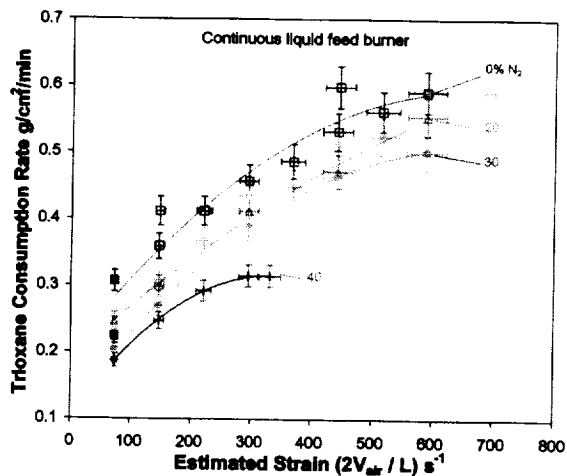


Figure 2 - Trioxane consumption vs. strain in liquid system at 0, 10, 20, 30, and 40% added N₂ in air.

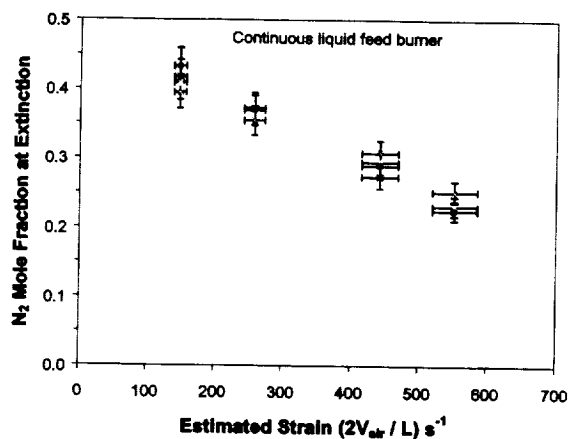


Figure 3 – Mole fraction of added N₂ in air vs. extinction strain rate for liquid trioxane burner.

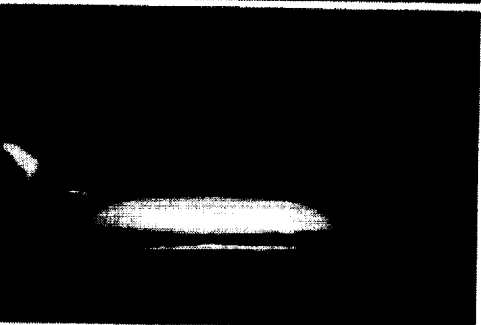
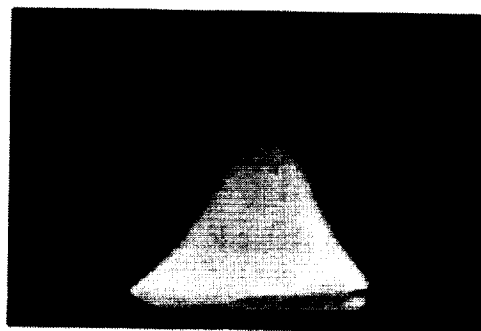


Figure 4 – Video images of trioxane-air flames. Top image is in 1-g with no imposed flow. The second through fourth from the top are in μ g, with imposed flows of 0, 640, and 1100 sccm

COMBUSTION OF UNCONFINED DROPLET CLUSTERS IN MICROGRAVITY

G. A. Ruff¹ and S. Liu²

¹NASA Glenn Research Center, Cleveland, OH (gary.a.ruff@grc.nasa.gov)

²Mechanical Engineering and Mechanics Department, Drexel University,
Philadelphia, PA (sg95x4sj@drexel.edu)

INTRODUCTION

Combustion experiments using arrays of droplets seek to provide a link between single droplet combustion phenomena and the behavior of complex spray combustion systems. Both single droplet and droplet array studies have been conducted in microgravity to better isolate the droplet interaction phenomena¹⁻⁴ and eliminate or reduce the confounding effects of buoyancy-induced convection. In most experiments involving droplet arrays, the droplets are supported on fibers to keep them stationary and close together before the combustion event. The presence of the fiber, however, disturbs the combustion process by introducing a source of heat transfer and asymmetry into the configuration. As the number of drops in a droplet array increases, supporting the drops on fibers becomes less practical because of the cumulative effect of the fibers on the combustion process. To eliminate the effect of the fiber, several researchers have conducted microgravity experiments using unsupported droplets. Jackson and Avedisian⁵ investigated single, unsupported drops while Nomura *et al.*⁶ studied droplet clouds formed by a condensation technique.

The overall objective of this research is to extend the study of unsupported drops by investigating the combustion of well-characterized drop clusters in a microgravity environment. Direct experimental observations and measurements of the combustion of droplet clusters would fill a large gap in our current understanding of droplet and spray combustion and provide unique experimental data for the verification and improvement of spray combustion models. In this work, the formation of drop clusters is precisely controlled using an acoustic levitation system so that dilute, as well as dense clusters can be created and stabilized before combustion in microgravity is begun. This paper describes the design and performance of the 1-g experimental apparatus, some preliminary 1-g results, and plans for testing in microgravity.

EXPERIMENTAL APPARATUS

To achieve the objectives stated above, it has been necessary to perform the following tasks: (1) design and fabricate a unique acoustic levitator that can stabilize a two-dimensional droplet cluster prior to combustion, (2) develop a method to introduce a specified number and size of droplets into the acoustic field, (3) develop a method to ignite the droplet cluster, and (4) assemble all of these components into a controllable experiment in a drop tower rig. The first three challenging items have been completed. Because of the unique nature and requirements of each of these components each task required the development and evaluation of new experimental apparatus. Work accomplished to date on these systems are described in this section.

Acoustic Levitator

As shown in Fig. 1, the single-axis acoustic driver assembly consists of two piezoelectric transducers in a sandwich configuration similar to that developed by Zhuyou *et al.*⁷ Aluminum

transmitter blocks are placed on both sides of the sandwich transducer and sized to create a plane standing wave in the material when oscillating at 20 kHz. A titanium stepped acoustic horn is tightly coupled to the forward transmitter to amplify the transducer displacement. The electrical power to the amplifier is provided by a 12-v battery. The signal generator has a dedicated internal battery. The tip of the horn is 29 mm in diameter and directs the acoustic wave towards the concave reflector (50-mm diameter). The shape of the reflector focuses the acoustic pressure field to produce an axially- and radially-varying pressure field between the driver and reflector that was quantified using a 3-mm diameter microphone. Because of the shape of the reflector, two axial pressure antinodes are produced when the driver and reflector are 20 mm apart. Radial sound pressure measurements were obtained at an antinode located 4 mm above the surface of the driver and are shown in Fig. 2. The pressure well that laterally stabilizes the droplet cluster is clearly seen and has a radius of approximately 4 mm. A sound pressure levels in excess of 160 dB can be produced in this apparatus.

Droplet Generator

An on-demand droplet generator was developed to introduce droplets into the acoustic levitator. Liquid fuel is placed in a 0.1-ml syringe having a 90-micron hypodermic needle attached at its end. The syringe assembly is mounted on a traversing stage controlled by a stepping motor. A piezoelectric screw positioner depresses the plunger of the syringe to form drops as small as 300 microns on the end of the needle. The liquid is charged to help break up the drop placed on the end of the hypodermic needle and to prevent the drops that are produced from coalescing in the antinode of the acoustic field. An induction charging system consisting of a copper ring mounted on the syringe and an adjustable 0 – 10 kV high voltage power supply charges the liquid as it passes through the needle.

Droplet Ignition

The droplet ignition system is practically the only component that can be copied from existing drop combustion experiments. However, most systems use two opposing hot wire coils to ignite drops. Because of the larger spatial distribution of drops in this experiment and the need to maintain symmetry of the heating process, two pairs of opposing hot wires were incorporated into the current ignition system.

Imaging system

The two-dimensional droplet cluster can be imaged from the side (along the plane of the cluster) and from the top (90 deg to the cluster) through a window mounted in the center of the reflector. A light sheet produced by a fiber optic illuminator is directed towards the plane of the droplet cluster. A 45-deg mirror is mounted above the acoustic reflector and allows the cluster to be viewed from the top through a window in the reflector. A CCD camera and microscope lens is positioned to view the cluster from either the side or the top. The image is transmitted to the computer to monitor the experiment and to a video recorder.

RESULTS AT ONE-G

As in several other microgravity investigations,^{1,2} methanol has been used in our initial tests of the acoustic levitator/droplet generator system. Figure 3 shows an image of a droplet

cluster containing 13 drops where the average drop size and spacing given in the caption. Based on the criteria given by Annamalai and Ryan,⁸ these clusters lie in the group combustion regime. More specifically, these conditions are between the internal and external group combustion regimes, where the flame front lies within the droplet cluster and both isolated drop and group combustion occurs. This will be investigated in future combustion experiments.

The evaporation rate of methanol drops was evaluated by forming single droplets and droplet clusters in the acoustic field and recording the time history of the decrease in drop size on video. Because these experiments are conducted in 1-g, the acoustic field was maintained during the evaporation process. Preliminary results for a single droplet and for both drops of a two-droplet array (Drop A and B) are shown in Fig. 4. The vaporization constant for the single drop in the acoustic field is very near the theoretical value for diffusion-controlled, quasi-steady droplet evaporation. Similar to Seaver *et al.*⁹ and Tian and Apfel,¹⁰ this implies that the acoustic field has little effect on the evaporation of a single, isolated drop. As expected, the vaporization rate for the two-drop array is less than that for the single drop with both drops evaporating at the same rate. However, this rate is below the theoretical vaporization rate for two droplets spaced at $l/d = 4.1$.¹¹ This will continue to be evaluated using clusters with increasing number of drops and containing drops of different composition.

CONTINUING WORK

While conducting tests at 1-g, work is progressing on the construction of the drop tower rig. In the drop tower, the droplet cluster will be formed and stabilized before the start of the drop event. As the experimental package begins to drop, the acoustic field can be terminated (or reduced substantially), making observations of the vaporization and combustion of unsupported clusters of large number of drops possible.

SUMMARY

In the current work, a single axis acoustic levitator has been designed and constructed. The design of the acoustic levitator provides both a vertical and lateral positioning force on the droplet cluster. By specifying the charge placed on the initial drop, stable clusters containing between 2 and 20 drops have been generated. Preliminary results of droplet vaporization in a resonant acoustic field at 1-g are consistent with those of previous researchers and will continue to be evaluated for larger numbers of drops in the cluster. Current work focuses on incorporating the entire apparatus into a drop tower test rig so that experiments can be conducted under microgravity.

REFERENCES

1. Dietrich, D. L., Struk, P.M., Kitano, K., and Ikegami, M. "Combustion of Interacting Droplet Arrays in a Microgravity Environment," Proceedings of the Fifth International Microgravity Combustion Workshop (NASA Conference Publication 1999-208917), Cleveland, Ohio, May 18 - 20, 1999.
2. Gokalp, I., Chauveau, C., Vieille, B., Kadota, T., and Segawa, D. "High Pressure Burning of Methanol Droplets: A Comparison between Parabolic Flight and Drop Tower Experiments," Proceedings of the Fourth International Microgravity Combustion Workshop (NASA Conference Publication 10194), Cleveland, Ohio, May 19-21, 1997.
3. Shaw, B. D. "Combustion of Two-Component Miscible Droplets in Reduced Gravity," Fifth International Microgravity Combustion Workshop," Cleveland, Ohio, May 18 - 20, 1999.

4. Wang, C. H. and Ueng, G. J., "An Experimental Investigation of Fuel Droplet Combustion Under Micro-Gravity," *Int. Comm. Heat Mass Transfer*, Vol. 24, No. 7, pp. 931-944, 1997.
5. Jackson, G. S. and Avedisian, C. T. "Combustion of Unsupported Water-in-n-Heptane Emulsion Droplets in a Convection-Free Environment," *Int. J. Heat Mass Transfer* **41**, pp. 2503-2515, 1998.
6. Nomura, H., Koyama, M., Ujiie, Y., Sato, J., Kono, M., and Yoda, S. (1999) "Microgravity Experiments on Combustion of Monodispersed and Mono-Sized Fuel Droplet Clouds," Fifth International Microgravity Combustion Workshop, Cleveland, Ohio, May 18 - 20, 1999.
7. Zhuyou, C., Shuqin, L., Zhimin, L., Mingli, G., Yulong, M., and Chenghao, W. "Development of an Acoustic Levitation Reactor," *Powder Technology* **69**, pp. 125 - 131, 1992.
8. Annamalai, K. and Ryan, W., "Interactive Processes in Gasification and Combustion. Part I: Liquid Drop Arrays and Clouds," *Progress in Energy and Combustion Science* Vol. 18, pp. 221, 1992.
9. Seaver, M., Galloway, A., and Manuccia, T.J. "Acoustic Levitation in a Free-Jet Wind Tunnel," *Rev. Sci. Instrum.* **60**, pp. 3452-3459, 1989.
10. Tian, Y. and Apfel, R. E. "A Novel Multiple Drop Levitator for the Study of Drop Arrays," *J. Aerosol Sci.*, **27**, pp. 721-737, 1996.
11. Samson, R. and Deutch, J. "Exact Solution for the Diffusion Controlled Rate into a Pair of Reacting Sinks," *J. Chem. Phys.* **67**, pp. 847-859, 1977.

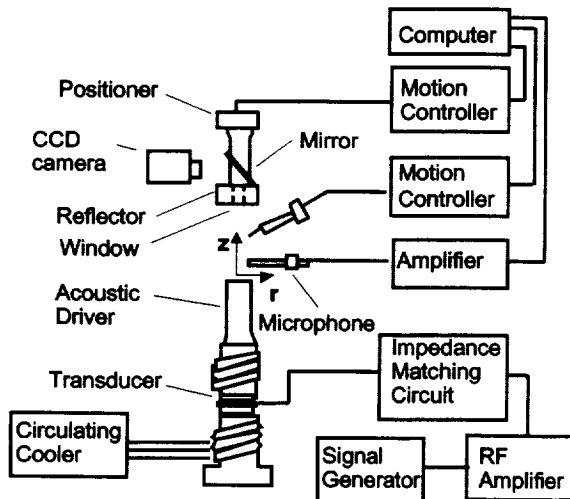


Figure 1. Drop levitation apparatus

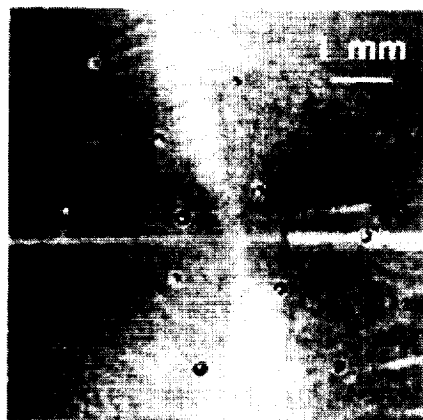


Figure 3. Droplet cluster containing 13 drops ($d_m = 190 \mu\text{m}$, $l/d = 11.7$, $G \approx 1.0$)

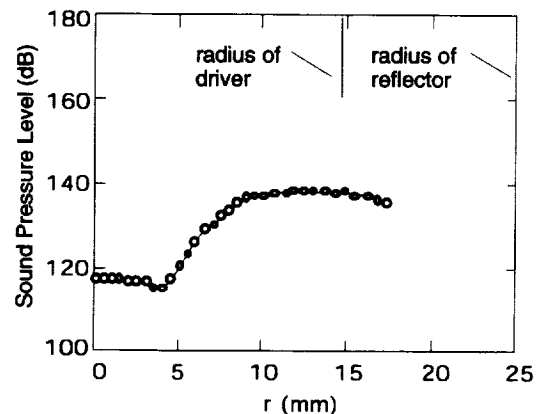


Figure 2. Radial sound pressure level 4 mm above the acoustic driver

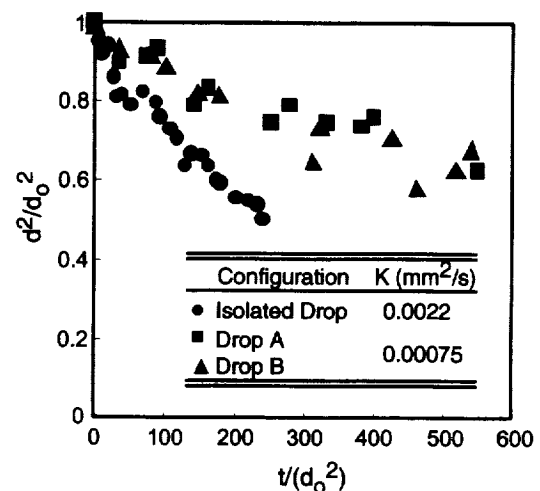


Figure 4. Comparison of methanol droplet evaporation (levitated single drop and two-drop array, $l/d = 4.1$)

HIGH PRESSURE, TRANSPORT PROPERTIES OF FLUIDS: THEORY AND DATA FROM LEVITATED FLUID-DROPS AT COMBUSTION-RELEVANT TEMPERATURES

J. Bellan^{*} and K. Ohaska⁺

^{*}Jet Propulsion Laboratory, Pasadena, CA 91109-8099

⁺University of Southern California, Los Angeles, CA 90089-1191

OBJECTIVES

The objective of this investigation is to derive a set of consistent mixing rules for calculating diffusivities and thermal diffusion factors over a thermodynamic regime encompassing the subcritical and supercritical ranges. These should serve for modeling purposes, and therefore for accurate simulations of high pressure phenomena such as fluid disintegration, turbulent flows and sprays. A particular consequence of this work will be the determination of effective Lewis numbers for supercritical conditions, thus enabling the examination of the relative importance of heat and mass transfer at supercritical pressures.

TECHNICAL DESCRIPTION

This investigation addresses some crucial issues in transport property calculations that lie at the core of understanding supercritical fluid behavior for combustion applications. Although the high pressure multicomponent fluid conservation equations have already been derived and approximately validated for binary mixtures by this PI (see Figs. 1 and 2 below, and Harstad and Bellan, 2000), the validation of the multicomponent theory is hampered by the lack of existing mixing rules for property calculations. Classical gas dynamics theory can provide property mixing rules at low pressures exclusively. While thermal conductivity and viscosity high-pressure mixing rules have been documented in the literature, there is no such equivalent for the diffusion coefficients and the thermal diffusion factors.

Therefore, the primary goal of this investigation is to extend the low pressure mixing rule theory to high pressures and validate the new theory with experimental data from levitated single drops. The two properties that will be addressed are the diffusion coefficients and the thermal diffusion factors. To validate the property calculations, ground-based experiments from levitated drops will be conducted. The levitated drops will be obtained using an electrostatic technique having the particular advantage of creating nearly spherical drops whose internal flow is minimized. The apparatus is sketched in Fig. 3. Additionally, it is planned to build a laboratory mini drop tower so as to allow the performance of initial microgravity experiments without traveling to NASA facilities; thus, saving time and expense. More importantly, this mini drop tower will allow the performance of time consuming on site calibrations which are necessary until a standard experimental procedure is established. The primary output of the experimental data will be the measurement of the drop diameter which will then be compared with the theoretical predictions.

Part of the database will be used to construct the mixing rule models while the remaining part will be used to validate the derived models. Such a strategy was already used by the PI in comparing theoretical predictions of free-floating drops with the suspended drop experiments of

Nomura et al., 1996. While these comparisons were promising (see Harstad and Bellan, 2000), they embedded the uncertainties of comparing numerical results from free drops with data from suspended drops. This uncertainty will be mitigated by the present experimental technique.

The regime of investigation will include subcritical as well as supercritical pressures at combustion relevant temperatures. The focus will be on evaporation/mass-emission experiments and on drop sizes varying from the large ones used in suspended drop experiments to small ones of size relevant to combustion engines. This range of parameters will bridge the gap between the current high pressure microgravity data which encompasses only combustion experiments for which there are no measurements of the flame temperature, and the data needed for model validation which requires the knowledge of drop effective-far-field conditions. The levitated drop experiments may also allow the utilization of drops that are about one order of magnitude smaller than those employed in suspended drop experiments, thereby further reducing buoyancy as well as making the range of parameters more relevant to combustion devices.

This study is in the spirit of a short exploratory program, focusing exclusively on binary mixtures. The plan of this exploratory investigation is to accomplish the following:

1. Accurate binary diffusion coefficients calculations – monoatomic species.

A formalism will be derived for the binary diffusion coefficients at all pressures. Calculations will be first performed for monoatomic compounds to obtain a baseline verification of our formalism; the predicted results will be compared with experimental measurements (Balenovic et al., 1970) for self diffusion in *Ar*, and binary diffusion in *Ar-Kr*, *Ar-He* and *He-Ar*. One of the important issues to be determined is the meaning of the quantities experimentally measured: (i) the diffusion coefficient, or (ii) the product of the diffusion coefficient by the mass diffusion factor (i.e. the effective coefficient of the Fick term). This issue is crucial at high pressures since mixtures show increasing non-ideality with increasing pressure, reducing the mass diffusion factor below the unity value characteristic of ideal mixtures at low pressures. Part of this study will include an exploration of the sensitivity of the prediction of the drop diameter to the uncertainties in the diffusion coefficient.

2. Accurate binary diffusion coefficients calculations – general species

The formalism derived in the first year of study will be here applied to a variety of binary systems such as: *He-N₂*, *Ar-N₂*, *N₂-He*, *N₂-H₂*, *He-CH₄*, *He-C₂H₆* and *He-C₃H₈*. Experimental data for verification exists for all these mixtures (Balenovic et al., 1970). Additionally, there is also experimental data quantifying the self diffusion in *CO₂*, *CH₄*, *C₂H₄* and *H₂O* (Liu and Macedo, 1995). Maynard and Grushka, 1975, present extensive tables of measured (using gas-chromatography broadening techniques) infinite dilution binary diffusion coefficients, some at high pressures; comparisons with this data will be performed as well. Recently, binary diffusion coefficients of naphthalene and biphenyl in *CO₂* at infinite dilution at 330 K and as a function of the *CO₂* density were published by Schneider, 1998. The diffusion coefficient of toluene in supercritical *CO₂* was plotted also as a function of the *CO₂* density by Bruno, 1993. During the course of this work, EOSs for all these compounds will be determined by using either data, or our own method for obtaining computationally simple, yet accurate EOSs (Harstad et al., 1997), or cubic EOSs, as appropriate. At the suggestion of the reviewers, part of this study will include an exploration of the sensitivity of the prediction of the drop diameter to the uncertainties in the diffusion coefficient.

3. Thermal diffusion factors for binary mixtures

During the last part of this exploratory study, the fluid drop model of Harstad and Bellan, 2000, embedding the validated diffusion coefficient model determined in the first two years of this investigation, will be applied to some binary mixtures of interest to combustion science. Calculations will be performed for hydrocarbon fluid-drops in nitrogen, and the calculated drop boundary as function of time will be compared to that measured during the levitated drop experiments conducted by the co-PI. The value of the thermal diffusion factor will be backed-up from this comparison by performing calculations for several values of the thermal diffusion factor and observing which one matches better the experiment. The experimental margin of error (error bars) will be transferred by the model into error bars on the determination of the thermal diffusion factor. Part of the data will be used for determining the value of the thermal diffusion factor, and the remaining data will be used for model validation. Because of this strategy, coordination with the experiment will be initiated as soon as the feasibility of the experiment has been ascertained (in the previous years of this exploratory study) to ensure that data are obtained at conditions encompassing both the determination and the validation aspects.

REFERENCES

- Balenovic, Z., Myers, M. N., and Giddings, J. C., Binary Diffusion in Dense Gases to 1360 atm by the Chromatographic Peak-Broadening Method, *J. Chem. Phys.*, 52(2), 915-922, 1970
- Bruno, T., Measurements of Diffusion in Supercritical Fluid Systems, AIAA 93-0809, 31st Aerospace Sciences Meeting, Reno, 1993
- Harstad, K. G., Miller, R. S. and Bellan, J., Efficient High-Pressure State Equations, *AIChE Journal*, 43(6), 1605-1610, 1997
- Harstad, K. and Bellan, J., An All-Pressures Fluid-Drop Model Applied to a Binary System: Heptane Fluid-Drops in Nitrogen, *Int. J. Multiphase Flow*, 26(10), 1675-1706, 2000
- Liu, H. and Macedo, E. A., Accurate Correlations for the Self-Diffusion Coefficients of CO_2 , CH_4 , C_2H_4 , H_2O , and D_2O over Wide Ranges of Temperature and Pressure" *J. Supercrit. Fluid.*, 8, 310-317, 1995
- Maynard, V. R. and Grushka, E., Measurement of Diffusion Coefficients by Gas-Chromatography Broadening Techniques: A Review, *Advances in Chromatography*, Vol. 12, 99-140, M. Dekker, 1975
- Nomura, H., Ujiie, Y., Rath, H. J., Sato, J. and Kono, M., Experimental study on high pressure droplet evaporation using microgravity conditions, 26th Symp. (Int.) on Comb., 1267-1273, 1996
- Schneider, G. M., High-pressure Investigations of Fluid Mixtures - Review and Recent Results, *Journal of Supercritical Fluids*, 13, 5-14, 1998

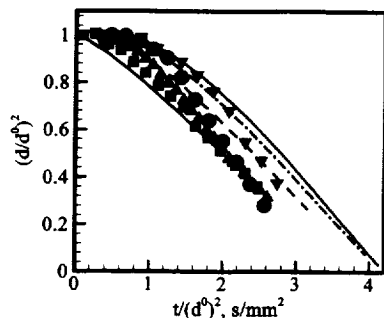


Figure 1. Comparison of moderate (~650K) temperature model predictions of Harstad and Bellan, 2000, with the data of Nomura et al., 1996. Details in Harstad and Bellan 2000.

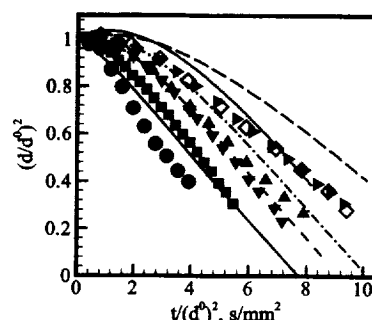


Figure 2. Comparison of low (~450K) temperature model predictions of Harstad and Bellan, 2000 with the data Nomura et al., 1996. Details in Harstad and Bellan, 2000.

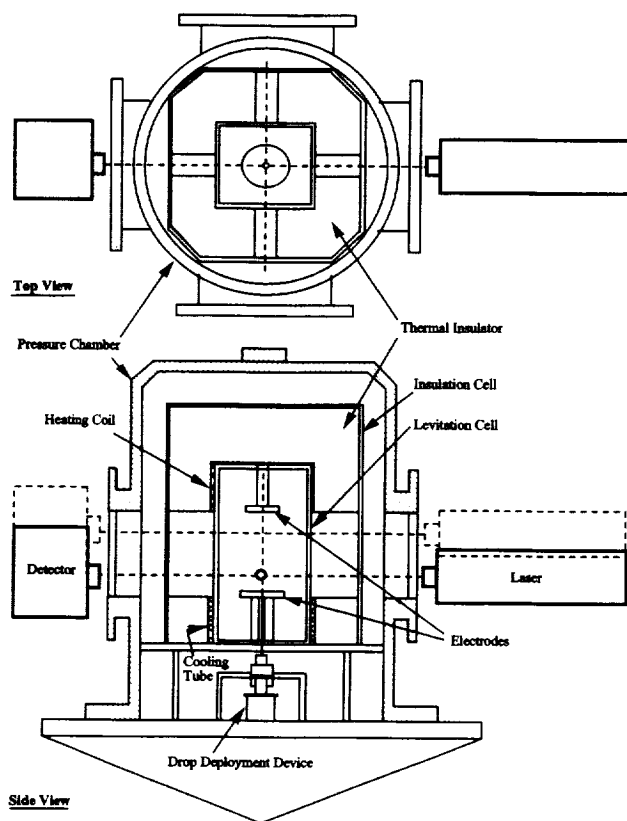


Figure 3. Schematics of the apparatus. A pair of electrodes is placed inside of the levitation cell made from quartz glass. The cell has a square cross section (as shown in the top view) for an undistorted view of a levitated drop. The top and bottom portions of the cell are wound by a heating coil and a cooling tube, respectively. These elements are used to create temperature gradients within the cell along the vertical axis at elevated temperatures. The cell is covered by thermal insulators except for 4 viewing ports. A drop deployment device is located under the levitation cell. The device consists of a syringe with a fine needle and two linear actuators. The drop deployment device and the insulation cell which houses the levitation cell are placed inside of a pressure chamber. A laser source and a detector are not a part of the dropping module but they are depicted here to show their functions.

Quenching of Particle-Gas Combustible Mixtures Using Electric Particulate Suspension (EPS) and Dispersion Methods

Gerald M. Colver

Department of Mechanical Engineering, Iowa State University, Ames IA., USA

Samuel Goroshin

Department of Mechanical Engineering, McGill University, Montreal, Canada

John H. S. Lee

Department of Mechanical Engineering, McGill University, Montreal, Canada

INTRODUCTION

A cooperative study is being carried out between Iowa State University and McGill University. The new study concerns wall and particle quenching effects in particle-gas mixtures. The primary objective is to measure and interpret flame quenching distances, flammability limits, and burning velocities in particulate suspensions. A secondary objective is to measure particle slip velocities and particle velocity distribution as these influence flame propagation. Two suspension techniques will be utilized and compared: electric particle suspension/EPS (ISU) and flow dispersion (McGill). Microgravity tests will permit testing of larger particles and higher and more uniform dust concentrations than is possible in normal gravity.

Cloud Uniformity and Modeling: Flame quenching distance for dusts is an important parameter in laminar flame theory as it closely relates to the characteristic flame thickness and structure. Achieving a uniform dust concentration has been identified as a key problem to be resolved in dust flame studies. This uniformity can be accomplished with ISU's electric particle suspension method (EPS). Results obtained with EPS will be compared with the flow dispersion technique developed at McGill. Reliable measurements of flame quenching distance and flammability limits will serve as a basis for theoretical modeling of the mechanisms for flame propagation in dust suspensions.

EXPERIMENTAL APPROACH

The EPS method perfected at ISU is fundamentally simple [1]. It utilizes a cylindrical test section enclosure comprised of two parallel plate electrodes (15 to 20 cm diameter) and Pyrex glass tubing for the insulated sides (Teflon and quartz are also used). Quenching distance is adjustable over distances of typically 0 to 6 cm. Both parallel plate and inert particle quenching are possible. During combustion, the test cell pressure is equalized to that of the ambient pressure. A dc supply drives the particle dispersion process. Spark ignition is utilized.

The McGill setup is a flow dispersal system in which a powder flame burns from one end of a tube (80 cm in length by 5 cm diameter) through a series of parallel plates having variable

separation distance in which quenching takes place. The powder dispersion system features acoustic flame damping and a unique powder dispersal method developed from McGill's current NASA and Canadian research programs.

DETAILED OBJECTIVES FOR MICROGRAVITY AND 1-g RESEARCH

Achieving uniform dust concentration has been identified as a key problem to be resolved in dust flame studies. This goal is addressed using a comparison of two distinct methods of powder dispersion, Iowa State's EPS method and McGill's powder dispersal method.

The specific objectives of the proposed microgravity and 1-g research investigation are:

- To compare parallel plate quenching distance and flame velocity measurements for combustible powders (e.g. aluminum, zirconium) using McGill's flow dispersion technique and ISU's EPS method in which the electric field strength is extrapolated to zero value.
- To evaluate the influence of inert particle concentration (glass, copper) on flame quenching/flame velocity of combustible gas mixtures (propane-air) using the EPS method.
- To quantify the effect of electrically controlled particle-gas slip velocity on quenching distance of powder flames using the EPS method (aluminum, zirconium, $10\ \mu\text{m} < d < 100\ \mu\text{m}$).
- To quantify the effect of electrically controlled particle-gas slip velocity on gas flame quenching (propane-air) by inert particles using the EPS method (glass, copper, $10\ \mu\text{m} < d < 100\ \mu\text{m}$).
- To characterize the particle velocity and particle velocity spread (velocity distribution) using the EPS method.

ELECTRIC PARTICULATE SUSPENSION (EPS METHOD)

The Electric Particulate Suspension (EPS) method permits the formation of steady-state uniform suspensions. It is well suited for small-volume testing of powders and consequently can be used to measure quenching distance. It also provides up to four methods for measuring and calibrating particle concentration [2]. Excellent reproducibility of powder concentration is possible by monitoring the attenuated signal from a laser beam passed through the suspension. This is an important testing advantage in the present research. At 1-g, laser attenuation scans of an EPS show that gravitational stratification occurs in particle concentration over the height of the test section (few centimeter plate separation) although the cloud remains visually uniform and steady. In microgravity, gravitational stratification is effectively eliminated, permitting the formation of steady-state particulate clouds of improved uniformity. Microgravity also extends the range of testing to $E = 0$, which is useful to extrapolate the EPS quenching results to the field-free case used by McGill.

PARTICLE SLIP VELOCITY AND VELOCITY DISTRIBUTION (EPS METHOD)

A slip velocity and velocity distribution between particles and gas is expected in certain conditions of larger particles flowing near walls and in vertical transport (against gravity) such as accelerating flows in burners and pulsating combustors. In a pulverized coal combustor, the

minimum scale of microturbulence is 10-100 times the diameter of a pulverized-coal particle, which is also the scale of particle separation so that the gas within this distance from the surface of the particle is non-turbulent relative to the particle. The present study permits a study of particle slip velocity using the applied electric field [3]. In principle, both the Sherwood (mass transfer) and Nusselt numbers (heat transfer) of particles can be increased by increasing the particle-gas relative velocity. Both ground-based and microgravity based studies will be considered as regards effects of slip and particle velocity distribution.

ISU'S KC-135 AND GROUND-BASED (1-g) APPARATUS

Studies to date at 1-g include the measurement of quenching and ignition energy curves for aluminum powder in various admixtures of oxygen, nitrogen, and carbon dioxide at ambient conditions of temperature and pressure. Aluminum powder 25-30 μm in concentrations of 150-3300 g/m^3 was tested with admixtures of oxygen, nitrogen, and carbon dioxide (mole ratio 0.21) [1]. Flammability curves were developed for lean to stoichiometric powder mixtures as shown in Fig. 1. Our quenching tests in 1-g using 17.5 μm spherical aluminum particles and 16.7 μm Illinois No. 6 coal used a system similar to that shown in the Fig. 2. The results indicated that both the quenching distance and lean flammability limit increase with particle size while the quenching distance of coal was observed to decrease with increasing volatile content.

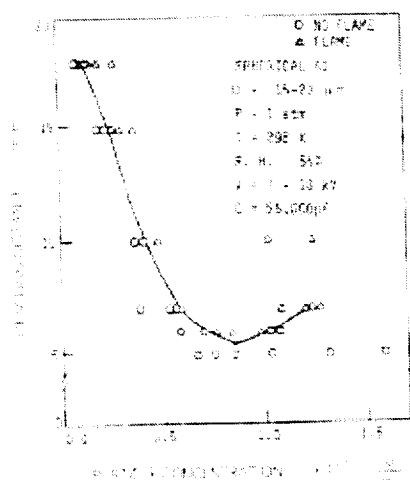


Fig. 1 Quenching distance using EPS 17.5 μm spherical aluminum particles.

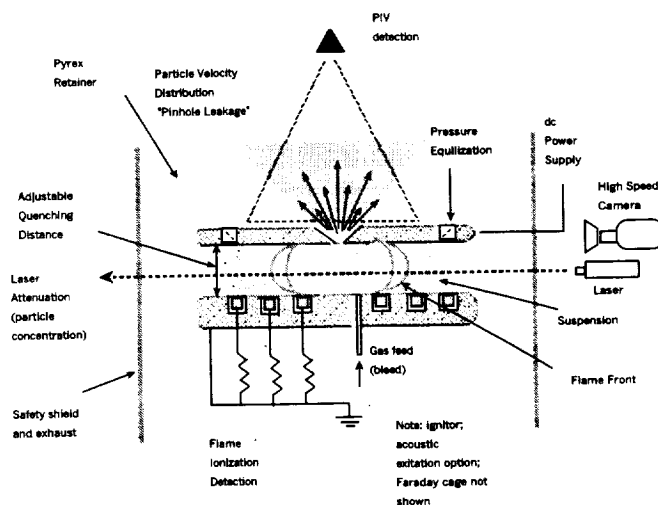


Fig. 2. EPS test facility (proposed)

MCGILL'S KC-135 AND GROUND-BASED (1-g) APPARATUS

A newly developed dispersion system at McGill has been used to measure quenching distances in uniform dust clouds at constant pressure Figs. 3 and 4. In microgravity, it is possible to extend the ground-based experiments to larger particle sizes and higher dust concentrations. Initial studies of microgravity dust combustion were based on constant volume combustion in a closed spherical bomb. A number of KC-135 campaigns have been flown since 1991 [4]. The main findings indicated that combustion of a quiescent dust cloud in microgravity was reproducible with peak combustion pressure and the rate of the pressure rise. However, the peak pressure obtained indicated that only a fraction of the dust used was being suspended. Microgravity experiments on the KC-135 have demonstrated that a uniform suspension of relatively large particles ($18\text{ }\mu\text{m}$) at dust concentrations as high as 1200 g/m^3 can be obtained with the present method. In normal gravity, small particles ($\leq 5\text{ }\mu\text{m}$) and lower concentrations ($< 600\text{ g/m}^3$) can be suspended uniformly to permit ground-based experiments to be conducted. A Beta-radiation probe in combination with laser light attenuation probe will be used for monitoring dust concentration in our experiments.

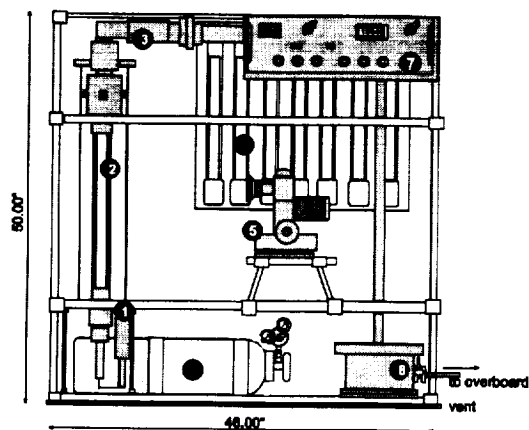


Fig. 3 McGill's Microgravity experimental package.

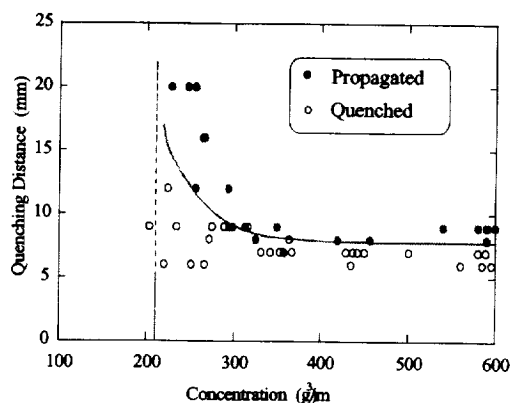


Fig. 4 Quenching distance in aluminum-oxygen-helium dust suspensions.

ACKNOWLEDGMENT

This study is supported by the NASA's Microgravity Combustion Science Program.

PUBLICATIONS

- [1] Colver, G. M., S. W. Kim, and Tae-U Yu, J. of Electrostatics, V. 37, 1996, pp. 151-172.
- [2] Colver, G. M., In Advances in the Mechanics and the Flow of Granular Materials, 1st Ed., Vol. 1. Trans-Tech., Ed. M. Shahinpoor, Clausthal-Zellerfeld, Federal Republic of Germany, Houston, Gulf Pub. Co. Houston, , 1983, pp. 355-373.
- [3] Colver, G. M. and L. J. Ehlinger, IEEE Trans. Ind. Appl., Vol. 24, No. 4, July/August 1988, pp. 732-739.
- [4] Goroshin, S., Kleine, H., Lee, J.H.S., Frost, D., NASA Conference Publication 10174, 1995, pp. 141-146.

“SMOKE:” Characterization of Smoke Particulate for Spacecraft Fire Detection

D.L. Urban¹, G. Mulholland², Z.G. Yuan³, J. Yang², T. Cleary²

¹NASA Glenn Research Center, Cleveland OH

²National Institute for Standards and Technology, Gaithersburg, MD

³National Center for Microgravity Research in Fluids and Combustion, Cleveland, OH

Introduction

“Smoke” is a flight definition investigation whose purpose is to characterize the smoke particulate from microgravity smoke sources to enable improved design of future space-craft smoke detectors. In the earliest missions (Mercury, Gemini and Apollo), the crew quarters were so cramped that it was considered reasonable that the astronauts would rapidly detect any fire. The Skylab module, however, included approximately 30 UV-sensing fire detectors (Friedman, 1992). The Space Shuttle Orbiter has 9 particle-ionization smoke detectors in the mid-deck and flight deck (Martin and DaLee 1993). The detectors for the US segments of the International Space Station (ISS) are laser-diode, forward-scattering, smoke detectors. Current plans for the ISS call for two detectors in the open area of the module, and detectors in racks that have cooling air-flow (McKinnie, 1997). Due to the complete absence of microgravity data, all three of these detector systems were designed based upon 1-g test data and experience. As planned mission durations and complexity increase and the volume of spacecraft increases, the need for and importance of effective, crew-independent, fire detection will grow significantly, necessitating more research into microgravity fire phenomena.

In 1997 the Comparative Soot Diagnostics Experiment (CSD) flew in the Orbiter Middeck as a Glovebox payload (Urban et al, 1997). The CSD experiment was designed to produce small quantities of smoke from several sources to obtain particulate samples and to determine the response of the ISS and Orbiter smoke detectors to these sources. Marked differences in the performance of the detectors compared to their behavior in 1-g were observed. In extreme cases, the detector used in the orbiter was completely blind to easily visible smoke from sources that were readily detected in 1-g. It is hypothesized but as yet unverified that this performance difference was due to enhanced growth of liquid smoke droplets in low-g. These CSD results clearly demonstrate that spacecraft smoke detector design cannot be based on 1-g experience.

Background

Other than the data from CSD, the smoke particulate studied from long-term microgravity sources is limited to soot from gas jet diffusion flames (Urban et al., 1997). Particulate have also been captured from over-heated wire insulations in the drop tower. (Paul et al., 1993 and Srivastava, McKinnon and Todd, 1998) but these data are limited by the short drop durations. Other than CSD, none of these investigations considered liquid droplet smokes. Since many overheated materials in low gravity can be expected to produce liquid droplet smokes, it is essential that the microgravity smoke droplet-size distribution be understood. In general, all of these studies have indicated that the particles are larger in low-gravity than in normal gravity. The results clear support the need for additional low-gravity smoke data.

Current Spacecraft Smoke Detector Designs

Both the ISS and the Orbiter smoke detectors were designed based upon the best data available at the time; nevertheless, their sensitivity to smoke particle size are very different.. The

Brunswick Defense design for the Orbiter consists of a dual-chamber ionization detector that is in the flow path created by a vane pump. Such detectors are most sensitive to high concentrations of small particles. This vane pump provides some active sampling capability and also the flow for an inertial separation system that is designed to make the detector insensitive to particulate larger than 1 to 2 μm , depending upon the particle density. It is a concern that this separator may remove a large fraction of some smokes produced microgravity conditions. The design developed for the ISS by Allied Signal consists of a 2-pass laser diode obscuration system that also has a photo-diode positioned to sense forward scattered light (30 degrees). The system is designed to alarm based on the magnitude of the scattered light signal with dust discrimination based on frequency analysis of the scattered light signal. The system is less sensitive to particles smaller than the wavelength of the laser (near IR) than it is to larger particles. The minimum reported sensitivity is 0.3 μm . Thus, it is seen that one detector is most sensitive to small smoke particles smaller than 0.3 μm and the other most sensitive to particle sizes larger than 0.3 μm .

CSD Experiment Results

In the CSD experiment, small samples of spacecraft materials were heated in a small duct that contained a thermophoretic sampler and was connected to the spacecraft smoke detectors. Results from two tests are shown in figures 1 and 2. In figure 1, the smoke detector response for overheated silicone rubber is shown. Low response by the ionization detector in low gravity is evident. In contrast, the results for a solid particle smoke (Kapton*) are shown in figure 2. In this case, both detectors performed well. These results are typical of the results seen for other smoke types. When the thermophoretic probes were returned to earth, the grids were removed and analyzed in a TEM to determine the primary particle and aggregate size distribution. Figure 3 contains TEM images of typical particulate from Teflon*, Kapton* and Candle tests. Table 1 summarizes the results for the tests for which comparable particulate samples were collected for 1-g and low-g. Significantly, despite strong smoke levels visible in the video record, no particulate material was found on the TEM grids for overheated paper and silicone rubber tests. The suspected cause of this is that the particulate for these materials is actually liquid droplets that later evaporated or spread out on the grids' surface, rendering them undetectable by the TEM. In summary, the CSD experiment demonstrated that smoke particulate properties can change with gravity level. The effect seems to be greater for liquid droplet smokes, however this was unverified since the droplet size distribution was not obtained for these smokes.

Material	Low-g Primary Diameter (nm)	1-g Primary Diameter (nm)	Low-g Aggregate Length (nm)	1-g Aggregate Length (nm)
Kapton	76	35	223	N/A
Candle	34	17	976	265
Teflon	136	75	662	277

Table 1 Properties of Smoke Particulate Generated in Reduced Gravity and in Normal Gravity
Shown in each column is the log-normal average diameter (geometric mean diameter).

Objectives of the flight investigation

Given the results of the CSD experiment, it is evident that more data on liquid droplet smoke in microgravity are critically needed. To address this issue, this investigation was proposed with the following four objectives. 1. Improve the reliability of future spacecraft smoke detectors by making measurements of the smoke particulate size distribution that are needed for rational

* Registered Trademarks

design of smoke detectors. 2. Compare the measured effect of μg on the size distribution of liquid aerosol smokes with the predicted effect. 3. Evaluate the performance of the two existing U.S. spacecraft smoke detector designs for the test conditions. 4. Evaluate other smoke detection/sensing devices at NASA's request for the test materials.

Description of the Planned Flight Experiment

The new investigation is based on the design heritage of the CSD experiment but will add new diagnostics to provide on-orbit measurements of critical moments of the smoke size distribution. The planned approach will use commercial particle measurement devices in the new Microgravity Science Glovebox (MSG) planned for ISS. The test samples will be similar to those used previously except more liquid smoke producers will be used and a reference sample will be designed. The added diagnostics will include a commercial condensation nucleus counter to measure the number concentration of the aerosol, the ionization smoke detector to measure a moment involving the particle concentration times the diameter, a commercial light scattering instrument with a signal approximately proportional to the number concentration times the particle volume, a heated thermophoretic sampling probe and potentially a particle classifier based upon MEMS technology. This combination of instruments is sufficient to allow computation of the critical smoke particle size parameters

Modeling of Aerosol Generation

To assist experimental design and to provide an analytical context for interpretation of the results from the reference sample, a numerical model is planned. The model will be used to predict the formation of aerosol (nucleation) and its subsequent growth (via condensation and coagulation). The numerical calculation will be carried out in two parts. The first part is to compute the vapor distribution, temperature distribution, and flow field using direct numerical simulation of the laminar flow. The second part of the calculation is to compute the time evolution of the growing droplets as they traverse through the vapor concentration-temperature field computed in the first part. Preliminary results with the model are shown in figure 4. These predictions were performed using the Fire Dynamics Simulator (McGrattan et al., 2000a, 2000b). The figure indicates that, 10 cm downstream of the source, the $\mu\text{-g}$ concentration field is circular with a larger peak value than the 1-g case (attributed to the buoyancy induced flow), suggesting that these conditions favor further droplet growth through coalescence.

References

- Friedman, R., 1992. *Journal of Applied Fire Science*, 2:243-259.
- Martin, C.E. and R.C. DaLee, 1993. SAE Technical Paper 932166, 23rd International Conference on Environmental Systems, Colorado Springs, CO, July 12-15.
- McGrattan, K.B., H.R. Baum, R.G. Rehm, A. Hamins, and G.P. Forney, 2000a. NISTIR 6467, U.S. Department of Commerce, Washington D.C.
- McGrattan, K.B. and G.P. Forney, 2000b. NISTIR 6469, U.S. Department of Commerce, Washington D.C.
- McKinnie, J., 1997. SAE Technical Paper 972334, 27th International Conference on Environmental Systems, Lake Tahoe, NV, July 14-17.
- Paul, M., F. Issacci, G. E. Apostolakis and I. Catton. 1993. *ASME-HTD* Vol. 235:59-66.
- Srivastava, R., J.T. McKinnon and P. Todd, 1998, AIAA 98-0814, Aerospace Sciences Meeting, Reno NV, Jan 12-15, 1998.
- Urban, D. L., D. W. Griffin and M.Y. Gard, 1997, Proceedings of the USML-2 and USMP-3 Joint Launch plus 1 Year Conference, National Academy of Science, Washington D.C. February.
- Urban, D.L., Z.G. Yuan, P.B. Sunderland, G.T. Linteris, J.E. Voss, K.-C. Lin, K. Sun and G.M. Faeth, 1998, *AIAA Journal*, V36 p1346-1360.

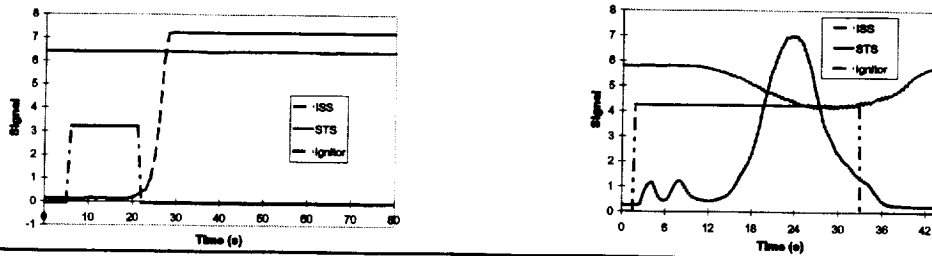


Figure 1: 0-g (left) and 1-g (right) results for silicone rubber. STS detector signal appears as a deviation downward, ISS signal increases with the particulate. The ignitor curve shows the power level. In 0-g the ISS detector saturated while the STS showed no signal. In 1-g both showed good signal.

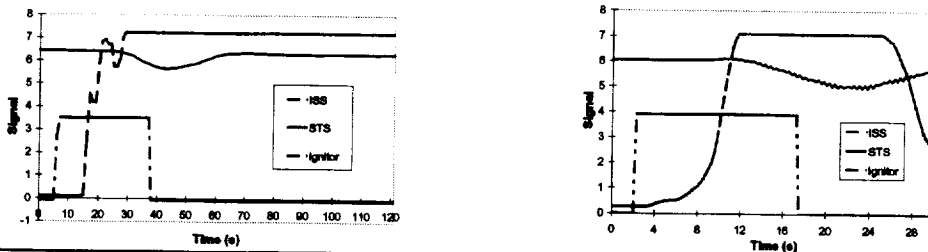


Figure 2: 0-g (left) and 1-g (right) results for Kapton. STS detector signal appears as a deviation downward, The ISS signal increases with the particulate. The ignitor curve shows the igniter power level.

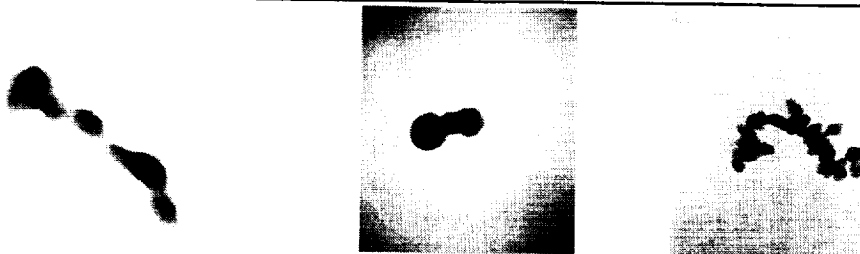


Figure 3: From left to right images of microgravity particulate from overheated Teflon and Kapton and candle soot. Images are at the same magnification

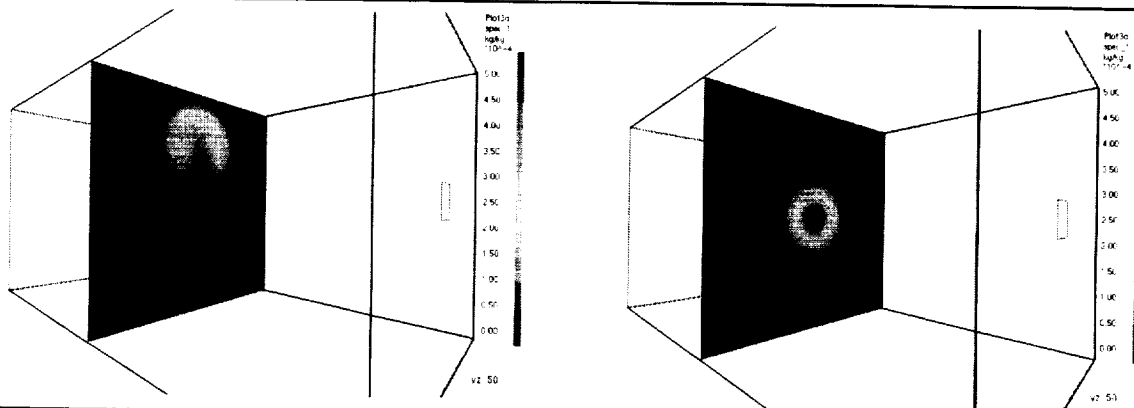


Figure 4: Plots of concentration of vapor 10 cm downstream of the source with a 5 cm/s cross flow. The source is 1 cm x cm and is water vapor at a temperature 50 degrees C above the ambient, (0 degrees C). The flow direction is perpendicular to the direction of gravity. Normal gravity results are on the left and low-gravity on the right.

FLAME SPREAD IN A MICROGRAVITY ENVIRONMENT- ROLE OF FUEL THICKNESS

SUBRATA BHATTACHARJEE
San Diego State University, San Diego, California

and

KAZUNORI WAKAI
SHUHEI TAKAHASHI
Gifu University, Gifu, Japan

INTRODUCTION: Fueled by a necessity to develop an understanding of flame spread in microgravity environment due to the fire safety aspects in manned spacecrafts, considerable work has been done during the last decade [1] on laminar flame spread over solid fuels. In this study, we present a simplified scale analysis and recently acquired spread rate data in the MGLAB, Japan [2] to address the role played by fuel thickness in opposed-flow flame spread with emphasis on the limiting case of the quiescent environment.

LENGTH AND TIME SCALES: To describe the heat-transfer limited mechanism, we focus our attention in Fig. 1 at the leading edge of the flame where the forward heat transfer[3] occurs. With respect to the flame the oxidizer approaches the flame with a velocity $V_r = V_g + V_f$ (V_g can be due to forced or buoyancy induced) and the fuel with a velocity V_f . Two control volumes, one in the gas phase of size $L_{gx} \times L_{gy} \times W$ and one in the solid phase of size $L_{sx} \times L_{sy} \times W$, are shown, W being the fuel-width in the z direction and the length scales, L_{gx} , L_{gy} , L_{sx} and L_{sy} , unknown at this point.

There are two characteristic resident times at the leading edge, $t_{res,g} \sim L_{gx} / V_r$ in the gas phase and $t_{res,s} \sim L_{sx} / V_f$ in the solid.

In the gas-phase, a balance between the conduction and convection in the x -direction at the leading edge yields the familiar[3] expression for L_{gx} , while L_{gy} can be obtained following Delichatsios[4] as the diffusion length in the y -direction within the available residence time. .

$$L_{gx} \sim \frac{\alpha_g}{V_r} \quad L_{gy} \sim \sqrt{\alpha_g t_{res,g}} = \frac{\alpha_g}{V_r} = L_{gx} \quad L_g \equiv L_{gx} = L_{gy} \quad (1).$$

The gas-phase conduction being the driving force under all but extreme situations [5], L_g is imposed on the solid phase making $L_{sx} \sim L_g$. The transverse length L_{sy} , derived in a manner similar to L_{gy} , however, cannot be greater than the half-thickness of the fuel. Therefore,

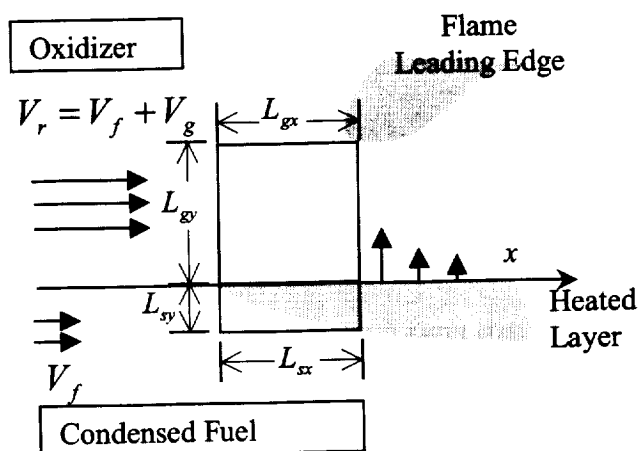


Fig. 1 Control volumes at the flame leading edge in the gas and the solid phases.

$$L_{sx} \sim L_g = \frac{\alpha_g}{V_r} \quad \text{and, } L_{sy} \sim \min \left[\tau, \sqrt{\alpha_s \frac{L_{sx}}{V_f}} \right] = \min \left[\tau, \sqrt{\frac{\alpha_s \alpha_g}{V_f V_r}} \right]. \quad (2).$$

THERMAL REGIME: In thermal regime $t_{res,g}$ is assumed large compared to the characteristic chemical time t_{comb} justifying the assumption of infinitely fast chemistry and small compared to the radiative time scales justifying the neglect of all radiative effects. of flame spread is based on a few simplifying assumptions. The characteristic vaporization time t_{vap} is assumed small compared to $t_{res,s}$ allowing the use of a constant vaporization temperature. An energy balance for the solid phase control volume yields the spread rate.

$$\lambda_g \frac{(T_f - T_v)}{L_{gy}} L_{gx} W \sim V_f \rho_s c_s L_{sy} W (T_v - T_{F,\infty}) \quad (3).$$

$$\text{Hence, } V_f \sim \frac{\lambda_g}{\rho_s c_s L_{sy}} F \quad \text{where, } F \equiv \frac{T_f - T_v}{T_v - T_{F,\infty}} \quad (4).$$

Substituting L_{sy} from Eq. (2) produces the familiar[6] thin and the thick limits.

$$V_{f,thin} \sim \frac{\lambda_g}{\rho_s c_s \tau} F \quad \text{and} \quad V_{f,thick} \sim V_r \frac{\lambda_g \rho_g c_g}{\lambda_s \rho_s c_s} F^2 \quad (5a,5b)$$

In order to reduce the errors in Eq. (5) resulting from the simplifying assumptions, Bhattacharjee et. al[5] proposed a simplified theory (EST), which replaced V_g with an equivalent velocity taking into account the boundary layer development, introduced a flame temperature correction and prescribed T_v as the appropriate temperature for property evaluation.

THICK VS. THIN FUELS: Equating the two limiting cases [Eqs. 5a and 5b], we obtain the scale for the transition thickness.

$$\tau_{cr,thin-thick} \sim \frac{\lambda_s L_g}{\lambda_g F}. \quad (6)$$

In non-dimensional terms, Eqs. 5(a) and 5(b) can be combined.

$$\eta \equiv \frac{V_f}{V_{f,thick,EST}} = \min \left(1, \frac{1}{T} \right) \quad \text{where, } T \equiv \tau / \tau_{cr,thin-thick,EST} \quad (7).$$

Computational results suggest that the fuel becomes thermally thick for $T \geq 2$, a conclusion that has been found to be independent of flow configuration. The recent data [7] for downward spread where the fuel thickness has been varied over a wide range is reproduced in Fig. 2. Although the spread rate is somewhat overpredicted by Eq. (7), the transition seems to be around $T \geq 2$ even though significant

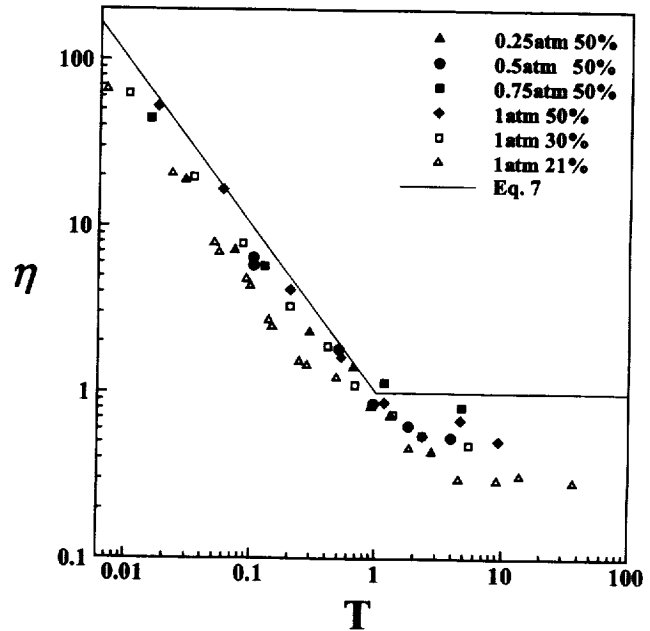


Fig. 2 Downward spread rate data over PMMA for different fuel thicknesses and ambient conditions.

kinetic effects are present. Unfortunately, there is no forced opposed-flow experiment in which the thickness of a fuel has been varied from the thin to the thick limit in the thermal regime.

QUIESCENT ENVIRONMENT: In the absence of forced or induced motion V_r (see Fig. 1) must be replaced with V_f . By substituting $V_{f,thin}$ from Eq. (5), an upper limit for V_f in Eq. (2), it can be shown that

$$L_{sy} \sim \min[\tau, \tau_0] = \tau \quad \text{because, } \tau_0 = \sqrt{\frac{\alpha_s \alpha_g}{V_f V_r}} > \sqrt{\frac{\alpha_s \alpha_g}{V_{f,Thin} V_r}} = \tau F \sqrt{\frac{\lambda_s \rho_s c_s}{\lambda_g \rho_g c_g}} > \tau \quad (6)$$

Fuels at any given thickness, therefore, can be expected to behave as thin fuels in a quiescent microgravity environment.

The energy balance of Eq. (3) should be adjusted for thin fuels, and must account for radiative losses, given the large residence times, $t_{res,g} = t_{res,s} \sim L_g / V_f$, possible in a quiescent environment. We include only solid reradiation in the energy balance to capture the radiative effects.

$$V_{f0} \rho_s c_s L_{sy} W (T_v - T_\infty) + \epsilon \sigma (T_v^4 - T_\infty^4) L_{gx} W \sim \lambda_g (T_f - T_v) W \quad (7)$$

$$\text{Or, } \eta_0 \equiv \frac{V_{f0}}{V_{f,Thin}} \sim \frac{1}{2} + \frac{1}{2} \sqrt{1 - 4\Re_0}, \quad \text{where, } \Re_0 = \frac{1}{F^2} \frac{\rho_g c_g}{\rho_s c_s} \frac{\epsilon \sigma \tau}{\lambda_g} \left(\frac{T_v^4 - T_\infty^4}{T_v - T_\infty} \right) \quad (8)$$

Equations (8) reveals several characteristics of flame spread in a completely quiescent environment. The radiative effects can be seen to reduce the spread rate from its thermal limit $V_{f,Thin}$, the severity depending on the parameter \Re_0 . The minimum spread rate is reached at $\Re_0 = 1/4$, when the spread rate becomes half its thermal limit. Any increase in \Re_0 beyond this critical value will produce an imaginary spread rate, indicating extinction. Equation (8) thus yields a critical fuel thickness above which steady spread cannot be sustained. There is no comprehensive data to validate this claim. However, the steady spread rate at quiescent-environment for thin cellulosic fuel[8] and extinction for thick PMMA[9] are qualitatively consistent with Eq. (8).

The MGLAB data[2] for spread over PMMA of three different thicknesses at several opposing velocities is reproduced in Table 1 and Fig. 3. The extinction reported in the table is accompanied by relatively high values of \Re_0 , qualitatively consistent with conclusion from Eq. (8). The reduction in spread rate from the 1-g to microgravity environment (see Table 1) lends further support to the prediction from Eq.

(8) that the spread rate decreases by 50% before extinction. The gradual reduction in spread rate, seen in Fig. 1, as the opposing velocity is reduced can be predicted from the energy balance equation (Eq. 7) by substituting $L_{gx} \sim \alpha_g / V_g$ for $V_g \gg V_f$, L_{sy} from Eq. (2), and treating the radiative term small compared to the sensible heating term in Eq. (7).

$$\eta_{thin} \equiv \frac{V_f}{V_{f,Thin,Thermal}} \sim 1 - \Re, \quad \eta_{thick} \equiv \frac{V_f}{V_{f,Thick,Thermal}} \sim 1 - 2\Re, \quad \Re = \frac{1}{F} \frac{\epsilon \sigma}{\rho_g c_g V_g} \left(\frac{T_v^4 - T_\infty^4}{T_v - T_\infty} \right) \quad (9)$$

Thickness O ₂ level	15μm	50μm	125μm
21%	extinct 13.4	extinct 4.2	extinct 1.4
30%	18.6 28.3	4.1 10.0	extinct 3.2
50%	39.1 55.1	18.9 22.8	Unsteady 8.1

Table 1. Spread rates in mm/s over PMMA in quiescent microgravity (upper number) and normal gravity conditions. Total pressure is 1 atm. Extinction occurs at high value of \Re_0 .

Note that while Eq. (8) clearly establishes thickness as an important parameter in the quiescent environment, the two limits in Eq. (9) also lend support this conclusion that the higher the fuel thickness, the higher is the radiative effects. Data shown in Fig. 2 is quite consistent with this conclusion.

SYMBOLS:

~ Equality within an order of magnitude
 \approx Approximately equal
 \equiv Definition

CONCLUSIONS: We present here a scale analysis and some recent data acquired in the MGLAB, Japan, to investigate the role played by fuel thickness in opposed-flow flame spread. The major conclusions, some yet to be validated through proposed experiments [10], are as follows. 1. The critical non-dimensional thickness at which transition between thin and thick fuels takes place is $T \approx 2$, where T depends on the fuel and environmental parameters according to Eq.(7). 2. In a quiescent microgravity environment all fuels are thin fuels. 3. Steady spread is impossible in a quiescent environment for fuels above a critical thickness. 4. In the presence of opposing flow, the radiative effect decreases according to Eq. (9), which indicates two different limits for thermally thin and thick fuels.

ACKNOWLEDGEMENT: We gratefully acknowledge the support of NASA, Glenn Research Center and Japan Space Forum, and our technical monitor from NASA, Dr. Sandra Olson.

REFERENCES:

- [1] Wichman, I.S., Prog. Energy Combust. Sci., Vol. 18, pp. 646-651 (1992).
- [2] Takahashi, S., Nagumo, T., Wakai, K., and Bhattacharjee, S., JSME Int. Journal, Series B, Vol. 43, No. 4., pp. 556-562, (2000).
- [3] Williams, F.A., Sixteenth Symposium (International) on Combustion, The Combustion Institute, Pittsburgh, PA, p. 1281, (1976)
- [4] Delichatsios, M.A., Twenty-Sixth Symposium (International) on Combustion, The Combustion Institute, Pittsburgh, PA, p. 1281, (1996).
- [5] Bhattacharjee, S., West, J., and Altenkirch, R.A., Twenty-Sixth (International) Symposium on Combustion, pp. 1477-1485, The Combustion Institute (1996).
- [6] de Ris, J.N., Twelfth Symposium (International) on Combustion, The Combustion Institute, Pittsburgh, PA, p. 241, (1969).
- [7] Bhattacharjee, S., King, M., Takahashi, S., Nagumo, T., and Wakai, K., A., Twenty-Seventh (International) Symposium on Combustion, The Combustion Institute (2000)
- [8] Bhattacharjee, S., and Altenkirch, R.A., Twenty-Fourth (International) Symposium on Combustion, Combustion Institute, Pittsburgh, PA, pp. 1669-1676, (1992).
- [9] Altenkirch, R.A., Tang, L., Sacksteder, K., Bhattacharjee, S., and Delichatsios, M.,A., Twenty-Seventh (International) Symposium on Combustion, The Combustion Institute (1998)
- [10] Bhattacharjee, S., Wakai, K., and Takahashi, S., *Dynamics of Flame Spread in Microgravity Environment*, Office of Space Science Applications, NASA , 2000-2003.

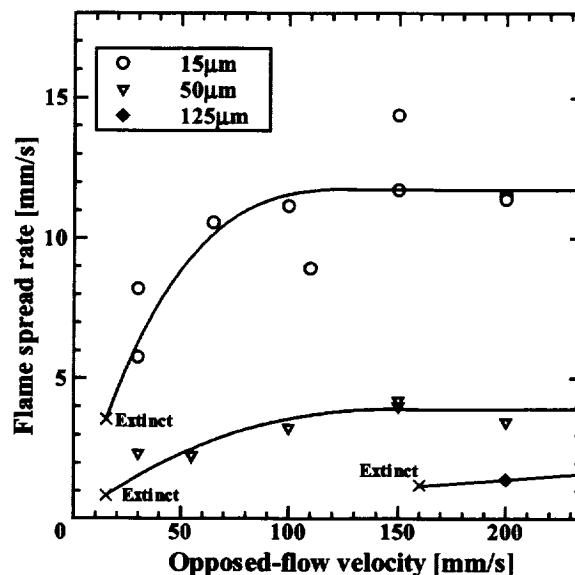


Fig. 3 Spread rate vs. opposed-flow velocity for PMMA in 21% O₂ and 1 atm. (Data obtained in MGLAB, Japan)

An Earth-Based Equivalent Low Stretch Apparatus to Assess Material Flammability for Microgravity & Extraterrestrial Fire-Safety Applications

S.L. Olson, NASA Glenn Research Center
H. Beeson, and J. Haas, NASA White Sands Test Facility

Abstract

One of the performance goals for NASA's enterprise of Human Exploration and Development of Space (HEDS) is to develop methods, data bases, and validating tests for material flammability characterization, hazard reduction, and fire detection/suppression strategies for spacecraft and extraterrestrial habitats. This work addresses these needs by applying the fundamental knowledge gained from low stretch experiments to the development of a normal gravity low stretch material flammability test method. The concept of the apparatus being developed uses the low stretch geometry [1] to simulate the conditions of the extraterrestrial environment through proper scaling of the sample dimensions to reduce the buoyant stretch in normal gravity. The apparatus uses controlled forced-air flow to augment the low stretch to levels which simulate Lunar or Martian gravity levels. In addition, the effect of imposed radiant heat flux on material flammability can be studied with the cone heater. After breadboard testing, the apparatus will be integrated into NASA's White Sands Test Facility's Atmosphere-Controlled Cone Calorimeter for evaluation as a new materials screening test method.

Applicability of the NASA's Upward Flammability Test

NASA's current methods of material screening determine fire resistance under conditions presenting a worst-case for normal gravity flammability- the upward flammability Test 1. The applicability of these Test 1 conditions to fires in microgravity and extraterrestrial environments, however, is uncertain because the relationship between these buoyancy-dominated tests and actual extraterrestrial fire hazards is not fully understood. Flames in microgravity are known to preferentially spread upwind [2], not downwind as in the normal gravity upward flammability screening Test 1. At low velocity flow, the Test 1 type flame spread was not viable over solid cylinders, as shown in Figure 1. However, the stagnation point flame at the tip of the cylinder (low stretch flame) was viable [3]. In addition, the maximum flammability in the upwind spread configuration is known to be at lower imposed flows and lower oxygen concentrations than occur in normal gravity [4].

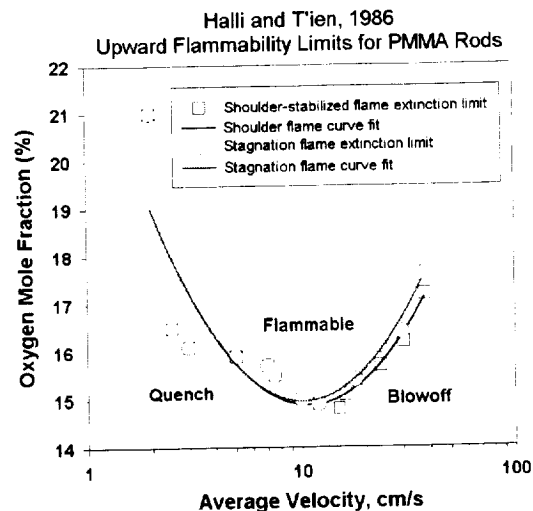


Figure 1: Upward flammability limits for flame spread along PMMA rods.

Theoretical Foundation

Theoretical predictions by Foutch and T'ien (1987)¹, shown in Figure 2, indicate that it is possible to understand a material's burning characteristics in the low stretch environment of spacecraft ($Fr=0$, non-buoyant, but with some movement induced by fans and crew disturbances) by understanding its burning characteristics in an equivalent Earth-based stretch environment ($Fr=\infty$, induced by normal gravity buoyancy). Similarly, Earth-based stretch environments can be made equivalent to those in Lunar- and Martian-surface stretch environments (which would induce partial-gravity buoyancy).

Equivalent Low Stretch Scaling

Equivalent stretch rates can be determined as a function of gravity, imposed flow, and geometry. For purely buoyant flow, the equivalent stretch rate is $a_b = [(\rho_c - \rho^*)/\rho_c] [g/R]^{1/2}$ [1,5]. For purely forced flow, the equivalent stretch rate is characterized by either $a_f = 2U_\infty/R$ for a cylinder^[5], or $a_f = U_{jet}/d_{jet}$ for a jet impinging on a planar surface^[6]. A generalized expression for stretch rate which captures mixed convection includes both buoyant and forced stretch is defined^[5] as $a_{mixed} = a_f(1 + a_b^2/a_f^2)^{1/2}$. In the normal gravity experiments to date, the buoyant stretch is varied through R , the radius of curvature, but the buoyant stretch could also be varied through g , the gravity level. In this way the effect of partial gravity, such as those found on the Moon ($1/6 g$) or Mars ($1/3 g$) can be captured in the definition of flame stretch.

Normal Gravity Low Stretch Results

Recent experimental results [1], shown in Figure 3, demonstrate the transition from a robust flame at stretch rates of $10\text{--}20 \text{ s}^{-1}$ to a quenched flame at very low stretch in the 21% oxygen environment tested.

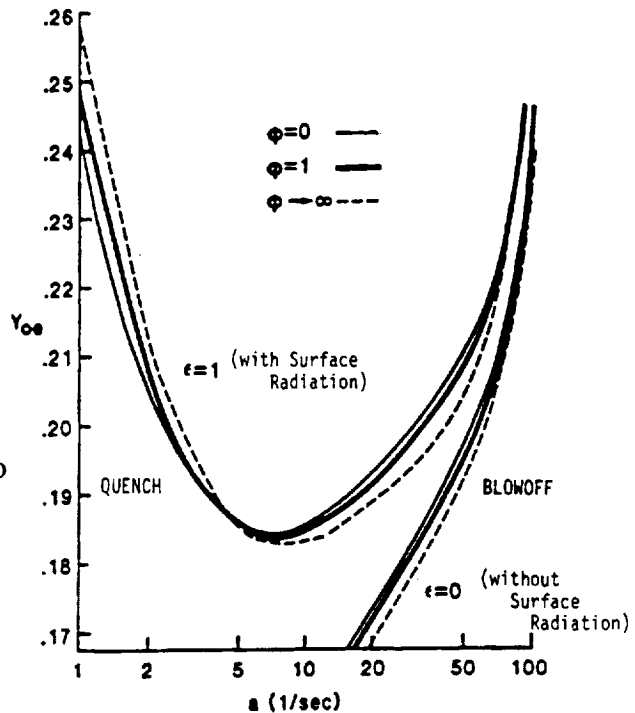


Figure 2: Extinction boundary as a function of ambient oxygen and forced (0), buoyant (∞), and mixed (1) convective stretch.

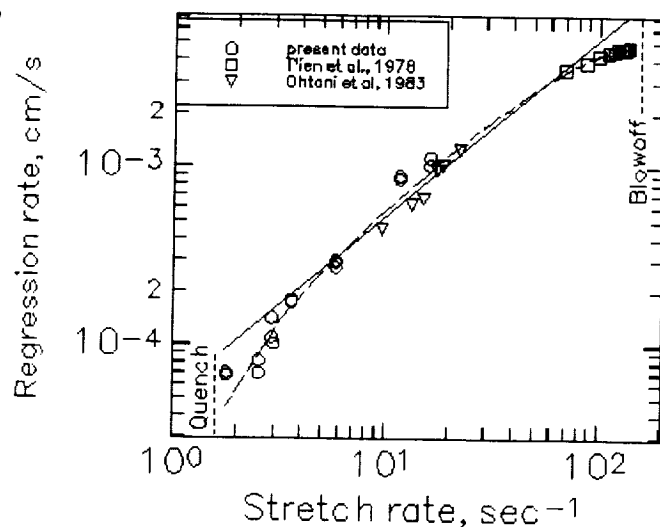


Figure 3: PMMA regression rates over the range of flammability in air.

Figure 3 captures the surface regression rates for PMMA over the full range of flammability in air, from blowoff at high stretch, to quenching at low stretch, observed for the first time in the above-mentioned experiments, which are represented by the data circles. Previous higher stretch results are represented by the squares and triangles. The solid line drawn through the central portion of the data ($3 < a < 100 \text{ s}^{-1}$) has a slope of unity, which indicates regression is proportional to stretch. Infinite kinetics theory and experiments find a square root relationship^[6] between regression and stretch at high stretch rates, but kinetics become important at low stretch rates and the dependence on flame stretch becomes stronger.

The figure coordinates assume the values of stretch are equivalent, whether derived from forced stretch^[6] or from buoyant stretch^[7]. The excellent correlation of the regression-rate data over the two-order-of-magnitude variation of stretch shows the reasonableness of this assumption.

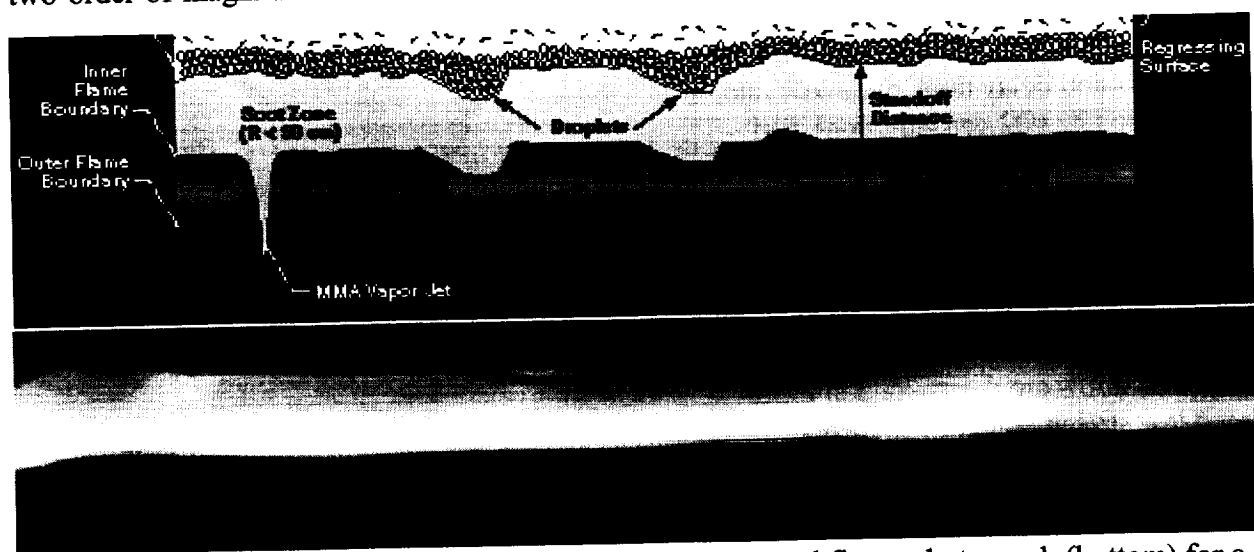


Figure 4: schematic of low stretch flame(top) along with actual flame photograph (bottom) for a stretch rate of 6 s^{-1} .

Buoyant low-stretch flames compare well with low-gravity low-stretch flames. A buoyant low stretch flame is shown in Fig.4. Through normal and microgravity testing we have found 1) flame standoff distances increase at low stretch, 2) reaction zones thicken at low stretch, 3) cooler flame temperatures at low stretch, 4) decreased heat flux back to the surface at low stretch, 5) decreased burning rates of fuel at low stretch, 6) increased relative heat loss at low stretch, and 7) quenching extinction is noted at low stretch rates of $1.5\text{-}2 \text{ s}^{-1}$.

Equivalent Low Stretch Apparatus Under Development

A concept of the apparatus is shown schematically in Figure 5. The concept uses the low stretch geometry [1] to simulate the conditions of the extraterrestrial environment through proper scaling of the sample dimensions to reduce the buoyant stretch in normal gravity. If successfully tested, the apparatus will be integrated into NASA's White Sands Test Facility's Atmosphere-Controlled Cone Calorimeter for evaluation as a new materials screening test method.

The apparatus uses controlled forced-air flow to augment the low stretch to levels which simulate Lunar or Martian gravity levels. In addition, the effect of imposed radiant heat flux on material flammability can be studied with the cone heater.

Primary variables include material tested, imposed forced stretch rate (effective gravity level), radiant flux level, and oxygen concentration.

Data from the Apparatus will include ignition delay time, mass loss rate, heat release rate (O₂ consumption), and product generation rates (CO, CO₂, soot, THC).

Ignition limits and material flammability limits will be measured for selected ideal/practical materials. If extinction limits are determined in Earth-based low stretch experiments as a function of the percent of heat flux conducted into the solid, we can identify critical percent heat flux values for spacecraft. It would then be possible to design safe-use configurations in space to ensure non-flammability (ie sufficiently thick materials or sufficiently conductive substrates).

In addition to the development of the apparatus, a predictive model will be developed to predict flammability limits for a given material, using specific material properties, desired atmospheric composition, and extraterrestrial gravity environments as inputs to the prediction. The experimental and predicted results will be compared to evaluate the test method and predictive capability.

References

- 1) Olson, S.L and T'ien, J.S.; *Combustion and Flame*, V. 121, pp. 439-452, 2000.
- 2) McGrattan, K.B., Kashiwagi, T., Baum, H.R., and Olson, S.L ; *Combustion and Flame*, Vol. 106, pp.377-391, 1996.
- 3) Halli, Y., and T'ien, J.S., NBS-GCR-86-507, Feb. 1986.
- 4) Olson, S.L., *Comb. Science and Tech.* V. 76, pp.233-249, 1991.
- 5) Foutch, D.W., and T'ien, J.S., *ALAA Journal*, Vol. 25, No. 7, pp. 972-976, 1987.
- 6) T'ien, J.S., Singhal, S.N., Harrold, D.P., and Prahl, J.M.; *Combustion and Flame*, Vol. 33, pp.55-68, 1978.
- 7) Ohtani, H., Akita, K., and Hirano, T., *Combustion and Flame*, Vol. 53, pp. 33-40, 1983.

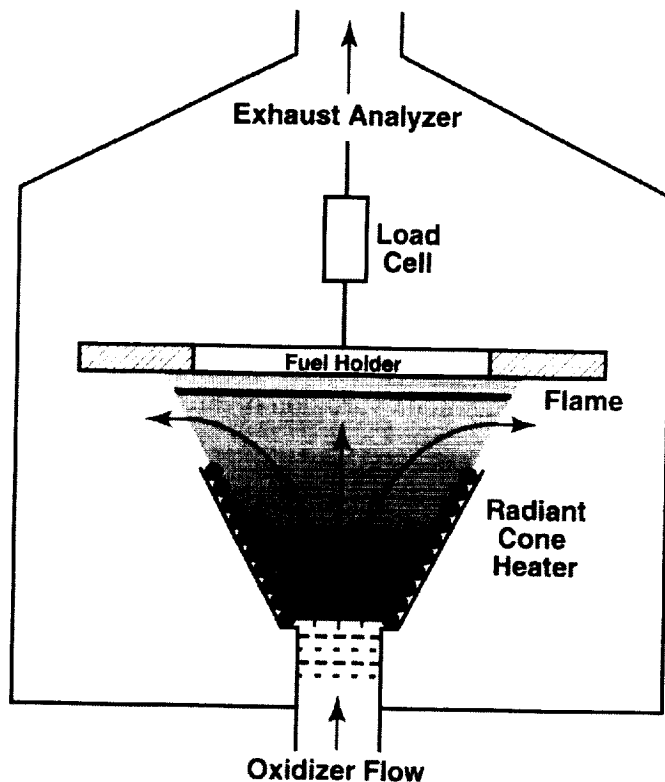


Figure 5: Equivalent Low Stretch Apparatus

Fire Accident Testing Evaluation (FATE)

H. D. Ross¹, W. Mell², R. Pettegrew³, M. Hicks¹ and D. Urban¹, ¹NASA Glenn Research Center; MS 500-115, 21000 Brookpark Road, Cleveland, OH 44135; Howard.D.Ross@grc.nasa.gov; ²University of Utah; 50 South Campus Drive; Salt Lake City, CA 84112 ³National Center for Microgravity Research; MS 110-3, 21000 Brookpark Road, Cleveland, OH 44135

INTRODUCTION

Over the past decade, NASA has sponsored a growing amount of microgravity combustion research that has afforded considerable insight into a wide variety of fundamental problems. The vast majority of earlier funded projects claimed strong 'relevance' to fire safety aboard spacecraft, but unfortunately the actual connections are often weak (their clear value is in the fundamental knowledge that is gained). In contrast, the experiments we plan are aimed directly at testing, understanding and improving NASA's existing policies and practices toward spacecraft fire safety. In this study, we examine several previously unaddressed issues regarding these fire safety practices and policies. Specifically,

- a. NASA Test 1 (an upward flame spread test) is the primary qualification test for materials' use on spacecraft. NASA Test 1, however, does not consider some possible fire sources and some of its assumptions remain unvalidated. These include, among others: a. Premixed fires can occur and heat and ignite solid materials, but these are unconsidered in Test 1; b. Solid materials may be heated well above normal spacecraft air temperatures at the time of an accidental exposure to an ignition source (again unconsidered); c. The effect of firebrands in 1g is assumed to be worst case.
- b. Configuration control in microgravity is unvalidated. NASA requires that flammable materials be separated by 5 cm or more, so that fire from one material cannot ignite a neighboring material.
- c. There are also concerns with the fire suppression practices and policies. For example, there is uncertainty about the time to extinguish a fire upon termination of ventilation. The application of a jet of suppressant may itself produce firebrands from molten or charring material, and cause an accidental spread of fire. Finally, carbon dioxide, the suppressant of choice for the International Space Station, behaves differently than other diluent, in regard to its impact on the range of oxygen concentrations that will support a flame [1].

The goal of the proposed research is to contribute to improved fire safety practices and policies for spacecraft and Martian habitat through the achievement of the following objectives:

1. Determine systematically the conditions that will ignite onboard flammable materials upon passage of an initial premixed gas, firebrand, or aerosol flame over these materials.
2. Test the effect of firebrands and configuration spacing.
3. Determine the effectiveness of the flow of CO₂ extinguisher or other extinguishing agents.

APPROACH AND PRELIMINARY RESULTS

Objective 3 may be the most important for immediate ISS application, so we are starting with this class of experiments for low-gravity tests. Using a facility that is already built and aircraft-tested (the Spacecraft Fire Safety Facility), we will utilize the configuration of Goldmeer et al[2], i.e. a 2 cm diameter PMMA cylinder over which air flows (stagnation flow geometry). After ignition in 1g and a predetermined time to establish a deeply preheated sample, the gas flow will be switched during an aircraft trajectory from normal air to a preset mixture of extinguishing agent and air (e.g. 20% CO₂, 80% air) and the time for the fire to extinguish will be determined. A variety of gas flow rates, oxygen concentrations, extinguishing agents, sample materials and preheats will be tested. The results will be compared with the depressurization test results of Goldmeer et al.

In support of Objective 1, we will use the same facility with a premixed gas combustion environment, and position secondary materials that are normally found on spacecraft within the environment. Upon ignition of the gas via hot wire, we will determine if a secondary fire occurs. Preliminary feasibility tests were performed in normal gravity. Paper samples were placed in the holder, and the chamber was sealed. After pumping down to vacuum, methanol was introduced into the chamber through a short heated section. The combination of high temperature and vacuum enabled the methanol to fully vaporize. The chamber was then filled to 0.5 atm with a selected gas mixture (the 0.5 atm was used in order to assure chamber safety). The amounts of methanol and air that were introduced were selected so that the mixture was fuel-lean. After several minutes of delay in order to assure that the environment was initially quiescent, a hot wire igniter was energized and ignited the methanol-oxygen-nitrogen mixture at the bottom of the chamber. The subsequent premixed gas flame passed over the paper sample. In a simple test with methanol-air, a double-thick paper sample was charred but did not ignite. This was because of the high speed of the premixed gas flame in 1g, the double-thickness of the paper, and the relatively low oxygen concentration. The test was then repeated with a gas mixture containing 26% oxygen and a single thickness sample. In this case, as shown in **figure 1**, the paper sample rapidly ignited and spread.

In support of Objective 2, we will also perform controlled firebrand experiments, substituting individual or a stream of burning fuel droplets, for the fragments of free-floating burning material that may occur in real spacecraft fires. A droplet generator has already been designed and is in fabrication. A range of configurations will be examined to check the criterion of separation distance required by NASA procedures.

In parallel with the experiments, we are developing a state-of-the-art simulation code for predicting and analyzing the experimental tests. It is recognized that no model presently exists for all of the types of experiments that are described above. Also, the governing equations need to be simplified to simulate the proposed experimental scenarios, not only because it would otherwise be prohibitively expensive to do the computations, but also because the thermo-physical properties are not all known in detail (e.g., thermal degradation of a printed circuit board). The computational efficiency gained by using simple kinetic and radiative transport models will allow the investigators to simulate the effects of obstacles and fuel spacing on the ambient wind and, therefore, transition to flame spread. The effects of obstacles on the delivery of CO₂ suppressant to the flame, in different gravity conditions, can also be investigated.

A simulation code currently under development for use in another NASA project [3] will be modified for use here. This code is the result of combining the numerical approaches of two proven codes developed at NIST: the NIST large eddy simulation fire code and a microgravity flame spread code. The flame spread code has been used to investigate the influence of varying the ambient wind speed (i.e., oxygen supply; [4-6]), the initial flame shape [6], and the width of the cellulosic sample [7] on flame spread, ignition, transition and extinction. Experimental trends have been reproduced and insight into the physics underlying the trends has been obtained. For example, with regard to fire safety, it has been found both experimentally and observed in the simulation results that under certain conditions flames along the open edges of the cellulosic sample spread faster and survive transition more easily than flames which are isolated from the open edges [8]. The simulation results clearly show this to be the result of an increased oxygen supply to the edge flames. Thus, it is expected that, with minor modifications, the simulation code currently under development can be used to obtain qualitative results.

As an illustrative example of how the numerical code will be used to investigate trends, a scenario similar to the aforementioned feasibility experiment was simulated with the two-dimensional version of the flame spread code. The code was used to simulate a fuel-lean gas mixture ignited at one end of the simulation domain and then the subsequent 0g flame traveled over a combustible solid phase fuel. Unlike the 1g feasibility experiments described above, however, the code here is used to examine behavior in zero gravity conditions¹. The solid-phase and gas-phase kinetic schemes were similar to those used in previous simulations of flame spread over a thermally thin, cellulosic sample. Three conditions were simulated: no ambient wind (**figure 2**); a 2 cm/s ambient wind with the premixed flame spreading in the same direction as the wind; then the premixed flame spreading in the opposite direction of the 2 cm/s wind (**figure 2**). On **figure 2**, color contours of the gas-phase reaction rates are shown for four successive times. The right column of line plots show the mass fraction of the solid phase fuel that is located along $z = 0$ cm. The 0g premixed flame (labeled P on the figure) travels from left to right. Ignition of the fuel gases from pyrolysis of the solid phase occurs at approximately $t = 3.2$ s. The resulting secondary fire (labeled D) spreads in both directions, with its two flame fronts anchored to the solid fuel. When an ambient wind is present, a premixed flame spreading with (against) a wind has less (more) time to heat the solid phase. It may be expected, therefore, that for concurrent winds above a certain speed, no solid-phase ignition will occur. The column on the left side of **figure 3** shows the case of a 2 cm/s wind traveling in the same direction as the 0g premixed flame. The times are the same as in **figure 3**. No ignition of the solid-phase occurred (it did occur when the concurrent wind was 1 cm/s). The column on the right shows the final case in which the premixed flame spreads in the opposite direction of the 2 cm/s ambient wind. In this situation the cellulosic solid ignited even sooner than with no wind (**figure 2**). Again, the secondary fire (labeled D) spreads, and is anchored to the solid fuel only at its leading edge. These results are meant to illustrate how the model could be used to investigate trends. In order to obtain more quantitative results, modifications to the model are needed – e.g. flame and combustion product radiation, improved kinetics, 3D effects, etc.

¹ The code requires modification before simulations with gravity levels of 1g can be performed.

SUMMARY

By performing parametric experiments both in normal gravity and reduced gravity on the KC-135 aircraft, as well as developing and analyzing related modeling, generality of the interpretation of the experimental findings will be pursued along with direct recommendations for fire safety practices and policies for fire safety on spacecraft and in Martian habitats. This is the principal value of the research.

REFERENCES

1. Honda, L.K. and P.D. Ronney, *Combustion Science and Technology*, 1998. 133: p. 267-291.
2. Goldmeier, J., Urban, D., and Tien, J., *Fire Safety Journ.*, 1999. 32: p. 61-88.
3. Mell, W.E., et al. *Simulation of combustion systems with realistic g-jitter*. in *Sixth Microgravity Combustion Workshop*. 2001. Cleveland, OH: NASA CP (this workshop).
4. McGrattan, K.B., et al., *Combustion and Flame*, 1996. 106: p. 377-391.
5. Kashiwagi, T., et al. *Effects of Slow Wind on Localized Radiative Ignition and Transition to Flame Spread in Microgravity*. in *Proceedings of the Combustion Institute*. 1996, 26.
6. Mell, W.E. and T. Kashiwagi. *Dimensional Effects on Microgravity Flame Transition*. in *Proceedings of the Combustion Institute*. 1998, 27.
7. Mell, W.E. and T. Kashiwagi. *Effects of Finite Sample Width on Transition and Flame Spread in Microgravity*. in *Proceedings of the Combustion Institute*. 2000. Edinburgh, Scotland: The Combustion Institute.
8. Mell, W.E., S.L. Olson, and T. Kashiwagi, *Flame Spread Along Free Edges of Thermally Thin Samples in Microgravity*. *Proceedings of the Combustion Institute*, 2000. 28.

Figure 1: A lean methanol-26% oxygen flame passing over a double-thickness tissue paper. Gravity force is to left of page. A. Ignition by hot wire. B. Methanol flame rising in chamber; C. Methanol flame covers paper and paper ignites at lower edge; D. Flame spread across paper begins; E. Flame spread continues rapidly; F. Paper burns completely. The additional oxygen sustained the paper burning.

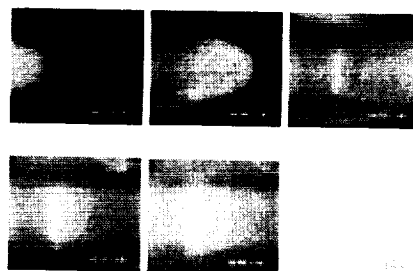


Figure 2: Color contours of the gas-phase reaction rate are shown on the left for four separate times, $t = 0.1$ s, 1.6 s, 3.2 s, and 4.7 s. The premixed flame is identified by a P and the diffusion flame, due to the thermal degradation and pyrolysis of the solid phase, is denoted by a D. Conditions are 0g with no ambient wind.

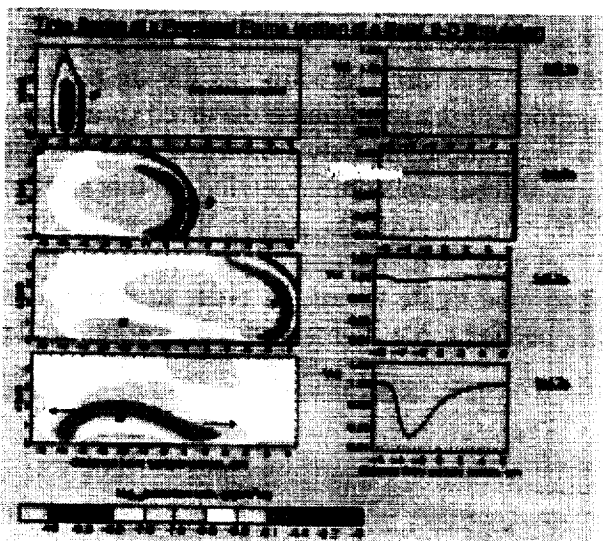
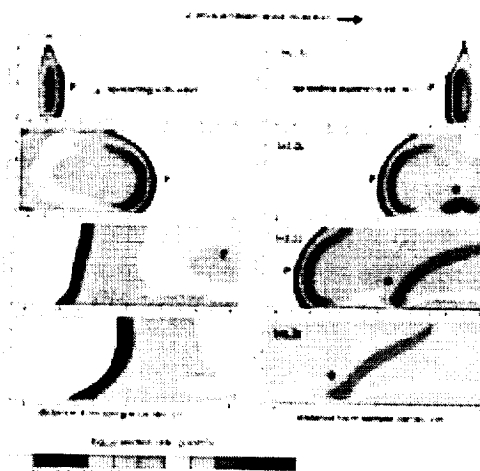


Figure 3: Color contours of the gas-phase reaction rate at four times. As before, the premixed flame is identified by a P and the diffusion flame is denoted by a D. Conditions are 0g with the premixed flame spreading in the same direction as a 2 cm/s ambient wind. Ignition of the solid phase occurs for the premixed flame spreading upwind, since it travels more slowly. Note that ignition occurs earlier for the case of no wind in the previous figure.



PHYSICAL AND CHEMICAL ASPECTS OF FIRE SUPPRESSION IN EXTRATERRESTRIAL ENVIRONMENTS

F. Takahashi¹, G. T. Linteris², and V. R. Katta³

¹National Center for Microgravity Research on Fluids and Combustion, Cleveland, Ohio

²National Institute of Standards and Technology, Washington, D.C.

³Innovative Scientific Solutions, Inc., Dayton, Ohio

INTRODUCTION

A fire, whether in a spacecraft or in occupied spaces on extraterrestrial bases, can lead to mission termination or loss of life. While the fire-safety record of US space missions has been excellent, the advent of longer duration missions to Mars, the moon, or aboard the International Space Station (ISS) increases the likelihood of fire events, with more limited mission termination options. The fire safety program of NASA's manned space flight program is based largely upon the principles of controlling the flammability of on-board materials and greatly eliminating sources of ignition. As a result, very little research has been conducted on fire suppression in the microgravity or reduced-gravity environment. The objectives of this study are: to obtain fundamental knowledge of physical and chemical processes of fire suppression, using gravity and oxygen concentration as independent variables to simulate various extraterrestrial environments, including spacecraft and surface bases in Mars and moon missions; to provide rigorous testing of analytical models, which include comprehensive descriptions of combustion and suppression chemistry; and to provide basic research results useful for technological advances in fire safety, including the development of new fire-extinguishing agents and approaches, in the microgravity environment associated with ISS and in the partial-gravity Martian and lunar environments.

MOTIVATION

As the planned extraterrestrial missions aim to establish long-term, human-occupied bases on Mars and the moon, fire incidents are possible. Friedman [1] reviewed the understanding and key issues of fire safety in the low-gravity extraterrestrial environments. Fire safety technology must be tailored to respond to the unusual fire characteristics in low-gravity environments. Unusual environmental conditions and agent usage peculiar to extraterrestrial applications may exert distinct influences on the flame structure, and, in turn, on the various physical and chemical processes in fire suppression and agent effectiveness.

Materials fire-spread tests on the ground at normal earth gravity (1 g) are justified by the view that the buoyancy-aided combustion represents a "worst case". However, because the flame structure significantly differs with the gravity level, various fire phenomena may not be simply interpolated from results in normal and microgravity. For example, the flammability and flame spread data for thin-paper fuels [2] showed that the maximum flame-spread rate occurred in partial-gravity (Martian) environments (0.38 g).

In quiescent microgravity environments, the solid fuel combustion intensities are reduced, yet a fire suppression agent and/or its decomposed inhibition species may also diffuse more slowly into the flame zone. Nonetheless, spacecraft and surface base atmospheres include forced convection (typically a continuous flow in the range of 6 to 20 cm/s) for atmospheric conditioning and component cooling [3]. For thin cellulosic fuels, low-velocity forced flow

greatly increases the flame spread rate and flammability range in microgravity [2]. In addition, application of a fire-extinguishing agent toward an established fire may cause a substantial current of agent-air mixture and alter the fire dynamics, changing the agent dispersion and interaction with the flame zone. Finally, for uncontrollable fires, a last-resort procedure is to evacuate the crew to a safe haven and then depressurize the module in an attempt to extinguish the fire [1, 4]. The depressurization may induce a significant airflow, which could augment burning, and stabilization of the fire in a recirculation zone behind an obstruction could also occur. In a 1-g experiment, a step-stabilized flame was very stable and attached to the obstruction at the free air velocity up to ~ 3 m/s [5, 6]. The unsteady vortex-flame interaction leading to local extinction has been studied numerically in 1 g [7], but unsteady suppression phenomena are unstudied for low-gravity environments.

Oxygen-enriched atmosphere, likely to be used in spacecraft and surface bases in the Mars missions, may result in intense burning and cause serious difficulties in suppression of established fires. The Space Shuttle and ISS environments that are prescribed for crew conditioning prior to extravehicular activities are 30-vol% oxygen in nitrogen at 70.3 kPa [3]. Such high oxygen concentration causes attendant increased fire hazards. The Mir fire in February 1997, caused by the failure of a solid-oxygen generator, is a good example of the difficulty in predicting potential fire scenarios in spacecraft [3] and suppressing the oxygen-assisted fires. Although microgravity flame-spread experiments in oxygen-enriched atmospheres have been conducted [2], the agent performance data is limited to the earth atmosphere [8].

A fire suppressant itself such as CO₂ may possibly be used in crew-compartment atmospheres. The effectiveness of various agent types needs to be studied in realistic extraterrestrial environments. The Space Shuttle uses fire extinguishers with halon 1301 (CF₃Br); the production of which has been banned due to its high stratospheric ozone depletion potential [9]. ISS uses CO₂ or H₂O as the agent, but these agents are relatively inefficient. Although the existing systems may continue to be used, new agents or techniques are ultimately needed to replace the Shuttle halon system; for long-duration missions aboard ISS, alternatives to the CO₂ systems are desirable [4]. Innovations can be developed for habitation and extinguishment of in-situ resource utilization using the Martian atmosphere (95.3-vol% CO₂) as the agent [4]. Although chemical agents can yield toxic and corrosive byproducts, and are unlikely to be used for long-duration missions, they are an order-of-magnitude more efficient and may be appropriate under some conditions.

RESEARCH APPROACH

In this study, both experimental and computational approaches are pursued. The experiments include both normal- and reduced-gravity tests using the drop tower and aircraft. For normal gravity conditions, the cup burner apparatus is the most widely used test for suppressant effectiveness by the fire protection community. An agent is generally introduced into the co-flowing oxidizer in the cup-burner system to determine the critical agent mole fraction at extinction. Because its structure resembles a fire, great faith has been placed in suppressant extinction concentrations determined in the cup burner experiment, and many codes and design standards are based on the cup-burner values [8]. Using a cup burner, the critical extinction mole fraction of fire suppression agents will be measured for selected fuels with variable gravity and

oxygen concentration in the oxidizer. Such cup-burner tests will connect the results in reduced gravity to the vast existing database on flame extinction obtained in 1 g. Then, physical and chemical effects of agents on flame structure and suppression processes will be determined with variable gravity and oxygen concentration in the oxidizer. Physical aspects include agent injection, dispersion, and entrainment as well as the thermal effects of the agent on flame structure. Chemical aspects include impacts on agent effectiveness, mechanistic processes of suppression (radical recombination and entrapping), and the effect of flame structure on a shift in important reactions.

Figure 1 shows conceptual schematics of the burner configurations. The axisymmetric cup burner is the standard burner used for the critical agent mole fraction measurements for various agents and fuels in normal gravity. The standard burner has the cup and chimney diameters of 30 mm and 80 mm, respectively. The 2D burners have a longer optical path along the flat flame sheet and uniform properties along the path, which are advantageous for optical measurements. In addition, an agent can be injected toward the flat flame formed on the step burner for the agent flow-flame interaction studies. Diagnostic techniques to be used include Mach-Zehnder interferometry, particle image velocimetry, standard color videography and high-speed digital color imaging.

Major parameters to be varied are the gravity level, oxygen mole fraction in the oxidizer, oxidizer velocity, and types of agent, fuel, and diluent. Fuels include gases: CH_4 , CH_4/N_2 , $\text{CH}_4/\text{N}_2/\text{O}_2$, liquids: $n\text{-C}_7\text{H}_{16}$, and solids: $3[\text{CH}_2\text{O}]$; and diluents include N_2 , CO_2 , He, and Ar. In addition to N_2 , CO_2 , H_2O , we will also study agents which have an increasing chemical contribution; namely CF_4 , CF_3H , CF_3Br , and $\text{Fe}(\text{CO})_5$ (or ferrocene). These halogenated compounds provide a homologous series with very similar physical contributions but increasing chemical effect. The iron compound is included, not to so much as a potential agent, but rather to determine the limit of what is possible through chemical inhibition. Recent research has shown that $\text{Fe}(\text{CO})_5$ up to 100 ppm behaves as a nearly ideal catalytic agent, with the radical recombination reactions proceeding at nearly gas-kinetic rates [10, 11]. Hence, it can be added as a diagnostic tool to determine the effect from gas-phase radical recombination alone.

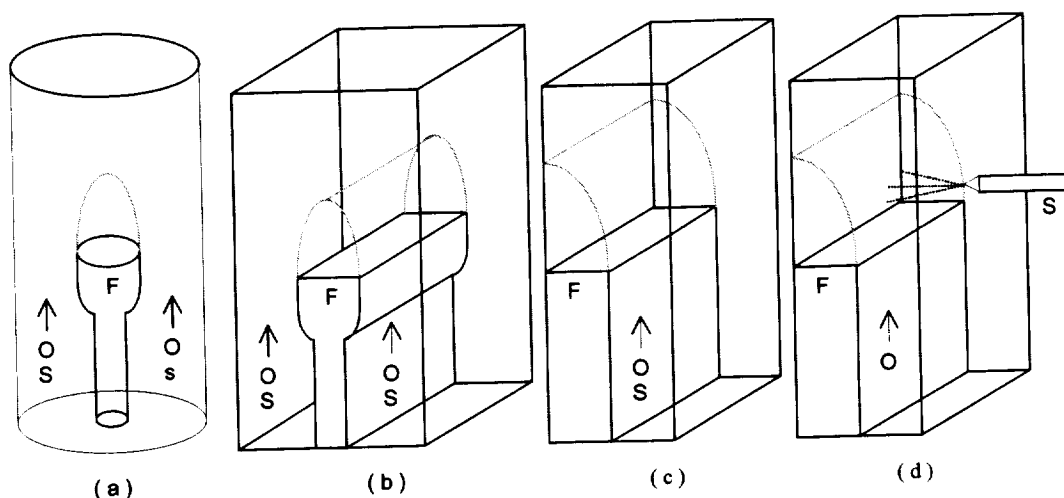


Fig. 1 Burner configurations. (a) Axisymmetric cup burner, (b) 2D cup burner, (c) step burner, (d) step burner with agent injection. F: fuel, O: oxidizer, and S: suppressant.

Computations of laminar, unsteady diffusion flames play an important role in understanding combustion and suppression phenomena. In this study, unsteady fire suppression processes in various flames will be simulated under different gravity and oxygen levels using an existing transient two-dimensional code (known as UNICORN [12]), which includes comprehensive kinetic models for the $\text{CH}_4\text{-O}_2$ combustion including diluents (GRI Mech) and halogenated agent chemistry (NIST CKMech). A periodically oscillating, pure-methane-air jet diffusion flame has been recently [13] studied to explore the chemical inhibition resulting from CHF_3 . Furthermore, additional goals of the project include extension of the code to higher hydrocarbon fuels such as C_3H_8 and $\text{n-C}_7\text{H}_{16}$, incorporation of a radiation model and the detailed kinetics models for various fire suppressants, and evaluation of various models developed in this study by a comparison with benchmark experiments.

ACKNOWLEDGMENTS

This work was supported by the Office of Biological and Physical Research, National Aeronautics and Space Administration, Washington, DC.

REFERENCES

1. Friedman, R., Fire safety in extraterrestrial environments, NASA/TM-1998-207417, 1998.
2. Sacksteder, K. R., and T'ien, J. S., "Buoyant downward diffusion flame spread and extinction in partial-gravity accelerations," *Proceedings of The Combustion Institute*, Vol. 25, 1685-1692 (1994).
3. Friedman, R., Fire safety in the low-gravity spacecraft environment, NASA/TM-1999-209285, 1999.
4. Annon., Workshop on research for space exploration: Physical Sciences and Process Technology, NASA/CP-1998-207431, 1998.
5. Takahashi, F., Schmoll, W. J., Strader, E., and Belovich, V. M., "Suppression of Step-Stabilized Nonpremixed Flames," *Combustion and Flame*, 122, 105-116 (2000).
6. Takahashi, F., Schmoll, W. J., Strader, E., and Belovich, V. M., "Suppression Behavior of Obstruction-Stabilized Pool Flames," *Combustion Science and Technology* (2000) (in press).
7. Takahashi, F., and Katta, V. R., "Unsteady extinction mechanisms of diffusion flames," *Proceedings of The Combustion Institute*, Vol. 26, 1151-1160 (1996).
8. NFPA, "Clean Agents Fire Extinguishing Systems," NFPA 2001, 1999.
9. United Nations Environment Programme (UNEP), Report of the Halon Fire Extinguishing Agents Technical Options Committee, 1994.
10. Babushok, V., Tsang, W., Linteris, G. T., and Reinelt, D., "Chemical limits to flame inhibition," *Combustion and Flame*, 115, 551 (1998).
11. Linteris, G. T., Rumminger, M. D., Babushok, V. I., and Tsang, W., "Flame inhibition by ferrocene, and blends of inert and catalytic agents," *Proceedings of The Combustion Institute*, Vol. 28 (2000) (in press).
12. Roquemore, W. M., and Katta, V. R., "Role of flow visualization in the development of UNICORN," *Journal of Visualization*, Vol. 2, No. 3/4, 257-272 (2000).
13. Katta, V. R., and Roquemore, W. M., "Role of CHF_3 in Extinguishing Diffusion and Premixed Flames," 39th AIAA Aerospace Sciences Meeting and Exhibit, Reno, NV, Paper No. AIAA-2001-1075, January 2001.

COOL FLAME QUENCHING

A Poster Presentation

Howard Pearlman[†]
University of Southern California
Department of Aerospace and Mechanical Engineering
Los Angeles, CA 90089
howard.pearlman@grc.nasa.gov

Richard Chapek
NASA Glenn Research Center
Cleveland, OH 44135

ABSTRACT

Cool flame quenching distances are generally presumed to be larger than those associated with hot flames, because the quenching distance scales with the inverse of the flame propagation speed, and cool flame propagation speeds are oftentimes slower than those associated with hot flames (Ryason, 1974, 1999). To date, this presumption has never been put to a rigorous test, because unstirred, non-isothermal cool flame studies on Earth are complicated by natural convection (Griffiths, 1971, 1982; Pearlman, 1999). Moreover, the critical Peclet number (Pe) for quenching of cool flames has never been established and may not be the same as that associated with wall quenching due to conduction heat loss in hot flames, $Pe \approx 40-60$ (Spalding, 1957; Ronney, 1988).

The objectives of this ground-based study are to: (1) better understand the role of conduction heat loss and species diffusion on cool flame quenching (i.e., Lewis number effects), (2) determine cool flame quenching distances (i.e., critical Peclet number, Pe) for different experimental parameters and vessel surface pretreatments, and (3) understand the mechanisms that govern the quenching distances in premixtures that support cool flames as well as hot flames induced by spark-ignition. Objective (3) poses a unique fire safety hazard if conditions exist where cool flame quenching distances are smaller than those associated with hot flames. For example, a significant, yet unexplored risk, can occur if a multi-stage ignition (a cool flame that transitions to a hot flame) occurs in a vessel size that is smaller than that associated with the hot quenching distance.

To accomplish the above objectives, a variety of hydrocarbon-air mixtures will be tested in a static reactor at elevated temperature in the laboratory (1g). In addition, reactions with chemical induction times that are sufficiently short will be tested aboard NASA's KC-135 microgravity (μg) aircraft. The μg results will be compared to a numerical model that includes species diffusion, heat conduction, and a skeletal kinetic mechanism, following the work on diffusion-controlled cool flames by Fairlie et al., 2000.

[†] Corresponding author

INTRODUCTION

Thermal and diffusional theories have been developed to account for heat and species loss on flame quenching (Spalding, 1957; Belles, 1959). While such theories are well-established for hot flames, they have not been extended or tested against cool flames and other low temperature reaction modes.

The purpose of this study is therefore to address the role of diffusive transport of heat and species on cool flame quenching. This requires that buoyant convection and its associated complexities are suppressed, which can only be accomplished in a μg environment. By reducing the effective gravitational acceleration (g), the Rayleigh number (Ra) associated with the reaction may be reduced to a value that is smaller than the critical Ra ($Ra_{cr} \approx 600$; Tyler, 1966, Fine, 1970) for onset of natural convection. Note that most unstirred cool flame and auto-ignition studies on Earth have a $Ra \sim 10^4$ - 10^5 , which is reduced by several orders of magnitude (depending on the facility) at μg (i.e., $Ra \sim g$). For additional discussion, refer to the article entitled "The Cool Flames Experiment" also included in this volume.

COOL FLAME QUENCHING DISTANCES

Hot flame quenching is controlled by heat loss and species transport. These mechanisms also regulate cool flames, although cool flames have an additional moderating mechanism. Namely, the negative temperature coefficient (ntc), which is known to exist for most hydrocarbon-air mixtures at low temperature (typically 275-350°C). In essence, the ntc regulates the self-acceleration of the low temperature reactions.

The ntc is demonstrated in Figure 1, taken from the original work of Pease (Pease, 1929). It is a plot of fuel consumption rate (overall reaction rate) versus temperature for propane oxidation and clearly shows that the reaction rate increases with decreasing temperature for a range of low temperatures.

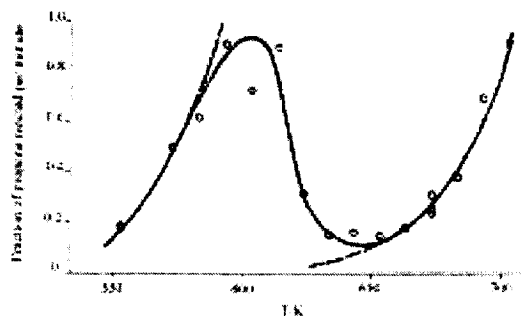


Fig.1. Propane consumption rate as a function of temperature in a propane-oxygen premixture (Pease, 1929) demonstrating the ntc.

The negative temperature coefficient could not be expected based on extrapolation of the high temperature fuel consumption rate to lower temperatures. Moreover, the nonlinearity associated with the ntc may also lead to "abnormal" quenching behavior of cool flames. Specifically, cool flame quenching distances may vary nonlinearly with temperature, because cool flame propagation speeds are expected to scale as the square root of the overall reaction rate, which itself varies nonlinearly with temperature (Fig.1).

Evidence to suggest that cool flame quenching may be characterized by a critical Pe can be found in existing literature. In particular, the ignition diagram associated with unstirred static reactor studies typically shifts towards lower pressures as the vessel size increases (Pilling, 1997). While these 1g results are complicated by natural convection, this shift towards lower pressure may be expected because the quenching distance scales inversely with pressure. This is because the quenching distance (d) scales with the diffusion coefficient (α) and the diffusion coefficient scales inversely with pressure ($\alpha \sim 1/p$). This phenomenological argument assumes that the limiting cool flame propagation speed at the boundary between the cool flame and slow reaction regimes is the roughly the same irrespective of the vessel size. This later assumption is approximately true for hot flames near their flammability limits, yet further quantitative studies are needed to validate this assumption for cool flames.

Lastly, cool flame quenching distances are also expected to vary with vessel treatment and material, since internal surfaces and intrusions can serve as sinks for termination of radical and branching species. Experimentally, different surface treatments will be tested to quantify and better understand the role of these surface effects.

At the time of this writing, the experimental hardware used to support laboratory and KC-135 aircraft cool flame experiments is being reconfigured to conduct this research (the reader is referred to the article entitled "The Cool Flames Experiment" also included in this volume for additional details). Results from these studies will be presented at the poster session of the conference.

ACKNOWLEDGMENTS

Special thanks to Professor John Griffiths at University of Leeds for inspirational and helpful discussions. This work is supported by NASA under NCC3-854.

REFERENCES

- Belles, F.E. and Swett, C.C. (1959) NACA Report 1300, ed. Barnett, H.C. and Hibbard, R.R., 83-93.
- Day, R.A. and Pease, R.N. (1940) Proc. Royal Society (London) **62**, 2334-2337.

Fairlie, R., Griffiths, J., and Pearlman, H. (2000) "A numerical study of cool flame development under microgravity," The Twenty-Eighth (International) Symposium on Combustion, The Combustion Institute, Scotland.

Frank-Kamenetskii, D.A. (1939) Zh. Fiz. Khim., **13**, 738.

Fine, D.H., Gray, P., MacKinven, R. (1970) Royal Soc. of London **A316**, 223-240.

Griffiths, J.F., Gray, B.F., and Gray, P. (1971) "Multistage ignition in hydrocarbon combustion: Temperature effects and theories of non-isothermal combustion," Thirteenth Symposium (International) on Combustion, 239-248.

Griffiths, J. and Hasegawa, K. (1982) Combustion and Flame **45**, 53-66.

McKay, G. (1977) Progress in Energy and Combustion Science **3**, 105-126.

Pearlman, H. (1999) Combustion and Flame **121** (1-2), 390-3.

Pearlman, H. (2000) Third International Seminar on Fire and Explosion Hazards of Substances, University of Central Lancashire, Preston, UK, April 10-14, 2000.

Pease, R.N. (1929) Journal of the American Chemical Society, **51**, 1839-1856; Pease, R.N. (1938) Journal of the American Chemical Society **60**, 2244.

Pilling, M.J., ed. (1997) Low-Temperature Combustion and Auto-ignition, Elsevier Science, 555-649.

Ronney, P. (1997) Transport Properties Fortran Code.

Ronney, P. (1988) "On the mechanisms of flame propagation limits and flame extinction at microgravity," Twenty Second Symposium (International) on Combustion, The Combustion Institute, 1615.

Ryason, P. and Hirsch, E. (1974) Combustion and Flame **22**, 131 -132.

Ryason, R.P. (1999) Personal Communication.

Spalding, D.B. (1957) Proceedings of the Royal Society of London **A240**, 83-100.

Tyler, B.J. (1966) Combustion and Flame **10**, 90-91.

SPHERICAL ETHYLENE/AIR DIFFUSION FLAMES SUBJECT TO CONCENTRIC DC ELECTRIC FIELD IN MICROGRAVITY[†]

Z. -G. Yuan, U. Hegde, National Center for Microgravity Research, MS 110-3,
Cleveland, OH 44135-3191

G. M. Faeth, Department of Aerospace Engineering, The University of Michigan,
Ann Arbor, MI 48109-2140

INTRODUCTION

It is well known that microgravity conditions, by eliminating buoyant flow, enable many combustion phenomena to be observed that are not possible to observe at normal gravity. One example is the spherical diffusion flame surrounding a porous spherical burner [1,2]. The present paper demonstrates that by superimposing a spherical electrical field on such a flame, the flame remains spherical so that we can study the interaction between the electric field and flame in a one-dimensional fashion. Flames are susceptible to electric fields that are much weaker than the breakdown field of the flame gases [3-7] owing to the presence of ions generated in the high temperature flame reaction zone. These ions and the electric current of the moving ions, in turn, significantly change the distribution of the electric field [8]. Thus, to understand the interplay between the electric field and the flame is challenging. Numerous experimental studies of the effect of electric fields on flames have been reported [9-15]. Unfortunately, they were all involved in complex geometries of both the flow field and the electric field, which hinders detailed study of the phenomena. In a one-dimensional domain, however, the electric field, the flow field, the thermal field and the chemical species field are all co-linear. Thus the problem is greatly simplified and becomes more tractable.

EXPERIMENTAL METHODS

Experiments with ethylene diffusion flames burning in air at atmospheric pressure subjected to under various voltages were conducted in the 2.2-second drop tower at NASA Glenn Research Center [16]. The fuel system on the drop rig includes a stainless steel fuel bottle, a pressure regulator, a metering valve, a solenoid valve and a spherical burner, which is a brass porous sphere, 12.7 mm in diameter. By adjusting the pressure regulator and the metering valve, the fuel system can provide the desired constant fuel flow rate during the drop test. Figure 1 shows the test section of the experiment, which consists of a pair of concentric spherical electrodes. The inner electrode utilizes the spherical burner, while the outer electrode is a spherical Faraday cage having a 63.5 mm ID, made of copper wires. A floating, adjustable, high DC-voltage source provides the desired voltage and polarity between the two electrodes, generating an electric field in the radial direction. By adjusting the applied voltage, the strength of the electric field can be controlled. The burner is connected to the fuel supply system using thin stainless-steel tubing having a 0.9 mm ID. To accommodate the fuel supply tube, the bottom part of the outer electrode has a 13 mm diameter opening where the copper wires turn to a direction parallel to the fuel tubing. The schematic drawing in Fig. 1 illustrates the relation between the flame and the electric field. During a test, the flame was ignited at normal gravity using a hot-wire igniter, which was

[†] The relevant NRA project is "Effects of Electric Field on Soot Processes in Non-buoyant Hydrocarbon-fueled Flames."

then retracted outside the outer electrode to avoid interfering with the flame and the electric field. Following ignition, the drop rig was released and the high DC-voltage turned on. The flame images were acquired at a rate of 30 frames per second using a CCD color camera on board the drop rig. The video signal from the camera was transmitted, via a fiber-optic cable system, to a computer on the ground, where the signal was digitized and stored in the hard drive of the computer for later analysis. A large number of drop tests were conducted with various fuel flow rates and applied voltages. Spherical flames and strong effects of the electric field on the flames were observed. The results of the tests are described in the next section.

RESULTS AND DISCUSSION

A series of screening tests with various ethylene flow rates were carried out in the absence of the electric field to establish a baseline flame commensurate with the above-mentioned electrode dimensions. The results of those tests show that a flame having a 2.5 mg/s ethylene fuel flow rate can serve as a proper baseline flame. It was observed that in about 0.2 seconds after the start of free fall, the flame changed from a teardrop shape typical of normal gravity conditions to a spherical shape typical of microgravity conditions. The flame radius increased slowly during the drop, similar to flames studied by other workers [2,17]. Due to the limited microgravity time, it is not clear if a quasi-steady state was reached. Figure 2a shows the flame image acquired at 1.6 seconds into free fall. The flame appears to be a blue sphere, about 38 mm in diameter, surrounding an orange-colored soot-containing region.

Flame images with three different applied voltages for each polarity are shown in Figures 2b-g. The electric voltages and polarities marked on each image represent those of the outer electrode with respect to the inner electrode. It can be seen that the upper portion of all these flames is quite spherical, especially when positive voltages are applied. However, the bottom portion of these flames deviates from a spherical shape due to the non-spherical distribution of the electric field. All these flame images were acquired at 1.8 seconds after the start of free fall. Figures 2b,d and f show the flame under positive 1.0, 1.5 and 2.0 kV, respectively. In these cases, the radius of the upper portion of the flame becomes slightly smaller than the zero-voltage flame (Fig. 2a). The flame becomes increasingly dimmer because the soot containing zone inside the flame diminishes with increasing voltages. Figures 2c, e and g show the corresponding flame images with negative applied voltages of 1.0, 1.5 and 2.0 kV, respectively. When the applied negative voltage increases, the radius of the upper portion of the flame decreases significantly, while the brightness of the flame increases. The flame becomes purely blue when the applied voltage is -1.5 and -2.0 kV. The observed flame shape change is likely due to the electric-field-induced body force, i.e. ionic wind effect [7]. The flame reaction zone is very thin in comparison with the distance between the flame and either electrode. The ions generated in the flame reaction zone are partially, or totally, removed from the flame by the electric force, depending on the amplitude of the applied voltage. The positive ions move toward the negative electrode, while the negative charge carriers, either electrons or negative ions, move toward the positive electrode. It is generally believed that in the flame reaction region, the negative charge carriers are mostly electrons [4-6]. After leaving the flame, electrons tend to attach to the molecules of either cold air or fuel gas, forming negative ions. Note that on each side of the flame, there is only one type of charge carrier, either positive or negative. When the ions move toward the electrodes, they collide with neutral molecules, resulting a body force from a macroscopic point of view. The additional gas movement caused by this body force is often referred to as ionic wind. In the

present configuration, the electric-field-induced body forces on the two sides of the flame are directed in opposite directions. The integrated results of the body force over the entire distance between the two electrodes should be responsible for the changes of the flame shape. The observed disappearance of soot is consistent with early experiments reported by other workers: Weinberg and co-workers [10,18,19] noticed that the electric field caused significant reductions of carbon deposition in their opposed-jet flame experiments; Saito et al. [12] observed similar reduced soot emissions when an electric field was applied in their jet diffusion flame experiments. In the present experiments, although the soot-containing zone diminishes with both electric polarities, the mechanisms seem to be different. When the outer electrode is negative the flame is relatively intense with modest heat losses and a relatively short residence time for the fuel in soot forming regions of the flame; the short residence time inhibits the formation of soot precursors and soot leading to a blue flame. In contrast, when the outer electrode is positive the rate of combustion per unit of flame surface is smaller; then radiation should be important and the lower flame temperatures reduce rates of soot precursor and soot formation even though residence times of fuel in potentially soot-forming regions are longer.

A system is presently under development to measure the electric current passing through the spherical portion of the flame, which will provide information on the distribution of the electric field. Subsequently, tests with different hydrocarbon fuels (i.e. propane, methane, etc) will be conducted to evaluate fuel effects.

ACKNOWLEDGMENTS

This work is supported by the Microgravity Research Division of the NASA Office of Life and Microgravity Science and Application. The authors greatly appreciate assistance of Eric D. Baumann and Andrew J. Jenkins in drop tests. Matthew Ellis, an intern with NASA Glenn, assisted with drop testing in the 2.2 Second Drop Tower.

REFERENCES

1. Sunderland, P. B., Axelbaum, R. L., and Urban, D. L., *Fifth International Microgravity Combustion Workshop*, NASA/CP-1999-208917, May 1999, p. 475.
2. Atreya, A., Agrawal, S., Sacksteder, K. R., and Baum, H. R., *AIAA 32nd Aerospace Science Meeting paper 94-0572*, Reno (1994).
3. Thomson, J. J., and Thomson, G. P., *Conduction of Electricity Through Gases*, Vol. I, Cambridge University Press, 1928, p. 399.
4. Calcote, H. F., *Proc. Combust. Inst.* 9:622(1963).
5. Lawton, J., and Weinberg, F. J., *Electrical Aspects of Combustion*, Clarendon Press, Oxford, 1969, p. 215.
6. Carleton, F. B. and Weinberg, F. J., *Nature* 330:635 (1987).
7. Lawton, J., Mayo, P. J., and Weinberg, F. J., *Proc. Roy. Soc. A* 303, 275 (1968).
8. Lawton, J. and Weinberg, F. J., *Proc. Roy. Soc. A* 277, 468 (1964).
9. Heinsohn, R. J., Wulffhorst, D. E., and Becker, P. M., *Combust. Flame* 11:288 (1967).
10. Mayo, P. J., and Weinberg, F. J., *Proc. Roy. Soc. Lond. A* 319, 351 (1970).
11. Heinsohn, R. J., Thillard, S. V., and Becker, P. M., *Combust. Flame* 13:442 (1969).
12. Saito, M., Arai, T., and Arai, M., *Combust. Flame* 119:356 (1999).
13. Heinsohn, R. J., Wilhelm, Jr, C. F., and Becker, P. M., *Combust. Flame* 14:341 (1970).
14. Calcote, H. F., and Pease, R. N., *Industrial and Engineering Chemistry*, 43:2726 (1951).
15. Carleton, F., Dunn-Rankin, D. and Weinberg, F., *Proc. Combust. Inst.* 27:2567 (1998).
16. NASA Technical Memorandum 106858, Glenn Research Center, 1995.
17. King, M. K., *Proc. Combust. Inst.* 26:1227 (1996).
18. Place, E. R., and Weinberg, F. J., *Proc. Combust. Inst.* 11:245 (1967).
19. Bowser, R. J., and Weinberg, F. J., *Nature* 249:339 (1974).

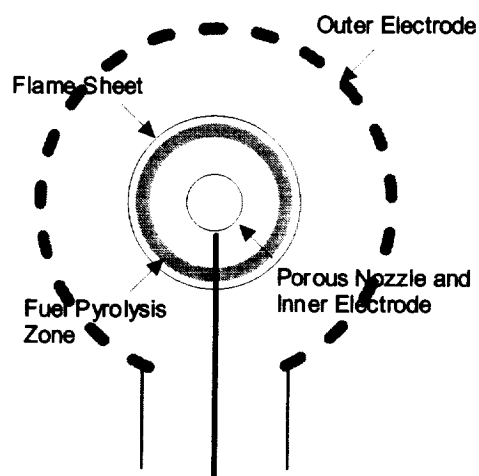
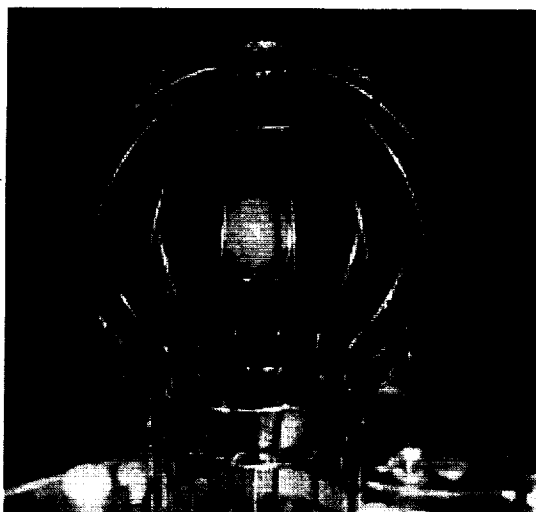


Figure 1. On the left is a photograph of the test section used to conduct the drop tests shown in Fig. 2. The OD of the porous spherical nozzle is 12.7 mm, while the ID of the outer electrode is 63.5 mm. On the right is a sketch illustrating the relationship between the flame and the two electrodes.

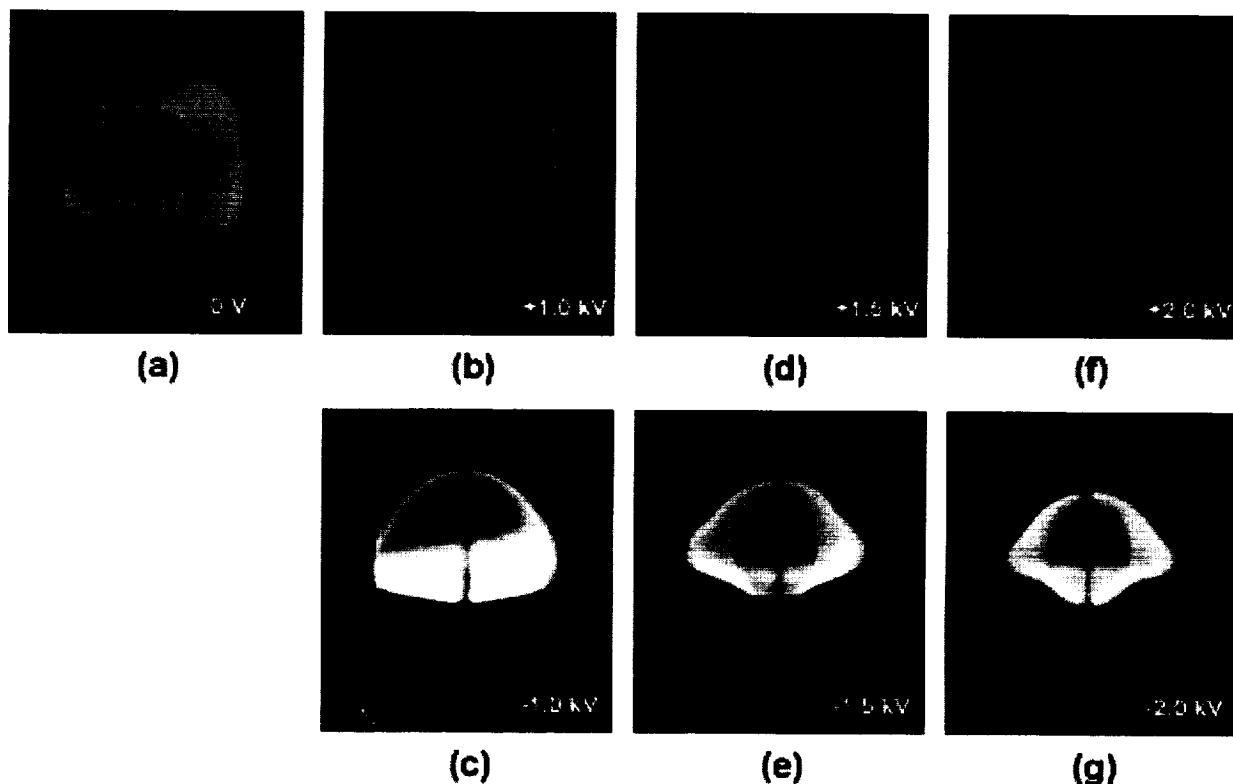


Figure 2. Images of non-buoyant ethylene diffusion flames from a porous spherical burner, subject to various DC voltages. The voltages marked on images are those of the outer electrode with respect to the inner electrode, i.e. the inner electrode is assumed to be at zero volts. The vertical dark lines are the out-of-focus elements of the Faraday cage. The darker center portion in the images is the porous spherical burner, which also is the inner electrode.

PARTICLE GENERATION AND EVOLUTION IN SILANE/ACETYLENE FLAMES IN MICROGRAVITY

D. G. Keil

AeroChem Research Laboratory, Titan Corp.
Princeton, NJ 08543

INTRODUCTION

The objective of this new experimental program is to advance the understanding of the formation of particles from gas phase combustion processes. The work will utilize the unique $\text{SiH}_4/\text{C}_2\text{H}_2$ combustion system which generates particulate products ranging from high purity, white SiC to carbonaceous soot depending on equivalence ratio (Ref. 1). A key goal of this work is to identify gas phase or particle formation processes that provide the enthalpy release necessary to drive the combustion wave, and to locate the parts of the particle formation process that determine SiC stoichiometry and crystallinity. In a real sense, these $\text{SiH}_4/\text{C}_2\text{H}_2$ flames act like "highly sooty" hydrocarbon flames, but with simpler chemistry. This simplification is expected to allow them to be used as surrogates to advance understanding of soot formation in such rich hydrocarbon flames. It is also expected that this improved understanding of SiC particle generation and evolution in these self-sustaining flames will advance the commercial potential of the flame process for the generation of high purity SiC powders.

BACKGROUND

We have previously investigated $\text{SiH}_4/\text{C}_2\text{H}_2$ flames in constant volume combustion experiments. In that work we found (Ref. 2) that $\text{SiH}_4/\text{C}_2\text{H}_2$ flames propagate over a wide range of stoichiometry ratios from 0.05 (acetylene-rich) to 2.5 (silane-rich). Burning velocities extracted from the pressure histories of combustion events exhibited an unusual dependence on the $\text{SiH}_4/\text{C}_2\text{H}_2$ reactant ratio as shown in Fig. 1. The major products of the combustion were hydrogen and fine powder containing most of the reactant mass of carbon and silicon. At the limits, this fine powder could be an atomic-level silicon-carbon mixture or a mixture of pure carbon and silicon particles. Either is consistent with the endothermic nature of the silane and acetylene reactants to decomposition to elemental silicon and carbon. Hence, over the range of stoichiometries observed to burn, a continuum of carbon-silicon compositions is produced. The homogeneity of the product must depend in part on the coupling between the silicon and carbon chemistries during the combustion and on the rates of elemental interdiffusion in nascent particles. For a very narrow range of $\text{SiH}_4/\text{C}_2\text{H}_2$ mixture ratios near 2.0 (equal silicon and carbon atomic concentrations), the powder product of the combustion was found to be stoichiometric nanocrystalline, cubic silicon carbide (SiC), consistent with intimate mixing on the atomic level. One possible mechanism to explain this would be parallel decomposition to carbon and silicon followed by rapid interatomic diffusion to produce stoichiometric SiC. We have presented evidence (Ref. 2) for coupling of the silicon and carbon chemistries, i.e., that the silicon-carbon bonds form early in the flame and have suggested that the such gas phase species determine the stoichiometry and crystallinity of the final product. There are problems with defining a suitable mechanism. Although a number of candidate small Si_xC_y species are known, they are high energy species which could present an significant energy barrier to the ultimate enthalpy-releasing process: formation of the condensed SiC phase. High molecular weight polyatomic silicon-carbon species are thermally unstable to dissociation, and unlikely

candidates for participating in particle formation. Insight into the mechanism of SiC formation may be gained through comparisons of flame data and the product properties for a series of related flames.

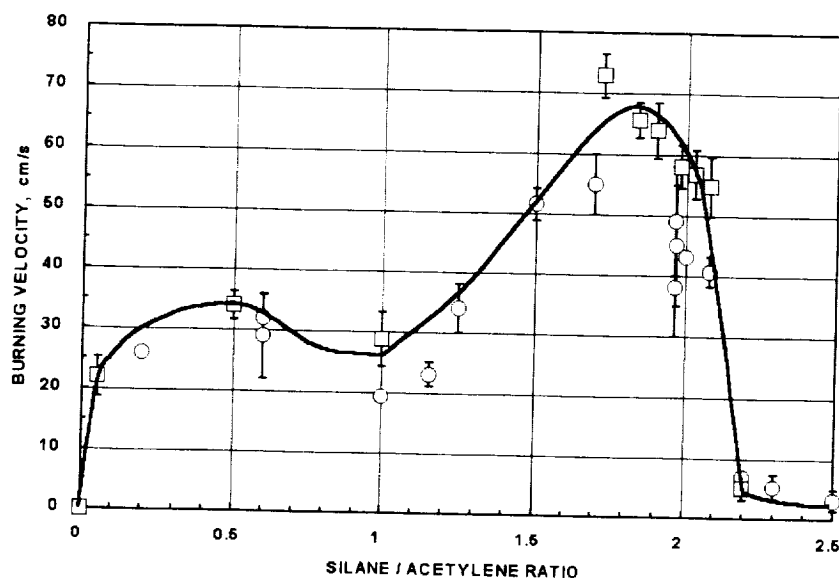


Figure 1 Experimental Silane/Acetylene Burning Velocities

It is difficult to obtain detailed flame structure information from constant volume combustion experiments like those described above. Instead, a steady-state, burner-supported flame is more suitable for accurate flame diagnostics. We previously established such constant pressure flames on a variety of burners in normal gravity, but found that laminar flames were extremely difficult to stabilize because of the interactions of buoyant product acceleration, settling and thermophoretic transport of the SiC powder product, and because of the apparent sensitivity of burning velocity to dilution and reactant mixture ratio. This sensitivity may arise from the close coupling of enthalpy release and particle formation that is unique to this combustion system. In the present microgravity studies, the complex effects of buoyancy, buoyancy induced mixing, and gravitational settling will be substantially reduced or eliminated. Less distorted and steadier flames that reflect the combustion chemistry and particle formation processes more than extraneous fluid transport effects are expected. It should be possible to obtain more accurate correlations among, e.g., reactant stoichiometry, added gases, burning velocities, flame temperatures, and the resultant powder properties. Several mechanistic questions will be addressed in this work: Are the enthalpy releasing particles formed from high energy small gas phase Si_xC_y species such as SiC(g) or large soot-like species? If the latter, at what stages in the particle formation are the one-to-one silicon to carbon ratio and the crystallinity developed? Based on the enthalpy release during particle formation, can the burning velocity be affected by increasing or decreasing the particle nucleation rate? This information will be used to improve our understanding of the heat release processes, and ultimately will provide an improved model picture of $\text{SiH}_4/\text{C}_2\text{H}_2$ flames to show whether and how a continuous burner process can produce high value SiC powder. The new understanding may help promote alternate approaches to commercial development of the synthesis flame process.

EXPERIMENTAL APPROACH

This program will focus on fundamental flame properties (burning velocity, particle and gas temperatures, flame species, and product characterizations). The key experimental challenges are to make reliable burning velocity measurements and to make useful measurements near the flame front to relate to the burning velocities of these particle-laden premixed flames. To make burning velocity measurements that reflect the adiabatic combustion chemistry, energy loss and thermophoretic transport to the burner must be minimized. Thus, multitubular burners are unsuitable for this purpose with these flames. In addition, flame front diagnostics require a geometry in which the pre-flame region is not obscured by the highly luminous particle cloud as with a Bunsen-type burner. A useful geometry that satisfies these requirements is that of inverted cone flame stabilized above a rod coaxial with the reactant flow, Fig. 2.

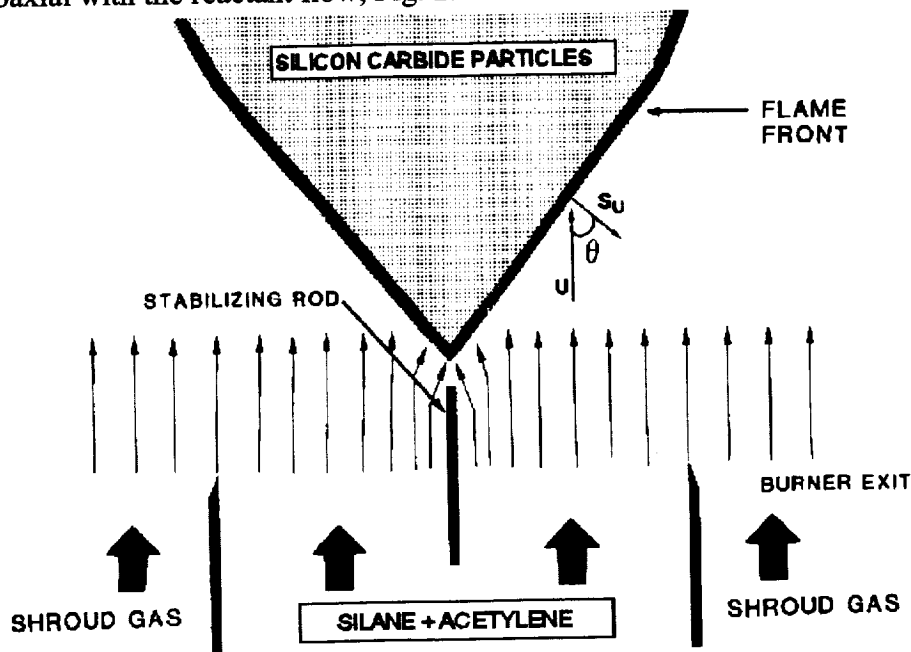


Figure 2 Inverted Flame Cone Geometry

The cone flame angle is related to the ratio of the flow velocity to the burning velocity. However, in normal gravity, the buoyant acceleration of the hot flame gases greatly distorts the cone angle. For the flames that will be investigated in this work, this normal gravity distortion would have a significant effect on a majority of the flames to be investigated and would dominate the lower velocity flames. These distortions would unpredictably affect each reactant mixture with its unique burning rate, flame products, and flame temperature, complicating the interpretation of measured differences among comparison flames. Therefore the microgravity environment is required to make burning velocity measurements suitable for flame comparisons and which predominantly reflect the fundamental flame chemistries and rates.

Measurements are planned to obtain overall structural information such as flame angle (measured from CCD camera images) to determine the burning velocity, preheat zone location (using schlieren imaging, thermocouples), particle temperatures (optical pyrometry), and particle volume fractions (laser extinction). The powder product from selected experiments will be collected and characterized as to particle size (N_2 surface area, TEM), material density (pycnometry), and

crystallinity (XRD, TEM). These properties will be compared to typical properties of powders produced in previous constant volume experiments and the comparisons interpreted in terms of differences in flame environments. Comparisons will also be made between the properties of $\text{SiH}_4/\text{C}_2\text{H}_2$ flames that produce pure SiC ($\text{SiH}_4/\text{C}_2\text{H}_2 \sim 2$) and acetylene-rich ($\text{SiH}_4/\text{C}_2\text{H}_2 < 0.1$) flames that produce predominantly carbon soot. Dilution with inert gas will permit comparison of the two types of flames at the same burning velocity. The effects of additives that can affect particle nucleation (e.g., carbon black particles, electric fields, aromatic hydrocarbons) on burning velocity, flame properties, and/or product properties may be investigated. Additional diagnostics may be employed, including flame spectra (flame species information), gas sampling with microprobes for post drop analysis, thermophoretic particle sampling onto TEM grids for microscopic characterization, and thermocouple gas temperature measurements. All the data will be interpreted using thermochemical and kinetic estimates establish possible initial particle nucleation routes (e.g., carbon soot, silicon aerosol, low molecular weight Si-C species), and to improve the model of the synthesis flame.

PRESENT PLANS

The experimental system for the 2.2 second drop tower will be capable of quickly stabilizing inverted $\text{SiH}_4/\text{C}_2\text{H}_2$ cone flames (Fig. 2) suitable for burning velocity measurements. A completely contained system will be designed because of the pyrophoric properties of silane. The flame experiments require that we provide constant laminar flows with precisely controlled $\text{SiH}_4/\text{C}_2\text{H}_2$ gas mixtures to the burner. To control the reactant mixture ratio, the (ignitable) mixture at about atmospheric pressure will be prepared (by partial pressures) in a reservoir. The reservoir will be designed to withstand the pressure of an accidental ignition. The reactant gas mixture will be fed at a constant rate to the burner by displacement using an inflatable internal bladder. The drop tower provides a limited time to establish a steady flame and record the flame measurements. For most planned and potential diagnostics, a sampling time on the order of one second will be adequate. Hence, the reactant flows must be stabilized and the flame ignited within a fraction of the first second of the drop. The burner (Fig. 2) will consist of a tube with flow straighteners at the reactant inlet and a converging nozzle to create a uniform velocity profile at the exit. The coaxial rod will act as a flame holder downstream of the burner exit. The flame will be supported in the sealed flame chamber in a stagnant or slowly flowing nitrogen atmosphere. In the short burning time the flame products are not expected to interfere with the flame or its observation with proper chamber size and geometry. The chamber pressure will be monitored with a pressure transducer.

ACKNOWLEDGMENTS

This research supported by NASA Contract NAS3-01092, Dr. Michael Hicks, NASA Microgravity Combustion Science Branch, technical monitor.

REFERENCES

1. Keil, D. G., Calcote, H. F. and Gill, R. J., *Mat. Res. Soc. Symp. Proc. Vol. 410*, Materials Research Society, Pittsburgh, 167 (1996).
2. Calcote, H.F. and Keil, D.G., "Combustion Synthesis of Silicon Carbide Powder," in Proceedings of the Joint NSF-NIST Conference of Nanoparticles: Synthesis, Processing into Functional Nanostructures, and Characterization, Arlington, VA, 12-13 May, 1997 p. 28.

COUPLED RADIATION AND THERMOPHORETIC EFFECTS IN SOOTING MICROGRAVITY FLAMES

D. W. Mackowski¹, V. Nayagam and P. B. Sunderland²

¹ Department of Mechanical Engineering, Auburn University, AL

² National Center for Microgravity Research, Cleveland, OH

INTRODUCTION

It is well established that radiative emission from soot particles can constitute a large fraction of total heat release from hydrocarbon flames. Because the soot particles act, through radiative emission, as a 'sink' through which sensible enthalpy is removed from the flame gases, the soot concentration field obviously can play an important governing role in the flame temperature field. The temperature field, in turn, can directly affect the soot concentration field as a result of particle thermophoresis, i.e., the movement of small particles down a temperature gradient. Consequently, the radiative emission from the soot particles can, in principle, indirectly act to alter the soot concentration field. An effect of such an interaction is relatively easy to visualize: radiative emission from the soot field – which will be proportional to the local soot concentration – will depress the local temperature of the gas. The resulting temperature gradients will lead to thermophoretic transport of the soot into the cooled regions. In this sense, radiation emission, coupled with thermophoretic transport, could act to 'destabilize' the soot concentration field – in that soot would become compressed into regions of increasing concentration.

Order-of-magnitude estimates suggest that the radiation/thermophoretic mechanism could contribute to the formation of 'superaggregates' in large-scale flames. The objective of the proposed work is to examine, both theoretically and through a series of microgravity-based experiments in laminar, hydrocarbon-air diffusion flames, the interactions and effects of radiative heat transfer on the transport and growth dynamics of soot particles.

THERMOPHORETIC COAGULATION

It has been observed in several recent investigations that exceptionally large soot aggregates can appear in microgravity diffusion flames [1, 2, 3]. This effect is illustrated in Fig. 1, in which we present pictures of the soot field formed by diffusion flame combustion of hydrocarbon fuels in microgravity. The photo in (a) shows a C_2H_4 gas diffusion flame produced on a 4 mm spherical burner in the 2.2 s drop tower [3], and (b) is a 4 mm *n*-heptane droplet burning in an O_2/He mixture during the MSL-1 mission. [2]. The soot field in both flames has a nonuniform, granular structure in which large (i.e., visible to the eye) aggregates are clearly evident. The aggregates appear to grow via the scavenging of smaller aggregates in their vicinity, which is observed (especially for the droplet case) in the 'coarsening' of the soot sheet with increasing distance from the soot inception zone. Formation of these aggregates could not occur from fluid shear as the strain rates in the flames are essentially zero, and it is highly unlikely that diffusion-limited aggregation could create particles of this size in the time span of the experiments. Furthermore, we do not believe that a gelation mechanism (i.e., the formation of aggregates via the break-up of a 'gel' state) could fully account for

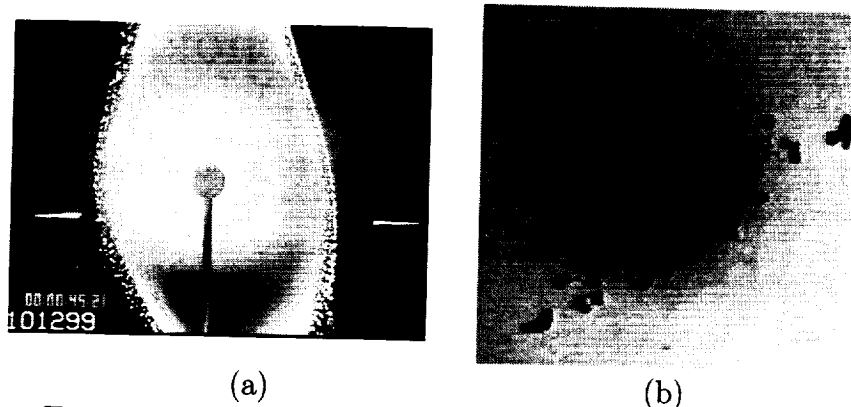


Fig. 1: Aggregate formation in microgravity diffusion flames

the continued growth of the aggregates as they are transported outwards [4].

It has been proposed that such aggregates could result from the coupled effects of radiative emission from the particles and thermophoretic transport of the particles [5]. The basic idea behind the mechanism is that the particles become heat sinks in the gas as a result of their radiative emission. The gas will respond by conducting heat into the particles, and the gas temperature gradients will drive a thermophoretic motion of the particles towards each other. A microscopic-level model of this effect is based on the assumption of a quasi-steady state between the radiatively-cooled particle and the surrounding gas, for which the gas temperature gradient extending from the particle will vary as $1/r^2$. Numerical solutions of the general dynamic equation for aerosol growth have shown that the radiation/thermophoretic mechanism can result in an explosive growth of large particles, i.e., the particle cloud can essentially condense into a single aggregate [5].

Detailed macroscopic-level examinations of radiation/thermophoretic effects in flames have not been performed. A simple order-of-magnitude analysis considers a plane layer of soot, initially having thickness d , suspended in a high-temperature gas and exchanging radiation with a cool background environment. We take the soot layer to be radiatively thin, neglect the effect of emission on the temperature distribution within the layer (i.e., the temperature is only slightly depressed relative to that of the surrounding gas), and assume that the gas and the soot are in a quasi-steady state. The conductive flux at the boundary of the layer must then balance the radiative flux, for which

$$k_g \frac{dT}{dx} = 2 \kappa_P d \sigma (T^4 - T_{env}^4) \quad (1)$$

where κ_P is the Planck mean absorption coefficient of the soot. The gas temperature gradient resulting from the radiation loss will drive a thermophoretic motion of the particles into the layer. Neglecting the effects of Brownian diffusion, the rate at which the layer recedes will be equal to the particle thermophoretic velocity V_T . A characteristic time for 'collapse' of the layer would therefore be $t_c = d/2V_T$, or

$$t_c = d \cdot \left(2 \frac{c_T \nu}{T} \frac{dT}{dx} \right)^{-1} = \frac{k_g T}{4 c_T \nu \kappa_P \sigma (T^4 - T_{env}^4)} \quad (2)$$

where ν is the gas kinematic viscosity and c_T is the dimensionless thermophoretic factor.

Detailed theories to predict c_T and κ_P for large-scale soot aggregates do not exist; a simple estimate can be obtained using equivalent-sphere approximations for which $c_T \sim 0.1 - 1$ and $\kappa_P \approx C_R T f$, where C_R is a constant. At typical diffusion flame conditions ($f = 10^{-6}$, $T = 1500$ K, $T_{env} = 1000$ K, air at 1 atm) the characteristic time t_c will be on the order of 1 s – which is somewhat longer than the residence times of normal-gravity, laminar jet and droplet diffusion flames yet comparable to or less than that for large-scale, turbulent diffusion flames and laminar flames in microgravity. We emphasize again that our time scale can be considered only an order-of-magnitude estimate – since it obviously neglects or vastly simplifies the important convective, kinetic, and radiative mechanisms which affect the thermal and transport dynamics of the soot field. Nevertheless, the model would suggest that radiation/thermophoretic effects on soot coagulation cannot be ruled out for flames of sufficiently long residence time.

Perhaps the most intriguing and salient feature of radiation/thermophoretic coupling is that it provides a mechanism to destabilize the soot field. That is, the coupling will act to amplify nonuniformities because soot is drawn towards regions of relatively high volume fraction. This basic concept is simple enough to visualize, yet a detailed understanding of the conditions under which such instabilities would occur, as well as a prediction of the effects on overall flame properties (i.e., aggregate size, soot release rates, radiation heat transfer) is completely lacking. This is certainly due to the fact that such effects have only recently been hypothesized. Perhaps more importantly, radiation/thermophoresis interactions would be difficult to both detect and model under the earth-bound conditions in which we believe they could become important, i.e., large-scale flames. In particular, the effects of such interactions would invariably be superimposed with (and obscured by) those due to convective transport and gelation. Clearly, an unmasking of the radiation/thermophoresis effects will require experimental conditions in which the effects can be isolated – and not compete with other transport mechanisms. A primary task of our proposed research will be to extend established microgravity diffusion flame experiments so that the existence (or lack of) radiation/thermophoretic coagulation mechanisms can be unambiguously determined.

RESEARCH PLAN

Our proposed research will involve three concurrent tasks; 1) an experimental determination of the existence and effects of thermophoretic aggregation in sooting microgravity diffusion flames; 2) development of analytical models for predicting the onset of radiation/thermophoretic instabilities in diffusion flames; and 3) a microscopic-level theoretical/numerical examination of radiation emission and thermophoretic transport for realistic soot aggregates.

The central task in our proposed research will be to conduct a series of experiments that are designed to examine radiation-induced thermophoretic aggregation of soot in flames. Our plan is to use a rig similar to that used to make the flames (and resulting ‘superaggregates’) in Fig. 1a, i.e., a 0.4 cm spherical diffusion flame burner in the 2.2 s drop tower at GRC [3]. We will test our hypothesis on radiation/thermophoretic interactions by manipulating the radiation environment of the flame. Specifically, we will attempt to offset the rate of thermal emission from soot particles with absorption of radiation from an external source. If radiative cooling is the mechanism for which large aggregates form in the flame, we expect that

a balancing of radiation emission with absorption will extinguish the mechanism and the flames will no longer produce large aggregates. Indeed, an absorption rate which exceeds the emission rate would overheat the particles relative to the gas, for which thermophoresis would lead to a net dispersal of the soot.

We will initially attempt to use a tungsten-filament bulb as the source of the external radiation. A parabolic mirror and lens will be used to produce a collimated sheet from the source, and this beam will be projected so that it intersects the top edge of the soot 'shell' formed about the flame. A key requirement of the experiments is the ability to measure characteristic sizes of large aggregates in the flame. Laser light scattering methods will not be feasible for the super- μm sized, sporadically-occurring particles seen in Fig. 1. Thermophoretic sampling techniques would be difficult to apply and may not collect the large aggregates of interest. Since, however, the aggregates in Fig. 1 are observable to the eye, we expect that image analysis techniques will be sufficient to qualitatively measure the largest aggregates occurring in the flame.

Numerical modeling of radiation/thermophoresis interactions in flames is complicated by the inherently 3-D nature of these effects, and also by the fact that they create a numerically stiff system. We will initially attempt to predict soot instabilities in a relatively simple (yet 3-D) model of the μg spherical diffusion flame. Likewise, an accurate prediction of the diffusive and thermophoretic transport properties of soot aggregates – which are needed for the flame models – is made difficult by the transitional Knudsen conditions that are characteristic of large aggregates in atmospheric-pressure flames. Our approach will be to develop analytical models in the slip-flow (or near-continuum) regime and numerical monte-carlo models for free molecular limit, and 'adjust' the continuum models so they extrapolate correctly to the FML. The validity of this approach will be tested by comparisons to direct simulation monte carlo predictions for simple aggregates in the transitional Knudsen regime.

- [1] O. Fujita, K. Ito, H. Ito, and Y. Takeshita. Effect of thermophoretic force on soot agglomeration process in diffusion flames under microgravity. In *NASA Conference Publication 10194*, pages 217–222. NASA, Cleveland, OH, USA, 1997.
- [2] V. Nayagam, J. Haggard, R. Colantonio, A. J. Marchese, B. L. Zhang, and F. A. Williams. *n*-heptane droplet combustion in oxygen helium mixtures at atmospheric pressure. *AIAA J.*, 36:1369–1378, 1998.
- [3] P. B. Sunderland, R. L. Axelbaum, and D. L. Urban. Effects of structure and hydrodynamics on the sooting behavior of spherical microgravity diffusion flames. submitted to Twenty-Fifth Symposium (International) on Combustion, 1999.
- [4] C. M. Sorensen, W. B. Hageman, T. J. Rush, H. Huang, and C. Oh. Aerogelation in a flame soot aerosol. *Phys. Rev. Lett.*, 80:1782, 1998.
- [5] D. W. Mackowski, D. E. Rosner, and M. Tassopolous. Effect of radiation heat transfer on the coagulation dynamics of combustion-generated particulates. *Aerosol Sci. Tech.*, 20:83–99, 1994.

LAMINAR FLAME SPEEDS OF SOOT-FORMING FLAMES

C. J. Sung^{1,2} and H. Wang³

¹ Department of Mechanical and Aerospace Engineering, Case Western Reserve University, Cleveland, OH 44106

² National Center for Microgravity Research on Fluids and Combustion, Cleveland, OH 44135

³ Department of Mechanical Engineering, University of Delaware, Newark, DE 19716

INTRODUCTION

The present study aims to gain fundamental understanding of the structure and dynamics of sooting premixed flames in simple, well-defined, one-dimensional, burner-supported, cylindrical and spherical flow fields. The research program consists of four components: (1) experimental determination of the fundamental sooting limits in the absence of conductive heat loss to the burner; (2) experimental determination of the laminar flame speed of soot-forming flames; (3) experimental mapping of sooting flame structure; and (4) detailed modeling of sooting flame propagation and soot formation. The work in components 1 and 2 will demonstrate a novel experimental approach under microgravity and generate fundamental flame and soot data that are suitable for model validation. This experimental approach eliminates the ambiguities associated with the boundary conditions in previous soot laminar premixed flame experiments and simulation.

The purely curved flames will be generated by discharging a gas mixture from a porous cylindrical/spherical burner into a quiescent ambience in microgravity [1]. The sooting phenomena of interest can be unambiguously studied without flame distortion and complication due to unwanted, buoyancy-driven flow. The flames are not aerodynamically strained. The standoff distance of the cylindrical and spherical flames can be several times of the corresponding flame thickness of a flat flame. These unique qualities along with the simplicity of the flame configuration enables us to stabilize flames which are close to be "adiabatic" with respect to conductive heat loss to the burner surface. It also facilitates a better spatial resolution for detailed diagnostics and a well-defined boundary condition for modeling purposes.

Conceptually these flame configurations allow us to define the sooting laminar flame speed as the velocity of flame-front propagation in absence of conductive heat loss. This definition accounts for the intrinsic radiative heat loss, which cannot be avoided experimentally even for non-sooting flames. The flame configuration also allow us to extend the previous sooting limit studies [2,3] to define the sooting limit as a fundamental property independent of conductive heat loss to the burner.

Results obtained for sooting premixed flames in a counterflow configuration are reported in this paper, which demonstrate the counterflow is inadequate for the purpose of the present research. As an integral part of this research program, we also developed the numerical formulation to account for thermal ionization in sooting flames and to examine the role of ionization on particle mass growth. These modeling results are also discussed here.

INVESTIGATION ON SOOTING FLAMES USING COUNTERFLOW CONFIGURATION

Experimental determination of the *one-dimensional laminar flame speed* s_u^0 has been one of the most active endeavors in combustion research [4]. The counterflow-based configuration has been widely used in recent years. All flame speed measurements were made for nonsooting flames. In this section, we discuss the feasibility of using counterflow configuration to determine the fundamental laminar flame speed for premixed fuel-air mixtures beyond their critical sooting limits.

Experimentally, premixed ethylene/air flames are established in the counterflow. Two-dimensional flow field is measured to simultaneously obtain the axial and radial velocity profiles using Digital Particle Image Velocimetry (DPIV). A typical DPIV image is shown in Fig. 1, which shows relatively-high stretched, blue ethylene/air flame of $\phi = 2.2$. Figure 2(a) shows the axial velocity profile along the centerline derived from the corresponding vector map. The minimum point in this axial velocity profile is conventionally used as the reference speed for the subsequent linear extrapolation. Figure 2(b) shows the radial velocity profile at that reference point, which is seen to be linear, and hence the radial velocity gradient yields the characteristic strain rate. The conventional axial velocity gradient based definition or

the stretch rate (K) is then equal to twice the radial velocity gradient.

Figure 3(a) delineates the methodology of linear extrapolation in the determination of laminar flame speed by plotting the reference speed against stretch rate, for $\phi = 2.2$ ethylene/air flames. Each data point is determined from the vector map of the instantaneous DPIV image. The laminar flame speed is then determined by linearly extrapolating the reference speed to $K = 0 \text{ s}^{-1}$. The insets in Fig. 3(a) show the direct photographs of representative flames and their schematics. We first note that no visible soot layer can be observed for the stretch rate range investigated herein when $\phi < \sim 1.92$. When $\phi > 1.92$, the flame/soot structure varies significantly with stretch rate. Figure 3(a) shows that in the low stretch regime a soot layer is observed which is sandwiched by twin blue flames. With increasing stretch rate, the separation distance between twin flames becomes smaller. Eventually and at approximately $K = 165 \text{ s}^{-1}$, the majority of the two flamelets merge and cannot be distinguished, while they are detached around the edge. The merged flames appear to be blue, but there exists a ring of soot layer around the merged flames.

Figure 3(b) is a counterpart plot for ethylene/air flames of $\phi = 2.4$, showing a more intricate structural variation with stretch rate. For all the stretch rates investigated, the twin flames merge completely, even including the edge. Additionally, the flame location is insensitive to the stretch rate variation. No flame exists when $K > 225 \text{ s}^{-1}$ because of blow off extinction. In the relatively high stretch rate regime, say ranging between 155 and 225 s^{-1} , a blue, flat, non-sooting, merged flamelet is observed. When the stretch rate is reduced to be within 130 and 155 s^{-1} , the merged flamelet is partially sooting in that the center part of the flame is blue while the edge of the luminous zone becomes orange. With decreasing stretch rate, the portion of blue flame shrinks and diminishes. At $K \approx 130 \text{ s}^{-1}$, the entire luminous zone becomes orange. Furthermore, the thickness of the orange luminous zone as well as its brightness increases with further decreasing stretch rate. Associated with the increase in flame thickness is that the flame surface becomes curved. More interestingly, there exists a critical stretch rate below which the flame quenches and cannot be established. The controlling mechanism leading to this low-stretch flame quenching is expected to result from excessive flame/soot radiation, which is different from that of the blow-off extinction. The DPIV image just before quenching shown in Fig. 4 clearly demonstrates that the flame is no more one-dimensional. It is also noted that the flame generally becomes more unstable as stretch rate is reduced, which is indicative of the larger scatter of the low-stretch data points shown in Fig. 3(b).

The above results indicate that there exist intrinsic limitations in applying counterflow configuration for the soot-forming flames. Especially, for a given fuel-rich mixture, with decreasing stretch rate the counterflow flame can change from to an originally permanently blue, non-sooting flame, to a donut-shaped partially sooting flame, then an orange sooting flame, and finally flame quenching. The appearance of partially sooting flame signifies the inherent, sooting non-uniformity in the counterflow flamelets. Specifically soot precursors experience longer residence times as they traverse in the radial direction. Clearly, we expect that the sooting non-uniformity influence the determination of laminar flame speed, as these flames are two-dimensional in nature. Furthermore, the 2-D effect renders the quantification of soot radiation impossible. Based on the above discussion, we conclude that the counterflow configuration is not suited for measuring flame speeds under sooting conditions.

To further demonstrate the concept of dual extinction limits observed experimentally and the radiation induced quenching, non-adiabatic, "non-sooting", rich methane/air flames are computed using GRI-Mech 1.2 and considering radiant loss from the combustion products, such as CO_2 , H_2O , and CO , in the optically-thin limit. Figure 5 shows that for $\phi > 1.68$ the non-adiabatic flames exhibit an isola response, with dual extinction turning points. The higher and lower values of the extinction stretch rate correspond to blow-off extinction and radiative quenching limits, respectively. In addition, it is seen that the isolas shrink with increasing ϕ such that steady burning will not be possible beyond $\phi \sim 1.87$. Note that this critical equivalence ratio is less than the flammability limit, ~ 2.38 , determined in this work on freely propagating flames.

PARTICLE THERMAL IONIZATION AND ITS EFFECT ON SOOT MASS GROWTH

It is well known that a large fraction of soot particles in flames are charged. Early studies [e.g., 5] showed that charged particles ($> 10,000 \text{ amu}$) and the number of charges on these particles could be satisfactorily accounted for by the Saha equation [6,7]. Depending on flame temperature, as much as 30% of flame soot may be thermally ionized [8]. These charged particles may exhibit large coagulation rates with neutral particles and particles of opposite charge because of collision enhancement related to

charge and charge-induced dipole and due to coulomb forces. Charged particles may also influence the surface reaction mechanism and rates. Previous studies [e.g., 9] showed that thermal ionization plays a minor role in soot mass growth. All of the analyses were based on assumed particle-size distribution functions (PSDFs). A more detailed analysis is yet to be conducted with size-resolved treatment of thermal ionization. In recent modeling studies on soot formation in laminar flames, thermal ionization was assumed to be unimportant and thus omitted from the model. This assumption needs to be verified by considering size-dependent thermal ionization kinetics and the dynamics of charged particles.

In this work, we developed a mathematical methodology for a combined neutral and charged system on the basis of a previously developed moment method [10]. The PSDFs of both uncharged and neutral particles are calculated and coupled by a reversible ionization reaction. The collision enhancement for charged-neutral and charged-charged interactions was estimated and incorporated in the Smoluchowski coagulation equation. Numerical simulations were conducted for soot formation in a low-pressure laminar premixed acetylene flame and results compared to the experimental data [11]. Figure 6 shows the relative volume fractions of neutral and charged particles. It is seen that the modeling results agree very well with the experimental data [11]. A comparison of the absolute number densities of charged and neutral particles also show good agreement between model and experiment.

Analysis of the rates of coagulation and mass growth led us to conclude that insofar as the simulation of soot formation in laminar premixed flames is concerned, the omission of thermal ionization does not lead to significant differences in the premixed soot mass growth. In most flames, thermal ionization leads to only a small number of charged particles, which coagulate with the neutrals at approximately the same rate as neutral-neutral coagulation. Only if the surface reaction between charged particle and gas molecules is enhanced should the thermal ionization play a more imminent role in soot mass growth.

REFERENCES

- [1] Eng, J. A., Zhu, D. L., and Law, C. K., *Proc. Combust. Inst.* 25: 1711-1718 (1994).
- [2] Milliken, R. C. *J. Phys. Chem.* 66: 794-801 (1962).
- [3] Takahashi, F. and Glassman, I. *Combust. Sci. Technol.* 37: 1-19 (1984).
- [4] Law, C. K. *Proc. Combust. Inst.* 22: 1381-1402 (1989).
- [5] Calcote, H. F., *Combust. Flame* 42: 215-242 (1981).
- [6] Sodha, M. S., Sagoo, M. S., Chandra, A., and Ghatak, A. K., *J. Appl. Phys.* 46:3806-3808 (1975).
- [7] Sodha, M. S., and Guha, S., *Adv. Plasma. Phys.* 4:219-309 (1971).
- [8] Calcote, H. F., Olson, D. B., and Keil, D. G., *Energy Fuel* 2: 494-504 (1988).
- [9] Prado, G. P., and Howard, J. B., in *Evaporation-Combustion of Fuels*, (J. T. Zung, Ed.), Advances in Chemistry Series 166, American Chemical Society, Washington, DC, 1978, pp.153-166.
- [10] Frenklach, M., and Wang, H., in *Soot Formation in Combustion—Mechanisms and Models*, (Bockhorn, H., Ed.) Springer-Verlag, Berlin, 1994, pp.165-190.
- [11] Homann, K. H., and Wolf, H., *Ber. Bunsenges. Phys. Chem.* 87:1073-1077 (1983).

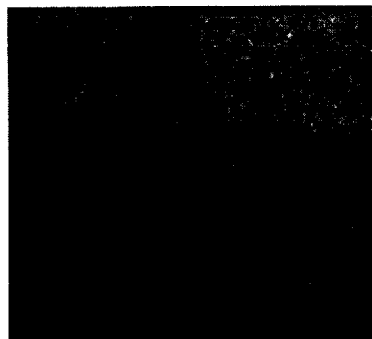
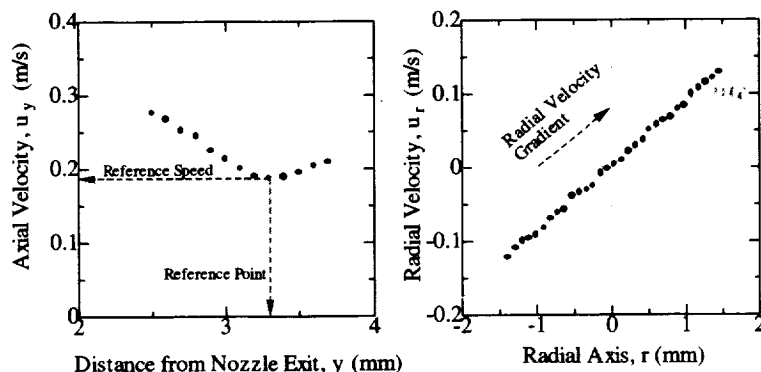


Figure 1. DPIV image of a $\phi = 2.2$ C_2H_4 /air counterflow flame at high stretch.



(a) Axial Velocity Profile (b) Radial Velocity Profile at the Reference Point
Figure 2. Axial velocity profile and radial velocity profile at the reference point for the image shown in Fig. 1.

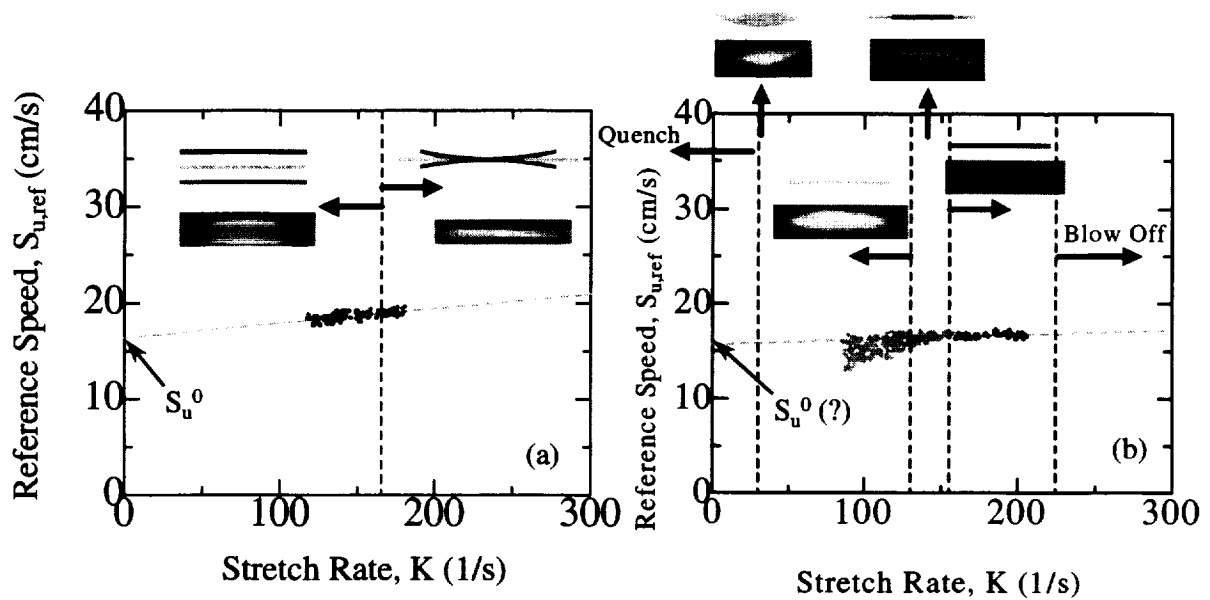


Figure 3 Variations of reference speed with stretch rate for rich ethylene/air flames: (a) $\phi = 2.2$ and (b) $\phi = 2.4$.

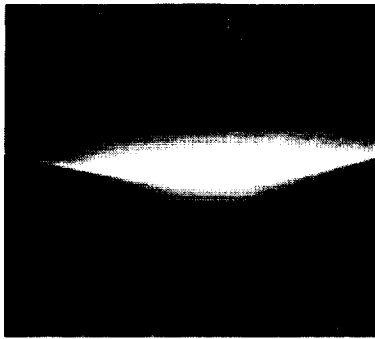


Figure 4. DPIV image of a $\phi = 2.4$ ethylene/air counterflow flame just before low-stretched quenching.

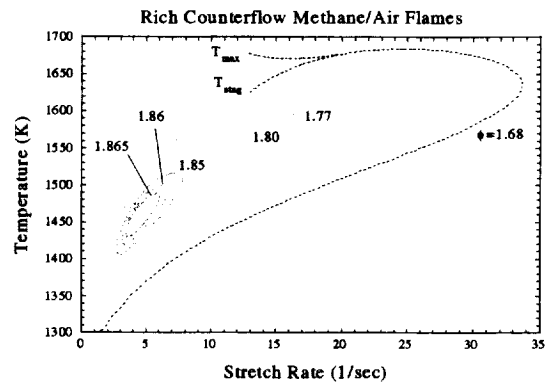


Figure 5. Flame temperature as a function of stretch rate for various rich methane/air mixtures.

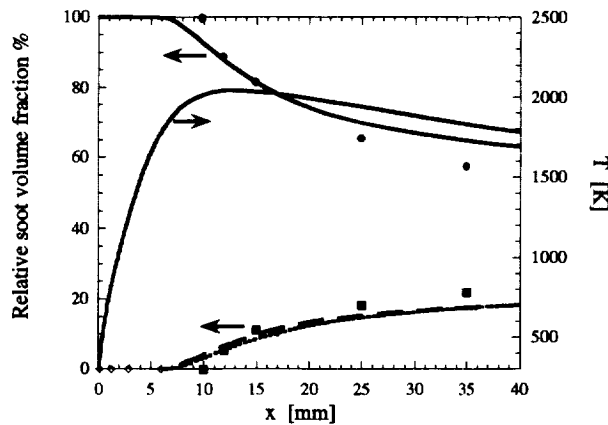


Figure 6. Computed (lines) and experimental (symbols, Ref 11) relative soot volume fractions: neutral particles—solid line circles; positively charged particles—dashed line and squares; negatively charged particles—dotted line and diamonds.

MICROGRAVITY PRODUCTION OF NANOPARTICLES OF NOVEL MATERIALS USING PLASMA SYNTHESIS

Michael Frenklach and Carlos Fernandez-Pello

Department of Mechanical Engineering
University of California at Berkeley
Berkeley, CA 94720-1740

The project has just been funded. The research goal is to study the formation in reduced gravity of high quality nanoparticulate of novel materials using plasma synthesis. Particular emphasis will be placed on the production of powders of non-oxide materials like diamond, SiC, SiN, c-BN, etc. The objective of the study is to investigate the effect of gravity on plasma synthesis of these materials, and to determine how the microgravity synthesis can improve the quality and yield of the nanoparticles. It is expected that the reduced gravity will aid in the understanding of the controlling mechanisms of plasma synthesis, and will increase the yield, and quality of the synthesized powder. These materials have properties of interest in several industrial applications, such as high temperature load bearings or high speed metal machining. Furthermore, because of the nano-meter size of the particulate produced in this process, they have specific application in the fabrication of MEMS based combustion systems, and in the development and growth of nano-systems and nano-structures of these materials. These are rapidly advancing research areas, and there is a great need for high quality nanoparticles of different materials.

One of the primary systems of interest in the project will be gas-phase synthesis of nanopowder of non-oxide materials. Under laboratory conditions, the best results have been obtained when synthesis took place in plasma-enhanced flame environments. Although the powder was of high quality, the yields were quite low and limited by the short length of the reaction zone and small residence time. Since in reduced gravity the flow residence times should be larger, as it has been observed with diffusion flames, it can be inferred that nanopowders formed in microgravity will have larger yields. Also, in microgravity the distribution of nucleates and the particle growth should be more uniform, as it has been observed which several other crystal growth processes, which should increase the quality of the powder. Furthermore, recent plasma reactors operate at atmospheric pressures, which although simplifies the reactor operation, has the disadvantage of the increased buoyancy that adversely affects the flame/plasma characteristics. In microgravity, this last deterring effect will be reduced. Thus, the operation of an elevated pressure plasma synthesis reactor in microgravity has the potential of producing a high yield, high quality, powder of other non-oxide materials, such as diamond, SiC, SiN, c-BN, since they have similar synthesis.

To accomplish the stated objectives, a plasma reactor, operating in the diffusion flame mode, will be designed and built at the University of California at Berkeley. The Berkeley team combines the experience in plasma synthesis of diamond and other non-oxide materials and in premixed, diffusion and condensed phase combustion in microgravity. The reactor will be designed, keeping in mind that it will be used in ground based microgravity facilities, to operate from low to near atmospheric pressure. The expectation is that the larger residence times and better nucleate uniformity obtained in microgravity, along with higher pressures, will result in powder of high yield and quality. Normal gravity experiments will be conducted to determine

the performance characteristics of the reactor, i.e., powder yield and quality, and to obtain data for comparison with the microgravity experiments. The initial experiments will be conducted with silicon carbide powder, which has similar synthesis to diamond but requires a somewhat simpler system. Upon successful accomplishment of this task, the experiments on diamond powder will be performed.

One critical parameter in the formation of significant quantities of these powders is time (of the order of hours), due to the small yield of the plasma synthesis process. For this reason, to produce significant amounts of powder, the synthesis must eventually be conducted in a facility with long microgravity operation periods, such as the Space Shuttle or Space Station. However, verification of the concepts supporting this proposal, and the reactor capabilities could be done in ground based microgravity facilities. We estimate that the total microgravity time provided by an aircraft parabolic flight, i.e., 30 to 40 parabolas with 20 to 30 seconds of microgravity each parabola, would be enough to determine the potential of the proposed system, and to obtain preliminary results. Thus the program is planned as a ground based research investigation. Given the industrial interest of these materials, and the current thrust in MEMS and nanotechnology, it is envisioned that the program could lead to advances in these fields, and perhaps the eventual commercial utilization of space based facilities to produce nanoparticles using the methodology presented here.

CARBON NANOSTRUCTURE: ITS EVOLUTION DURING AND ITS IMPACT UPON SOOT GROWTH AND OXIDATION

R. L. Vander Wal

The National Center for Microgravity Research at The NASA-Glenn Research Center

Introduction

Soot impacts the performance of power and propulsion systems, is a hazard of unwanted fires and is the main combustion generated pollutant. Responsible for an estimated 60,000 deaths per year in the U.S. alone, the EPA's new PM 2.5 criteria for particulate matter reflects increasing recognition of the health hazards associated with soot. Combustor ignitors and fuel injectors can become fouled with flame generated soot. Continuum radiation from soot is the main heat load upon combustor components and linings and is ultimately responsible for their failure. The spread of unwanted fires largely occurs through preheating from soot radiation. While an unwanted pollutant, soot also causes the release of substantial CO emissions from fires and unburned hydrocarbons in engines.

As most practical flames are turbulent diffusion flames, soot processes within such flames are of great relevance. Given the prevalent fuel-rich conditions at elevated temperatures within such flames, soot formation is inevitable. In contrast to seeking control of soot inception and growth, an alternative strategy is to focus on soot removal through oxidation. For example, modification of fuel/air mixing, reburning and exhaust gas recirculation represent parameters and processes that can be adjusted in existing practical devices to facilitate soot burnout by both O₂ and OH. Such process control and design require accurate models of soot oxidation processes. Current models for soot oxidation are inhibited by widely varying values for soot oxidation rates [1]. Values for OH collision efficiencies vary widely, ranging from 0.13 in premixed flames [2], to 0.3 in shock tubes [3] while from 0.11 to 0.01 in diffusion flames [4]. Similar uncertainties exist in O₂ oxidation rates with rates varying by factors of +6 to - 20 relative to the Nagle Strickland-Constable rate for graphite oxidation [5].

An entirely neglected aspect in the relatively few oxidation studies performed to-date is soot nanostructure, its evolution during combustion and its impact on oxidation. Soot nanostructure is defined here as the local spatial arrangement and orientation of nanoscale graphene layers. In contrast, the relation between carbon structure and reactivity is well-known in carbon science from thermal and oxidative studies of coal, char and graphite [6-8]. Similarly for soot, as the nanostructure evolves, the relative number and accessibility of potential reactive carbon layer edge sites (aryl C-H bonds) changes. It is these sites that are potentially accessible for H-atom abstraction followed by molecular (acetylene) addition (HACA mechanism) [9], potential rearrangement and/or bonding with adjacent layer planes (graphene layer plane growth, i.e. graphitization) or for reaction with O₂ or OH (oxidation). Larger (longer) graphene layer planes, larger (and hence fewer) crystallites and concentrically oriented crystallites (lower edge site accessibility) result in fewer potential reaction sites for these reactions. In contrast, such structures are desirable towards purposeful synthesis of ordered carbon materials such as fullerenic structures [10].

To-date, there has been little systematic study of the soot nanostructure evolution during combustion as a function of thermal or oxidative treatments. Given this, it is not surprising that there is also an absence of detailed data regarding the impact of soot nanostructure upon oxidation processes (and rates) and upon purposeful growth of highly ordered carbon materials. Buoyancy-induced convection prevents logical independent variation of the temperature and residence time necessary for defining the range of conditions under which such changes occur. Consequently nanostructural changes in soot have yet to be directly studied within combustion processes and their impact quantified.

OBJECTIVES

In response to this void of knowledge and potential impact, it is main goal of the proposed research to demonstrate the importance of soot particle nanostructure by defining its degree of impact on oxidation and growth. Secondly, this research will examine the effect of chemical environment and temperature-time history upon the development of desirable ordered carbonaceous (fullerenic) nanostructures.

APPROACH

Microgravity will be used to provide a range of conditions for studying the influence of growth species, temperature conditions, their individual and combined effect upon the oxidation of the soot and synthesis of ordered carbon materials. Microgravity will allow the independent control of temperature and residence time for separating the solid state and gas-phase processes. In the absence of buoyancy, spatial gradients are relaxed to allow resolution of the soot nanostructure development. Temperature gradients are greatly reduced allowing intelligible temperature-time trajectories. Finally, residence times can be extended to investigate kinetic temperature dependencies.

In contrast to past experimental studies, these experiments will use direct measurements from transmission electron microscopy (TEM) images rather than inferences based only on light extinction and scattering for oxidation measurements and extraction-based procedures for fullerenic materials. High-resolution TEM (HRTEM) and image analysis will be used to quantify the soot graphitization and order levels in response to growth conditions, thermal and oxidative treatment, to assess the impact of nanostructure upon oxidation and to search for fullerenic structures through variation of inception/growth conditions. Soot surface nanostructure will be probed by scanning tunnelling microscopy (STEM). The soot collection will be performed by thermophoretic sampling. Flame measurements will consist of temperature via thermocouples and 2-wavelength pyrometry. The oxidizing species concentration and temperature will be measured directly using diode laser absorption spectroscopy. Combined with a characterized chemical environment, quantitative analysis of the impact of nanostructure upon soot oxidation and purposeful growth along specific trajectories in chemical environments at known temperatures will be enabled. Armed with experimental data, model development of soot oxidation including nanostructural changes can be developed and tested. The experimental configurations will consist of various dual flame configurations.

SUMMARY

The proposed work is a ground-based study to define and quantify soot nanostructural changes in response to growth conditions, thermal and oxidative treatments and to quantify their impact upon further oxidation and growth of highly ordered carbon materials. Experimental data relating soot oxidation rates to multiple oxidizing species concentrations will directly test for additive or synergistic soot oxidation rates. Such validation is central for assessing the applicability of individual soot oxidation rates and designing oxidative strategies for controlling soot loadings in and emissions from turbulent combustion processes. Through these experiments, new insights into soot nanostructure evolution during and its impact upon oxidation by O₂ and OH will be realized. It is expected that the results of this effort will spawn new research directions in future microgravity and 1g environments. Issues raised by positive or even negative demonstration of the hypotheses of this proposal have direct bearing on modelling and controlling soot formation and its destruction in nearly every combustion process producing soot.

ACKNOWLEDGEMENTS

This work is supported by a NASA NRA 99-HEDs-01 combustion award administered through NASA cooperative agreement NAC3-544 with The National Center for Microgravity Research on Fluids and Combustion (NCMR) at The NASA-Glenn Research Center.

REFERENCES

1. Kennedy, I. M., Prog. Energy Combust. Sci. 23:95 (1997).
2. Neoh, K. G., Howard, J. B. and Sarofim, A. F., in Particulate Carbon, D. C. Siegla and G. W. Smith (eds.) Plenum Press, New York p. 261 (1981).
3. Roth, P., Brandt, O. and Gersum, S. Von., Twenty-Third Symposium (International) on Combustion, The Combustion Institute, Pittsburgh, PA p. 1485 (1990).
4. Haudiquert, M., Cessou, A., Stepowski, D. and Coppalle, A., Combust. and Flame 111:139 (1997).
5. Levendis, Y. A., Flagan, R. C. and Gavalas, G. R., Combust. and Flame 76:221 (1989).
6. Ljubisa, R., Walker, P. L. and Jenkins, R. G., Fuel 62:849 (1983).
7. Hurt, R. H., Dudek, D. R., Longwell, J. P. and Sarofim, A. F., Carbon, 26:433 (1988).
8. Rosner, D. E. and Allendorf, H. D., AIAA Journal 6:650 (1968).
9. Frenklach, M. and Wang, H., Twenty-Third Symposium (International) on Combustion, The Combustion Institute p. 1559 (1990).
10. Grieco, W. J., Howard, J. B., Rainey, L. C., Vander Sande, J. B., Carbon 38:597 (2000).-----

ELECTRIC FIELD EFFECTS IN SELF-PROPAGATING HIGH-TEMPERATURE COMBUSTION SYNTHESIS UNDER MICROGRAVITY CONDITIONS

Z. A. Munir and B. D. Shaw, University of California, Davis

INTRODUCTION

Self-propagating high-temperature synthesis (SHS) has been used to form many materials [1]. SHS generally involves mixing reactants together (e.g., metal powders) and igniting the mixture such that a deflagration wave passes through the mixture. The imposition of an electric field (AC or DC) across SHS reactants has been shown to have a marked effect on the dynamics of wave propagation and on the nature, composition, and homogeneity of the product (e.g., [2-5]). The use of an electric field with SHS has been termed "field-assisted SHS".

A schematic of the field-assisted SHS process is shown in Fig. 1. The field overcomes thermodynamic and kinetic limitations of the SHS process, making possible the synthesis of materials that could not otherwise be prepared with SHS. In such cases, combustion waves are initiated above a threshold field value and wave velocities and temperatures are directly affected by the field magnitude. The degree of activation by the field (e.g., combustion rate) is related to the current density distribution within the sample, and is therefore related to the temperature-dependent spatial distribution of the effective electrical conductivity of reactants and products.

The electric field has been shown to influence the nature of the product, the composition of phases in a composite, and the homogeneity (elemental distribution) in solid solutions. Furthermore, the field can influence other important SHS-related phenomena including capillary flow, mass-transport in porous media, and Marangoni flows. These phenomena are influenced by gravity in conventional SHS processes (i.e., without electric fields) [6-9]. As a result the influence of the field on SHS under reduced gravity is expected to be different than under normal gravity. It is also known that heat loss rates from samples, which can depend significantly on gravity, can influence final products in SHS (e.g., [10]). For these reasons, it is useful to study field-assisted SHS processes under conditions where gravity effects are reduced to small levels.

This research program is focused on studying field-assisted SHS under reduced gravity conditions. The broad objective of this research program is to understand the role of an electric field in SHS reactions under conditions where gravity-related effects are suppressed. The research will allow increased understanding of fundamental aspects of field-assisted SHS processes as well as synthesis of materials that cannot be formed in normal gravity.

RESEARCH EFFORTS

The research will investigate the following topics.

- (a) The effect of the field on the dynamics of SHS waves in the absence of gravitationally induced buoyancy and phase separation effects. This aspect of the work includes the effect of the field on wave velocity and temperature, on the mode of propagation (e.g., planar or spinning) and its transition, and on the conversion profile. Implied in this part of the research is a significant effect of the field on interfacial energies, capillary spreading, mass transport in porous media, and electrically-induced Marangoni flows.

- (b) The effect of the field on phase formation and structure evolution in SHS: This research has practical implications as well as fundamental implications. We plan to investigate the role of the field on product formation (nature of the product, composition of phases, homogeneity of the phase(s), and grain size).

The planned work includes both terrestrial and reduced gravity experiments. The latter will be carried out in parabolic flights and in drop towers. The parabolic flight experiments will use existing facilities (COSYMTM, developed by Guigne International, Ltd.) in NASA's KC-135 aircraft. Modifications will be made to accommodate the requirements for electric field application, interferometry and thermistor temperature measurements. Drop tower experiments will be carried out in the NASA Glenn Research Center 2.2 s Drop-Tower, and additional drop tower experiments will be carried out in Japan by one of the collaborating scientists (collaborations are described in a later section).

The research topics will be investigated with different systems that will produce varied amounts of liquid during combustion. For example, the system Si + C will allow investigation of the case where one reactant melts and the other does not, the system Ta + C will allow investigation of a system where neither the reactants nor the products melt, and the system FeAl will allow investigation of the case where both reactants and products melt. These systems are expected to respond to the gravity level in different ways, e.g., through liquid transport effects.

It is also planned that quenching experiments will be performed. This will be accomplished by turning off the electric field during the combustion process. The removal of the field will cause the deflagration wave to quench under certain conditions, essentially freezing the structure of the wave. Wave structure will be analyzed using XRD, SEM and EPMA.

We plan to quantify temperature fields near samples with interferometry techniques [11]. These techniques will be used in the parabolic flight experiments as well as the drop tower experiments. Because the composition of the gas phase should not change appreciably, the interferometry measurements can be used to infer gas-phase temperature profiles, which will be verified with the point measurements from thermistors. In this way, temperature gradients, and thus convective heat fluxes, can be evaluated at the sample surfaces. The interferometry experiments should also provide some information on gas-phase velocity profiles. Density fields near the samples should be approximately two-dimensional so that interferometry methods can be used to determine gas temperature fields (and thus heat transfer rates) near and at sample surfaces with reasonable accuracy. For simplicity as well as for robustness in microgravity, a point diffraction interferometer (PDI) system will be used. The interferometer system will be comprised of a low-power visible laser with associated optical components [12]. A schematic of the apparatus to be used in the NASA Glenn 2.2 s Drop Tower is shown in Fig. 2.

A radiometer will also be installed in the parabolic flight apparatus. The radiometer will allow radiant heat loss rates from sample surfaces to be measured. One other system to be used in the parabolic flight apparatus as well as in the ground experiments is a miniature spectrometer coupled to a fiber optic probe; the probe will be focused on small areas of the surface of a sample. This will allow measurement of surface temperatures through multi-wavelength pyrometry. These measurements may also provide an indication of intermediate species present during the combustion. Through changes in buoyant heat transfer rates, it is expected that there will be significant changes in radiant heat loss characteristics as gravity levels are altered.

We also plan to do modeling studies. This will include both computational and asymptotic efforts. The computational efforts will involve extending and using previously developed

numerical models [3,13,14] to account for phenomena such as melting, capillary flows, and buoyant flows. The model will also be extended to three spatial dimensions, which will allow simulation of spin combustion. The present numerical model is based on finite-difference methods. This methodology will be maintained in the extension of the model. However, we now plan to use adaptive gridding or overset grid techniques, which will allow more accurate resolution of thin zones without significantly compromising overall computation times.

The asymptotic studies will be concerned with determining the influences of electric fields on stability and extinction of field-assisted SHS waves. Only one study has been published in this area [15]. However, the referenced work did not consider many phenomena that are relevant to field-assisted SHS, especially when a liquid zone is present. For example, it did not consider capillary transport of liquids as well as local variations in surface tension and contact angles from thermal or electrical effects. These factors will be included in the asymptotic analyses.

COLLABORATION

This research program represents a collaborative effort between the PIs at UC Davis and scientists and engineers in Canada, Italy, Germany, Japan, and the US. The UC Davis work represents an interdisciplinary approach with expertise from Materials Science (Z. A. Munir: self-propagating combustion synthesis; field-activated SHS) and Mechanical Engineering (B. D. Shaw: gravity effects in combustion; fluid flow and heat transfer). In Japan, Professor Makino (Mechanical Engineering, Shizuoka University) will be involved in modeling aspects and plans to carry out drop-tower experiments (pending funding from NEDO) on systems without field activation to provide a well-characterized baseline. In Italy, Professor Cao (Chemical Engineering, University of Cagliari) will use European aerospace facilities to conduct quenching experiments in reduced gravity using the copper-wedge technique. Doctor Zell of the Daimler Chrysler Company (Friedrichshafen, Germany) and Doctor Guigne of Guigne International (Newfoundland, Canada) will provide expertise on reduced gravity experiments, and the motivation of an industrial interest and possible technology transfer. Collaboration with Professor Moore of the Colorado School of Mines will provide a link to NASA's Center for Commercial Applications of Combustion in Space (CCACS).

REFERENCES

1. *Combustion and Plasma Synthesis of High-Temperature Materials*, edited by Z. A. Munir and J. B. Holt, VCH Publishers (1990).
2. Z. A. Munir, W. Lai, and K. Ewald, *U.S. Patent* No. 5,380,409, January 10, 1995.
3. A. Feng and Z. A. Munir, *Metall. Mater. Trans.*, **27B**, 581 (1995).
4. Z. A. Munir, *Z. Phys. Chem.*, **207**: 39 (1998).
5. H. Xue and Z. A. Munir, *J. Euro. Ceram. Soc.*, **17**: 1787 (1997).
6. K. G. Shkadinsky, G. V. Shkadinskaya, and B. J. Matkowsky, *Combust. Sci. Tech.*, **118**: 313 (1996).
7. O. Odawara, K. Mori, A. Tanji, and S. Yoda, *J. Mater. Synth. Process.*, **1**: 203 (1993).
8. K. R. Hunter and J. J. Moore, *J. Mater. Synth. Process.*, **2**: 355 (1994).
9. A. Mukasyan, A. Pelekh, A. Varma, A. Rogachev, and A. Jenkins, *AIAA J.*, **35**: 1821 (1997).

10. H. C. Yi, T. C. Woodger, J. J. Moore, and J. Y. Guigne, *Metall. Mater. Trans.*, **29B**: 889 (1998).
11. R. J. Goldstein and T. H. Keuhn, "Optical Systems for Flow Measurement: Shadowgraph, Schlieren and Interferometric Techniques," Chapter 7 of *Fluid Mechanics Measurements*, 2nd ed., R. J. Goldstein, ed., Taylor and Francis (1996).
12. J. S. Goldmeer, D. L. Urban, and Z.-G. Yuan, *AIAA Journal* (submitted).
13. A. Feng, O.A. Graeve, and Z. A. Munir, *Comput. Mater.Sci.*, **12**: 137 (1998).
14. E. M. Carrillo-Heian, O.A. Graeve, A. Feng, J. A. Faghih, and Z. A. Munir, *J. Mater. Res.*, **14**: 1949 (1999).
15. I. A. Filimonov and N. I. Kidin, Twenty-Fourth Symposium (International) on Combustion, The Combustion Institute, Pittsburgh, p. 1893 (1992).

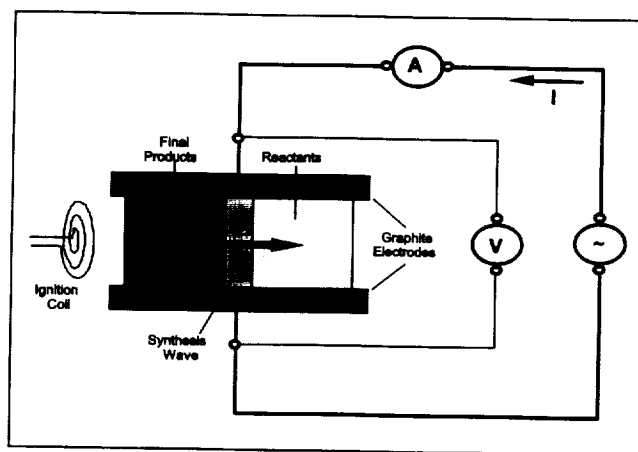


Figure 1 – Schematic representation of the field-assisted SHS process.

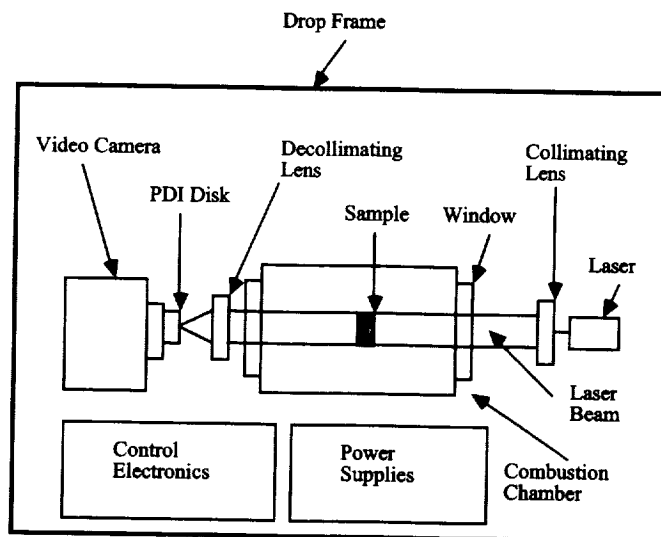


Figure 2. Schematic of the drop rig to be used in the NASA Glenn 2.2 s Drop Tower. For clarity, some components are not shown.

INVESTIGATION OF THE LIFTOFF AND BLOWOUT OF TRANSITIONAL AND TURBULENT JET FLAMES

James J. Riley, George Kosály, and John C. Kramlich

University of Washington

INTRODUCTION

The problems of turbulent jet flame liftoff and blowout are of critical importance to the safety and reliability of a variety of combustion devices. Developing a fundamental explanation of the factors governing these phenomena has, however, been surprisingly difficult. Competing theories focusing on both premixed and non-premixed behavior at the base of the flame have been proposed. The more recent finding that liftoff and blowout are influenced by buoyancy [1,2,3] was unexpected by many researchers. An examination of the data from this finding suggests the hypothesis that gravity influences flame extinction and stabilization through the role buoyancy plays in transition to turbulence. In this study we are applying three-dimensional direct numerical simulation (DNS) and concurrent theoretical analysis to (1) test this and other hypotheses, (2) identify the governing mechanisms for liftoff and blowout, (3) determine which of the various modeling approaches are most consistent with the governing mechanisms, and (4) devise means for controlling liftoff and blowout (*e.g.*, via harmonic forcing of the jet). Further expected outputs are the use of the numerical results to suggest critical experiments for low-gravity environments, and the use of numerical simulation to guide planned low-gravity experiments.

Although DNS cannot be a complete substitute for experiments, it does have the unique advantage of providing the full three-dimensional, time-resolved field of all flow properties. Thus, it forms an ideal complement to physical experiments since it can be used to critically test mechanistic ideas and models for turbulent reacting flows. Continuing advances in computer speed, and the development of algorithms that take full advantage of today's massively parallel computers (*e.g.*, the Cray T3E), have made it possible to numerically resolve a turbulent reacting jet at moderate Reynolds numbers. With regard to developing a means for controlling the processes, one of the most important findings over the past several decades in turbulence research is that turbulence can be controlled in various ways, *e.g.*, by application of forcing at specific frequencies that are tuned to flow instabilities. This suggests that low-energy forcing at specific frequencies could significantly impact liftoff and blowout, and lead to means for controlling these processes (*e.g.*, extending stability limits).

LIFTOFF AND BLOWOUT OF TURBULENT DIFFUSION FLAMES

At a sufficiently low exit velocity a jet diffusion flame is attached to the nozzle. When the exit velocity is increased above a certain value, the flame lifts off and stabilizes at a distance from the nozzle referred to as the liftoff height; the liftoff height increases with increasing exit velocity. Between the nozzle exit and the liftoff height, partial premixing takes place. When the velocity becomes higher than a certain value (the blowout velocity), the flame extinguishes. In recent years liftoff, and the accompanying stabilization of turbulent diffusion flames at the liftoff height, has become the canonical problem for studying partially premixed combustion [4].

The normal gravity experimental results regarding the liftoff and blowout of turbulent flames have been summarized in the correlations of Kalghatgi [5,6]. The Kalghatgi correlations appear to accurately describe the extinction-reignition behavior of turbulent flames without accounting for buoyancy. Recent laboratory results of Bahadori et al.[1] and Hegde et al.[2,3], however, in both normal gravity and microgravity, indicate a strong effect of buoyancy on the results, and establish that gravitational effects on flames are more ubiquitous than commonly thought.

RESEARCH

To explain this unexpected influence of buoyancy on jet flame liftoff and blowout, it is hypothesized that buoyancy modifies the transition to turbulence. We have recently initiated a study which employs direct numerical simulations and accompanying theoretical analysis to (1) test this and other hypotheses, (2) address flame stabilization mechanisms, (3) evaluate models which predict these phenomena, and (4) develop concepts (*e.g.*, forcing) to control these processes. In particular the research consists of linear stability analysis, direct numerical simulations, and theoretical modeling.

Linear stability analysis

The microgravity experiments addressing reacting turbulent jets appear to be in the transitional regime. It is possible, therefore, that the effect of buoyancy under normal gravity is to cause the flow to more readily transition to fully-developed turbulence. Under microgravity, where buoyancy is inhibited, the flow never becomes fully turbulent, at least upstream of the location of liftoff. This could explain the observed differences in the experiments. To understand the effect of buoyancy on transition, it is important to understand the stability characteristics of the basic flow. Furthermore, in order to simulate transitional and turbulent jet flows, and to learn how to control the turbulence, it is again important to know these stability characteristics. Thus we are first performing linear stability analysis of the reacting buoyant and non-buoyant jets; methods similar to those employed by previous researchers who have addressed the stability of reacting mixing layers are being utilized (*e.g.*, Papas et al.[7]; Day et al.[8]), including some recent research in the Microgravity Combustion Science Program [2]. This analysis will be carried out for a range of the acceleration of gravity g , and thus the effects of buoyancy on flow stability will be determined. In addition, from the analysis the relevant unstable modes and their corresponding frequencies would be obtained; these can then be used to guide the inflow and forcing conditions for simulating transitional and turbulent flows. For example, typical outputs from such analyses could be plots of growth rates versus frequency for progressively increasing values of g , demonstrating how g influences the instabilities in the jet flame.

Direct numerical simulations

One goal of the direct numerical simulations is to address the various questions and hypotheses that have been raised regarding the effects of buoyancy on reacting, turbulent jets. For example, are the differences in the experiments reported by Bahadori et al.[9] due to gravity influencing flame extinction and stabilization through the role that buoyancy plays in the transition to turbulence? If so, is this effect due to the buoyancy in the exiting jet, or due to the buoyancy downstream caused by the chemical reaction? Can the nature of the

end flames be resolved in direct numerical simulations? Does it have a triple flame structure? If so, why have not PLIF-type observations resolved this structure? Does buoyancy alter the structure of the end flame?

To address hypotheses and issues such as these, we are initiating two series of direct numerical simulations. The first series will involve simulating three-dimensional, transitioning flows. The flow conditions will be similar to the conditions for the experiments of Bahadori et al.[9], with similar chemical composition, and similar Reynolds and Froude numbers at the nozzle exit. Results from the linear stability analysis, especially with regard to the frequency and shape of unstable disturbances, will be employed in the inlet boundary conditions. Also, models for intermittent turbulent slugs exiting from the pipe flow, as observed in the experiments, will be used as inlet conditions to mimic these observations. Simulations will be carried out for a range of the acceleration of gravity (from $-g$, through μg and to $+g$), and for a range of inlet conditions. The results from these simulations will be analyzed with special emphasis on interpreting the laboratory experiments of Bahadori et al., and determining how flow modulation affects the flow field and chemical reactions.

The second series of simulations will address fully turbulent jet flames. Again similar conditions to the laboratory experiments being carried out in the Microgravity Combustion Research Program will be utilized, in terms of chemical composition and of the outflow Froude number. The Reynolds number will be made as high as the numerical methods will allow, although it is realized that it will not be possible to match the Reynolds numbers of some of the laboratory experiments. It is felt, however, that, due to the Reynolds number similarity of higher Reynolds number free shear flows, these lower Reynolds number simulations should still provide qualitatively and semi-quantitatively accurate results. Again simulations will be performed for a range of the acceleration of gravity (from $-g$, through μg , and to $+g$), and for a range of forcing parameters. The latter will be chosen based upon the results of the transiting flow simulations.

At this point, various hypotheses, such as the one regarding the influence of buoyancy on transition, can be tested. For example, simulations with $1g$ and μg , and accompanying stability analysis, can determine whether and how buoyancy affects transition to turbulence. Furthermore, the simulations can also determine if liftoff and blowout are affected by gravity, and if so, why. The simulations will be analyzed with special emphasis on: interpreting the laboratory experiments; distinguishing the various liftoff and blowout mechanisms; and determining how to best modulate the flows to control liftoff and blowout. In addition, if found to be appropriate, direct numerical simulations will be performed to help interpret and to guide the planning of future laboratory experiments.

Modeling

Although we are planning to consider other modeling as well, our main approach will be to apply the method of Peters [4] to compute liftoff in $1g$ and μg flames. In turbulent jet flames in normal gravity, the $k-\epsilon-g$ turbulence model (Kent and Bilger [10]) with Rodi's [11] correction is applicable and can be used to compute the averages and root means squares appearing in Peter's theory. The modeling of microgravity flames would, however, necessitate new tuning of one of the coefficients, due to the change in entrainment rates. Unfortunately, the measured microgravity flames appear to be more transitional than turbulent; therefore they cannot be used with confidence to tune the RANS coefficients. Direct numerical simulation

may offer an attractive way out of this difficulty.

Whether the new procedure of Peters will validly predict liftoff heights depends on two issues. (a) Are the physical ideas that form the basis for the assumptions in the theory valid? (b) Can the averages and root mean squares appearing in the theory validly computed? Using DNS we can take the parameters directly from the simulations and attack the basic physical question of the validity the assumptions

References

- [1] Bahadori, M. Y., D. P. Stocker, D. F. Vaughan, L. Zhou and R. B. Edelman. 1993. in *Modern Developments in Energy, Combustion and Spectroscopy*, Pergamon Press, pp. 46-66.
- [2] Hegde, U., L. Zhou and M. Y. Bahadori. 1994. *Comb. Sci. and Tech.*, Vol. 102, pp. 95-113.
- [3] Hegde, U., Z. G. Yuan, D. P. Stocker and M. Y. Bahadori. 1999. *5th International Microgravity Combustion Workshop*, pp. 259-262.
- [4] Peters, N. 2000. *Turbulent Combustion*, Cambridge University Press.
- [5] Kalghatgi, G. T. 1981. *Combust. Sci. Tech.*, Vol. 26, pp. 233-239.
- [6] Kalghatgi, G. T. 1984. *Combust. Sci. Tech.*, Vol. 41, pp. 17-29.
- [7] Papas, P., P. A. Monkewitz and A. G. Tomboulides. 1999. New instability modes of a diffusion flame near extinction. *Phys. Fluids*, Vol. 11, pp. 2818-2820.
- [8] Day, M. J., W. C. Reynolds and N. N. Mansour. 1998. The structure of the compressible reacting mixing layer: insights from linear stability analysis. *Phys. Fluids*, Vol. 10, pp. 993-1007.
- [9] Bahadori, M. Y., U. Hegde and D. P. Stocker. 1997. Structure of microgravity transitional and pulsed jet diffusion flames. Fourth International Microgravity Combustion Conference, pp. 179-184.
- [10] Kent, J. H., and R. W. Bilger. 1976. The prediction of turbulent diffusion flame fields and nitric oxide formation. *Proceedings of the Combustion Institute*, Vol. 16, pp. 1643-1656.
- [11] Rodi, W. 1980. in *Prediction Methods for Turbulent Flows*, (W. Kollmann, Ed.), Hemisphere, 1980.

UNSTEADY MULTIDIMENSIONAL NUMERICAL SIMULATIONS OF FLAME VORTEX INTERACTIONS – A NEW STUDY

G. Patnaik and K. Kailasanath

The Laboratory for Computational Physics and Fluid Dynamics

Naval Research Laboratory

Washington, D.C. 20375

INTRODUCTION

Theoretical analysis, experimental observations, and numerical simulations have all indicated that flame-vortex interactions play an important role in the propagation and extinguishment of turbulent flames in microgravity [1]. Although significant progress has been made, there are still a number of poorly understood phenomena that need to be studied. Most studies of flame-vortex interactions ignore the effects of gravity and experiments are usually conducted in Earth gravity. Recently, Sinibaldi et al. [2] and Driscoll and coworkers [3] have reported the results of drop-tower experiments that show that for some vortex strengths, the reduction in gravity can significantly alter the structure of the flame produced by the flame-vortex interaction.

There are a number of plausible and often conflicting explanations for the differences between the dynamics and extinction of flames interacting with a vortex in microgravity and on Earth. Both experimental and numerical studies indicate the need to study systematically the relative importance of strain rate, heat losses, and gravity in premixed flame-vortex interaction. A numerical study, in which the various effects, such as gravity, can be independently controlled and isolated, will help answer some of these questions. Zero-gravity can be easily set up in numerical simulations. Better control of initial and boundary conditions are also possible numerically, leading to “cleaner” experiments.

In our study, started February 2001, we will use detailed time-dependent, multi-dimensional numerical simulations to investigate the relative importance of the processes occurring in flame-vortex interactions in normal gravity and microgravity. A richer understanding of flame-vortex interactions is possible if the numerical simulations closely complement laboratory experiments. The results of our numerical simulations will be correlated qualitatively and, whenever possible, quantitatively with the past and current experiments in the NASA Microgravity Combustion Sciences program, such as those by Prof. Driscoll (University of Michigan). The simulations may also be used as a tool to guide future microgravity experiments.

COMPUTATIONAL TOOLS

The numerical simulations will be performed using the computational model developed at NRL, FLAME3D. FLAME3D is a parallel multi-dimensional (either two- or three-dimensional) flame

model based on FLIC2D [4], which has been used extensively to study the structure and stability of premixed hydrogen and methane flames. Many sub-models in FLAME3D are based on FLAME1D [5], a one-dimensional, time-dependent Lagrangian model that has been validated and applied to various studies of flame phenomena

FLAME3D uses the BIC-FCT method for convection [6], which combines an explicit high-order, nonlinear multidimensional FCT method [7] with an implicit correction process. This maintains high-order accuracy and yet removes timestep limitations imposed by sound speed.

In FLAME3D, thermal conductivity of the individual species is modeled by a polynomial fit in temperature to existing experimental data. Individual conductivities are then averaged using a mixture rule [5, 9] to get the thermal conductivity coefficient of the gas mixture. A similar process is used to obtain the mixture viscosity from individual viscosities. Heat and momentum diffusion are then calculated explicitly using these coefficients.

Binary mass-diffusion coefficients are represented by an exponential fit to experimental data, and the individual species-diffusion coefficients are obtained by applying mixture rules [5]. The individual species-diffusion velocities are determined explicitly by applying Fick's law followed by a correction procedure to ensure zero net flux [8].

Radiative heat losses from H_2O and CO_2 are included using an optically thin model.

The chemical reaction-rate equations are modeled and solved using CHEMEQ [9]. Because of the complexity of the reaction scheme and the large number of computational cells, the solution of the chemical rate equations takes a large fraction of the total computational time.

All of the chemical and physical processes are solved sequentially and then coupled asymptotically by timestep splitting [10].

PREVIOUS WORK

In our previous work, sponsored by NASA, we examined the effect of gravity on the flame-vortex interaction in lean methane-air flames [11]. We examined the interaction of downward propagating flames with vortices of different strengths and then compared these results to those for zero gravity and upward propagating flames. All our simulations indicated that buoyancy controls the flame shape after the flame-vortex interaction. Gravity has the strongest effect on weak vortices with small Froude numbers.

These computational studies were restricted to the examination of an idealized flame and vortex. Qualitative agreement with experiments of Driscoll and coworkers [4] was satisfactory, with better agreement observed for weaker vortices. Figure 1 below shows comparison of numerical and experimental OH concentration in a downward propagating flame interacting with an intermediate strength vortex strength.

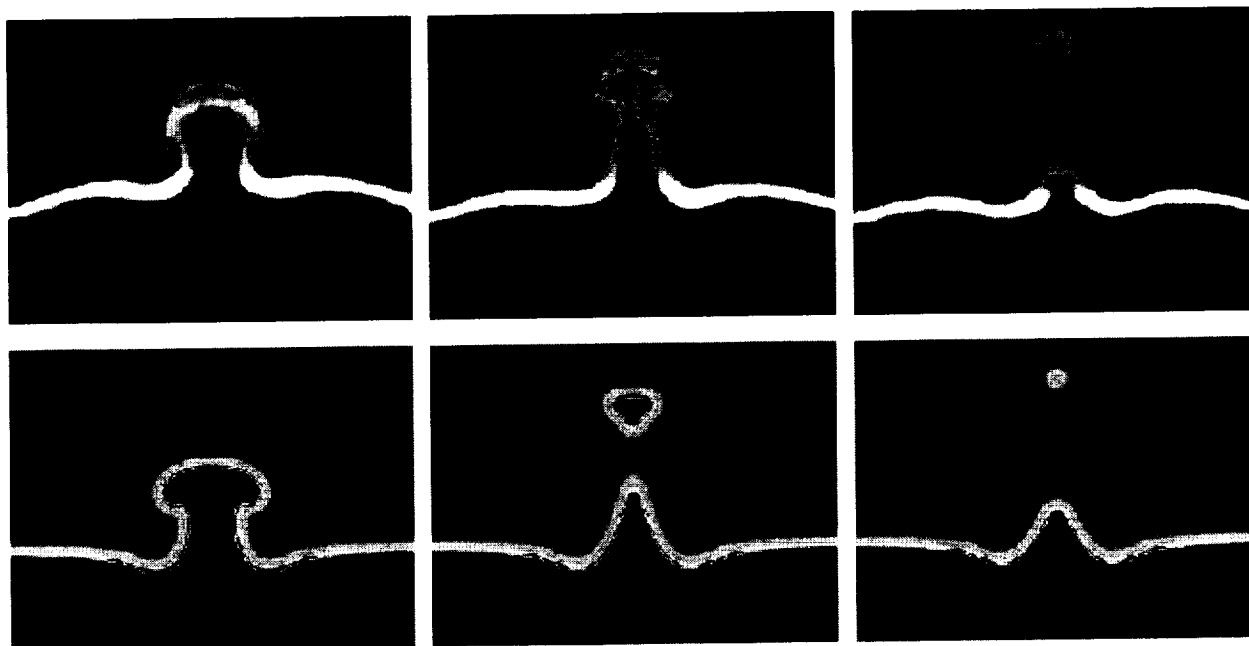


Fig. 1. Experimental (above) and numerical (below) comparison of OH concentration.

INITIAL RESULTS

An important goal of this study is to perform complete simulations of current microgravity flame-vortex experiments including the effects of flame curvature. In our earlier simulations, the flame is initially planar, being generated from a one-dimensional steady-state simulation. In the experiments, the microgravity flame is highly curved even before the interaction with the vortex. For vortices of sufficient size, the flame curvature can affect the flame-vortex interaction.

This flame curvature may be due to the initiation of the flame. So, in the current simulations, we propagate the flame from a small one-dimensional spherical flame and let it evolve into a curved shape. Figure 2 shows the interaction of an intermediate strength vortex with an initially-planar flame and with a curved flame resulting from the propagation from a small kernel. The vortex interacting with the initially-planar flame is 50% stronger than the one interacting with the curved flame. In both cases, pocket formation is observed. No pocket formation is observed in the initially-planar flame case if the vortex strength is kept the same as in the curved flame case.

FUTURE WORK

Complete simulations will be performed spanning the duration of the microgravity experiment. This will include the evolution of the vortex ring and the curved flame and the flame-vortex interaction itself. The goal is to obtain quantitative agreement with the microgravity and Earth gravity experiments. The simulations will be analyzed to obtain quantitative information on outstanding issues such as baroclinic vorticity production and the change in turbulent transport.

Flame-generated vorticity and its role when combined with the pressure gradient induced by gravity will be examined. The contribution of the initial flame curvature will be quantified.

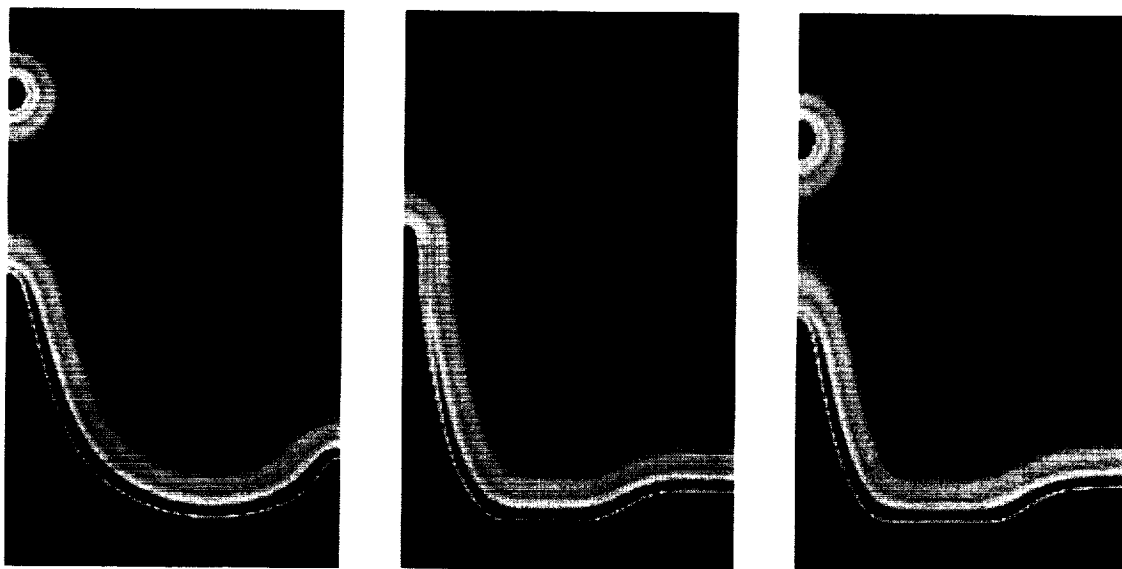


Fig. 2. OH mole fractions. Curved flame (left), planar flame (center), planar strong vortex (right)

- [1] Marble F., Growth of a Diffusion Flame in the Field of a Vortex, in *Recent Advances in Aerospace Science*, C. Bruno and C. Casci, Editors. 1985, Plenum, NY. pp. 395-413.
- [2] Sinibaldi, J., Driscoll, J., Mueller, C., and Tulkki, A., Flame-Vortex Interactions: Effects of Buoyancy from Microgravity Imaging Studies, AIAA Paper No. 97-0669, AIAA, 1997.
- [3] Driscoll, J., Private Communication, 1997.
- [4] Patnaik, G., Laskey, K., Kailasanath, K., Oran, E., and Brun, T., FLIC — A detailed, Two-Dimensional Flame Model, Memorandum Report No. 6555, NRL, Washington, DC, 1989.
- [5] Kailasanath, K., Oran, E. S., and Boris, J. P., A One-Dimensional Time-Dependent Model for Flame Initiation, Propagation, and Quenching, Memorandum Report No. 4910, Naval Research Laboratory, Washington, DC, 1982.
- [6] Patnaik, G., Guirguis, R. H., Boris, J. P., and Oran, E. S., *J. Comput. Phys.* 71:1-20, 1987.
- [7] Boris, J. and Book, D., Solution of Convective Equations by the Method of Flux Corrected Transport, in *Methods in Computational Physics*. 1976, Academic Press, NY, p 85.
- [8] Kee, R., Dixon-Lewis, G., Warnatz, J., Coltrin, M., and Miller, J., A FORTRAN Computer Code Package for the Evaluation of Gas-Phase Multi-Component Transport Properties, Sandia Report No. SAND86-8246, Sandia National Laboratories, Albuquerque, NM, 1986.
- [9] Young, T., CHEMEQ – A Subroutine for Solving Stiff Ordinary Equations, Memorandum Report No. 4091, Naval Research Laboratory, Washington DC, 1980.
- [10] Oran, E. and Boris, J., *Numerical Simulation of Reactive Flow*, Elsevier, NY, 1987.
- [11] Patnaik, G. and Kailasanath, K., Role of Gravity in Premixed Methane-Air Flame-Vortex Interactions, AIAA Paper No. 98-0742, AIAA, 1998.

FLAME PROPAGATION IN LOW-INTENSITY TURBULENCE UNDER MICROGRAVITY CONDITIONS

R. C. Aldredge

Mechanical & Aeronautical Engineering
University of California, Davis

INTRODUCTION

The goal of the research is to understand the influences of the hydrodynamic instability on premixed-flame propagation. It is known that coupling between flame and flow-field dynamics in association with the hydrodynamic instability may lead to flame-generated turbulence, flame acceleration and enhancement of burning rates [1]. As a result of such hydrodynamic coupling the transition from initially planar or wrinkled laminar flames to fast turbulent flames or detonations is possible, even when diffusive-thermal effects associated with non-unity reactant Lewis numbers are not destabilizing. It is important to identify methods of suppressing the hydrodynamic instability so as to insure fire safety, particularly in space.

Under normal-gravity conditions, it is generally possible to suppress the hydrodynamic instability by sufficient reduction of the flow cross-sectional area, thereby restricting flow disturbances to wavelengths below the unstable range, or by dilution of the reactants so as to limit the heat released by the flame [2]. However, these approaches are at the expense of increased heat loss and decreased reactant consumption rates. Furthermore, the effectiveness of these approaches may be severely limited in space, since under microgravity conditions there is no stabilizing influence of buoyancy and, as a result, the influence of the hydrodynamic instability may be stronger.

It has been demonstrated recently that one-dimensional acoustic waves can suppress the hydrodynamic instability and prevent the growth of flame-surface wrinkles under normal-gravity conditions [3]. An objective of the present work is to determine the effectiveness of such acoustic waves in suppressing the influence of the hydrodynamic instability on planar and weakly wrinkled flames under microgravity conditions, where the instability is expected to be stronger. Another objective of the work is to examine the influence of the hydrodynamic instability on flame propagation in low-intensity turbulent flow. In particular, it is of interest to determine the relationship between the burning rate and the intensity of turbulence and how this relationship is influenced by the hydrodynamic instability. Theoretical analyses neglecting hydrodynamic coupling have predicted two fundamentally different relationships, depending on the extent of randomness of the velocity fluctuations [4,5]. A third objective of the proposed work is to examine the effectiveness of low-intensity turbulence in suppressing the hydrodynamic instability. It is expected that high-intensity velocity fluctuations in the reactant flow, relative to the laminar burning speed, will suppress the influence of the hydrodynamic instability. It is of interest to determine the level of intensity required and if low levels of intensity could be used to enhance burning rates while also providing flame stability.

BACKGROUND

Freely propagating planar flames are known to be unstable to large-scale flow-field fluctuations, such that small-amplitude wrinkles that develop in the flame surface will grow and result in acceleration of the flame [6]. This is because the reactant flow speed decreases (increases) along streamlines approaching the flame in regions where the flame surface is convex (concave) toward the reactants, and as the motion of the flame is governed primarily by the local reactant flow speed, the flame will tend to become more wrinkled, as both convex and concave bulges grow in amplitude and variations in the local reactant flow speed increase over time. Acceleration of the flame is a consequence of the resulting increase in flame surface area. This instability associated with coupling between the dynamics of the flame and the incompressible reactant flow was discovered independently by Darrieus [7] and Landau [8].

A planar flame will be unstable to reactant-flow fluctuations and undergo wrinkling and acceleration if the Darrieus-Landau hydrodynamic instability is weaker than any existing stabilizing influences which act to suppress flame wrinkling. Two stabilizing mechanisms are well known, those associated with thermal-diffusive effects and buoyancy [6], and a third mechanism associated with one-dimensional acoustic waves has been recently established [3,9]. Small-wavelength wrinkles are stabilized by thermal-diffusive effects for sufficiently large reactant Lewis numbers, while large-wavelength wrinkles are stabilized by buoyancy for downward flame propagation. Acoustic waves propagating along the axis of flame propagation act similarly to buoyancy-induced gravity waves, by inducing a local oscillating acceleration field which dampens flame wrinkles [10]. Unlike buoyancy, however, the influence of these one-dimensional acoustic waves is expected to be stabilizing even for flames that are not propagating downward and, thus, is independent of the presence of or direction of a gravitational field [10]. The strength of the hydrodynamic instability itself increases with the strength of the reactant mixture, as represented by the amount of heat released per mass of reactants or the value of the planar, laminar flame speed. Therefore, whether flame propagation in a given reactant mixture will be stable or not depends on the strength of the mixture, as determined by the equivalence ratio and the extent of heat loss to the burner walls, as well as the size of the combustor and the presence of a gravitational or acoustic acceleration field.

RESEARCH PLAN

Fig. 1 shows a schematic diagram of the Taylor-Couette (TC) combustor to be used for the experiments. It is a modified version of a TC combustor that has been used in our laboratory to study flame propagation under normal gravity conditions. It will consist of two vertically oriented, concentric cylinders capable of independent rotation in either direction. The inner cylinder will be made of aluminum, with an anodized outer surface, and the outer cylinder made of glass to allow optical access to the annulus gap separating the two cylinders. The annulus gap is sealed at the bottom of the combustor and open to the atmosphere at the top. Reactants are introduced into the annulus through many small holes in the bottom of the inner cylinder and flow upward toward the top of the combustor where the flame is ignited. The flame will be first stabilized in the top section of the combustor by weak straining of the flow, in the region of changing annulus area, while the hydrodynamic instability is suppressed with longitudinal acoustic waves introduced into the annulus by an array of loud speakers above the combustor. In this way, a planar or weakly wrinkled stable flame can be established in the upper section of the combustor before downward propagation through the smaller-area region and development of

the hydrodynamic instability under microgravity conditions occurs. Pre-ignition turbulence intensities will be controlled by counter rotation of the TC cylinders, and the propagation of the flame through the combustor will be measured with a high-speed film or CCD camera. The flame speed will be measured from video records and correlated with levels of pre-ignition turbulence intensity and reactant-mixture properties which determine the strength of the hydrodynamic instability, such as heat released per mass of reactants and reactant Lewis numbers. Experiments will be conducted with and without acoustic-wave suppression of the hydrodynamic instability during propagation in order to evaluate the influence of hydrodynamic coupling.

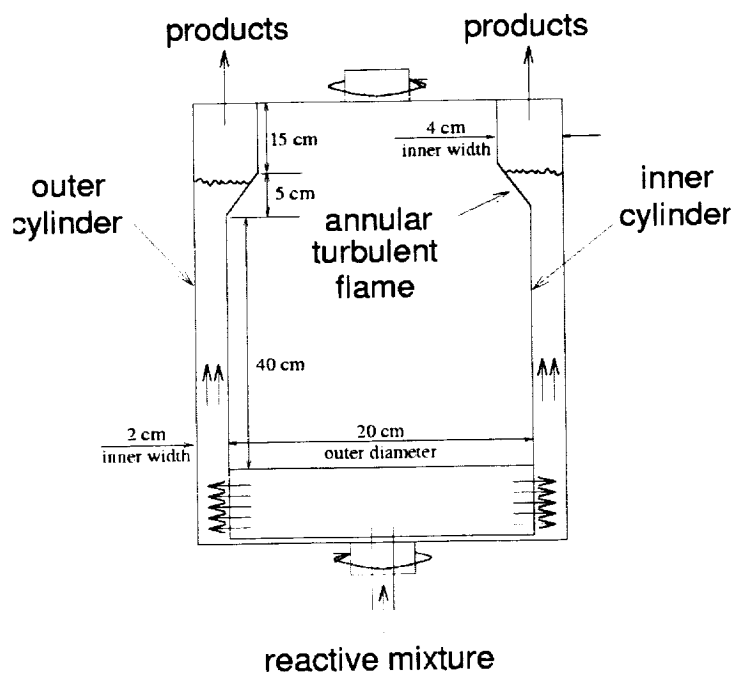


FIG. 1

With the dimensions chosen for the TC combustor, as represented in Fig. 1, the time required for a flame to propagate through the lower section of the combustor will be no longer than about 4 sec for the weakest methane-air and propane-air mixtures to be considered (having burning speeds as low as 10 cm/s), but less than 1 sec for flame propagation in stronger mixtures; stabilization of the flame in the variable-area section of the combustor will be accomplished prior to attaining microgravity conditions. Therefore, many of the experiments can be conducted in the 2.2-sec NASA drop tower, although the 5.18-sec drop tower will be necessary for a few with weak reactant mixtures and no appreciable flame-wrinkling.

REFERENCES

1. Aldredge, R.C., and Williams, F.A., "Influences of Wrinkled Premixed-Flame Dynamics on Large-Scale, Low-Intensity Turbulent Flow," *J. Fluid Mech.* **228**, pp. 487-511 (1991)
2. Pelce, P., and Clavin, P., "Influence of Hydrodynamics and Diffusion upon the Stability Limits of Laminar Premixed Flames," *J. Fluid. Mech.* **124**, pp. 219-237 (1982)
3. Clanet, C., and Searby, G., "First Experimental Study of the Darrieus-Landau Instability," *Phys. Rev. Lett.* **17**, no. 80, pp. 3867-3870 (1998)
4. Clavin, P. and Williams, F. A., "Effects of Molecular Diffusion and of Thermal Expansion on the structure and dynamics of premixed flames in Turbulent flows of large scale and low intensity," *J. Fluid. Mech.* **116**, pp. 251-282 (1982)
5. Kerstein, A. R., and Ashurst, Wm. T., "Propagation Rate of Growing Interfaces in Stirred Fluids," *Phys. Rev. Lett.* **68**, pp. 934-937 (1992)
6. Williams, F.A., *Combustion Theory*, 2nd ed., Addison-Wesley, Reading, MA, 1985, chap. 9
7. Darrieus, G., "Propagation d'un front de flamme," unpublished work presented at the meeting *La Technique Moderne* in France (1938)
8. Landau, L. D., "On the Theory of Slow Combustion," *Acta Physicochimica URSS* **19**, pp. 77-85 (1944)
9. Vaezi, V., and Aldredge, R.C., "Laminar-Flame Instabilities in a Taylor-Couette Combustor," *Comb. & Flame* **121**, pp.356-366 (2000)
10. Searby, G. and Rochwerger, D., "A Parametric Acoustic Instability in Premixed Flames," *J. Fluid Mech.* **231**, pp. 529-543 (1991)

PIV Measurement of Transient 3-D (Liquid and Gas Phases) Flow Structures Created by a Spreading Flame over 1-Propanol

M. I. Hassan, K. Kuwana, and K. Saito

Department of Mechanical Engineering, University of Kentucky
Lexington, Kentucky

ABSTRACT

In the past, we measured three-D flow structure in the liquid and gas phases that were created by a spreading flame over liquid fuels [1]. In that effort, we employed several different techniques including our original laser sheet particle tracking (LSPT) technique, which is capable of measuring transient 2-D flow structures. Recently we obtained a state-of-the-art integrated particle image velocimetry (IPIV), whose function is similar to LSPT, but it has an integrated data recording and processing system. To evaluate the accuracy of our IPIV system, we conducted a series of flame spread tests using the same experimental apparatus that we used in our previous flame spread studies [1] and obtained a series of 2-D flow profiles corresponding to our previous LSPT measurements.

We confirmed that both LSPT and IPIV techniques produced similar data, but IPIV data contains more detailed flow structures than LSPT data. Here we present some of newly obtained IPIV flow structure data, and discuss the role of gravity in the flame-induced flow structures. Note that the application of IPIV to our flame spread problems is not straightforward, and it required several preliminary tests for its accuracy including this IPIV comparison to LSPT.

FLAME-SPREAD EXPERIMENT

We employed a fuel tray whose side-wall is Pyrex (300mm long x 10 mm high x 2mm thick) and bottom is PMMA. To test the effect of tray width on the flow structure, two different tray widths (5 and 20 mm) were used without changing the tray length and height. 1-propanol was placed in the tray just before the experiment and its initial temperature was measured by a 50 μ m-diameter type-K thermocouple that was placed just below the fuel surface. The initial temperature of propanol was changed between 10°C and 20°C in which temperature range, the flame-spread behavior is either uniform or pulsating. To achieve repeatable experimental data, we enclosed the fuel tray with an opaque box of 250 mm wide x 250 mm high x 400 mm long with two transparent PMMA windows for observation and recording.

IPIV FLOW MEASUREMENT

IPIV technique requires seeding for both air and liquid; hollow glass particles (8-12 μ m diameter) for liquid and smoke particles (1-2 μ m) for air were used. Two laser pulses were sequenced to track trajectories of the seeding particles that were distributed in a 2-D laser illuminated plane. Figure 1 shows a schematic of our flame-spread apparatus and IPIV system that were applied to the flow measurement. Using two independent laser sheets, one for the top (x - z) view and the other for the side (x - y) view, a 3-D flow field can be obtained. In this study, however, we only report 2-D flow data in order to compare it with LSPT data.

SOME EXPERIMENTAL RESULTS

Here we report some of our IPIV data. IPIV detected a liquid circulation, which is consistent with our previous LSPT [1] and HI [2] results. We also found that the flame-induced liquid flow structures are quite different between the 5mm wide tray and the 20mm wide tray, supporting previous study's results by NASA [3,4] and our group [1,2].

Figure 2 shows 2-D velocity profiles measured by IPIV for (a) gas and (b) liquid propanol. The initial propanol temperature was 14°C (flame is in pulsating spread region) and the fuel tray width was 20mm. There was an approximately 2mm-diameter re-circulation cell in the gas phase, while in the liquid phase there was a large circulation whose center is located just ahead of the flame leading edge and approximately in 3mm deep. Schiller et al. [4] predicted the existence of the existence of a small gas-phase re-circulation cell. They explain that this re-circulation cell is driven by a combination of buoyancy-driven flow opposed to the flame propagation direction and the flow in the same direction as flame spread induced by thermocapillary-driven motion at the liquid surface. Our IPIV experiment confirmed that this gas-phase cell exists as long as the flame spreads in pulsating mode in the 20-mm fuel tray, but not in the uniform region.

Figure 3 shows 2-D velocity profiles for (a) gas and (b) liquid propanol at its initial propanol temperature 19 °C (flame is in uniform spread region). Again there was no re-circulation cell in the gas phase, but there was a liquid circulation whose diameter was somewhat smaller than the pulsating spread case and center is located behind of the flame leading edge. For the pulsating spread, the relative location of the liquid circulation center to the flame leading edge changes, so the figure 2 (b) is not representative in nature. However, in both cases the liquid circulation always ahead the flame leading edge indicating the flame spread to be driven by the liquid circulation.

In the upstream gas phase near the fuel surface in Fig. 2 (a), airflow is parallel to the fuel surface and is concurrent to the flame spreading direction. The concurrent airflow is likely induced by the liquid circulation (but not by the flame), because the velocity of the concurrent airflow decreased with an increase of the initial propanol temperature. In the uniform spread region, a millimeter-order gas-phase circulation, which was formed just ahead of the flame leading edge was found only for the 5-mm wide tray, but not for the 20-mm wide tray. For the 5mm wide tray, viscose effect may be more dominant than the 20mm wide tray and flow structure is rather 2-D, while for the 20mm wide tray the viscose effect is rather weak and the flow structure is 3-D. The 3-D flow structure in the 20mm wide tray helps to distribute the fluid momentum across the space in front of the flame leading edge.

Both the length (L) and velocity (V) of liquid surface flow were measured from IPIV diagrams and plotted as a function of the initial propanol temperature (Fig. 4). It is interesting to see the subsurface liquid flow to always ahead in the very similar way the flame leading edge for both tray width cases, despite the fact that there is a big difference in gas phase flow structure between both tray width cases. This suggests the flame spread to be controlled by the liquid flow, but not by gas phase heat transfer.

Acknowledgements

This study was partially supported by both Kentucky-NASA EPSCoR program and a special equipment grant from the University of Kentucky.

References

- [1] T. Konishi, G. Tashtoush, A. Ito, A. Narumi and K. Saito, *Proc. The 28th International Symposium on Combustion*, The Combustion Institute. 2000.
- [2] A. Ito, D. Masuda and K. Saito, *Combustion and Flame*, 83: 375-389 (1991).
- [3] F.J. Miller and H. Ross, *Proc. Combust. Inst.* 27: 2715-2722 (1998).
- [4] D.N. Schiller, H. Ross and W.A. Sirignano, *Combust. Sci. Tech.*, 118: 205 (1996).

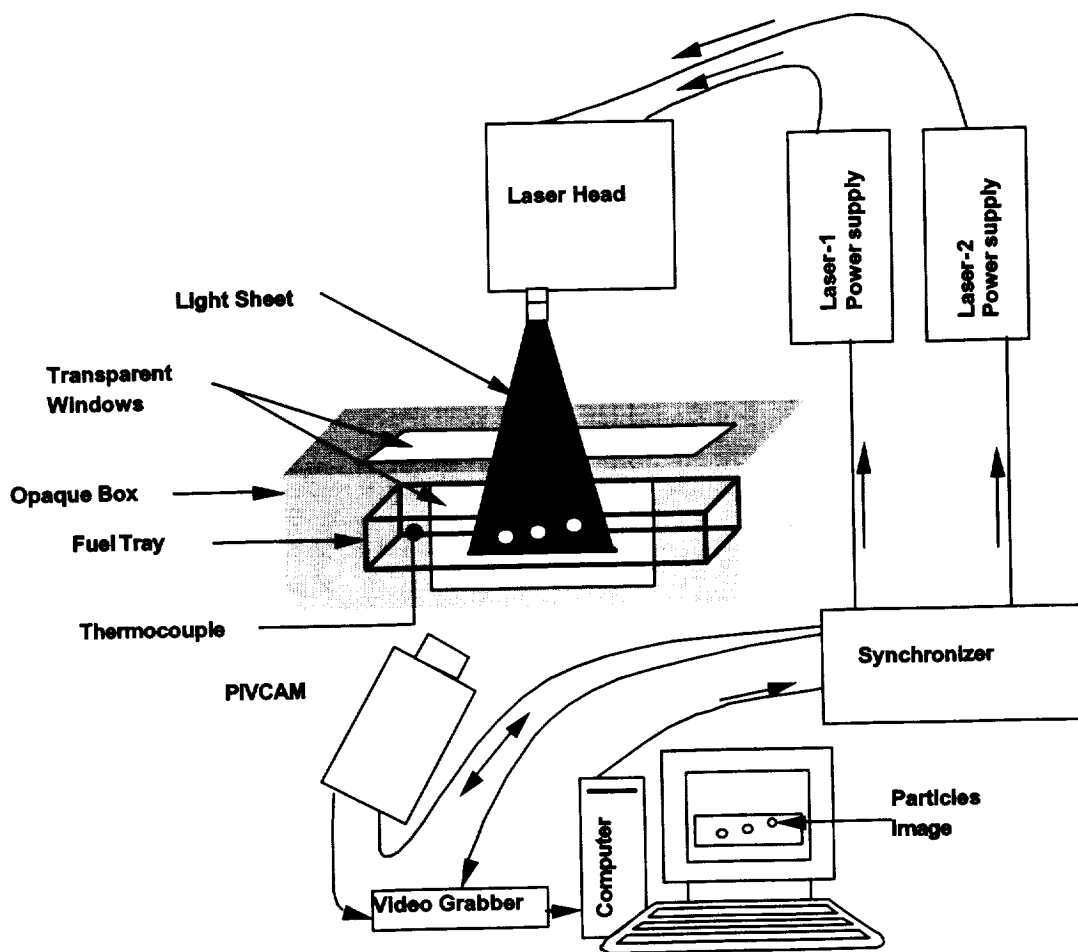


Fig. 1 Flame spread apparatus and an integrated particle image velocimetry.

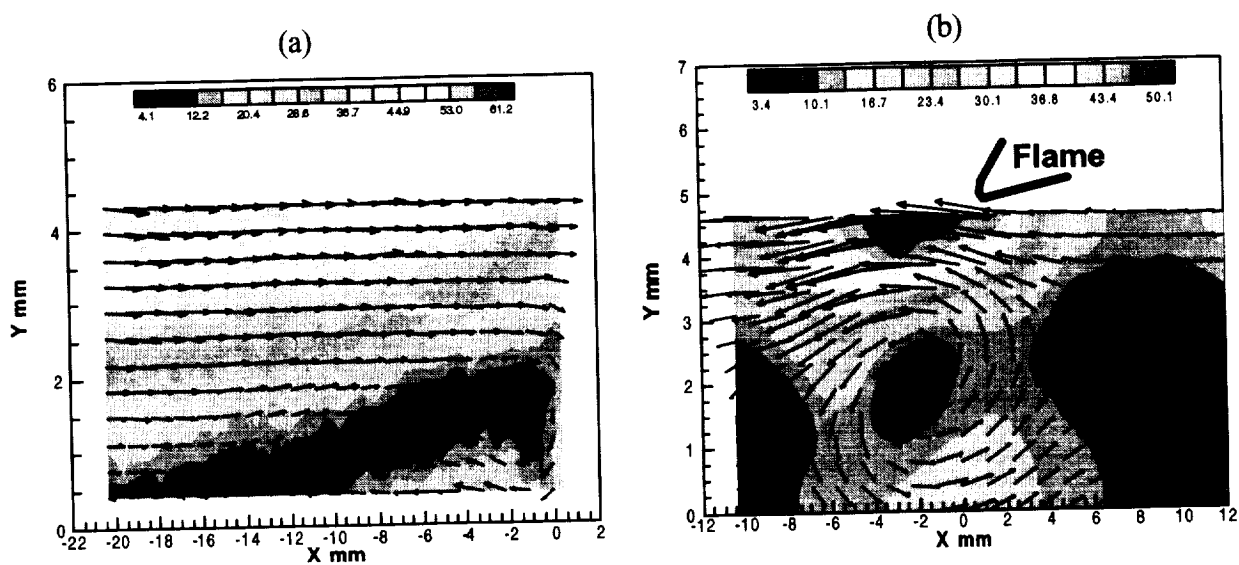


Fig. 2 Two-D velocity profiles for (a) gas and (b) propanol using a 20-mm wide tray. The initial propanol temperature was 14°C.

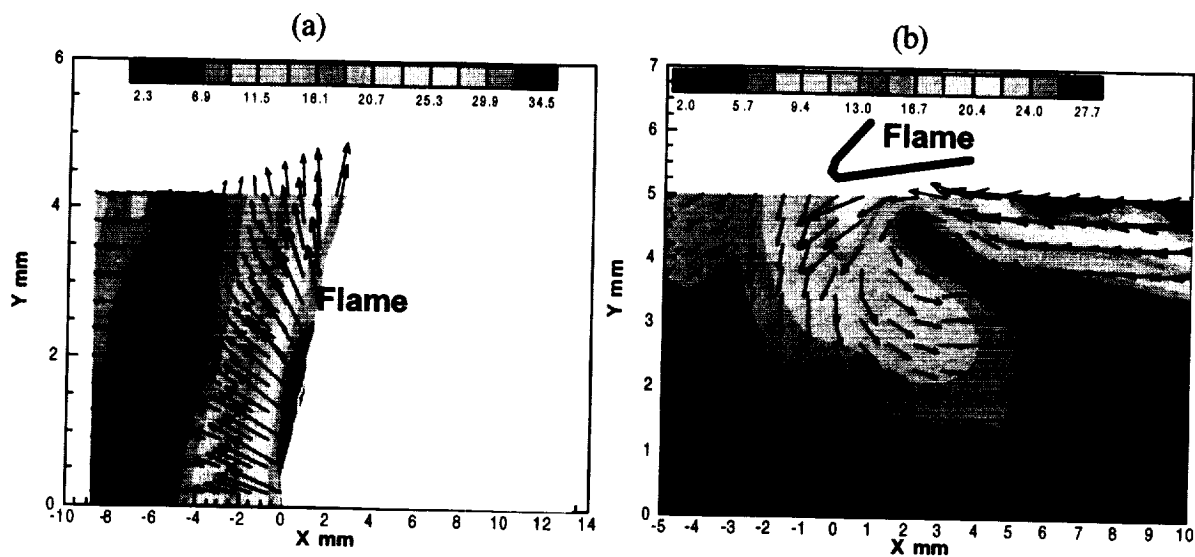


Fig. 3 Two-D velocity profiles for (a) gas and (b) propanol using a 20-mm wide tray. The initial propanol temperature was 19°C.

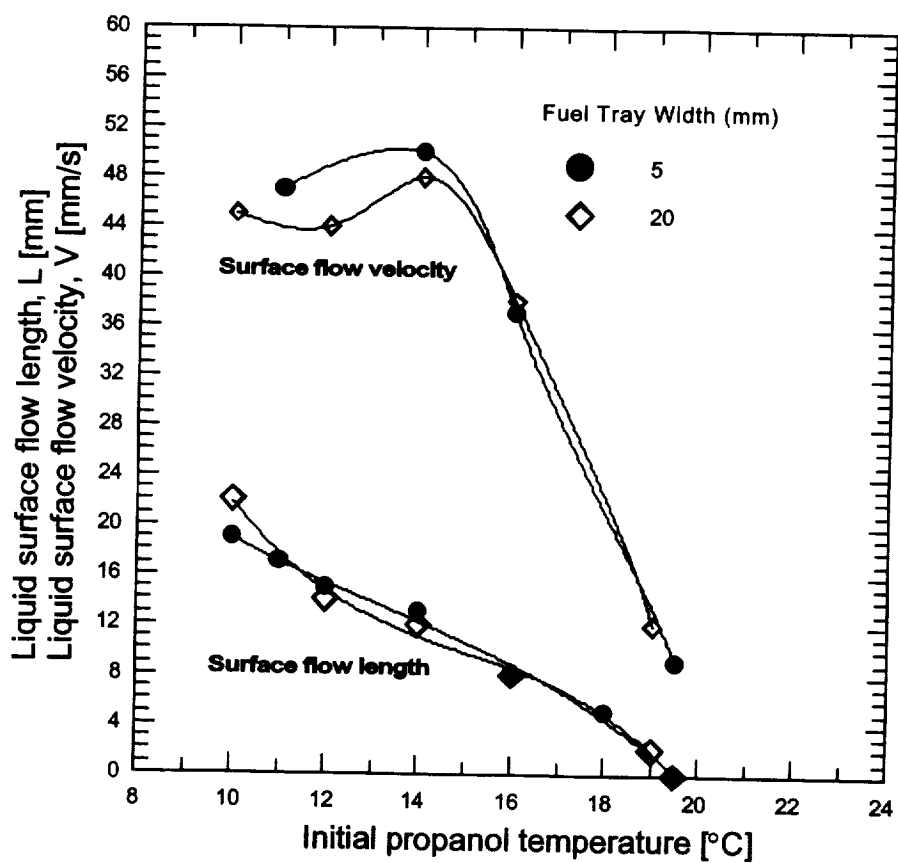


Fig. 4 Liquid surface flow velocity and horizontal distance of liquid surface-flow from a flame leading edge.

Author Index

- Abbud-Madrid, A. 105
 Abbud-Madrid, A. 269
 Abid, M. 309
 Ackerman, M. 237
 Aggarwal, S.K. 317
 Aldredge, R.C. 459
 Alford, J.M. 293
 Allen, M.G. 57
 Ananth, R. 373
 Andac, M.G. 109
 Annen, K.D. 365
 Apfel, R.E. 209
 Arias-Zugasti, M. 265
 Armstrong, J.B. 93
 Atreya, A. 113
 Aung, K. 309
 Avedisian, C.T. 249
 Axelbaum, R.L. 153, 297
 Ayers, R. 273
 Bae, J.H. 249
 Bahadori, M.Y. 129, 149
 Baker, J. 361, 381
 Bar-Ilan, A. 21
 Baum, H.R. 81, 333
 Bedir, H. 9
 Beeson, H. 409
 Bellan, J. 393
 Berhan, S. 113
 Bhattacharjee, S. 405
 Blevins, L.G. 177
 Boxx, I.G. 133
 Branch, M.C. 269
 Buckmaster, J. 341
 Bundy, M. 101
 Cai, J. 5
 Calvert, M.E. 361, 381
 Campbell, C.S. 109
 Cao, G. 285
 Carrea, E. 225
 Castillo, M. 273
 Chang, P. 329
 Chao, B.H. 153, 297
 Chapek, R. 313, 421
 Chauveau, C. 225
 Chelliah, H.K. 213
 Chen, J.-Y. 349
 Chen, L.-D. 165
 Chen, R. 153
 Chen, S.-J. 61, 65
 Cheng, R.K. 121
 Chernovsky, M. 113
 Chiaverini, M.J. 189
 Choi, C.W. 317
 Choi, M.Y. 245
 Christiansen, E.W. 157
 Cincotti, A. 285
 Cleary, T. 401
 Clemens, N.T. 133
 Colver, G.M. 397
 Conant, J.A. 365
 Cordeiro, P. 29
 Crosley, D.R. 69
 Cuenot, B. 25
 Dahm, W.J.A. 61, 65
 Dai, Z. 173
 Daily, J.W. 269
 Datterajan, S. 241
 Davidson, R. 357
 Davis, R.W. 177
 Delisle, A.J. 213
 Dietrich, D.L. 193, 197, 261, 329
 Dimalanta, R. 121
 Dobashi, R. 245
 Dong, Y. 25
 Dreizin, E.L. 217
 Dreyer, C.B. 269
 Driscoll, J.F. 125
 Dryer, F.L. 233, 245
 Dunn-Rankin, D. 181
 Easton, J. 321
 Echekki, T. 349
 Egolfopoulos, F.N. 25, 109
 Eigenbrod, Ch. 353
 El-Leathy, A.M. 169, 325
 Enomoto, H. 205
 Everett, P. 357
 Faeth, G.M. 169, 173, 325, 425
 Feier, I.I. 37

Feikema, D.A.	293	Kaib, N.	237
Ferkul, P.	9, 33	Kailasanath, K.	373, 455
Fernandez, M.G.	177	Kaiser, C.	309
Fernandez-Pello, A.C.	21, 85, 441	Karagozian, A.R.	241
Frate, D.	9	Kashiwagi, T.	17, 81
Frenklach, M.	441	Katta, V.R.	117, 417
Fujita, O.	17	Kazakov, A.	233, 245
Ghenai, C.	241	Kee, R.J.	105
Giesen, A.	49, 53	Keil, D.G.	429
Givi, P.	145	Kennedy, I.M.	137
Gökalp, I.	225	Kleinhenz, J.	9
Gökoğlu, S.	105	Knuth, W.H.	189
Goldshleger, U.	225	Kobayashi, H.	201
Goroshin, S.	221, 397	Kolbe, M.	221
Goswami, K.	77	Kollmann, W.	137
Gramer, D.J.	189	König, J.	49, 53, 353
Grebner, D.	49, 53	Kosály, G.	451
Greenberg, P.S.	45, 121	Kramlich, J.C.	451
Guigné, J.	357	Kufner, E.	353
Gupta, A.K.	377	Kulis, M.	321
Gustafson, R.J.	189	Kumar, A.	9
Haas, J.	409	Kumfer, B.M.	297
Haggard, Jr., J.B.	237	Kuwana, K.	463
Hamins, A.	101	La Mantia, B.	265
Hanson-Parr, D.M.	185	Lau, C.	277
Hassan, M.I.	463	Law, C.K.	157, 305
Hegde, U.	129, 141, 149, 317, 349, 425	Lawrence, W.G.	57
Hermanson, J.C.	141	Lee, J.H.S.	221, 397
Hicks, M.C.	237, 413	Legrand, B.	225
Hoffman, V.K.	217	Lieberman, R.	77
Honda, L.K.	13	Lim, J.	369
Honma, S.	193, 261	Linteris, G.T.	385, 417
Idicheria, C.A.	133	Liu, F.	5
Ikeda, K.	193, 261	Liu, J.-B.	309
Ikegami, M.	193, 261	Liu, S.	153
Ito, K.	17	Liu, S.	389
Iwahashi, T.	201	Lo, T.L.	21
Jaberi, F.A.	145	Lobbia, R.	241
Jagodzinski, J.	41	Locci, A.	285
Jeffries, J.B.	69	Luque, J.	69
Jia, K.	165	Mackowski, D.W.	433
Johannsen, I.	49, 53	Malecki, M.M.	189
Johari, H.	141	Marchese, A.	321
Joseph, R.	369	Margolis, S.B.	337
Joulain, P.	29	Marinelli, W.J.	57
Kadota, T.	205	Mason, G.R.	293

Matalon, M.	161	Rawlins, W.T.	57
Matkowsky, B.J.	281	Rice, E.E.	189
McGrattan, K.B.	81, 101, 333	Riedel, E.P.	105
McKinnon, J.T.	105	Riley, J.J.	451
Medda, E.	285	Ronney, P.D.	13, 309
Mell, W.E.	81, 333, 413	Rosner, D.E.	265
Miller, F.J.	1, 213, 321	Ross, H.D.	1, 85, 321, 329, 413
Modak, A.	269	Rouan, J.P.	225
Moore, E.F.	177	Rozenchan, G.	305
Moore, J.J.	273	Rubstov, V.	77
Mounaim-Rousselle, C.	225	Ruff, G.A.	389
Mukasyan, A.S.	277	Rumminger, M.D.	385
Mulholland, G.	177, 289, 401	Ryan, B.J.	165
Müller, D.	49	Sacksteder, K.R.	9, 37, 113
Munir, Z.A.	447	Saito, K.	361, 381, 463
Murdy, R.S.	217	Sangras, R.	141
Nagaishi, H.	193, 261	Schowengerdt, F.D.	273
Nagashima, T.	141	Scott, J.H.J.	177, 289
Nagata, H.	205	Segawa, D.	205
Nakamura, Y.	81, 333	Shafirovich, E.	225
Nam, S.	89	Sharif, J.	309
Narayanan, V.	369	Shaw, B.D.	253, 257, 447
Nayagam, V.	97, 237, 433	Sheredy, W.	313
Ndubizu, C.C.	373	Shih, H.-Y.	9, 37
Neville, D.	313	Shoshin, Y.L.	217
Niioka, T.	201	Silver, J.A.	61, 65
Nishizawa, K.	17	Sirignano, W.A.	5
Obata, S.	141	Sivathanu, Y.	289, 369
Oerther, J.	33	Smith, G.P.	69
Ohaska, K.	393	Smith, O.I.	241
Olson, S.	345	Smooke, M.D.	185
Olson, S.L.	17, 81, 93, 409	Son, Y.	13
Oravec-Simpkins, L.	345	Spedding, G.	25
Orru, R.	285	St. Clair, C.P.	189
Park, W.C.	101	Steel, E.B.	177
Parr, T.P.	185	Stocker, D.P.	129, 141, 149
Patnaik, G.	373, 455	Struk, P.M.	193, 261
Pearlman, H.	313, 421	Sun, Z.	297
Perry, D.	321	Sunderland, P.B.	45, 153, 433
Peterson, K.A.	73	Sung, C.J.	437
Pettegrew, R.	9, 33, 413	T'ien, J.S.	9, 37, 93, 329
Pilgrim, J.S.	73	Takahashi, F.	117, 417
Piltch, N.D.	9, 77, 61, 65	Takahashi, S.	405
Poinsot, T.	25	Takeshita, Y.	261
Puri, I.K.	101, 317	Tatem, P.A.	373
Rath, H.J.	353	Tewarson, A.	89

Ticich, T.M.	301	Wernet, M.P.	45, 121
Torero, J.L.	29, 85	Whitbeck, M.	89
Tornabene, R.	313	Wichman, I.S.	345
Triebel, W.	49, 53	Williams, F.A.	97, 197, 229, 237
Tse, S.D.	157, 305	Wood, W.R.	61
Urban, B.D.	233	Wu, M.-S.	313
Urban, D.L.	21, 45, 153, 385, 401, 413	Xu, F.	169, 173, 325
Usowicz, J.E.	141	Xu, G.	261
Vander Wal, R.L.	65, 137, 301, 361, 381, 443	Yang, J.C.	289, 401
Varghese, P.L.	41	Yang, W.	105
Varma, A.	277	Yanis, W.	45
Venuturumilli, R.	165	Yetter, R.A.	185
Voevodkin, G.	77	Yoo, W.S.	157
Wakai, K.	405	Yozgatligil, A.	245
Walther, D.C.	21, 85	Yuan, Z.-G.	129, 401, 425
Wang, H.	437	Zhang, X.	273
Wang, Y.	377	Zheng, Y.	209
Weiland, K.J.	365	Zhou, Y.Y.	85
Weinberg, F.J.	181	Zhu, D.L.	305

REPORT DOCUMENTATION PAGE			Form Approved OMB No. 0704-0188	
Public reporting burden for this collection of information is estimated to average 1 hour per response, including the time for reviewing instructions, searching existing data sources, gathering and maintaining the data needed, and completing and reviewing the collection of information. Send comments regarding this burden estimate or any other aspect of this collection of information, including suggestions for reducing this burden, to Washington Headquarters Services, Directorate for Information Operations and Reports, 1215 Jefferson Davis Highway, Suite 1204, Arlington, VA 22202-4302, and to the Office of Management and Budget, Paperwork Reduction Project (0704-0188), Washington, DC 20503.				
1. AGENCY USE ONLY (Leave blank)		2. REPORT DATE May 2001		3. REPORT TYPE AND DATES COVERED Conference Publication
4. TITLE AND SUBTITLE Sixth International Microgravity Combustion Workshop			5. FUNDING NUMBERS WU-101-52-00-00 NCC-544	
6. AUTHOR(S) Kurt Sacksteder, Compiler				
7. PERFORMING ORGANIZATION NAME(S) AND ADDRESS(ES) National Aeronautics and Space Administration John H. Glenn Research Center at Lewis Field Cleveland, Ohio 44135-3191			8. PERFORMING ORGANIZATION REPORT NUMBER E-12750	
9. SPONSORING/MONITORING AGENCY NAME(S) AND ADDRESS(ES) National Aeronautics and Space Administration Washington, DC 20546-0001			10. SPONSORING/MONITORING AGENCY REPORT NUMBER NASA CP-2001-210826	
11. SUPPLEMENTARY NOTES Responsible person, Jack Salzman, organization code 6700, 216-433-2868.				
12a. DISTRIBUTION/AVAILABILITY STATEMENT Unclassified - Unlimited Subject Category: 29 Available electronically at http://gltrs.grc.nasa.gov/GLTRS This publication is available from the NASA Center for AeroSpace Information, 301-621-0390.			12b. DISTRIBUTION CODE	
13. ABSTRACT (Maximum 200 words) This conference proceedings document is a compilation of papers presented orally or as poster displays to the Sixth International Microgravity Combustion Workshop held in Cleveland, Ohio on May 22-24, 2001. The purpose of the workshop is to present and exchange research results from theoretical and experimental work in combustion science using the reduced-gravity environment as a research tool. The results are contributed by researchers funded by NASA throughout the United States at universities, industry and government research agencies, and by researchers from international partner countries that are also participating in the microgravity combustion science research discipline. These research results are intended for use by public and private sector organizations for academic purposes, for the development of technologies needed for Human Exploration and Development of Space, and to improve Earth-bound combustion and fire-safety related technologies.				
14. SUBJECT TERMS Microgravity; Combustion; Fires; Flammability			15. NUMBER OF PAGES 487	
			16. PRICE CODE	
17. SECURITY CLASSIFICATION OF REPORT Unclassified	18. SECURITY CLASSIFICATION OF THIS PAGE Unclassified	19. SECURITY CLASSIFICATION OF ABSTRACT Unclassified	20. LIMITATION OF ABSTRACT	